

# BULGARIAN CHEMICAL COMMUNICATIONS

2015 Volume 47 / Number 3

*Journal of the Chemical Institutes  
of the Bulgarian Academy of Sciences  
and of the Union of Chemists in Bulgaria*



## In Memoriam

### **Academician Panayot R. Bontchev**

(31.12.1933–11.04.2015)



Panayot R. Bontchev was born on 31.12.1933 in Burgas, Bulgaria. He graduated with excellent scores at the University of Sofia in 1956 and defended his scientific degrees obtained in 1965 (PhD) and 1975 (DSc). For over 46 years P. R. Bontchev has been affiliated to the Department of Analytical Chemistry of the “St. Kliment Ohridski” University of Sofia: Assistant Professor (1956), Associate Professor (1969) and Full Professor of Analytical Chemistry (1979–2002). Professor Bontchev was elected a Corresponding Member of the Bulgarian Academy of Sciences (BAS) (1995–2003) and Academician of BAS (since 2003); he is also Fellow of the Bulgarian National Academy of Medicine (since 1995). Prof. Bontchev has established and lectured several University courses for graduate students: Coordination in Analytical Chemistry (1965–1980), Analytical Chemistry (1970–2004), Biocoordination (Bioinorganic) Chemistry (1978–2002), Structure and Reactivity of Chemical Compounds (1985). His textbook “*Introduction to Analytical Chemistry*” (three editions in 1972, 1979, 1985) and a Russian translation in 1978, has been widely consulted for over four decades. Prof. Bontchev also lectured in two other Bulgarian Universities: in “Episkop Konstantin Preslavski” University of Shumen (1972–1987) and South-West University in Blagoevgrad (1988–2001). After his retirement from the “St. Kliment Ohridski” University of Sofia (2002) he was a Visiting Professor at the Institute of General and Inorganic Chemistry of Bulgarian Academy of Sciences (1978–2002) and the “Academician Angel Balevski” Institute of Metal Science of BAS (2003).

Professor Bontchev is widely known for his research in the field of analytical, coordination and bio-coordination chemistry: catalytic methods of analytical chemistry (1959–1980), complexation and catalytic activity in homogenous catalysis (1962–1980), coordination chemistry of Cr(V) (1970–1986), analytical determination of antibiotics (1975–1985), coordination chemistry of Pt and Pd (1980–), metal complexes of bioligands in biology and medicine (1980–). He has published over 200 scientific articles in Bulgarian, Russian and international journals, three monographs and has co-authored four specialized books. His monograph “*Complexation and Catalytic Activity*” (1972) has also been translated in Russian (1975). He is a holder of 11 Authors’ Certificates and patents. Professor Bontchev has been lecturing in 21 universities abroad, being a Honorary Ostwald Professor at the University of Leipzig, Germany (1981). He has participated in 90 scientific conferences with 24 plenary and 17 keynote lectures, over 50 oral presentations and posters. His publications have been widely cited in over 2000 relevant texts in the world’s scientific literature, among them in over 15 prestigious textbooks in analytical chemistry such as Charlot (France), Laitinen and Harris (USA), Sandell and Onishi (USA), Christian and O’Reilly (USA), Wilson and Wilson (USA), Zolotov (Russia), Bussev (Russia), Kreingold & Bozhevov (Russia), Vassilev (Russia), “*Analyticum*” (Germany) etc.

A scientific school on catalytic analysis has been established in Bulgaria in the beginning of the career of P.R. Bontchev. It has been recognized as one of the world’s leading schools in this field, resulting in six PhD and 2 DSc theses and two professorships. These studies have been acknowledged at a later stage in the monographs on catalymetry by Yatsimirskii (Moscow), M. Peres-Bendito and Valcarcel (Spain), D. Peres-Bendito and Silva (UK), H. Mueller, M. Otto and G. Werner (Germany), etc.

A well-known Bulgarian school in coordination and bio-coordination chemistry has been established by Prof. Bontchev, resulting in nine PhD and one DSc theses, and numerous papers in international journals. These results have been cited in the textbooks on inorganic and coordination chemistry: Cotton and Wilkinson (USA), Peterson

(USA), M. Tobi (UK), Horvath and Stickenson (USA), Kryukov, Kutchmii and Dilung (Kiev); in “*Comprehensive Coordination Chemistry*” (Wilkinson, Ed.), “*Encyclopedia of Inorganic Chemistry*” (Bruce-King, Ed.), “*Structure and Chemical Bonds*” (Germany), “*Toxicity of Inorganic Compounds*” (USA) etc. On the basis of Prof. Bontchev’s research have been initiated studies by scientists in Germany, UK, Japan, USSR, Poland, Greece, India, France, etc.

The administrative and organizational activity of Prof. Bontchev is well known: he has been Vice-Dean of the Faculty of Chemistry (1976–1979), Vice-Rector of the University of Sofia (1989–1991 and 1995–1999), Head of the Department of Analytical Chemistry (1991–1999); Chairman of the Specialized Council for Conferment of PhD and DSc in Inorganic and Analytical Chemistry in Bulgaria (1991–1995, 2001–2004); President of the Chemistry Commission of the Bulgarian Supreme Certification Committee (1995–2000); Member and Vice-President of the Chemistry Commission of the National Research Foundation (1990–1995); Member of the National UNESCO Commission (1990–) and National IUPAC Committee (1990);

Member of the International Organizing Committee for the International Conferences of Coordination Chemistry (ICCC) (1970–2001); Director of the American-European Alliance “Universities for Democracy” (1990–2001). Prof. Bontchev has been a Member of the Editorial Board of “*Talanta*” (1979–1992) and “*Chimika Chronika – Newseries*” (1992). He has been decorated with numerous national and international medals and awards.

Complete bibliography and bibliographic data for Prof. P. R. Bontchev have been published elsewhere (*Ann. Univ. de Sofia, Fac. Chimie*, **97** (2), 17–30 (2005) <<http://www.chem.uni-sofia.bg/annual/>>; In: “*Almanac of Analytical Chemistry in Bulgaria*”, G. Naydenov (Ed.), Europress, Plovdiv, 2006, pp. 67–71, ISBN 978-954-9357-10-3).

Academician Panayot R. Bontchev passed away at the age of 81 on April 11th, 2015 in Sofia. He will be remembered as a dearest teacher of many hundreds of students and post graduates and a prominent scientist in the field of chemistry.

D. L. Tsalev

## Labeling, quality control and biological evaluation of $^{99m}\text{Tc}$ -vibramycin for infection sites imaging

S. Hina<sup>1\*</sup>, M. I. Rajoka<sup>1</sup>, P. B. Savage<sup>2</sup>, S. Roohi<sup>3</sup>, T. H. Bokhari<sup>4</sup>,

<sup>1</sup>Department of Bioinformatics and Biotechnology, Government College University, Faisalabad, Pakistan

<sup>2</sup>Department of Chemistry and Biochemistry, Brigham Young University, C100, BNSN Provo, UT, 84602, USA

<sup>3</sup>Quality Control Labs, IPD, Pakistan Institute of Nuclear Science and Technology, P.O. Nilore, Islamabad, Pakistan

<sup>4</sup>Department of Chemistry, Government College University, Faisalabad, Pakistan

Received June 11, 2014, Revised November 15, 2014

The use of radiolabeled antibiotics as diagnostic agents is an emerging area of medical research. Vibramycin is a semisynthetic antibiotic of the tetracycline family prescribed to treat a variety of infections. We present in this study a new technetium-99m labeled vibramycin radiopharmaceutical using  $\text{SnCl}_2 \cdot 2\text{H}_2\text{O}$  as a reducing agent. The stability of  $^{99m}\text{Tc}$ -vibramycin was evaluated in human serum at 37 °C. Biodistribution studies of  $^{99m}\text{Tc}$ -vibramycin were performed on a model of bacterially infected Sprague-Dawley rats. *In vitro* studies were performed to determine the binding interaction of the labeled antibiotic with bacteria and its stability. Scintigraphic study was done with a  $\gamma$ -camera 1 h, 4 h and 24 h after radiotracer injection in rats having infectious intramuscular lesions. It was confirmed through this study that  $^{99m}\text{Tc}$ -vibramycin possesses high radiolabeling yield (95%) as determined by instant thin-layer chromatography. The binding assay shows good binding with *S. aureus*. Scintigraphy in rabbits showed uptake of  $^{99m}\text{Tc}$ -vibramycin in the infectious lesions 1 h, 4 h and 24 h after injection. Biodistribution studies of  $^{99m}\text{Tc}$ -vibramycin revealed that the radiopharmaceutical accumulated significantly at the infection sites and showed the renal route of excretion. Target-to-non target ratios for  $^{99m}\text{Tc}$ -vibramycin for the infectious lesion and the control muscle were found to be significantly different. The study demonstrated that  $^{99m}\text{Tc}$ -vibramycin shows preferential binding to living bacteria. The biological activity (*in vitro*) of  $^{99m}\text{Tc}$ -vibramycin was studied using the optimized parameters and the  $^{99m}\text{Tc}$ -vibramycin was found to be a good infection imaging agent.

**Key Words:**  $^{99m}\text{Tc}$ -vibramycin; biodistribution; *Staphylococcus aureus*; infection imaging; ascorbic acid; scintigraphy.

### INTRODUCTION

Infection is well-defined as an injury caused by bacteria, viruses, fungi and parasites leading to trauma, ischemia, and neoplasm. Signs and symptoms such as fever, swelling and pain may also appear and the diagnosis is regularly based on clinical, pathological and microbiological results. Due to lack of specificity, the diagnosis of infection is a major challenge in clinical practices. In molecular biology, immunology and medical biotechnology various approaches offer new insights for infection and inflammation imaging. Morphologic imaging and functional imaging tests are used for infection diagnosis. Morphologic imaging tests rely on structural abnormalities of tissues as a result of combination of microbial invasion and inflammatory reaction of the host such as ultrasonography, magnetic resonance imaging (MRI) and computed tomography (CT). Functional imaging studies use small quantities of radioactive material that is taken up by body cells, tissues, and

organs directly, or attaches to other substances and migrates to the site of infection. Nuclear medicinal techniques can be used for *in vivo* characterization of cellular structure, function and biological changes at molecular level on infection associated tissues [1]. Radiopharmaceuticals are unique medicinal preparations comprising a radionuclide and a nonradioactive part and are designed to interact with a biological pathway, or target molecule in the body. Radiopharmaceuticals labeled with technetium-99m are used for medical imaging due to its superior properties of labeling and availability. Technetium-99m is normally eluted from a commercially available  $^{99}\text{Mo}/^{99m}\text{Tc}$  generator system and is available at all radiopharmacy centers. Nuclear medical imaging techniques require radionuclides which decay with single photon emission and  $^{99m}\text{Tc}$  is the radioisotope universally used in nuclear medical centers for gamma imaging [2]. Various technetium-99m biomolecules, such as cytokines, chemotactic peptides [3], monoclonal and polyclonal immunoglobulins, human defensin [4-6] and antibiotics [7] have been introduced for

\* To whom all correspondence should be sent:  
E-mail: sairahina@yahoo.com

infection imaging. Radiolabeled antibiotics are an accurate tool for detection of infectious diseases, because they precisely bind to the bacterial machineries making possible the discrimination of bacterial infection and sterile inflammation [8],  $^{99m}\text{Tc}$  labeled antibiotics such as  $^{99m}\text{Tc}$ -ceflizoxime [9],  $^{99m}\text{Tc}$ -cefuroxime and  $^{99m}\text{Tc}$ -sitaflloxacin kit [10],  $^{99m}\text{Tc}$ -ciprofloxacin [11,12],  $^{99m}\text{Tc}$ -dextran [13],  $^{99m}\text{Tc}$ -enrofloxacin [14],  $^{99m}\text{Tc}$ -ethambutol [15],  $^{99m}\text{Tc}$ -erythromycin [16],  $^{99m}\text{Tc}$ -flucanazole [17],  $^{99m}\text{Tc}$ -infecton [18],  $^{99m}\text{Tc}$ -kanamycin [19],  $^{99m}\text{Tc}$ -lomefloxacin,  $^{99m}\text{Tc}$ -ofloxacin complexes [20],  $^{99m}\text{Tc}$ -pefloxacin [21],  $^{99m}\text{Tc}$ -piroxicam [22],  $^{99m}\text{Tc}$ -tetrofosmin [23], and  $^{99m}\text{Tc}$ -vancomycin [24] have been developed for imaging purposes and some of them are routinely employed in diagnostic nuclear medical centers [25,26]. Vibramycin is a wide-spectrum antibiotic of the family of tetracycline synthesized from oxytetracycline that controls the ability of bacteria to produce proteins crucial to them. Vibramycin has pronounced activity against a broad range of gram-positive and gram-negative organisms. Vibramycin is used to treat infections of the urinary tract, genitals, lungs, or eyes caused by infecting bacteria [27].

The present work aims at labeling vibramycin with technetium-99m, characterization, quality control, biodistribution and scintigraphic studies of  $^{99m}\text{Tc}$ -vibramycin for infection sites diagnosis.

## EXPERIMENTAL

Vibramycin for intravenous injection was obtained from Ameer Medical and Superstores, Islamabad, Pakistan.  $\text{Na}^{99m}\text{TcO}_4$  was eluted from a locally produced fission based PAKGEN  $^{99}\text{Mo}/^{99m}\text{Tc}$  generator, with 0.9% saline. All other reagents used were of analytical grade and acquired from E. Merck, Germany. *Staphylococcus aureus* was obtained from the National Institute of Health, Islamabad. All animal experiments were performed following the principles of laboratory animal care and were approved by the Institutional Animal Ethics committee. Three animals (rabbits and rats) were used for each set of experiments for biodistribution and scintigraphy. The animals were kept under standard conditions with free access to food and water. Tissue and organ radioactivity was measured with a  $\gamma$ -counter (Ludlum model-261). Gamma scintillation camera (Capintec Caprac-R1) was used for imaging of experimental animals.

### *Labeling of vibramycin with technetium-99m*

Vibramycin (0.2 mg) was directly labeled with  $^{99m}\text{Tc}$ . Optional amount of 2-4  $\mu\text{g}$  of  $\text{SnCl}_2 \cdot 2\text{H}_2\text{O}$

was used as a reducing agent (pH 3). Ascorbic acid (4 mg) was used as a stabilizer in the mixture. After addition of all reagents  $\sim 370 \text{ MBq } ^{99m}\text{TcO}_4^-$  in saline was injected into the vial at room temperature.

### *Determining labeling efficiency by ITLC analysis*

Stability and labeling yield of  $^{99m}\text{Tc}$ -vibramycin was done by instant thin-layer chromatography. One  $\mu\text{L}$  sample of the preparation was spotted on ITLC strips (Gelman Laboratories) using 0.5M NaOH as the mobile phase. In this system,  $^{99m}\text{Tc}$ -vibramycin migrated with the solvent front of the mobile phase ( $R_f = 1.0$ ) and the colloid was found at the origin of the strip ( $R_f = 0$ ). To determine the pertechnetate content of the preparations, a strip of Whatman Paper No. 3 was developed using acetone as the mobile phase. In this system, pertechnetate migrated with the solvent front of the mobile phase ( $R_f = 1.0$ ).

### *Electrophoresis*

Electrophoresis of the prepared  $^{99m}\text{Tc}$ -vibramycin was done on Whatman No. 1 paper in phosphate buffer (pH 6.8) in a deluxe electrophoresis chamber (Gelman) system. Whatman No. 1 paper of 30 cm was marked as L at the left side of the strip and R at the right side of the strip. A drop of  $^{99m}\text{Tc}$ -vibramycin was applied to the middle of the strip which was put in the midpoint of the electrophoresis chamber having buffer in such a way that the left side was dipped at anode and right side at cathode. The electrophoresis was run for 60 to 90 min at a voltage of 300V. After completion of electrophoresis, the strip was scanned by using  $2\pi$  scanner to identify the charge on vibramycin.

### *Stability of $^{99m}\text{Tc}$ -vibramycin in human serum*

The stability of  $^{99m}\text{Tc}$ -vibramycin was checked in human serum at 37 °C. Normal human serum (1.8 mL) was mixed with 0.2 mL of  $^{99m}\text{Tc}$ -vibramycin and incubated for 30 min. Aliquots of 0.2 mL were withdrawn during the incubation at different time intervals up to 24 h and subjected to ITLC analysis for the determination of  $^{99m}\text{Tc}$ -vibramycin, reduced/hydrolyzed  $^{99m}\text{Tc}$  and free  $^{99m}\text{TcO}_4^-$ . The increase in the amount of free pertechnetate indicated the degree of degradation.

### *Bacterial strains*

Bacterial strain of *Staphylococcus aureus* is frequently used in different microbiology labs. It was obtained from the American Type Culture Collection. Overnight cultures of the strain were

prepared in brain heart infusion broth (BHI, Oxoid) at 37 °C in a shaking water bath. Aliquots of suspensions containing the viable stationary phase bacteria were rapidly frozen in liquid nitrogen and stored at -70 °C. Before use, an aliquot of this suspension was immediately thawed in a water bath at 37 °C and diluted with sodium phosphate buffer.

#### *Bacterial binding assay*

Bacterial binding of Tc-99m-vibramycin was assessed using *S. aureus*. Sodium phosphate buffer (0.1 mL) containing ~5MBq of <sup>99m</sup>Tc-vibramycin was transferred to a test tube. A known volume (0.8 mL) of acetic acid (0.01M) in Na-PB containing around  $1 \times 10^8$  viable bacteria was added to the above tube. The mixture was incubated at 4 °C for 1 h and centrifuged for 10 min. The supernatant was removed and the bacterial pellet was gently resuspended in 1 mL of ice cooled Na-PB and recentrifuged. The supernatant was removed and the radioactivity in the bacterial pellet and the supernatant was measured by gamma-counter. The radioactivity related to bacteria was expressed in percent of the added <sup>99m</sup>Tc activity to viable bacteria with respect to total <sup>99m</sup>Tc activity. For comparison purposes binding of <sup>99m</sup>Tc-ascorbic acid to bacteria was also performed. Ascorbic acid (1 mg) was dissolved in 1 mL of pure water, the pH adjusted to 5 with 0.1 M NH<sub>4</sub>OH solution, and then 0.2 mL of SnCl<sub>2</sub>·H<sub>2</sub>O (1 mg/1 mL 0.1 M HCl) and 0.5 mL of Na<sup>99m</sup>TcO<sub>4</sub> (100 MBq) in saline were added to the vial. The reaction vial was left at 25°C for 20 min. The radiochemical purity of the labeled compound was checked with TLC [28].

#### *Induction of infection with live S.aureus*

A single clinical isolation of *S.aureus* from biological samples was used to produce focal infection. Individual colonies were further diluted to obtain a turbid suspension containing  $2 \times 10^8$  colony-forming units (cfu) of *S. aureus* in 0.2 mL of saline and were intramuscularly injected into the left thigh of rats [29, 30]. Then, the rats were left for 24 h to get a visible swelling in the infected thigh. Three rats were used for one set of experiments.

#### *Induction of non-infected inflammation with heat killed S.aureus*

*Staphylococcus aureus* suspension was heated at 100°C for 2 h to obtain killed *S. aureus*. Sterile inflammation was induced by injecting 0.2 mL of heat killed *S.aureus*, intramuscularly in the left thigh muscle of the rats. Two days later, swelling appeared.

#### *Induction of non-infected inflammation with irradiated S. aureus*

*Staphylococcus aureus* (1 mL suspension) containing about  $2 \times 10^8$  colony-forming units (cfu) was gamma irradiated with a 3 KGy dose to get irradiated *S. aureus*. The non-viability of bacteria was tested by cultivating them in different media and 0.2 mL suspension were injected intramuscularly in the left thigh of rats.

#### *Induction of inflammation with turpentine oil*

Sterile inflammation was induced intramuscularly by injecting 0.2 mL of turpentine oil [31] in the left thigh muscle of the rats. After two days the swelling appeared.

#### *Biodistribution studies in animal models*

The animals were intravenously injected with 0.2 mL of <sup>99m</sup>Tc-vibramycin (~38 MBq) via the tail vein. After a definite time, the rats were sacrificed at 1, 4 and 24-h post-injection after ether anesthesia and biodistribution study was done. Blood (1 mL) was taken by cardiac puncture and activity in total blood was calculated by assuming blood volume equal to 6.34% of body weight. Samples of weighed infected muscle, normal muscle, liver, spleen, kidney, stomach, intestine, heart, brain, bladder and lungs were taken and activity was measured by the use of a gamma counter. The results were expressed as the percent uptake of injected dose per organ. The results of the bacterial uptake of <sup>99m</sup>Tc-vibramycin and other compounds were analyzed by analysis of variance setting the level of significance at 0.05.

#### *Induction of experimental infection in rabbit*

Saline (0.6 mL) containing viable *S. aureus* ( $4 \times 10^8$  cfu) was injected into the left thigh muscle of each rabbit. After 72 h when significant swelling appeared at the site of injection, scintigraphy was done.

#### *<sup>99m</sup>Tc-vibramycin scintigraphy*

The model animal in triplicate was placed on a flat hard surface with both hind legs spread out and was fixed with the help of a surgical tape. Diazepam (5 mg) was injected into the right thigh muscle. Saline (0.2 mL) containing 15 MBq of <sup>99m</sup>Tc-vibramycin was then injected intravenously into the marginal ear vein. A single headed Siemens Integrated ORBITER Gamma Camera System interfaced with high-resolution parallel hole collimator and an on-line dedicated computer was used for imaging. Immediately after injection, dynamic acquisition with both thighs in focus was

done for 120 min. For the biodistribution study of the radiotracer, whole body acquisition was done at 1, 4 and 24 h after injection.

## RESULTS AND DISCUSSION

Vibramycin (Fig. 1) was labeled with technetium-99m and labeling efficiency of 95 % was achieved (Fig. 2, 3). The effect of pH is shown in Fig. 4. At pH 2 the minimum labeling efficiency was achieved (80%), while at pH 3-4 the labeling efficiency of  $^{99m}\text{Tc}$ -vibramycin increased to > 95%. In basic media (pH 8) the labeling efficiency decreased to 68%. A known quantity of 2-3  $\mu\text{g}$  of reducing agent,  $\text{SnCl}_2 \cdot 2\text{H}_2\text{O}$  gave the highest labeling efficiency, and thus the value of 2.5  $\mu\text{g}$  of  $\text{SnCl}_2 \cdot 2\text{H}_2\text{O}$  was chosen for further procedures (Fig. 5). The highest labeling efficiency was achieved at 200  $\mu\text{g}$  of ligand (Fig. 6). The complexation of  $^{99m}\text{Tc}$  with vibramycin was achieved after about 30 min and retained for up to 12 h (Fig. 7).

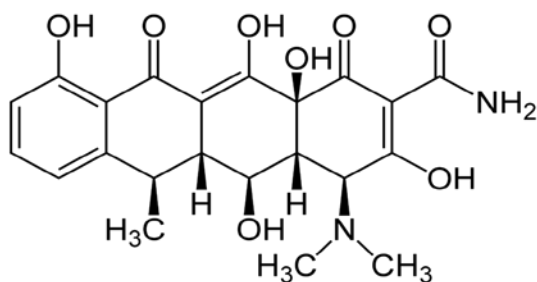


Fig. 1. Structure of vibramycin

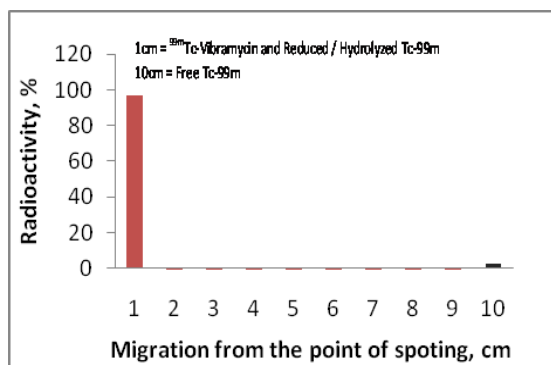


Fig.2. Paper chromatography pattern of the  $^{99m}\text{Tc}$ -vibramycin, free, reduced/hydrolyzed  $^{99m}\text{Tc}$ .

The radiochemical purity was assessed by a combination of ascending paper chromatography and instant thin-layer chromatography on silica gel. In paper chromatography acetone was used as solvent for free  $^{99m}\text{TcO}_4^-$  while in ITLC-SG 0.5M NaOH was the solvent used for  $^{99m}\text{Tc}$ -vibramycin and reduced/hydrolyzed  $^{99m}\text{Tc}$ . By following the above mentioned procedures the results were in excellent agreement. In this study, vibramycin was labeled with  $^{99m}\text{Tc}$  with high radiochemical yields. During the labeling of vibramycin <2% colloid and <2% free pertechnetate were observed.

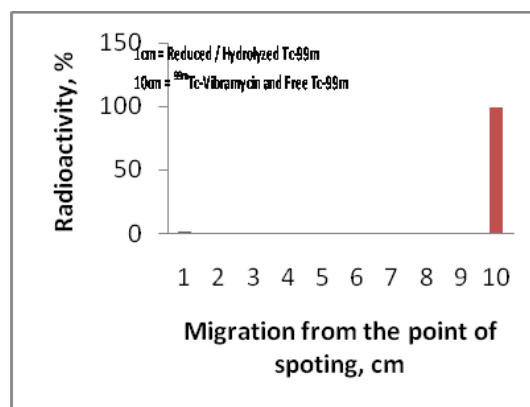


Fig.3. ITLC-SG pattern of the  $^{99m}\text{Tc}$ -vibramycin, free, reduced/hydrolyzed  $^{99m}\text{Tc}$ .

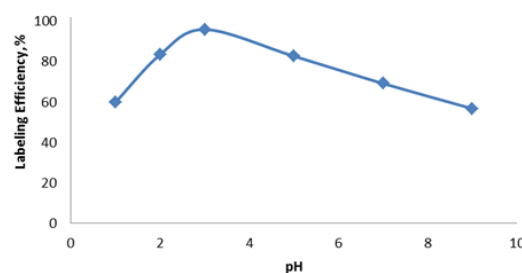


Fig.4. Effect of pH on the labeling efficiency of  $^{99m}\text{Tc}$ -vibramycin

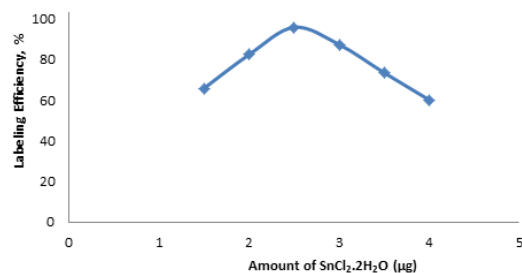


Fig.5. Effect of amount of stannous chloride dihydrate on the labeling efficiency of  $^{99m}\text{Tc}$ -vibramycin

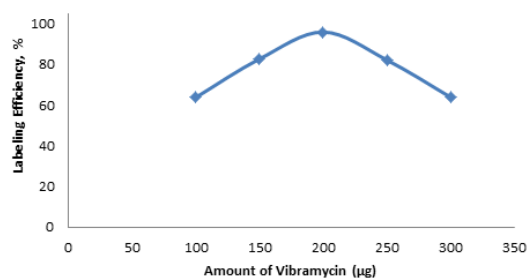
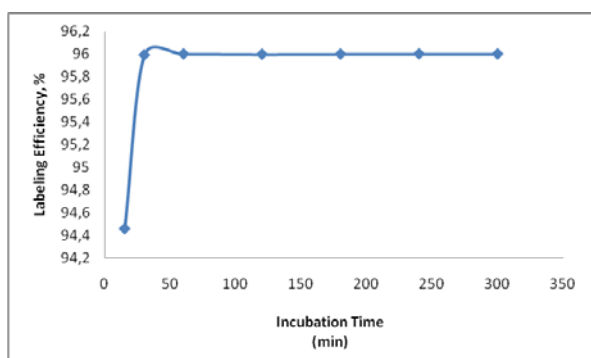


Fig.6. Effect of amount of ligand on the labeling efficiency of  $^{99m}\text{Tc}$ -vibramycin

The stability of the radiopharmaceutical was checked by its incubation in human serum.  $^{99m}\text{Tc}$ -vibramycin was found to be fully stable as determined by ITLC. Up to 98% labeling was found at 24 h of incubation at  $37^\circ\text{C}$  and there was almost no increase in reduced/hydrolyzed  $^{99m}\text{Tc}$ ,



while very little increase in free pertechnetate was observed. The total impurities were  $<2\%$  (Table 1). The results of electrophoresis illustrate the neutral behavior of the ligand (Fig. 8).



**Fig.7.** Rate of complexation and stability of  $^{99m}\text{Tc}$ -vibramycin at room temperature.

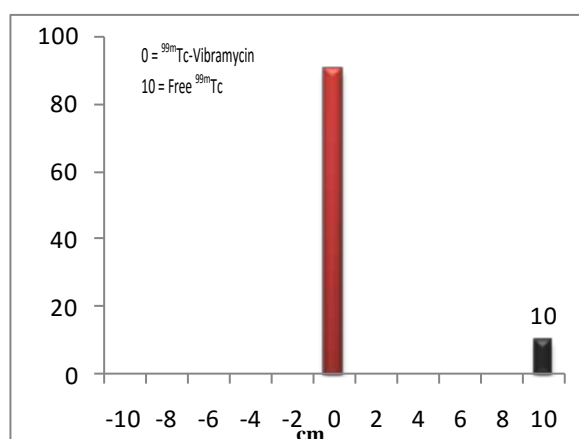


**Fig.8.** Electrophoresis of radiolabeled compound ( $^{99m}\text{Tc}$ -vibramycin at 0 cm;  $^{99m}\text{TcO}_4^-$  at 10 cm).

**Table 1.** *In vitro* stability of  $^{99m}\text{Tc}$ -vibramycin in normal human serum

Incubation time (h)	$^{99m}\text{Tc}$ -vibramycin	Free pertechnetate	Colloid
0.5	$99.9 \pm 0.1$	$0.1 \pm 0.0$	0.0
1	$99.8 \pm 0.2$	$0.2 \pm 0.01$	0.0
2	$99.7 \pm 0.3$	$0.3 \pm 0.03$	0.0
4	$99.6 \pm 0.4$	$0.4 \pm 0.04$	0.0
24	$99.5 \pm 0.5$	$0.5 \pm 0.06$	0.0

*In vitro* binding of  $^{99m}\text{Tc}$ -vibramycin to bacteria was comparable to that of  $^{99m}\text{Tc}$ -ascorbic acid. Binding of varying amounts of  $^{99m}\text{Tc}$ -vibramycin with *S. aureus* was in the range of 97-99% (Fig. 9), while binding of  $^{99m}\text{Tc}$ -ascorbic acid was  $<5\%$  (Table 2).

**Table 2.** *In vitro* binding of  $^{99m}\text{Tc}$ -ascorbic acid to viable *Staphylococcus aureus*

$^{99m}\text{Tc}$ -ascorbic acid	<i>Staphylococcus aureus</i>		
	1 h	4 h	24 h
10 $\mu\text{g}$	0.25	0.18	0.10
50 $\mu\text{g}$	0.39	0.29	0.16
100 $\mu\text{g}$	4.7	3.6	1.2

Significant uptake of  $^{99m}\text{Tc}$ -vibramycin was observed in liver, stomach, lungs and heart during biodistribution studies. *In vivo* stability of  $^{99m}\text{Tc}$ -vibramycin was noticed in the body since stomach, lungs and intestine showed significant activity. The biodistribution results (% injected activity/g) of  $^{99m}\text{Tc}$ -vibramycin in different organs of the animals infected with living, heat killed *S.aureus* and turpentine oil induced, 1, 4 and 24 h after intravenous administration are shown in Table 3. The results show that  $^{99m}\text{Tc}$ -vibramycin accumulates significantly at the infected thigh muscle as compared to heat killed *S.aureus* and turpentine oil infected group of animals. Our studies in rats with intramuscular infection indicated that the uptake in the infected tissue is attributed to specific binding to living bacteria. Whole body images of infected rabbits at 1, 4, and 24 h post  $^{99m}\text{Tc}$ -vibramycin administration are presented in Fig. 10 a, b and c, respectively. *S. aureus* infection in rabbit left thigh was visualized as the area of increased tracer accumulation just after injecting labeled vibramycin as shown in Fig 11. The infection is clearly visible 3 h post administration. The rats with infectious lesions injected with  $^{99m}\text{Tc}$ -vibramycin showed a mean target-to-non target (T/NT) ratio of  $2.6 \pm 0.3$ , 1 h post injection (Table 3).  $^{99m}\text{Tc}$ -vibramycin shows a higher T/NT ratio in the infected muscle (live *S.aureus*) at all time intervals than that of sterile inflamed muscle (heat killed *S.aureus* and turpentine oil). This  $^{99m}\text{Tc}$ -vibramycin showed higher uptake in infected tissue than  $^{99m}\text{Tc}$ -streptomycin (T/NT =  $2.4 \pm 0.1$ ) [32]. The high T/NT ratio for the live *S. aureus* model as compared to turpentine, irradiated and heat killed *S. aureus* models provides evidence that  $^{99m}\text{Tc}$ -vibramycin accumulated at the infectious site due to its specific binding to bacterial cells. Thus, in this study we can establish the basis for the potential of  $^{99m}\text{Tc}$ -vibramycin to distinguish bacterial from non-bacterial infection.

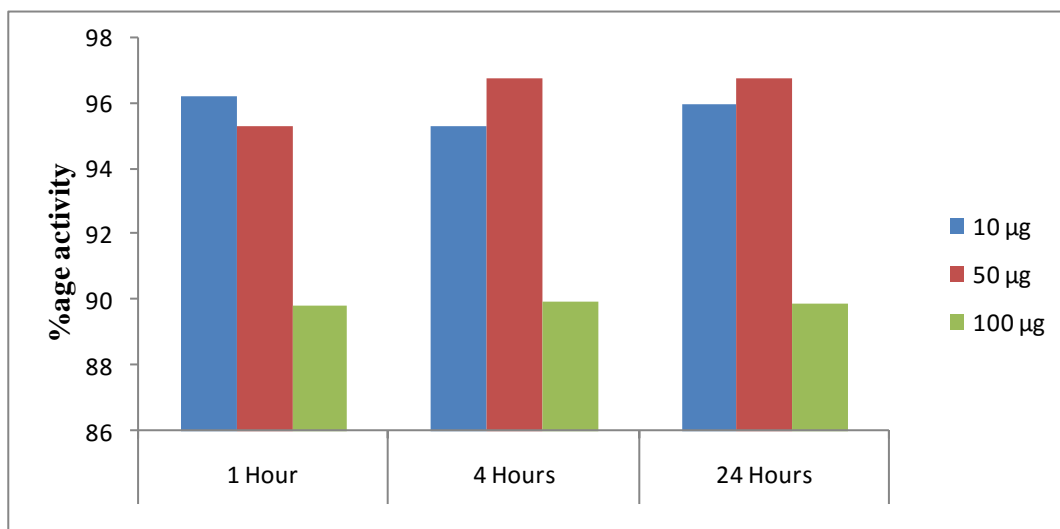


**Fig.9.** *In vitro* binding of  $^{99m}\text{Tc}$ -vibramycin to viable *Staphylococcus aureus*

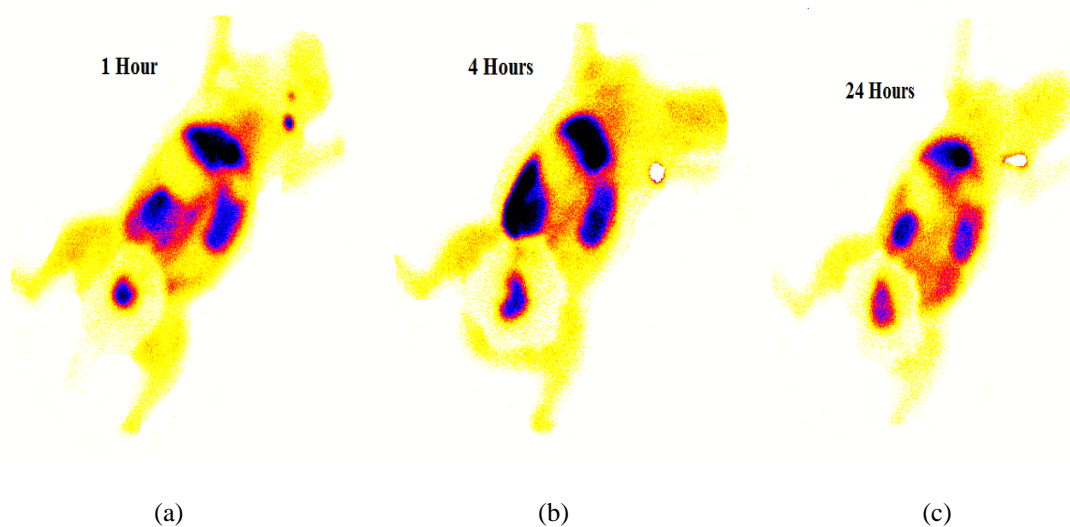


**Fig.10.** Whole body gamma camera image of rabbit injection with  $^{99m}\text{Tc}$ -vibramycin 1 h post administration (a), 4 h post administration (b), and 24 h post administration (c).

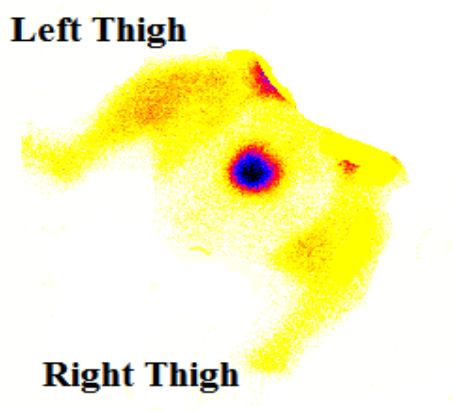


**Fig.11.** *S. aureus* infection in rabbit left thigh and right thigh visualized as area of increased tracer accumulation 3 h post injection of  $^{99m}\text{Tc}$ -vibramycin

**Table 3.** Biodistribution of <sup>99m</sup>Tc-vibramycin in live *S.aureus*, heat killed *S.aureus*, irradiated *S.aureus* and turpentine oil inflamed rats at different time intervals (mean ± SD), (% ID/g).

Organs	Percentage of injected dose per gram of tissue weight (n = 3 at time, interval, hr)											
	Live <i>S.aureus</i>			Heat Killed <i>S.aureus</i>			Irradiated <i>S.aureus</i>			Turpentine oil		
	1h	4h	24h	1h	4h	24h	1h	4h	24h	1h	4h	24h
Liver	4.60 ± 0.8	3.52 ± 1.2	1.48 ± 0.6	4.32 ± 0.4	3.55 ± 0.8	0.80 ± 0.1	3.06 ± 0.6	2.5 ± 0.6	1.18 ± 0.5	3.88 ± 0.8	2.25 ± 0.2	0.50 ± 0.9
Spleen	0.20 ± 0.6	0.19 ± 0.05	0.12 ± 0.03	0.10 ± 0.2	0.15 ± 0.2	0.05 ± 0.5	0.12 ± 0.5	0.10 ± 0.06	0.10 ± 0.2	0.05 ± 0.4	0.09 ± 0.8	0.03 ± 0.1
Stomach	0.19 ± 0.2	0.18 ± 0.03	0.11 ± 0.01	0.90 ± 0.3	1.09 ± 0.9	0.9 ± 0.1	0.25 ± 0.9	0.15 ± 0.1	0.09 ± 0.02	0.50 ± 0.5	0.77 ± 0.8	0.32 ± 0.2
Intestine	4.28 ± 1.1	3.81 ± 0.9	1.98 ± 0.4	3.59 ± 1.0	3.1 ± 1.5	1.50 ± 0.3	1.05 ± 0.3	1.30 ± 0.4	1.01 ± 0.12	2.99 ± 0.1	2.50 ± 0.7	0.95 ± 0.5
Lungs	2.29 ± 0.9	2.20 ± 0.8	1.85 ± 0.8	1.97 ± 1.0	1.90 ± 1.6	1.73 ± 0.4	1.75 ± 1.2	1.05 ± 0.2	1.09 ± 1.1	6.96 ± 1.7	1.05 ± 1.7	1.28 ± 0.1
Kidney	0.64 ± 0.1	0.99 ± 0.2	1.35 ± 0.65	0.58 ± 1.3	0.5 ± 0.2	0.96 ± 0.6	0.20 ± 0.2	0.5 ± 0.1	1.40 ± 0.3	0.25 ± 1.5	0.01 ± 0.1	0.54 ± 0.2
Bladder	7.28 ± 2.3	1.34 ± 0.6	3.56 ± 1.21	6.16 ± 0.1	0.78 ± 0.6	2.75 ± 0.5	5.25 ± 0.7	1.16 ± 0.1	3.06 ± 0.4	5.06 ± 0.2	0.26 ± 0.3	1.93 ± 0.3
Heart	0.18 ± 0.03	0.11 ± 0.05	0.07 ± 0.03	1.2 ± 0.1	0.40 ± 0.3	0.13 ± 0.9	0.10 ± 0.06	0.07 ± 0.01	0.04 ± 0.01	0.60 ± 0.4	0.30 ± 0.1	0.10 ± 0.1
Brain	0.06 ± 0.01	0.04 ± 0.02	0.04 ± 0.01	0.03 ± 0.5	0.09 ± 0.5	1.04 ± 0.2	0.02 ± 0.1	0.42 ± 1.0	0.03 ± 0.01	0.90 ± 1.6	0.02 ± 0.6	1.57 ± 0.7
Blood	5.46 ± 1.5	2.71 ± 1.6	1.22 ± 0.48	4.95 ± 0.01	1.97 ± 0.5	1.10 ± 1.6	1.79 ± 0.5	1.01 ± 0.1	1.09 ± 0.2	3.30 ± 0.5	1.05 ± 0.2	0.80 ± 0.4
Body	0.91 ± 0.3	0.57 ± 0.09	0.38 ± 0.05	0.65 ± 0.4	0.54 ± 1.2	1.26 ± 1.6	1.15 ± 0.4	1.15 ± 0.4	1.15 ± 0.4	1.82 ± 0.5	2.41 ± 1.0	2.05 ± 1.4
Inflamed muscle	0.66 ± 0.2	0.54 ± 0.01	0.36 ± 0.11	0.41 ± 1.2	0.34 ± 0.4	0.32 ± 4.0	0.21 ± 1.0	0.25 ± 0.2	0.15 ± 0.2	0.47 ± 0.02	0.42 ± 0.2	0.40 ± 0.4
Control muscle	0.25 ± 0.1	0.24 ± 0.03	0.19 ± 0.04	0.19 ± 0.3	0.16 ± 1.0	0.15 ± 1.0	0.11 ± 0.1	0.12 ± 0.02	0.09 ± 0.1	0.26 ± 0.8	0.18 ± 0.5	0.29 ± 0.9

<sup>1</sup>values represent the mean ± standard deviation of data from 3 animals.

## CONCLUSION

<sup>99m</sup>Tc-vibramycin prepared by a direct method possesses high radiochemical purity of 95%. The <sup>99m</sup>Tc-vibramycin was stable and ≥95% labeling was maintained for up to 12 h and there was no need of post-labeling. The biological activity of <sup>99m</sup>Tc-vibramycin and <sup>99m</sup>Tc-ascorbic acid was comparable. The <sup>99m</sup>Tc-vibramycin was found to have greater ability to localize in bacterial infection sites induced by *S. aureus* in animal models. Thus data obtained from bio-evaluation studies showed that the prepared <sup>99m</sup>Tc-vibramycin is accumulated at the infectious site and may be a good bacterial infection imaging agent due to its specific binding to bacterial cells.

**Acknowledgement:** This research work was supported by Higher Education Commission of Pakistan under international research support initiative program (No: 1-8/HEC/HRD/20143402; PIN: IRSIP 27 BMS 18).

## REFERENCES

- V. G. Barreto, G. Rabiller, F.Iglesias, V.Soroa, F.Tubau, M.Roca, J. Martin-Comin, *Rev. Esp. Med. Nucl.*, **24**, 312 (2005).
- W.C.Eckelman, *Cardiovas. Imag.*, 364 (2009).
- S. Vallabhajosula, *J. Nucl. Med.*, **38**, 1322 (1997).
- W. Calame, M. Welling, H.I. Feitsma, G.J. Ensing, E.K. Pauwels, *Eur. J. Nucl. Med.*, **20**, 490 (1993)
- M. Welling, H. Feitsma, W. Calame, E.Pauwels, *Nucl.Med. Commun.*, **18**, 1057 (1997).
- M.Welling, H. I. Feitsma, W. Calame, E. K. Pauwels, *Nucl. Med. Biol.*, **24**, 649 (1997).
- M.M.Welling, P.H.Nibbering, A.Paulusma-Annema, P.S.Hiemstra, E.Pauwels, W.Calame, *Int. J. Nucl. Med.*, **40**, 2073 (1999).
- S. Vinjamuri, K.Solanki, J.Bomanji, Q.Siraj, K.Britton, A.Hall, E. O'Shaughnessy, S.Das, *The Lancet*, **347**, 233 (1996).
- V. G. Barreto, G. Rabiller, F.Iglesias, V.Soroa, F.Tubau, M.Roca, J.Martin-Comin, *Rev. Esp. Med. Nucl.*, **24**, 312 (2005).
- S.Qaiser, A.Khan, M.Khan, *J. Radioanal. Chem.*, **284**, 189 (2010).
- S.J. Oh, J. S. Ryu, J. W. Shin, E. J. Yoon, H. J. Ha, J. H.Cheon, H. K. Lee, *Appl. Radiat. Isot.*, **57**, 193 (2002).
- K. Sonmezoglu, M. Sonmezoglu, M. Halac, I. Akgün, C. Türkmen, C. Önsel, B. Kanmaz, K. Solanki, K. E. Britton, I. Uslu, *J. Nucl. Med.*, **42**, 567 (2001).
- A. Bhatnagar, D. Lahoti, A. K. Singh, L. R. Shankar, B. Sharma, T. Singh, *Clin. Nucl. Med.*, **20**, 1070-1073 (1995).
- R. H. Siaens, H. J. Rennen, O. C. Boerman, R. Dierckx, G. Slegers, *J. Nucl. Med.*, **45**, 2088 (2004).
- J. Verma, A. Bhatnagar, A Singh, *World J. Nucl. Med.*, **4**, 35 (2005).
- M. T. Ercan, T. Aras, I. S. Unsal, *Int. J. Rad. Appl. Instrument. Part B*, **19**, 803 (1992).
- A. Lupetti, M. M. Welling, U. Mazzi, P. H. Nibbering, E. K. Pauwels, *Eur. J. Nucl. Med. Mol. Imaging*, **29**, 674 (2002).
- A. Hall, K. Solanki, S. Vinjamuri, K. Britton, S. Das, *J. Clin. Path.*, **51**, 215 (1998).
- S. Roohi, A. Mushtaq, M. Jehangir, S. Malik, *J. Radioanal. Chem.*, **267**, 561 (2006).
- M. Motaleb, *J. Radioanal. Chem.*, **272**, 95 (2007).
- E. El-Ghany, M. El-Kolaly, A. Amine, A.El-Sayed, F.Abdel-Gelil, *J. Radioanal. Chem.*, **266**, 131 (2005).
- E. El-Ghany, A. Amine, A.El-Sayed, M.El-Kolaly, F.Abdel-Gelil, *J. Radioanal. Chem.*, **266**, 125 (2005).
- B. Degirmenci, O. Kilinc, K. A. Cirak, G. Capa, O. Akpinar, H. Halilcolar, H. Durak, A. Akkochu, E. Derebek, E. S. Ucan, *J. Nucl. Med.*, **39**, 2116 (1998).
- S. Roohi, A. Mushtaq, S. A. Malik, *Radiochim. Acta*, **93**, 415 (2005).
- T. H. Bokhari, M. Ahmad, S. Hina, I. H. Bokhari, M. Yousaf, I. Ahmad, N. Rasool, M. Zubair, A. Raza, A. Fawad, *J. Chem. Soc. Pak.*, **34**, 473.(2012).
- M. M. Welling, G. Ferro-Flores, I. Pirmettis, C. P. Brouwer, *Anti-Inf. Agen. Med. Chem.*, **8**, 272 (2009).

26. M. J. Quarterman, D. W. Johnson, D. C. Abele, J. L. Leshner, Jr, D. S. Hull, L. S. Davis, *Arch Dermat.*, **133**, 49 (1997).
27. S. Y. Ugur, Y. L. Fatma, Ü. Perihan, Z. B. Fazilet, I. M. Emin, C. Berkan, *Chem. Pharm. Bull.* **54**, 1 (2006).
28. P. B. Chantal, J. J. M. Huub, C. B. Otto, A. B. Wymenga, E. P. Visser, H. B. Johannes, J. W. M. van der Meer, F. H. M. Corstens, W. J. G. Oyen, *J. Nucl. Med.*, **48**, 337 (2007).
29. W. J. G. Oyen, O. C. Boerman, F. H. M. Corstens, *J. Microbiol. Meth.*, **47**, 151 (2001).
30. M. Asikoglu, F. Yurt, O. Cagliyan, P. Unak, H. Ozkilig. *Appl. Radiat. Isot.*, **53**, 411 (2000).
31. T. Meral, T. Ercan, S. U. Isil, *J. Nucl. Med. Biol.*, **19**, 802 (1992).

## БЕЛЯЗАНЕ, КАЧЕСТВЕН КОНТРОЛ И БИОЛОГИЧНА ОЦЕНКА НА <sup>99m</sup>Tc-ВИБРАМИЦИН ЗА ОПРЕДЕЛЯНЕ НА ИНФЕКТИРАНИ ЗОНИ

С. Хина<sup>1\*</sup>, М. И. Раджока<sup>1</sup>, П. Б. Саваж<sup>2</sup>, С. Рухи<sup>3</sup>, Т. Х. Бокхари<sup>4</sup>

<sup>1</sup>Департамент по биоинформатика и биотехнология, Правителствен университет, Файсалабад, Пакистан

<sup>2</sup>Департамент по химия и биохимия, Университет Бригам Янг, Ц100, БНСН Прово, ЮТ, 84605, САЩ

<sup>3</sup>Лаборатории за качествен контрол, ИПД, Пакистански институт по ядрени изследвания и технологии, П.О. Найлор, Исламабад, Пакистан

<sup>4</sup>Департамент по химия, Правителствен университет, Файсалабад, Пакистан

Постъпила на 11 юни, 2014 г.; коригирана на 15 ноември, 2014 г.

(Резюме)

Използването на белязани антибиотици като диагностициращи агенти е развиваща се дейност в медицинските изследвания. Вибрамицинът е полу-синтетичен антибиотик от групата на тетрациклините, предписван за лечението на различни инфекции. В настоящата работа се представя нов вибрамицин, белязан с <sup>99m</sup>Tc-технеций и използващ SnCl<sub>2</sub>·2H<sub>2</sub>O като редуктор. Стабилността на белязания вибрамицин е оценена върху човешки серум при 37°C. Изследвано е биологичното разпределение на <sup>99m</sup>Tc-вибрамицина върху Sprague-Dawley плъхове, заразени с бактериална инфекция. *In vitro*-изследванията са извършени, за да се определи свързващото взаимодействие на белязания антибиотик с бактериите и неговата стабилност. Извършено е сцинтиграфско изследване с γ-самега един, четири и двадесет и четири часа след инжектирането на радиотрейсера в плъхове с инфекциозни поражения на мускулите. Потвърдено е чрез моментна тънкослойна хроматография, че <sup>99m</sup>Tc-вибрамицинът притежава висок добив на белязване (95%). Пробите показват добро свързване с *S. aureus*. Сцинтиграфията при зайци показва поглъщане на <sup>99m</sup>Tc-вибрамицина в инфектирани тъкани един, четири и двадесет и четири часа след инжектирането. Биоразпределението на <sup>99m</sup>Tc-вибрамицин показва, че радиоактивният препарат значително се натрупва в инфектираните места и се изхвърля чрез бъбреците. Отлагането при целево към нецелево използване на <sup>99m</sup>Tc-вибрамицина в засегнатите места и в контролните мускули се различават значително. Изследването показва, че <sup>99m</sup>Tc-вибрамицинът се свързва предимно с живи бактерии. Биологичната активност *in vitro* на <sup>99m</sup>Tc-вибрамицина е изследвана при оптимизирани параметри и е установено качеството му на добър агент за изобразяването на инфекции.

## Some problems in the column apparatuses modeling

Chr. B. Boyadjiev<sup>1\*</sup>, M. D. Doichinova<sup>1</sup>, B. Chr. Boyadjiev

<sup>1</sup>*Institute of Chemical Engineering, Bulgarian Academy of Sciences,  
Acad. St. Angelov str., Bl. 103, 1113 Sofia, Bulgaria*

Received October 15, 2013, Revised September 25, 2014

The solutions of some theoretical problems of the column apparatuses modeling in the cases of one-, two- and three-phase processes are presented in the approximation of the mechanics of continua. The effect of the radial non-uniformity of the velocity distribution, the effect of the tangential flow and simultaneous mass and heat transfer processes in one-phase column are analyzed. The possibility for obtaining the interphase distribution of the mass transfer resistances in two-phase columns is shown. An iterative numerical algorithm for non-stationary processes modeling in three-phase columns is also presented.

**Key words:** modeling, column apparatus, one phase, two phases, three phases, mass transfer, heat transfer.

### INTRODUCTION

The fundamental modeling problems in column apparatuses are a result of the complicated hydrodynamic behavior of the flows in the columns. The presence of different phases (gas, liquid and solid) leads to the necessity for formulation of two or three phases hydrodynamic problem. At the other side the equations of the interphase surface, where boundary conditions must be formulated, are practically unknown. As a result the solution of the interphase mass transfer problem is not possible because the velocity function in the convection-diffusion equation is unknown.

The interphase mass transfer problem in column apparatuses may be modeled using a new approach based on the approximations of the mechanics of continua [1-4], where the mathematical point is equivalent to a small (elementary) physical volume, sufficiently small with respect to the apparatus volume, but at the same time sufficiently large with respect to the intermolecular volumes of the medium. As a result the mathematical description of the processes presents the mass balance in this elementary volume in the form of a convection-diffusion type of model, using the convection-diffusion equations. These types of models [1-4] allow a qualitative analysis of the process in order to obtain the main, small and slight physical effects (mathematical operators in the models), and to reject the slight effects (operators).

The use of the convection-diffusion type of models for modeling (quantifying) of the processes in column apparatuses is not possible because the velocity function in the convection-diffusion

equations is unknown. The problem can be avoided if the average values of the velocities and concentrations over the cross-sectional area of the column are used, i.e. the medium elementary volume (in the physical approximations of the mechanics of continua [1-4]) will be equivalent to a small cylinder with radius  $r_0$  and a height, which is sufficiently small with respect to the column height and at the same time sufficiently large with respect to the intermolecular distances in the medium.

The main part of the problems in one-phase columns is the decrease of the processes efficiency as a result of the effect of radial non-uniformity of the velocity distribution. This problem can be avoided by using a tangential inlet of the flow in the column, which is very useful in the cases of simultaneous mass and heat transfer processes.

Theoretical analysis of the interphase distribution of the mass transfer resistances in two-phase columns allows obtaining the optimal gas-liquid dispersion, i.e. a system of gas-liquid drops (liquid-gas bubbles) in the case when the main part of the interphase mass transfer resistance is in the gas (liquid) phase.

### ONE-PHASE MODEL

Let's consider a liquid motion in a column reactor with radius  $r_0$  (m) and height  $l$  (m), where a homogeneous chemical reaction between two liquid components is realized. If the difference between the component concentrations is very large, then the chemical reaction will be of first order.

\* To whom all correspondence should be sent:  
E-mail: chboyadj@bas.bg

Convection–diffusion type of model

If the velocity  $u$  [m.s<sup>-1</sup>] and concentration  $c$  [kg.m<sup>-3</sup>] distributions in the column are defined as:

$$u = u(r), \quad c = c(r, z), \quad (1)$$

the convection–diffusion type of model [4] can be expressed as:

$$u \frac{\partial c}{\partial z} = D \left( \frac{\partial^2 c}{\partial z^2} + \frac{1}{r} \frac{\partial c}{\partial r} + \frac{\partial^2 c}{\partial r^2} \right) - kc;$$

$$z = 0, \quad c(r, 0) \equiv c_0, \quad \bar{u} c_0 \equiv u c_0 - D \frac{\partial c}{\partial z};$$

$$r = 0, \quad \frac{\partial c}{\partial r} \equiv 0; \quad r = r_0, \quad \frac{\partial c}{\partial r} \equiv 0, \quad (2)$$

where  $D$  [m<sup>2</sup>.s<sup>-1</sup>] is diffusivity,  $k$  [s<sup>-1</sup>] – chemical reaction rate constant,  $\bar{u}$ ,  $c_0$  – input values of the average velocity and concentration.

The qualitative analysis of the model (2) will be made using generalized variables:

$$r = r_0 R, \quad z = lZ, \quad u(r) = u(r_0 R) = \bar{u} U(R),$$

$$c(r, z) = c(r_0 R, lZ) = c_0 C(R, Z), \quad \varepsilon = \left( \frac{r_0}{l} \right)^2, \quad (3)$$

Where  $r_0$ ,  $l$ ,  $\bar{u}$ ,  $c_0$  are the characteristic (inherent) scales (maximal or average values) of the variables. Introducing the generalized variables (3) in (2), the convection–diffusion type of model can be written as:

$$U(R) \frac{\partial C}{\partial Z} = \text{Fo} \left( \varepsilon \frac{\partial^2 C}{\partial Z^2} + \frac{1}{R} \frac{\partial C}{\partial R} + \frac{\partial^2 C}{\partial R^2} \right) - \text{Da} C;$$

$$Z = 0, \quad C \equiv 1, \quad 1 \equiv U - \text{Pe}^{-1} \frac{\partial C}{\partial Z};$$

$$R = 0, \quad \frac{\partial C}{\partial R} \equiv 0; \quad R = 1, \quad \frac{\partial C}{\partial R} \equiv 0, \quad (4)$$

where  $\varepsilon = \text{Fo}^{-1} \text{Pe}^{-1}$ ,  $\text{Fo} = \frac{Dl}{\bar{u} r_0^2}$ ,  $\text{Pe} = \frac{\bar{u} l}{D}$ ,  $\text{Da} = \frac{kl}{\bar{u}}$  are the

Fourier, Damkohler and Peclet numbers, respectively.

In the cases of big values of the average velocity ( $0 = \text{Fo} \leq 10^{-2}$ ), from the convection–diffusion type of model (4) may obtain a convection type of model:

$$U(R) \frac{\partial C}{\partial Z} = -\text{Da} C; \quad Z = 0, \quad C \equiv 1. \quad (5)$$

The effect of the chemical reaction rate is negligible if  $0 = \text{Da} \leq 10^{-2}$  and as a result  $C \equiv 1$ .

When a fast chemical reaction takes place ( $\text{Da} \geq 10^2$ ), the terms in the model must be divided by  $\text{Da}$  and the approximation  $0 = \text{Da} \leq 10^{-2}$  has to be applied.

The result is:

$$0 = \frac{\text{Fo}}{\text{Da}} \left( \frac{1}{R} \frac{dC}{dR} + \frac{d^2 C}{dR^2} \right) - C;$$

$$R = 0, \quad \frac{dC}{dR} = 0; \quad R = 1, \quad \frac{dC}{dR} = 0, \quad (6)$$

i.e. the model (6) is diffusion type.

Average concentration model

The average velocity and concentration at the column cross-sectional area can be presented as

$$\bar{u} = \frac{2}{r_0^2} \int_0^{r_0} r u(r) dr, \quad \bar{c}(z) = \frac{2}{r_0^2} \int_0^{r_0} r c(r, z) dr. \quad (7)$$

The convection–diffusion type of model (2) assumes the velocities and concentration distributions to be presented [3, 4] by the average functions (7):

$$u(r) = \bar{u} \tilde{u}(r), \quad c(r, z) = \bar{c}(z) \tilde{c}(r, z), \quad (8)$$

where  $\tilde{u}(r)$  and  $\tilde{c}(r, z)$  represent the radial non-uniformity of both the velocity and the concentration distributions, satisfying the conditions:

$$\frac{2}{r_0^2} \int_0^{r_0} r \tilde{u}(r) dr = 1, \quad \frac{2}{r_0^2} \int_0^{r_0} r \tilde{c}(r, z) dr = 1. \quad (9)$$

An average concentration model may be obtained [1-4] if the expressions (8) were placed into the model equations (2) and then multiplied by  $r$  and integrated with respect to  $r$  over the interval  $[0, r_0]$ . The result is:

$$\alpha \bar{u} \frac{\partial \bar{c}}{\partial z} + \frac{d\alpha}{dz} \bar{u} \bar{c} = D \frac{\partial^2 \bar{c}}{\partial z^2} - k \bar{c};$$

$$z = 0, \quad \bar{c}(0) = c_0, \quad \frac{\partial \bar{c}}{\partial z} = 0, \quad (10)$$

where

$$\alpha = \alpha(z) = \frac{2}{r_0^2} \int_0^{r_0} r \tilde{u} \tilde{c} dr. \quad (11)$$

The use of the generalized variables:

$$Z = \frac{z}{l}, \quad \bar{C} = \frac{\bar{c}}{c_0}, \quad \alpha(z) = \alpha(lZ) = A(Z), \quad (12)$$

leads to:

$$A \frac{d\bar{C}}{dZ} + \frac{dA}{dZ} \bar{C} = \text{Pe}^{-1} \frac{d^2 \bar{C}}{dZ^2} - \text{Da} \bar{C};$$

$$Z = 0, \quad \bar{C} = 1, \quad \frac{d\bar{C}}{dZ} = 0. \quad (13)$$

In the cases

$$0 = \text{Fo} \leq 10^{-2}, \quad 0 = \text{Pe}^{-1} = \varepsilon \text{Fo} \leq 10^{-2}, \quad \varepsilon < 1$$

(see (5)) the model (13) has the convective form:

$$A \frac{d\bar{C}}{dZ} + \frac{dA}{dZ} \bar{C} = -\text{Da} \bar{C}; \quad Z = 0, \quad \bar{C} = 1. \quad (14)$$

The function  $A(Z)$  in (13, 14) represents the effect of the velocity radial non-uniformity on the mass transfer efficiency in the column apparatus:

$$A(Z) = \alpha(z) = \frac{2}{r_0^2} \int_0^{r_0} r \tilde{u} \tilde{c} dr, \quad (15)$$

where

$$\tilde{u}(r) = \frac{u(r)}{\bar{u}} = U(R),$$

$$\tilde{c}(r, z) = \frac{c(r, z)}{\bar{c}(z)} = \frac{C(R, Z)}{\bar{C}(Z)},$$

$$\bar{C}(Z) = \frac{\bar{c}(z)}{c_0} = 2 \int_0^1 RC(R, Z) dR \quad (16)$$

and as a result one can obtain the following equation:

$$A(Z) = 2 \int_0^1 RU(R) \frac{C(R, Z)}{\bar{C}(Z)} dR. \quad (17)$$

#### Effect of the radial non-uniformity of the velocity distribution

The case of parabolic velocity distribution (Poiseuille flow) will be used as an example:

$$u(r) = \bar{u} \left( 2 - 2 \frac{r^2}{r_0^2} \right). \quad (18)$$

From (3, 18) follows:

$$U(R) = 2 - 2R^2. \quad (19)$$

The model (4) may raise several particular cases that permit to obtain  $C(R, Z)$ ,  $\bar{C}(Z)$  and to present results for  $A(Z) \geq 1$ , using different approximations:

$$\text{Fo} = 1, \quad \text{Da} = 1, 2, \quad A(Z) = a_0,$$

$$a_0 = \frac{1}{N} \sum_{n=1}^N A(Z_n);$$

$$\text{Fo} = 0, 0.1, \quad \text{Da} = 1, 2, \quad A(Z) = 1 + aZ,$$

$$a = \frac{1}{N} \sum_{n=1}^N \frac{A(Z_n) - 1}{Z_n}; \quad 0 < Z_n < 1. \quad (20)$$

The obtained values of  $a$ ,  $a_0$  in (20) are shown in Table 1.

The equations (13, 14) allow to obtain expressions for the concentration axial gradient:

$$\frac{d\bar{C}}{dZ} = -A^{-1} \frac{dA}{dZ} \bar{C} + A^{-1} \text{Pe}^{-1} \frac{d^2\bar{C}}{dZ^2} - A^{-1} \text{Da} \bar{C};$$

$$\frac{d\bar{C}}{dZ} = -A^{-1} \frac{dA}{dZ} \bar{C} - A^{-1} \text{Da} \bar{C}. \quad (21)$$

From (8) follows that  $\tilde{u}=1$  if the velocity radial non-uniformity is absent ( $u=\bar{u}$ ), i.e.  $A=a=1$  (see (9, 11, 15)). The presence of a radial non-uniformity of the axial velocity in the columns leads to  $A>1$ , i.e. a decrease of the concentration axial gradient and process efficiency [4]. In Table 1 are shown the process efficiencies (conversion degree) in the cases of presence ( $G$ ) and absence ( $G_0$ ) of a radial non-uniformity of the axial velocity in the column:

$$G = 1 - 2 \int_0^1 RU(R)C(R, 1) dR, \quad G_0 = 1 - \bar{C}(1). \quad (22)$$

**Table 1.** Parameter values and values of process efficiencies (conversion degree)

	$a$	$a_0$	$G$	$G_0$
Da=1, Fo=0	0.5511		0.5568	0.6734
Da=1, Fo=0.1	0.2463		0.5938	0.6452
Da=1, Fo=1		1.02	0.6211	0.6281
Da=2, Fo=0	1.3623		0.7806	0.8516
Da=2, Fo=0.1	0.4547		0.8115	0.8502
Da=2, Fo=1		1.04	0.8481	0.8538

The values in Table 1 demonstrate that the radial non-uniformity of the axial velocity component leads to a substantial decrease of the conversion degree.

#### Effect of the tangential flow

Let's consider a cylindrical column with axial input of gas (liquid) flow (Fig.1a). The axial and radial velocity components  $u_z=u_z(r, z)$ ,  $u_r=u_r(r, z)$  satisfy the continuity equation:

$$\frac{\partial u_z}{\partial z} + \frac{\partial u_r}{\partial r} + \frac{u_r}{r} = 0;$$

$$z = 0, \quad u_z(r, 0) = u_z^0(r), \quad r = r_0, \quad u_r(r_0, z) \equiv 0, \quad (23)$$

where  $u_z^0(r)$  is the input distribution of the axial velocity component as a result of the geometric conditions at the axial input of the column. The velocity components  $u_z(r, z)$ ,  $u_r(r, z)$  can be obtained as a solution of the Navier-Stokes equations in boundary layer approximation, i.e. to solve the problem of the gas (liquid) jet in immobile gas (liquid). As a result the radial non-uniformity of the axial velocity component exists for the columns with limited height. In these conditions the conversion degree increase is related to the decrease of the radial non-uniformity of the axial velocity component (special geometric conditions at the axial input of the column).

A possibility for a partial reduction of the radial non-uniformity of the axial velocity component is to use a column with tangential enter [5] of the gas (liquid) flow (Fig.1b) in the column input.

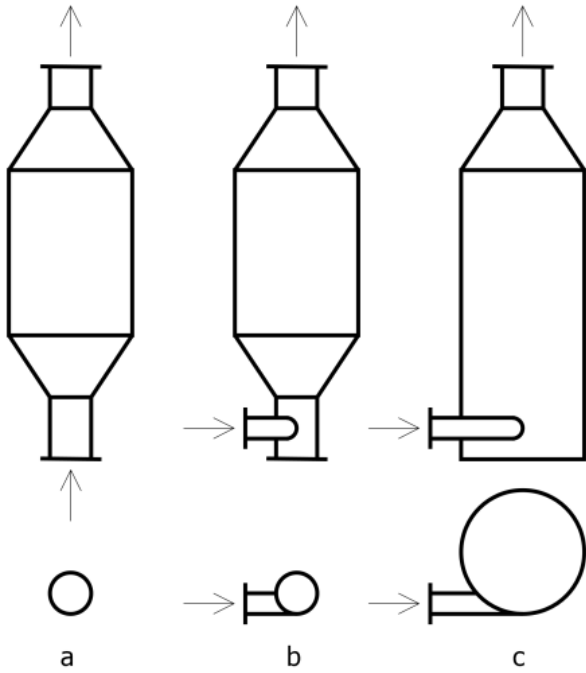


**Fig. 1.** Cylindrical column with: **a** - axial gas (liquid) flow; **b** - tangential gas (liquid) flow in column inlet; **c** - tangential gas (liquid) flow in the column working area.

A maximal reduction of the radial non-uniformity of the axial velocity component is to use a column with tangential enter [6] of the gas (liquid) flow (Fig.1c) in the column working area. In the cases of tangential input of the flow in the column, the velocity components  $u_z=u_z(r,z,\varphi)$ ,  $u_r=u_r(r,z,\varphi)$ ,  $u_\varphi=u_\varphi(r,z,\varphi)$  satisfy the continuity equation:

$$\frac{\partial u_z}{\partial z} + \frac{1}{r} \frac{\partial u_\varphi}{\partial \varphi} + \frac{\partial u_r}{\partial r} + \frac{u_r}{r} = 0;$$

$$z = 0, \quad 0 \leq r < r_0, \quad 0 \leq \varphi \leq 2\pi,$$

$$u_z(0, r, \varphi) \equiv \bar{u} = \frac{Q}{\pi r_0^2};$$

$$r = r_0, \quad 0 < z \leq l, \quad 0 \leq \varphi \leq 2\pi, \quad u_r(z, r_0, \varphi) \equiv 0;$$

$$\varphi = 0, \quad u_\varphi(0, r_0, 0) \equiv u_\varphi^0 = \frac{Q}{\pi r_{00}^2}, \quad (24)$$

where  $Q$  ( $\text{m}^3 \cdot \text{s}^{-1}$ ) is gas (liquid) flow rate in the column and  $r_{00}$  is the column inlet radius.

The applying of generalized variables:

$$z = lZ, \quad r = r_0R, \quad \varphi = 2\pi\Phi, \quad (25)$$

$$u_z = \bar{u}U_z, \quad u_r = \bar{u} \frac{r_0}{l} U_r, \quad u_\varphi = u_\varphi^0 U_\varphi,$$

leads to

$$\frac{1}{R} \frac{\partial U_\varphi}{\partial \varphi} + 2\pi \frac{\bar{u}r_0}{u_\varphi^0 l} \left( \frac{\partial U_z}{\partial Z} + \frac{\partial U_r}{\partial R} + \frac{U_r}{R} \right) = 0;$$

$$Z = 0, \quad 0 \leq R < 1, \quad 0 \leq \Phi \leq 1, \quad U_z(0, R, \Phi) \equiv 1;$$

$$R = 1, \quad 0 < Z \leq 1, \quad 0 \leq \Phi \leq 1, \quad U_r(Z, 1, \Phi) \equiv 0;$$

$$\Phi = 0, \quad U_\varphi(0, 1, 0) \equiv 1. \quad (26)$$

Practically  $\bar{u} \square u_\varphi^0$  and the following approximation can be used:

$$0 = 2\pi \frac{\bar{u}r_0}{u_\varphi^0 l} \leq 10^{-2}, \quad (27)$$

$$\text{i.e.} \quad \frac{\partial U_\varphi}{\partial \varphi} = 0 \quad (28)$$

and from (26) follows:

$$\frac{\partial U_z}{\partial Z} + \frac{\partial U_r}{\partial R} + \frac{U_r}{R} = 0;$$

$$Z = 0, \quad 0 \leq R < 1, \quad U_z(0, R) \equiv 1;$$

$$R = 1, \quad 0 < Z \leq 1, \quad U_r(Z, 1) \equiv 0. \quad (29)$$

From model (29) follows that practically  $U_z(R, Z) \equiv 1$ ,  $U_r(Z, R) \equiv 0$  (except for the thin boundary layer at the wall).

The presented theoretical analysis shows that using tangential input of the flow in the column area leads to a significant decrease of the velocity radial non-uniformity and as a result to an increase of the conversion degree in the columns.

#### Simultaneous mass and heat transfer processes

The heat and mass transfer kinetics theory shows [3], that the process rate depends on the characteristic velocity in the boundary layer. The big difference between these velocities leads to a substantial increase of the heat transfer rate through the column wall in the cases of axial and tangential input of the flows ( $\bar{u} \square u_\varphi^0$ ).

Let's consider simultaneous mass and heat transfer processes in a column chemical reactor, where the velocity, concentration and temperature  $t$  (deg) distributions in the column are denoted as:

$$u = u(r), \quad c = c(r, z), \quad t = t(r, z). \quad (30)$$

The mass and heat transfer model in the physical approximations of the mechanics of continua [1-4] can be expressed as:

$$u \frac{\partial c}{\partial z} = D \left( \frac{\partial^2 c}{\partial z^2} + \frac{1}{r} \frac{\partial c}{\partial r} + \frac{\partial^2 c}{\partial r^2} \right) - kc;$$



$$z = 0, \quad c(r,0) \equiv c_0, \quad \bar{u} c_0 \equiv u c_0 - D \frac{\partial c}{\partial z},$$

$$r = 0, \quad \frac{\partial c}{\partial r} \equiv 0; \quad r = r_0, \quad \frac{\partial c}{\partial r} \equiv 0. \quad (31)$$

$$u \frac{\partial t}{\partial z} = \frac{\lambda}{\rho c_p} \left( \frac{\partial^2 t}{\partial z^2} + \frac{1}{r} \frac{\partial t}{\partial r} + \frac{\partial^2 t}{\partial r^2} \right) + \frac{q}{\rho c_p} k c;$$

$$z = 0, \quad t(r,0) \equiv t_0, \quad \bar{u} t_0 \equiv u t_0 - \frac{\lambda}{\rho c_p} \frac{\partial t}{\partial z};$$

$$r = r_0, \quad t \equiv t_s; \quad -\lambda \frac{\partial t}{\partial r} \equiv k_0, \quad (32)$$

where  $\rho$  (kg.m<sup>3</sup>) is density,  $c_p$  [J.kg<sup>-1</sup>.deg<sup>-1</sup>] – specific heat at constant pressure,  $\lambda$  [J.m<sup>-1</sup>.s<sup>-1</sup>.deg<sup>-1</sup>] – thermal conductivity,  $q$  [J.kg<sup>-1</sup>] – heat effect of the chemical reaction,  $k_0$  [J.m<sup>-2</sup>.s<sup>-1</sup>] – local heat transfer flux. In the model (31, 32)  $D, k, \lambda, \rho, c_p, q, k_0$  are temperature functions, where  $t_0 \leq t \leq t_s$  or  $t_s \leq t \leq t_0$  in the case of endothermic ( $q < 0$ ) or exothermic ( $q > 0$ ) chemical reaction. Practically the difference  $|t_0 - t_s|$  is not so big and in (31, 32) may use constant values of  $D, k, \lambda, \rho, c_p, q, k_0$  at  $t^* = (t_0 + t_s)/2$ .

From the condition  $t_s = \text{const}$  follows that the volume heat generation in the column is equal to the interface heat transfer through the column wall:

$$2\pi \int_0^{r_0} r q k c dr = -2\pi r_0 \lambda \left( \frac{\partial t}{\partial r} \right)_{r=r_0},$$

$$-\lambda \left( \frac{\partial t}{\partial r} \right)_{r=r_0} = \frac{r_0 q k}{2} \bar{c}(z) = k_0(z). \quad (33)$$

A qualitative analysis of the model (31, 32) will be made using generalized variables:

$$r = r_0 R, \quad z = l Z, \quad u(r) = u(r_0 R) = \bar{u} U(R),$$

$$c(r, z) = c(r_0 R, l Z) = c_0 C(R, Z),$$

$$t(r, z) = t(r_0 R, l Z) = t^* T(R, Z), \quad (34)$$

where  $r_0, l, \bar{u}, c_0, t^*$  are the characteristic (inherent) scales (maximal or average values) of the variables. The introduction of generalized variables (34) in (31, 32) leads to:

$$U(R) \frac{\partial C}{\partial Z} = \frac{Dl}{\bar{u} r_0^2} \left( \frac{r_0^2}{l^2} \frac{\partial^2 C}{\partial Z^2} + \frac{1}{R} \frac{\partial C}{\partial R} + \frac{\partial^2 C}{\partial R^2} \right) - \frac{kl}{\bar{u}} C;$$

$$Z = 0, \quad C(R,0) \equiv 1, \quad 1 \equiv U(R) - \frac{D}{\bar{u} l} \frac{\partial C}{\partial Z};$$

$$R = 0, \quad \frac{\partial C}{\partial R} \equiv 0; \quad R = 1, \quad \frac{\partial C}{\partial R} \equiv 0. \quad (35)$$

$$U(R) \frac{\partial T}{\partial Z} = \frac{\lambda}{\bar{u} \rho c_p r_0^2} \left( \frac{r_0^2}{l^2} \frac{\partial^2 T}{\partial Z^2} + \frac{1}{R} \frac{\partial T}{\partial R} + \frac{\partial^2 T}{\partial R^2} \right) + \frac{q l k c_0}{\bar{u} \rho c_p t^*} C;$$

$$Z = 0, \quad T(R,0) \equiv T_0, \quad 1 \equiv U(R) - \frac{\lambda}{T_0 \bar{u} \rho c_p l} \frac{\partial T}{\partial Z}, \quad T_0 = \frac{t_0}{t^*}.$$

$$R = 1, \quad T \equiv T_s; \quad \frac{\partial T}{\partial R} \equiv -\frac{r_0^2 q k c_0}{2 \lambda t^*} \bar{C}(Z), \quad T_s = \frac{t_s}{t^*}. \quad (36)$$

In the cases of very high columns it may use the approximation  $0 = \frac{r_0^2}{l^2} \leq 10^{-2}$  and the models (35, 36) are of parabolic type. If the average velocity  $\bar{u}$  is very high, it may use the approximations  $0 = \frac{Dl}{\bar{u} r_0^2} \leq 10^{-2}$  and  $0 = \frac{\lambda}{\bar{u} \rho c_p r_0^2} \leq 10^{-2}$ , i.e. the models (32, 33) are of convective type:

$$U(R) \frac{\partial C}{\partial Z} = -\frac{kl}{\bar{u}} C; \quad Z = 0, \quad C(R,0) \equiv 1. \quad (37)$$

$$U(R) \frac{\partial T}{\partial Z} = \frac{q l k c_0}{\bar{u} \rho c_p t^*} C; \quad Z = 0, \quad T(R,0) \equiv T_0. \quad (38)$$

#### Average temperature model

The average temperature at the column cross-sectional area can be presented as

$$\bar{t}(z) = \frac{2}{r_0^2} \int_0^{r_0} r t(r, z) dr. \quad (39)$$

The velocities and temperature distributions can be presented by the average functions (7, 39):

$$u(r) = \bar{u} \tilde{u}(r), \quad t(r, z) = \bar{t}(z) \tilde{t}(r, z), \quad (40)$$

where  $\tilde{u}(r, z)$  and  $\tilde{t}(r, z)$  represent the radial non-uniformity of both the velocity and the temperature distributions, satisfying the conditions:

$$\frac{2}{r_0^2} \int_0^{r_0} r \tilde{u}(r) dr = 1, \quad \frac{2}{r_0^2} \int_0^{r_0} r \tilde{t}(r, z) dr = 1. \quad (41)$$

An average temperature model may be obtained if the expressions (40) are put into the model equations (32) and then multiplied by  $r$  and integrated with respect to  $r$  over the interval  $[0, r_0]$ . The result is:

$$\alpha_t \bar{u} \frac{d\bar{t}}{dz} + \frac{d\alpha_t}{dz} \bar{u} \bar{t} = \frac{\lambda}{\rho c_p} \frac{d^2 \bar{t}}{dz^2};$$

$$z = 0, \quad \bar{t}(0) = t_0, \quad \frac{d\bar{t}}{dz} = 0, \quad (42)$$

where

$$\alpha_i = \alpha_i(z) = \frac{2}{r_0^2} \int_0^{r_0} r \tilde{u} \tilde{t} dr. \quad (43)$$

The use of generalized variables:

$$Z = \frac{z}{l}, \quad \bar{T} = \frac{\tilde{t}}{t_0}, \quad \alpha_i(z) = \alpha_i(lZ) = A_i(Z), \quad (44)$$

leads to:

$$A_i \frac{d\bar{T}}{dZ} + \frac{dA_i}{dZ} \bar{T} = \frac{\lambda t_0}{\rho c_p \bar{u} l^2} \frac{d^2 T}{dZ^2};$$

$$Z = 0, \quad \bar{T} = 1, \quad \frac{d\bar{T}}{dZ} = 0. \quad (45)$$

Similar to (17) the function  $A_i(Z)$  may be obtained after solution of the problems (35) and (36):

$$A_i(Z) = 2 \int_0^1 RU(R) \frac{T(R,Z)}{\bar{T}(Z)} dR,$$

$$\bar{T}(Z) = \frac{\bar{t}(z)}{t^*} = 2 \int_0^1 RT(R,Z) dR. \quad (46)$$

### TWO-PHASE MODEL

The convection-diffusion models are used [6-11] for qualitative analysis of the processes in two-phase columns. A new possibility is the determination of the interphase distribution of the mass transfer resistances in gas-liquid systems.

#### Interphase distribution of the mass transfer resistances

Let's consider a physical absorption in a co-current gas-liquid bubble column with a radius  $r_0$  and working zone height  $l$ , where the interphase mass transfer rate across the gas-liquid boundary is  $k(c_1 - \chi c_2)$  and  $\chi$  is the Henry's constant. If  $\varepsilon_1$  and  $\varepsilon_2$  are the gas and liquid parts of the medium elementary volume ( $\varepsilon_1 + \varepsilon_2 = 1$ ) in the column (gas and liquid holdup coefficients), the convection-diffusion equations have the forms:

$$\varepsilon_1 u_1 \frac{\partial c_1}{\partial z} = \varepsilon_1 D_1 \left( \frac{\partial^2 c_1}{\partial z^2} + \frac{1}{r} \frac{\partial c_1}{\partial r} + \frac{\partial^2 c_1}{\partial r^2} \right) - k(c_1 - \chi c_2),$$

$$\varepsilon_2 u_2 \frac{\partial c_2}{\partial z} = \varepsilon_2 D_2 \left( \frac{\partial^2 c_2}{\partial z^2} + \frac{1}{r} \frac{\partial c_2}{\partial r} + \frac{\partial^2 c_2}{\partial r^2} \right) + k(c_1 - \chi c_2), \quad (47)$$

where  $u_1(r)$ ,  $u_2(r)$  are velocity distributions in the gas and liquid phases,  $c_i(z,r)$  and  $D_i(i=1,2)$  are the concentration distributions and the diffusivities of the absorbed substance in the gas and liquid. The boundary conditions of the model equations have the form:

$$z=0, \quad c_1(0,r) \equiv c_1^0, \quad \bar{u}_1 c_1^0 \equiv u_1(r) c_1^0 - D_1 \left( \frac{\partial c_1}{\partial z} \right)_{z=0};$$

$$z=0, \quad c_2(0,r) \equiv c_2^0, \quad \bar{u}_2 c_2^0 \equiv u_2(r) c_2^0 - D_2 \left( \frac{\partial c_2}{\partial z} \right)_{z=0};$$

$$r=0, \quad \frac{\partial c_1}{\partial r} = \frac{\partial c_2}{\partial r} \equiv 0; \quad r=r_0, \quad \frac{\partial c_1}{\partial r} = \frac{\partial c_2}{\partial r} \equiv 0, \quad (48)$$

where  $\bar{u}_i$ ,  $c_i^0$ ,  $i=1,2$  are the average velocities and the input concentrations in the gas and liquid phases. Practically  $c_2^0=0$ .

A qualitative analysis of the model may be made, using dimensionless (generalized) variables:

$$R = \frac{r}{r_0}, \quad Z = \frac{z}{l}, \quad U_1 = \frac{u_1}{\bar{u}_1}, \quad U_2 = \frac{u_2}{\bar{u}_2}, \quad C_1 = \frac{c_1}{c_1^0}, \quad C_2 = \frac{c_2 \chi}{c_1^0}. \quad (49)$$

The model (47, 48) in generalized variables (49) has the form:

$$U_1(R) \frac{\partial C_1}{\partial Z} = \text{Fo}_1 \left( \varepsilon \frac{\partial^2 C_1}{\partial Z^2} + \frac{1}{R} \frac{\partial C_1}{\partial R} + \frac{\partial^2 C_1}{\partial R^2} \right) - K(C_1 - C_2);$$

$$U_2(R) \frac{\partial C_2}{\partial Z} = \text{Fo}_2 \left( \varepsilon \frac{\partial^2 C_2}{\partial Z^2} + \frac{1}{R} \frac{\partial C_2}{\partial R} + \frac{\partial^2 C_2}{\partial R^2} \right) + K \frac{\varepsilon_1 \bar{u}_1 \chi}{\varepsilon_2 \bar{u}_2} (C_1 - C_2);$$

$$Z=0, \quad C_1(0,R) \equiv 1, \quad 1 = U_1(R) - \text{Pe}_1^{-1} \left( \frac{\partial C_1}{\partial Z} \right)_{Z=0};$$

$$Z=0, \quad C_2(0,R) \equiv 0, \quad \left( \frac{\partial C_2}{\partial Z} \right)_{Z=0} \equiv 0;$$

$$R=0, \quad \frac{\partial C_i}{\partial R} \equiv 0; \quad R=1, \quad \frac{\partial C_i}{\partial R} \equiv 0; \quad i=1,2, \quad (50)$$

where

$$K = \frac{k_0 l}{\varepsilon_1 \bar{u}_1}, \quad \text{Fo}_i = \frac{D_i l}{\bar{u}_i r_0^2}, \quad \text{Pe}_i = \frac{\bar{u}_i l}{D_i}, \quad i=1,2. \quad (51)$$

If denote:

$$\rho_0 = \frac{\varepsilon_1 \bar{u}_1 \chi}{\varepsilon_2 \bar{u}_2}, \quad \rho_1 = K, \quad \rho_2 = \rho_0 \rho_1,$$

$$\rho_1 + \rho_2 = 1, \quad \rho_1 = \frac{1}{1 + \rho_0}, \quad \rho_2 = \frac{\rho_0}{1 + \rho_0}, \quad (52)$$

the parameters  $\rho_1$  and  $\rho_2$  can be considered as mass transfer resistances in the gas and liquid phases and from (50) it may obtain directly models of the physical absorption in the cases of highly ( $\chi \rightarrow 0$ ,  $\rho_0 \rightarrow 0$ ,  $\rho_2 \rightarrow 0$ ,  $C_2 \equiv 0$ ) and slightly ( $\chi \rightarrow \infty$ ,  $\rho_0 \rightarrow \infty$ ,  $\rho_1 \rightarrow 0$ ,  $C_1 \equiv 1$ ) soluble gases. The use of model (50) for prediction of the distribution of mass transfer resistances allows an optimal organization of the absorption process, i.e. absorption in gas-liquid drops systems, when the resistance is in the gas phase ( $\rho_2 \leq 10^{-2}$ ,  $\rho_0 \leq 10^{-2}$ ), or absorption in liquid-

gas bubble systems, when the resistance is in the liquid phase ( $\rho_1 \leq 10^{-2}, \rho_0 \geq 10^2$ ).

### THREE-PHASE MODEL

The convection-diffusion models in three -phase systems [12, 13] are very often characterized by a fixed solid phase, where there is no diffusion transfer. As a result, the process in the solid phase is usually non-stationary. One of the main problems in these cases is the solution of the set of model equations.

#### Non-stationary processes modeling

Let's consider a non-stationary absorption-adsorption process in column apparatuses in a cylindrical coordinate system  $(\tau, z, r)$ , where  $\tau$  (s) is the time. A co-current liquid-gas bubbles flow moves through a fixed solid adsorbent particles bed. A component of the gas phase absorbs physically in the liquid phase and after that adsorbs physically in the adsorbent particles. A chemical reaction takes place in the adsorbent particles between adsorbed component and the active centers (AC) in the adsorbent.

The concentrations of the absorbed component in the gas ( $i=1$ ) and liquid ( $i=2$ ) phases are  $c_i(\tau, z, r)$ , while  $c_3(\tau, z, r)$  and  $c_0(\tau, z, r)$  are the concentrations of the absorbed component and AC in the solid phase, respectively. The interphase mass transfer rates of the physical absorption and adsorption are  $k(c_1 - \chi c_2)$  and  $k_a(c_2 - c_3)$ .

The chemical reaction rate in the solid phase is  $k_0 c_3 c_0$ . As a result the convection-diffusion model of this absorption-adsorption process has the form:

$$\begin{aligned} \varepsilon_1 \frac{\partial c_1}{\partial \tau} + \varepsilon_1 u_1 \frac{\partial c_1}{\partial z} &= \\ &= \varepsilon_1 D_1 \left( \frac{\partial^2 c_1}{\partial z^2} + \frac{1}{r} \frac{\partial c_1}{\partial r} + \frac{\partial^2 c_1}{\partial r^2} \right) - k(c_1 - \chi c_2), \\ \varepsilon_2 \frac{\partial c_2}{\partial \tau} + \varepsilon_2 u_2 \frac{\partial c_2}{\partial z} &= \varepsilon_2 D_2 \left( \frac{\partial^2 c_2}{\partial z^2} + \frac{1}{r} \frac{\partial c_2}{\partial r} + \frac{\partial^2 c_2}{\partial r^2} \right) + \\ &+ k(c_1 - \chi c_2) - k_a(c_2 - c_3), \\ \varepsilon_0 \frac{\partial c_3}{\partial \tau} &= k_a(c_2 - c_3) - k_0 c_3 c_0, \\ \varepsilon_0 \frac{\partial c_0}{\partial \tau} &= -k_0 c_3 c_0, \quad \varepsilon_0 + \varepsilon_1 + \varepsilon_2 = 1, \end{aligned}$$

with initial and boundaries conditions

$$\tau \equiv 0, \quad c_1 \equiv c_1^0, \quad c_2 \equiv 0, \quad c_3 \equiv 0, \quad c_0 \equiv c_0^0;$$

$$z = 0, \quad c_1 \equiv c_1^0, \quad \bar{u}_1 c_1^0 \equiv u_1(r) c_1^0 - D_1 \left( \frac{\partial c_1}{\partial z} \right)_{z=0};$$

$$z = 0, \quad c_2 \equiv 0, \quad \left( \frac{\partial c_2}{\partial z} \right)_{z=0} \equiv 0;$$

$$r = 0, \quad \frac{\partial c_1}{\partial r} = \frac{\partial c_2}{\partial r} \equiv 0; \quad r = r_0, \quad \frac{\partial c_1}{\partial r} = \frac{\partial c_2}{\partial r} \equiv 0. \tag{54}$$

In the presented model (53, 54)  $\varepsilon_i, D_i$  are phase part and diffusivity in the solid ( $i=0$ ), gas ( $i=1$ ) and liquid ( $i=2$ ) phases ( $D_0=0$ ),  $k, k_a, k_0$ - absorption and adsorption interphase mass transfer coefficients and a chemical reaction rate constant, respectively.

The use of dimensionless (generalized) variables permit a qualitative analysis of the model (53, 54) to be made, where as characteristic scales average velocities, initial concentrations, characteristic time  $\tau_0$  (s) and column parameters  $(r_0, h)$  are used:

$$\begin{aligned} T = \frac{\tau}{\tau_0}, \quad R = \frac{r}{r_0}, \quad Z = \frac{z}{l}, \quad U_i(R) = \frac{u_i(r)}{\bar{u}_i}, \\ C_i(T, Z, R) = \frac{c_i(\tau, z, r)}{c_i^0}, \quad c_2^0 = \frac{c_1^0}{\chi}, \\ C_3(T, Z, R) = \frac{c_3(\tau, z, r)}{c_3^0}, \quad C_0(T, Z, R) = \frac{c_0(\tau, z, r)}{c_0^0}, \\ i = 1, 2. \end{aligned} \tag{55}$$

The convection-diffusion model in dimensionless variables can be written in the following way:

$$\begin{aligned} \frac{l}{\bar{u}_1 \tau_0} \frac{\partial C_1}{\partial T} + U_1 \frac{\partial C_1}{\partial Z} &= \\ &= \frac{D_1 l}{\bar{u}_1 r_0^2} \left( \frac{\partial^2 C_1}{\partial Z^2} + \frac{1}{R} \frac{\partial C_1}{\partial R} + \frac{\partial^2 C_1}{\partial R^2} \right) - \frac{kl}{\varepsilon_1 \bar{u}_1} (C_1 - C_2), \\ \frac{l}{\bar{u}_2 \tau_0} \frac{\partial C_2}{\partial T} + U_2 \frac{\partial C_2}{\partial Z} &= \\ &= \frac{D_2 l}{\bar{u}_2 r_0^2} \left( \frac{\partial^2 C_2}{\partial Z^2} + \frac{1}{R} \frac{\partial C_2}{\partial R} + \frac{\partial^2 C_2}{\partial R^2} \right) + \\ &+ \frac{kl\chi}{\varepsilon_2 \bar{u}_2} (C_1 - C_2) - \frac{k_a l}{\varepsilon_2 \bar{u}_2} \left( C_2 - \frac{\chi c_3^0}{c_1^0} C_3 \right), \\ \frac{\partial C_3}{\partial T} &= \frac{k_a \tau_0}{\varepsilon_0} \left( \frac{c_1^0}{\chi c_3^0} C_2 - C_3 \right) - \frac{k_0 \tau_0 c_0^0}{\varepsilon_0} C_3 C_0, \\ \frac{\partial C_0}{\partial T} &= - \frac{k_0 \tau_0 c_3^0}{\varepsilon_0} C_3 C_0. \end{aligned} \tag{56}$$

$$\begin{aligned}
 T = 0, \quad C_1 \equiv 1, \quad C_2 \equiv 0, \quad C_3 \equiv 0, \quad C_0 \equiv 1; \\
 Z = 0, \quad C_1 \equiv 1, \quad 1 \equiv U_1(R) - \frac{D_1}{\bar{u}_1 l} \left( \frac{\partial C_1}{\partial Z} \right)_{Z=0}; \\
 Z = 0, \quad C_2 \equiv 0, \quad \left( \frac{\partial C_2}{\partial Z} \right)_{Z=0} \equiv 0; \\
 R = 0, \quad \frac{\partial C_1}{\partial R} = \frac{\partial C_2}{\partial R} \equiv 0; \quad R = 1, \quad \frac{\partial C_1}{\partial R} = \frac{\partial C_2}{\partial R} \equiv 0.
 \end{aligned} \tag{57}$$

The presented model (56, 57) is the basis for a qualitative analysis of the mass transfer processes in three-phase column apparatuses, i.e. the role of the different physical effects in the complicated absorption-adsorption process.

One of the main problems in three-phase systems is the long-time process. In this case approximations must be used:

$$0 = \frac{l}{\bar{u}_1 \tau_0} \leq 10^{-2}, \quad 0 = \frac{l}{\bar{u}_2 \tau_0} \leq 10^{-2} \tag{58}$$

and the model (56, 57) has the form:

$$\begin{aligned}
 U_1 \frac{\partial C_1}{\partial Z} = \frac{D_1 l}{\bar{u}_1 r_0^2} \left( r_0^2 \frac{\partial^2 C_1}{\partial Z^2} + \frac{1}{R} \frac{\partial C_1}{\partial R} + \frac{\partial^2 C_1}{\partial R^2} \right) - \frac{kl}{\varepsilon_1 \bar{u}_1} (C_1 - C_2); \\
 Z = 0, \quad C_1 \equiv 1, \quad 1 \equiv U_1(R) - \frac{D_1}{\bar{u}_1 l} \left( \frac{\partial C_1}{\partial Z} \right)_{Z=0}; \\
 R = 0, \quad \frac{\partial C_1}{\partial R} \equiv 0; \quad R = 1, \quad \frac{\partial C_1}{\partial R} \equiv 0.
 \end{aligned} \tag{59}$$

$$\begin{aligned}
 U_2 \frac{\partial C_2}{\partial Z} = \frac{D_2 l}{\bar{u}_2 r_0^2} \left( r_0^2 \frac{\partial^2 C_2}{\partial Z^2} + \frac{1}{R} \frac{\partial C_2}{\partial R} + \frac{\partial^2 C_2}{\partial R^2} \right) + \\
 + \frac{kl\chi}{\varepsilon_2 \bar{u}_2} (C_1 - C_2) - \frac{k_a l}{\varepsilon_2 \bar{u}_2} \left( C_2 - \frac{\chi c_3^0}{c_1^0} C_3 \right); \\
 Z = 0, \quad C_2 \equiv 0, \quad \left( \frac{\partial C_2}{\partial Z} \right)_{Z=0} \equiv 0; \\
 R = 0, \quad \frac{\partial C_2}{\partial R} \equiv 0; \quad R = 1, \quad \frac{\partial C_2}{\partial R} \equiv 0.
 \end{aligned} \tag{60}$$

$$\frac{dC_3}{dT} = \frac{k_a \tau_0}{\varepsilon_0} \left( \frac{c_1^0}{\chi c_3^0} C_2 - C_3 \right) - \frac{k_0 \tau_0 c_0^0}{\varepsilon_0} C_3 C_0; \tag{61}$$

$$\frac{dC_0}{dT} = -\frac{k_0 \tau_0 c_3^0}{\varepsilon_0} C_3 C_0; \quad T = 0, \quad C_0 \equiv 1. \tag{62}$$

Considering problems (59, 60)  $T$  is parameter, while in (61, 62) the parameters are  $Z$  and  $R$ . The presented convection-diffusion model (59-62) may be used for qualitative analysis only, but it is the base for the creation of average concentration model.

#### Average concentration model

Using the dimensionless form of average concentrations the concentrations in (59-62) can be written as:

$$\begin{aligned}
 C_i(T, Z, R) = \bar{C}_i(T, Z) \tilde{C}_i(R), \\
 \bar{C}_i(T, Z) = 2 \int_0^1 R C_i(T, Z, R) dR, \\
 2 \int_0^1 R \tilde{C}_i(R) dR = 1, \quad i = 0, 1, 2, 3.
 \end{aligned} \tag{63}$$

The average concentration model can be obtained if the expressions (63) are put into the model equations (59-62) and then multiplied by  $R$  and integrated with respect to  $R$  over the interval  $[0, 1]$ . The result is:

$$\begin{aligned}
 A_1 \frac{d\bar{C}_1}{dZ} + \frac{dA_1}{dZ} \bar{C}_1 = \text{Pe}_1^{-1} \frac{d^2 \bar{C}_1}{dZ^2} - K_1 (\bar{C}_1 - \bar{C}_2); \\
 Z = 0, \quad \bar{C}_1 \equiv 1, \quad \frac{d\bar{C}_1}{dZ} \equiv 0.
 \end{aligned} \tag{64}$$

$$\begin{aligned}
 A_2 \frac{d\bar{C}_2}{dZ} + \frac{dA_2}{dZ} \bar{C}_2 = \\
 = \text{Pe}_2^{-1} \frac{d^2 \bar{C}_2}{dZ^2} + K_2 (\bar{C}_1 - \bar{C}_2) - K_a (\bar{C}_2 - K_3 \bar{C}_3); \\
 Z = 0, \quad \bar{C}_2 \equiv 0, \quad \frac{d\bar{C}_2}{dZ} \equiv 0.
 \end{aligned} \tag{65}$$

$$\begin{aligned}
 \frac{d\bar{C}_3}{dT} = K_0 \frac{k_a}{k_0} (K_3^{-1} \bar{C}_2 - \bar{C}_3) - K_0 c_0^0 B \bar{C}_3 \bar{C}_0; \\
 T = 0, \quad \bar{C}_3 \equiv 0.
 \end{aligned} \tag{66}$$

$$\frac{d\bar{C}_0}{dT} = -K_0 c_3^0 B \bar{C}_3 \bar{C}_0; \quad T = 0, \quad \bar{C}_0 \equiv 1. \tag{67}$$

In the problems (64-67) the expressions are used:

$$\begin{aligned}
 A_i(Z) = 2 \int_0^1 R U_i(R) \frac{C_i(T, Z, R)}{\bar{C}_i(T, Z)} dR, \quad \text{Pe}_i = \frac{\bar{u}_i l}{D_i}, \quad i = 1, 2, \\
 B(Z) = 2 \int_0^1 R \frac{C_3(T, Z, R) C_0(T, Z, R)}{\bar{C}_3(T, Z) \bar{C}_0(T, Z)} dR, \quad K_a = \frac{k_a l}{\varepsilon_2 \bar{u}_2}, \\
 K_0 = \frac{k_0 \tau_0}{\varepsilon_0}, \quad K_1 = \frac{kl}{\varepsilon_1 \bar{u}_1}, \quad K_2 = \frac{kl\chi}{\varepsilon_2 \bar{u}_2}, \quad K_3 = \frac{\chi c_3^0}{c_1^0}.
 \end{aligned} \tag{68}$$

In the problems (64, 65)  $T$  is parameter, while in (66, 67) the parameter is  $Z$  and for solution of the set of equations (64-67) will be used a numerical iterative algorithm.

*Iterative algorithm*

The solution of (64-67) may be obtained as four matrix forms:

$$\begin{aligned} \bar{C}_1(T, Z) &= \|\bar{C}_{10\zeta}\|, & \bar{C}_2(T, Z) &= \|\bar{C}_{20\zeta}\|, \\ \bar{C}_3(T, Z) &= \|\bar{C}_{30\zeta}\|, & \bar{C}_0(T, Z) &= \|\bar{C}_{00\zeta}\|; \\ T &= 0.01\theta, \theta = 1, 2, \dots, 100; & Z &= 0.01\zeta, \zeta = 1, 2, \dots, 100 \end{aligned} \quad (69)$$

A multi-step approach for different values of  $T = 0.01\theta$ , ( $\theta = 1, 2, \dots, 100$ ) will be used, where the upper index ( $\theta$ ) will be the step number too. As a zero step ( $\theta=0$ ) will be used:

$$\begin{aligned} \bar{C}_1^0(T, Z) &= \|\bar{C}_{(1)0\zeta}\|, & \bar{C}_2^0(T, Z) &= \|\bar{C}_{(2)0\zeta}\|, \\ \bar{C}_3^0 &= \|\bar{C}_{(3)0\zeta}\| \equiv 0, & \bar{C}_0^0(T, Z) &= \|\bar{C}_{(0)0\zeta}\| \equiv 1 \\ Z &= 0.01\zeta, \zeta = 1, 2, \dots, 100, \end{aligned} \quad (70)$$

where  $\bar{C}_1^0(T, Z) = \|\bar{C}_{(1)0\zeta}\|$ ,  $\bar{C}_2^0(T, Z) = \|\bar{C}_{(2)0\zeta}\|$  are solutions of (64, 65) for  $\bar{C}_3^0 = \|\bar{C}_{(3)0\zeta}\| \equiv 0$ :

$$\begin{aligned} A_1 \frac{d\bar{C}_1^0}{dZ} + \frac{dA_1}{dZ} \bar{C}_1^0 &= \text{Pe}_1^{-1} \frac{d^2 \bar{C}_1^0}{dZ^2} - K_1 (\bar{C}_1^0 - \bar{C}_2^0); \\ Z = 0, \bar{C}_1^0 &\equiv 1, \frac{d\bar{C}_1^0}{dZ} \equiv 0. \\ A_2 \frac{d\bar{C}_2^0}{dZ} + \frac{dA_2}{dZ} \bar{C}_2^0 &= \text{Pe}_2^{-1} \frac{d^2 \bar{C}_2^0}{dZ^2} + K_2 (\bar{C}_1^0 - \bar{C}_2^0) - K_a \bar{C}_2^0; \\ Z = 0, \bar{C}_2^0 &\equiv 0, \frac{d\bar{C}_2^0}{dZ} \equiv 0. \end{aligned} \quad (71)$$

The first step is the solutions of (66, 67)  $\bar{C}_3^1(T, Z) = \|\bar{C}_{(3)\theta\zeta}\|$ ,  $\bar{C}_0^1(T, Z) = \|\bar{C}_{(0)\theta\zeta}\|$  for  $\bar{C}_2 = \bar{C}_2^0(T, Z) = \|\bar{C}_{(2)0\zeta}\|$ ,  $Z = 0.01\zeta$ ,  $\zeta = 1, 2, \dots, 100$ :

$$\begin{aligned} \frac{d\bar{C}_3^1}{dT} &= K_0 \frac{k_a}{k_0} (K_3^{-1} \bar{C}_2^0 - \bar{C}_3^1) - K_0 c_0^0 B \bar{C}_3^1 \bar{C}_0^1; \\ T = 0, \bar{C}_3^1 &\equiv 0. \\ \frac{d\bar{C}_0^1}{dT} &= -K_0 c_3^0 B \bar{C}_3^1 \bar{C}_0^1; \quad T = 0, \bar{C}_0^1 \equiv 1. \end{aligned} \quad (72)$$

As a result the solutions for  $T=0.01 - \hat{C}_0^1(Z)$  and the polynomial approximation  $\hat{C}_3^1(Z)$  may be obtained:

$$\begin{aligned} \hat{C}_3^1(Z) &= \bar{C}_3^1(0.01, Z) = \|\bar{C}_{(3)1\zeta}^1\| = \sum_{j=1}^5 \bar{\theta}_j^{(1)} Z^{j-1}, \\ \hat{C}_0^1(Z) &= \bar{C}_0^1(0.01, Z) = \|\bar{C}_{(0)1\zeta}^1\|, \\ Z &= 0.01\zeta, \zeta = 1, 2, \dots, 100. \end{aligned} \quad (73)$$

The solution of (64, 65) at the first step leads to:

$$\begin{aligned} A_1 \frac{d\bar{C}_1^1}{dZ} + \frac{dA_1}{dZ} \bar{C}_1^1 &= \text{Pe}_1^{-1} \frac{d^2 \bar{C}_1^1}{dZ^2} - K_1 (\bar{C}_1^1 - \bar{C}_2^1); \\ Z = 0, \bar{C}_1^1 &\equiv 1, \frac{d\bar{C}_1^1}{dZ} \equiv 0. \\ A_2 \frac{d\bar{C}_2^1}{dZ} + \frac{dA_2}{dZ} \bar{C}_2^1 &= \\ = \text{Pe}_2^{-1} \frac{d^2 \bar{C}_2^1}{dZ^2} + K_2 (\bar{C}_1^1 - \bar{C}_2^1) - K_a \left( \bar{C}_2^1 - \sum_{j=1}^5 \bar{\theta}_j^{(1)} Z^{j-1} \right); \\ Z = 0, \bar{C}_2^1 &\equiv 0, \frac{d\bar{C}_2^1}{dZ} \equiv 0. \end{aligned} \quad (74)$$

The step ( $\theta$ ) is the solutions of (66, 67)  $\bar{C}_3^\theta(T, Z) = \|\bar{C}_{(3)\theta\zeta}^\theta\|$ ,  $\bar{C}_0^\theta(T, Z) = \|\bar{C}_{(0)\theta\zeta}^\theta\|$  for  $\bar{C}_2 = \bar{C}_2^{\theta-1}(T, Z) = \|\bar{C}_{(2)(\theta-1)\zeta}\|$ ,  $Z = 0.01\zeta$ ,  $\zeta = 1, 2, \dots, 100$ :

$$\begin{aligned} \frac{d\bar{C}_3^\theta}{dT} &= K_0 \frac{k_a}{k_0} (K_3^{-1} \bar{C}_2^{\theta-1} - \bar{C}_3^\theta) - K_0 c_0^0 B \bar{C}_3^\theta \bar{C}_0^\theta; \\ T = 0, \bar{C}_3^\theta &= \hat{C}_3^{\theta-1}(Z). \\ \frac{d\bar{C}_0^\theta}{dT} &= -K_0 c_3^0 B \bar{C}_3^\theta \bar{C}_0^\theta; \quad T = 0, \bar{C}_0^\theta = \hat{C}_0^{\theta-1}(Z). \end{aligned} \quad (75)$$

As a result the solutions for  $T=0.01 - \hat{C}_0^\theta(Z)$  and the polynomial approximations  $\hat{C}_3^\theta(Z)$  may be obtained:

$$\begin{aligned} \hat{C}_3^\theta(Z) &= \bar{C}_3^\theta(0.01, Z) = \|\bar{C}_{(3)\theta\zeta}^\theta\| = \sum_{j=1}^5 \bar{\theta}_j^{(\theta)} Z^{j-1}, \\ \hat{C}_0^\theta(Z) &= \bar{C}_0^\theta(0.01, Z) = \|\bar{C}_{(0)\theta\zeta}^\theta\|, \\ Z &= 0.01\zeta, \zeta = 1, 2, \dots, 100. \end{aligned} \quad (76)$$

At the step  $\theta$  the solution of (64, 65) leads to:

$$\begin{aligned} A_1 \frac{d\bar{C}_1^\theta}{dZ} + \frac{dA_1}{dZ} \bar{C}_1^\theta &= \text{Pe}_1^{-1} \frac{d^2 \bar{C}_1^\theta}{dZ^2} - K_1 (\bar{C}_1^\theta - \bar{C}_2^\theta); \\ Z = 0, \bar{C}_1^\theta &\equiv 1, \frac{d\bar{C}_1^\theta}{dZ} \equiv 0. \end{aligned}$$

$$A_2 \frac{d\bar{C}_2^\theta}{dZ} + \frac{dA_2}{dZ} \bar{C}_2^\theta =$$

$$= \text{Pe}_2^{-1} \frac{d^2 \bar{C}_2^\theta}{dZ^2} + K_2 (\bar{C}_1^\theta - \bar{C}_2^\theta) - K_a \left( \bar{C}_2^\theta - \sum_{j=1}^5 \bar{\theta}_j^{(\theta)} Z^{j-1} \right);$$

$$Z = 0, \quad \bar{C}_2^\theta \equiv 0, \quad \frac{d\bar{C}_2^\theta}{dZ} \equiv 0. \quad (77)$$

The stop criterion is  $\theta=100$ .

The obtained results can be presented as:

$$\|\check{\bar{C}}_{(1)\theta\zeta}\| = \|\bar{C}_{(1)\theta\zeta}^{(\theta)}\|, \quad \|\check{\bar{C}}_{(2)\theta\zeta}\| = \|\bar{C}_{(2)\theta\zeta}^{(\theta)}\|,$$

$$\|\check{\bar{C}}_{(3)\theta\zeta}\| = \|\bar{C}_{(3)\theta\zeta}^{(\theta)}\|, \quad \|\check{\bar{C}}_{(0)\theta\zeta}\| = \|\bar{C}_{(0)\theta\zeta}^{(\theta)}\|;$$

$$\theta = 1, \dots, 100; \quad \zeta = 1, \dots, 100.$$

### CONCLUSIONS

The solutions of some theoretical problems of the column apparatuses modeling in the cases of one-, two- and three-phase processes are presented in the approximation of the mechanics of continua. In the cases of one-phase processes the effect of the radial non-uniformity of the velocity distribution, the effect of the tangential flow and the simultaneous mass and heat transfer processes are shown.

A possibility to obtain the interphase distribution of the mass transfer resistances in two-phase columns is shown.

The modeling of three-phase processes in column apparatuses is analysed. An iterative

numerical algorithm for non-stationary processes modeling is presented.

The presented approach is used for solution of the SO<sub>2</sub> problem in power engineering [14, 15].

### REFERENCES

1. Chr. Boyadjiev, *Int. J. HeatMass Transfer*, **49**, 796 (2006).
2. Chr. Boyadjiev, *Transactions of Academenergo*, **3**, 7 (2009).
3. Chr. Boyadjiev, Springer-Verlag, Berlin Heidelberg, 2010, p. 594.
4. M. Doichinova, Chr. Boyadjiev, *Int. J. HeatMass Transfer*, **55**, 6705 (2012).
5. Lietuvos Respublika, Patent No3884, 1994.
6. Chr. Boyadjiev, J. Merchuk, *Journal of Engineering Thermophysics*, **17** (2), 134 (2008).
7. Chr. Boyadjiev, *Int. J. HeatMass Transfer*, **49**, 2053 (2006).
8. K. Panayotova, M. Doichinova, Chr. Boyadjiev, *Int. J. HeatMass Transfer*, **52**, 543 (2009).
9. K. Panayotova, M. Doichinova, Chr. Boyadjiev, *Int. J. HeatMass Transfer*, **52**, 2358 (2009).
10. K. Panayotova, M. Doichinova, Chr. Boyadjiev, *Int. J. HeatMass Transfer*, **53**, 2128 (2010).
11. Chr. Boyadjiev, *Transactions of Academenergo*, **3**, 7 (2009).
12. Chr. Boyadjiev, *Theor. Found. Chem. Eng.*, **40**, 673 (2006).
13. Chr. Boyadjiev, *Int. J. HeatMass Transfer*, **54**, 3004 (2011).
14. Chr. Boyadjiev, M. Doichinova, P. Popova, *Transactions of Academenergo*, **2**, 44 (2012).
15. Chr. Boyadjiev, Proceedings, 15<sup>th</sup> Workshop on Transport Phenomena in Two-Phase Flow, Sunny Beach Resort, Bulgaria, Sept. 17-22, 2011, p. 125.

## ПРОБЛЕМИ ПРИ МОДЕЛИРАНЕ НА КОЛОННИ АПАРАТИ

Хр. Б. Бояджиев<sup>1</sup>, М. Д. Дойчинова<sup>1</sup>, Б. Хр. Бояджиев

<sup>1</sup>*Институт по инженерна химия, Българска академия на науките,  
ул. Акад. Ст. Ангелов, бл. 103, 1113 София*

Постъпила на 15 октомври 2013 г., преработена на 25 септември 2014 г.

(Резюме)

В приближенията на механиката на непрекъснатите среди са представени теоретични решения при моделирането на колонни апарати в случаите на една, две и три фази. Анализирани са ефектите от разпределението на радиалната неравномерност на скоростта, наличието на тангенциален поток, както и топло и масопреносните процеси в колона с една фаза. Показана е възможността за получаване на съпротивленията при междуфазно масопренасяне в колона с две фази. Представен е числен алгоритъм за моделиране на нестационарни процеси в колона с три фази.

## Kinetics of oxidation of sulfide ions in model solutions of sea water

N. Dr. Dermendzhieva\*, E. N. Razkazova-Velkova, V. N. Beschkov

*Institute of Chemical Engineering, Bulgarian Academy of Sciences, Sofia 1113, Bulgaria*

Received September 25, 2014; Revised November 18, 2014

The possibility of catalytic oxidation of sulfide ions from model solutions of seawater is studied. ZrO<sub>2</sub> catalyst incorporated into a matrix of activated carbon is synthesized. The surface of the catalyst is characterized by iodine adsorption. The effect of the deposited catalyst is studied. Experiments at different initial concentrations of sulfide ions and temperatures are conducted in two regimes - continuous aeration or stirring at the same speed without aeration. The reaction products in the case of continuous aeration are 90% of sulfate ions relative to the initial quantity of sulfides. The reaction products at stirring without aeration at the same temperatures are stable reducers that should not be dumped into the sea water. The oxidation in the regime of continuous aeration follows the kinetics of a first order reaction with relatively low activation energy.

**Keywords:** kinetics, oxidation, sea water, sulfide ions, ZrO<sub>2</sub> - catalyst

### INTRODUCTION

Hydrogen sulfide is common in some geothermal springs and closed deep water basins. Deep Black Sea waters contain significant amount of hydrogen sulfide [1,2]. This is the reason for the lack of aquatic life below a certain depth. The latest data show that the level of the "dead zone" is constantly rising. Different methods are used for catalytic decomposition of hydrogen sulfide to harmless products [3-6]. In many of them the end product is elemental sulfur [3]. However, elemental sulfur is undesirable because it inhibits the catalytic oxidation by blocking the active sites of the catalyst. Moreover, sulfur is not of particular interest as a commercial product and its back return into the Black Sea water is inappropriate from an environmental point of view. In the present work no elemental sulfur is formed in all experiments. The sulfates are the desirable product because they are naturally present in the sea water.

It is known according to the literature [2, 7] that Me<sup>2+</sup> cations (Me: Mn, Co, Ni, Fe, Cu) catalyze the process of sulfide to sulfate oxidation. As the reaction between the metals and the sulfide produces precipitates it is not preferable to add them in the form of salts. On the other hand, it is not environmentally acceptable to use large quantities of catalyst and dumping it into the water. The research for stable catalysts that can be subsequently incorporated into electrodes working under these conditions imposed synthesis of metal oxides incorporated in matrices of activated carbon.

A further advantage is that the activated carbon is also a catalyst in this case [8]. The principle of obtaining such catalysts includes impregnation of the initial organic material with a salt of the given metal and subsequent pyrolysis with simultaneous activation [9].

This study is part of collaborated efforts to clean the waters of the Black Sea by oxidation of the sulfide anions of the seawater. The aim of this work is to study the catalytic oxidation of the sulfide ions to sulfite and sulfate with high enough concentrations and yields. This goal requires the selection of a suitable catalyst, its optimal amount, as well as establishing the optimum conditions for the process.

### EXPERIMENTAL PART

#### *Experimental conditions*

The kinetics of the oxidation process of sulfide ions was investigated. In order to select the proper catalyst the experiments were carried out at room temperature and constant stirring speed. After the proper catalyst and its amount were chosen two types of experiments were carried out for determination of the kinetic parameters – by continuous aeration and by stirring at the same speed without aeration. The flow rate of the air was 120 l.h<sup>-1</sup> corresponding to 10 vvm. The experiments were carried out in a stirred cell at different temperatures (20, 30 and 60°C) maintained by a thermostat. The volume of the solution in the cell was 200 ml. A sketch of the experimental set-up is shown in Fig. 1.

\* To whom all correspondence should be sent.

E-mail: nastemi1@abv.bg



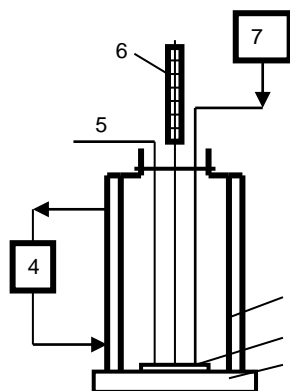


**Fig. 1.** Scheme of the experimental set-up. 1- thermostated cell; 2,3- magnetic stirrer; 4- thermostat; 5- sampling outlet; 6- thermometer; 7- aerator.

The experiments were carried out in model solutions imitating sea water prepared by dissolving NaCl to attain a concentration of  $16.5 \text{ g dm}^{-3}$ , corresponding to the Black Sea salinity (i.e.  $15\text{-}17 \text{ g dm}^{-3}$ ) [10, 11]. Sulfide was added by dissolving sodium sulfide nonahydrate ( $\text{Na}_2\text{S}\cdot 9\text{H}_2\text{O}$  reagent ACS  $\geq 98\%$ ) in the model sea water. The experiments were performed within the concentration range of sulfides  $25\text{-}120 \text{ mg dm}^{-3}$  which is 5-20 times higher than their actual concentration (i.e. between  $5$  and  $15 \text{ mg dm}^{-3}$ ) [2, 12].

The metal containing catalysts incorporated in a matrix of activated carbon were obtained according to [9]. The principle of the preparation of the catalysts on the carbon matrix consists of impregnation of the initial organic material with a metal salt - precursor and subsequent pyrolysis with simultaneous activation. The metal ions are in the form of oxides. The obtained catalysts incorporated in a matrix of activated carbon were characterized by iodine adsorption. The obtained specific surface area of the  $\text{ZrO}_2$  - catalyst is  $780.66 \text{ m}^2 \text{ g}^{-1}$ . The cobalt and manganese catalysts are spinel type oxides with 30 % concentration of the active components. The specific surface area of the Co - catalyst is  $897.98 \text{ m}^2 \text{ g}^{-1}$ .

The annually averaged ion content in the natural Black Sea surface water close to the Bulgarian coast is shown in Table 1 [13, p. 44].

**Table 1.** Data for the concentrations of major ions in the seawater.

Components	Content, ‰
Chloride	9.96
Sulfate	1.39
Hydrocarbonate	0.16
Carbonate	0.0204
Sodium	5.49
Magnesium	0.68
Calcium	0.269
Potassium	0.200

Samples from the reacting solution were taken periodically. The concentration of the total sulfur containing reducing substances was determined iodometrically. The sulfide ( $\text{S}^{2-}$ ) content was determined photometrically [14] and the presence of sulfate ions was detected qualitatively by addition of barium chloride solution. Sulfates were determined quantitatively by addition of barium chloride and back-titration of the excess of  $\text{Ba}^{2+}$  ions with EDTA using Eriochrom Black T as indicator.

## RESULTS AND DISCUSSIONS

While screening for the proper catalyst four types of metal oxides incorporated into an activated carbon matrix were investigated. The use of the activated carbon from the same origin was also studied. The results are shown in Fig.2. The oxidation rate for the non-catalyzed process at the same conditions is given for comparison. The initial concentration was chosen to be  $65 \text{ mg l}^{-1}$  because at this concentration there is no retard of the oxidation rate due to parallel processes [8,12]. The amount of the catalyst was the same ( $0.5 \text{ g l}^{-1}$ ) for all experiments.

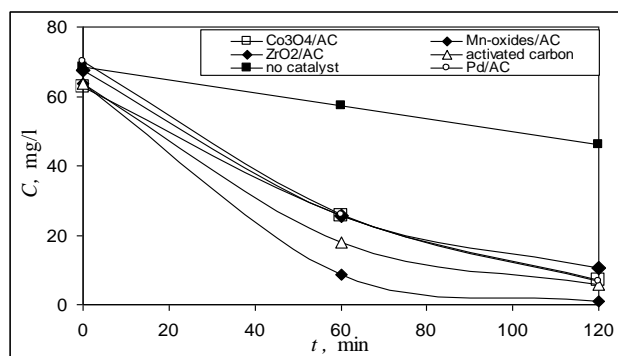


**Fig. 2.** Influence of the type of catalyst on the oxidation rate. AC means activated carbon.

Figure 2 shows that the oxidation of sulfide ions without catalyst is slow (about 10 % reduction of the sulfide ions in the first sixty minutes). The addition of the catalyst into the reactor volume leads to a considerable acceleration of the process (from 50 to 90% reduction of the sulfide ions in the first sixty min). The effect of the  $\text{Co}^{2+}$ ,  $\text{Mn}^{2+}$  and  $\text{Pd}^{2+}$  catalysts was comparable and the activated carbon also had good catalytic activity. As a catalyst for the further experiments  $\text{ZrO}_2$  was used, because it provided the highest oxidation rate (by 40% higher than all other metal catalysts).

The influence of the initial concentration of sulfide at the same amount of catalyst was investigated and the results are shown in Fig. 3.

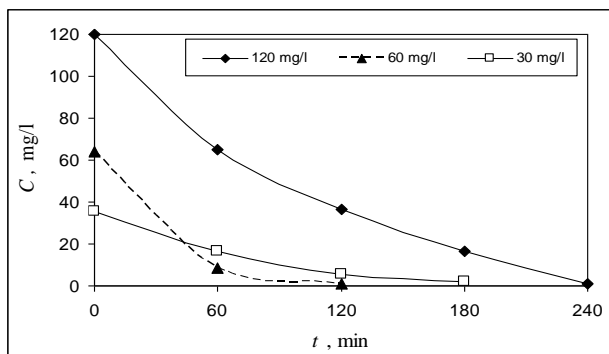


**Fig. 3.** Influence of the initial concentration of sulfide on the rate of oxidation at the same amount of  $ZrO_2$  catalyst.

It appears that at low and high concentrations, 50% of the sulfides are oxidized for 1 hour while at  $60\text{ mg l}^{-1}$  the oxidation rate is 90%. The reason for the low rate of oxidation is probably the accumulation of intermediates, competitive reaction or catalyst poisoning by the intermediates, e.g. elemental sulfur. Therefore a concentration of about  $60\text{--}70\text{ mg l}^{-1}$  was found suitable for conducting the process.

The influence of the  $ZrO_2$  catalyst on the rate of oxidation of sulfide ions at an initial concentration of  $65\text{ mg l}^{-1}$  was investigated (Fig.4).

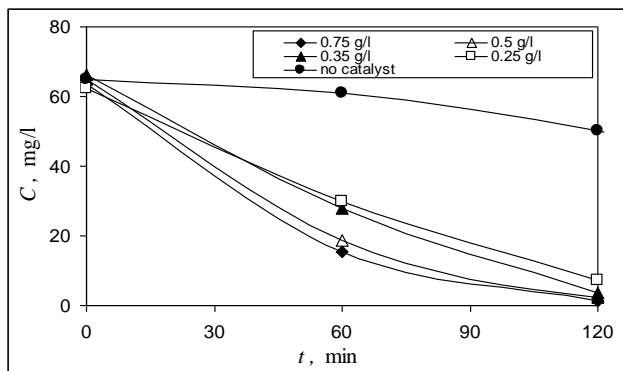


**Fig. 4.** Influence of the amount of  $ZrO_2$  catalyst on the oxidation rate at initial concentration of  $60\text{ mg l}^{-1}$ .

The optimum amount of  $ZrO_2$  catalyst which provided a satisfactory rate of oxidation was  $0.75\text{ g l}^{-1}$  as shown in Figure 4. In the further experiments a catalyst amount of  $0.5\text{ g l}^{-1}$  was used which provided a rate of oxidation comparable to that of  $0.75\text{ g l}^{-1}$  of catalyst. The oxidation rate was low with a lower amount of catalyst and did not change significantly at a higher amount.

The catalyst was characterized by X-ray analysis in order to establish the proper crystallographic structure (Fig.5).

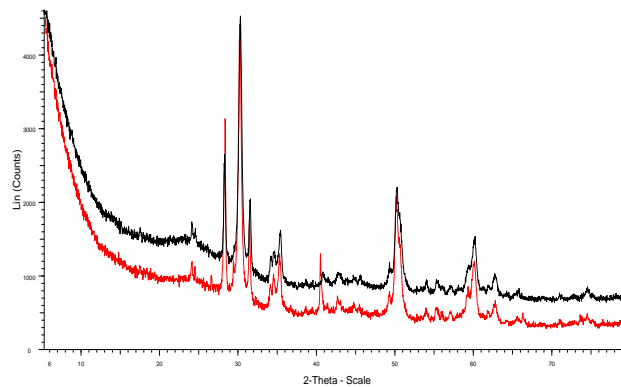


**Fig. 5.** XRD patterns of the  $ZrO_2$  catalyst before (upper X-ray gram, black) and after sulfide oxidation process (lower X-ray gram, red).

The  $ZrO_2$  is in monoclinic and tetragonal form. Comparison before and after conducting the oxidation process is also shown in Fig.5. As it can be seen, the structure and the composition of the catalyst are the same before and after performing sulfide oxidation. This means that there is no transformation of its surface.

A comparison of the oxidation rates for both regimes at  $120\text{ mg l}^{-1}$ , and different temperatures is presented in Fig.6.

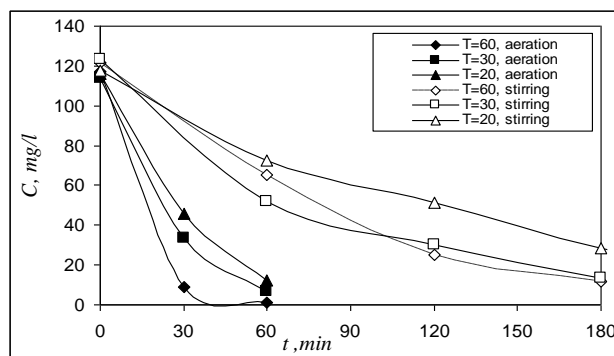


**Fig. 6.** Oxidation rates at different aeration rates and stirring.

It shows that the process at constant stirring is about 2 times slower than that with aeration. For this reason the kinetic parameters for aeration were derived for concentrations  $120\text{ mg l}^{-1}$ ,  $200\text{ mg l}^{-1}$ , and those with stirring - at  $60\text{ mg l}^{-1}$  and  $120\text{ mg l}^{-1}$  and temperatures  $20, 30, 60\text{ }^\circ\text{C}$ .

The oxidation with aeration follows the kinetics of first order reaction with rate constants  $k = 0.0269\text{ min}^{-1}$  for  $20\text{ }^\circ\text{C}$ ,  $k = 0.0358\text{ min}^{-1}$  for  $30\text{ }^\circ\text{C}$ ,  $k = 0.0813\text{ min}^{-1}$  for  $60\text{ }^\circ\text{C}$ .

$$\frac{dC}{dt} = kC$$

The Arrhenius plot for the studied reaction is presented on Fig.7.

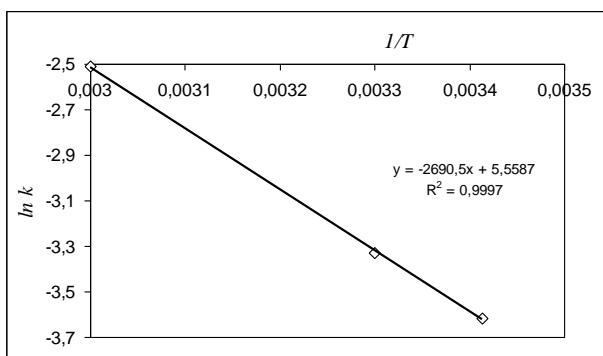


**Fig. 7.** Arrhenius plot for the reaction with zirconia containing catalyst.

The reaction products are 90% of sulfate ions relative to the initial quantity of sulfides. Since sulfate ions are naturally present in seawater they can be fed back into it without harming the environment, restoring the sulfur cycle. Based on the experimental data obtained from the kinetic curves, the apparent activation energy of the reaction was calculated as 22 kJ mol<sup>-1</sup>.

In the second case with continuous stirring at constant speed for the same temperatures the reaction products were stable reducers which were determined iodometrically and should not be dumped into the sea water. The obtained rate constants are not alike for the different concentrations, i.e. the process is limited by the amount of dissolved oxygen in the cell. Therefore, in this case the Arrhenius dependence does not fit the experimental data properly.

### CONCLUSION

Best results for sulfide to sulfate oxidation were obtained when using ZrO<sub>2</sub> as a catalyst embedded into charcoal.

The optimum amount of ZrO<sub>2</sub> catalyst which provides a satisfactory oxidation rate is 0.5 g l<sup>-1</sup>. The oxidation rate of the sulfide ion is relatively high up to a concentration of 60-70 mg l<sup>-1</sup>.

In all experiments no elemental sulfur was observed. In the case of continuous aeration the sulfide conversion into sulfate was over 90% according to the initial sulfide concentration, whereas at continuous stirring without aeration the products of the reaction were stable reducers but no sulfate was obtained.

The oxidation follows the kinetics of a first

order reaction with relatively small activation energy – 22 kJ mol<sup>-1</sup>.

**Acknowledgment:** This work was accomplished within the project HYSULFCELL supported by the program BS-ERA.NET (FP7 of the European Union), grant of the Ministry of Education, Youth and Science (contract DNS7RP 01/32/2011), Republic of Bulgaria.

### REFERENCES

1. A. Demirbas, Energy Sources, Part A: Recovery, Utilization, and Environmental Effects, Volume 31, Issue 20, 1866-1872, 2009.
2. U.S. National Research Council, Hydrogen sulphide. Committee on Medical and Biologic Effects of Environmental Pollutants, Subcommittee on Hydrogen Sulphide. University Park Press, Baltimore, MD, 1979.
3. P. K. Dutta, K. Rabaey, Zh. Yuan, J. Keller, *Water Research* **42**, 4965 (2008).
4. B. G. Ateya, F. M. Al-Kharafi, R. M. Abdallah, A. S. Al-Azab, *Journal of Applied Electrochemistry* **35**, 297 (2005); DOI 10.1007/s10800-004-7273-6.
5. S. Ouali, S. Chader, M. Belhamel, M. Benziada, *Int. J. Hydrogen Energy*, **36**, (2011).
6. R.E. Linga, V.M. Biju, Ch. Subrahmanyam, *Int. J. Hydrogen Energy*, **37**, 2204 (2012).
7. A. Goifman, J. Gun, F. Gelman, I. Ekeltchik, O. Leva, J. Donner, H. Börnick, E. Worch, *Appl. Catalysis B: Environmental*, **63**, 296 (2006).
8. N. Dermendzhieva, E. Razkazova-Velkova, M. Martinov, L. Ljutzkanov, V. Beschkov, *J. Chem. Technol. Metallurgy*, **48**, 465 (2013).
9. L.A. Ljutzkanov, Method for Treatment of Carbon – Containing Materials, *BG patent* № 63594 /26.06.2002.
10. P.J. Mudie, A. Rochon, A.E. Aksu, H. Gillespie, *Marine Geology*, **190**, 203 (2002).
11. S.P. Young, T.I.J. Smith, J.R. Tomasso, *Aquaculture*, **258**, 646 (2006).
12. E. N. Razkazova-Velkova, M. S. Martinov, L. A. Ljutzkanov, N. Dr. Dermendzhieva, V. N. Beschkov, *J. Internat.Sci. Publi.: Materials, Methods & Technologies*, **7**, Part 1, ISSN 1313 (2013).
13. A. Rozhdestvenskiy, Hydrochemistry of the Bulgarian Sector of the Black Sea (in Bulgarian), BAS Publishing House, Sofia, 1986, p. 33.
14. T. D. Rees, A. B. Gyllenpetz, A. C. Dochery, *Analyst*, **96**, 201 (1971).

## КИНЕТИКА НА ОКИСЛЕНИЕТО НА СУЛФИДНИ ЙОНИ ОТ МОДЕЛНИ РАЗТВОРИ НА МОРСКА ВОДА

Н. Др. Дерменджиева\*, Ел. Н. Разказова – Велкова, В. Н. Бешков

*Институт по инженерна химия – Българска Академия на Науките, София 1113, България*

Постъпила на 25 септември, 2014 г.; Коригирана 18 ноември, 2014 г.

(Резюме)

Изследвано е каталитичното окисление на сулфидни йони от моделни разтвори на морска вода. Синтезиран е  $ZrO_2$  катализатор, инкорпориран в матрица от активен въглен. Повърхността на катализатора се охарактеризира чрез адсорбция по йод. Експериментите са проведени при различни начални концентрации на сулфидните йони и температури. Работено е при два режима на работа – непрекъсната аерация и разбъркване при едни и същи обороти без аерация. Продуктите на реакцията при процес с непрекъснато аериране са 90 % сулфатни йони, стехиометрично изчислени спрямо първоначалното количество сулфиди. Реакционните продукти при същите условия, но при процес с разбъркване, без аерация, са стабилни редуктори и са неприемливи от екологична гледна точка като крайни продукти. Окислението на сулфидни йони в режим на непрекъснато аериране следва кинетика на реакция от първи порядък с относително малка активизираща енергия.

## Analysis in terms of environmental awareness of farmers' decisions and attitudes in pesticide use: the case of Turkey

H. Yilmaz\*

*Department of Agricultural Economics, Faculty of Agriculture, Süleyman Demirel University, Isparta, Turkey.*

Received January 25, 2014, Revised October 12, 2014

The aim of this study was to analyze in terms of environmental consciousness farmers' decisions and attitudes in pesticide use. Data were obtained from melon growers of the villages of Cankiri Province of Turkey. The farms were chosen by the random sampling method. Chi-square test ( $\chi^2$ ) was used for analyzing the relationships between some selected socio-economic characteristics and the decisions and attitudes in pesticide use. The decision-making of pesticide application time showed significant relationships between the information sources used by the farmers, their age, education and farm size. A relationship was also found between the information sources used by the farmers and their experience in identifying diseases or insect pest. An intensification of extension services to educate farmers on safe use of pesticides in melon production is recommended. A communication gap between the farmers and research centers was established. Extension programs, brochures and field visits are the sources of information that farmers rely on.

**Keywords:** environmental awareness, pesticide use decisions, attitudes, Turkey

### INTRODUCTION

Vegetable cultivation is one the most economically important and dynamic branches of agriculture. It has become an important source of income for both farmers and field laborers, serving as a vehicle for reducing poverty in rural areas. At the same time, vegetable cultivation is becoming more costly due to the increased use of purchased inputs, such as pesticides and fertilizers, to sustain production levels. If used improperly, many of these inputs have deleterious effects on human health and environment.

Vegetable farmers use a wide range of pesticides at different levels to reduce losses from pests and diseases. However, despite the contribution of pesticides to agricultural production, evidences in the last few decades have shown that they could also be detrimental to human health and the ecosystem. [1]

Pesticides have substantially contributed to control pests and increase crop yields in meeting the food demand of escalating population and control of diseases. Exposure to pesticides is one of the most important occupational risks among farmers in developing countries. [2,3]

Pesticide usage is inevitable in modern agriculture. However, both crop protection against pests and diseases and human health and environment should be considered in pesticide treatments. Excessive use

of pesticides has shown negative effects on the environment and human health. [4] The environmental effects include damage to agricultural land, fisheries, fauna and flora. Increased mortality and morbidity of humans due to exposure to pesticides are also recorded, especially in several developing countries. [5] In developed countries, old techniques have been replaced by new systems that are based on minimum use of chemical ingredients and new pesticides that are less persistent in the environment. On the other hand, farmers in developing countries still use classic pesticides that are cheaper but carry more risks for the environment and health. [6] In developing countries, from the viewpoint of farmers, pesticides continue to be regarded both as a guarantee against crop loss, for maximum efficiency to be gained from cultivation. [7]

Agricultural and rural development for many developing countries depends on modern technologies and innovations proposed by research institutes and universities, or imported by developed countries. Two key factors may play major role on the use of technology by farm operators; one of them is the availability of public or private organizations disseminating recent innovations to rural areas; and the other factor is farm operators' socio-economic characteristics and information seeking behavior influencing their decisions for using information sources. [8] Agricultural development achieved through these initiatives also created an interest on the use of

\* To whom all correspondence should be sent:  
E-mail: hasanyilmaz@ziraat.sdu.edu.tr

sophisticated chemical input and technologies to replace old traditional agriculture with modern high input based agriculture.

This paper focuses on the analysis of farmers' information sources as the most important factor in pest management. This study examines to which information sources farmers resorted for the use of pesticides and how they got the decisions regarding the use of sources of information. The analysis was focused on comparing the characteristics of farmers using both modern and traditional information sources. In addition, farmers' pest management practices, attitudes and decisions about pesticide use and the resulting effects on the environment were discussed.

## MATERIALS AND METHODS

In this study, the central district of Cankiri province and the eleven villages of Kızılırmak were selected considering the distances from the district center, agricultural potential, population intensity, and socio-economic characteristics of the villages. Taking farm size as the criterion, and using [9] stratified sample size determination formula, 87 farmers were chosen for sample data collection. In the study a questionnaire developed by a panel of experts was used. The survey was conducted in October 2009. Data were collected through face to face interviews with farmers at their farms. In Cankiri Province, the mean annual rainfall, humidity and temperature are 397 mm, 63.7 % and 22 °C, respectively.

For this analysis, information sources were divided into two categories such as information acquired from modern sources and traditional sources. Modern sources included extension agents, farmer cooperatives, input dealers, mass media, and the internet. Traditional sources, on the other hand, included information coming from farmers' own personal experience, own family members, and neighbor farmers.

Contingency tables were prepared to evaluate the association between the variables and Chi-square test <sup>[10]</sup> ( $\chi^2$ ) was used to analyze the relationships between the socio-economic variables. Age of the farmer's (AGE), was categorized as: (20-40), (41-60), (61 and over) According to educational level (ED), farmers were grouped as: primary school (5 years), secondary school (8 years), and high school (11 years). None of the respondents in the sample had any university degree.

According to farmer's experience (FE), the grouping was: (less than 10 years), (between 11-20 years), (21 years and over)

According to the size of melon production (MPS), the grouping was: (1-10 decare), (11-20 decare), (21 and more decare)

According to farm size (FS) the grouping was: (1-50 decare), (51-100 decare), (101 and more decare)

## RESULTS AND DISCUSSION

### Basic characteristics of farms

The average age of farmers was 47.59 years and the average experience of farmers in agriculture was 27.75 years. Their average years of education were 6.34. The average size of the farms was 119.41 decare. The average melon production area was 16.55 decare.

**Table 1.** General characteristics of surveyed farms

Component	mean	St. d.
Farm size (decare)	119.41	73.19
Melon production area (decare)	16.55	13.15
Farmer's age (years)	47.59	12.83
Farmer's experience (years)	27.75	14.03
Farmer's education (years)	6.34	2.46

A decare is 1.000 square meters; 10 decares is 1 hectare.

### Most common pesticides used by melon farmers

A common way of summarizing pesticide use is by summing the pounds of active ingredient for all pesticides used. This allows for some aggregation of the numerous pesticide products used in agriculture. Using conversion factors it is quite simple to summarize pesticides with common active ingredients in terms of kilograms of that active ingredient.[11] In the study area, the most commonly used trade names and active ingredients are listed in Table 2. The pesticide commonly used by the farmers was identified as Fenthion (86.21 % of the farmers). Other pesticides used were Chlorpyrifos ethyl (18.39%) and Diazinon (2.30%). This is an indication that pesticides play an important role in the control of pests and for increasing crop yields. [12]

**Table 2.** Pesticides used by melon farmers in Cankiri province.

Trade Name	Active ingredient	*Frequency	Percentage
Lebaycid EC 50	Fenthion	75	86.21
Dursban 4	Chlorpyrifos ethyl	16	18.39
Basudin 60 EM	Diazinon	2	2.30

\* Multiple responses

### Opinions of farmers on pesticide application and their information sources and attitudes

Data presented in Table 3 indicate the attitudes and opinions of farmers in pesticide application. Farmers have used traditional information sources

as main information sources for deciding pesticide application time (72.41%), identifying the disease or insect pest (62.07%), pesticide choice (49.43%) and pesticide application dosage (70.11%). This means that farmers used more information from farmers' own personal experience, own family members, and neighbor farmers. As the table shows, the rate of farmers who exactly fulfilled the instructions was 74.71%. The reason for this is that farmers consider excessive pesticide as harmful for the crops. Despite this fact, 25.29% of the farmers stated that sometimes they use more or less than the recommended dosage. Most of the farmers who use more than the recommended dosage assume that resistance might be developed against pesticide by pests and suggested dosage might be ineffective in this region.

Table 3 shows farmers' answers to the question whether to leave or not residues harmful to human health on the crops. While 31.03% of farmers stated no opinion on the issue, approximately two third of them (68.97%) declared may leave harmful residues of some pesticides on the crops.

Table 3 shows farmers' answers to whether there are harmful effects of pesticides on the environment and human health. While 85.06% of the farmers stated that excessive and incorrect pesticide application will harm environment and human health, 14.94% of the farmers considered no damage.

Disposal of empty containers was also an important issue of environmental and health concern. Therefore, the utilization of empty pesticide containers after application was also examined. 51.72% of the farmers were throwing the empty containers to the environment carelessly, while 48.28% buried the packages in the ground after applying the pesticide (Table 3).

Table 4 shows the chi-square ( $\chi^2$ ) test of relationships between attitudes and opinions of farmers in pesticide application and their selected socio-economic characteristics.

In addition, relationships were looked for between information sources used by farmers on pesticide use and farmer's age, education, experience, melon production area and farm size. For education, experience, and melon production area there was no statistically significant relationship. Age and farm size were found statistically significant ( $p < 0.05$ ).

No statistically significant relationship was found between pesticide choice, pesticide application dosage and compliance recommended with farmer's age, education, experience, melon production area and farm size ( $p > 0.05$ ). No

statistically significant relationship was found between identifying the disease or insect pest and farmer's age, education, melon production area and farm size ( $p > 0.05$ ). However, farmer's experience was a statistically significant factor ( $p < 0.01$ ). Farming experience was also found to have significant influence on farmers' pesticide applications. The reason for this can be attributed to the experiences gained in the past by farmers on pesticide hazards.

The opinions of farmers on harmful residues of pesticides were compared in terms of farmer's age, education, experience, melon production area, and farm size. Statistical analysis (chi-square test,  $p > 0.05$  there is not any association) indicated that farmers' opinions regarding harmful residues of pesticides do not have any impact on selected socio-economic characteristics. The opinions of farmers about the environmental and human health harm of pesticides were compared with the farmer's age, education, experience, melon production area, and farm size. Results of statistical analysis indicated that there was a relationship between farmer's age, education and experience variables (chi-square test,  $p < 0.05$  and  $p < 0.01$ ). Chi-square results pointed to a significant association between age variable and farmers' opinions. This means that about the environmental hazards of pesticides due to accumulated knowledge and experience of farming systems, the elder farmers are much better perceived compared to the young farmers.[1] Education had also a significant influence on farmers' opinions. This might be due to the ability of the literate farmers to read and follow the instructions on pesticides containers. But no statistically significant relationship was found between melon production area and farm size ( $p > 0.05$ ). We also analyzed whether or not there is an association between destruction methods for pesticide packages and farmer's age, education, experience, melon production area, and farm size. No statistically significant relationship was found between destruction methods used by farmers for pesticide packages with selected socio-economic characteristics ( $p > 0.05$ ).

## CONCLUSION

The study shows that melon farmers use traditional information sources more than modern sources for decisions and attitudes on pesticide use. Farmers used traditional information as main information sources for deciding on pesticide application time (72.41%), identifying the disease or insect pest (62.07%), pesticide choice (49.43%) and pesticide application dosage (70.11%)

**Table 3.** Information sources on pesticide management practices

Attitudes and Opinions of Farmers on Pesticide Application	A		B	
	N	%	N	%
Decisions on pesticide application time (DPAT)	63	72.41	24	27.59
Identifying the disease or insect pest (IDIP)	54	62.07	33	37.93
Decisions on pesticide choice (DPC)	43	49.43	44	50.57
Decisions on pesticide application dosage (DPAD)	61	70.11	26	29.89
<i>A: traditional information sources; B: modern information sources</i>				
Compliance with recommended dosage (CRD)	C		D	
	N	%	N	%
	65	74.71	22	25.29
<i>C: recommendations exactly implemented; D: recommendations not exactly implemented</i>				
Farmers' opinions about the residues of pesticides used. (FORPU)	E		F	
	N	%	N	%
	27	31.03	60	68.97
<i>E: I have no information about the problem of left residuals of pesticides on the products</i>				
<i>F: Some pesticides may leave residuals</i>				
Farmers' opinions about the environmental and human health harm of pesticides used (FOEHPU)	G		H	
	N	%	N	%
	74	85.06	13	14.94
<i>G: Pesticides are harmful to environment and human health;</i>				
<i>H: Pesticides are not harmful to environment and human health</i>				
Destruction methods used by farmers for pesticide packages (DMFPP)	I		J	
	N	%	N	%
	45	51.72	42	48.28
<i>I: Throwing packages to the environment carelessly after applying pesticide;</i>				
<i>J: Destroying the packages by burning and burying the packages in the ground after applying pesticide</i>				

**Table 4.** Results of chi-square ( $\chi^2$ ) test showing associations between attitudes and opinions of farmers in pesticide application and selected socio-economic characteristics of the farmers

Attitudes and Opinions of Farmers	AGE		ED		FE		MPS		FS	
	$\chi^2$	P	$\chi^2$	P	$\chi^2$	P	$\chi^2$	P	$\chi^2$	P
$\chi^2$ (df=2, N=87)										
DPAT	7.284	0.026*	1.919	0.383	1.182	0.554	3.403	0.182	6.535	0.038*
IDIP	3.468	0.177	5.304	0.071	8.972	0.011**	0.230	0.891	4.164	0.125
DPC	1.532	0.465	2.052	0.358	5.245	0.073	1.280	0.527	5.371	0.068
DPAD	1.300	0.532	1.495	0.474	1.812	0.404	0.290	0.865	1.127	0.569
CRD	4.697	0.096	0.884	0.643	0.833	0.639	0.128	0.938	0.832	0.660
FORPU	5.636	0.060	3.197	0.202	4.615	0.100	2.934	0.231	0.079	0.961
FOEHPU	8.351	0.015*	7.883	0.019*	10.095	0.006**	3.594	0.166	4.046	0.132
DMFPP	2.182	0.336	0.707	0.702	5.206	0.074	0.244	0.885	0.018	0.991

\*  $p < 0.05$ , \*\* $p < 0.01$ ; Variables; Age of farmers (AGE), Education level (ED), Farmer's experience (FE), Melon production size (MPS), Farm size (FS)

Other factors that may influence the use of farmers' information sources as age, education, farm size, and farmers' experience were found to significantly affect the decision to use information sources.

The decisions on pesticide application time by farmers revealed positively significant associations between farmers' age, farm size and the used information sources. There were significant relationships between their experience and the information sources used for identifying the disease or insect pest. Furthermore, there were significant associations between farmer's age, education and farmers' experience and their opinions on the

environmental and human health harm of pesticides.

Therefore, the ideas of farmers on environmental issues should be taken into consideration before deciding agro-environmental policies. Survey results showed that melon growers need more information about technical issues. The significant influence of information sources on farmers' pesticide management is indicative that extension systems must be strengthened to increase farmers' knowledge and understanding of the effects of pesticides on the environment.



REFERENCES

1. R. G Adeola, *Global Journal of Science Frontier Research Agriculture & Biology*, **12** (4), (2012).
2. F. Konradsen, W. Van der Hoek, D. C. Cole, Hutchinson, G. Daisley, S. H. Singh, M. Eddleston, *Toxicology*, **192**, 249 (2003).
3. G. D. Coronado, B. Thompson. L. Strong. W. C Griffith, I. Islas, *Environmental Health Perspectives*. **112**,142 (2004).
4. E. Lichtenberg, R. Zimmerman, *Risk Analysis*, **19**(2), 283 (1999).
5. C. Wilson, C. Tisdell, *Ecological Economics*, **39**(3), 449 (2001).
6. F. P. Carvalho, *Environmental Science & Policy*, **9**, 685 (2006).
7. P. Pingali, R.V. Gerpacio, *Food Policy*, **22** (2), 107 (1997).
8. İ. Boz, O. Ozcatalbas, *African Journal of Agricultural Research*, **5** (10), 980 (2010).
9. T. Yamane, Elementary sampling methods (Turkish translation). Literature Yayincilik, Dagitim Pazarlama Sanayi ve Ticaret Ltd. Sti, Istanbul, 2001.
10. M.Koseoglu, R. Yamak,. Uygulamalı İstatistik. Celepler Matbaacılık, 3. Baskı. Trabzon (Tr), 2008.
11. G.K Agnew, P. B. Baker, The University of Arizona Cooperative Extension Service publication series. **257** (2000).
12. N. Mahantesh, S. Alka, *Agricultural Science*, **32**, 63 (2009).

## АНАЛИЗ НА ЕКОЛОГИЧНО СЪОБРАЗЕНИТЕ РЕШЕНИЯ НА ФЕРМЕРИТЕ В ТУРЦИЯ ЗА УПОТРЕБАТА НА ПЕСТИЦИДИ

Х. Йилмаз

*Департамент по агрономическа икономика, Агрономически факултет, Университет „Сюлейман Демирел“,  
Испарта, Турция*

Постъпила на 25 януари, 2014 г.; коригирана на 12 октомври, 2014 г.

(Резюме)

Целта на тази работа е да се анализират от гледна точка екологичното съзнание решенията и отношението на фермерите за употребата на пестициди. Данните са събрани от гледачи на пълеши от делата в провинция Джанкири в Турция. Фермите са подбрани на случаен принцип. Използван е  $\chi^2$ -критерия за анализ на връзките между някои подбрани социо-икономически характеристики и решенията спрямо употребата на пестициди. Взимането на решения за прилагането на пестициди показва значителна зависимост между информационните източници, използвани от фермерите, тяхната възраст, образование и размер на фермата. Освен това е намерена връзка между използваните информационни източници и опита на фермерите за определяне на болести и насекоми-вредители. Препоръчва се информационна кампания за образование на фермерите за безопасна употреба на пестициди. Установена е празнота в комуникацията между фермерите и изследователските центрове.

## Effect of $\text{H}_3\text{BO}_3$ and $\text{Na}_3\text{citrate}$ on the conditions of electrodeposition of Ni-Co alloy from citrate electrolyte

K. Ignatova

UCTM – Sofia, Department of Electrochemistry

Received February 25, 2014, Revised March 5, 2015

The article reports the results from the examination on the effect of background additive ( $\text{H}_3\text{BO}_3$ ) and complexation agent  $\text{Na}_3\text{citrate}$  on the type of Ni and Co complexes at either pH=5.0 or pH=7.0. It is found that at pH=5.0 in an electrolyte containing both additives,  $\text{NiCit}^-$  and  $\text{CoCit}^-$  prevail ( $\lg K_{\text{inst}(\text{Ni})} = -5,379$ ;  $\lg K_{\text{inst}(\text{Co})} = -4,38$ ). At pH=7.0, simultaneously with  $\text{NiCit}^-$ , complexes of the type  $\text{NiCit}_2^{4-}$  and  $\text{CoCit}_2^{4-}$  with a lower constant of unsteadiness are also formed ( $\lg K_{\text{inst}(\text{Ni})} = -8,193$ ;  $\lg K_{\text{inst}(\text{Co})} = -7,103$ ).

It was found that the simultaneous presence of  $\text{H}_3\text{BO}_3$  and  $\text{Na}_3\text{citrate}$  results in increased buffer capacity of the electrolyte compared to that containing the complexation agent ( $\text{Na}_3\text{citrate}$ ) only and increases the rate of deposition of Ni and decreases that of Co, which is beneficial for alloy formation. It is proved through SEM images that the addition of  $\text{H}_3\text{BO}_3$  results in formation of needle-shaped crystals up to 500 nm, as the share of crystals of dimensions below 100 nm increases above 50%. This additive also leads to an increase in the Ni content in the Ni-Co alloy at comparable conditions.

**Key words:** buffer capacity, potentiometry, cyclic voltammetry, morphology of alloys.

### INTRODUCTION

The Ni-Co alloys have been examined for several decades for their unique properties: hardness, wear resistance, heat conductivity [1], electrocatalytic activity [2], as well as for their magnetic properties, whence they are widely used in production of sensors, inductors, recording devices [3].

The choice of electrolyte depends on the intended use of the coating and the associated requirements for its properties. The more important electrolytes for deposition of high quality Ni-Co coatings are sulfamate electrolyte [4] and sulfate electrolyte, chloride electrolyte [3, 5], Watts-type bath [6]. The latter includes boric acid as additive and is recommended for preparation of coatings with low internal tensions.

Both the citrate electrolytes and phosphate electrolytes have a lot of advantages for preparation of coatings with good quality, high content of Ni and high usability of current [7]. Although some disadvantages of those electrolytes are indicated in the reference sources, i.e. low conductance and low stability [7, 15, 19], their obvious advantages in terms of quality of the obtained coatings support the interest in them [8-14]. The citrate electrolytes exhibit complex properties of bleaching [8],

structure-defining [9], and buffering [10] agents. The buffering and complexation impacts of the citrate ions are applied in electroless deposition of nickel [11], as well as in electrodeposition of Fe-alloys [12], Ni-W [13] and Cu-Ni alloys [14]. The issue with the use of citrate electrolyte is its instability [15]. It is found in case of electrodeposition of Cu-Ni alloy that the electrolytes with pH<4 are unstable. In an electrolyte with pH  $\approx$  6, soluble  $\text{NiCit}^-$  complexes are formed ( $\lg K_{\text{inst}} = -5.35$ ), as the solution remains stable for a few weeks and can be used for deposition of Cu-Ni alloys at almost 100% usability of current [15]. Some authors have obtained very helpful results for the values of the stability constants of nickel [16] and cobalt [17] with the citrate ions. Thus, according to [16], at pH<4.5 the forms  $\text{Ni}^{2+}$  and  $\text{NiHCit}^-$  prevail in citrate solutions, correspondingly the forms being  $\text{Co}^{2+}$  and  $\text{CoHCit}^-$  [17] in the case of cobalt. When pH increases to 5÷6,5, ions of the type  $\text{NiCit}^-$  ( $\lg K_{\text{st}} = 5.35$ ) are present, correspondingly  $\text{CoCit}^-$  ( $\lg K_{\text{st}} = 4.63$ ) [17]. According to another source [15], when pH increases to about and above 7, complexes of the type  $\text{NiCit}_2^{4-}$  ( $\lg K_{\text{st}} = 8.11$ ) are formed, as increasing the share of less soluble forms like  $\text{Ni}(\text{OH})\text{SO}_4^-$  is also possible.

The conclusion from the review of the literature suggests that the electrodeposition of Ni-Co alloy in

\* To whom all correspondence should be sent:  
E-mail: katya59ignatova@gmail.com

presence of each of H<sub>3</sub>BO<sub>3</sub> and Na<sub>3</sub> citrate is widely investigated and discussed in the literature but there are fewer and incomplete data for their joint influence on the electrodeposition of Ni-Co. That is why we set the goal in this paper to investigate the joint effect of H<sub>3</sub>BO<sub>3</sub> and Na<sub>3</sub> citrate on the complexation of Ni and Co, as well as their buffer effect on the kinetics of deposition of the metals.

## EXPERIMENTAL DETAILS

The experimental research is carried out in a three-electrode cell of total volume 150 dm<sup>3</sup> at room temperature (18-20° C). In order to examine the kinetics of deposition, we used disk-shaped cathodes of electrolytic copper (by kinetics examination), Ni-plated and Co-plated copper (by the potentiometric method) with surface area of 1 cm<sup>2</sup>. The surface of the platinum anode is ≈ 30 times larger than that of the working electrode. Saturated calomel electrode (SCE) is used as a comparative electrode (E<sub>SCE</sub> = 0.241 V). The surfaces of the copper cathodes are prepared beforehand through polishing, etching in especially prepared etching solution for copper, and washing with double distilled water. Prior to each experiment, the anode is cleaned in hot 1M HNO<sub>3</sub> and then is washed with water. The impact of H<sub>3</sub>BO<sub>3</sub> and Na<sub>3</sub> citrate on the kinetics of deposition of Ni and Co is examined on the following compositions of electrolytes:

**For cobalt:** **1:** 0.2M Co (as CoSO<sub>4</sub>·7H<sub>2</sub>O), background of 0.2 M Na<sub>3</sub> citrate (as Na<sub>3</sub> citrate. H<sub>2</sub>O) and 0.485M H<sub>3</sub>BO<sub>3</sub>; **2:** 0.2M Co, background of 0.2M Na<sub>3</sub> citrate; **3:** 0.2M Co, background of 0.485M H<sub>3</sub>BO<sub>3</sub>.

**For nickel:** **1\*:** 0.2M Ni (as NiSO<sub>4</sub>·2H<sub>2</sub>O), background of 0.2 Na<sub>3</sub> citrate, M and 0.485M H<sub>3</sub>BO<sub>3</sub>; **2\*:** 0.2M Co, background of 0.2M Na<sub>3</sub> citrate; **3\*:** 0.2 M Co, background of 0.485M H<sub>3</sub>BO<sub>3</sub>.

The data for the buffering behavior of each solution were obtained through pH-metric titration and building the dependencies pH-V<sub>0,5MNaOH</sub>.

The constants of instability of the citrate complexes of Ni and Co were determined through application of a potentiometric method, whilst having in mind that this method does not yield precise data regarding the internal mechanism of building complexes. The potentiometric method is based on measurement of equilibrium potentials of the working electrodes (Ni-plated copper for Ni-electrolytes and Co-plated copper for Co-electrolytes, thickness of 4-5 μm) both in presence and in absence of complexation agent, i.e. citrate ion introduced as Na<sub>3</sub> citrate with increasing

concentration (0.0M; 0.1M; 0.2M; 0.3M and 0.4M). The difference ΔE<sup>k-o</sup> between the potentials in presence and in absence of complexation agent at i=0 is related to the constant of instability of the complex Me<sub>x</sub>[Cit]<sub>y</sub> upon the equation:

$$\Delta E^{k-o} = E^k - E^o = \frac{0,058}{n} \cdot \lg K_{inst} - y \cdot \frac{0,058}{n} \cdot \lg C_{cit} \quad (1)$$

After building the dependencies ΔE<sup>k-o</sup> - lgC<sub>cit</sub> according to equation (1), we obtain the constant of instability, K<sub>inst</sub>, from the segment at lgC<sub>cit</sub>= 0.

The kinetics of deposition was examined by linear and cyclic chronovoltammetry using the Wenking Electrochemical Analysis System (Germany). The rates of potential scanning applied are v=30mV s<sup>-1</sup>.

The morphology of Ni-Co alloys was examined by means of a Scanning Electron Microscope (SEM) with equipment of Oxford Instruments, JSM-6390-Jeol.

## RESULTS AND DISCUSSION

### *Potentiometric determination of the type and stability of the complexes of Ni and Co*

With the increase in Na<sub>3</sub> citrate concentration from 0.0 to 0.4M (with a step of 0.1M), the equilibrium potentials of the Ni-plated copper electrode for Ni-electrolytes and Co-plated copper electrode for Co-electrolytes and the differences in electrolytes containing only Ni or only Co at pH=5.0 and pH=7.0 were measured.

The dependencies ΔE<sup>k-o</sup> - lgC<sub>cit</sub> are displayed in Fig. 1. The constants of instability of the complexes of Ni and Co were computed from the segments of the obtained straight lines at lg C<sub>cit</sub>=0 and after comparing the values obtained with the reference data [15-17] we can make a suggestion about their possible structure. The final results are displayed in Table 1.

As is seen from the results in Table 1, at pH=5.0 the prevailing complex in the electrolyte for deposition of Ni is NiCit<sup>-</sup> (lg K<sub>inst</sub> = -5,379, K<sub>inst</sub> = 4,18·10<sup>-6</sup>); and at pH=7.0 the complexes of the type NiCit<sub>2</sub><sup>4-</sup> with lower constant of instability lg K<sub>inst</sub> = -8,193; K<sub>inst(Co)}</sub> = 6,0·10<sup>-9</sup> prevail. These results agree well with the reference data [15, 16]. The latter also suggest that with the increase in pH, it is possible that the complexes turn into insoluble forms of the type Ni(OH)SO<sub>4</sub><sup>-</sup>, thus decreasing the stability of the solutions. The data obtained for cobalt indicate the formation of the same complexes as is the case with nickel, as a certain difference between the values of the constants of instability is observed (Table 1).

Based on the results obtained we can draw the important conclusion that at pH=5.0 and pH=7.0 the complexes of Ni exhibit higher stability compared to those of Co, although the difference is not very large. This can be one of the reasons leading to greater difficulties in the deposition of Ni compared to that of Co and consequently to the anomalous co-deposition of both metals in the alloy that we found. As a basis for these conclusions not only the voltammograms, but also the data for the chemical content of the Ni-Co alloy [20] are used.

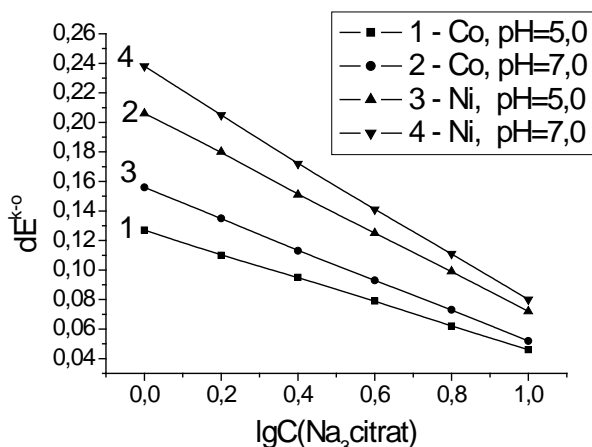


**Fig. 1.** Dependence  $\Delta E^{k-o} - \lg C_{cit}$  in electrolytes of compositions: **0.2M Co**; 0.485M  $H_3BO_3$  (curve 1 for pH=5 and curve 2 for pH=7), and **0.2M Ni**; 0.485M  $H_3BO_3$  (curve 3 for pH=5 and curve 4 for pH=7).

The results obtained are in accordance with the data given by Golodnitsky [4] for the difference between the electronic structures of Co(II) and Ni(II) and the instability of their aqueous complexes based on the ligand field theory. This is also consistent with the conclusions made by Vazquez-Arenas and Pritzker [18] regarding the rate constants for aqueous phase exchange and substitution reactions of complexes containing Fe(II), Co(II), and Ni (II).

*Effect of the background additive ( $H_3BO_3$ ) and  $Na_3$  citrate on the buffer capacity of the electrolyte*

In order to ascertain the buffer capacity of the background additive  $H_3BO_3$  and the complexation agent  $Na_3$  citrate, the electrolytes for self-deposition of Co (1-3) and Ni (1\*-3\*) with contents presented in Section 2 were subjected to pH-metric titration

with 0.5M NaOH. The dependencies obtained are presented in Fig. 2. The data indicate that when only  $H_3BO_3$  is present in the electrolyte (Fig. 2, curves 3,3\*), the buffer capacity of the Co- and Ni-solutions is insignificant and pH increases rapidly after addition of small quantities of NaOH. In the electrolyte with addition of 0.2M  $Na_3$ citrate only (curve 2 for Co and curve 2\* for Ni), the buffer capacity rapidly increases, which is more pronounced in the case of Co (Fig. 2, curve 2). In this case pH remains constant at values about 5.0 and in the range 5.5-6.0. There is a slight retention of pH about 5.5, and 6.0, and at 6.5.

The behavior of the electrolytes for deposition of Ni and Co in presence of the two additives (Fig.2: curve 1 for Co and curve 1\* for Ni) is also of interest. In this case, the solutions exhibit maximum buffer capacity, which is demonstrated by the slight increase of pH with addition of 0.5M NaOH.

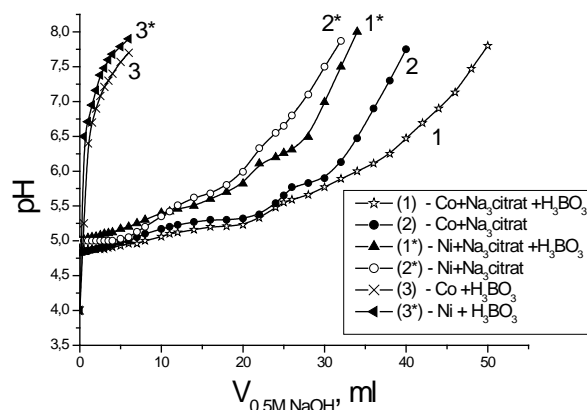


**Fig. 2.** pH -  $V_{0.5M NaOH}$  dependencies in electrolytes for self-deposition of Co (1-3 electrolytes) and Ni (1\*-3\*electrolytes).

The results obtained evidence that the addition of 0.485M boric acid to the citrate electrolyte enhances the buffer capacity of the electrolyte.

Our observations also indicate that in case of continuous operation, the electrolytes containing boric acid remain stable longer (up to 4-5 weeks) than in the case without boric acid (up to 1-2 weeks).

**Table 1.** Constants of instability determined from the experimental data and from the references.

pH	$\lg K_{unst}(Co_x Cit_y)$	$\lg K_{unst}(Ni_x Cit_y)$	Reference
5.0	-4.38	-5.379	[17](Co)
Complex →	$CoCit^-$	$NiCit^-$	[15,16] (Ni)
7.0	-7.103	-8.193	[17](Co)
Complex →	$CoCit_2^{4-}$	$NiCit_2^{4-}$	[15,16] (Ni)

This is valid especially for the electrolyte for Co deposition without boric acid in which sediment is formed within less than 2 weeks after preparation. The reason for such behavior of the solution can be justified by comparing the obtained data to the type and stability of the complexes of nickel and cobalt ions with citrate ions (Table 1) and the curves in Figure 1.

Introduction of boric acid in the citrate solution more reliably maintains the pH within the range where the soluble complexes of the metals prevail: at pH=5.0 they are  $CoCit^-$  and  $NiCit^-$ . In case of continuous operation, pH within the space around the electrode increases due to the parallel reaction of hydrogen evolution on the cathode. In absence of boric acid, a more rapid increase of pH is possible, as it reaching values about and above 7.0 leads to formation of not only soluble complexes of the metals  $CoCit_2^{4-}$  and  $NiCit_2^{4-}$ , but also to formation of less soluble forms of the type  $Co(OH)SO_4^-$  or  $Ni(OH)SO_4^-$ , as [15,16] indicate. That justifies the necessity of working with citrate electrolytes with addition of boric acid, which is an important circumstance that we have to consider during the final optimization of the electrolyte.

*Effect of the background additive ( $H_3BO_3$ ) and  $Na_3$  citrate on the kinetics of self-deposition of Ni and Co*

The influence of the presence of  $H_3BO_3$  and  $Na_3$  citrate on the kinetics of self-deposition of Ni and Co in the citrate electrolyte was examined. The cyclic voltammograms in the range of potentials from 0.6 V to -2.0 V in electrolytes for deposition of Ni (Fig. 3) and Co (Fig. 4) with addition of boric acid only (Figs. 3,4 curve 3);  $Na_3$ citrate only (Figs. 3,4 curve 2); and with both  $H_3BO_3$  and  $Na_3$ citrate (Figs. 3,4 curve 1) are shown. The voltammograms obtained indicate a characteristic impact of each background additive on the kinetics of self-deposition of the metals.

*Self-deposition of Ni*

In the case of Ni (Fig. 3) in presence of boric acid only (curve 3), a long initial polarization is observed. Then the current increases slightly and reaches a plateau at about -1,5V (SCE). In presence of  $Na_3$  citrate only (curve 2), the curve passes through two cathode peaks, i.e. at about -0.300 V and -1.150 V. The first cathode peak is associated with the induction of copper ions obtained at high anode potentials. This peak is reproduced even after a few cycles of the curve (4-5), which is not typical

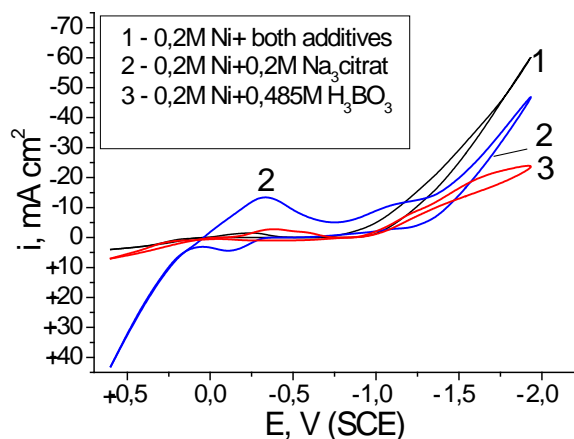


Fig. 3. Voltammograms ( $v=30$  mV/s) in electrolyte for self-deposition of Ni in presence of the different background additives (1 – electrolyte 1\*; 2 – electrolyte 2\*; 3 – electrolyte 3\*).

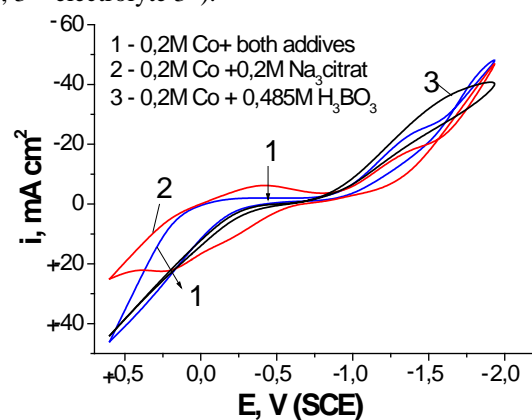


Fig. 4. Voltammograms ( $v=30$  mV s<sup>-1</sup>) in the electrolyte for self-deposition of Co in presence of the different background additives (1 – electrolyte 1; 2 – electrolyte 2; 3 – electrolyte 3).

for the rest compositions of the electrolyte. The second cathodic peak at 1.150V is associated with the reduction of the nickel complex ions to nickel. The deposition of nickel proceeds at low rate and according to our observations at those high enough cathodic potentials, the coating on the cathode has low density and adhesion and is virtually almost absent. The copper electrode remains active within almost the whole range of potentials. There are two consecutive retentions occurring in anode direction: at -0.200 V and at 0.100 V, that might be associated with the solution of nickel and copper correspondingly. As a whole, in the electrolyte containing no  $H_3BO_3$  but only  $Na_3$  citrate, the surface is active and sufficiently dense Ni coatings are not formed.

In presence of both  $H_3BO_3$  and  $Na_3$  citrate simultaneously in the electrolyte for deposition of Ni (Fig. 3, curve 1), the dependence features long cathodic and anodic polarization, and absence of cathodic and anodic peaks, which most probably suggests a completely different control of

deposition, and most probably an activation one. There is a decrease of the total polarization observed, which is also associated with the evolution of hydrogen together with nickel. Visually, a dense nickel coating with high adhesion is observed on the cathode in case of retention of the cathodic potential at high values above -1,250 V (SCE).

#### Self-deposition of Co

In an electrolyte for self-deposition of cobalt (Fig.4), the typical impact of each additive is also observed. In presence of boric acid only (Fig. 4 curve 3), the lowest total and initial polarization and the highest currents are achieved. This impact is completely opposite to that of boric acid on deposition of Ni (Fig. 3, curve 3). In presence of  $Na_3$  citrate only (Fig. 4, curve 2) the curve passes through two cathodic peaks at about -0,300 V and -1,150 V, like in the case with the nickel electrolyte (Fig. 3, curve 2). In case of cobalt, the first plateau is the result of reduction of copper ions obtained at the high anodic potentials and the second is the result of deposition of cobalt. In the anodic direction, two subsequent retentions of the current are obtained at -0.300 V and at 0.100 V, which might be associated with the solution of cobalt and copper, correspondingly. In the electrolyte containing  $Na_3$  citrate only, the cobalt coatings deposited at high cathodic potentials, unlike the nickel coatings deposited in the same conditions, are dense and have a very good adhesion which is demonstrated in their difficult dissolution through etching.

In presence of  $H_3BO_3$  and  $Na_3citrate$  (Fig. 4, curve 1) in the Co solution, the curve passes through a long initial polarization and a plateau at -1,250V, as the rate of the process of cobalt deposition is lower in comparison with that in presence of boric acid only. This is an evidence for the formation of stable citrate complexes of Co with a rate of reduction lower than that of the single cobalt ions only.

These difficulties in the deposition of cobalt associated with the complex formation in presence of citrate ions could result in formation of a fine grain structure of the coatings in presence of the total background (with both additives).

#### Determination of the conditions for deposition of Ni-Co alloy

Based on the data above proving the advantages of the simultaneous presence of  $H_3BO_3$  and  $Na_3$  citrate, the conditions for co-deposition of the two metals are determined in this electrolyte. For this purpose, the voltammograms in electrolytes for

self- and co-deposition of Ni and Co are taken in comparable conditions and the deposition potentials of the metals are registered in both cases.

The cyclic voltammograms in electrolytes at the same rate of potential scanning  $v= 30 \text{ mV s}^{-1}$  are presented in Fig. 5 (c.1 for Ni; c.2 for Co; c.3 for Ni-Co).

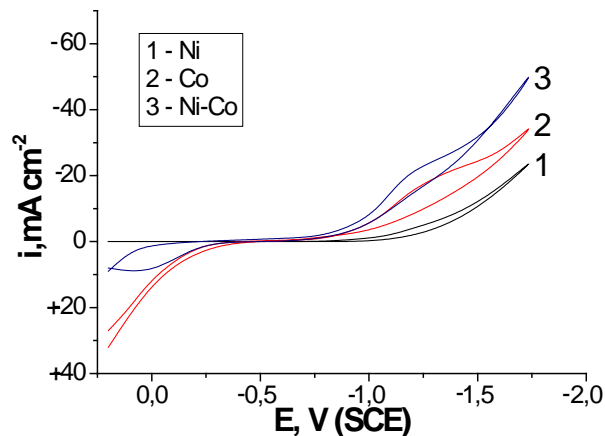
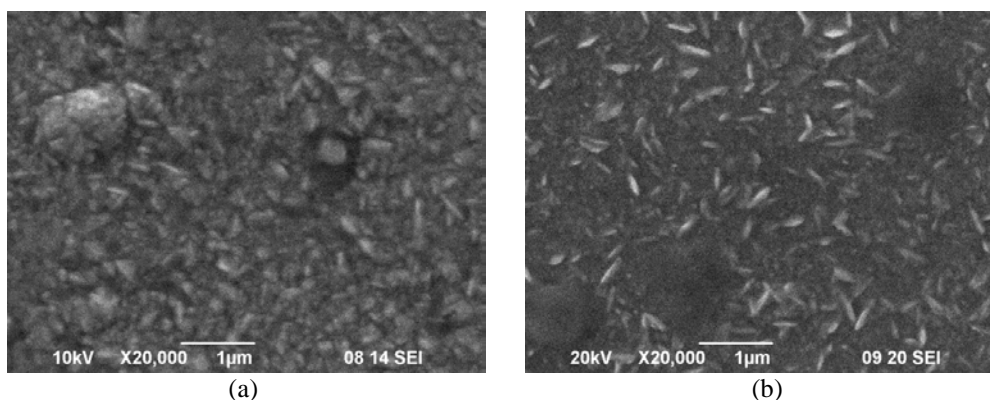


Fig. 5. Voltammograms in electrolytes for self-deposition of Ni in electrolyte 1\* (1); of Co in electrolyte 1 (2); and of Ni-Co in electrolyte composition: 0,2M Ni; 0,2M Co; 0,2M  $Na_3citrate$  and 0.485M boric acid,  $pH=5\div 5,5$  ( $v= 30 \text{ mV s}^{-1}$ ).

The comparison of the dependencies obtained indicates that in the electrolyte for self-deposition of Ni (Fig. 5, curve 1), long initial cathodic and anodic polarizations are observed; however in the case of cobalt both polarizations are lower and the current begins to increase in anodic direction at -0,250V (SCE), which is associated with its anodic increase (Fig.5, curve 2). In the curve for co-deposition of the two metals (Fig.5, curve 3), the anodic current increases at the same potential which means that Co first begins dissolving from the two metals deposited in the alloy. The initial increase of the current associated with the beginning of deposition of the metals points to anomalous deposition, which is characteristic for both electrolytes examined [14] and the alloys from the iron group as a whole [12-14]. Thus the potential for beginning the deposition of Ni is about -1,150V (SCE), while that of deposition of Co is about -0,980 V(SCE), i.e. more positive than the dynamically predetermined potential of Ni. The reasons might be associated with the larger difficulties for deposition of Ni in the composition examined related to the determined higher stability constants. The reasons for the long initial polarization in case of Ni compared to that of cobalt are the possible adsorption processes of the citrate complexes of Ni and even of hydrocitrate nickel compounds with low solubility.



**Fig. 6.** SEM images of Ni-Co coatings in an electrolyte containing: 0.2M Ni, 0.2M Co, 0.2M  $Na_3$  citrate: (a) in absence of  $H_3BO_3$  and (b) in presence of 0.485M  $H_3BO_3$ , pH=5÷5.5 at  $E=-1.250$  V (SCE); Elemental composition of Ni-Co alloys: (a) 86.79wt% Co-13.21wt% Ni; (b) and (b) 81.15wt% Co-18.85wt% Ni.

The greater difficulties during the deposition of nickel compared to cobalt and the conditions when that difference was the largest constituted the base for optimization of the content of citrate electrolyte. It was found in the course of the examinations that the ratio of concentrations of  $Na_3$  citrate and each metal ( $C_{Na_3citrat}/C_{Me^{z+}}$ ) should not exceed 1 in order to allow their deposition in coatings. In case  $C_{Na_3citrat}/C_{Me^{z+}} > 1$ , the deposition of the metals and especially the deposition of Ni is extremely difficult and practically does not occur. The increase in concentration of the components up to 0.3M and maintaining the concentration 0.2M for the sodium citrate is beneficial for both the stability of the electrolyte and the deposition of metal itself. The positive influence of boric acid on the stability of the electrolyte and the quality of coatings proven during the examination point to the following optimal content: 0.2÷0.3M Ni; 0.1÷0.3M Co; 0.485M  $H_3BO_3$  and 0.2M  $Na_3citrate$ , pH=5÷5.5.

#### *Effect of boric acid on the morphology of the Ni-Co coatings*

In Fig. 6 the SEM images of Ni-Co coatings deposited in stationary potentiostatic mode at potential  $E= -1,250$  V (SCE) in electrolyte in absence of boric acid (Fig. 6,a) and in presence of 0.485M boric acid are shown (Fig. 6,b). The images taken indicate that the presence of boric acid leads to formation of a more fine-grain structure, as the share of smaller size crystals greatly increases (Fig. 6,b). The higher density of distribution of crystals in the presence of boric acid can explain the resistance of the coatings against etching, i.e. their better adhesion.

#### CONCLUSIONS

The type and stability of the citrate complexes of Ni and Co at two values of pH are determined. It is found that the simultaneous presence of  $H_3BO_3$

and  $Na_3citrate$  increases both the buffer capacity of the electrolyte and its stability during extended operation. It is shown that each additive has a characteristic impact on the kinetics of deposition. The presence of  $H_3BO_3$  in the citrate electrolyte increases the rate of deposition of Ni and Co, which has beneficial effect on the alloy formation. It is found through SEM images that the addition of  $H_3BO_3$  leads to more than 50% increase of the share of crystals with dimensions less than 100 nm. The addition of  $H_3BO_3$  leads to about 6% increase of Ni content in comparable conditions.

#### REFERENCES:

1. L. Wang, Y. Gao, Q. Xue, H. Liu, T. Xu, *Applied Surface Science*, **242**, 326 (2005).
2. D. Golodnitsky, Yu. Rosenberg, A. Ulus, *Electrochem. Acta*, **47**, 2707 (2002).
3. S. Armyanov, *Electrochim. Acta*, **45**, 3323 (2000).
4. D. Golodnitsky, N. V. Gudin, G. A. Volyanuk, *J. Electrochem. Soc.*, **147-11**, 4156 (2000).
5. W. T. B. Hansal, M. Halmdienst, M. Versanyi, W. Kautek, *Electrochim. Acta*, **52**, 1145 (2006).
6. B. V. Tilak, A. S. Gendron, M. A. Mosoiu, *J. Appl. Electrochem.*, **7**, 495 (1977).
7. A. Brenner, *Electrodeposition of Alloys*, Acad. Press, New York, 1963, p. 558.
8. M. Ishikawa, H. Enomoto, M. Matsuoka, C. Iwakura, *Electrochem Acta*, **40**, 1663 (1995).
9. A. R. Despic, V. D. Jovic, S. Spaic, *This Journal*, **136**, 1651 (1989).
10. M. Pushpavanam, K. Balakrishnan, *J. Appl. Electrochem*, **26**, 1065 (1996).
11. R. Tarozaitė, O. Gyliene, G. Stalnionis, *Surface & Coatings Technology*, **200**, 2208 (2005).
12. M. Grobani, A. G. Dolati, A. Afshar, *Russian Journal of Electrochemistry*, **8**, 11, 1173 (2004).
13. O. Younes, E. Gileadi, *J. Electrochem. Soc.*, **149-2**, C100 (2002).
14. [14] R.Y., Ying, *J. Electrochem. Soc.*, **135**, 12, 2957-2964 (1988)
15. T. A. Green, A. E Russel, S. Roy, *J. Electrochem. Soc.*, **145**, 3, 875 (1998).

16. O. Yu. Zelenin, *Russian Journal of Coordination Chem.*, **33**, 5, 346 (2007).  
17. N. Kotsakis, C. P. Raptopoulou, V. Tangoulis, A. Terzis, J. Giapintzakis, T. Jakusch, *Inorganic Chemistry*, **42**, 22 (2003).  
18. J. Vazquez-Arenas, M. Pritzker, *Journal of Solid State Electrochemistry*, **17**, 419-433 (2013).  
19. R. Orinakova, A. Turonova, D. Kladekova, M. Galova, R. Smith, *J. Appl. Electrochem.*, **36**, 957 (2006).  
20. K. Ignatova, Y. Marcheva, *Bulgarian Chemical Communications*, **47**, 678 (2015).

## ЕФЕКТ НА $H_3BO_3$ И $Na_3$ ЦИТРАТ ВЪРХУ УСЛОВИЯТА НА ЕЛЕКТРОЛИТНО ОТЛАГАНЕ НА Ni-Co СПЛАВИ ОТ ЦИТРАТЕН ЕЛЕКТРОЛИТ

К. Игнатова

Катедра по електрохимия, ХТМУ – София

Получена на 25 февруари 2014 г., ревизирана на 5 март 2015 г.

(Резюме)

В статията се докладват резултатите за влиянието на  $H_3BO_3$  и комплексообразуващия агент  $Na_3$ цитрат върху вида на комплексите на Ni и Co при две стойности на pH (5,0 и 7,0). Установено е, че при pH=5,0 в електролит, в който присъстват и двете добавки преобладават комплекси от типа  $NiCit^-$  и  $CoCit^-$  ( $\lg K_{unst(Ni)} = -5,379$  и  $\lg K_{unst(Co)} = -4,38$ ). При pH=7,0, заедно с  $NiCit^-$  се образуват комплекси от вида  $NiCit_2^{4-}$  и  $CoCit_2^{4-}$  с по-ниска константа на неустойчивост ( $\lg K_{unst(Ni)} = -8,193$  и  $\lg K_{unst(Co)} = -7,103$ ).

Установено е, че присъствието на  $H_3BO_3$  едновременно с  $Na_3$ цитрат повишава буферния капацитет на електролита в сравнение с електролит, в който присъства само  $Na_3$ цитрат. Особено силен е този ефект в електролит за самостоятелно отлагане на Co. Чрез снемане на циклични хроноволтамперометрични зависимости е показано, че присъствието на  $H_3BO_3$  едновременно с  $Na_3$ цитрат повишава скоростта на отлагане на Ni в по-висока степен, отколкото на Co, което има за ефект повишаване на процента на никел в сплавта. Чрез SEM е установено, че добавката от  $H_3BO_3$  води до формиране на кристали с игловидна форма с размери до 500 nm. Делът на кристалите с размери под 100nm нараства до над 50%. Добавката на  $H_3BO_3$  води и до нарастване съдържанието на Ni с около 5 % при съпоставими условия.



## Inhibition mechanism and molecular modeling studies of the interactions of 6-(propan-2-yl)-3-methyl-morpholine-2,5-dione with xanthine oxidase

Ž. Šmelcerović<sup>1\*</sup>, M. Rangelov<sup>2</sup>, E. Cherneva<sup>3</sup>, G. Kocić<sup>4</sup>, S. Stojanović<sup>4</sup>, T. Jevtović-Stoimenov<sup>1,4</sup>, Ž. Petronijević<sup>5</sup>, D. Yancheva<sup>2</sup>

<sup>1</sup>Center for Biomedical Science, Faculty of Medicine, University of Niš, Bulevar Dr Zorana Djindjica 81, 18000 Niš, Serbia

<sup>2</sup>Institute of Organic Chemistry with Centre of Phytochemistry, Bulgarian Academy of Sciences, Acad. G. Bonchev Str., Build. 9, 1113 Sofia, Bulgaria

<sup>3</sup>Faculty of Pharmacy, Medical University of Sofia, 2 Dunav Str., 1000 Sofia, Bulgaria

<sup>4</sup>Institute of Biochemistry, Faculty of Medicine, University of Niš, Bulevar Dr Zorana Djindjica 81, 18000 Niš, Serbia

<sup>5</sup>Faculty of Technology, University of Niš, Bulevar Oslobođenja 124, 16000 Leskovac, Serbia

Received April 11, 2014, Revised April 27, 2015

Xanthine oxidase (XO) is an enzyme which catalyzes oxidation of hypoxanthine to xanthine and then to uric acid, and plays a key role in hyperuricemia. The inhibition of XO activity in rat liver homogenate by 6-(propan-2-yl)-3-methyl-morpholine-2,5-dione (**1**) was evaluated and compared with that of two previously studied cyclodipeptides, 3,6-di(propan-2-yl)-4-methyl-morpholine-2,5-dione (**2**) and 3-(2-methylpropyl)-6-(propan-2-yl)-4-methyl-morpholine-2,5-dione (**3**), and allopurinol. Compound **1** showed significant inhibitory activity against rat liver XO ( $IC_{50} = 49.82 \mu\text{g/mL}$ ), comparable with the activity of **2** and **3**. Allopurinol, a widely used XO inhibitor and drug to treat gout, exhibited a stronger inhibitory effect on rat liver XO than **1-3**. Compound **1** was synthesized as a mixture of two diastereoisomers, (3*S*,6*R*) and (3*S*,6*S*), and molecular docking studies were performed to gain an insight into their binding modes with XO. Lineweaver–Burk plot analysis of the inhibition kinetics data demonstrated that the studied compound (**1**) was a competitive inhibitor of XO. Both forms of **1** bind in the entrance of the narrow tunnel towards the dioxothiomolybdenum moiety of the active center of XO, blocking in this way the approach of the substrates toward the metal atom.

**Keywords:** inhibition kinetics; molecular modeling; 6-(propan-2-yl)-3-methyl-morpholine-2,5-dione; xanthine oxidase inhibition.

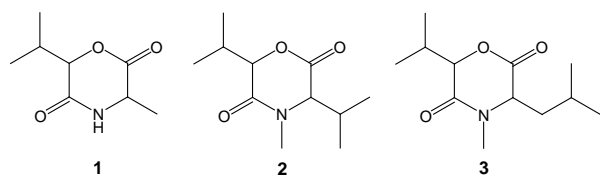
### INTRODUCTION

Cyclodipeptides are the simplest ones in the cyclodipeptide family containing one residue of amino acid and one residue of lactic,  $\alpha$ -hydroxyisovaleric or other  $\alpha$ -hydroxy acid. There are reports on their antioxidant [1], antimicrobial [2,3] and immunomodulatory [2,4,5] activities, as well as inhibitory activities towards acyl-CoA:cholesterol acyltransferase [6],  $\alpha$ -glucosidase [7-9] and platelet aggregation [10]. Recently, we synthesized a novel cyclodipeptide, 6-(propan-2-yl)-3-methyl-morpholine-2,5-dione (**1**;  $C_8H_{13}NO_3$ ,  $M = 171.19$ ) (Scheme 1), containing an alanine moiety [3]. Xanthine oxidase (XO) is a key enzyme which can catalyze oxidation of xanthine to uric acid causing hyperuricemia in humans [11] and recently, we evaluated two synthetic cyclodipeptides 3,6-di-(propan-2-yl)-4-methyl-morpholine-2,5-dione (**2**;  $C_{11}H_{19}NO_3$ ,  $M = 213.27$ ) and 3-(2-methylpropyl)-6-(propan-2-yl)-4-

methyl-morpholine-2,5-dione (**3**;  $C_{12}H_{21}NO_3$ ,  $M = 227.30$ ) [12] for inhibitory activity against commercial enzyme XO *in vitro* and XO in rat liver homogenate as well as anti-inflammatory response on human peripheral blood mononuclear cells (PBMCs) [13]. The two cyclodipeptides were excellent inhibitors of XO and significantly suppressed the nuclear factor of  $\kappa\text{B}$  (NF- $\kappa\text{B}$ ) activation. Based on molecular docking study, the binding modes of **2** and **3** with XO were clarified and recommendations for future structure-guided design of new morpholine-dione inhibitors of XO were drawn [13].

In this paper, we investigated the inhibition of xanthine oxidase (XO) activity in rat liver homogenate by compound **1** and compared with that by cyclodipeptides **2** and **3**, as well as allopurinol, a widely used XO inhibitor and drug to treat gout. Inhibition kinetics of compound **1** with XO was studied in order to determine the type of enzyme inhibition, while the molecular docking studies were performed in order to examine the binding mode of **1** with XO.

\* To whom all correspondence should be sent:  
E-mail: zsmelcerovic@yahoo.com



**Scheme 1.** Chemical structure of cyclodipeptides **1-3**

## EXPERIMENTAL

### *Evaluation of xanthine oxidase inhibition*

Inhibition of XO activity in rat liver homogenate was evaluated using a spectrophotometric method [14], by measuring uric acid formation at 293 nm. The reaction mixture (volume 2200  $\mu\text{L}$ ) was prepared by allocating the following test sample groups: i) Test sample group contained 100  $\mu\text{L}$  of 10 % rat liver homogenate, one of the studied compounds (**1-3**) diluted in DMSO (the final concentration of DMSO in the assay was 4.55 % v/v), 454.5  $\mu\text{M}$  of xanthine (Serva), and 45.5 mM TRIS-HCl buffer (pH 7.8); ii) Solvent control group contained the same amount of rat liver homogenate, appropriate amount of DMSO, xanthine and TRIS-HCl buffer; iii) Control group contained the same amount of rat liver homogenate, xanthine and TRIS-HCl buffer adjusted to the same volume. Corresponding blank samples were prepared for each group in the same way as the test solutions (i-iii). The obtained inhibition was calculated as a percent change of the control which involves the effect of appropriate amount of DMSO. All samples were assayed for XO inhibitory activity at concentration of 50  $\mu\text{g}/\text{mL}$ . Those showing greater than 50 % inhibition at this concentration were tested further to ascertain the corresponding  $\text{IC}_{50}$  values.  $\text{IC}_{50}$  curves were generated using three concentrations of studied compounds (50, 40 and 25  $\mu\text{g}/\text{mL}$ ). Allopurinol was used as positive control. All experiments were performed in triplicate and averaged.

### *Lineweaver–Burk plots*

To determine the mode of inhibition by compound **1**, Lineweaver–Burk plot analysis was performed. This kinetics study was carried out in the absence and presence of the inhibitor with varying concentrations of xanthine as the substrate. Commercial bovine milk XO, purchased from Sigma-Aldrich, was employed for *in vitro* evaluation of enzyme inhibition. The inhibition was studied in a series of test-tubes with the reaction mixture (total volumen 2150  $\mu\text{L}$ ) containing 0.01 units of XO and 46.5 mM TRIS-HCl buffer (pH 7.8). Xanthine concentration was varied (0, 18.6, 46.5, 93, 232.5 or 930  $\mu\text{M}$ ) at three series of fixed

concentrations of compound **1** (0, 13.6 and 54.4  $\mu\text{M}$ ). Amount of generated uric acid formation was measured at 293 nm.

### *Molecular docking*

Molecular docking was carried out into the salicylic acid active site of XO (PDB entry code 1FIQ) using MOE software [15]. Water molecules from initial pdb were removed. Conformational search for preparation of the ligands was carried out by LowModelMD method which performs molecular dynamics perturbations along with low frequency vibrational modes with energy window 7 kCal/mol, and conformational limits of 1000. Placement of conformers was prepared according to alpha-triangle method on selected pharmacophores. Docking was done using the induced-fit docking protocol allowing the side-chain and backbone movement in the receptor to accommodate the ligand. Scoring of docking poses was performed by affinity dG, calculated with MMFF94x force field.

## RESULTS AND DISCUSSION

Compound **1** showed a significant inhibitory activity against rat liver XO ( $\text{IC}_{50} = 49.82 \mu\text{g}/\text{mL}$  (291  $\mu\text{M}$ )), comparable with activity of **2** ( $\text{IC}_{50} = 41.88 \mu\text{g}/\text{mL}$  (196  $\mu\text{M}$ )) and **3** ( $\text{IC}_{50} = 46.66 \mu\text{g}/\text{mL}$  (205  $\mu\text{M}$ )). As cyclodipeptides **1-3** have a common part of the structure (6-(propan-2-yl)morpholine-2,5-dione core), it can be concluded that the presence of isopropyl groups at position 3 and a methyl group at position 4 of morpholine ring (structural characteristics of compound **2**) are more favorable for XO inhibition then the presence of isobutyl group at position 3 and a methyl group at position 4 of morpholine ring (structural characteristics of compound **3**) or the presence of a methyl group at position 3 and the absence of substituents at position 4 of morpholine ring (structural characteristics of compound **1**).

Allopurinol ( $\text{IC}_{50} = 0.79 \mu\text{g}/\text{mL}$  (5.8  $\mu\text{M}$ )), a widely used XO inhibitor and drug to treat gout, exhibited stronger inhibitory effect on rat liver XO than **1-3**. However, allopurinol does have a number of serious side effects, and the cellular and molecular mechanisms of these side effects are incompletely understood. Some data indicate that the renal toxicity of allopurinol is related to impairment of pyrimidine metabolism [16]. There are no reliable or rapid screening tools that would predict the safety profile of novel XO inhibitors in terms of hypersensitivity reactions or organ toxicity; contact hypersensitivity mouse ear models and toxicity studies in rodents are being used to predict such side effects [17]. Intuitively, one

would predict that novel XO inhibitors that would move away from the purine-based inhibitor structure may have fewer of the allopurinol-like side effects (of course, they may introduce new types of side effects or toxicities) [18]. In the recent literature there are data on non-purine XO inhibitors [19-22].

We also determined the type of enzyme inhibition. The related inhibition type of the title compound on XO was identified from Lineweaver–Burk plots (Fig. 1). The compound **1** was a competitive inhibitor of XO.

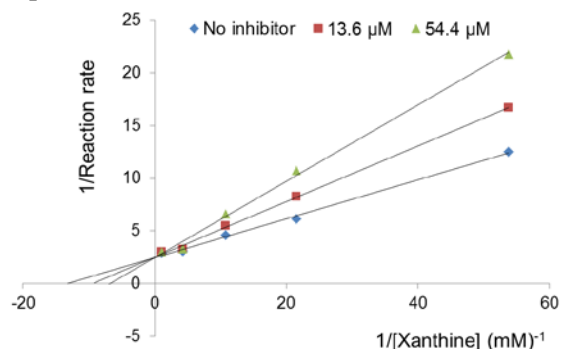


**Fig. 1.** Lineweaver–Burk plots for the inhibition of xanthine oxidase by compound **1** with xanthine as substrate (see the Methods and Materials section for details)

The interaction of the inhibitor with the XO was studied also by molecular docking into the salicylic acid active site of the bovine milk enzyme (PDB entry code 1FIQ) [23]. Based on recent spectral and computational studies, it is known that the keto form of the title compound is much more energetically favored than the corresponding enol form. The reported NMR and IR data show no evidences for enol formation neither in polar nor in nonpolar medium (3). For this reason only the keto forms of the two diastereoisomers of **1**, (3*S*,6*R*) and (3*S*,6*S*), were taken into consideration in the molecular docking studies. The docking poses of the ligands **1**(3*S*,6*R*) and **1**(3*S*,6*S*), are presented in Fig. 2.

Both forms of **1** bind in the entrance of the narrow tunnel towards the dioxothiomolybdenum moiety of the active center of XO, blocking in this way the approach of the substrates toward the metal atom (Fig. 2). As can be seen from the 2D 2D representation of the ligand interactions in the pocket (Fig. 3), the ligand-pocket binding of both diastereoisomers is stabilized via hydrogen bonds with Thr1010 and Arg880 and a number of lipophilic interactions with neighboring amino acid residues. In the case of **1**(3*S*,6*R*) the hydrogen bond is formed between the amide O-atom and Thr1010, while **1**(3*S*,6*S*) interacts with Thr1010 and Arg880 through its ester carbonyl group (Fig. 3). **1**(3*S*,6*S*)

enters deeper in the cavity. The molecular interactions of title compound to XO resemble those found by crystallographic studies on complexes of XO with other inhibitors not forming a covalent bond with the molybdenum atom such as salicylic acid [23] and febuxostat [24]. These results demonstrate that both diastereoisomers have good binding capacity toward the XO.

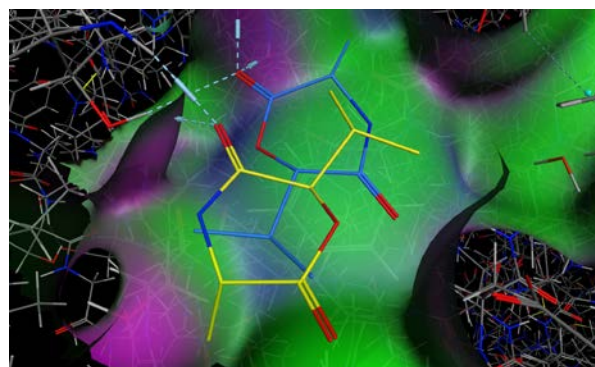


**Fig. 2.** Docking poses of: **1**(3*S*,6*R*) - yellow carbons; **1**(3*S*,6*S*) - blue carbons

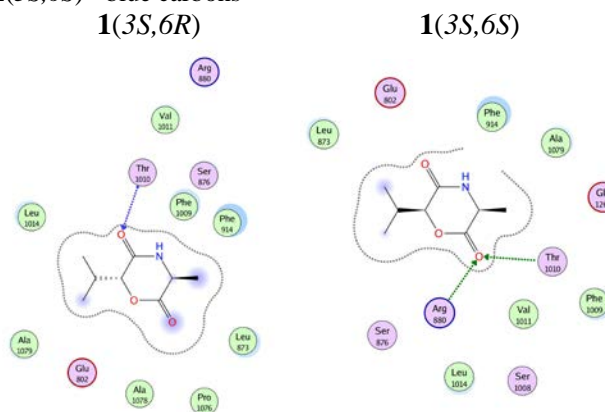


**Fig. 3.** 2D representation of the ligand interactions in the pocket.

## CONCLUSIONS

Cyclodipeptide **1** showed a potent inhibitory effect on XO in a competitive mode. Both diastereoisomers, **1**(3*S*,6*R*) and **1**(3*S*,6*S*), bind in the entrance of the narrow tunnel towards the dioxothiomolybdenum moiety of the active center of XO, blocking in this way the approach of the substrates toward the metal atom. Allopurinol was found to be more active against rat liver XO than **1**-**3**. Chronic allopurinol administration for the inhibition of XO is clinically effective against the hyperuricemia associated with gout, but undesirable side effects have prompted efforts to isolate or synthesise other types of XO inhibitors [25]. Therefore, the results of this study as well as results of our previous study [13] may suggest that 6-(propan-2-yl)-morpholine-2,5-diones are likely to be adopted as candidates to treat gout and may be

taken for further evaluation by using *in vivo* studies. The synthesis of new morpholine-diones derivatives as well as evaluation of their potential for inhibition of XO activity will be part of our further investigation.

**Acknowledgements:** The financial support of this work by National Science Fund of Bulgaria (Contract DMU-03/66) and Ministry of Science and Technological Development of Serbia (Projects OI 172044 and TR 31060) is gratefully acknowledged.

#### REFERENCES

1. V. Stankov-Jovanovic, J.C. Tabet, P. Dzodic, L. Daskalova, E. Cherneva, D. Yancheva, A. Smelcerovic, *Acta Chim. Slov.*, **59**, 939 (2012).
2. V. Pavlovic, A. Djordjevic, E. Cherneva, D. Yancheva, A. Smelcerovic, *Food Chem. Toxicol.*, **50**, 761 (2012).
3. D. Yancheva, L. Daskalova, E. Cherneva, B. Mikhova, A. Djordjevic, Z. Smelcerovic, A. Smelcerovic, *J. Mol. Struct.*, **1016**, 147 (2012).
4. M. Iijima, T. Masuda, H. Nakamura, H. Naganawa, S. Kurasawa, Y. Okami, M. Ishizuka, T. Takeuchi, Y. Iitaka, *J. Antibiot.*, **45**, 1553 (1992).
5. V. Pavlovic, E. Cherneva, D. Yancheva, A. Smelcerovic, *Food Chem. Toxicol.*, **50**, 3014 (2012).
6. K. Hasumi, C. Shinohara, T. Iwanaga, A. Endo, *J. Antibiot.*, **46**, 1782 (1993).
7. A. Arcelli, D. Balducci, A. Grandi, G. Porzi, M. Sandri, S. Sandri, *Monatsh. Chem.*, **135**, 951 (2004).
8. A. Arcelli, D. Balducci, A. Grandi, G. Porzi, M. Sandri, S. Sandri, *Tetrahedron: Asymmetry*, **16**, 1495 (2005).
9. A. Arcelli, D. Balducci, S.F.E. Neto, G. Porzi, M. Sandri, *Tetrahedron: Asymmetry*, **18**, 562 (2007).
10. T. Kagamizono, E. Nishino, K. Matsumoto, A. Kawashima, M. Kishimoto, N. Sakai, B.-M. He, Z.-X. Chen, T. Adachi, S. Morimoto, K. Hanada, *J. Antibiot.*, **48**, 1407 (1995).
11. J.-F. Hsieh, S.-H. Wu, Y.-L. Yang, K.-F. Choong, S.-T. Chen, *Bioorg. Med. Chem.*, **15**, 3450 (2007).
12. A. Smelcerovic, D. Yancheva, E. Cherneva, Z. Petronijevic, M. Lamshoef, D. Herebian, *J. Mol. Struct.*, **985**, 397 (2011).
13. A. Smelcerovic, M. Rangelov, Z. Smelcerovic, A. Veljkovic, E. Cherneva, D. Yancheva, G.M. Nikolic, Z. Petronijevic, G. Kocic, *Food Chem. Toxicol.*, **55**, 493 (2013).
14. Z. Smelcerovic, A. Veljkovic, G. Kocic, D. Yancheva, Z. Petronijevic, M. Anderluh, A. Smelcerovic, *Chem.-Biol. Interact.*, **229**, 73 (2015).
15. Molecular Operating Environment (MOE), 2011.10; Chemical Computing Group Inc., 1010 Sherbooke St. West, Suite #910, Montreal, QC, Canada, H3A 2R7, 2011.
16. H. Horiuchi, M. Ota, S. Nishimura, H. Kaneko, Y. Kasahara, T. Ohta, K. Komoriya, *Life Sci.*, **66**, 2051 (2000).
17. H. Horiuchi, M. Ota, S. Kitahara, T. Ohta, M. Kiyoki, K. Komoriya, *Biol. Pharm. Bull.*, **22**, 810 (1999).
18. P. Pacher, A. Nivorozhkin, C. Szabo, *Pharmacol. Rev.*, **58**, 87 (2006).
19. K. Nepali, G. Singh, A. Turan, A. Agarwal, S. Sapra, R. Kumar, U.C. Banerjee, P.K. Verma, N.K. Satti, M.K. Gupta, O.P. Suri, K.L. Dhar, *Bioorg. Med. Chem.*, **19**, 1950 (2011).
20. K. Nepali, A. Agarwal, S. Sapra, V. Mittal, R. Kumar, U.C. Banerjee, M.K. Gupta, N.K. Satti, O.P. Suri, K.L. Dhar, *Bioorg. Med. Chem.*, **19**, 5569 (2011).
21. S. Sharma, K. Sharma, R. Ojha, D. Kumar, G. Singh, K. Nepali, P.M.S. Bedi, *Bioorg. Med. Chem. Lett.*, **24**, 495 (2014).
22. H. Singh, S. Sharma, R. Ojha, M.K. Gupta, K. Nepali, P.M.S. Bedi, *Bioorg. Med. Chem. Lett.*, **24**, 4192 (2014).
23. C. Enroth, B.T. Eger, K. Okamoto, T. Nishino, T. Nishino, E.F. Pai, *Proc. Natl. Acad. Sci. USA*, **97**, 10723 (2000).
24. K. Okamoto, B.T. Eger, T. Nishino, S. Kondo, E.F. Pai, T. Nishino, *J. Biol. Chem.*, **278**, 1848 (2003).
25. F. Borges, E. Fernandes, F. Roleira, *Curr. Med. Chem.*, **9**, 195 (2002).

МЕХАНИЗМИ НА ИНХИБИРАНЕ И МОЛЕКУЛНО МОДЕЛИРАНЕ НА НА  
ВЗАИМОДЕЙСТВИЯТА НА 6-(ПРОПАН-2-ИЛ)-3-МЕТИЛ-МОРФОЛИН-2,5-ДИОН С  
КСАНТИН ОКСИДАЗА

Ж. Шмелцерович<sup>1\*</sup>, М. Рангелов<sup>2</sup>, Е. Чернева<sup>3</sup>, Г. Коцич<sup>4</sup>, С. Стоянович<sup>4</sup>, Т. Йевтович-Стоименов<sup>1,4</sup>,  
Ж. Петрониевич<sup>5</sup>, Д. Янчева<sup>2</sup>

<sup>1</sup>Център за биомедицински науки, Медицински факултет, Университет в Ниш, Сърбия

<sup>2</sup>Институт по органична химия с Център по фитохимия, Българска академия на науките, 1113 София,  
България

<sup>3</sup>Факултет по фармация, Медицински университет в София, 1000 София, България

<sup>4</sup>Институт по биохимия, Медицински факултет, Университет в Ниш, Сърбия

<sup>5</sup>Технологичен факултет, Университет в Ниш, Сърбия

Постъпила на 11 април 2014 г.; коригирана на 27 април, 2015 г.

(Резюме)

Ксантин оксидазата (ХО) е ензим, катализиращ окислението на хипоксантина до ксантин, а след това до пикочна киселина. С това той има ключова роля при хиперурициемията. Оценено е инхибирането на активността на ХО в препарат от черен дроб на плъхове чрез 6-(пропан-2-ил)-3-метил-морфолин-2,5-дион (**1**) и е сравнено с това на две по-рано изследвани цикло-дипепсипептиди: 3,6-ди(пропан-2-ил)-4-метил-морфолин-2,5-дион (**2**) и 3-(2-метилпропил)-6-(пропан-2-ил)-4-метил-морфолин-2,5-дион (**3**) и алопуринол. Съединението **1** показва значителна инхибираща активност спрямо ХО от плъхове ( $IC_{50} = 49.82 \mu\text{g/mL}$ ), сравнима с активността на **2** и **3**. Алопуринолът, като широко използван инхибитор на ХО и лекарство за лечение на подагра проявява по-силен инхибиращ ефект върху ХО от съединенията **1-3**. Съединенията **1** са синтезирани като смес от два диастереоизомера (*3S,6R*) и (*3S,6S*). Молекулно моделиране е приложено за да даде поглед върху връзките им с ензимните активни центрове. Обработката на данните с помощта на координатите на Lineweaver–Burk показват, че съединение (**1**) е конкурентен инхибитор на ХО. Двете форми на **1** се свързват с входа на тесен „тунел“ към диоксо-тиомолибденовата половина на активния център на ХО, блокирайки по този начин достъпа на субстратите до металния атом.

## Anaerobic co-digestion of waste fruits and vegetables and swine manure in a pilot-scale bioreactor

V. N. Hubenov \*, S. N. Mihaylova, I. S. Simeonov

*The Stephan Angeloff Institute of Microbiology, Bulgarian Academy of Sciences  
Acad. G. Bonchev, bl. 26, Sofia 1113, Bulgaria*

Received May 8, 2014, Revised March 9, 2015

Anaerobic digestion (AD) of mixtures of different substrates is a new trend in biogas production. It gives possibilities to stimulate the AD of materials not easily susceptible to this process by mixing them with other substances which are easier degradable or to improve the content of compounds, C/N ratio and thus the process stability. In this study, swine manure (SM) and a specific mixture of waste fruits and vegetables (WFV) were used as single substrates and in a mixture at various ratios. The mixture of WFV was with a constant ratio of 40% waste potatoes (WP), 20% waste tomatoes (WT), 20% waste cucumbers (WC) and 20% waste apples (WA). The results showed that the increase of the WFV in the inlet organics mixture led to an increase of the specific daily biogas flow rate at a slight decrease of methane and small increase of the carbon dioxide content in the biogas obtained. The optimal mix ratio for co-digestion of SM and WFV maximizing the biogas and the methane yields obtained from a unit of biodegraded organics was found to be SM:WFV = 70:30. Under this conditions, the biogas and methane yields from a unit of degraded organics reached 1.090 m<sup>3</sup>/kgVS.day and 0.65 m<sup>3</sup>/kgVS.day, respectively. The co-digestion of SM and WFV not only improved the stability of the anaerobic process, but also led to a higher methane production.

**Keywords:** Anaerobic co-digestion, swine manure, waste fruits and vegetables, biogas, methane, biodegradation, optimum

### INTRODUCTION

Anaerobic digestion (AD) is an effective biotechnological process for treating different agricultural, municipal and industrial wastes [1, 2, 3]. It combines environmental depollution (ecological aspect) with production of renewable energy – biogas, the main component of which is methane (energetical aspect).

Another ecological effect of AD is the reduction of methane (a strong greenhouse gas) emissions [4].

However, AD is a very unstable process in regard to the biogas reactor operation due to the complicated interactions between different microbial species, as well as to the complex transformations of the organic matter affected by a variety of environmental factors [5].

AD has been widely used for the biodegradation of cattle manure (CM), swine manure (SM), poultry litter (PL) and activated sludge (AS) from wastewater treatment plants. Traditionally, the process is a single substrate treatment [1, 2], but recently many authors reported that AS, CM and food waste can be used as main co-substrates in the anaerobic co-digestion of waste fruits and vegetables (WFV) [6, 7, 8, 9].

AD of mixtures of different substrates is a new trend in biogas production. It gives possibilities to stimulate the AD of materials not easily susceptible to this process by mixing them with other substances which are easier degradable. The other advantages of the co-digestion are in that potential inhibitor compounds can be diluted, nutrient balance can be improved and biogas yield increased [10].

WFV are produced in large quantities in markets in many big cities [10, 11, 12] and are inadequately treated by land application.

AD reduces the need of waste disposal and leads to the formation of biogas and digestate (potential manure). Our previous studies demonstrated good performances of AD of WFV and either CM or AS in mesophilic conditions [17, 20]. However, until now, very few studies have been carried out concerning the optimal ratio of different co-substrates [15, 16].

The aim of this paper was to study the anaerobic co-digestion of SM and a mixture of WFV at various ratios under mesophilic conditions in a pilot-scale continuously stirred-tank bioreactor in view of obtaining an optimal ratio for maximizing the methane production.

---

\* To whom all correspondence should be sent:  
E-mail: vhubenov@microbio.bas.bg

## MATERIALS AND METHODS

### MATERIALS

#### Specificity and pretreatment of SM and WFV as substrates for AD

In this study, the substrates used for AD were SM and a mixture of WFV at various ratios. The mixture of WFV was at a constant ratio of 40% waste potatoes (WP), 20% waste tomatoes (WT), 20% waste cucumbers (WC) and 20% waste apples (WA). All components of the mixture of WFV were mixed with an appropriate amount of water, ground with mixer and filtered through a coarse sieve. The SM was obtained from a little farm nearby Sofia. The WFV were collected from markets in Sofia. The material was homogenized in an electric blender. The samples were stored at 4°C in a refrigerator until usage.

The following parameters were determined using analytical methods: total solids (TS), volatile solids (VS), *pH*. Total biogas production and biogas composition (CH<sub>4</sub> and CO<sub>2</sub>) were measured using appropriate devices.

#### Experimental setup (pilot-scale bioreactor)

The experiments were carried out in a 100-L pilot-scale continuously stirred-tank anaerobic bioreactor (ABR) with a working volume of 80 L in mesophilic conditions (34 ± 0.5°C) [24]. The ABR was operated in semi-continuous mode. The scheme of the pilot-scale ABR is shown on Fig. 1.

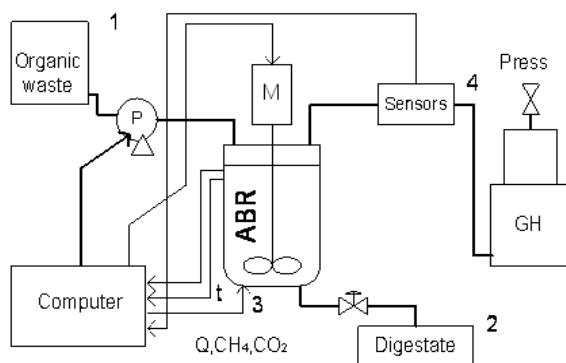


**Fig. 1.** Experimental setup of pilot scale ABR  
1 – vessel for the influent (substrate); 2 – vessel for the effluent (digestate); 3 – heater control; 4 – sensors for Q, CH<sub>4</sub>, CO<sub>2</sub>, ABR – anaerobic bioreactor; GH – gas holder; M – AC drive of the stirrer; P – peristaltic or progressive cavity type pump, t – sensor for the temperature in the bioreactor; Press – sensor for the pressure in the bioreactor

The substrate (organic waste) was stored in a plastic can of 25 L placed in the influent line of the ABR. The digestate taken out of it during semi-continuous operation (feeding one to 24 times daily) was stored in a plastic can of 50 L in the

next-door auxiliary service premises of the biogas plant.

A biogas outlet from the upper bioreactor flange led off the biogas to a 200 L metal gas holder (GH) operating on the water displacement principle (the inner vessel, placed in a vessel with water, is displaced vertically by the biogas).

The biogas flow rate was measured through transformation of the linear shift of the inlet vessel of the GH into normalized electrical signal (sensor developed by our team).

Samples for *pH* measurements and biochemical analyses were taken from the effluent of the bioreactor (digestate). Corrections of *pH* were done (if necessary) with additions of 2 N NaOH to the influent.

## METHODS

### Analytical methods

**TS and VS.** TS and VS were measured according to standard methods (APHA-AWWA-WPCF, 1985).

**Biogas yield.** Total biogas production was measured by the water displacement technique (graduated gas holder) and by a sensor developed by our team [24].

**Biogas composition.** The biogas composition was measured with computerized devices of MSR (Germany) with infrared sensors.

*pH* in the bioreactors was measured daily in the effluent with a laboratory *pH*-meter. *pH* of the influent was also measured daily.

**Chemicals.** All chemicals used were of analytical grade and were obtained from commercial sources.

### Calculations

For comparison of data, some parameters were calculated according to the following formulas:

- degree of biodegradation (DBD):

$$DBD = \frac{VS_{infl} - VS_{effl}}{VS_{infl}} \cdot 100 [\%],$$

where  $VS_{infl}$  and  $VS_{effl}$ , [g/L] are volatile solids, per 1 L of the working volume, of the influent and of the effluent, respectively;

- specific biogas production:

$$Q_{biogas}^{sp} = \frac{Q_{biogas}^{spV}}{VS_{effl}(t-1) - VS_{effl}(t) + VS_{infl}},$$

where  $Q_{biogas}^{sp}$  [dm<sup>3</sup> biogas/g VS.day] – specific flow rate of methane obtained from 1 L of the working volume of the bioreactor per 1 g biodegraded organics, per day;

- specific methane production:

$$Q_{CH_4}^{sp} = \frac{Q_{CH_4}^{spV}}{VS_{effl}(t-1) - VS_{effl}(t) + VS_{infl}}$$

where  $Q_{CH_4}^{sp}$  [dm<sup>3</sup> CH<sub>4</sub>/g VS.day] – specific flow rate of methane obtained from 1 L of the working volume of the bioreactor and from 1 g biodegraded organics;  $Q_{biogas}^{spV}$  and  $Q_{CH_4}^{spV}$  - specific flow rate of biogas and methane, respectively, obtained from 1 L of the working volume of the bioreactor per day and were calculated as follows:

$$Q_{biogas}^{spV} = \frac{Q_{biogas}}{V_{work}}, \quad Q_{CH_4}^{spV} = \frac{Q_{CH_4}}{V_{work}}$$

## RESULTS AND DISCUSSION

### Startup

The startup of the ABR was done with SM using the natural microbial community in this substrate. After the start of the AD of SM, this process was stabilized as a continuous one with a dilution rate  $D = 0.025 \text{ day}^{-1}$  in the next 60 days.

### Experiments with mixtures of SM and WFV

After the stabilization of the continuous process of AD of SM with  $D = 0.025 \text{ day}^{-1}$ , addition of WFV in various ratios was started as follows:

- co-digestion of SM and WFV in a ratio of 90:10 was started and stabilized during the next 30 days;
- the same was done for ratios SM:WFV = 70:30, 50:50 and 25:75;
- operation with AD of a mixture only of WFV was performed in the last phase of this experiment.

During the whole incubation period, the specific daily biogas flow rate  $Q_{biogas}^{spV}$  increased proportionally with the increase of WFV percentage in the feeding substrate. At the same time, there was a slight decrease in the CH<sub>4</sub> content and slight increase in the CO<sub>2</sub> content. These may have been due to the higher content of VS in the WFV mixture than in SM.

There was also an increase of the specific daily methane flow rate  $Q_{CH_4}^{spV}$  despite the small increase of the CO<sub>2</sub> content in the biogas obtained.

The organic load of the pilot ABR, the average specific daily biogas and methane yields, as well as the degree of biodegradation for anaerobic co-digestion of mixtures with different ratio of SM and WFV and for  $D = 0.025 \text{ day}^{-1}$  are presented in Table 1.

The maximal biogas yield from a unit of degraded organics in the anaerobic co-digestion of mixtures of SM and WFV was at a ratio SM:WFV = 70:30 with a value of 0.65 m<sup>3</sup>/kgVS/day. This result is comparable with that obtained by Bouallagui *et al.* [23] – biogas yield of 0.61 m<sup>3</sup>/kgVS/day from a mixture of WFV and abattoir wastes at the ratio of 30:70.

In our case the biogas yield was by 38.5% higher at this ratio in comparison with SM as a single substrate, and by 16.5% higher in comparison with WFV as a single substrate. In spite of the decrease of methane content in the biogas with the increase of WFV in the mixture, the yield of methane from unit degraded organics was maximal at the same ratio and was higher than the methane yields from WFV and SM as single substrates with 20.0 % and 35.4%, respectively.

Bouallagui *et al.* [23] reported 34.4 % higher methane yield for the mixture with the highest result than for the anaerobic digestion of WFV as a single substrate. The methane yield for WFV as a single substrate was about 0.52 m<sup>3</sup>/kgVS/day which is higher than that for SM as a single substrate with 19.2%. Kafle *et al.* [24] considered that co-digestion of SM and apple waste at 67:33 ratio (bioreactor operated at continuous mode and HRT=30 days) leads to 16 % higher methane yield than AD of SM.

The degree of biodegradation at the optimal ratio with respect to biogas and methane yields (SM:WFV = 70:30), was lower, compared to the degree of pure substrates biodegradation (SM or WFV).

**Table 1.** Biodegradation, biogas and methane yield for different ratios of SM and WFV for  $D = 0.025 \text{ day}^{-1}$

Substrate	Organic load, kgVS/m <sup>3</sup> .day	Biogas yield, m <sup>3</sup> /kgVS.day	Content of CH <sub>4</sub> , vol %	Yield of CH <sub>4</sub> , m <sup>3</sup> /kgVS.day	DBD, %
SM	0.446	0.67	62	0.42	72.3
90% SM + 10% WFV	0.500	0.726	61	0.44	50.3
70% SM + 30% WFV	0.466	1.090	60	0.65	60.3
50% SM + 50% WFV	0.970	0.536	59	0.32	70.6
25% SM+ 75% WFV	1.290	0.580	58	0.34	83.1
WFV	1.15	0.91	57	0.52	78.9



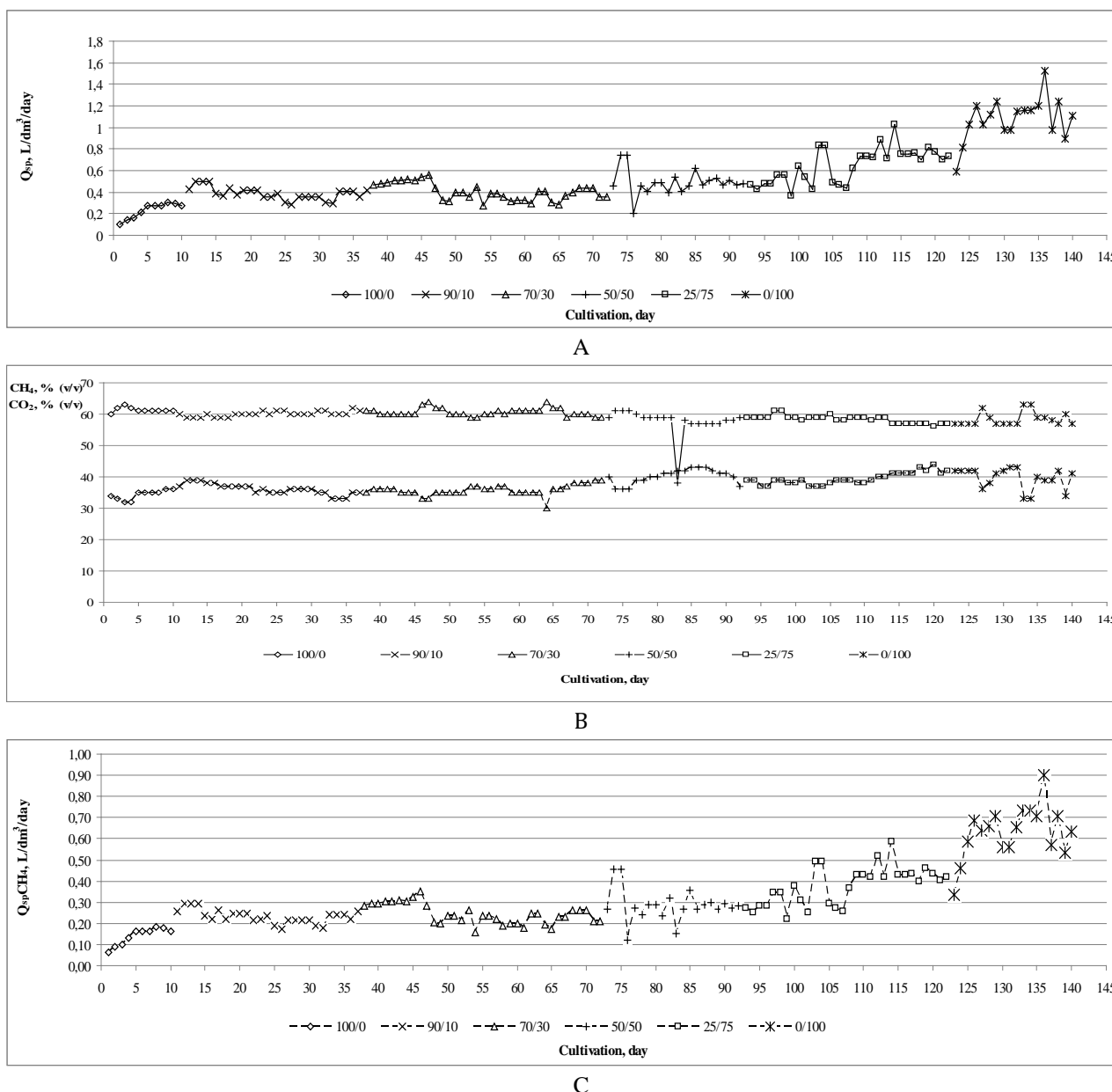


Fig. 2. A. Specific flow rate of biogas  $Q_{biogas}^{spV}$  [L/dm<sup>3</sup>/day] for different ratios of SM and WFV in the substrate;  
 B. Content of methane and carbon dioxide in the biogas;  
 C. Specific flow rate of methane  $Q_{CH_4}^{spV}$  [L/dm<sup>3</sup>/day] for different ratios of SM and WFV in the substrate

### CONCLUSION

Generation of methane gas from mixtures of SM and WFV is a stable and effective biomethanization process.

The optimal ratio for co-digestion of SM and WFV maximizing the biogas and the methane yields obtained from a unit of biodegraded organics was found to be SM:WFV = 70:30. Under this condition, the biogas and methane yields from a unit of degraded organics amounted to 1.090 m<sup>3</sup>/kgVS.day and 0.65 m<sup>3</sup>/kgVS.day, respectively. The co-digestion of SM and WFV not only improved the stability of the anaerobic process, but also led to a higher methane production.

However, the degree of biodegradation at that optimal ratio (DBD=60.3 %) was lower compared to the degree of single substrates biodegradation (DBD = 72.3 % for SM as a single substrate and DBD = 78.9 % for WFV as a single substrate).

These results were object of a utility model of the patent administration of the Republic of Bulgaria [25].

**Acknowledgements:** The authors gratefully acknowledge the financial support of this work by the Bulgarian National Science Fund, contract No DFNI-E02/13.

## REFERENCES

1. B. Ahring, (Ed.). Biomethanation, I and II, Springer – Verlag Berlin – Heidelberg, 2003.
2. D. Deublein, A. Steinhauser. Biogas from waste and renewable resources. Wiley-VCH Verlag, Weinheim, 2008.
3. I. Simeonov, in: Contemporary approaches to modeling, optimization and control of biotechnological processes. S. Tzonkov (Ed.), Prof. Marin Drinov Acad. Publ. House, Sofia, 2010.
4. A. Zahariev, D. Penkov, A. Aladjadjian, *Annual Research & Review in Biology*, **4**, 709 (2014).
5. M. H. Gerardi. The microbiology of anaerobic digesters. John Wiley&Sons, Inc. New Jersey, 2003.
6. F. Callaghan, D. Wase, K. Thayanithy, C. Forster, *Biomass Bioenergy*, **22**, 71 (2002).
7. F. Shen, H. Yuan, Y. Pang, S. Chen, B. Zhu, D. Zou, Y. Liu, J. Ma, L. Yu, X. Li, *Bioresour. Technol.*, **144**, 80 (2013).
8. C. Gomez-Lahoz, B. Fernandez-Gimenez, F. Garcia-Herruzo, J. Rodriguez-Maroto, C. Vereda-Alonso, *J. Environ. Sci. Health., Part A*, **42**, 481, (2007).
9. Y. Jiang, S. Heaven, C.J. Banks, *Renew Energ*, **44**, 206 (2012)
10. S. Berlian, S. Sukandar, D. Panjaitan, *Energy Procedia* **32**, 176 (2013).
11. H. Bouallagui, R. Ben Cheikh, L. Marouani, M. Hamdi, *Bioresour. Technol.*, **86**, 85 (2003).
12. E. A. Scano, C. Asquer, A. Pistis, L. Ortu, V. Demontis, D. Cocco, *Energy Convers. Manage.*, **77**, 22 (2014).
13. APHA, Standard methods for the examination of waste and wastewater. American Public Health Association, Washington, DC, 2005.
14. E. I. Garcia-Peña, P. Parameswaran, D.W. Kang, M. Canul-Chan, R. Krajmalnik-Brown, *Bioresour. Technol.*, **102**, 9447, (2011).
15. J. Lin, J. Zuo, L. Gan, L. Peng, L. Fenglin, K. Wang, L. Chen, H. Gan, *J. Environ. Sci.*, **23**, 1403 (2011).
16. M. Rizk, R. Bergamasco, C. Tavares, *Int. J. Chem. React. Eng.*, **5** (2007).
17. M. Saev, B. Koumanova, I. Simeonov, *J. Univ. Chem. Technol. Metallurgy*, **44**, 55 (2009).
18. M. Saev, B. Koumanova, I. Simeonov, *Biotechnol. Biotechnol. Equip.*, special issue, **23**, 832 (2009).
19. M. Saev, I. Simeonov, B. Koumanova, *J. Biotechnol.*, **150**, Supplement, 171 (2010).
20. I. Simeonov, S. Mihaylova, B. Kalchev, E. Chorukova, S. Marinova, Study on the Anaerobic Co-Digestion of Waste Fruits and Vegetables, 5<sup>th</sup> International scientific conference on Water, Climate and Environment issues (BALWOIS 2012), Ohrid, 28 May – 2 June 2012 (on flash).
21. U. D. Akpubio, A. E. Akpakpan, G. N. Emin, *J. Basic Appl. Sci. Res.*, **2**, 4839 (2012).
22. I. Simeonov, B. Kalchev, S. Mihaylova, V. Hubenov, A. Aleksandrov, R. Georgiev, N. Christov, Pilot-scale Biogas Plant for the Research and Development of New Technologies, *Int. J. Bioautomation*, **16**, 187 (2012).
23. H. Bouallagui, H. Lahdheb, E. Ben Romdan, B. Rachdi, M. Hamdi, *J. Environ. Manage.*, **90**, 1844 (2009).
24. G. Kafle, S. Kim, *Appl. Energ.*, **103**, 61 (2013).
25. I. Simeonov, D. Denchev, S. Mihaylova, V. Hubenov, E. Chorukova, *Utility model № 1814/22.01.2014 of the patent administration of the Republic of Bulgaria* (2014).

## АНАЕРОБНА БИОДЕГРАДАЦИЯ НА СМЕСИ ОТ ОТПАДНИ ПЛОДОВЕ И ЗЕЛЕНЧУЦИ И СВИНСКИ ТОР В ПИЛОТЕН БИОРЕАКТОР

В. Н. Хубенов \*, С. Н. Михайлова, И. С. Симеонов

*Институт по микробиология „Стефан Ангелов“, Българска академия на науките  
Ул. Акад.Г. Бончев, бл. 26, София 1113, България*

Постъпила на 8 май, 2014. Коригирана на 9 март, 2015

(Резюме)

Анаеробната биодegradация (АБД) на смеси от различни субстрати е нов подход при получаването на биогаз. Това дава възможност да се стимулира АБД на трудно разградими субстрати, чрез смесването им с други субстанции, които се поддават по-лесно на АБД или да се подобри състава, съотношението C/N и от там и стабилността на процеса. В настоящото изследване в качеството на субстрати бяха използвани свински тор (СТ) и специфична смес от отпадни плодове и зеленчуци (ОПЗ), както самостоятелно, така и под формата на смеси в различни съотношения. Сместа от ОПЗ беше с постоянно съотношение на отпадни картофи – 40%, отпадни домати – 20%, отпадни краставици – 20% и отпадни ябълки – 20%. Резултатите показват, че увеличаването на съдържанието на ОПЗ в подавания субстрат води до увеличаване и на специфичния добив на биогаз, паралелно със слабо понижаване на CH<sub>4</sub> и малко повишаване на CO<sub>2</sub> в биогаза. Беше установено, че оптималното съотношение между свинския тор и ОПЗ, по отношение на получаване на максимален добив на биогаз и CH<sub>4</sub>, е СТ:ОПЗ = 70:30. При тези условия добивите на биогаз и CH<sub>4</sub> от единица разградена органика достигаха съответно 1.090 м<sup>3</sup>/кг.ден и 0.65 м<sup>3</sup>/кг.ден. Съвместната АБД на СТ и ОПЗ не само подобрява стабилността на анаеробния процес, но води и до по-висока продукция на CH<sub>4</sub>.

## Pressure drop of highly efficient Raschig Super-Ring packing for column apparatuses

D. B. Dzhonova-Atanasova\*, Sv. Ts. Nakov, E. N. Razkazova-Velkova, N. N. Kolev

*Institute of Chemical Engineering, Bulgarian Academy of Sciences,  
Acad. G. Bonchev St., Bl. 103, 1113 Sofia, Bulgaria*

Received March 28, 2014, Revised June 23, 2015

The present work presents and generalizes own experimental data for the pressure drop of highly efficient metal Raschig Super-Ring (RSR) packing for packed columns. The contemporary demands from the chemical industry for environment protection and waste free production lead to focusing on application of these apparatuses in purification of flue gases and waste water. RSR is modern high-performance random packing of latest generation, which combines effective mass transfer, large interfacial area and uniform distribution of the phases over the column cross section. There is no universal methodology for calculating the performance characteristics of this packing. The constants of the existing equations for practical calculations are obtained for each individual packing size. The aim of the present work is to propose more precise equations for prediction of the pressure drop of RSR packing, which are common for all investigated sizes and reflect the influence of the packing geometry and the column redumping.

**Keywords:** Packed columns; Random packing; Pressure drop; Experiments, Equations for dry and irrigated RSR packing.

### INTRODUCTION

Packed bed columns are apparatuses with very large area of application for heat and mass transfer processes in gas-liquid systems. The requirements for industry sustainability lead to their wide employment for solving problems connected with reducing the environmental pollution and increasing the energy efficiency of industrial processes using conventional and renewable energy resources. The development of packings of special materials and designs is of great importance for the modern applications of packed columns.

The present work presents, discusses and generalizes the obtained own experimental data for the pressure drop of metal Raschig Super-Ring (RSR) packing. This is modern high-performance packing introduced in 1995 and classified in [1] as the first random packing of forth generation, which combines effective mass transfer, large interfacial area and uniform distribution of the phases over the column cross section. The high loading capacity and exceptionally low pressure drop, approaching that of structured packings, result in high column throughputs at low operating costs. A comparison with Intalox Metal Tower Packing (IMTP) with the same specific surface area [2] shows that the effective surface of the RSR is about 15 % higher. The advantages of RSR are explained in [1] with the hydrodynamic optimization of the packing geometry. The form of the packing element

consisting of sinus strips enables formation of continuous films (characteristic for structured packings). The recurring connection points of the strips promote turbulence. The open geometry provides uninterrupted cleaning of the packing surface preventing from fouling and reduces drops formation, which suppresses foaming. The place of RSR packing is evident from the selection of its industrial applications in [1], which includes Natural gas plant, Methanol plant, Refinery plant, Synthesis gas plant, Effluent water treatment, Effluent gas plant, Sulfur plant, Ammonia plant, Ethanol plant etc.

There is no universal methodology for calculating the performance characteristics of RSR packing. The equations for practical calculations proposed in [3, 4, 5] are obtained on the base of a uniform theoretical approach for random and arranged packings with packing specific constants for each individual packing type and size. A prediction of the pressure drop of RSR packings is presented in [5] with the assumption that the flow through the packing is regarded as a flow through a bundle of identical channels and the relation for an empty tube is applicable. For the pressure drop of dry packing the following equation (in our notation) is proposed:

$$\frac{\Delta P_0}{H} = C_{P,0} \left( \frac{64}{Re_{G1}} + \frac{1.8}{Re_{G1}^{0.08}} \right) \frac{a}{\varepsilon^3} \frac{F_{G1}^2}{2} \frac{1}{K_p}, \quad (1)$$

where  $\Delta P_0$  is dry packing pressure drop, Pa,  $H$  is packing height, m;  $Re_{G1}$  is gas flow Reynolds number

\* To whom all correspondence should be sent:

E-mail: dzhonova@bas.bg

$$Re_{G1} = \frac{w_0 d_{p1}}{(1-\varepsilon) \nu_G}, \quad (2)$$

where  $w_0$  is gas velocity with reference to the column cross section,  $m^3/m^2s$ ;  $d_{p1}$  is particle diameter defined as:

$$d_{p1} = 6 \frac{1-\varepsilon}{a}. \quad (3)$$

Here  $\varepsilon$  is packing void fraction;  $\nu_G$  is gas phase kinematic viscosity,  $m^2/s$ ;  $F_G = w_0 \sqrt{\rho_G}$  is gas velocity factor,  $Pa^{0.5}$ ;  $\rho_G$  is gas density,  $kg/m^3$ ;  $K_p$  is wall factor, given by the relation

$$\frac{1}{K_p} = 1 + \frac{2}{3} \frac{1}{1-\varepsilon} \frac{d_{p1}}{d_c}, \quad (4)$$

where  $d_c$  is the column diameter, m.

For calculation of the pressure drop under and over the loading point of irrigated packings Billet and Schultes [5] offered the following equation:

$$\frac{\Delta P}{H} = C_{P,0} \left( \frac{64}{Re_{G1}} + \frac{1.8}{Re_{G1}^{0.08}} \right) \left( \frac{\varepsilon - H_t}{\varepsilon} \right)^{1.5} \left( \frac{H_t}{H_{t0}} \right)^{0.3} \times \exp \left( \frac{13300}{a^{3/2} \sqrt{Fr_L}} \right) \quad (5)$$

where  $Fr_L = \frac{L^2 a}{g}$  is the Froude number;  $H_{t0}$  is the

total holdup under the loading point  $m^3/m^3$ ;  $H_t$  is the total holdup for the corresponding regime,  $m^3/m^3$ ;  $L$  is the liquid superficial velocity,  $m^3/m^2s$ ;  $a$  is packing specific surface area,  $m^2/m^3$ ;  $g$  is acceleration of gravity,  $m/s^2$ .

The packing specific constant  $C_{P,0}$ , has been obtained by processing experimental data, including data for 6 metal and plastic RSR packings, and the constant's values are given in [5] for each packing type and size.

The aim of the present study is on the basis of own experimental data to propose general equations for calculation of the pressure drop of metal Raschig Super-Ring packings, which are common for all investigated sizes shown in Table 1 and reflect the influence of the packing geometry and the column redumping.

## EXPERIMENTAL

The experimental data are obtained in a column of a 470 mm diameter with a system air-water, scheme presented in [6]. The liquid superficial velocity varies between 0 and 120  $m^3/(m^2h)$ . The packing height is 2400 mm. The liquid phase packing pressure drop was measured by means of an optical differential manometer with an accuracy of 0.1 Pa. The distributor ensures 923 drip points per  $m^2$ . At a pressure drop higher than

200 Pa, a conventional U-tube differential manometer was used. The investigated packing is shown in Fig. 1, [7]. It can be seen that there are three packing geometries differing in number of strips and undulation pattern.



Fig. 1. Metal Raschig Super-Ring packings, source [7]

The packing geometrical characteristics are shown in Table 1. Here  $h_s$  denotes the strip width in m, and  $h$ - the height of the packing element, m, Fig. 2.

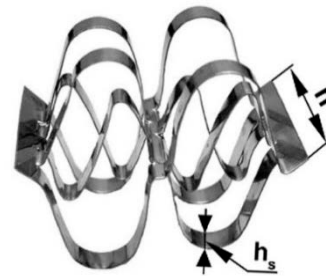


Fig. 2. RSR packing element

The nominal diameter  $d_n$  is the diameter of the inscribed circle in the packing element in m. All other geometrical characteristics are defined as averages obtained from triplicate redumping of the packing in the column.

Figs. 3 to 9 present our experimental results for the pressure drop of all investigated packings at different liquid superficial velocities versus the gas velocity factor  $F_G$ . The obtained lines are typical for random packings. They are in good agreement with the data of the manufacturer Rraschig GmbH [7] for close values of column diameters. It is shown in [1] that the pressure drop of RSR is lower compared to similar sizes of other high performance packings, e.g. the pressure drop of RSR No. 2 is 38% of the pressure drop of 50-mm Pall-ring, (system cyclohexane/ *n*-heptane, 1.65 bar, total reflux).

**Table 1.** Geometrical characteristics of the investigated metal RSR packing

Name	Surface area $a$ $m^2/m^3$	Free volume $\epsilon\%$	Element height $h$ mm	Number of strips $n$	Strip width $h_s$ mm	Diameter of inscribed circle $d_n$ mm	Hydraulic Diameter $d_h$ mm
Raschig Super-Ring No. 0.5	236.2	96.5	15	4	3.8	21	16.3
Raschig Super-Ring No. 0.6	180.5	97.5	20	6	3.3	27	21.6
Raschig Super-Ring No. 0.7	175.9	97.7	20	5	4.0	34	22.2
Raschig Super-Ring No.1	155.5	98.0	25	6	4.2	34	25.2
Raschig Super-Ring No. 1.5	105.8	97.9	30	5	6.0	48	37.0
Raschig Super-Ring No. 2	100.6	98.0	38	6	6.3	50	39.0
Raschig Super-Ring No. 3	74.9	98.0	50	6	8.3	65	52.3

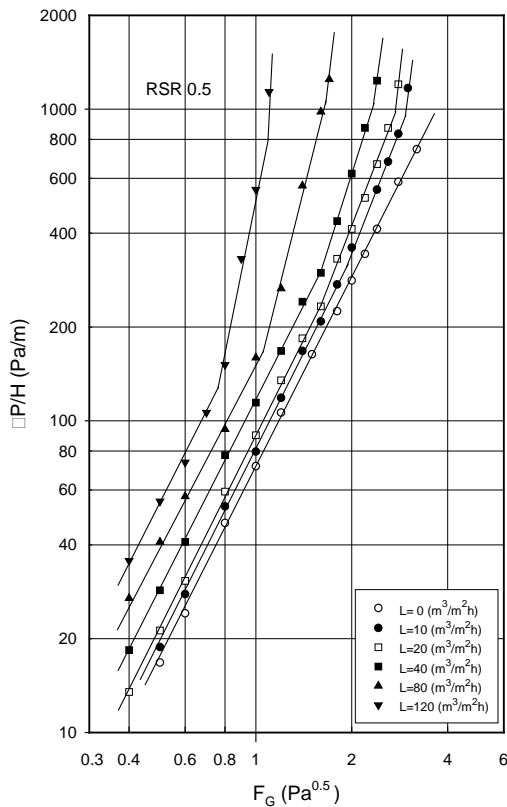


**Fig. 3.** Pressure drop of metal RSR 0.5 at various superficial liquid velocities vs. gas velocity factor.

It was found in [6] that at comparable values of the specific area and the liquid superficial velocities RSR juxtaposed to IMTP, have about 15% higher effective area and over 35 % lower pressure drop versus effective area, at the same gas velocity.

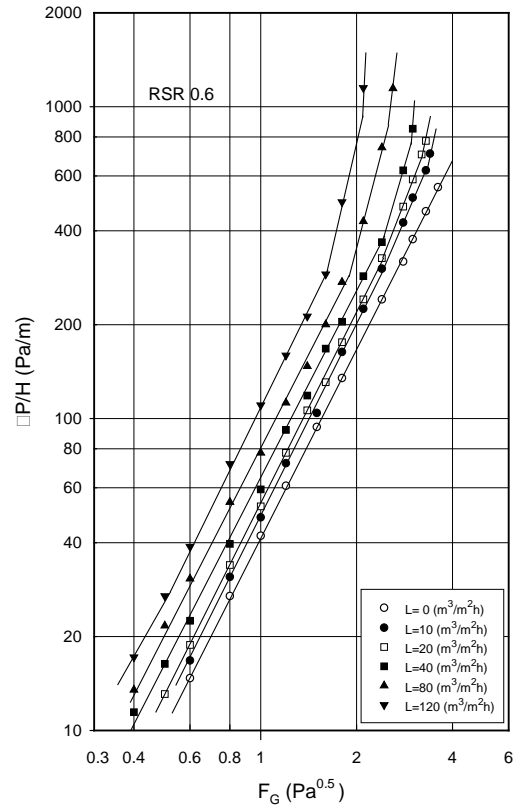


**Fig. 4.** Pressure drop of metal RSR 0.6 at various superficial liquid velocities vs. gas velocity factor.

EQUATIONS

The present work accepts the usual channel model for the flow through the packing, where  $H$  is the height and  $d_h$  the diameter of the hypothetical vertical channels and therefore the relation for the dry packing pressure drop is:

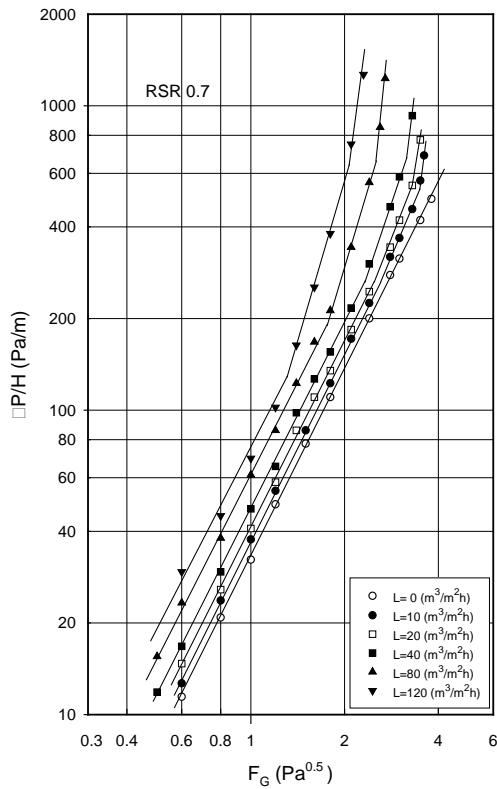


**Fig. 5.** Pressure drop of metal RSR 0.7 at various superficial liquid velocities vs. gas velocity factor.

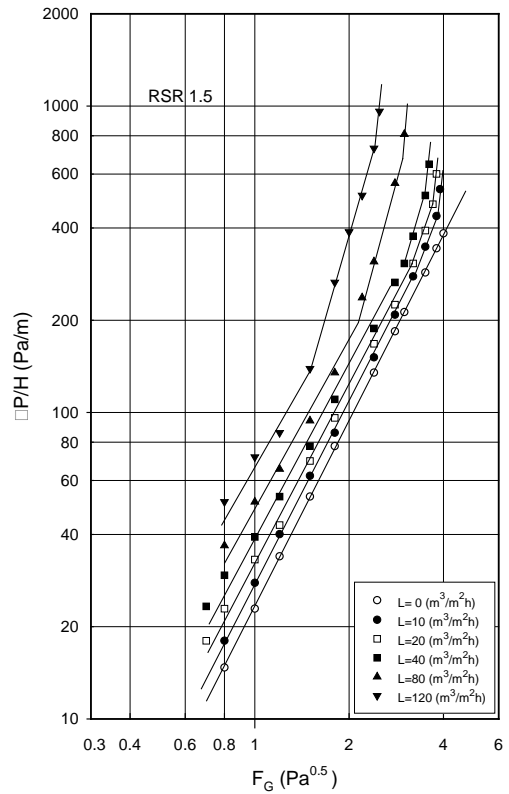


**Fig. 7.** Pressure drop of metal RSR 1.5 at various superficial liquid velocities vs. gas velocity factor.

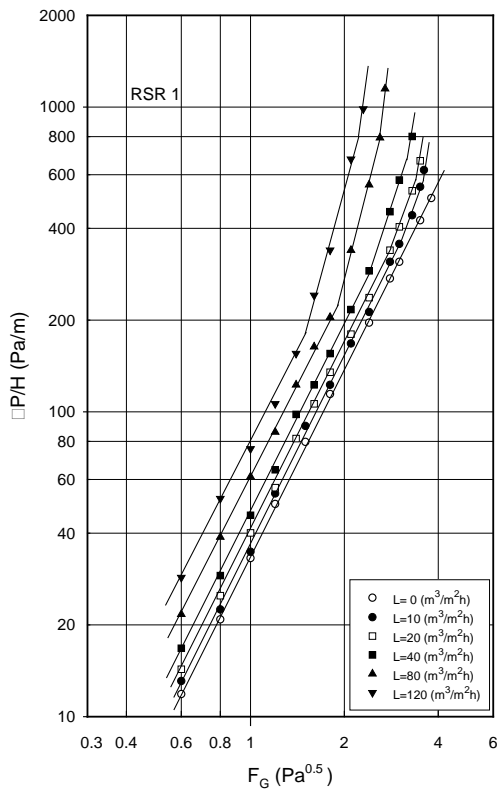


**Fig. 6.** Pressure drop of metal RSR 1 at various superficial liquid velocities vs. gas velocity factor

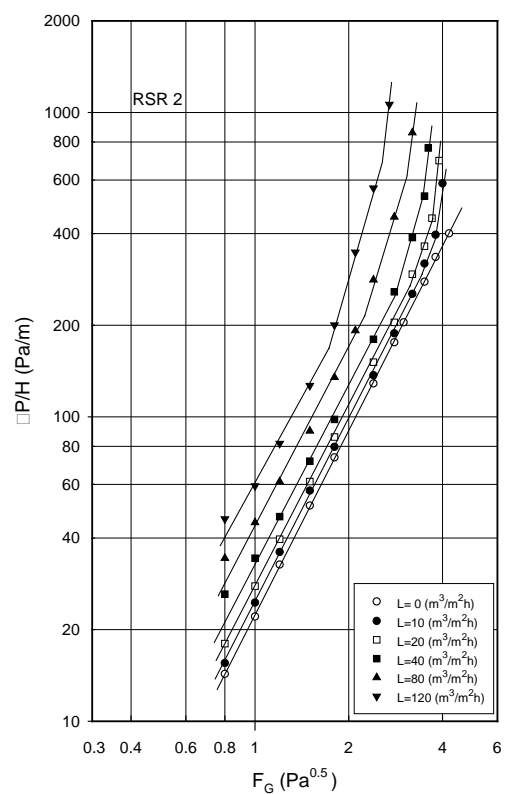


**Fig. 8.** Pressure drop of metal RSR 2 at various superficial liquid velocities vs. gas velocity factor.

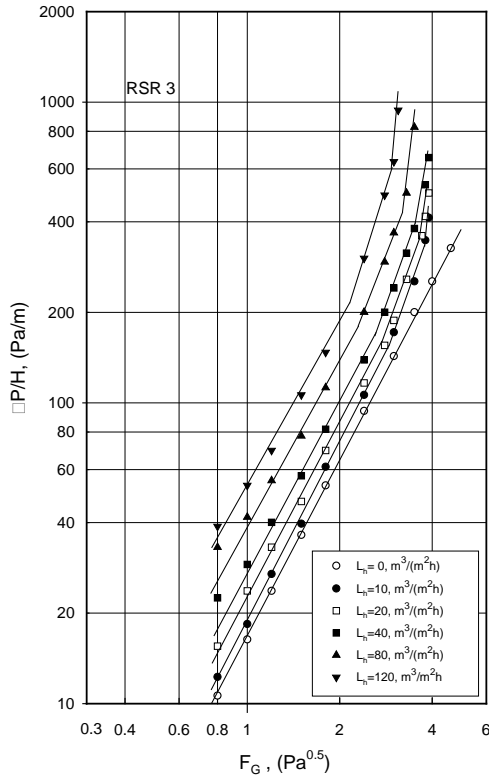


Fig. 9. Pressure drop of metal RSR 3 at various superficial liquid velocities vs. gas velocity factor.

$$\frac{\Delta P_0}{H} = \psi \frac{\rho_G (w_0 / \varepsilon)^2}{2d_h}, \quad (6)$$

where  $\psi = \frac{\Delta P_0 d_h}{2H \rho_G (w_0 / \varepsilon)^2}$  is the resistance factor, equivalent to Euler number,  $\Delta P_0$  is dry packing pressure drop, Pa;  $d_h = \frac{4\varepsilon}{a}$  is packing hydraulic diameter, m.

On the basis of dimensional analysis and processing the experimental data for dry packings by regression analysis, the following equation was obtained:

$$\psi = 4.0 \left( \frac{h_s}{d_n} \right)^{0.72} (ad_n)^{-0.48} \quad (7)$$

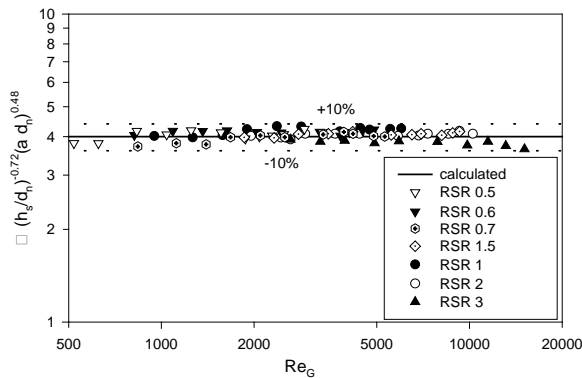


Fig. 10. Comparison of experimental data for dry packings with results calculated by Eq. (7).

Fig. 10 presents a comparison of Equation (7) with the data obtained for all the studied packings, where  $Re_G = \frac{w_0 d_h}{\nu_G \varepsilon}$  is Reynolds number for the gas phase.

The mean deviation of Equation (7) is 4.1%. The precision of the obtained experimental constants at 95% statistical reliability is given below:

$$4.0 \pm 0.46; \quad 0.72 \pm 0.028; \quad -0.48 \pm 0.075.$$

It was found that the resistance factor depends on the geometrical characteristics of the packing elements expressed by the simplexes  $h_s/d_n$  and  $ad_n$ , and is independent of  $Re_G$ , which speaks for turbulent hydrodynamic regime of the gas flow in the dry packing bed [8]. The range of  $Re_G$  in Fig. 10 exhibits some lower limit of the fully developed turbulent regime than that defined in [9] as  $Re_G > 1200$ , which confirms again that the form of RSR promotes turbulence, [1].

The equations for determination of the irrigated packing pressure drop under and over the loading point are obtained using the relation proposed by Zhavoronkov et al. [10]:

$$\Delta P = \frac{\Delta P_0}{(1-A)^3} \quad (8)$$

where  $A$  is a dimensionless value related to the liquid holdup and represents the packing void fraction occupied by the liquid phase. In [10, 11] it is presented as a sum:

$$A = A_0 + \Delta A \quad (9)$$

$A_0$  is the value of  $A$  under the loading point and  $\Delta A$  - the increasing of  $A$  over the loading point.

Applying dimensional analysis and processing the experimental data for packing pressure drop below the loading point with regression analysis the following expression was obtained:

$$A_0 = 0.26 Re_L^{0.17} Fr_L^{0.27}, \quad (10)$$

where  $Re_L = \frac{4L}{av_L}$  is Reynolds number for the liquid phase;  $Fr_L = \frac{L^2 a}{g \nu_L}$  is Froude number for the liquid phase;  $\nu_L$  is liquid phase kinematic viscosity,  $m^2/s$ .

The mean deviation of Equation (10) is 9.3%. The precision of the obtained experimental constants at 95% statistical reliability is given below:

$$0.26 \pm 0.051; \quad 0.17 \pm 0.024; \quad 0.27 \pm 0.015.$$

For the experimental data for packing pressure drop over the loading point the following equation was obtained:

$$\Delta A_0 = 0.17 Fr_L^{0.30} \left( \frac{w_0^2}{\varepsilon^2 g d_h} \right)^{0.30} \quad (11)$$

The mean deviation of Equation (11) is 28%. This value is acceptable because it corresponds to only 8.9% mean deviation of  $\Delta P$ . The precision of the obtained experimental constants at 95% statistical reliability is given below:

$$0.17 \pm 0.040; \quad 0.30 \pm 0.040; \quad 0.30 \pm 0.110.$$

Fig. 11 shows the good agreement of the predicted pressure drop of irrigated packing by using Eqs. (8) to (11) with our experimental data below and over the loading point in the film regime and the loading regime according to the definitions in [11].

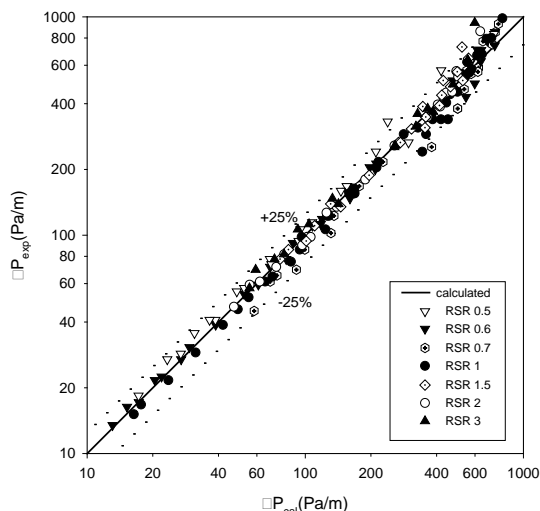


**Fig. 11.** Comparison of the experimental data for the pressure drop of irrigated packings below and above the loading point with the results calculated by Eqs. (8) to (11).

### CONCLUSION

The experimental data for the packing pressure drop obtained by the presented investigation have proven the qualities and advantages of RSR packing. Equations have been proposed, which generalize our pressure drop data from 7 sizes of metal RSR packing and constitute simple and sufficiently precise mathematical model for pressure drop prediction for engineering purposes.

Equation (7) is in good agreement with our measurements for the pressure drop of dry packing with mean deviation of 4.1%, and the resistance factor is independent of  $Re_G$ , which speaks for turbulent gas flow in the column. The equations for the pressure drop of irrigated packing describe well our experimental data under and over the loading point with mean deviation of 8.9% in respect to the pressure drop.

### REFERENCES

1. M. Schultes, *Trans IChemE*, **81**, Part A, 48 (Jan. 2003)
2. N. Kolev, *Packed bed columns for absorption, desorption, rectification and direct heat transfer*, Elsevier, 2006
3. R. Billet, *Packed Column Analysis and Design*, Ruhr-University Bochum, 1989
4. R. Billet, *Packed Towers in Processing and Environmental Technology*, Weinheim, 1995
5. R. Billet, M. Schultes, *Trans. IChemE*, **77**, Part A, (Sept. 1999)
6. Sv. Nakov, N. Kolev, L. Ljutzkanov, D. Kolev, *Chem. Eng and Process.*, **46**, (12), 1385, (2007).
7. Raschig Super-Ring, Product Bulletin 250, (accessed 16/12/2013) <http://s341789233.online.de/editor/assets/Info%20Raschig%20Super-Ring-250.pdf>
8. J. Mackowiak, *Fluid Dynamics of Packed Columns: Principles of the Fluid Dynamic Design of Columns for Gas/ Liquid and Liquid/Liquid Systems*, Springer, 2010
9. M. E. Aerov, O. M. Todes, *Hydrodynamic and thermal foundations of operation of apparatuses with stationary fluidized granular bed*, Leningrad: Himia, 1968, (Russ)
10. M. Zhavoronkov, M. E. Aerov, N. N. Umnik, *Chim. Prom.* 10, 294, (1948). (Russ)
11. N. Kolev, *Verfahrenstechnik*, **3** (4), 163, (1969)
12. A. M. Kagan, A. G. Laptev, A. S. Pushnov, M. I. Farahov, *Contact Packing of Industrial Heat and Mass Transfer Apparatuses*, Kazan: Otechestvo, 2013, (Russ)



## ХИДРАВЛИЧНО СЪПРОТИВЛЕНИЕ НА ВИСОКОЕФЕКТИВНИЯ ПЪЛНЕЖ RASCHIG SUPER-RING ЗА КОЛОННИ АПАРАТИ

Д. Б. Джонова-Атанасова\*, Св. Ц. Наков, Е. Н. Разказова-Велкова, Н. Н. Колев

*Институт по инженерна химия, Българска академия на науките  
ул. "Акад. Г. Бончев" бл. 103, 1113 София*

Постъпила на 28 март 2014 г., преработена на 23 юни 2015 г.

(Резюме)

В настоящата работа са представени и обобщени собствени експериментални данни за хидравличното съпротивление на високо ефективен метален пълнеж Raschig Super-Ring (RSR) за колони с пълнеж. Съвременните изисквания към химическата промишленост за опазване на околната среда и безотпадно производство, водят до засилване на интереса към тези апарати за цели като пречистване на димни газове и отпадни води. RSR е модерен високоефективен насипен пълнеж от последно поколение, който съчетава ефективен масообмен, голяма междуфазна повърхност и равномерно разпределение на фазите по напречно сечение на апарата. Не съществува универсална методика за пресмятане на работните характеристики на тези пълнежи. Съществуващите уравнения съдържат константи, определени за всеки отделен размер. Целта на настоящата работа е да се получат по-точни уравнения за пресмятане на хидравличното съпротивление на пълнеж RSR, общи за всички размери, които да отразяват геометрията на пълнежа и презареждането на колоната.

## A model to predict the solubility of drugs in ethanol + propylene glycol mixtures at various temperatures

A. Jouyban<sup>\*1,2</sup>, M. Khoubnasabjafari<sup>3</sup>, F. Martinez<sup>4</sup>

<sup>1</sup> Pharmaceutical Analysis Research Center and Faculty of Pharmacy, Tabriz University of Medical Sciences, Tabriz 51664, Iran

<sup>2</sup> Kimia Idea Pardaz Azarbayjan (KIPA) Science Based Company, Tabriz University of Medical Sciences, Tabriz 51664, Iran

<sup>3</sup> Tuberculosis and Lung Disease Research Center, Tabriz University of Medical Sciences, Tabriz, Iran.

<sup>4</sup> Grupo de Investigaciones Farmacéutico-Físicoquímicas, Departamento de Farmacia, Facultad de Ciencias, Universidad Nacional de Colombia, A.A. 14490, Bogotá, D.C., Colombia

Received July 16, 2014, Revised January 7, 2015

A trained version of Jouyban-Acree model is proposed employing 32 solubility data sets of 5 drugs in ethanol + propylene glycol mixtures at various temperatures. Using this model, the solubilities of a drug in the mono-solvents and the Abraham solvation parameters are required to predict the solubility in the binary solvent mixtures. The overall mean percentage deviation for the correlated data was 11.0 %, and that of a predicted data set was 11.2 %.

**Key words:** Solubility prediction, Abraham solvation parameters, Jouyban-Acree model, Ethanol + propylene glycol.

### INTRODUCTION

Solubility of a drug/drug candidate in a non-aqueous solvent mixture is an interesting topic for a pharmaceutical technologist. These solutions are used in pharmaceutical formulations such as soft gel capsules or to prepare liquid formulations of ester, amide or other drugs to prevent their possible hydrolysis. In addition, these mixtures provide some facilities in crystallization or separation processes in the pharmaceutical industry. Temperature variation is another factor affecting the solubility of pharmaceuticals in mixed solvents. In spite of experimental determination of solubility in mixed solvents at various temperatures, a number of computational models have been presented to calculate the solubility values [1, 2]. Previous results showed that the Jouyban-Acree model is the most accurate one among similar algorithms [1]. The model requires a number of experimental data points to compute the numerical values of its constants.

### DISCUSSIONS

To cover this limitation, trained versions of the model were reported to predict the solubility of drugs. The aim of this communication is to present such a generally trained model for predicting the solubility of drugs in ethanol + propylene glycol

mixtures at various temperatures and discuss on the capability of these types of model to be extended for predicting the solubility in ternary solvent mixtures. It is noteworthy that ethanol and propylene glycol are the more widely used cosolvents in the liquid dosage forms [3, 4]. Available solubility data of pharmaceuticals in ethanol + propylene glycol mixtures at various temperatures were collected from our earlier works and used to train or check the prediction capability of the trained model.

The Jouyban-Acree model is presented as [2]:

$$\log X_{m,T} = f_1 \log X_{1,T} + f_2 \log X_{2,T} + \left( \frac{f_1 f_2}{T} \right) [A_0 + A_1(f_1 - f_2) + A_2(f_1 - f_2)^2] \quad (1)$$

where  $X_{m,T}$ ,  $X_{1,T}$  and  $X_{2,T}$  are the mole fraction solubilities of the solute in the solvent mixture, solvents 1 and 2 at temperature ( $T$ , K),  $f_1$  and  $f_2$  are the solute free fractions of solvents 1 and 2,  $A_0$ ,  $A_1$  and  $A_2$  are the model constants computed using a no-intercept least square analysis [5]. The solute solubility in the solvent with higher solubility is defined as  $X_{1,T}$  and for all solvent systems  $X_{1,T} > X_{2,T}$ . The trained versions of Eq. (1) were reported for different solvent mixtures [2, 6]. In derivation of the constants of Eq. (1) for these mixtures, it is assumed that the solute-solvent interactions of various drugs are the same and no indicator parameter of the solutes was included in the model. However this is not the case for drugs, water and pharmaceutical cosolvents since they have various functional groups and the solubility of a drug

\* To whom all correspondence should be sent:  
E-mail: ajouyban@hotmail.com

depends on its physical and chemical properties and on those of the solvent system [7-10]. These properties could be represented using various computational physico-chemical properties such as those reported by Abraham *et al.* [11]. The Abraham solvation parameter models provided numerical methods for prediction of solutes' solubility in a wide variety of neat organic solvents. The Abraham models employ five parameters for each solute and six solvent coefficients that were computed for a number of common solvents [11]. The basic model proposed for processes within condensed phases is:

$$\log\left(\frac{C_s}{C_w}\right) = c + e \cdot E + s \cdot S + a \cdot A + b \cdot B + v \cdot V, \quad (2)$$

where  $C_s$  and  $C_w$  are the solute solubility in the organic solvent and water (in mole per liter), respectively,  $E$  is the excess molar refraction,  $S$  is dipolarity/polarizability of solute,  $A$  denotes the solute's hydrogen-bond acidity,  $B$  stands for the solute's hydrogen-bond basicity and  $V$  is the McGowan volume of the solute (for numerical values of the Abraham parameters computed by PharmaAlgorithm [12] see Table 1).

**Table 1.** The Abraham solvation parameters of the investigated drugs computed using PharmaAlgorithm software [12]

Solute	$E$	$S$	$A$	$B$	$V$
Acetaminophen	1.12	1.66	0.91	0.93	1.17
Carvedilol	3.08	3.00	0.62	2.09	3.10
Ibuprofen	0.78	1.01	0.57	0.51	1.78
Indomethacin	2.44	2.49	0.57	1.24	2.53
Lamotrigine	2.79	2.81	0.50	1.09	1.65
Naproxen	1.54	1.49	0.57	0.75	1.78
Phenothiazine	1.95	1.53	0.13	0.50	1.48
Salicylic Acid	0.91	1.10	0.70	0.40	0.99
Triclocarban	2.00	2.23	0.77	0.71	2.05

As noted above, in Eq. (1), there is no solute property to present the effects of different functional groups on the solute-solvent interactions in the solution. To include the possible interactions using Abraham solute parameters, it is possible to re-write Eq. (1) as:

$$\begin{aligned} \log X_{m,T} = & f_1 \log X_{1,T} + f_2 \log X_{2,T} \\ & + \left(\frac{f_1 f_2}{T}\right) [J_1 + J_2 E + J_3 S + J_4 A + J_5 B + J_6 V] \\ & + \left(\frac{f_1 f_2 (f_1 - f_2)}{T}\right) [J_7 + J_8 E + J_9 S + J_{10} A + J_{11} B + J_{12} V] \\ & + \left(\frac{f_1 f_2 (f_1 - f_2)^2}{T}\right) [J_{13} + J_{14} E + J_{15} S + J_{16} A + J_{17} B + J_{18} V] \end{aligned} \quad (3)$$

where  $J$  terms are the model constants. Solubilities of acetaminophen [13], ibuprofen [14], indomethacin [15], naproxen [14], triclocarban [16], carvedilol [17], phenothiazine [18], lamotrigine [19], and salicylic acid [20] in ethanol + propylene glycol mixtures were fitted to Eq. (3) and the constants with the significance level of  $< 0.10$  were included in the final model which is:

$$\begin{aligned} \log X_{m,T} = & f_1 \log X_{1,T} + f_2 \log X_{2,T} \\ & + \left(\frac{f_1 f_2}{T}\right) [-491.408 + 913.350E - 1014.694S] \\ & + \left(\frac{f_1 f_2 (f_1 - f_2)}{T}\right) [-27.372E] \\ & + \left(\frac{f_1 f_2 (f_1 - f_2)^2}{T}\right) [35.146E] \end{aligned} \quad (4)$$

The back-calculated solubilities using Eq. (4) were compared with the corresponding experimental values using the mean percentage deviation ( $MPD$ ):

$$MPD = \frac{100}{N} \sum \frac{|X_{m,T}^{Predicted} - X_{m,T}^{Observed}|}{X_{m,T}^{Observed}} \quad (5)$$

as an accuracy criterion. The maximum (25.2 %)  $MPD$  was observed for carvedilol at 25 °C and the overall  $MPD$  ( $\pm SD$ ) was  $11.0 \pm 5.7$  % (details are listed in Table 2). Equation (4) was trained using mole fraction solubility data of drugs in the binary solvent mixtures and the solvent compositions were expressed as mass fractions, however it is capable of calculating the molar solubility of drugs and the obtained  $MPD$  was  $11.2 \pm 6.0$  %. There was no significant difference between 11.0 % (mole fraction unit) and 11.2 % (molar unit) (t-test,  $p > 0.05$ ), revealing that the trained model using mole fraction data could be used to predict the solubility of drugs in molarity. This is due to the presence of experimental values of  $X_{1,T}$  and  $X_{2,T}$  in the model which normalize the data.

Theoretically, Eq. (4) could be used to predict the solubility of drugs in ethanol + propylene glycol mixtures at any temperature of interest. In most pharmaceutical applications, the temperature range lies at 20-40 °C, however due to the existence of  $T$  term in the equation and linear relationship of solubility and reciprocal absolute temperature (according to van't Hoff equation [22]), one might use the developed Eq. (4) for solubility prediction at temperatures  $< 20$  and  $> 40$  °C.

To test the prediction capability of Eq. (4) for other data, the solubility of acetaminophen in ethanol + propylene glycol at 25 °C [21] was predicted. It should be added that none of these data points was used in the training process of Eq. (4),

**Table 2.** Details of the investigated solubility data sets, number of data points in each set ( $N$ ) and mean percentage deviations ( $MRD$ ) for mole fraction and molar solubilities

Solute	Solvent 1	T (°C)	N	Ref	Eq.(4) (mole fraction data)	Eq. (4) (molar data)
Acetaminophen	Ethanol	20	11	[13]	1.3	3.7
		25	11	[13]	1.0	3.4
		30	11	[13]	3.3	6.3
		35	11	[13]	3.7	4.5
		40	11	[13]	6.8	5.4
Carvedilol	Ethanol	25	11	[17]	25.2	20.5
		30	11	[17]	13.6	10.4
		35	11	[17]	11.4	8.6
		40	11	[17]	14.5	8.2
Ibuprofen	Ethanol	20	6	[14]	14.6	12.6
		25	6	[14]	12.0	10.0
		30	6	[14]	7.4	5.6
		35	6	[14]	4.9	3.6
		40	6	[14]	6.4	4.1
Indomethacin	Ethanol	20	11	[15]	18.8	22.1
		25	11	[15]	15.4	18.3
		30	11	[15]	14.7	17.7
		35	11	[15]	13.4	16.7
		40	11	[15]	8.7	13.2
Lamotrigine	Propylene Glyc	25	9	[19]	.	14.9
Naproxen	Ethanol	20	6	[14]	17.4	8.8
		25	6	[14]	16.7	8.2
Naproxen	Ethanol	30	6	[14]	14.3	6.1
		35	6	[14]	16.7	8.2
		40	6	[14]	11.9	4.8
Phenothiazine	Ethanol	25	12	[10.2]	13.9	10.0
Salicylic acid	Ethanol	25	11	[20]	.	9.7
Triclocarban	Propylene glycol	20	11	[16]	12.0	17.6
		25	11	[16]	9.5	18.6
		30	11	[16]	7.8	17.7
		35	11	[16]	6.0	19.9
		40	11	[16]	5.1	20.0
Overall ( $\pm$ SD)					11.0 ( $\pm$ 5.7)	11.2 ( $\pm$ 6.0)

and the only required data was the solubilities in neat ethanol and propylene glycol. The obtained  $MPD$  was  $7.1 (\pm 5.6) \%$  ( $N=11$ ). It should be noted that the solvent composition of the predicted data set was expressed as volume fraction. When these fractions were converted to mass fractions, and the solubilities were predicted, the obtained  $MPD$  was  $6.1 (\pm 5.3) \%$  and there was borderline difference between two  $MPD$  values (paired t-test,  $p=0.12$ ) revealing that in order to obtain more accurate predictions, the solvent composition of the solvent mixture should be expressed as it was in the training data set.

#### CONCLUSION

In conclusion, the trained model was capable of providing accurate predictions for solubility of

drugs in ethanol + propylene glycol mixtures at various temperatures and could be recommended for relevant computations and the required input data are the solubilities in the neat mono-solvents and the Abraham solvation parameters which could be easily computed using an online software.

**Acknowledgment:** The authors would like to thank PharmaAlgorithms Inc. for providing the trial version of the software.

#### REFERENCES

1. A. Jouyban-Gharamaleki, L. Valaee, M. Barzegar-Jalali, B. J. Clark, W. E. Acree Jr., *Int. J. Pharm.*, **177**, 93 (1999).
2. A. Jouyban A., W. E. Acree Jr., *J. Drug Del. Sci. Tech.*, **17**, 159 (2007).

3. J. T. Rubino, Cosolvents and cosolvency, in: Encyclopedia of Pharmaceutical Technology, J. Swarbrick, J. C. Boylan (eds), vol 3, Marcel Dekker, Inc., New York, 1988.
4. S. H. Yalkowsky, Solubility and Solubilization in Aqueous Media, American Chemical Society and Oxford University Press, New York, 1999.
5. A. Jouyban-Gharamaleki, J. Hanaee, *Int. J. Pharm.*, **154**, 245 (1997).
6. Sh. Soltanpour, A. Jouyban, *J. Solution Chem.*, **40**, 2032 (2011).
7. S. H. Yalkowsky, T. J. Roseman, Solubilization of drugs by cosolvents, in: Techniques of Solubilization of Drugs, S. H. Yalkowsky (ed), Marcel Dekker, New York, 1981.
8. A. Martin, P. Bustamante, A. H. C. Chun, Physical Chemical Principles in the Pharmaceutical Sciences, 4th edition, Lea & Febiger, Philadelphia, 1993.
9. Y. Marcus, The Properties of Solvents, John Wiley & Sons, Chichester, 1998.
10. K. A. Connors, Thermodynamics of Pharmaceutical Systems: An Introduction for Students of Pharmacy, Wiley-Interscience, Hoboken, NJ, 2002.
11. D. M. Stovall, W. E. Acree Jr., M. H. Abraham, *Fluid Phase Equilib.*, **232**, 113 (2005).
12. PharmaAlgorithms, ADME Boxes, Version 3.0, PharmaAlgorithms Inc., 591 Indian Road, Toronto, ON M6P 2C4, Canada, 2006.
13. J. A. Jiménez, F. Martínez, *J. Solution Chem.*, **35**, 335 (2006).
14. D. P. Pacheco, Y. J. Manrique, F. Martínez, *Fluid Phase Equilib.*, **262**, 23 (2007).
15. E. A. Cantillo, D. R. Delgado, F. Martinez, *J. Mol. Liq.*, **181**, 62 (2013).
16. A. R. Holguín., D. R. Delgado, F. Martínez, *Quím. Nova*, **35**, 280 (2012).
17. S. Vahdati, A. Shayanfar, J. Hanaee, F. Martínez, W. E. Acree, Jr., A. Jouyban, *Ind. Eng. Chem. Res.*, **52**, 16630 (2013).
18. S. Ahmadian, V. Panahi-Azar, M. A. A. Fakhree, W. E. Acree, Jr., A. Jouyban, *J. Chem. Eng. Data*, **56**, 4352 (2011).
19. F. Ghaderi, M. Barzegar-Jalali, A. Jouyban, *Lat. Am. J. Pharm.*, **33**, 1392 (2014).
20. A. Jouyban, V. Panahi-Azar, F. Khonsari, *J. Mol. Liq.*, **160**, 14 (2011).
21. A. Jouyban, H. K. Chan, N. Y. K. Chew, M. Khoubnasabjafari, W. E. Acree Jr., *Chem. Pharm. Bull.*, **54**, 428 (2006).
22. D. J. W. Grant, M. Mehdizadeh, A. H. L. Chow, J. E. Fairbrother, *Int. J. Pharm.*, **18**, 25 (1984).

## МОДЕЛ ЗА ПРЕДСКАЗВАНЕ НА РАЗТВОРИМОСТТА НА ЛЕКАРСТВА В СМЕСИ ОТ ЕТАНОЛ И ПРОПИЛЕН-ГЛИКОЛ ПРИ РАЗЛИЧНИ ТЕМПЕРАТУРИ

А. Джуйбан<sup>\*1,2</sup>, М. Хубнасабджафари<sup>3</sup>, Ф. Мартинез<sup>4</sup>

<sup>1</sup>Изследователски център за фармацевтични анализи и факултет по фармация, Медицински университет в Табриз, Табриз 51664, Иран

<sup>2</sup>Идея химия Пардаз Азърбайджан (КІРА) Научно базирана компания, Медицински университет в Табриз, Табриз 51664, Иран

<sup>3</sup>Изследователски център по белодробни заболявания и туберкулоза, Медицински университет в Табриз, Табриз, Иран

<sup>4</sup>Група за фармако-физикохимични изследвания, Департамент по фармация, Национален университет на Колумбия, Богота, Колумбия

Постъпила на 16 юли, 2014 г.; коригирана на 7 януари, 2014 г.

(Резюме)

Предложена е тренирана версия на модела на Jouyban-Acree, използваща набор от 32 разтворимости на пет лекарства в смеси от етанол и пропилен-гликол при различни температури. Предсказването на разтворимостите в бинарните смеси чрез използването на този модел предполага познаването на разтворимостта в единични разтворители и солватационните параметри по Abraham. Общото средно процентно отклонение за обработените данни е 11.0 %, а за предсказаните данни е 1.2 %.

## Efficient one-pot room-temperature synthesis of 2-imidazolines from aldehydes

H. Alinezhad<sup>1\*</sup>, K. Nemati<sup>1</sup>, M. Zare<sup>2</sup>

<sup>1</sup>Department of Organic Chemistry, Faculty of Chemistry, University of Mazandaran, Babolsar, Iran

<sup>2</sup>Department of Basic Science, Faculty of Herbs, Amol University of Special Modern Technologies, Amol, Iran

Received August 12, 2014, Revised May 14, 2015

The reactions of various aromatic and aliphatic aldehydes with ethylenediamine followed by *N*-iodosaccharin treatment proceed at room temperature to give the corresponding dihydroimidazoles in high yields. The process is simple, fast and convenient.

**Key words:** Imidazoline, Aldehyde, Ethylenediamine, *N*-Iodosaccharin.

### INTRODUCTION

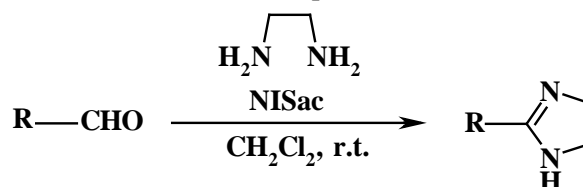
Imidazoline derivatives exhibit significant biological and pharmacological properties including antihypertension, antihistamine, antihyperglycemia, antiinflammation, antidepression and antitumor activities [1]. They are also used as synthetic intermediates [2], chiral catalysts [3] and ligands for asymmetric catalysis [4] in organic synthesis.

Many methodologies for the synthesis of 2-imidazolines from nitriles [1], esters [5], carboxylic acids [6], aldehydes [7], hydroxy amides [8] and benzimidate [9] as starting materials have been developed. Recently, several protocols for the synthesis of imidazoline derivatives have been reported by condensation of aldehydes with ethylenediamine using various oxidants and catalysts such as NBS [10], ceric ammonium nitrate (CAN) [11], I<sub>2</sub> [12,13], H<sub>2</sub>O<sub>2</sub> [14], K<sub>4</sub>[Fe(CN)<sub>6</sub>] [15], and Al<sub>2</sub>O<sub>3</sub>-OK [16], etc. Some of these procedures suffer from limitations including long reaction time, high temperature, N<sub>2</sub> atmosphere, use of strong oxidizing agent, difficult work-up and limitation in the use of aliphatic and heteroaromatic aldehydes as a substrate.

*N*-Halosaccharins (NXSac, X = Cl, Br, I) are stable crystalline compounds, soluble in most common organic solvents, insoluble in water [17, 18] and more electrophilic than their analogues such as *N*-haloamides. *N*-halosaccharins are oxidizing [19] and halogenating agents which are often employed for the halogenation of alkenes, activated aromatic compounds, enol acetates, 1,3-diones, etc. [18, 20].

Herein, we report an efficient one-pot method

for the synthesis of 2-imidazolines from various aldehydes and ethylenediamine using *N*-iodosaccharin at room temperature (Scheme 1).



**R :aryl,alkyl**

### Scheme 1

### EXPERIMENTAL

Materials were purchased from Fluka and Merck companies. NISac was prepared according to the reported procedure [17b]. Products were characterized by their spectroscopic data (<sup>1</sup>H NMR, <sup>13</sup>C NMR and FT-IR) and physical properties and comparison with authentic samples.

#### General procedure for the synthesis of imidazoline

A mixture of aldehyde (1 mmol), ethylenediamine (2 mmol) and *N*-iodosaccharin (2 mmol) in CH<sub>2</sub>Cl<sub>2</sub> was stirred at room temperature for the appropriate time according to Table 1. After completion of the reaction, NaOH (10%) aq or sat. NaHCO<sub>3</sub> was added to the reaction mixture and extracted with CH<sub>2</sub>Cl<sub>2</sub>. The organic layer was dried over Na<sub>2</sub>SO<sub>4</sub>, the solvent was removed under reduced pressure and the corresponding 2-imidazoline was obtained in 90-95% yield.

#### Some Product Characterization Data

**2-(4-Bromophenyl)imidazoline (Table 2, entry 10):** IR (KBr): 3150, 2930, 2870, 1625, 1475, 1290, 820 cm<sup>-1</sup>. <sup>1</sup>H NMR (400MHz, CDCl<sub>3</sub>): δ=7.66 (d, *J*=8.4 Hz, 2H), 7.56 (d, *J*=8.4 Hz, 2H), 3.811(s,

\* To whom all correspondence should be sent:  
E-mail: heshmat@umz.ac.ir

4H).  $^{13}\text{C}$  NMR (100 MHz,  $\text{CDCl}_3$ ):  $\delta$ = 161.8, 131.6, 130.6, 128.0, 124.0.

**2-(4-Cyanophenyl)imidazoline (Table 2, entry 12):** IR (KBr): 3150, 2930, 2200, 1590, 1270, 840  $\text{cm}^{-1}$ .  $^1\text{H}$  NMR (400MHz,  $\text{CDCl}_3$ ):  $\delta$ =7.9 (d,  $J$ =8.4 Hz, 2H), 7.6 (d,  $J$ =8.4 Hz, 2H), 3.729 (s, 4H).  $^{13}\text{C}$  NMR (100 MHz,  $\text{CDCl}_3$ ): 164.0, 135.5, 131.2, 125.7, 119.1, 114.0.

**2-(2-Furyl)imidazoline (Table 2, entry 15):** IR (KBr): 3125, 2925, 2860, 1640, 1505, 1170, 975  $\text{cm}^{-1}$ .  $^1\text{H}$  NMR (400MHz,  $\text{CDCl}_3$ ):  $\delta$ =7.49 (d,  $J$ =4, 1H), 7.02 (d,  $J$ =4 Hz, 1H), 6.5 (q,  $J$ =4 Hz, 1H), 3.79 (s, 4H).

## RESULTS AND DISCUSSION

The reaction conditions were optimized using ethylenediamine and benzaldehyde as model substrates. Therefore, benzaldehyde (1 mmol) was treated with ethylenediamine (2 mmol) in the presence of different amounts of *N*-iodosaccharin in various solvents at room temperature. It was observed that this reaction goes well in dichloromethane among the commonly used organic solvents such as dichloroethane, ethanol and acetonitrile (Table 1, entries 1–4).

After choosing the solvent, we changed the amount of NISac to 1, 1.5 and 2.5 mmol and the product was obtained in 50–93% yields (Table 1 entries 5-7). Using higher amounts of NISac did not affect the yield and reaction time (Table 1, entry 7). Also, we decreased the amount of ethylenediamine from 2 to 1.5 mmol and the yield of the reaction decreased, while the reaction time increased (Table 1, entry 8).

After optimization of the reaction conditions, the reaction of other aldehydes with ethylenediamine was carried out in the presence of NISac and the results are presented in Table 2. As shown in Table 2, several substituted aromatic, heteroaromatic and aliphatic aldehydes were used successfully in this procedure.

Aromatic aldehydes having electron donating groups such as methoxy and methyl (Table 2, entries 2-7) or electron withdrawing groups such as chloro, bromo and nitro (Table 2, entries 8-12) were converted to the corresponding imidazolines in excellent yields. Similarly, heteroaromatic aldehydes such as pyridine, furan and thiophen carbaldehyde reacted with ethylenediamine to give the desired compounds without any problem in 93–95% yields (Table 2, entries 13-16). Finally, butanal as an aliphatic aldehyde (Table 2, entry 17) successfully afforded 2-propylimidazoline in excellent yield under the optimal reaction conditions. It is important to note that no iodinated or over-oxidized products (i.e. imidazole) were found in the reaction mixtures. The yields of the reactions were dependent on the substituents present on the substrates. Reactions with substrates having electron-withdrawing groups proceeded at faster rates than those with electron-donating groups.

In Table 3, we compared our results with those obtained by a reported procedure for the synthesis of 2-(2-pyridyl)imidazoline. The data presented in this table show the promising feature of this method in terms of reaction rate and the yield of product compared with that reported in the literature.

**Table 1:** Optimization of reaction conditions.

Entry	Solvent	NISac (mmol)	Ethylenediamine (mmol)	Time (h)	Yield (%) <sup>a</sup>
1	MeOH	2	2	5	70
2	$\text{CH}_3\text{CN}$	2	2	5	73
3	$\text{ClCH}_2\text{CH}_2\text{Cl}$	2	2	5	75
4	$\text{CH}_2\text{Cl}_2$	2	2	2	93
5	$\text{CH}_2\text{Cl}_2$	1	2	4	65
6	$\text{CH}_2\text{Cl}_2$	1.5	2	4	75
7	$\text{CH}_2\text{Cl}_2$	2.5	2	2	93
8	$\text{CH}_2\text{Cl}_2$	2	1.5	5	70

<sup>a</sup>Yields refer to isolated products.

**Table 2.** Reaction of aldehydes with ethylenediamine in the presence of NISac <sup>a</sup>

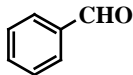
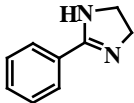
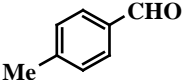
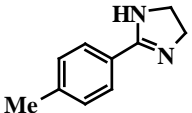
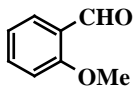
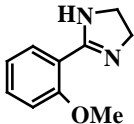
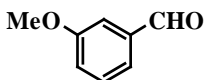
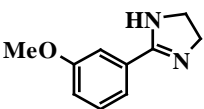
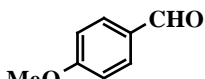
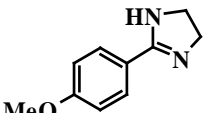
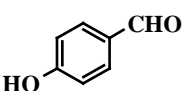
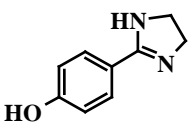
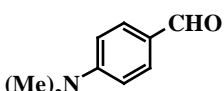
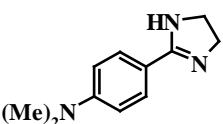
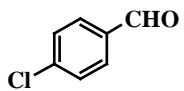
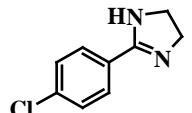
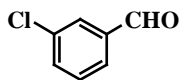
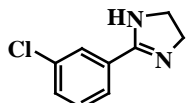
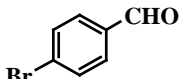
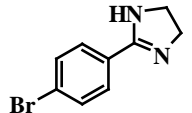
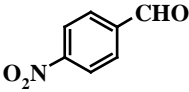
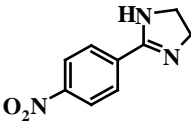
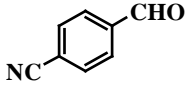
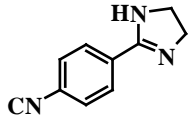
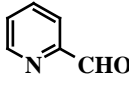
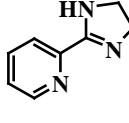
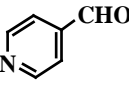
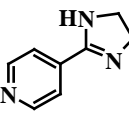
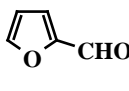
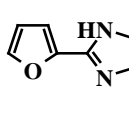
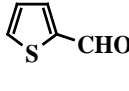
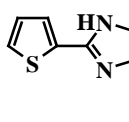
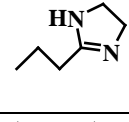
Entry	Substrate	Product	Time (h)	Yield (%)	M.p. (°C) [Ref.]
1			2	93	100-102 [10a]
2			3.5	92	181-182 [13]
3			0.2	90	72-74 [10a]
4			1.5	90	100-102 [10a]
5			4	90	135-137 [10a]
6			2.5	90	299-301 [1a]
7			2	93	255-257 [13]
8			2.5	92	183-185 [10a]
9			2.5	90	134-136 [21]
10			1.5	90	239-241 [7a]



Table 2 continued

Entry	Substrate	Product	Time (h)	Yield (%)	M.p. (°C) [Ref.]
11			1	95	232-233 [7a]
12			1	90	196-198 [7a]
13			0.25	95	99-100 [22]
14			0.25	93	135-136 [22]
15			3	93	180-181 [22]
16			3	94	175-176 [22]
17	$\text{CH}_3(\text{CH}_2)_2\text{CHO}$		1	90	43-45 [23]

<sup>a</sup>The reaction was carried out at room temperature using aldehyde (1 mmol), ethylenediamine (2 mmol), NISac (2 mmol) and  $\text{CH}_2\text{Cl}_2$  (5 mL).

**Table 3.** Comparison of some other procedures with the present method for synthesis of 2-(2-pyridyl)imidazoline from 2-pyridine carbaldehyde.

Entry	Oxidant	Reaction conditions	Time	Yield(%) [Ref]
1	NISac	rt	15 min	95
2	$\text{I}_2$	$70^\circ\text{C}$ (under Ar)	3 h	97 [12]
3	NBS	$0^\circ\text{C}$ -rt	overnight	100 [10]
4	CAN	reflux	50 min	65 [11]

### CONCLUSION

We have developed a mild, simple one-pot method for the synthesis of 2-imidazoline from aldehydes and ethylenediamine using an efficient oxidizing agent (NISac). This method is performed at room temperature and many functional groups such as halogen, amine and nitrile can be introduced without any problem. It needs no heat or inert atmosphere and has high product yields and short reaction time.

**Acknowledgements:** This work was supported by a Research Grant from University of Mazandaran, Iran.

### REFERENCES

- (a) M. Sun, H. D. Wei, Li, Y. Zheng, J. Cai, M. Ji, *Synthetic Commun.*, **38**, 3151 (2008). (b) T. Shalina Begum, U.C.A. Jaleel and P.M. Shafi, *Int. J. Pharm. Biomed. Sci.*, **4(1)**, 40 (2013).
- (a) R. C. F. Jones, J. R. Nichols, *Tetrahedron Lett.*, **31**, 1771 (1990). (b) M. E. Jung, A. Huang, *Org. Lett.*, **2**, 2659 (2000).
- E. J. Corey, M. J. Grogan, *Org. Lett.*, **1**, 157 (1999).
- Bastero, C. Claver, A. Ruiz, S. Castillon, E. Daura, C. Bo, *Chem. Eur. J.*, **10**, 3747 (2004).
- G. Neef, U. Eder, G. Sauer, *J. Org. Chem.*, **46**, 2824 (1981).
- H. Vorbruggen, K. A. Krolkiewicz, *Tetrahedron Lett.*, **22**, 4471 (1981).
- (a) M. Ishihara, H. Togo, *Tetrahedron*, **63**, 1474 (2007). (b) H. Fujioka, K. Murai, O. Kubo, Y. Ohla, Y. Kita, *Tetrahedron*, **63**, 638 (2007).

8. N. A. Boland, M. Casey, S. J. Hynes, J. W. Matthews, M. P. A. Smyth, *J. Org. Chem.*, **67**, 3919 (2002).
9. (a) J. Szychala, *Synthetic Commun.*, **30**, 1083 (2000).
10. H. Fujioka, K. Murai, Y. Ohba, *Tetrahedron Lett.*, **46**, 2197 (2005) (b) G. S. Sant'Anna, P. Machado, P. D. Sauzem, F. A. Rosa, M. A. Rubin, J. Ferreira, H. G. Bonacorso, N. Zanatta, M. A. P. Martins, *Bioorg. Med. Chem. Lett.*, **19**, 546 (2009).
11. R. Kumar, Y. C. Joshi, *E. J. Chem.*, **4**, 606 (2007).
12. M. Ishihara and H. Togo, *Tetrahedron*, **63** 1474 (2007).
13. P. Gogoi, D. Konwar, *Tetrahedron Lett.*, **47**, 79 (2006).
14. G. Bai, K. Xu, G. Chen, Y. Yang, T. Li, *Synthesis*, 1599 (2011).
15. Kabeer Shaikh, A. Vishal Patil, *Org. Commun.*, **5:1**, 12 (2012).
16. P. J. Das, A. Baruah, *Indian J. Chem.* **51**, 752 (2012).
17. (a) D. Dolenc, *Synlett*, **4**, 544 (2000). (b) S. Soraia, S. Jaoquim and D. Marco, *Synth. Commun.*, **33**, 935 (2003).
18. D. Dolene, B. Sket, *Synlett*, 327 (1995).
19. V. Manoharan, N. Venkatasubramanian, *Indian Chem. Soc.*, **63**, 613 (1986).
20. (a) I. Mozek, B. Sket, *Synthetic Commun.*, **22**, 2513 (1992). (b) D. Dolenc, *Synth. Commun.*, **33**, 2917 (2003).
21. S. Haneda, A. Okui, C. Ueba, M. Hayashi, *Tetrahedron*, **63**, 2414 (2007).
22. M. Anastasiadou, S. Danoum, L. Crane, G. Baziard-mouysset, M. Payard, D. H. Caignard, M. C. Rettori, P. Renard, *Bioorg. Med. Chem.*, **9**, 585 (2001).
23. A. Grigorev, G. I. Shchukin, L. B. Volodarskii, *Izv. Akad. Nauk SSSR. Ser. Khim.*, **5**, 1140 (1983).

## ЕФЕКТИВНА ЕДНОСТАДИЙНА СИНТЕЗА ПРИ СТАЙНА ТЕМПЕРАТУРА НА 2-ИМИДАЗОЛИНИ ОТ АЛДЕХИДИ

Х. Алинежад<sup>1\*</sup>, К. Немати<sup>1</sup>, М. Заре<sup>2</sup>

<sup>1</sup>Отделение по органична химия, Химически факултет, Университет на Мазандаран, Баболсар, Иран  
<sup>2</sup>Катедра по основни науки, Факултет Наука и билки, Университет Специални Съвременни технологии в Амол, Амол, Иран

Получена на 12 август, 2014, ревизирана на 14 май 2015

(Резюме)

Реакциите на различни ароматни и алифатни алдехиди с етилендиамин, последвано от третиране с N-йодозахарин, проведено при стайна температура, за да се получат съответните дихидроимидазоли с високи добиви. Процесът е прост, бърз и удобен.

## Barium aluminate nano-spheres grown on the surface of BaAl<sub>2</sub>O<sub>4</sub>: a versatile catalyst for the Knoevenagel condensation reaction of malononitrile with benzaldehyde

M. Momayezan<sup>1</sup>, M. Ghashang\*<sup>2</sup>, S. A. Hassanzadeh-Tabrizi<sup>2</sup>

<sup>1</sup>Advanced Materials Research Center, Materials Engineering Department, Najafabad Branch, Islamic Azad University, Najafabad, Iran

<sup>2</sup>Department of Chemistry, Faculty of Sciences, Najafabad Branch, Islamic Azad University, P.O. Box: 517; Najafabad, Esfahan, Iran

Received August 20, 2014, Revised December 3, 2014

In this study, barium aluminate nano-powder was synthesized *via* homogeneous precipitation method and was investigated for its activity on the Knoevenagel condensation reaction of malononitrile with benzaldehyde. The obtained samples were characterized by X-ray diffraction (XRD), field emission scanning electron microscopy (FE-SEM), Fourier transform infrared spectroscopy (FT-IR) and energy-dispersive X-ray spectroscopy (EDAX). The XRD pattern showed a single phase of hexagonal structure. Two distinctive phases of BaAl<sub>2</sub>O<sub>4</sub> are present in the FE-SEM micrographs. The first phase is an irregular shape of agglomerated BaAl<sub>2</sub>O<sub>4</sub> nano-powders, and the second - diffused nano-spheres of BaAl<sub>2</sub>O<sub>4</sub> on the outer surface of the nano-powder. The BaAl<sub>2</sub>O<sub>4</sub> nano-spheres have an average size of about 70 nm. The BaAl<sub>2</sub>O<sub>4</sub> nano-powder was shown to be a highly efficient catalyst for the Knoevenagel condensation reaction of malononitrile with benzaldehyde under reflux conditions in ethanol as solvent. The effects of catalyst concentration, temperature and solvent on the reaction were investigated.

**Keywords:** BaAl<sub>2</sub>O<sub>4</sub>; Knoevenagel reaction; malononitrile; benzaldehyde

### INTRODUCTION

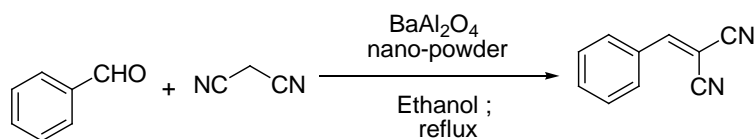
In view of homogenous and heterogeneous catalysis, basic-type catalysts and especially solid base catalysts are a challenging goal of catalysis to play a conclusive role in a lot of chemical reactions. Various solid base catalytic systems such as hydroxides, zeolites, mixed oxides, immobilized amines, metal-organic frameworks and clays are samples of the reported references [1-7].

Nowadays there is a driving force for using heterogeneous catalysts in various industries due to the environmentally friendly effect achieved, thus replacing traditional homogeneous-catalyzed reactions. Noncorrosive and environmentally benign characteristics which create fewer disposal problems are the main advantages that patronize this driving force. In addition, heterogeneous catalysts usually have higher activity, selectivity and longer catalyst life over liquid homogeneous catalysts [8-11]. However, among various acid and base heterogeneous catalysts, solid base catalysts

get much fewer applications in chemical reactions. Solid base catalysts are non-stoichiometric, non-corrosive and reusable which can be a good option for the replacement of liquid bases [12-14].

Aluminates are known to have mild basic characteristics among various bases. They are widely used in ceramics, cements, pigments, glazes, and also as industrial catalysts with superior physical properties. Among various aluminates barium aluminate (BaAl<sub>2</sub>O<sub>4</sub>) is of great interest in catalysis as it can be used in the treatment of air pollutions as a catalyst, for the preparation of humidity sensors and phosphor materials [15-21].

In view of the above advantages, in the present study an investigation on the phase formation of barium aluminate nano-powders and evaluation of their catalytic activity in the Knoevenagel condensation reaction of malononitrile with benzaldehyde [22-25] was taken up (Scheme 1).



**Scheme 1.** Knoevenagel condensation reaction of malononitrile with benzaldehyde

\* To whom all correspondence should be sent:  
E-mail: ghashangmajid@gmail.com

## EXPERIMENTAL

All reagents were purchased from Merck and Aldrich and were used without further purification. The powder X-Ray diffraction patterns were recorded with Bruker AXS D<sub>8</sub> Advance diffractometer using Cu-K $\alpha$  irradiation. FE-SEM was taken on a Hitachi S-4160 instrument to examine the shape and metallic composition of the samples. The FT-IR spectra of the materials were recorded by the standard KBr pellet technique with a Perkin Elmer 781 spectrophotometer in the range of 400-4000 cm<sup>-1</sup>.

### *Preparation of BaAl<sub>2</sub>O<sub>4</sub> nano-powder*

Two different solutions were prepared as follows: solution A: a solution of Ba(II), and Al(III) was prepared by dissolving barium chloride (20 mmol), and aluminum chloride (20 mmol) in 50 mL of water. Solution B: a solution of 2-amino ethanol (100 mmol) in 50 ml of ethanol / water (50/50 v/v). Solution B was slowly poured into solution A under vigorous magnetic stirring. The resulting mixture was aged for 5 h until a gel was formed. Finally, the gel was filtered, washed with water three times, dried and calcinated at 700 °C for 2 h.

*Knoevenagel condensation reaction of malononitrile with benzaldehyde: typical procedure*  
A mixture of benzaldehyde (1 mmol), malononitrile (1.3 mmol) and BaAl<sub>2</sub>O<sub>4</sub> nano-powder (0.01 – 0.1 g) was refluxed for 10 h. The progress of the reaction was monitored by TLC. After completion of the reaction, the catalyst was separated by simple filtration. Removal of the solvent under reduced pressure afforded the pure product as a white solid after recrystallization from ethanol.

## RESULTS AND DISCUSSION

The XRD spectrum of the BaAl<sub>2</sub>O<sub>4</sub> nano-powder is presented in Figure 1. The diffraction patterns demonstrated the formation of a single phase, as peak splitting for the presence of two phases could not be detected. It can be seen from the patterns that the synthesized material showed hexagonal structure with the corresponding diffractions of 28.3, 34.3, 39.8, 40.1, 45.0, 54.5, 57.8, 89.4 (2Theta [°]).

The morphology of the nano-particles was investigated using FE-SEM analysis (Figure 2). As can be seen from the FE-SEM micrographs, two distinctive particles of BaAl<sub>2</sub>O<sub>4</sub> are present. The first phase is an irregularly shaped agglomerate of BaAl<sub>2</sub>O<sub>4</sub> nano-powders, and the second is diffused

nano-spheres of BaAl<sub>2</sub>O<sub>4</sub> on the outer surface of the nano-powder. As can be seen in Figure 2, the BaAl<sub>2</sub>O<sub>4</sub> nano-spheres have an average size of about 70 nm for 20 particles.

The FT-IR absorption spectrum of the sample calcinated at 700 °C for 2 h is presented in Figure 3. The peak appeared at 1630 cm<sup>-1</sup> is related to the Al–O stretching vibration and the other peak at around 1437 cm<sup>-1</sup> indicated the formation of the BaAl<sub>2</sub>O<sub>4</sub> phase. The intense and broad peaks observed in the 400- 900 cm<sup>-1</sup> region may be due to the stretching and bending vibrations of Al-O and Ba-O bonds [26-27].

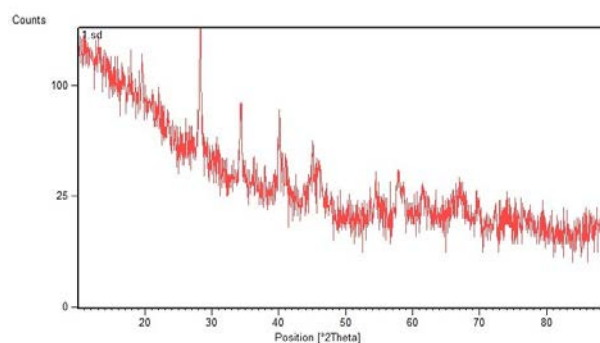


**Fig. 1.** XRD pattern of BaAl<sub>2</sub>O<sub>4</sub> nano-powder calcined at 700 °C

### *Catalytic test*

The BaAl<sub>2</sub>O<sub>4</sub> nano-powder was assessed for its catalytic activity by studying the Knoevenagel condensation reaction of malononitrile with benzaldehyde to form 2-benzylidenemalononitrile as the targeted molecule (Scheme 1).

### *Solvent Selection*

Initially the Knoevenagel condensation reaction of benzaldehyde and malononitrile was carried out in different solvents such as acetonitrile, ethanol, ethyl acetate, dichloromethane, *n*-hexane, H<sub>2</sub>O and solvent-free using BaAl<sub>2</sub>O<sub>4</sub> nano-powder as a catalyst (Table 1). The reaction was carried out under reflux conditions, until the starting materials disappeared (TLC indicating technique). In order to compare the catalytic performances of the different solvents, the yield of the reaction was used as indicator of catalytic activity. The use of solvent media led to higher product yields when compared with solvent-free conditions. Among the various solvents screened, ethanol was chosen as the approved reaction medium due to its higher product yield (Table 1).

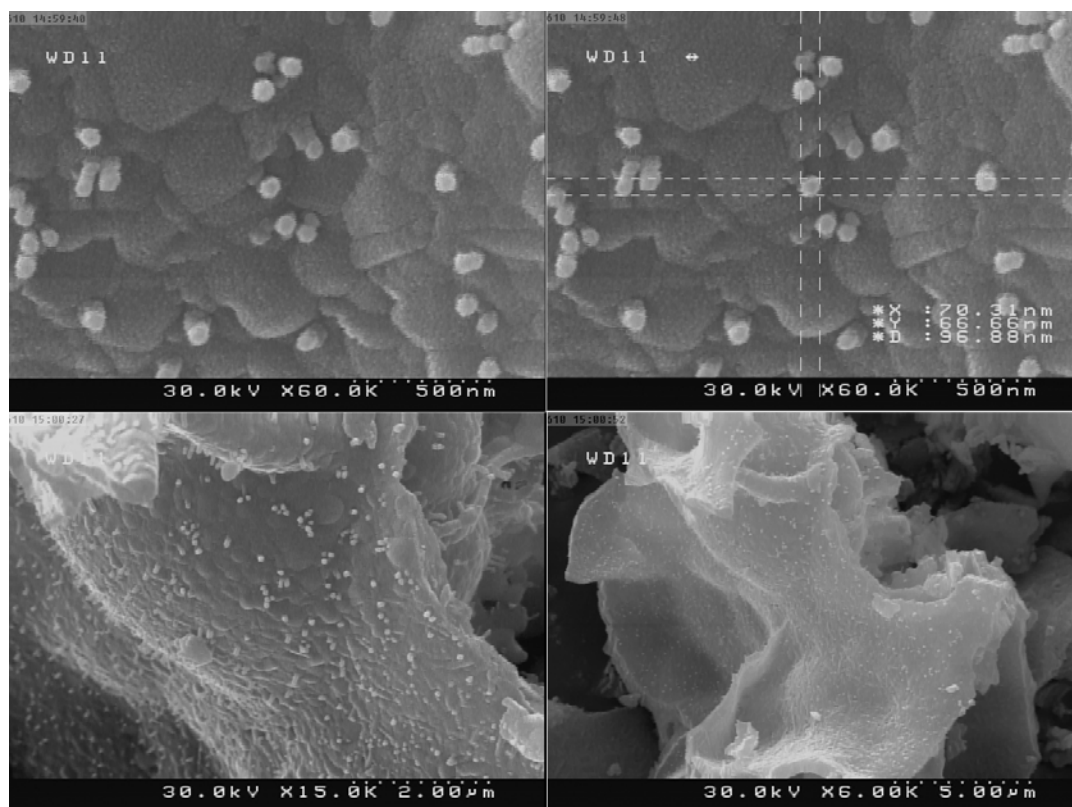


**Fig. 2.** FE-SEM photographs of BaAl<sub>2</sub>O<sub>4</sub> nano-powder calcined at 700 °C for 2 h

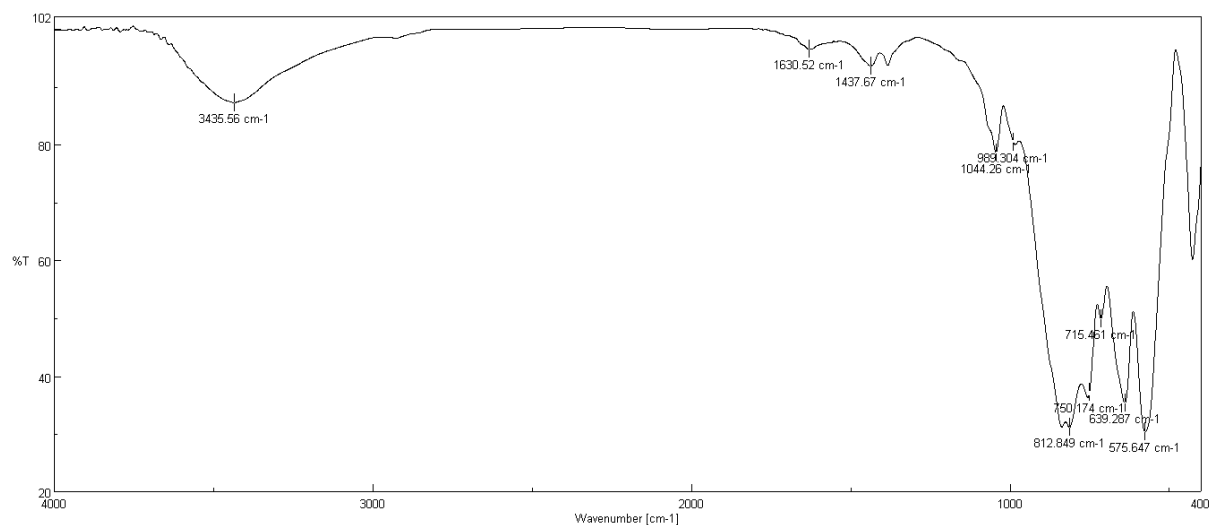


**Fig. 3** FT-IR spectra of BaAl<sub>2</sub>O<sub>4</sub> nano-powder calcined at 700 °C

**Table 1.** Solvent screening

Entry	Conditions	Yield (%) <sup>a</sup>
1	BaAl <sub>2</sub> O <sub>4</sub> nano-powder (0.20 mmol, 0.05 g), Ethanol (10 ml), reflux	80
2	BaAl <sub>2</sub> O <sub>4</sub> nano-powder (0.20 mmol, 0.05 g), Acetonitrile (10 ml), reflux	71
3	BaAl <sub>2</sub> O <sub>4</sub> nano-powder (0.20 mmol, 0.05 g), Ethyl acetate (10 ml), reflux	61
4	BaAl <sub>2</sub> O <sub>4</sub> nano-powder (0.20 mmol, 0.05 g), Dichloromethane (10 ml), reflux	10
5	BaAl <sub>2</sub> O <sub>4</sub> nano-powder (0.20 mmol, 0.05 g), <i>n</i> -Hexane (10 ml), reflux	15
6	BaAl <sub>2</sub> O <sub>4</sub> nano-powder (0.20 mmol, 0.05 g), H <sub>2</sub> O (10 ml), reflux	45
7	BaAl <sub>2</sub> O <sub>4</sub> nano-powder (0.20 mmol, 0.05 g), Solvent-free, (80 °C)	55

<sup>a</sup>Isolated yield, reaction time: 10 h

### Influence of temperature and catalyst concentration

To clarify the effect of catalyst concentration, the Knoevenagel condensation reaction of benzaldehyde and malononitrile over BaAl<sub>2</sub>O<sub>4</sub> nano-powder was carried out using ethanol as a solvent.

Initially, in order to determine the conditions for maximum conversion of benzaldehyde, the reaction was performed at a temperature ranging from 25 to 80 °C for 10 h with a catalyst concentration of 0.05 g (Figure 4). As it is seen from Figure 4, with increasing temperature, the conversion increased and the complete conversion was achieved at a temperature of 80 °C.

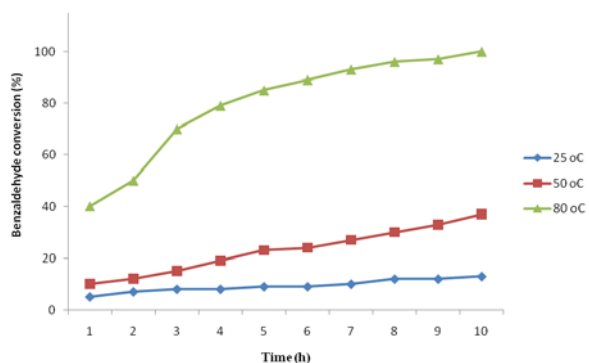


**Fig. 4.** Benzaldehyde conversion as a function of time for different reaction temperatures. Reaction conditions: BaAl<sub>2</sub>O<sub>4</sub> nano-powder (0.05 g), ethanol (10 mL), reflux, 10 h

The percentage of benzaldehyde conversion was calculated as follows:

$$\text{Benzaldehyde conversion (\%)}: [1 - n_t] \times 100$$

where  $n_t$  is the remaining amount (in mmol) of benzaldehyde at time  $t$ .

The benzaldehyde conversion capacity of BaAl<sub>2</sub>O<sub>4</sub> nano-powder was calculated using following equation:

$$\text{Benzaldehyde conversion capacity: } [1 - n_t] \times V/m$$

$V$  is the volume of the reaction solvent and  $m$  is the mass of the catalyst in g (Figure 5).

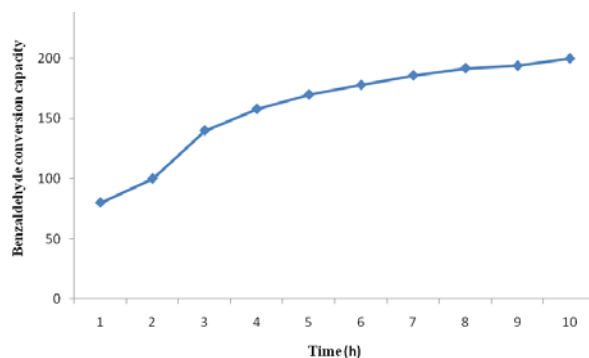


**Fig. 5.** Benzaldehyde conversion capacity of BaAl<sub>2</sub>O<sub>4</sub> nano-powder as a function of time. Reaction conditions: BaAl<sub>2</sub>O<sub>4</sub> nano-powder (0.05 g), ethanol (10 mL), reflux (80 °C), 10 h

To perform a kinetic analysis of the Knoevenagel condensation reaction, an excess of malononitrile was used to achieve pseudo first-order conditions. The data from the benzaldehyde conversion was further used to analyze the rate of the reaction by the following equation which can be further simplified as follows:

$$\text{Rate} = \frac{dC}{dt} = kC$$



$$\ln \frac{C_0}{C_t} = kt \longrightarrow \ln \frac{0.1}{C_t} = kt \longrightarrow \ln \frac{1}{n_t} = kt \longrightarrow \ln n_t = -kt$$

$C_t$  can be calculated from the division operator of  $n_t$  (mmol amount of benzaldehyde at time  $t$ ) to 10 mL (volume of ethanol as solvent).

The kinetic study shows that the conversion of benzaldehyde follows pseudo-first order kinetics and nearly linear relation of  $-\ln(n_t)$  vs.  $t$  is observed (Figure 6).

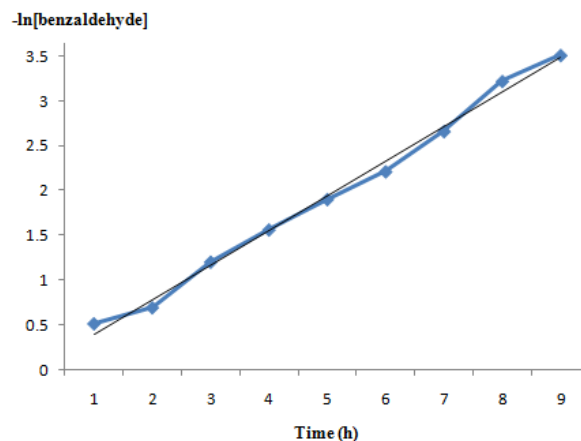


**Fig. 6.** Pseudo first order kinetics of  $-\ln$ [benzaldehyde] vs time for the Knoevenagel condensation reaction of malononitrile with benzaldehyde. Reaction conditions: BaAl<sub>2</sub>O<sub>4</sub> nano-powder (0.05 g), ethanol (10 mL), reflux (80 °C), 10 h

Since  $n_t$  is the remaining amount (in mmol) of benzaldehyde at time  $t$  and  $t$  is the time of reaction process.

It was observed that this relationship follows from the equation:

$$-\ln(n_t) = kt \quad \text{or} \quad -\ln[\text{benzaldehyde}] = kt$$

The nearly linear relationship between  $-\ln(n_t)$  and  $t$  indicates that the conversion of benzaldehyde follows first-order kinetics.  $k$  is the constant of the reaction rate and can be determined from the straight-line slope of the fitted values by means of linear regression. The  $k$  value was determined as 0.007 (s<sup>-1</sup>).

With these results in hand and in order to find the conditions for complete conversion of benzaldehyde, five experiments with different

concentrations of catalyst were performed at 80 °C (reflux conditions) for 10 h. The molar ratio of benzaldehyde / malononitrile was 1/1.3. The results are shown in Figure 7. It shows that the initial reaction rates increase with increasing catalyst concentration. At a catalyst amount lower than 0.025 g, the conversion of benzaldehyde is low (43%). With increasing the catalyst amount above 0.025 g, complete conversion of benzaldehyde was achieved. The increase in the number of active sites of the catalyst at higher catalyst dosage leads to an increase in the conversion of the starting materials.

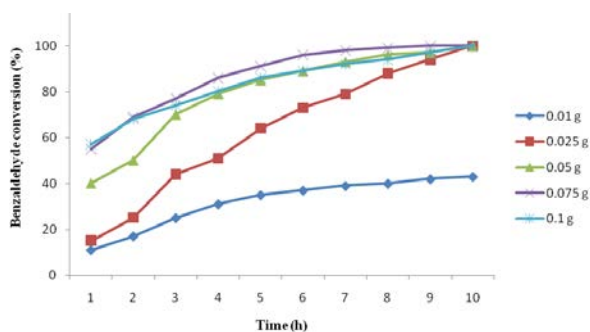


**Fig. 7.** Benzaldehyde conversion as a function of time for different catalyst concentrations. Reaction conditions: ethanol (10 mL), reflux (80 °C), 10 h.

The effect of catalyst concentration on the product yield was investigated by performing four runs of the Knoevenagel condensation reaction of benzaldehyde and malononitrile over different dosages of BaAl<sub>2</sub>O<sub>4</sub> nano-powder ranging from 0.025-0.1 g (Table 2). Higher yield was obtained using 0.05 g of catalyst and increasing the amount of catalyst did not significantly improve the yield.

**Table 2.** Effect of the amount of BaAl<sub>2</sub>O<sub>4</sub> nano-powder as a catalyst on the product yield (%)

Entry	Catalyst (g)	Yield (%) <sup>a</sup>
1	0.025	72
2	0.05	80
3	0.075	73
4	0.1	70

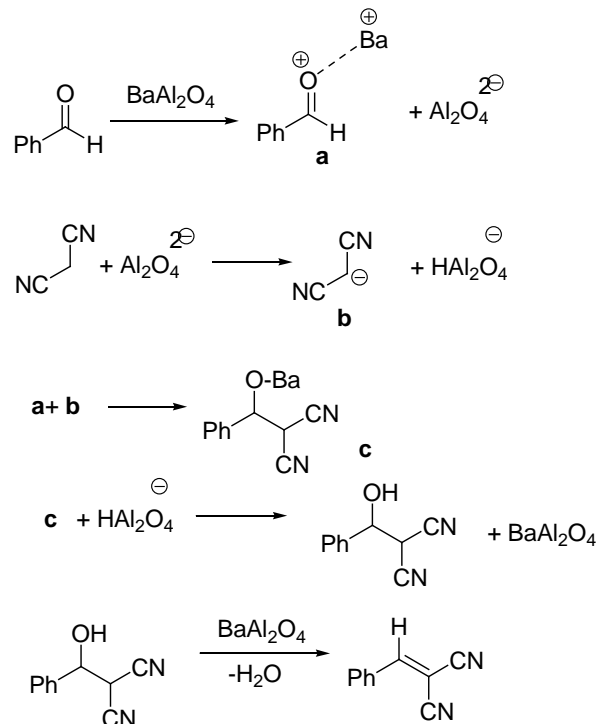
<sup>a</sup>Isolated yield, reaction conditions: time: 10 h, solvent: ethanol (10 ml), reflux (80 °C)

Thus the optimized conditions are: 0.05 g of BaAl<sub>2</sub>O<sub>4</sub> nano-powder as the catalyst and ethanol as solvent under reflux.

It was found that complete conversion of benzaldehyde can be achieved when BaAl<sub>2</sub>O<sub>4</sub> nano-powder (0.05 g, 0.2 mmol) was used. With other metal oxides such as BaO (0.2 mmol, 80%), CaO (0.2 mmol, 89%) and Al<sub>2</sub>O<sub>3</sub> (0.2 mmol, 30%) in the same conditions a lower conversion efficiency was achieved.

The proposed mechanism for the Knoevenagel condensation reaction of benzaldehyde and malononitrile over BaAl<sub>2</sub>O<sub>4</sub> nano-powder is shown in Scheme 2. In this reaction, BaAl<sub>2</sub>O<sub>4</sub> could act as a bifunctional catalyst, by activating both the carbonyl oxygen in the aldehyde and the acidic hydrogen in malononitrile. Since BaAl<sub>2</sub>O<sub>4</sub> contains Ba atoms attached to O atoms, it is likely that Ba<sup>2+</sup> would be released *in situ*, and this species would act as a catalyst in the reaction medium leading to a considerable increase in the electrophilicity of the aldehyde (intermediate **a**).

It is proposed that BaAl<sub>2</sub>O<sub>4</sub> produces two different species: Ba<sup>2+</sup> and Al<sub>2</sub>O<sub>4</sub><sup>2-</sup>. The latter species reacts with malononitrile to form a carbanion form (intermediate **b**). This reaction is followed by the attack of intermediate **b** on the activated carbonyl to afford intermediate (**c**). The reaction proceeds till the recovery of BaAl<sub>2</sub>O<sub>4</sub> and the formation of 2-(hydroxy(phenyl)methyl) malononitrile. The reaction could be continued with the removal of water to afford the targeted molecules, as is shown in scheme 2.



**Scheme 2:** Plausible Knoevenagel condensation reaction of benzaldehyde and malononitrile over BaAl<sub>2</sub>O<sub>4</sub> nano-powder as a catalyst.

#### Catalyst reusability

Our attention then turned to the possibility of recycling the catalyst from the reaction medium since the recovery and reuse of the catalyst are preferable for a green process. At the completion of the reaction, the solid catalyst was separated by

simple filtration, dried and reused for subsequent reactions. The reusability of the catalyst was investigated in the Knoevenagel condensation reaction of malononitrile with benzaldehyde. After 10 recycles, the catalyst still had a high activity and gave the corresponding product in good yield (Figure 8).

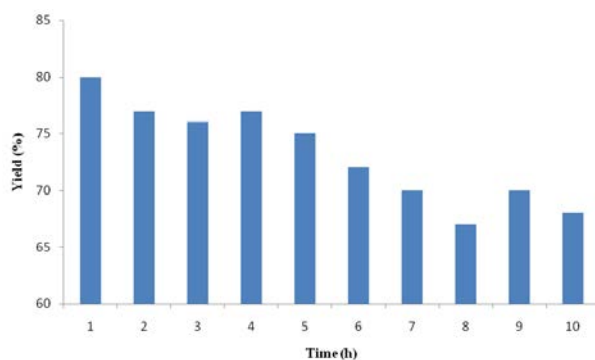


Fig. 8. Reusability of BaAl<sub>2</sub>O<sub>4</sub> nano-powder.

## CONCLUSION

The *in-situ* preparation of BaAl<sub>2</sub>O<sub>4</sub> nano-powder via homogeneous precipitation was reported. The prepared sample was characterized using XRD, FT-IR, FE-SEM and EDAX analysis. The XRD pattern shows only hexagonal phase of BaAl<sub>2</sub>O<sub>4</sub>. The average particle size determined by FE-SEM is about 70 nm. The BaAl<sub>2</sub>O<sub>4</sub> nano-powder was shown to be a highly efficient catalyst for the Knoevenagel condensation reaction of malononitrile with benzaldehyde under reflux conditions in ethanol as a solvent.

**Acknowledgements:** We are thankful to the Najafabad Branch, Islamic Azad University research council for partial support of this research

## REFERENCES

- H. Hattori, *Chem Rev.*, **95**(3), 537 (1995).
- S. Inagaki, K. Thomas, V. Ruaux, G. Clet, T. Wakihara, S. Shinoda, S. Okamura, Y. Kubota, V. Valtchev, *ACS Catal.*, **4** (7), 2333 (2014).
- M. J. Climent, A. Corma, S. Iborra, M. J. Sabater, *ACS Catal.*, **4** (3), 870 (2014).
- Y. C. Sharma, B. Singh, J. Korstad. *Fuel*, **90**, 1309 (2011).
- A. C. Alba-Rubio, J. Santamaría-González, J. M. Mérida-Robles, R. Moreno-Tost, D. Martín-Alonso, A. Jiménez-López, P. Maireles-Torres, *Catal. Today*, **149**, 281 (2010).
- M. Bolognini, F. Cavani, D. Scagliarini, C. Flego, C. Perego, M. Saba, *Catal. Today*, **75**, 103 (2002).
- D. Wang, X. Zhang, W. Wei, Y. Sun, *Catal. Commun.*, **28**, 159 (2012).
- M. R. M. Shafiee, M. Ghashang, A. Fazlinia, *Curr. Nanosci.*, **9**, 197 (2013).
- M. Ghashang, *Curr. Org. Synth.*, **9**, 727 (2012).
- M. R. M. Shafiee, A. Fazlinia, N. Yaghooti, M. Ghashang, *Lett. Org. Chem.*, **9**, 351 (2012).
- M. Ghashang, *Lett. Org. Chem.*, **9**, 497 (2012).
- D. G. Morrell, *Catalysis of Organic Reactions*, CRC Press, 2002.
- M. Lancaster, *Green Chemistry: An Introductory Text*, Royal Society of Chemistry, 2010.
- K. Wilson, A. F. Lee, *Heterogeneous Catalysts for Clean Technology: Spectroscopy, Design, and Monitoring*. John Wiley & Sons, 2013.
- S. Hodjati, P. Bernhardt, C. Petit, V. Pitchon, A. Kiennemann, *Appl Catal B: Environ.*, **19**, 209 (1998).
- M. Mohapatra, D. M. Pattanaik, S. Anand, R. P. Das. *Ceram. Inter.*, **33**, 531 (2007).
- M. Casapu, J. D. Grunwaldt, M. Maciejewski, M. Wittrock, U. Gobel, A. Baiker, *Appl. Catal. B: Environ.*, **63**, 232 (2006).
- J. J. Vijaya, L. J. Kennedy, G. Sekaran, K. S. Nagaraja, *Sens. Actuators B: Chem.*, **124**: 542 (2007).
- S. Y. Raghvendra, S. K. Pandey, A. C. Pandey, *J. Lumin.*, **131**, 1998 (2011).
- V. Singh, V. Natarajan, J. J. Zhu, *Opt. Mater*, **29**, 1447 (2007).
- Z. Qiu, Y. Zhou, M. Lu, A. Zhang, Q. Ma, *Acta Mater*, **55**, 2615 (2007).
- Sk. I. Manirul, A. R. Singha, R. D. Chandra, S. Pau, *J. Molec. Catal. A: Chem.*, **394**, 66 (2014).
- J. Zhao, J. Xie, C-T. Au, S-F. Yin, *Appl. Catal. A: Gen.*, **467**, 33 (2013).
- Y. Tan, Z. Fu, J. Zhang, *Inorg. Chem. Commun.*, **14**: 1966 (2011).
- J. Xu, K. Shen, B. Xue, Y-X. Li, *J. Molec. Catal. A: Chem*, **372**: 105 (2013).
- L-W. Zhang, L. Wang, Y-F. Zhu, *Adv. Funct. Mater.*, **17**, 3781 (2007).
- R. Stefani, L.C.V. Rodrigues, C.A.A. Carvalho, M.C.F.C. Felinto, H.F. Brito, M. Lastusaari, J. Holsa, *Opt. Mater.*, **31**, 1815 (2009).



НАНОСФЕРИ ОТ БАРИЕВ АЛУМИНАТ, ИЗРАСТНАЛИ НА ПОВЪРХНОСТТА НА  
BaAl<sub>2</sub>O<sub>4</sub>: ОБЩО ПРИЛОЖИМ КАТАЛИЗАТОР ЗА КОНДЕНЗАЦИЯТА ПО  
KNOEVENAGEL НА МАЛОНИТРИЛ С БЕНЗАЛДЕХИД

М. Момаезян<sup>1</sup>, М. Гашанг\*<sup>2</sup>, С.А. Хасанзаде-Табризи<sup>2</sup>

<sup>1</sup> *Разширен изследователски център по материалознание, Факултет по материалознание и инженерство, Клон Наджафабад, Ислямски университет „Азад“, Наджафабад, Иран*

<sup>2</sup> *Департамент по химия, Научен факултет, Клон Наджафабад, Ислямски университет „Азад“, Наджафабад, Есфахан, Иран*

Постъпила на 20 август, 2014 г.; коригирана на 3 декември, 2014 г.

(Резюме)

Синтезиран е нано-прах от бариев алуминат по метода на хомогенното утаяване и изследван каталитичната му активност за кондензацията по Knoevenagel на малонитрил с бензалдехид. Получените образци са охарактеризирани чрез рентгено-структурен анализ (XRD), полева емисионна сканираща електронна микроскопия (FE-SEM), инфрачервена спектроскопия с Фурие-трансформация (FT-IR) и дисперсионна рентгенова спектроскопия (EDAX). Рентгенограмите показват единична фаза с хексагонална структура. Две обособени фази на BaAl<sub>2</sub>O<sub>4</sub> са налице на FE-SEM-микроснимките. Първата фаза има нерегулярни форми на агломериран нано-прах от BaAl<sub>2</sub>O<sub>4</sub>, а втората – дифузни нано-сфери от BaAl<sub>2</sub>O<sub>4</sub> на външната повърхност на нано-праховете. Сферите от BaAl<sub>2</sub>O<sub>4</sub> имат среден размер около 70 nm. Показано е, че нано-прахът от BaAl<sub>2</sub>O<sub>4</sub> е високо-ефективен катализатор на кондензационната реакция на Knoevenagel между малонитрил и бензалдехид с рефлукс на разтворителя (етанол). Изследвано е влиянието на концентрацията на катализатора, температурата и разтворителя върху реакцията.

## Preparation and optical properties of colloidal europium(III) diphenanthroline nitrate hydrate

S. Gutzov<sup>1\*</sup>, P. Stoyanova<sup>1</sup>, K. Balashev<sup>1</sup>, N. Danchova<sup>1</sup>, S. Stoyanov<sup>2</sup>

<sup>1</sup>Department of Physical Chemistry, Faculty of Chemistry and Pharmacy, University of Sofia “St Kliment Ohridski”, J. Bourchier Blvd 1, 1164 Sofia, Bulgaria

<sup>2</sup>Department of Organic Chemistry, Faculty of Chemistry and Pharmacy, University of Sofia “St Kliment Ohridski”, J. Bourchier Blvd 1, 1164 Sofia, Bulgaria

Received August 6, 2014, Revised November 25, 2014

Preparation and optical properties of  $[\text{Eu}(\text{phen})_2](\text{NO}_3)_3 \cdot x\text{H}_2\text{O}$  colloids with potential application as an attractive UV sensor is discussed depending on preparation conditions. Excitation / luminescence spectroscopy, UV-Vis spectroscopy and AFM – microscopy including roughness analysis are used to characterize the hybrid colloidal microparticles. Luminescence / excitation spectroscopy confirms formation of red emitting hybrid Eu(III) luminescence centers with site symmetry  $C_{2v}$  or lower during preparation. A strong energy transfer from the organic ligand to europium at 350 nm excitation is demonstrated.

**Key words:** Sol-Gel, Europium, Hybrid Composites, UV sensor.

### INTRODUCTION

Sol-gel technology is a powerful method for preparation of hybrid materials at room temperature. By variation of synthesis conditions different kinds of amorphous or nanocrystalline materials such as hybrid composites, thin films, xerogels or aerogels can be obtained. The strong luminescence of hybrid materials which contain lanthanide complexes incorporated in sol-gel networks, is based on an efficient energy transfer. These hybrid composite materials usually contain two components – amorphous or nanocrystalline matrix /sol-gel silica or zirconia/ and an optical active complex. Often, rare earth ion complexes are used as an optical active component due to their strong pure emission:  $\text{Eu}^{3+}$  (615 nm),  $\text{Tb}^{3+}$  (540 nm),  $\text{Ho}^{3+}$  (540 nm),  $\text{Sm}^{3+}$  (590 nm) [1-4].

Lanthanide complexes, however, display some disadvantages which have to be compensated for during sol-gel preparation by variation of pH, temperature and drying conditions. Many lanthanide complexes have very low solubility and low kinetic stability in solid matrices, thus the optical properties of the obtained complexes strongly depend on the preparation procedure which concerns the optical properties of  $\text{SiO}_2:[\text{Eu}(\text{ntac})_3][\text{pphendcn}]$  [1-3]. As it was previously described in our prior studies, we proposed a new method for functionalization of

$\text{Eu}^{3+}$  doped silica nanoparticles with 1,10-phenanthroline with a quantum efficiency of 20-40% [1]. The concept of this method was to replace the doping procedure of the complex by a surface functionalization of inorganic oxides, containing lanthanide ions, as  $\text{SiO}_2:\text{Eu}$  or  $\text{ZrO}_2:\text{Eu}$ . The organic ligands (e.g. 1, 10 – phenanthroline) can be used as surface functionalization agents for *in situ* formation of complexes. Thus, by applying the method of surface functionalization of europium doped silica microparticles we achieved a high time stability and improved the luminescent properties of the prepared material  $\text{SiO}_2:[\text{Eu}(\text{phen})_2](\text{NO}_3)_3$  [1 - 9].

A third way for preparation of hybrid sol-gel composites is by incorporation into silica or zirconia matrices of functionalized microparticles containing rare earth ions with a high quantum yield [5-8]. Appropriate materials for such an incorporation could be microparticles containing  $\text{Eu}(\text{phen})_2(\text{NO}_3)_3 \cdot x\text{H}_2\text{O}$  because of the excellent optical properties of this complex. Such approach, however, requires physico-chemical characterization of colloidal  $\text{Eu}(\text{phen})_2(\text{NO}_3)_3 \cdot x\text{H}_2\text{O}$  materials, but also additional efforts for obtaining reproducible results.

The aim of this contribution is to obtain reproducible colloidal  $[\text{Eu}(\text{phen})_2](\text{NO}_3)_3 \cdot x\text{H}_2\text{O}$  microparticles starting from  $\text{Eu}_2\text{O}_3$  and to describe their optical properties depending on the preparation strategy in the framework of preparation and characterization of high-quantum yield hybrid materials.

\* To whom all correspondence should be sent:  
E-mail: sgutzov@chem.uni-sofia.bg

## EXPERIMENTAL

The preparation of red emitting  $\text{Eu}(\text{NO}_3)_3 \cdot x\text{H}_2\text{O}$  microparticles functionalized with 1,10-phenanthroline was performed in several steps (figure 1). First, a 0.57 M solution with  $\text{pH} = 2-3$  was prepared using  $\text{Eu}_2\text{O}_3$  as precursor and  $\text{HNO}_3$  at  $40-50^\circ\text{C}$ . After that, 10 ml of EtOH was added to 10 ml of the initial 0.57 M aqueous solution of  $\text{Eu}(\text{NO}_3)_3$ . The so formed solid  $\text{Eu}(\text{NO}_3)_3 \cdot x\text{H}_2\text{O}$  was dried at that temperature for 1 h. After this the solid  $\text{Eu}(\text{NO}_3)_3 \cdot x\text{H}_2\text{O}$  was dissolved in EtOH. The next step of the preparation of the colloidal solution was to add a mild alkalizing agent – 450  $\mu\text{l}$  of 0.14 M EtOH solution of  $\text{NH}_3$ . Note that this colloidal solution does not display visible red emission even after excitation with UV light. To achieve a strong red emission at UV light excitation the colloidal  $\text{Eu}(\text{NO}_3)_3 \cdot x\text{H}_2\text{O}$  solution was impregnated with EtOH solution of 1.1 M 1,10-phenanthroline for 48 h under constant stirring at room temperature.

The impregnation procedure was done in excess of 1,10-phenanthroline in  $n_{\text{Eu}}/n_{\text{phen}}=9.4 \cdot 10^{-3}$ . The final concentration of europium in the functionalized solution was  $c_3=0.01$  M.

As a result of the ammonia addition, the composition of the so prepared colloidal particles could be  $\text{Eu}(\text{OH})_x(\text{NO}_3)_{3-x}$ . The functionalization with 1,10-phenanthroline leads to a formation of  $[\text{Eu}(\text{phen})_2](\text{OH})_x(\text{NO}_3)_{3-x}$ . According to general chemical considerations, and the chemistry of  $[\text{Eu}(\text{phen})_2](\text{NO}_3)_3$ , the transformation of  $[\text{Eu}(\text{phen})_2](\text{OH})_x(\text{NO}_3)_{3-x}$  with time to the thermodynamically stable  $[\text{Eu}(\text{phen})_2](\text{NO}_3)_3 \cdot x\text{H}_2\text{O}$  is very probable [5-8]. The exact microcomposition determination, however, needs additional investigations, which will be published in a next contribution.

In a second scheme,  $\text{Eu}_2\text{O}_3$  micropowders were used instead of  $\text{Eu}(\text{OH})_x(\text{NO}_3)_{3-x}$  microparticles, but the functionalization conditions remained the same. The resulting sol did not luminesce, which means that the process of functionalization has not been successful. This means that the ammonia addition, which led to the formation of  $\text{Eu}(\text{OH})_x(\text{NO}_3)_{3-x}$  microparticles, is an important step in the functionalization process.

A Varian Cary Eclipse spectrophotometer was used for excitation/luminescence spectra measurements of the sol at room temperature. Room temperature UV/Vis absorption spectra of solutions were measured on a Perkin Elmer Lambda 35 spectrophotometer. The Eu content in all prepared samples was checked using an LA-ICP-MS unit.



**Fig. 1.** Preparation of colloidal solution of  $[\text{Eu}(\text{phen})_2](\text{NO}_3)_3 \cdot x\text{H}_2\text{O}$ . The calculated Eu concentration is given in the different steps of preparation.

The sample preparation for AFM imaging involved a deposition of colloidal solution of  $\text{Eu}(\text{OH})_x(\text{NO}_3)_{3-x}$  or  $[\text{Eu}(\text{phen})_2](\text{NO}_3)_3 \cdot \text{H}_2\text{O}$  on freshly cleaved mica surface. Freshly cleaved quadratic mica Grade V-4 Muscovite (Structure Probe Inc. / SPI Supplies, West Chester, PA) with sizes  $10 \times 10$  mm glued to the metal pads were used for the deposition of about 100  $\mu\text{L}$  of colloidal solution. Then the samples were left for 10 min and were gently blown with a flow of nitrogen gas to dry out. AFM imaging was performed on the NanoScopeV system (Bruker Inc.) operating in tapping mode in air at room temperature. We used silicon cantilevers (Tap 300 Al-G, Budget Sensors, Innovative solutions Ltd, Bulgaria) with 30 nm thick aluminum reflex coating. According to the producer's datasheet the cantilever spring constant was in the range of  $1.5-15$  N/m and the resonance frequency was  $150 \pm 75$  kHz. The tip radius was less than 10 nm. The scan rate was set at 1 Hz and the images were captured in height mode with  $512 \times 512$  pixels in a JPEG format. Subsequently, all the images were flattened by means of Nanoscope software.

## RESULTS AND DISCUSSION

In Figure 2, absorption, excitation and luminescence spectra of the prepared colloidal  $[\text{Eu}(\text{phen})_2](\text{NO}_3)_3 \cdot x\text{H}_2\text{O}$  are shown. The absorption spectrum shows peaks at 231 nm (strong), 265 nm

(strong), 324 nm (weak) and 350 nm (shoulder). The absorption peaks of the colloidal  $[\text{Eu}(\text{phen})_2](\text{NO}_3)_3 \cdot x\text{H}_2\text{O}$  in this study are close to those of the  $\text{SiO}_2: [\text{Eu}(\text{phen})_2](\text{NO}_3)_3$  and  $\text{ZrO}_2: [\text{Eu}(\text{phen})_2](\text{NO}_3)_3$  [1-3]. More details about the optical properties of this complex are given in [5].

There are significant differences in the excitation spectrum of colloidal  $[\text{Eu}(\text{phen})_2](\text{NO}_3)_3 \cdot x\text{H}_2\text{O}$  compared to that of bulk  $[\text{Eu}(\text{phen})_2](\text{NO}_3)_3$  or hybrid sol-gel materials containing  $[\text{Eu}(\text{phen})_2](\text{NO}_3)_3$ . In the excitation spectra of  $[\text{Eu}(\text{phen})_2](\text{NO}_3)_3 \cdot x\text{H}_2\text{O}$ , only one sharp excitation band at 350 nm is visible and it is in agreement with the absorption spectra shoulder at the same wavelength. The excitation channels at  $\lambda < 330$  nm are closed in the case of colloidal solution (figure 2).

In the excitation spectra of the bulk polycrystalline powders a broad excitation window down to 270 nm has been described [1]. In the excitation spectra of  $\text{ZrO}_2: [\text{Eu}(\text{phen})_2](\text{NO}_3)_3$ ,  $\text{SiO}_2: [\text{Eu}(\text{phen})_2](\text{NO}_3)_3$  a broad band between 270 nm and 370 nm, also centered at 350 nm [1-3] has been detected. In this way the as prepared colloids could be an attractive sensor for 350 nm radiation. The differences in the excitation spectra of bulk and colloidal  $[\text{Eu}(\text{phen})_2](\text{NO}_3)_3 \cdot x\text{H}_2\text{O}$  require additional theoretical and experimental investigations.

The absorption and excitation spectrum in fig. 2 confirms the occurrence of a strong energy transfer in the colloidal  $[\text{Eu}(\text{phen})_2](\text{NO}_3)_3 \cdot x\text{H}_2\text{O}$  solution, where the excitation energy is absorbed by the 1,10 – phenanthroline molecule ( $T_1$  level, 265 nm) followed by inter-system crossing (ISC) to the  $S_1$  level at 350 nm and transfer to the  $^5D_2$  term of the  $\text{Eu}^{3+}$  ion [5,9,10].

The luminescence spectrum of the colloidal  $[\text{Eu}(\text{phen})_2](\text{NO}_3)_3 \cdot x\text{H}_2\text{O}$  solution consists of a strong red emission, coming from the well-known  $\text{Eu}^{3+} \ ^5D_0 \rightarrow ^7F_1$  electronic transitions. We detected one peak in the region of the  $^5D_0 \rightarrow ^7F_0$  transition (582 nm), two lines in the region of the  $^5D_0 \rightarrow ^7F_1$  transition (594 nm), one peak in the region of the  $^5D_0 \rightarrow ^7F_2$  transition (615 nm), one weak peak at 650 nm ( $^5D_0 \rightarrow ^7F_3$ ) and two lines in the  $^5D_0 \rightarrow ^7F_4$  transition (684 nm and 700 nm) using second derivative luminescence spectrum analysis. The results of luminescence spectra – structure analysis suggest a site symmetry  $C_{2v}$  or lower of europium ions [11-13]. The spectra – structure analysis results in this study are in agreement with our

recent results, which suggests that the most probable site symmetry in the case of  $\text{ZrO}_2: [\text{Eu}(\text{phen})_2](\text{NO}_3)_3$ ,  $\text{SiO}_2: [\text{Eu}(\text{phen})_2](\text{NO}_3)_3$  and bulk  $[\text{Eu}(\text{phen})_2](\text{NO}_3)_3$  is  $C_{2v}$  or  $D_2$  [11-13]. The  $^5D_0 \rightarrow ^7F_0$  transition in colloidal  $[\text{Eu}(\text{phen})_2](\text{NO}_3)_3 \cdot x\text{H}_2\text{O}$ , however, shows a site symmetry lowering and / or a change of chemical surroundings.

In the luminescence spectrum of colloidal  $[\text{Eu}(\text{phen})_2](\text{NO}_3)_3 \cdot x\text{H}_2\text{O}$  a weak blue emission with maximum at about 420 nm, coming from the 1,10 – phenanthroline ligand is visible, which is close to the blue luminescence described in our recent contribution [2,14].

The morphology of the films from nanoparticles deposited on freshly cleaved mica surface was investigated by Atomic Force Microscopy (AFM). Typical topographical images of non-functionalized  $\text{Eu}(\text{OH})_x(\text{NO}_3)_{3-x}$  and functionalized with 1,10 – phenanthroline  $[\text{Eu}(\text{phen})_2](\text{NO}_3)_3 \cdot x\text{H}_2\text{O}$  films are depicted in figures 3A÷C and figures 3D÷F, respectively where the significant differences in topography of the obtained films are easily detectable. In figures 3A÷C are presented typical AFM height images of non-functionalized  $\text{Eu}(\text{OH})_x(\text{NO}_3)_{3-x}$  films where the height images are presented in 2D- (figure 3A) and 3D- format (figure 3C) and also images of functionalized with 1,10 – phenanthroline  $\text{Eu}(\text{OH})_x(\text{NO}_3)_{3-x}$  films (figures 3D, F). The images are accompanied with sections across the films' surface presented in figure 3B and figure 3E, respectively. The films from non-functionalized  $\text{Eu}(\text{OH})_x(\text{NO}_3)_{3-x}$  have relatively flat morphology. Only few individual 3D-structures (white spots in figure 3A) with heights of about 25÷40 nm which are spread irregularly on the film surface can be observed. On the contrary, the films obtained from  $[\text{Eu}(\text{phen})_2](\text{NO}_3)_3 \cdot x\text{H}_2\text{O}$  exhibit a granule-like pattern and are composed of heterodisperse nanoparticles with different shapes and sizes in the range of 40 nm to more than 100 nm.

The roughness analysis of the height AFM images also showed a profound difference in the film structure. It gives reasoning for various non-functionalized  $\text{Eu}(\text{OH})_x(\text{NO}_3)_{3-x}$  films. The main roughness  $R_a$  value is 4.5 nm, while for functionalized  $[\text{Eu}(\text{phen})_2](\text{NO}_3)_3 \cdot x\text{H}_2\text{O}$  it is more than 6 times bigger, i.e.  $R_a = 31$  nm.

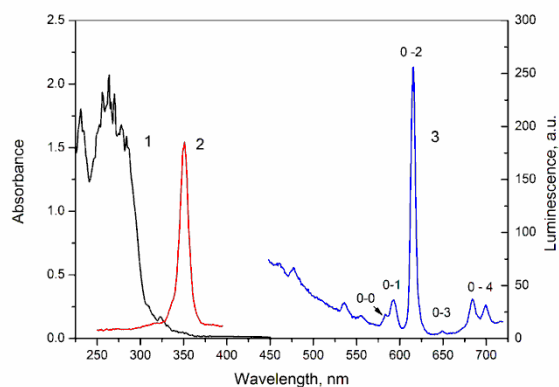


**Fig. 2.** Optical spectra of  $[\text{Eu}(\text{phen})_2](\text{NO}_3)_3 \cdot x\text{H}_2\text{O}$  colloidal solutions. Luminescence spectrum at 355 nm excitation (3) and excitation spectrum monitoring the 615 nm transition (2) are displayed. The  ${}^5\text{D}_0 \rightarrow {}^7\text{F}_j$  emission transitions of  $\text{Eu}^{3+}$  ion are denoted as 0-1, 0-2, 0-3 and 0-4. The Eu – concentration is  $5 \cdot 10^{-6}$  mol/l in absorption spectra measurements (1) and 0.01 mol/l in excitation / luminescence spectra measurements (2,3).

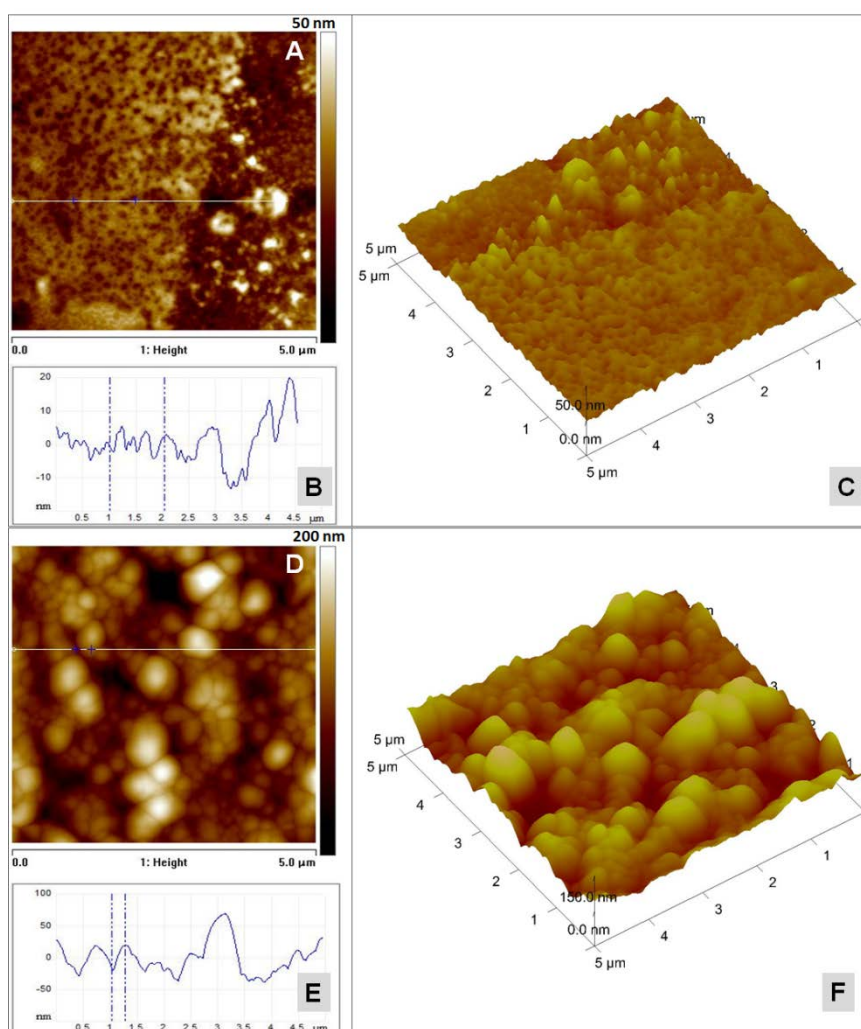


**Fig. 3.** AFM images of non-functionalized  $\text{Eu}(\text{OH})_x(\text{NO}_3)_{3-x}$  and functionalized with 1,10 - phenanthroline  $[\text{Eu}(\text{phen})_2](\text{NO}_3)_3 \cdot x\text{H}_2\text{O}$  films. (A) 2D height image of non-functionalized  $\text{Eu}(\text{OH})_x(\text{NO}_3)_{3-x}$  film with the scanning XY area  $5 \times 5 \mu\text{m}^2$  and the z-range  $z=50$  nm; (B) Cross-section of image (A); (C) 3D height image of the same non-functionalized  $\text{Eu}(\text{OH})_x(\text{NO}_3)_{3-x}$  film; (D) 2D height image of functionalized with 1,10-phenanthroline  $[\text{Eu}(\text{phen})_2](\text{NO}_3)_3 \cdot x\text{H}_2\text{O}$  film with the scanning XY area  $5 \times 5 \mu\text{m}^2$  and the z-range  $z=200$  nm; (E) Cross section of image (E); (F) 3D height image of the same functionalized with 1,10 - phenanthroline  $[\text{Eu}(\text{phen})_2](\text{NO}_3)_3 \cdot x\text{H}_2\text{O}$  film.

## CONCLUSIONS

In the present article we demonstrate a promising sol-gel technique for colloidal preparation of a red emitting sol containing  $[\text{Eu}(\text{phen})_2](\text{NO}_3)_3 \cdot x\text{H}_2\text{O}$  with potential application as an attractive UV sensor. The preparation procedure is based on intermediate formation of  $\text{Eu}(\text{OH})_x(\text{NO}_3)_{3-x}$  microparticles. The most probable symmetry of the  $\text{Eu}^{3+}$  ion in the hybrid colloidal microparticles is  $C_{2v}$  or lower. A strong energy transfer from the organic ligand at 350 nm excitation is demonstrated. There are differences in the optical properties of colloidal  $[\text{Eu}(\text{phen})_2](\text{NO}_3)_3 \cdot x\text{H}_2\text{O}$ , compared to that of bulk  $[\text{Eu}(\text{phen})_2](\text{NO}_3)_3$ . AFM height images of non-functionalized  $\text{Eu}(\text{OH})_x(\text{NO}_3)_{3-x}$  films exhibit relatively flat morphology with a small number of individual 3D-structures with irregular shapes and sizes of about 25÷40 nm, while the films from  $[\text{Eu}(\text{phen})_2](\text{NO}_3)_3 \cdot x\text{H}_2\text{O}$  are composed of nanoparticles with sizes in the range of 40 ÷ 100 nm.

## REFERENCES

1. N. Danchova, S. Gutzov, K. Matras-Postolek, M. Bredol, N. Lesev, S. Kaloyanova, T. Deligeorgiev, *J. Incl. Phenom. Macrocycl. Chem.*, **78**, 381 (2014).
2. N. Petkova, S. Gutzov, N. Lesev, S. Kaloyanova, S. Stoyanov, T. Deligeorgiev, *Opt. Mater.*, **33**, 1715 (2011).
3. N. Danchova, S. Gutzov, *Z. Naturforsch.*, B, **69**, 224 (2014).
4. J. C. G. Bunzli, in: Lanthanide Probes in Life, J. C. G. Bunzli, G. R. Choppin (Eds.), Chemical and Earth Sciences. Theory and Practice, Elsevier Science Publ. B.V., Amsterdam, 1989, p. 219.
5. A. G. Mirochnik, P. A. Bukvetskii, P. A. Zhikareva, V. E. Karasev, *Russian Journal of Coordination Chemistry*, **27**, 475 (2001).
6. T. Yan, D. Zhang, L. Shi, H. Li, *Journal of Alloys and Compounds*, **487**, 483 (2009).
7. D. Zhang, T. Yan, L. Shi, H. Li, J. F. Chiang, *Journal of Alloys and Compounds*, **506**, 446 (2010).
8. J. Yu, D. Parker, R. Pal, R. A. Poole, M. J. Cann, *J. Am. Chem. Soc.*, **128**, 2294 (2006).
9. K. Binnemans, *Chem. Rev.*, **109**, 4283 (2009).
10. R. Reisfeld, *J. Fluoresc.*, **12**, 317 (2002).
11. G. Blasse, B. Grabmaier, *Luminescent materials*. Springer Verlag, New York, 1994.
12. W. Schmidt, *Optische Spektroskopie*, Wiley-VCH, Weinheim, 1995.
13. N. A. Stump, G. K. Schweitzer, J. K. Gibson, R. G. Haire, J. R. Peterson, *Appl. Spectrosc.*, **48**, 937 (1994).
14. H. Li, D. Ueda, S. Inoue, *Bull. Chem. Soc. Japan.*, **75**, 161 (2002).

## ПРИГОТВЯНЕ И ОПТИЧНИ СВОЙСТВА НА КОЛОИДЕН ЕВРОПИЕВ (III) НИТРАТ ДИФЕНАНТРОЛИН ХИДРАТ

С. Гуцов<sup>1\*</sup>, П. Стоянова<sup>1</sup>, К. Балашев<sup>1</sup>, Н. Данчова<sup>1</sup>, С. Стоянов<sup>2</sup>

<sup>1</sup>Катедра по физикохимия, Софийски университет „Св. Климент Охридски“, Факултет по химия и фармация  
бул. Дж. Баучер №1, 1164 София, България

<sup>2</sup>Катедра по органична химия, Софийски университет „Св. Климент Охридски“, Факултет по химия и фармация,  
бул. Дж. Баучер 1, 1164 София, България

Получена на 6 август 2014 г., ревизирана на 25 ноември 2014 г.

(Резюме)

Дискутирана е връзката между условия за получаване и оптични свойства на колоидни микрочастици със състав  $[\text{Eu}(\text{phen})_2](\text{NO}_3)_3 \cdot x\text{H}_2\text{O}$  с потенциално приложение като луминесцентни сензори за ултравиолетово лъчение. Хибридният колоидни микрочастици са охарактеризирани с помощта на луминесцентна спектроскопия и спектри на възбуждане, ултравиолетова спектроскопия и атомно-силова микроскопия. Използваните спектроскопски методи доказват, че симетрията на европиевия йон в получените материали с интензивна червена луминесценция е  $C_{2v}$ . Наблюдаван е ефективен енергиен трансфер от органичните лиганди към европиевия йон при 350 nm.

## Application of cyclic voltammetry for determination of the mitochondrial redox activity during subcellular fractionation of yeast cultivated as biocatalysts

Y. V. Hubenova<sup>1\*</sup>, M. Y. Mitov<sup>2</sup>

<sup>1</sup>Department of Biochemistry and Microbiology, "Paisii Hilendarski" University of Plovdiv, 24 Tzar Asen Str., 4000 Plovdiv, Bulgaria,

<sup>2</sup>Department of Chemistry, South-West University "Neofit Rilski", 66 Ivan Mihajlov Str., 2700 Blagoevgrad, Bulgaria,

Received June 21, 2014, Revised September 10, 2014

In this study, cyclic voltammetry is proposed as an alternative method for determination of mitochondrial localization during subcellular fractionation of *Candida melibiosica* 2491 yeast cultivated under polarization. The obtained electrochemical activity of the fractions is compared to the determined cytochrome *c* activity in the presence and absence of rotenone.

**Keywords:** yeast-based biofuel cell; mitochondrial electrochemical activity; cytochrome *c* oxidase.

### INTRODUCTION

Mitochondria play a crucial role in eukaryotic cellular bioenergetics. Most eukaryotic cells rely on mitochondrial oxidative phosphorylation as the major pathway for synthesis of adenosine triphosphate (ATP) – the main energy source for the cellular metabolism. Recent advances in the proteomic analyses provide important information about the mitochondrial function, as well as the species and tissue specificity of mitochondrial protein composition [1-3]. However, the precise mechanisms, by which mitochondrial respiration and ATP synthesis are controlled in the cells, are still not completely understood [4]. Besides elucidation of these mechanisms, in recent years there has been an increase in research of mitochondria, concerning their involvement in cell aging or apoptosis [5, 6]. A key technique used is the subcellular fractionation, by which the cellular proteins are separated into defined enriched subcellular fractions. In most cases, the protocols for purification of mitochondrial fractions are based on disruption (homogenization) of the intact cells or tissue samples followed by consecutive differential and density gradient centrifugation of the cell homogenate [7, 8]. The purity of the obtained mitochondrial fractions is usually demonstrated by enzymatic marker detection assay, most often by a cytochrome *c* oxidase (COX) assay [9, 10]. Although the COX activity is wide-accepted as a primary marker for localization of intact

mitochondria in isolated subcellular fractions, some complications connected with the isolation procedure [11-13], rearrangement of light and heavy mitochondria in different subcellular fractions [14] and fast electron transport from the ferricytochrome *c* to the oxygen may compromise the data acquisition and interpretation.

In this paper, we propose an alternative approach for determination of mitochondria localization in subcellular fractions, based on the measurement of their electrochemical activity in the presence and absence of specific mitochondrial inhibitor. The presented results, obtained by means of cyclic voltammetry (CV) carried out with subcellular fractions isolated from *Candida melibiosica* 2491 yeast, cultivated under polarization conditions in biofuel cell in the presence and absence of rotenone, are compared with data collected by colorimetric COX activity assay.

### EXPERIMENTAL

#### *Cultivation of Candida melibiosica* 2491 in biofuel cell

*C. melibiosica* 2491 yeast cells were cultivated in the anodic compartment of double-chamber biofuel cell. The yeast was suspended in 50 ml of a YP<sub>fm</sub> sterile medium previously determined as optimal [15]. The quantity of yeast inoculum was unified by adjusting its optical density OD<sub>600</sub> to 0.670. 0.1M K<sub>3</sub>[Fe(CN)<sub>6</sub>] in PBS, pH 7, served as a catholyte. The biofuel cell compartments were

\* To whom all correspondence should be sent:  
E-mail: jolinahubenova@yahoo.com

connected with a salt bridge to avoid any possible mixing of the anolyte and the catholyte. Pieces of carbon felt (SPC-7011, 30 g/m<sup>2</sup>, Weibgerber GmbH & Co. KG) with a rectangular shape (4 × 4 cm) were used as both anodes and cathodes. The cultivation was carried out in a thermostat at 28°C on an orbital shaker at 100 rpm in the presence and absence of 30 μM rotenone (Sigma-Aldrich: R8875). The yeast suspension was cultivated in a batch-regime under constant polarization by switching on 1 kΩ load resistor.

#### *Subcellular fractionation*

Two ml of anolyte from yeast suspension cultivated in biofuel cells in the presence and absence of rotenone were collected and centrifuged at 5100 g for 5 min. After washing the cells with PBS buffer (pH 6.8), the obtained yeast pellets were re-suspended in homogenizing buffer, consisting of 0.4 M sucrose, 50 mM Tris-HCl (pH 7.5), 3 mM EDTA and 1 mM PMSF, in proportion 1:4, and disintegrated by sonication (5-times, 10 s, in an ice-bath). The homogenates were centrifuged at 1000 g for 10 min. After nuclei removal, the supernatants were centrifuged at 3000 g for 5 min. The obtained supernatants in this step were further centrifuged at 10000 g for 20 min. The obtained pellets (P<sub>10000</sub>) were mixed with homogenization buffer and introduced on a freshly prepared sucrose density gradient, composed of overlaid 45%, 35% and 25% sucrose solutions. The fractionation was carried out by centrifugation at 13000 g for 30 min. The sucrose density fractions were collected and investigated for COX activity and protein content. In parallel, the fractions were analyzed by means of cyclic voltammetry.

#### *Specific cytochrome c oxidase activity*

The COX activity was determined by means of colorimetric assay, based on observation of the decrease in absorbance at 550 nm of ferrocytochrome *c* caused by its oxidation to ferricytochrome *c* by cytochrome *c* oxidase. The substrate stock solution was freshly prepared from cytochrome *c* (Sigma 30398) in concentration 2.7 mg/ml and reduced prior to use by addition of 12 μl of 10 mg/ml sodium hydrosulfite. The reaction mixture consisted of 0.25 % Triton X-100/PBS (pH 6.8), 0.25 M sucrose, reduced cytochrome *c* (90:9:10) and 10 μl sample. The absorption decay was recorded spectrophotometrically at 550 nm during the first 10 sec of the reaction. The COX activity, defined as 1.0 μmol oxidized cytochrome *c* per min at 25 °C

and pH 6.8, was estimated by the following equation:

$$\text{Units/ml} = (\Delta A_{550}/\text{min}) \times V_{\text{react}} / V_{\text{samp}} \times 18.5$$

where  $\Delta A_{550}/\text{min} = A_{550}/\text{min}$  (sample) -  $A_{550}/\text{min}$  (blank);  $V_{\text{react}}$  is the reaction volume in ml;  $V_{\text{samp}}$  is the volume of sample in ml; 18.5 mM<sup>-1</sup> cm<sup>-1</sup> is the difference in millimolar absorptivity between reduced and oxidized cytochrome *c* [16].

The specific cytochrome *c* oxidase activity is presented as enzyme activity per milligram protein (Units/mg). The protein content was determined by using a modified Bradford method (Merck 1.10306.0500). The intracellular protein concentration was estimated in mg/ml by using BSA- calibration curve.

#### *Electrochemical analyses*

The electrochemical behavior of the yeast fractions was investigated by means of cyclic voltammetry (CV). The CV was carried out in a three electrode arrangement, using Pt-wires as working and counter electrodes and Ag/AgCl as a reference electrode. PalmSens handheld potentiostat/galvanostat was used for the analyses. The potential was swept with a scan rate 10 mV/s.

The experiments were performed in duplicate.

## RESULTS AND DISCUSSION

Yeast cells were harvested from the suspension used as an anolyte in the biofuel cell and fractionated by means of differential centrifugation for gathering the cellular organelles. The organelle enriched fractions were further fractionated by sucrose density centrifugation, i.e. rearranged due to the specific organelle density [17]. For determination of the mitochondrial location during this procedure, the COX activity of all obtained fractions was analyzed (Fig. 1, solid columns). The purification factor was expressed for the individual step - the specific COX activity of the P<sub>10000</sub> fraction was admitted as unit of measurement. The highest specific activity was observed in 35%-sucrose gradient fraction. The purification factor of this fraction amounted to 0.9 and denoted as mitochondrial fraction. The results show that the most yeast mitochondria are situated in the fraction with density 1.1513 g/cm<sup>3</sup>. The light mitochondria were located in the 25% fraction, however the purification factor was twice lower (0.4). The negligible values of the determined COX activity in the 15%- and 45%- fractions lead to the supposition that these fractions do not contain mitochondria.



In the presence of rotenone, the COX activity of P<sub>10000</sub> was lower with two orders of magnitude. As an inhibitor of electron transport chain (ETC) complex I, the addition of rotenone to the yeast suspension leads to dysfunction of the ETCs. Having in mind that rotenone blocks the electron passage from Fe-S centers of complex I to ubiquinone (CoQ), the lower electron passage between the ETC complexes leads to COX activity deactivation (Fig. 1, sparse columns).

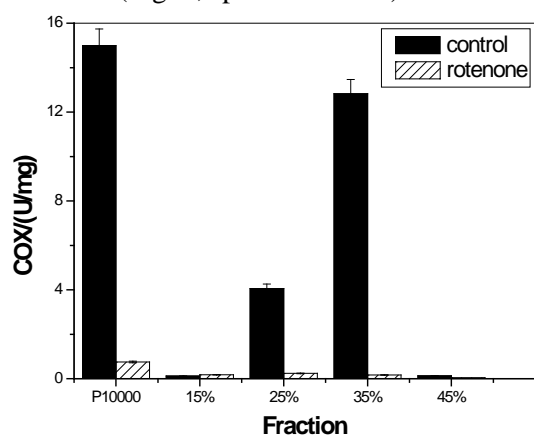


**Fig. 1.** Specific COX activity of the sucrose density gradient fractions in the presence and absence of rotenone.

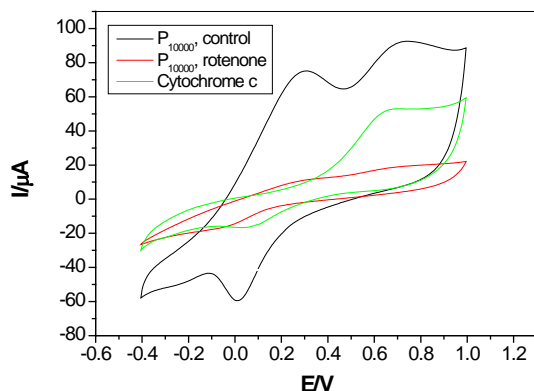


**Fig. 2.** Cyclic voltammograms of the organelle enriched fractions (P<sub>10000</sub>) obtained in the presence and absence of rotenone compared to cytochrome *c* as a standard.

In parallel, the electrochemical activity of the organelle enriched fractions (P<sub>10000</sub>) in the presence and absence of rotenone was analysed by means of cyclic voltammetry (Fig. 2). Two anodic peaks at potentials 0.3 V and 0.7 V and one cathodic peak at 0.03V were clearly observed on the voltammograms in the case without inhibition. We considered that the anodic peak at 0.7 V and the cathodic peak at 0.03 V represent the oxidation and reduction of cytochrome *c*. Fig. 2 clearly shows that the rotenone addition significantly decreased the redox activity of the fraction in comparison with that of the same fraction without inhibitor.

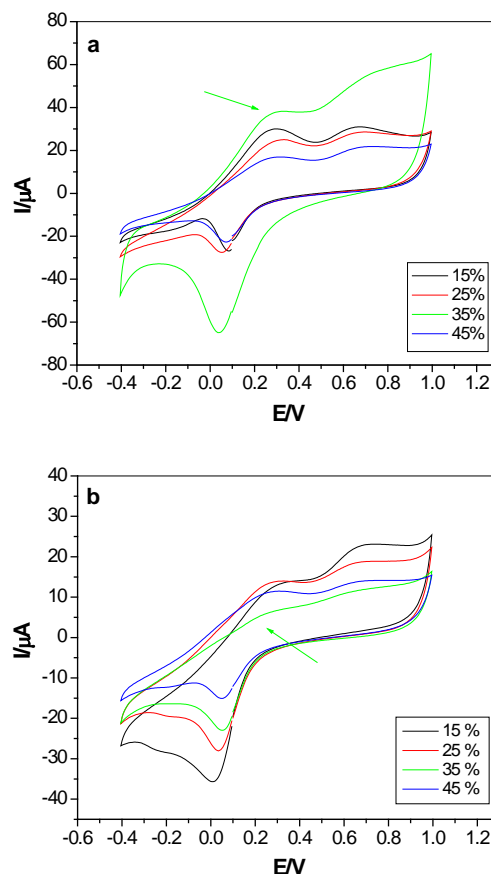


**Fig.3.** Cyclic voltammograms of the sucrose density gradient fractions obtained from yeast cultivated in biofuel cells: a) without inhibition; b) in the presence of rotenone.

After establishing the differences in the peaks on the CV in the presence and absence of inhibitor, cyclic voltammetry was carried out with the sucrose density fractions (Fig. 3). Identical to P<sub>10000</sub> anodic peaks appeared on the voltammograms of the fractions in the case without inhibition (Fig. 3a). The observed electrochemical activity demonstrated the presence of cytochrome *c* type molecules. It was considered that the peaks appeared at relatively low concentrations of the protein ( $5 \times 10^{-9}$  mol/l) as described by Brabec et al. [18], corresponding to a catalytic reaction, in which some of haemins of ferricytochrome *c* were reduced to haems. These haemins could be regenerated by chemical oxidation of the haem residues with oxygen [18]. The decreased current height of the peaks ( $I_p$ ) of the 15 %, 25 %, and 45 % fractions showed significantly lower concentrations of redox components. At the same time, the obtained peaks' currents of the mitochondrial fraction were much higher than those of the rest fractions. The highest electrochemical activity of the mitochondrial fraction overlaps the determined highest COX activity.

The electrochemical activity of the sucrose density gradient fractions obtained from yeast cultivated in the presence of rotenone was also explored (Fig.3b). The current height of the observed peaks of the 15 %, 25 %, and 45 % fractions was 50 % lower in comparison with the same fractions without inhibitor. The 35 % (mitochondrial) fraction, however did not express the anodic peak at a potential of 0.3 V. As far as rotenone is a specific mitochondrial NADH:ubiquinone oxidoreductase inhibitor, the result reveals that this peak represents the activity of the oxidoreductase reaction [19]. The lack of anodic peak on the CV of the mitochondrial fraction coincided with the significantly decreased specific COX activity determined in the presence of rotenone.

### CONCLUSION

The results obtained in this study offer a new fast approach for determination of the mitochondrial localization during fractionation. The conduction of cyclic voltammetry in the presence and absence of rotenone definitely shows the rearrangement of these organelles due to their maximal (without) and at the same time minimal (with inhibitor) redox activity. The cyclic voltammetry could be applied as an alternative method to the conventional enzymatic method for determination of cytochrome *c* oxidase activity.

### REFERENCES

1. T. Hajek, D. Honys, V. Capkova, *Plant Sci.*, **167**, 389 (2004).
2. J. Bardel, M. Louwagie, M. Jaquinod, A. Jourdain, S. Luche, T. Rabilloud, D. Macherel, J. Garin, J. Bourguignon, *Proteomics*, **2**, 880 (2002).
3. L. Jansch, V. Krufft, U.K. Schmitz, H.-P. Braun, *Plant J.*, **9**, 357 (1996)
4. C. Cardenas, J. Yang, R. A. Miller, I. Parker, I. Smith, C. B. Thompson, T. Bui, J. Molgo, M. J. Birnbaum, M. Muller, K. R. Hallows, H. Vais, K.-H. Cheung, J. K. Foskett, *Cell*, **142**, 270 (2010).
5. U. Brandt, *Annu. Rev. Biochem.*, **75**, 69 (2006).
6. D. J. Granville, B. A. Cassidy, D. O. Ruehlmann, J. C. Choy, C. Brenner, G. Kroemer, C. van Breemen, P. Margaron, D. W. Hunt, B. M. McManus, *Am. J. Pathol.*, **159**, 305 (2001).
7. T. Hajek, D. Honys, V. Capkova, *Plant Sci.*, **167**, 389 (2004).
8. M. Neuburger, F. Rebeille, A. Jourdain, S. Nakamura, R. Douce, *J. Biol. Chem.*, **271**, 9466 (1996).
9. R. Douce, E.L. Christensen, W.D. Bonner, *Biochim. Biophys. Acta*, **275**, 148 (1972).
10. R. S. Balaban, V. K. Mootha, A. Arai, *Anal. Biochem.*, **237**, 274 (1996).
11. T. Hajek, D. Honys, V. Capkova, *Plant Sci.*, **167**, 389 (2004).
12. A. J. Yang, R. M. Mulligan, *Nucleic Acids Res.*, **24**, 3601 (1996).
13. R. Benz, *Biochim. Biophys. Acta*, **291**, 167 (1994).
14. M. Luisa Bonet, F. Serra, J. C. Matamala, F. J. Garcia-Palmer, A. Palou, *Biochem. J.*, **311**, 327 (1995).
15. Y. Hubenova, M. Mitov, *Bioelectrochemistry*, **78**, 57 (2010).
16. R.M. Zabinski-Snopko, G.H. Czerlinski, *J. Biol. Phys.*, **9**, 155 (1981).
17. B. Storrie, E. Madden, *Methods Enzymol.*, **182**, 203 (1990).
18. V. Brabec, P. Bianco, J. Haladjian, *Gen. Physiol. Biophys.*, **1**, 269 (1982).
19. Y. Hubenova, DSc Thesis, Sofia University "St. Kliment Ohridski", Sofia, 2013, ISBN 978-954-322-696-2.

## ПРИЛОЖЕНИЕ НА ЦИКЛИЧНАТА ВОЛТАМПЕРОМЕТРИЯ ЗА ОПРЕДЕЛЯНЕ НА МИТОХОНДРИАЛНА РЕДОКС АКТИВНОСТ ПО ВРЕМЕ НА ВЪТРЕКЛЕТЪЧНО ФРАКЦИОНИРАНЕ НА ДРОЖДИ КУЛТИВИРАНИ КАТО БИОКАТАЛИЗАТОРИ

Й. В. Хубенова<sup>1</sup>, М. Й. Митов<sup>2</sup>

<sup>1</sup>Катедра по Биохимия и микробиология, Пловдивски университет "Паусий Хилендарски", ул. Цар Асен №24, 4000 Пловдив, България,

<sup>2</sup>Катедра по Химия, Югозападен университет "Неофит Рилски", ул. Иван Михайлов №66, 2700 Благоевград, България

Получена на 21 юни 2014 г.; коригирана на 10 септември 2014 г.

(Резюме)

В настоящата разработка е предложен алтернативен метод за определяне на митохондриалната локализация във фракции, получени чрез вътреклетъчно фракциониране на дрожди *Candida melibiosica* 2491, култивирани при поляризация. Електрохимичната активност на фракциите е сравнена с цитохром *c* оксидазната им активност в присъствие и отсъствие на rotenon.

## Synthesis and characterization of dip-coated CoB-, NiB- and CoNiB-carbon felt catalysts

M. Y. Mitov<sup>1\*</sup>, E. Y. Chorbadzhiyska<sup>1</sup>, L. Nalbandian<sup>2</sup>, Y. V. Hubenova<sup>3</sup>

<sup>1</sup>Department of Chemistry, South-West University "Neofit Rilski", Blagoevgrad, Bulgaria

<sup>2</sup>Laboratory of Inorganic Materials (LIM), Chemical Process & Energy Resources Institute, Center for Research and Technology - Hellas (CPERI / CERTH), Thessaloniki, Greece

<sup>3</sup>Department of Biochemistry and Microbiology, Plovdiv University "Paisii Hilendarski", Plovdiv, Bulgaria

Received June 21, 2014, Revised September 10, 2014

In the present study, CoB, NiB and CoNiB catalysts were dip-coated on carbon felt by borohydride reduction. The morphology and the elemental composition of the synthesized coatings were characterized by scanning electron microscopy and energy-dispersive X-ray spectroscopy. The electrocatalytic activity of the produced materials towards hydrogen evolution reaction in neutral electrolyte was investigated by means of linear voltammetry and chronoamperometry. The highest intrinsic activity was evaluated for the NiB catalysts.

**Keywords:** dip-coated catalysts, borohydride reduction, electrocatalytic activity, hydrogen evolution reaction, neutral electrolyte.

### INTRODUCTION

Over the past few years, bioelectrochemical systems (BESs), such as microbial fuel cells (MFCs) and microbial electrolysis cells (MECs), have attracted an increasing attention as a novel and promising approach for utilization of organic materials in wastewaters for production of electrical energy or valuable chemicals [1-3]. Hydrogen production in MECs is considered as a main goal of this strategy. Although laboratory-scale MECs operate with high electrical energy efficiency at applied voltages even below the theoretical electromotive force of water electrolysis (1.23 V), numerous challenges need to be faced before the microbial electrolysis can achieve practical implementation as a feasible hydrogen production technology. Because all types of BESs are based on the same microbial-assisted anodic reactions, the major task for improving the MECs performance is connected with a development of high catalytically active and cost-effective cathodes [3,4]. The replacement of the expensive platinum-catalyzed cathodes with alternative precious-metal free catalysts is one of the main strategies in the field.

Nickel-based materials have been extensively studied as cost-effective cathodes for hydrogen production in MECs [1,3,4]. Promising results have been reported for the use of different stainless steel and nickel alloys [5], commercially available nickel

and stainless steel powder supported on carbon cloth [6], NiMo and NiW electrodeposited onto a carbon cloth [7] or carbon felt [8]. Recently, we have demonstrated that carbon supported NiFe-, NiFeP- and NiFeCoP-nanocomposites possess high catalytic activity towards HER in neutral and weak acidic solutions and could be applied as cathodes in MECs [9]. Jeremiasse et al. [10] reported NiFeMo and CoMo alloys as possible HER catalysts in an MEC around neutral and mild alkaline pH.

Nanofabrication is considered as a perspective approach for producing efficient electrocatalysts due to the fact that nanomaterials possess unique chemical, structural and electrical properties [11]. In our previous studies [12, 13], it was established that CoB nanoparticles, produced by borohydride reduction, could be applied as an electrode material in alkaline batteries due to their ability for electrochemically reversible hydrogen absorption/desorption. An electrocatalytic activity of electrodes prepared from NiB nanosized powders towards HER and hydrogenation of some organic compounds was also found [14-16].

In the present study, CoB, NiB and CoNiB catalysts were dip-coated on carbon felt by borohydride reduction. The morphology and the elemental composition of the produced coatings were characterized and their electrocatalytic activity towards HER in neutral electrolyte was evaluated and compared.

\* To whom all correspondence should be sent:  
E-mail: mitovmario@mail.bg

## EXPERIMENTAL

Cobalt- and nickel-containing coatings were deposited on carbon felt (SPC-7011, 30 g/m<sup>2</sup>, Weibgerber GmbH & Co. KG) by borohydride reduction. 10% Co(NO<sub>3</sub>)<sub>2</sub> and 10% Ni(NO<sub>3</sub>)<sub>2</sub> or a mixture of both solutions in a volume ratio of 1:1 were used as a metallic precursor, and 5% NaBH<sub>4</sub> in 1% NaOH was the reducing agent. Prior to use the carbon felt samples (round-shaped with geometric area of 1.4 cm<sup>2</sup>) were sonicated in ethanol:acetone 1:1 (v/v) mixture for 10 min and then rinsed with DI water. The carbon felt was subsequently immersed into the precursor and the reducing solutions for 10 s and finally washed with DI water. The dip-coating procedure was repeated several times in order to produce substantial catalyst loading. The prepared catalysts were heated at 100 °C for 2 h to enhance the adhesion between the coatings and the support [17]. The weight difference before and after the deposition was used to calculate the catalyst loading.

The morphology of the developed materials was analyzed by scanning electron microscopy (SEM) using JEOL 6300 microscope. In addition, the elemental content of the coatings was analyzed by energy-dispersive X-ray spectroscopy (EDS).

The electrocatalytic activity of the produced materials towards hydrogen evolution reaction (HER) in phosphate buffer solution (PBS, pH 7.0) was explored by means of linear voltammetry (LV) and chronoamperometry (CA). The electrochemical examinations were performed in a three-electrode cell by using PJT 35-2 potentiostat/galvanostat (Radiometer-Tacussel) by automatic data acquisition via IMT-101 electrochemical interface. The investigated material was connected as a

working electrode; a platinum wire was used as a counter electrode and Ag/AgCl (3 M KCl) as a reference electrode.

The LV was carried out in a negative direction with a scan rate of 2 mV/s. Three subsequent scans were performed for each sample and the third scan was used for data analysis. During chronoamperometric measurements, the working electrode was polarized from -0.6 V to -1.2 V (vs. Ag/AgCl) for 10 min at each potential step and the current response was recorded. The hydrogen generation rate at each potential was calculated from the coulombs, determined by integration of areas under CA curves, applying the Faraday's law.

## RESULTS AND DISCUSSION

### *Production and characterization of CoB-, NiB- and CoNiB-coated carbon felt*

Preliminary experiments have shown that a single dip-coating cycle with the Co-containing precursor results in approximately double catalyst loading in comparison with the use of Ni-containing solution. The results reported hereafter in the paper are obtained with catalysts produced by 20 repetitions of the dip-coating process with the Ni precursor and 10 repetitions with the Co and mixed Co-Ni solution. The estimated loadings of the coatings, obtained as a result of the described procedure, are 9.6, 9.7 and 5.8 mg/cm<sup>2</sup> for the Ni-, Co- and CoNi-containing catalysts, respectively. These results indicate that the presence of Ni in the precursor solutions suppresses the coating deposition on the carbon felt, probably due to more favorable implementation of the reduction process in the solution volume than on the support surface.

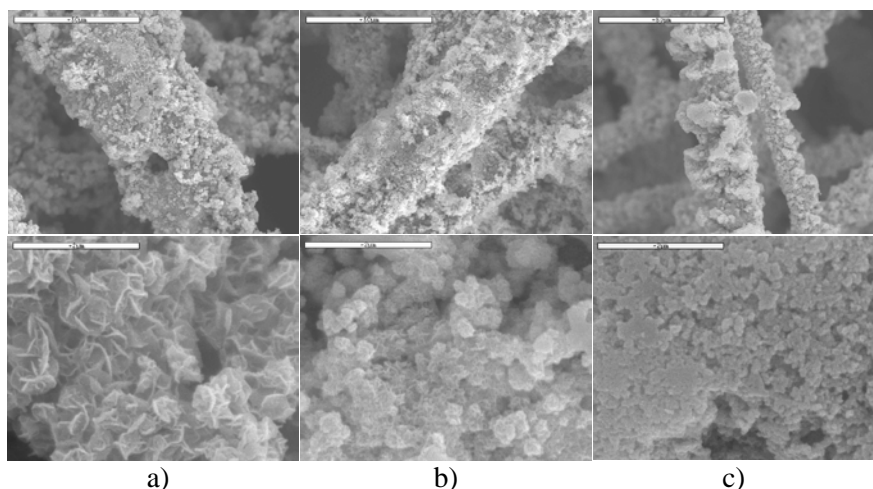
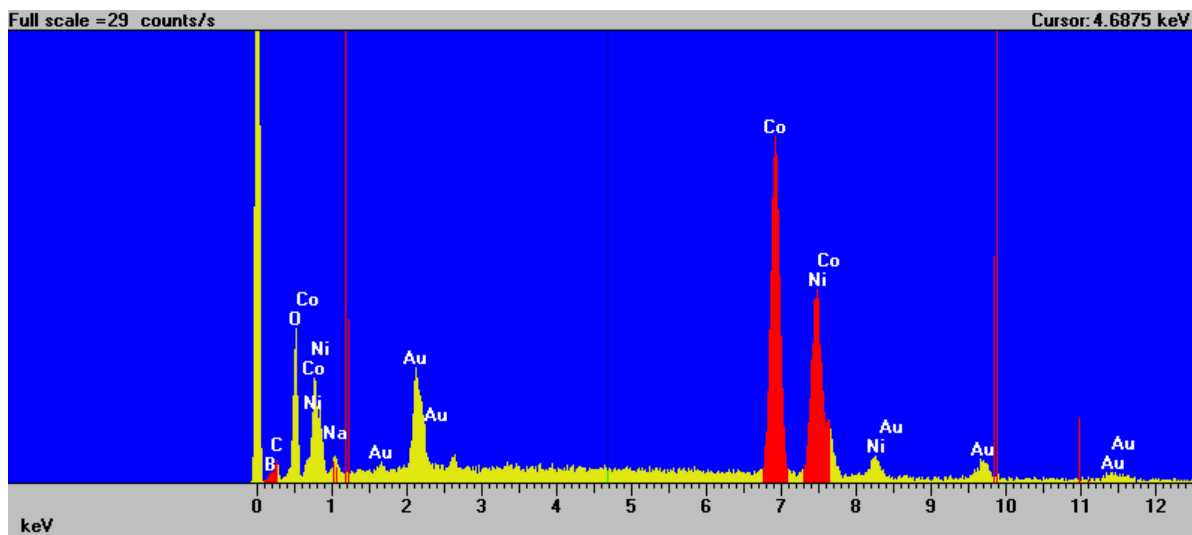


**Fig. 1.** SEM images of the investigated materials: a) CoB; b) CoNiB; c) NiB. Magnification: × 1000 (top) and × 25000 (down).



SEM images of the developed materials taken at different magnifications are presented in Fig. 1. The carbon felt used consists of randomly dispersed fibres with a diameter between 8 and 10  $\mu\text{m}$  [18, 19], which provides a large surface area. The SEM observations show that rugged coatings are formed from all applied precursors, which cover not only the surface, but also the fibres in a depth of the carbon felt. The thickness of the coated fibres increases from ca. 15  $\mu\text{m}$  for the deposits produced from Ni precursor to over 50  $\mu\text{m}$  for those prepared from Co-containing solution, suggesting a preferential reduction of Co(II) on the carbon surface. The developed CoNi-coatings enlarge the fibres' diameter to ca. 30  $\mu\text{m}$ . The higher magnification reveals that the Co-containing deposits possess a flakes-like shape, while the Ni-based ones have a more dense cauliflower-like structure. The CoNi-coating structure resembles that of Co-deposits, however, the inclusion of nickel results in a decrease of the flakes size.

The obtained EDS-spectra of the investigated materials confirm the presence of cobalt and nickel, and also indicate an existence of boron in the deposits (Fig. 2). These findings suggest that the produced coatings consist of CoB and NiB (nano)particles, as previously described [12,13,20]. Assuming this, the coatings obtained in this study will be further denoted as CoB, NiB and CoNiB. Besides the close molar percentages of Co and Ni in the mixed precursor solution, the atomic ratio of both metals in the produced CoNiB-deposits was determined as 61.7:38.3. The enriched Co content supports the supposition for preferential deposition of Co(II) on the carbon felt surface.

### *Electrocatalytic properties for HER in neutral electrolyte*

The electrochemical behavior of the produced coated carbon felt samples in neutral PBS was investigated by means of LV. Linear voltammograms, presenting the performance of the studied electrodes in the cathodic region of potentials, are plotted on Fig. 3. The electrocatalytic activity in respect to HER was evaluated by the onset potential ( $V_e$ ) needed to initiate hydrogen production as a measure of the relative overpotential [21] and the current density obtained at -1.0 V (vs. Ag/AgCl). The values of both quantities, derived from LVs, are summarized in Table 1.

**Table 1.** Values of  $V_e$  and current density at -1.0 V (vs. Ag/AgCl), derived from LVs.

Material	$V_e$ , V (vs. Ag/AgCl)	Current density, $\text{mA cm}^{-2}$
NiB/C-felt	-0.467	1.53
CoNiB/C-felt	-0.551	1.40
CoB/C-felt	-0.695	1.34
C-felt	-0.762	0.14

The obtained results indicate that CoB possesses the highest overpotential for HER among the explored modified electrodes. The increase of the Ni content in the deposits shifts the  $V_e$  values in positive direction, thus, the hydrogen production on NiB electrodes starts at the lowest onset potential -0.467 V (vs. Ag/AgCl). The augmentation of nickel also results in enhancing the hydrogen current production rate, evaluated by the current density at -1.0 V (vs. Ag/AgCl). All dip-coated electrodes exhibit lower overpotentials and HER

rates with an order of magnitude higher than the bare carbon felt.

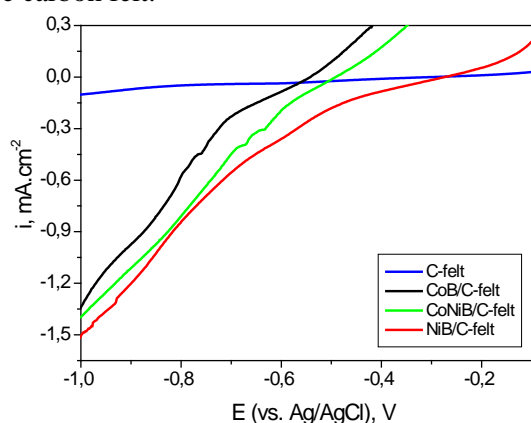


**Fig.3.** Linear voltammograms obtained with investigated materials in PBS, scan rate 2 mV/s.

The catalytic properties of the studied materials towards HER were more precisely evaluated by chronoamperometric measurements [22], performed in the potential range from -0.6 to -1.2 V (vs. Ag/AgCl). The chronoamperograms recorded at the highest cathodic potential applied are presented in Fig. 4. The electric charge values, obtained by integration of the areas under the current-time plots, were used for estimation of the hydrogen production rates at different potentials, shown in Fig. 5a. In general, the obtained results confirm the findings from the LV-studies that the electrocatalytic activity of the dip-coated electrodes surpasses that of the non-modified carbon felt. The highest hydrogen production rates at all applied potentials were achieved with the NiB/carbon felt electrodes, exceeding over twice those obtained

with the CoB- and CoNiB-catalysts. In order to evaluate the intrinsic electrocatalytic activity of the explored materials, the hydrogen production rates were normalized to catalyst loadings. The results, presented in Fig. 5b, show that the co-deposition of Co and Ni enhances the intrinsic activity in comparison to that of CoB, however, the highest values were achieved with NiB catalysts. Although these values are lower than those previously reported for Pd-Au/carbon felt electrodes [22], the absence of precious metals and the easy production by the dip-coating method supposes the NiB/carbon felt as a promising cost-effective cathode material for hydrogen production from neutral electrolytes, i.e. in microbial electrolysis cells.

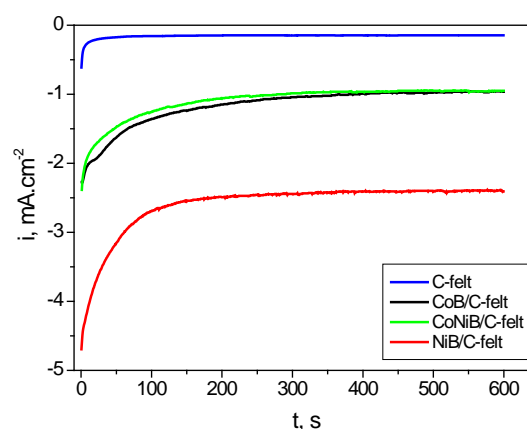
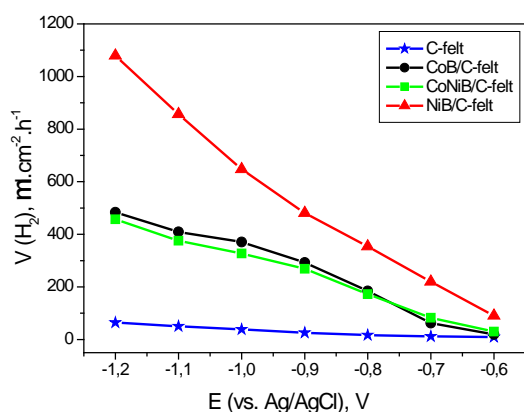
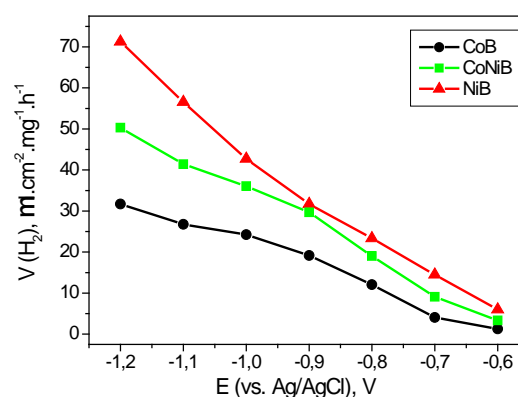


**Fig. 4.** Chronoamperograms obtained with different materials at a potential of -1.2 V (vs. Ag/AgCl) in PBS.



a)



b)

**Fig. 5.** a) Hydrogen evolution rates at different applied potentials, estimated from chronoamperometric measurements; b) Intrinsic electrocatalytic activity of the investigated dip-coated catalysts towards HER, expressed as a volume of generated hydrogen per hour normalized to the weight of the deposits and geometric area of the support.

## CONCLUSION

Carbon supported CoB, CoNiB and NiB catalysts can be produced by borohydride reduction applying a dip-coating procedure. The catalyst loading increases with augmentation of Co in the precursor solution. The intrinsic electrocatalytic activity of the synthesized catalysts towards HER in neutral electrolyte increases in the order CoB < CoNiB < NiB. The achieved hydrogen production rates suggest the NiB/carbon felt as a promising cost-effective cathode material for hydrogen production from neutral electrolytes.

**Acknowledgements:** This study was funded by the program "Hydrogen Economy Cooperation Network for Research - Public Awareness - Business Opportunities across Greek-Bulgarian borders – HYDECON". The Project is co-funded by the European Regional Development Fund and by national funds of the countries participating in the ETCP "Greece-Bulgaria 2007-2013" through contract B1.33.01.

## REFERENCES

1. R.A. Rozendal, H.V.M. Hamelers, K. Rabaey, J. Keller, C.J.N. Buisman, *Trends Biotechnol.*, **26**, 450 (2008).
2. K. Rabaey, R.A. Rozendal, *Nat. Rev. Microbiol.*, **8**, 706 (2010).
3. B.E. Logan, *Appl. Microbiol. Biotechnol.*, **85**, 1665 (2010).
4. A. Kundu, J.N. Sahu, G. Redzwan, M.A. Hashim, *Int. J. Hydrogen Energy*, **38**, 1745 (2013).
5. P.A. Selembo, M.D. Merrill, B.E. Logan, *J Power Sources*, **190**, 271 (2009).
6. P.A. Selembo, M.D. Merrill, B.E. Logan, *Int. J. Hydrogen Energy*, **35**, 428 (2010).
7. H. Hu, Y. Fan, H. Liu, *Int. J. Hydrogen Energy*, **34**, 8535 (2009).
8. E. Chorbadzhiyska, M. Mitov, Y. Hubenova, L. Nalbandian, in: Proc. 5<sup>th</sup> Int. Sci. Conf. FMNS 2013, South-West University "Neofit Rilski" Blagoevgrad, 2013, vol. 4, p. 88.
9. M. Mitov, E. Chorbadzhiyska, R. Rashkov, Y. Hubenova, *Int. J. Hydrogen Energy*, **37**, 16522 (2012).
10. A.W. Jeremiasse, J. Bergsma, J.N. Kleijn, M. Saakes, C.J.N. Buisman, *Int. J. Hydrogen Energy*, **36**, 10482 (2011).
11. Y. Fan, S. Xu, R. Schaller, J. Jiao, F. Chaplen, H. Liu, *Biosens. Bioelectron.*, **26**, 1908 (2011).
12. M. Mitov, A. Popov, I. Dragieva, *J. Appl. Electrochem.*, **29**, 59 (1999).
13. M. Mitov, A. Popov, I. Dragieva, *Colloid. Surface A*, **149**, 413 (1999).
14. P. Los, A. Lasia, *J. Electroanal. Chem.*, **333**, 115 (1992).
15. J.J. Borodzinski, A. Lasia, *J. Appl. Electrochem.*, **24**, 1267 (1994).
16. B. Mahdavi, P. Chambrion, J. Binette, E. Martel, J. Lessard, *Can. J. Chem.*, **73**, 846 (1995).
17. J. Lee, K. Kong, C. Jung, E. Cho, S. Yoon, J. Han, T. Lee, S. Nam, *Catal. Today*, **120**, 305 (2007).
18. Y. Hubenova, R. Rashkov, V. Buchvarov, M. Arnaudova, S. Babanova, M. Mitov, *Ind. Eng. Chem. Res.*, **50**, 557 (2011).
19. Y. Hubenova, R. Rashkov, V. Buchvarov, S. Babanova, M. Mitov, *J. Mater. Sci.*, **46**, 7074 (2011).
20. I. Dragieva, G. Ivanova, S. Bliznakov, E. Lefterova, Z. Stojnov, I. Markova, M. Pankova, *Phys. Chem. Glasses*, **41**, 264 (2000).
21. Y. Zhang, M. Merrill, B. Logan, *Int. J. Hydrogen Energy*, **35**, 12020 (2010).
22. E. Chorbadzhiyska, M. Mitov, G. Hristov, N. Dimcheva, L. Nalbandian, A. Evdou, Y. Hubenova, *Int. J. Electrochem.*, **2014**, Article ID 239270, 6 pages. <http://dx.doi.org/10.1155/2014/239270>

## СИНТЕЗ И ОХАРАКТЕРИЗИРАНЕ НА CoB-, NiB- И CoNiB- КАТАЛИЗАТОРИ ОТЛОЖЕНИ ВЪРХУ ВЪГЛЕРОДНО КЕЧЕ

М. Й. Митов<sup>1\*</sup>, Е. Й. Чорбаджийска<sup>1</sup>, Л. Налбандиан<sup>2</sup>, Й. В. Хубенова<sup>3</sup>

<sup>1</sup>Катедра Химия, Югозападен университет „Неофит Рилски“, Благоевград, България

<sup>2</sup>Лаборатория по неорганични материали, Институт по химични процеси и енергийни ресурси, Научно-изследователски и технологичен център – Хелас, Терми-Солун, Гърция

<sup>3</sup>Катедра Биохимия и Микробиология, Пловдивски Университет, Пловдив, България

Получена на 21 юни 2014 г.; коригирана на 10 септември 2014 г.

(Резюме)

В настоящата разработка, CoB, NiB и CoNiB катализатори са отложени върху въглеродно кечче чрез борхидридна редукция. Морфологията и елементният състав на синтезираните покрития са охарактеризирани чрез сканираща електронна микроскопия и енергийно-дисперсионна рентгенова спектроскопия. Електрохимичната активност на произведените материали по отношение катодното отделяне на водород в неутрален електролит е изследвана чрез линейна волтаперометрия и хроноамперометрия. Най-голяма специфична активност е установена за NiB катализатори.

## Solvent-free one-pot synthesis of highly functionalized benzothiazolodiamides via Ugi four-component reaction

F. Sheikholeslami-Farahani<sup>\*1</sup>, A. S. Shahvelayati<sup>2</sup>

<sup>1</sup>Department of Chemistry, Firoozkooh Branch, Islamic Azad University, Firoozkooh, Iran

<sup>2</sup>Department of Chemistry, Islamic Azad University Shahr-e Rey Branch, Tehran, Iran.

Received September 17, 2014, Revised January 2, 2015

4-Benzothiazol-2-ylamino-4-oxo-2-butenoic acid, prepared by reaction of 2-aminobenzothiazole and maleic anhydride, is used as an acid component in Ugi reaction, under solvent-free conditions, to produce unsaturated  $\alpha$ -benzothiazoleamidodipeptides in good yields using a tandem sequence.

**Keywords:** Ugi reaction, One-pot, Maleic anhydride, 2-Aminobenzothiazole, Solvent-free.

### INTRODUCTION

There has been tremendous interest in developing highly efficient transformations for the preparation of organic compounds and biologically active materials with potential application in the pharmaceutical or agrochemical industries from commercially available compounds. There is also a need for synthetic chemists to find new, efficient, and strategically important processes, which are environmentally benign and lead to greater structural variation in a short period of time with high yields and simple work-up procedures. Significant advances have been made to chemical processes to achieve the ultimate goal of hazard-free, waste-free, and energy-efficient syntheses [1]. In this context, multicomponent reactions [2-7] have played an important role in these processes [8]. The Ugi four-component reaction (U-4CR) [9] is one of the milestones in this field and great efforts have been devoted to the exploration of the potential of this transformation [10]. In the U-4CR, a primary amine, an aldehyde, a carboxylic acid and an isocyanide react simultaneously to afford peptide-like structures in high diversity. Small peptides (oligopeptides) are a group of omnipresent compounds in medicinal chemistry. Among them, compounds with various activities can be found [11-17]. Thus, the synthesis of  $\alpha$ -benzothiazoleamidodipeptides that mimic natural dipeptides, is very attractive. In recent years several modifications of the classical U-4CR have been described. Such modifications include variations of one of the components or the introduction of a linkage between two of them [18], the use of

polyfunctional building blocks [19, 20] and the employment of non-classical starting units [21]. As part of our continuing interest in isocyanide-based multi-component reactions [22-24], we describe the synthesis of a dipeptide mimetic library based on 4-benzothiazol-2-ylamino-4-oxo-2-butenoic acid, as a new acid component in the Ugi reaction under solvent-free conditions in a tandem reaction (Scheme 1).

### EXPERIMENTAL

#### *Apparatus and analysis*

Amines, alkyl isocyanides, and ketones were obtained from Merck and were used without further purification. 4-Benzothiazol-2-ylamino-4-oxo-2-butenoic acid was synthesized by reaction of 2-aminobenzothiazole and furan-2,5-dione. Melting points were recorded on an Electrothermal-9100 apparatus. IR spectra were recorded with a Shimadzu IR-460 spectrometer. <sup>1</sup>H- and <sup>13</sup>C-NMR spectra were recorded with a Bruker DRX-300 Avance instrument using CDCl<sub>3</sub> as the deuterated solvent containing tetramethylsilane as internal standard, at 300 and 75 MHz, respectively;  $\delta$  in parts per million,  $J$  in Hertz. EIMS (70 eV): Mass spectra were obtained with a Finnigan-MAT-8430 mass spectrometer, in  $m/z$ . Elemental analyses (C, H, N) were performed with a Heraeus CHN-O-Rapid analyzer.

#### *General procedure for preparation of compound 1*

A mixture of 2-aminobenzothiazole (0.30 g, 2 mmol) and maleic anhydride (0.20 g, 2 mmol) in 5 mL of CH<sub>3</sub>CN was stirred for 12 h at r.t. The yellow precipitate was filtered and washed with cold CH<sub>3</sub>CN. The product 1 was used in the next step without further purification.

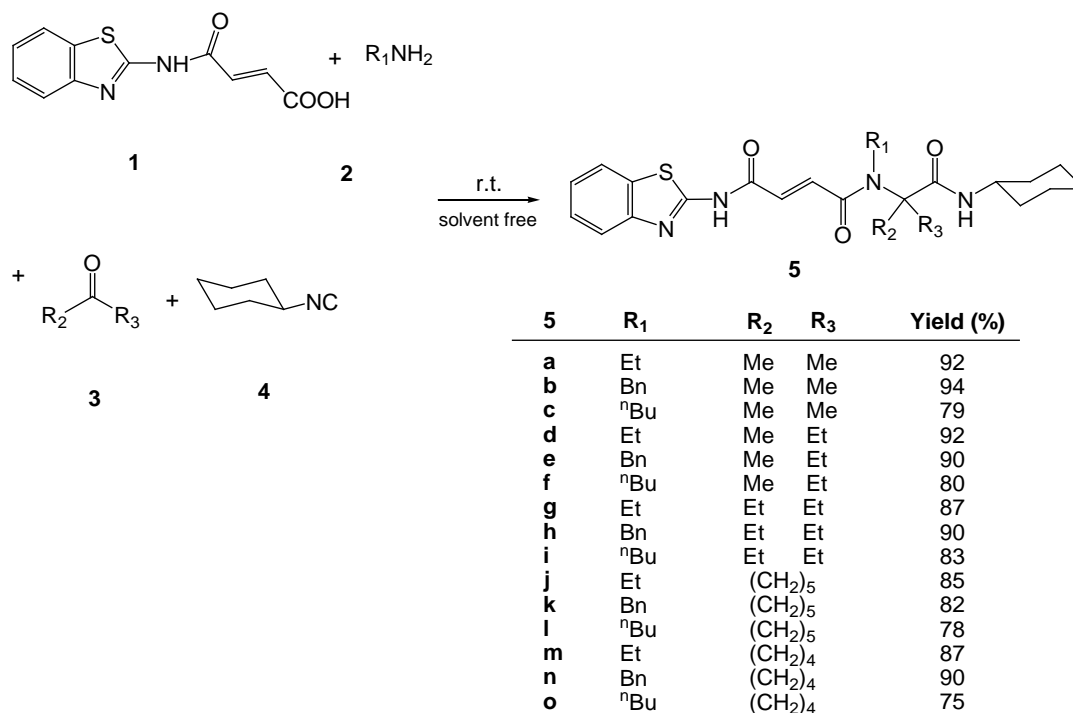
\* To whom all correspondence should be sent:  
E-mail: sheikholeslami@yahoo.com



General procedure for the preparation of compounds 5

The carboxylic acid (**1**, 1 mmol) was added to a mixture of amine (**2**, 1 mmol) and 0.5 ml (excess) of ketone or aldehyde **3**. Then, the alkyl isocyanide (**4**, 1 mmol) was added. The mixture was stirred for

12 h at r.t. The volatiles were evaporated under reduced pressure at 50 °C to leave a residue that was purified by column chromatography (SiO<sub>2</sub>; hexane/EtOAc 5:2) to afford pure desired products.



Scheme 1. Ugi reaction of isocyanide and ketones in the presence of amines.

*N*<sub>1</sub>-(Benzothiazol-2-yl)-*N*<sub>4</sub>-(1-(cyclohexylamino)-2-methyl-1-oxopropan-2-yl)-*N*<sub>4</sub>-ethyl fumaramide (**5a**)

Light yellow solid; m.p: 160-163 °C; yield: 0.40 g (92%); IR (KBr): ( $\nu_{\max}/\text{cm}^{-1}$ ) = 3365, 3173, 1637, 1543, 1435, 1266, 1180, 754; EI-MS:  $m/z$  (%) = 442 (M<sup>+</sup>, 1.2), 294 (32), 231 (58), 211 (18), 168 (24), 148 (100), 29 (23); Anal. calcd. for C<sub>23</sub>H<sub>30</sub>N<sub>4</sub>O<sub>3</sub>S (442.57): C, 62.42; H, 6.83; N, 12.66; Found: C, 62.58; H, 7.04; N, 12.98%; <sup>1</sup>H NMR (CDCl<sub>3</sub>):  $\delta$  = 1.16-1.97 (10 H, m, 5 CH<sub>2</sub>), 1.20 (3 H, t, <sup>3</sup>J 6.9 Hz, CH<sub>3</sub>), 1.45 (6 H, s, 2 CH<sub>3</sub>), 3.54 (2 H, q, <sup>3</sup>J 6.9 Hz, CH<sub>2</sub>N), 3.79-3.82 (1 H, m, CH), 6.40 (1 H, d, <sup>3</sup>J 12.0 Hz, CH), 6.65 (1 H, d, <sup>3</sup>J 12.0 Hz, CH), 6.86 (1 H, d, <sup>3</sup>J 8.6 Hz, NH), 7.28-7.84 (4 H, m, 4 CH), 8.53 (1 H, br s, NH) ppm; <sup>13</sup>C NMR (CDCl<sub>3</sub>):  $\delta$  = 17.1 (CH<sub>3</sub>), 25.2 (CH<sub>2</sub>), 25.8 (2 CH<sub>3</sub>), 26.0 (2 CH<sub>2</sub>), 33.0 (2 CH<sub>2</sub>), 40.9 (CH<sub>2</sub>), 49.4 (CH), 63.1 (C), 120.9 (CH), 121.8 (CH), 123.7 (CH), 124.9 (CH), 127.1 (CH), 131.9 (CH), 139.4 (C), 147.6 (C), 158.9 (C=N), 163.1 (C=O), 167.4 (C=O), 174.3 (C=O) ppm.

*N*<sub>1</sub>-(Benzothiazol-2-yl)-*N*<sub>4</sub>-benzyl-*N*<sub>4</sub>-(1-(cyclohexylamino)-2-methyl-1-oxopropan-2-yl) fumaramide (**5b**)

Light yellow solid; m.p: 180-182 °C; yield: 0.47 g (94%); IR (KBr): ( $\nu_{\max}/\text{cm}^{-1}$ ) = 3347, 3127, 1655, 1635, 1550, 1266, 1173; EI-MS:  $m/z$  (%) = 504 (M<sup>+</sup>, 1), 355 (23), 273 (22), 231 (26), 168 (10), 148 (100), 91 (59); Anal. calcd. for C<sub>28</sub>H<sub>32</sub>N<sub>4</sub>O<sub>3</sub>S (504.64): C, 66.64; H, 6.39; N, 11.10; Found: C, 66.89; H, 6.94; N, 11.73%; <sup>1</sup>H NMR (CDCl<sub>3</sub>):  $\delta$  = 1.19-2.01 (10 H, m, 5 CH<sub>2</sub>), 1.56 (6 H, s, 2 CH<sub>3</sub>), 3.83-3.86 (1 H, m, CH), 4.78 (2 H, s, CH<sub>2</sub>N), 6.22 (1 H, d, <sup>3</sup>J 16.0 Hz, CH), 6.61 (1 H, d, <sup>3</sup>J 16.0 Hz, CH), 6.66 (1 H, br s, NH), 7.36-7.86 (9 H, m, 9 CH), 8.61 (1 H, br s, NH) ppm; <sup>13</sup>C NMR (CDCl<sub>3</sub>):  $\delta$  = 25.0 (2 CH<sub>3</sub>), 25.8 (2 CH<sub>2</sub>), 26.0 (CH<sub>2</sub>), 33.1 (2 CH<sub>2</sub>), 49.3 (CH<sub>2</sub>N), 50.3 (CH), 63.9 (C), 121.1 (CH), 122.8 (CH), 124.4 (CH), 124.8 (CH), 126.6 (2 CH), 126.9 (CH), 127.5 (C), 127.9 (CH), 129.3 (2 CH), 132.2 (CH), 138.1 (C), 148.1 (C), 158.9 (C=N), 163.2 (C=O), 168.2 (C=O), 174.0 (C=O) ppm.

*N*<sub>1</sub>-(Benzo[d]thiazol-2-yl)-*N*<sub>4</sub>-butyl-*N*<sub>4</sub>-(1-(cyclohexylamino)-2-methyl-1-oxopropan-2-yl)fumaramide (5c)

Light yellow solid; m.p: 160-163 °C; yield: 0.37 g (79%); IR (KBr): ( $\nu_{\max}/\text{cm}^{-1}$ ) = 3382, 3214, 1782, 1659, 1543, 1252, 1183; EI-MS:  $m/z$  (%) = 470 ( $M^+$ , 1.4), 320 (25), 239 (19), 231 (56), 168 (20), 148 (100), 57 (24); Anal. calcd. for C<sub>25</sub>H<sub>34</sub>N<sub>4</sub>O<sub>3</sub>S (470.24): C, 63.42; H, 6.83; N, 12.66; Found: C, 63.98; H, 7.24; N, 13.08%; <sup>1</sup>H NMR (CDCl<sub>3</sub>):  $\delta$  = 0.93 (3 H, t, <sup>3</sup>J 6.9 Hz, CH<sub>3</sub>), 1.13-1.95 (14 H, m, 7 CH<sub>2</sub>), 1.62 (6 H, s, 2 CH<sub>3</sub>), 3.45 (2 H, t, <sup>3</sup>J 7.2 Hz, CH<sub>2</sub>N), 3.81-3.84 (1 H, m, CH), 6.48 (2 H, ABq, <sup>3</sup>J 12.1 Hz,  $\Delta\nu$  96.3 Hz, 2 CH), 6.85 (1 H, d, <sup>3</sup>J 7.8 Hz, NH), 7.38 (1 H, t, <sup>3</sup>J 7.3 Hz, CH), 7.46 (1 H, t, <sup>3</sup>J 7.6 Hz, CH), 7.82 (1 H, d, <sup>3</sup>J 7.3 Hz, CH), 7.85 (1 H, d, <sup>3</sup>J 7.6 Hz, CH), 10.95 (1 H, br s, NH) ppm; <sup>13</sup>C NMR (CDCl<sub>3</sub>):  $\delta$  = 12.9 (CH<sub>3</sub>), 19.1 (CH<sub>2</sub>), 23.9 (CH<sub>2</sub>), 25.1 (CH<sub>2</sub>), 25.5 (2 CH<sub>3</sub>), 26.1 (2 CH<sub>2</sub>), 33.2 (2 CH<sub>2</sub>), 44.5 (CH<sub>2</sub>), 49.5 (CH), 64.3 (C), 121.5 (CH), 122.0 (CH), 123.6 (CH), 125.1 (CH), 126.8 (CH), 130.8 (CH), 138.5 (C), 145.7 (C), 158.5 (C=N), 162.5 (C=O), 166.7 (C=O), 174.2 (C=O) ppm.

*N*<sub>1</sub>-(Benzo[d]thiazol-2-yl)-*N*<sub>4</sub>-(1-(cyclohexylamino)-2-methyl-1-oxobutan-2-yl)-*N*<sub>4</sub>-ethyl fumaramide (5d)

Light yellow solid; m.p: 229-230 °C; yield: 0.43 g (92%); IR (KBr): ( $\nu_{\max}/\text{cm}^{-1}$ ) = 3410, 3207, 1665, 1557, 1432, 1244, 1174; EI-MS:  $m/z$  (%) = 456 ( $M^+$ , 1.5), 330 (16), 306 (26), 231 (60), 225 (28), 182 (22), 148 (100), 29 (18); Anal. calcd. for C<sub>24</sub>H<sub>32</sub>N<sub>4</sub>O<sub>3</sub>S (456.60): C, 63.13; H, 7.06; N, 12.27; Found: C, 63.98; H, 7.54; N, 12.98%; <sup>1</sup>H NMR (CDCl<sub>3</sub>):  $\delta$  = 0.93 (3 H, t, <sup>3</sup>J 7.3 Hz, CH<sub>3</sub>), 1.20-1.98 (10 H, m, 5 CH<sub>2</sub>), 1.24 (3 H, t, <sup>3</sup>J 7.0 Hz, CH<sub>3</sub>), 1.27 (2 H, q, <sup>3</sup>J 7.3 Hz, CH<sub>2</sub>), 1.58 (3 H, s, CH<sub>3</sub>), 3.52 (2 H, q, <sup>3</sup>J 7.0 Hz, CH<sub>2</sub>N), 3.78-3.84 (1 H, m, CH), 6.32 (1 H, d, <sup>3</sup>J 12.1 Hz, CH), 6.68 (1 H, d, <sup>3</sup>J 12.1 Hz, CH), 6.75 (1 H, d, <sup>3</sup>J 7.3 Hz, NH), 7.38 (1 H, t, <sup>3</sup>J 7.5 Hz, CH), 7.48 (1 H, t, <sup>3</sup>J 8.0 Hz, CH), 7.81 (1 H, d, <sup>3</sup>J 8.0 Hz, CH), 7.84 (1 H, d, <sup>3</sup>J 7.5 Hz, CH), 11.96 (1 H, br s, NH) ppm; <sup>13</sup>C NMR (CDCl<sub>3</sub>):  $\delta$  = 10.8 (CH<sub>3</sub>), 17.6 (CH<sub>3</sub>), 24.8 (2 CH<sub>2</sub>), 25.3 (CH<sub>3</sub>), 25.5 (CH<sub>2</sub>), 26.0 (CH<sub>2</sub>), 32.5 (2 CH<sub>2</sub>), 41.7 (CH<sub>2</sub>), 50.1 (CH), 64.6 (C), 119.8 (CH), 121.8 (CH), 124.6 (CH), 125.8 (CH), 126.5 (CH), 131.6 (CH), 138.2 (C), 145.8 (C), 159.1 (C=N), 162.4 (C=O), 166.5 (C=O), 173.2 (C=O) ppm.

*N*<sub>1</sub>-(Benzo[d]thiazol-2-yl)-*N*<sub>4</sub>-benzyl-*N*<sub>4</sub>-(1-(cyclohexylamino)-2-methyl-1-oxobutan-2-yl)fumaramide (5e)

Light yellow solid; m.p: 179-181 °C; yield: 0.47 g (90%); IR (KBr): ( $\nu_{\max}/\text{cm}^{-1}$ ) = 3337, 3118, 1645, 1624, 1540, 1256, 1163; EI-MS:  $m/z$  (%) = 518 ( $M^+$ , 1.3), 392 (23), 368 (25), 287 (31), 231 (29), 182 (11), 148 (100), 91 (61), 29 (8); Anal. calcd. for C<sub>29</sub>H<sub>34</sub>N<sub>4</sub>O<sub>3</sub>S (518.67): C, 67.15; H, 6.61; N, 10.81; Found: C, 67.45; H, 7.01; N, 10.89%; <sup>1</sup>H NMR (CDCl<sub>3</sub>):  $\delta$  = 0.91 (3 H, t, <sup>3</sup>J 7.1 Hz, CH<sub>3</sub>), 1.11-1.93 (10 H, m, 5 CH<sub>2</sub>), 1.46 (3 H, s, CH<sub>3</sub>), 1.77 (2 H, q, <sup>3</sup>J 7.2 Hz, CH<sub>2</sub>), 3.73-3.76 (1 H, m, CH), 4.65 (2 H, s, CH<sub>2</sub>N), 6.33 (1 H, d, <sup>3</sup>J 16.0 Hz, CH), 6.71 (1 H, d, <sup>3</sup>J 16.0 Hz, CH), 6.86 (1 H, br s, NH), 7.21-7.88 (9 H, m, 9 CH), 9.51 (1 H, br s, NH) ppm; <sup>13</sup>C NMR (CDCl<sub>3</sub>):  $\delta$  = 9.9 (CH<sub>3</sub>), 21.2 (CH<sub>3</sub>), 24.8 (2 CH<sub>2</sub>), 25.7 (CH<sub>2</sub>), 27.4 (CH<sub>2</sub>), 33.3 (2 CH<sub>2</sub>), 46.6 (CH<sub>2</sub>N), 50.3 (CH), 72.3 (C), 119.3 (CH), 121.8 (CH), 123.3 (CH), 124.5 (CH), 127.0 (CH), 127.9 (2 CH), 128.5 (2 CH), 130.8 (C), 134.5 (2 CH), 138.4 (C), 149.2 (C), 158.8 (C=N), 162.2 (C=O), 166.3 (C=O), 174.0 (C=O) ppm.

*N*<sub>1</sub>-(Benzo[d]thiazol-2-yl)-*N*<sub>4</sub>-butyl-*N*<sub>4</sub>-(1-(cyclohexylamino)-2-methyl-1-oxobutan-2-yl)fumaramide (5f)

Light yellow solid; m.p: 170-172 °C; yield: 0.39 g (80%); IR (KBr): ( $\nu_{\max}/\text{cm}^{-1}$ ) = 3378, 3185, 1746, 1672, 1590, 1251, 1143; EI-MS:  $m/z$  (%) = 484 ( $M^+$ , 1.5), 358 (18), 333 (27), 253 (38), 231 (51), 182 (23), 148 (100), 57 (21), 29 (10); Anal. calcd. for C<sub>26</sub>H<sub>36</sub>N<sub>4</sub>O<sub>3</sub>S (484.65): C, 64.43; H, 7.49; N, 11.56; Found: C, 63.95; H, 7.85; N, 11.23 %; <sup>1</sup>H NMR (CDCl<sub>3</sub>):  $\delta$  = 0.91 (3 H, t, <sup>3</sup>J 7.1 Hz, CH<sub>3</sub>), 0.94 (3 H, t, <sup>3</sup>J 6.9 Hz, CH<sub>3</sub>), 1.10-1.95 (14 H, m, 7 CH<sub>2</sub>), 1.44 (3 H, s, CH<sub>3</sub>), 1.76 (2 H, q, <sup>3</sup>J 7.2 Hz, CH<sub>2</sub>), 3.60 (2 H, t, <sup>3</sup>J 7.2 Hz, CH<sub>2</sub>N), 3.81-3.84 (1 H, m, CH), 6.48 (2 H, ABq, <sup>3</sup>J 12.1 Hz,  $\Delta\nu$  96.3 Hz, 2 CH), 6.86 (1 H, d, <sup>3</sup>J 7.8 Hz, NH), 7.38 (1 H, t, <sup>3</sup>J 7.3 Hz, CH), 7.46 (1 H, t, <sup>3</sup>J 7.6 Hz, CH), 7.82 (1 H, d, <sup>3</sup>J 7.3 Hz, CH), 7.85 (1 H, d, <sup>3</sup>J 7.6 Hz, CH), 10.93 (1 H, br s, NH) ppm; <sup>13</sup>C NMR (CDCl<sub>3</sub>):  $\delta$  = 9.5 (CH<sub>3</sub>), 13.6 (CH<sub>3</sub>), 20.1 (CH<sub>2</sub>), 24.2 (CH<sub>2</sub>), 25.1 (2 CH<sub>2</sub>), 25.7 (CH<sub>3</sub>), 26.1 (CH<sub>2</sub>), 29.5 (CH<sub>2</sub>), 33.2 (2 CH<sub>2</sub>), 44.5 (CH<sub>2</sub>N), 49.8 (CH), 70.3 (C), 121.4 (CH), 122.2 (CH), 123.5 (CH), 125.6 (CH), 126.9 (CH), 130.7 (CH), 138.5 (C), 146.3 (C), 159.3 (C=N), 163.5 (C=O), 165.7 (C=O), 174.1 (C=O) ppm.

*N*<sub>1</sub>-(Benzothiazol-2-yl)-*N*<sub>4</sub>-(3-(cyclohexylcarbamoyl)pentan-3-yl)-*N*<sub>4</sub>-ethylfumaramide (5g)

Light yellow solid; mp: 160-163 °C; yield: 0.43 g (87%); IR (KBr): ( $\nu_{\max}/\text{cm}^{-1}$ ) = 3380, 3187, 1742, 1674, 1592, 1257, 1148; EI-MS:  $m/z$  (%) = 470 ( $M^+$ , 1.1), 344 (17), 320 (25), 239 (36), 231 (49), 196 (21), 148 (100), 29 (19); Anal. calcd. for  $C_{25}H_{34}N_4O_3S$  (470.63): C, 63.80; H, 7.28; N, 11.90; Found: C, 64.08; H, 8.78; N, 12.28%;  $^1H$  NMR ( $CDCl_3$ ):  $\delta$  = 0.89 (6 H, t,  $^3J$  7.2 Hz, 2  $CH_3$ ), 1.08-1.97 (10 H, m, 5  $CH_2$ ), 1.31 (3 H, t,  $^3J$  6.7 Hz,  $CH_3$ ), 1.77 (2 H, q,  $^3J$  7.3 Hz, 2  $CH_2$ ), 3.50 (2 H, q,  $^3J$  6.7 Hz,  $CH_2N$ ), 3.79-3.81 (1 H, m, CH), 6.18 (1 H, br s, NH), 6.56 (2 H, ABq,  $^3J$  12.5 Hz,  $\Delta\nu$  139.0 Hz, 2 CH), 7.37-7.87 (4 H, m, 4 CH), 11.51 (1 H, br s, NH) ppm;  $^{13}C$  NMR ( $CDCl_3$ ):  $\delta$  = 11.8 (2  $CH_3$ ), 17.6 ( $CH_3$ ), 25.8 (2  $CH_2$ ), 26.1 ( $CH_2$ ), 30.6 (2  $CH_2$ ), 33.5 (2  $CH_2$ ), 40.9 ( $CH_2$ ), 49.3 (CH), 67.6 (C), 120.5 (CH), 122.1 (CH), 124.7 (CH), 124.8 (CH), 126.7 (CH), 131.5 (CH), 138.4 (C), 145.7 (C), 158.6 (C=N), 163.4 (C=O), 166.4 (C=O), 172.4 (C=O) ppm.

*N*<sub>1</sub>-(Benzo[d]thiazol-2-yl)-*N*<sub>4</sub>-benzyl-*N*<sub>4</sub>-(3-(cyclohexylcarbamoyl)pentan-3-yl)fumaramide (5h)

Light yellow solid; m.p: 183-185 °C; yield: 0.48 g (90%); IR (KBr): ( $\nu_{\max}/\text{cm}^{-1}$ ) = 3340, 3125, 1658, 1629, 1540, 1262, 1175; EI-MS:  $m/z$  (%) = 532 ( $M^+$ , 1.5), 406 (25), 382 (22), 301 (20), 231 (28), 196 (12), 148 (100), 91 (58), 29 (15); Anal. calcd. for  $C_{30}H_{36}N_4O_3S$  (532.7): C, 67.64; H, 6.81; N, 10.52; Found: C, 67.04; H, 6.92; N, 10.32 %;  $^1H$  NMR ( $CDCl_3$ ):  $\delta$  = 0.93 (6 H, t,  $^3J$  7.2 Hz, 2 $CH_3$ ), 1.19-2.02 (10 H, m, 5  $CH_2$ ), 1.76 (4 H, t,  $^3J$  7.3 Hz, 2  $CH_2$ ), 3.83-3.86 (1 H, m, CH), 4.78 (2 H, s,  $CH_2N$ ), 6.22 (1 H, d,  $^3J$  16.0 Hz, CH), 6.61 (1 H, d,  $^3J$  16.0 Hz, CH), 6.66 (1 H, br s, NH), 7.36-7.86 (9 H, m, 9 CH), 8.72 (1 H, br s, NH) ppm;  $^{13}C$  NMR ( $CDCl_3$ ):  $\delta$  = 10.4 (2  $CH_3$ ), 24.9 (2  $CH_2$ ), 25.8 (2  $CH_2$ ), 26.0 ( $CH_2$ ), 33.1 (2  $CH_2$ ), 49.3 ( $CH_2N$ ), 50.3 (CH), 74.5 (C), 122.1 (CH), 124.5 (CH), 124.8 (CH), 124.9 (CH), 126.7 (2 CH), 126.9 (CH), 127.5 (C), 127.9 (CH), 129.4 (2 CH), 132.3 (CH), 138.2 (C), 149.1 (C), 158.9 (C=N), 164.2 (C=O), 168.3 (C=O), 174.1 (C=O) ppm.

*N*<sub>1</sub>-(Benzo[d]thiazol-2-yl)-*N*<sub>4</sub>-butyl-*N*<sub>4</sub>-(3-(cyclohexylcarbamoyl)pentan-3-yl) fumaramide (5i)

Cream powder; m.p: 165-167 °C; yield: 0.41 g (83%); IR (KBr): ( $\nu_{\max}/\text{cm}^{-1}$ ) = 3370, 3185, 1740, 1672, 1590, 1253, 1143; EI-MS:  $m/z$  (%) = 498 ( $M^+$ , 1.2), 372 (18), 348 (26), 267 (37), 231 (50), 196 (22), 148 (100), 57 (21), 29 (15); Anal. calcd.

for  $C_{27}H_{38}N_4O_3S$  (498.68): C, 65.03; H, 7.68; N, 11.24; Found: C, 64.54; H, 7.86; N, 11.35 %;  $^1H$  NMR ( $CDCl_3$ ):  $\delta$  = 0.90 (6 H, t,  $^3J$  7.2 Hz, 2  $CH_3$ ), 0.93 (3 H, t,  $^3J$  6.9 Hz,  $CH_3$ ), 1.08-1.97 (14 H, m, 7  $CH_2$ ), 1.75 (4 H, t,  $^3J$  7.2 Hz, 2  $CH_2$ ), 3.50 (2 H, t,  $^3J$  6.7 Hz,  $CH_2N$ ), 3.79-3.81 (1 H, m, CH), 6.18 (1 H, br s, NH), 6.58 (2 H, ABq,  $^3J$  12.5 Hz,  $\Delta\nu$  139.0 Hz, 2 CH), 7.37-7.87 (4 H, m, 4 CH), 11.45 (1 H, br s, NH) ppm;  $^{13}C$  NMR ( $CDCl_3$ ):  $\delta$  = 10.5 (2  $CH_3$ ), 13.5 ( $CH_3$ ), 20.1 ( $CH_2$ ), 24.7 (2  $CH_2$ ), 25.6 ( $CH_2$ ), 27.2 (2  $CH_2$ ), 29.5 ( $CH_2$ ), 33.3 (2  $CH_2$ ), 43.9 ( $CH_2N$ ), 49.5 (CH), 65.6 (C), 121.5 (CH), 122.0 (CH), 123.6 (CH), 125.1 (CH), 126.8 (CH), 130.8 (CH), 138.5 (C), 145.7 (C), 158.5 (C=N), 162.5 (C=O), 166.7 (C=O), 174.2 (C=O) ppm.

*N*<sub>1</sub>-(Benzothiazol-2-yl)-*N*<sub>4</sub>-(1-(cyclohexylcarbamoyl)cyclohexyl)-*N*<sub>4</sub>-ethylfumaramide (5j)

Light yellow solid; m.p: 167-169 °C; yield: 0.41 g (85%); IR (KBr): ( $\nu_{\max}/\text{cm}^{-1}$ ) = 3380, 3173, 1732, 1631, 1542, 1265, 1164; EI-MS:  $m/z$  (%) = 482 ( $M^+$ , 1.8), 356 (15), 332 (24), 251 (30), 231 (58), 208 (18), 148 (100), 83 (17), 29 (16); Anal. calcd. for  $C_{26}H_{34}N_4O_3S$  (482.64): C, 64.70; H, 7.10; N, 11.16; Found: C, 64.93; H, 7.35; N, 11.03%;  $^1H$  NMR ( $CDCl_3$ ):  $\delta$  = 1.12-2.20 (20 H, m, 10  $CH_2$ ), 1.35 (3 H, t,  $^3J$  7.0 Hz,  $CH_3$ ), 3.71 (2 H, q,  $^3J$  7.0 Hz,  $CH_2N$ ), 3.79-3.82 (1 H, m, CH), 6.54 (2 H, ABq,  $^3J$  12.2 Hz,  $\Delta\nu$  108.6 Hz, 2 CH), 7.05 (1 H, d,  $^3J$  8.3 Hz, NH), 7.32-7.90 (4 H, m, 4 CH), 9.89 (1 H, br s, NH) ppm;  $^{13}C$  NMR ( $CDCl_3$ ):  $\delta$  = 16.5 ( $CH_3$ ), 21.6 (2  $CH_2$ ), 24.7 (2  $CH_2$ ), 25.3 ( $CH_2$ ), 26.0 ( $CH_2$ ), 31.2 (2  $CH_2$ ), 33.1 (2  $CH_2$ ), 41.5 ( $CH_2N$ ), 50.2 (CH), 69.5 (C), 121.0 (CH), 122.5 (CH), 123.9 (CH), 125.8 (CH), 127.7 (CH), 131.4 (CH), 134.9 (C), 144.9 (C), 158.9 (C=N), 162.5 (C=O), 166.1 (C=O), 172.6 (C=O) ppm.

*N*<sub>1</sub>-(Benzo[d]thiazol-2-yl)-*N*<sub>4</sub>-benzyl-*N*<sub>4</sub>-(1-(cyclohexylcarbamoyl)cyclohexyl)fumaramide (5k)

Light yellow solid; m.p: 187-189 °C; yield: 0.45 g (82%); IR (KBr): ( $\nu_{\max}/\text{cm}^{-1}$ ) = 3352, 3127, 1655, 1634, 1542, 1258, 1174; EI-MS:  $m/z$  (%) = 544 ( $M^+$ , 1.1), 394 (25), 313 (20), 231 (28), 208 (15), 148 (100), 91 (57); Anal. calcd. for  $C_{31}H_{36}N_4O_3S$  (544.71): C, 68.35; H, 6.66; N, 10.29; Found: C, 68.75; H, 7.11; N, 10.39%;  $^1H$  NMR ( $CDCl_3$ ):  $\delta$  = 1.09-2.35 (20 H, m, 10  $CH_2$ ), 3.74-3.77 (1 H, m, CH), 4.35 (2 H, s,  $CH_2N$ ), 6.25 (1 H, d,  $^3J$  16.0 Hz, CH), 6.53 (1 H, d,  $^3J$  16.0 Hz, CH), 6.85 (1 H, br s, NH), 7.21-7.88 (9 H, m, 9 CH), 9.65 (1 H, br s, NH) ppm;  $^{13}C$  NMR ( $CDCl_3$ ):  $\delta$  = 21.5 (2  $CH_2$ ), 24.6 (2  $CH_2$ ), 25.8 ( $CH_2$ ), 26.2 ( $CH_2$ ), 33.1 (2  $CH_2$ ), 34.2 (2 $CH_2$ ), 47.8 ( $CH_2N$ ), 49.9 (CH), 69.2 (C),

120.1 (CH), 121.8 (CH), 124.2 (CH), 124.6 (CH), 126.7 (2 CH), 126.9 (CH), 127.8 (CH), 129.2 (2 CH), 132.2 (CH), 135.3 (C), 138.4 (C), 149.5 (C), 158.8 (C=N), 162.9 (C=O), 165.6 (C=O), 173.7 (C=O) ppm.

*N1-(Benzo[d]thiazol-2-yl)-N4-butyl-N4-(1-(cyclohexylcarbamoyl)cyclohexyl)fumaramide (5l)*

Cream powder; m.p: 170-172 °C; yield: 0.40 g (78%); IR (KBr): ( $\nu_{\max}/\text{cm}^{-1}$ ) = 3382, 3217, 1782, 1651, 1545, 1258, 1176; EI-MS:  $m/z$  (%) = 510 ( $M^+$ , 1.6), 360 (24), 279 (19), 231 (58), 208 (22), 148 (100), 57 (26); Anal. calcd. for  $C_{28}H_{38}N_4O_3S$  (510.69): C, 65.85; H, 7.50; N, 10.97; Found: C, 66.13; H, 7.78; N, 10.82%;  $^1\text{H NMR}$  ( $\text{CDCl}_3$ ):  $\delta$  = 0.94 (3 H, t,  $^3J$  6.8 Hz,  $\text{CH}_3$ ), 1.11-2.22 (24 H, m, 12  $\text{CH}_2$ ), 3.29 (2 H, t,  $^3J$  7.2 Hz,  $\text{CH}_2\text{N}$ ), 3.65-3.68 (1 H, m, CH), 6.52 (2 H, ABq,  $^3J$  12.1 Hz,  $\Delta\nu$  96.4 Hz, 2 CH), 6.93 (1 H, d,  $^3J$  7.8 Hz, NH), 7.36 (1 H, t,  $^3J$  7.3 Hz, CH), 7.44 (1 H, t,  $^3J$  7.6 Hz, CH), 7.79 (1 H, d,  $^3J$  7.3 Hz, CH), 7.89 (1 H, d,  $^3J$  7.6 Hz, CH), 10.75 (1 H, br s, NH) ppm;  $^{13}\text{C NMR}$  ( $\text{CDCl}_3$ ):  $\delta$  = 12.7 ( $\text{CH}_3$ ), 19.5 ( $\text{CH}_2$ ), 20.9 (2  $\text{CH}_2$ ), 24.7 (2  $\text{CH}_2$ ), 25.0 ( $\text{CH}_2$ ), 25.6 ( $\text{CH}_2$ ), 26.2 ( $\text{CH}_2$ ), 30.3 (2  $\text{CH}_2$ ), 33.2 (2  $\text{CH}_2$ ), 43.8 ( $\text{CH}_2\text{N}$ ), 49.9 (CH), 68.9 (C), 120.3 (CH), 122.2 (CH), 123.8 (CH), 125.7 (CH), 127.8 (CH), 132.8 (CH), 138.6 (C), 148.8 (C), 158.8 (C=N), 163.5 (C=O), 164.7 (C=O), 173.7 (C=O) ppm.

*N1-(Benzo[d]thiazol-2-yl)-N4-(1-(cyclohexylcarbamoyl)cyclopentyl)-N4-ethylfumaramide (5m)*

Cream powder; mp: 160-163 °C; yield: 0.43 g (87%); IR (KBr): ( $\nu_{\max}/\text{cm}^{-1}$ ) = 3371, 3174, 1734, 1634, 1543, 1262, 1167; EI-MS:  $m/z$  (%) = 468 ( $M^+$ , 1.8), 342 (12), 319 (23), 237 (27), 231 (56), 194 (16), 148 (100), 29 (15); Anal. calcd. for  $C_{25}H_{32}N_4O_3S$  (468.61): C, 64.08; H, 6.88; N, 11.96; Found: C, 64.38; H, 7.04; N, 12.08%;  $^1\text{H NMR}$  ( $\text{CDCl}_3$ ):  $\delta$  = 1.23 (3 H, t,  $^3J$  7.0 Hz,  $\text{CH}_3$ ), 1.38 (4 H, t,  $^3J$  9.1 Hz, 2  $\text{CH}_2$ ), 1.41-2.74 (14 H, m, 7  $\text{CH}_2$ ), 3.51 (2 H, q,  $^3J$  7.0 Hz,  $\text{CH}_2\text{N}$ ), 3.78-3.80 (1 H, m, CH), 6.54 (2 H, ABq,  $^3J$  12.2 Hz,  $\Delta\nu$  108.6 Hz, 2 CH), 7.01 (1 H, d,  $^3J$  8.3 Hz, NH), 7.34-7.90 (4 H, m, 4 CH), 11.91 (1 H, br s, NH) ppm;  $^{13}\text{C NMR}$  ( $\text{CDCl}_3$ ):  $\delta$  = 19.2 ( $\text{CH}_3$ ), 25.1 (2  $\text{CH}_2$ ), 25.8 (2  $\text{CH}_2$ ), 26.0 ( $\text{CH}_2$ ), 33.1 (2  $\text{CH}_2$ ), 35.4 (2  $\text{CH}_2$ ), 41.5 ( $\text{CH}_2$ ), 49.3 (CH), 73.7 (C), 121.1 (CH), 122.4 (CH), 123.8 (CH), 125.6 (CH), 127.8 (CH), 130.4 (CH), 132.9 (C), 143.9 (C), 158.9 (C=N), 163.3 (C=O), 164.8 (C=O), 172.2 (C=O) ppm.

*N1-(Benzo[d]thiazol-2-yl)-N4-benzyl-N4-(1-(cyclohexylcarbamoyl)cyclopentyl)fumaramide (5n)*

Cream powder; m.p: 182-184 °C; yield: 0.48 g (90%); IR (KBr): ( $\nu_{\max}/\text{cm}^{-1}$ ) = 3350, 3125, 1653, 1632, 1540, 1256, 1172; EI-MS:  $m/z$  (%) = 530 ( $M^+$ , 1.2), 380 (22), 299 (25), 231 (29), 194 (12), 148 (100), 91 (54); Anal. calcd for  $C_{30}H_{34}N_4O_3S$  (530.68): C, 67.83; H, 6.46; N, 10.56; Found: C, 67.85; H, 6.57; N, 10.73%;  $^1\text{H NMR}$  ( $\text{CDCl}_3$ ):  $\delta$  = 1.19-2.25 (18 H, m, 9  $\text{CH}_2$ ), 3.84-3.87 (1 H, m, CH), 4.67 (2 H, s,  $\text{CH}_2\text{N}$ ), 6.13 (1 H, d,  $^3J$  16.0 Hz, CH), 6.32 (1 H, d,  $^3J$  16.0 Hz, CH), 6.89 (1 H, br s, NH), 7.23-7.89 (9 H, m, 9 CH), 9.15 (1 H, br s, NH) ppm;  $^{13}\text{C NMR}$  ( $\text{CDCl}_3$ ):  $\delta$  = 24.8 (2  $\text{CH}_2$ ), 25.3 (2  $\text{CH}_2$ ), 26.0 ( $\text{CH}_2$ ), 33.1 (2  $\text{CH}_2$ ), 35.4 (2  $\text{CH}_2$ ), 46.6 ( $\text{CH}_2\text{N}$ ), 49.9 (CH), 72.1 (C), 121.2 (CH), 122.8 (CH), 124.4 (CH), 124.8 (CH), 126.6 (2 CH), 126.9 (CH), 127.5 (C), 127.9 (CH), 129.2 (2 CH), 132.2 (CH), 138.1 (C), 148.7 (C), 158.9 (C=N), 162.5 (C=O), 166.4 (C=O), 172.0 (C=O) ppm.

*N1-(Benzo[d]thiazol-2-yl)-N4-butyl-N4-(1-(cyclohexylcarbamoyl)cyclopentyl)fumaramide (5o)*

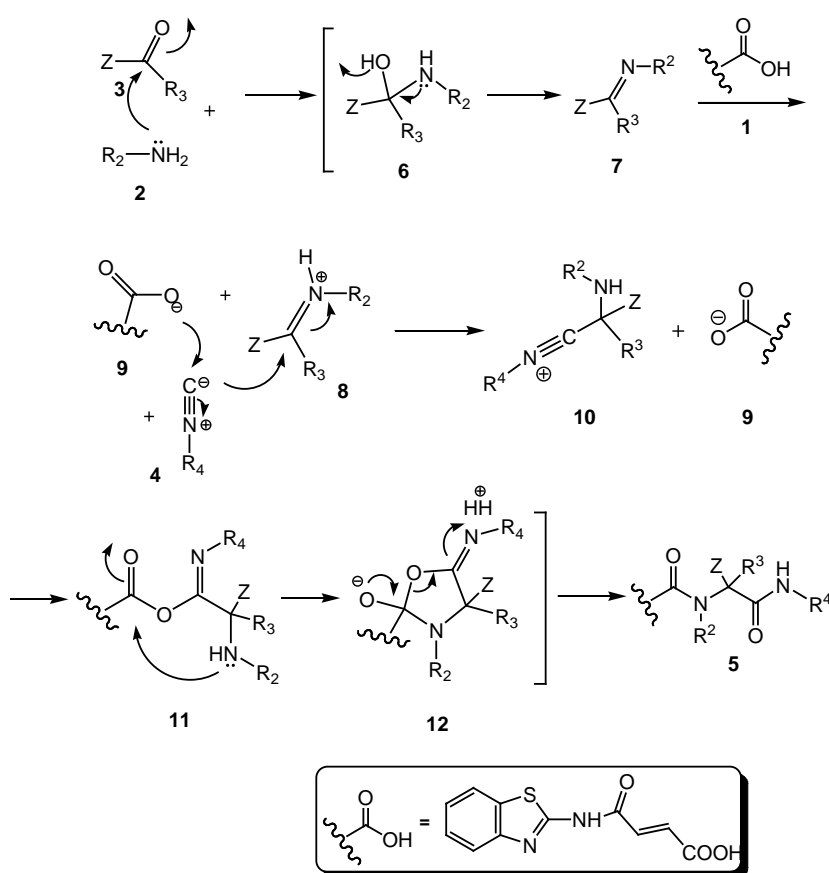
Cream powder; m.p: 158-160 °C; yield: 0.37 g (75%); IR (KBr):( $\nu_{\max}/\text{cm}^{-1}$ ) = 3372, 3215, 1772, 1649, 1540, 1255, 1173; EI-MS:  $m/z$  (%) = 496 ( $M^+$ , 1.5), 346 (24), 265 (18), 231 (58), 194 (21), 148 (100), 57 (25); Anal. calcd. for  $C_{27}H_{36}N_4O_3S$  (496.66): C, 65.29; H, 7.31; N, 11.28; Found: C, 64.93; H, 7.55; N, 11.35%;  $^1\text{H NMR}$  ( $\text{CDCl}_3$ ):  $\delta$  = 0.92 (3 H, t,  $^3J$  6.8 Hz,  $\text{CH}_3$ ), 1.21-2.15 (22 H, m, 11  $\text{CH}_2$ ), 3.35 (2 H, t,  $^3J$  7.2 Hz,  $\text{CH}_2\text{N}$ ), 3.80-3.83 (1 H, m, CH), 6.43 (2 H, ABq,  $^3J$  12.1 Hz,  $\Delta\nu$  96.3 Hz, 2 CH), 6.87 (1 H, d,  $^3J$  7.8 Hz, NH), 7.38 (1 H, t,  $^3J$  7.3 Hz, CH), 7.45 (1 H, t,  $^3J$  7.6 Hz, CH), 7.82 (1 H, d,  $^3J$  7.3 Hz, CH), 7.86 (1 H, d,  $^3J$  7.6 Hz, CH), 10.85 (1 H, br s, NH) ppm;  $^{13}\text{C NMR}$  ( $\text{CDCl}_3$ ):  $\delta$  = 13.8 ( $\text{CH}_3$ ), 19.7 ( $\text{CH}_2$ ), 23.9 ( $\text{CH}_2$ ), 24.7 (2  $\text{CH}_2$ ), 25.3 (2  $\text{CH}_2$ ), 25.9 ( $\text{CH}_2$ ), 33.2 (2  $\text{CH}_2$ ), 35.3 (2  $\text{CH}_2$ ), 43.9 ( $\text{CH}_2\text{N}$ ), 50.1 (CH), 72.4 (C), 121.4 (CH), 122.1 (CH), 123.6 (CH), 125.2 (CH), 126.7 (CH), 131.8 (CH), 138.5 (C), 148.7 (C), 158.7 (C=N), 162.7 (C=O), 165.6 (C=O), 173.2 (C=O) ppm.

## RESULTS AND DISCUSSION

The optimized reactant ratios were found to be 1.0 equiv. benzaldehyde, 1.0 equiv. benzamidine, and 1.0 equiv. malononitrile in the presence of potassium carbonate (20 mol %) in 3 ml of aqueous ethanol (1:1,  $\text{H}_2\text{O}$ -EtOH). The expected 4-amino-2,6-diphenyl-5-pyrimidinecarbonitrile was produced in 90% yield after 5 min at 40 °C (Scheme 1).

Structures of compounds **5a-5o** were characterized by IR,  $^1\text{H-NMR}$  and  $^{13}\text{C-NMR}$  spectral data. The mass spectra of compounds **5a-5o** displayed molecular ion peaks at appropriate  $m/z$  values. The IR and  $^1\text{H NMR}$  spectra of **5a-5o** exhibited three characteristic peaks NH moieties. The  $^1\text{H NMR}$  spectra of **5a-5o** exhibited two doublets with  $^3J = 12-16$  Hz, which confirms the *trans* geometry for the carbon-carbon double bond. The proton decoupled  $^{13}\text{C NMR}$  spectra of **5a-5o** showed four distinct resonances for  $\text{C}=\text{O}$  and  $\text{C}=\text{N}$  groups. For example, the IR spectrum of **5b** indicated two absorption bands ( $\nu_{\text{max}} = 3127, 3347 \text{ cm}^{-1}$ ) for NH stretching frequencies. The  $^1\text{H NMR}$  spectrum of **5b** in  $\text{CDCl}_3$  showed a singlet ( $\delta = 1.56$  ppm) for two identical methyl groups, a singlet ( $\delta = 4.78$  ppm) for methylene protons of the  $\text{ArCH}_2\text{N}$  moiety and two doublets ( $\delta = 6.22, 6.61$  ppm) with  $^3J = 16.0$  Hz for the vinylic CH along with two signals ( $\delta = 6.66, 8.61$  ppm) for NH protons. The CH proton chemical shifts of double bond in some of the products are close together and have created

ABq system. For example the  $^1\text{H NMR}$  spectrum of **5c** in  $\text{CDCl}_3$  showed an ABq ( $\delta = 6.48$  ppm,  $^3J = 12.1$  Hz,  $\Delta\nu = 96.3$  Hz) for the protons of CHs double bond. The protons of phenyl groups for **5b** exhibited certain signals in areas ( $\delta = 7.36-7.86$  ppm). The  $^{13}\text{C-NMR}$  spectrum of **5b** showed 23 signals in agreement with the proposed structure. Partial assignments of aromatic,  $\text{C}=\text{N}$ , carbonyl, and cyclohexyl resonances are given in the experimental section. Although the mechanistic details of the above reaction are unknown, a plausible pathway may be advanced to rationalize product formation (Scheme 2). Presumably, the imine **6** produced from the reaction between the amine **2** and the oxo compound **3** is protonated by acid **1** to generate intermediate **8**. This intermediate is attacked by the isocyanide **4** to afford **10**, which is attacked by the anion **9** to produce **11**. The latter would then undergo acyl transfer reaction to form dioxolane derivative **12**, which is converted to  $\alpha$ -benzothiazoleamidodipeptides **5** by ring opening.



Scheme 2. Proposed mechanism for synthesis of **5**

## CONCLUSION

In conclusion, we report a simple and highly efficient one-pot approach to the synthesis of complex  $\alpha$ -benzothiazoleamidodipeptides from simple and readily available inputs without any activation or modifications. The work-up procedure is fairly simple and the products do not require further purification. The advantage of the present procedure is that the reaction is performed without solvent by simple mixing of the starting materials.

**Acknowledgements:** This research is supported by the Islamic Azad University, Firoozkooh Branch.

## REFERENCES

1. D. J. Adams, P. J. Dyson, S. J. Tavener, Chemistry in alternative reaction media, Wiley-VCH Verlag GmbH & Co. Weinheim., 2004, p.1.
2. J. Zhu, H. Bienayme, Multicomponent reactions, Wiley-VCH: Weinheim, 2005, p. 169.
3. H. Bienayme, C. Hulme, G. Oddon, P. Schmitt, *Chem. Eur. J.*, **6**, 3321 (2000).
4. A. Domling, I. Ugi, *Angew. Chem. Int. Ed.*, **39**, 3168 (2000).
5. J. Zhu, *Eur. J. Org. Chem.*, **7**, 1133 (2003).
6. R. V. Orru, M. de Greef, *Synthesis QSAR Comb.Sci.*, **25**, 432 (2006).
7. D. J. Ramon, M. Yus, *Angew. Chem. Int. Ed.*, **44**, 1602 (2005).
8. L. Weber, M. Illgen, M. Almstetter, *Synlett.*, 366 (1999).
9. I. Ugi, *Angew. Chem. Int. Ed.*, **1**, 8 (1962).
10. A. Dömling, *Chem. Rev.*, **106**, 17 (2006).
11. S. Marcaccini, T. Torroba, *Nat. Protoc.*, **2**, 632 (2007).
12. C. Valente, R. C. Guedes, R. Moreira, J. Iley, I. Gutc, P. J. Rosenthal, *Bioorg. Med. Chem. Lett.*, **16**, 4115 (2006).
13. S. Hanessian, K. Ersmark, X. Wang, J. R. Del Valle, N. Blomberg, Y. Xuec, O. Fjellstrom, *Bioorg. Med. Chem. Lett.*, **17**, 3480 (2007).
14. P. F. van Swieten, E. Samuel, R.O. Hernández, M. A. Leeuwenburgh, G. A. van der Marel, B.M. Kessler, H. S. Overkleefta, A.F. Kisselev, *Bioorg. Med. Chem. Lett.*, **17**, 3402 (2007).
15. R. M. Freidinger, *J med Chem.*, **46**, 5553 (2003).
16. V. Huruby, *Acc Chem Res.*, **34**, 389 (2001).
17. R.S. Roy, P.J. Balarm, *Pept Res.*, **63**, 279 (2004).
18. R.W. Armstrong, A. P. Combs, P. A. Tempest, S. D. Brown, T. A. Keating, *Acc. Chem. Res.*, **29**, 123 (1996).
19. S. Berlozecki, W. Szymanski, R. Ostaszewski, *Tetrahedron*, **64**, 9780 (2008).
20. P. R. Krishna, G. Dayaker, P.V. N. Reddy, *Tetrahedron Lett.*, **47**, 5977 (2006).
21. C. Lamberth, A. Jeanguenat, F. Cederbaum, A. De mesmaeker, M. Zeller, H. J. Kempfc, R. Zeunc, *Bioorg. Med. Chem.*, **16**, 1531(2008).
22. [22] I. Yavari, L. Moradi, F. Nasiri, H. Djahaniani, *Mendeleev Commun.*, **15**, 156 (2005).
23. [23] I. Yavari, F. Nasiri, H. Djahaniani, *Mol Divers.*, **8**, 431 (2004).
24. [24] I. Yavari, H. Djahaniani, F. Nasiri, *Monatsh. Chem.* **134**, 543 (2004).

## ЕДНОСТАДИЙНА СИНТЕЗА НА ВИСОКО-ФУНКЦИОНАЛНИ БЕНЗОТИАЗОЛ-ДИАМИДИ БЕЗ РАЗТВОРИТЕЛ ЧРЕЗ ЧЕТИРИ-КОМПОНЕНТНА РЕАКЦИЯ НА UGI

Ф. Шейхолеслами-Фарахани<sup>\*1</sup>, А.С. Шахвеляти<sup>2</sup>

<sup>1</sup>Департамент по химия, Клон Фирузку, Ислямски университет „Азад“, Фирузку, Иран

<sup>2</sup>Департамент по химия, Ислямски университет „Азад“, Клон Шахр-е Рей, Иран

Постъпила на 17 септември, 2014 г.; коригирана на 2 януари, 2015 г.

(Резюме)

4-бензотиазол-2-ил amino-4-оксо-2-бутенова киселина, получена чрез реакция на 2-аминобензотиазол и малеинов анхидрид е използвана като киселинен компонент в реакцията на Ugi в условия без разтворител за получаването на ненаситени  $\alpha$ -бензотиазол-амидодипептиди с добър добив.

## QSAR study, synthesis and anti-depressant studies of some novel Schiff base derivatives of benzothiazepine

N. S. Dighe<sup>\*1</sup>, P. S. Shinde<sup>1</sup>, S. B. Vikhe<sup>1</sup>, S. B. Dighe<sup>2</sup>, D. S. Musmade<sup>3</sup>

<sup>1</sup>Department of Pharmaceutical Chemistry, Pravara Rural College of Pharmacy, Loni, MS, India-413736.

<sup>2</sup>Department of Pharmacology, Pravara Rural College of Pharmacy, Loni, MS, India-413736.

<sup>3</sup>Department of Pharmaceutical Chemistry, Sanjivani college of pharmaceutical education and research, Kopargaon, M S, India

Received January 16, 2015, Revised April 29, 2015

This study was designed to synthesize, characterize and evaluate the pharmacological activity of schiff base derivatives of benzothiazepine. Purity of the synthesized compounds was ascertained by TLC and melting points were determined by an open capillary tube method. The compounds were characterized by IR, NMR and mass spectroscopic methods. Antidepressant activity of all synthesized compounds was evaluated by despair swim test using *Sprague Dawley Rats*. Standard drug imipramine was used as the control. In the despair swim test, all synthesized derivatives showed antidepressant activity. QSAR for the title compounds was performed using TSAR 3.3 software and results were found satisfactory. These results are useful for the future investigations.

**Keywords:** Antidepressant activity, Despair swim test, QSAR, *Sprague Dawley Rat*.

### INTRODUCTION

As estimated by WHO, depression shall become the second largest illness in terms of morbidity by another decade in the world; already one out of every five women, and every twelve men have depression. Not only adults, but two percent of school children, and five percent of teenagers also suffer from depression, and these mostly go unidentified. Depression has been the commonest reason why people come to a psychiatrist, although the common man's perception is that all psychological problems are depression [1-2]. Current treatments for depression either fail to produce recovery or induce unwanted side effects. So there is still a large unmet clinical need [3-5]. The main aims in the development of new antidepressants are greater efficacy, absence of side effects, lack of toxicity in over dose and earlier onset of action [7]. Elaborate research work has been carried out in the past and continues in the present to synthesize new compounds to meet depression. The forced swim test (behavioral despair test) in the rat is widely used for the initial screening of antidepressants. These tests have good predictive validity and allow rapid and economical detection of substances with potential antidepressant-like activity. The majority of clinically used antidepressants decrease the duration of immobility [4].

### EXPERIMENTAL

#### *Materials & Methods*

Melting points were determined by an open capillary method and are uncorrected. The <sup>1</sup>H-NMR spectra were recorded on the sophisticated multinuclear FT-NMR spectrometer model Advance-II (Bruker) using dimethylsulfoxide-*d*<sub>6</sub> as solvent and tetramethylsilane as internal standard. IR spectra were recorded on Jasco FT-IR-spectrophotometer using KBr disc method. Antidepressant activity of all synthesized compounds was evaluated by despair swim test using *Sprague Dawley Rats*. Pharmacological screening values therein were converted into log (% Inh) and were used for multiple correlation analysis with descriptors generated using TSAR 3.3 software.

#### *QSAR Methodology*

All molecules were drawn in Chem draw ultra 8.0 module in Chemoffice 2004 software and imported into TSAR software. Charges were derived using Charge 2-Derive charges option and optimized by using Cosmic-optimize 3 D option in the structure menu of the project table. Substituents were defined and descriptors were calculated for the whole molecule as well as for the substituents. Several equations were generated correlating both log (% Inh) with physicochemical parameters (descriptors) by multiple linear regression analysis

\* To whom all correspondence should be sent:  
E-mail: nachiket1111@rediffmail.com

(MLR) method. Data was standardized by range and one method was used for cross validation. Models were excluded if correlation was exceeding 0.9 for more rigorous analysis. Correlation matrix was generated to find any intercorrelation between the descriptors. Intercorrelation between the descriptors in the final equation was less than 0.2 [7].

**Pharmacology:** Rat-Sprague Dawley (220-255 gm), 8-12 weeks old, were obtained from the National Institute of Bioscience, Pune. They were housed in autoclaved polypropylene cages in groups of 2-3 rats per cage and kept in a room maintained at 19 to 25 °C and humidity 45 to 65 % with a 12-h light/dark cycle. They were allowed to acclimatize for four days before the experiments and were given free access to a standard sterilized extruded rodent diet provided *ad libitum*. Reverse osmosis water treated with UV light was provided *ad libitum* in autoclaved polypropylene bottles and autoclaved corn cob was used as bedding material. All procedures of the present study were in accordance with the standard operating procedures of the Prado Pvt. Ltd. guidelines provided by the Committee for the Purpose of Control and Supervision of Experiments on Animals (CPCSEA) as published in The Gazette of India, December 15, 1998. Prior approval of the Institutional Animal Ethics Committee (IAEC) was obtained before initiation of the study (IAEC-13-004)

**Antidepressant Activity (Forced Swim Test in Rat):**

Behavioral despair or forced swim test (FST) was proposed as a model to test antidepressant activity by Porsolt et al. [8]. It was suggested that mice or rats when forced to swim in a restricted space from where they cannot escape are induced to a characteristic behavior of immobility. This behavior reflects a state of despair which can be reduced by several agents which are therapeutically effective in human depression. The behavioral despair test is employed to assess the antidepressant activity of synthesized derivatives. *Sprague-Dawley rats* of 200-270 g in a group of two each were used and on the first day of the experiment (pretest session), rats were individually placed in a cylindrical recipient (plexiglass cylinder) of dimensions (diameter, 10 cm; height, 25 cm) containing 10 cm of water at 25°C. The animals were left to swim for 6 min before being removed, dried and returned to their cages. The procedure was repeated 24 h later, in a 5 min swim session (test session). The synthesized compounds (25 mg kg<sup>-1</sup>), and imipramine, as a reference antidepressant drug (25 mg kg<sup>-1</sup>) were suspended in a 0.5 % aqueous solution of Na CMC (carboxy

methyl cellulose). The drugs were given by gavage in a standard volume of 10 ml/kg body weight, 1 h prior to the test. Control animals received 0.5 % aqueous solution of Na CMC. This test was performed after 1 h, 5 h and 24 h of dose administration. For individual animals video recording was made. Then, the rats were dropped individually into the plexiglass cylinder and left in the water for 6 min. After the first 2 min of the initial vigorous struggling, the animals were immobile. Immobility time is the time spent by rat floating in water without struggling, making only those movements necessary to keep the head above the water. The total duration of immobility was recorded during the last 5 min of the 6 min test session.

**Step I: Synthesis of ethyl-4-methyl-2-substituted -2,5-dihydro-1,5-benzothiazepine-3 carboxylate.**

An equimolar mixture of 2-aminothiophenol, substituted benzaldehydes and ethyl acetoacetate, in 20 ml ethyl alcohol was refluxed for 50 min at 70-90°C. Completion of the reaction was monitored by TLC [eluent: ethyl acetate/petr. ether (3:7)]. After completion of the reaction, the reaction mixture was poured onto crushed ice; the solid crude product was washed with water. The crude product was purified by recrystallisation with hot ethanol. (I<sub>1</sub>)

**Step II: Synthesis of 4-methyl-2-substituted -2,5-dihydro-1,5-benzothiazepine-3-carbohydrazide**

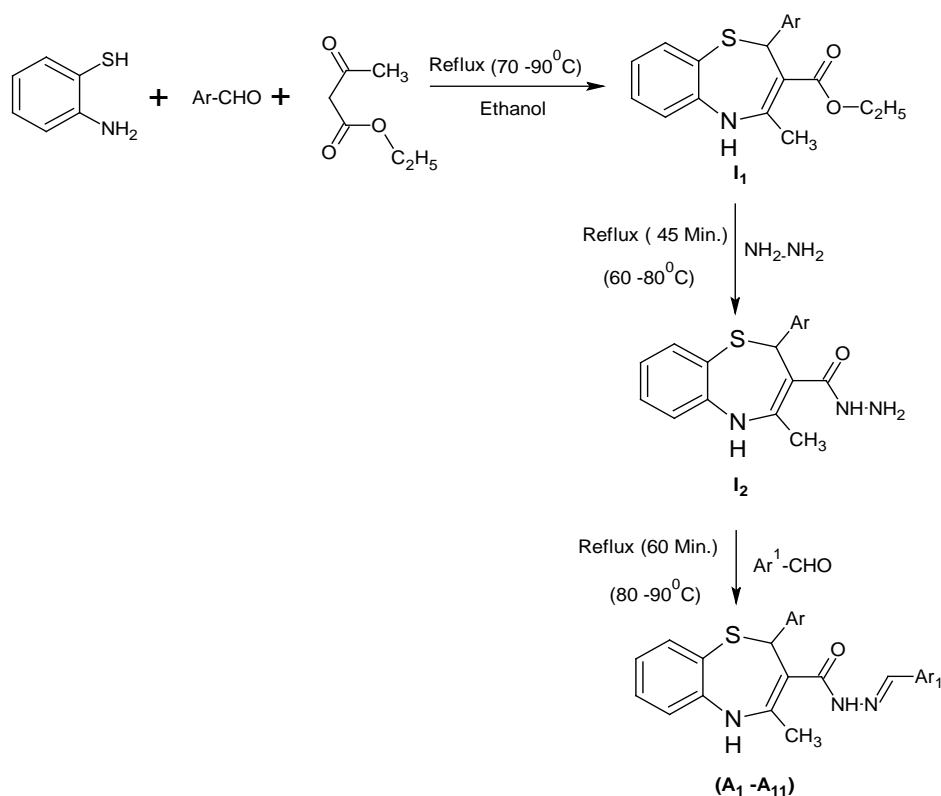
A mixture of 0.01 mole of I<sub>1</sub> and 0.01 mole of hydrazine was added in 05 ml ethyl alcohol. The reaction mixture was refluxed at 60-80 °C for 45 min. The reaction mixture was cooled to room temperature, the residue was poured onto crushed ice and the solid separated was filtered and dried through pump to afford the corresponding 4-methyl-2-substituted-2,5-dihydro-1,5-benzothiazepine-3-carbohydrazide. (I<sub>2</sub>)

**Step III: Synthesis of 4-methyl-2-phenyl-N'-[(E)-phenylmethylidene]-2,5-dihydro-1,5-benzothiazepine-3-carbohydrazide**

A mixture of 0.01 mole of I<sub>2</sub> and 0.01 mole of substituted benzaldehydes was added in 05 ml ethyl alcohol. The reaction mixture was refluxed at 80-90 °C for 60 min. The reaction mixture was cooled to room temperature, the residue was poured onto crushed ice and the solid separated was filtered and dried through pump to afford the corresponding schiff base derivatives of 1,5-benzothiazepine. (A<sub>1</sub>-A<sub>11</sub>).



Scheme



Comp Code	Ar	Ar'	Comp Code	Ar	Ar'
A <sub>1</sub>			A <sub>7</sub>		
A <sub>2</sub>			A <sub>8</sub>		
A <sub>3</sub>			A <sub>9</sub>		
A <sub>4</sub>			A <sub>10</sub>		
A <sub>5</sub>			A <sub>11</sub>		
A <sub>6</sub>					

*Spectral data*

**A<sub>1</sub>:** IR (KBr) cm<sup>-1</sup>: 3213.45 (-NH str.), 3010.23 (Ar-CH str.), 1682.11 (-C=O str.), 1525.32 (-C=N str), 3565.23 (-OH str.), 1245.36 (-C-N str). <sup>1</sup>H NMR: 4.50 (1H thiazipine), 8.54 (1H-N=CH), 9.61 (1H -NH sec. amine), 8.54 (1H-NH sec. amide), 9.43 (1H-OH), 6.8-7.2 (12H phenyl), 3.66 (3H-CH<sub>3</sub>-C-N), 2.26 (3H CH<sub>3</sub>). m/e(100%): 367.14

**A<sub>2</sub>:** IR (KBr) cm<sup>-1</sup>: 3010.23 (Ar-CH str.), 1682.11 (-C=O str.), 3213.45 (-NH str.), 1525.32 (-C=N str), 1245.36 (-C-N str), 3600.24 (-OH str.), 1260.02 (-C-O str). <sup>1</sup>H NMR: 4.50 (1H thiazipine), 8.54 (1H-N=CH), 9.61 (1H-NH sec. amine), 8.54 (1H-NH sec. amide), 9.43 (1H-OH), 6.8-7.2 (12H phenyl), 2.26 (3H CH<sub>3</sub>). m/e(100%): 353.13

**A<sub>3</sub>:** IR (KBr) cm<sup>-1</sup>: 3310.23 (-CH=CH str.), 3213.45 (-NH str.), 3010.23 (Ar-CH str.), 1682.11 (-C=O str.), 1525.32 (-C=N str), 3650.12 (-OH str.), 1245.36 (-C-N str). <sup>1</sup>H NMR: 6.32-6.53 (-2H -CH=CH), 3.90 (1H thiazipine), 8.54 (1H-N=CH), 9.61 (1H-NH sec. amine), 8.54 (1H-NH sec. amide), 11.43 (1H-OH), 6.8-7.2 (13H phenyl), 2.26 (3H CH<sub>3</sub>). m/e(100%): 366.15

**A<sub>4</sub>:** IR (KBr) cm<sup>-1</sup>: 3213.45 (-NH str.), 3010.23 (Ar-CH str.), 1682.11 (-C=O str.), 1525.32 (-C=N str), 1245.36 (-C-N str), 940.23 (-C-Cl str.), 3620.32 (-OH str.). <sup>1</sup>H NMR: 4.50 (1H thiazipine), 8.54 (1H-N=CH), 9.61 (1H -NH sec. amine), 8.54 (1H -NH sec. amide), 9.43 (1H-OH), 6.8-7.2 (12H phenyl), 3.66 (3H-CH<sub>3</sub>, -C-N), 2.26 (3H CH<sub>3</sub>). m/e(100%): 371.14

**A<sub>5</sub>:** IR (KBr) cm<sup>-1</sup>: 3010.23 (Ar-CH str.), 1682.11 (-C=O str.), 1525.32 (-C=N str), 1245.36 (-C-N str), 930.21 (-C-Cl str.), 1260.02 (-C-O str), <sup>1</sup>H NMR: 4.50 (1H thiazipine), 8.54 (1H-N=CH), 9.61 (1H-NH sec. amine), 8.54 (1H-NH sec. amide), 6.8-7.2 (12H phenyl), 2.26 (3H CH<sub>3</sub>). m/e(100%): 357.12

**A<sub>6</sub>:** IR (KBr) cm<sup>-1</sup>: 3213.45 (-NH str.), 3010.23 (Ar-CH str.), 1682.11 (-C=O str), 1525.32 (-C=N str), 1245.36 (-C-N str), 1260.02 (-C-O str), 1255.36 (-N-O str). <sup>1</sup>H NMR: 4.50 (1H thiazipine), 8.54 (1H-N=CH), 9.61 (1H-NH sec. amine), 8.54 (1H-NH sec. amide), 6.8-7.2 (12H phenyl), 3.82 (3H-CH<sub>3</sub>, -C-O), 2.26 (3H CH<sub>3</sub>). m/e(100%): 355.13

**A<sub>7</sub>:** IR (KBr) cm<sup>-1</sup>: 3213.45 (-NH str.), 3010.23 (Ar-CH str.), 1682.11 (-C=O str.), 1525.32 (-C=N str), 1245.36 (-C-N str), 940.21 (C-Cl str.), 3600.12 (-OH str.). <sup>1</sup>H NMR: 4.50 (1H thiazipine), 8.54 (1H-N=CH), 9.61 (1H-NH sec. amine), 8.54 (1H-NH sec. amide), 9.43 (1H-OH), 6.8-7.2 (12H phenyl), 3.86 (3H-CH<sub>3</sub>, -C-O), 2.26 (3H CH<sub>3</sub>).m/e(100%): 331.11

**A<sub>8</sub>:** IR (KBr) cm<sup>-1</sup>: 3010.23 (Ar-CH str.), 1682.11 (-C=O str.), 1255.36 (-N-O str.), 1525.32 (-C=N

str), 1245.36 (-C-N str), 3616.11 (-OH str.). <sup>1</sup>H NMR: 4.50 (1H thiazipine), 8.54 (1H-N=CH), 9.61 (1H-NH sec. amine), 8.54 (1H-NH sec. amide), 9.43 (1H-OH), 6.8-7.2 (12H phenyl), 2.26 (3H CH<sub>3</sub>).m/e(100%): 317.09

**A<sub>9</sub>:** IR (KBr) cm<sup>-1</sup>: 3213.45 (-NH str.), 3010.23 (Ar-CH str.), 1682.11 (-C=O str.), 1525.32 (-C=N str), 1245.36 (-C-N str), 3616.11 (-OH str.).<sup>1</sup>H NMR: 4.50 (1H thiazipine), 8.54 (1H-N=CH), 9.61 (1H-NH sec. amine), 8.54 (1H -NH sec. amide), 9.43 (1H-OH), 6.8-7.2 (12H phenyl), 2.26 (3H CH<sub>3</sub>). m/e(100%): 315.10

**A<sub>10</sub>:** IR (KBr) cm<sup>-1</sup>: 3010.23 (Ar-CH str.), 1689.78 (-C=O str), 1525.32 (-C=N str), 1245.36 (-C-N str), 1255.36 (-N-O str.), 940.21 (-C-Cl str.). <sup>1</sup>H NMR: 4.50 (1H thiazipine), 8.54 (1H -N=CH), 9.61 (1H-NH sec. amine), 8.54 (1H-NH sec. amide), 6.8-7.2 (12H phenyl), 2.26 (3H CH<sub>3</sub>).m/e(100%): 354.14

**A<sub>11</sub>:** IR (KBr) cm<sup>-1</sup>: 3208.12 (-NH<sub>2</sub> str.), 3010.23 (Ar-CH str.), 1689.78 (-C=O str), 1525.32 (-C=N str), 1245.36 (-C-N str), 3600.12 (-OH str.). <sup>1</sup>H NMR: 4.50 (1H thiazipine), 8.54 (1H-N=CH), 9.61 (1H-NH sec. amine), 8.54 (1H-NH sec. amide), 9.43 (1H-OH), 6.8-7.2 (12H phenyl), 2.26 (3H CH<sub>3</sub>). m/e(100%): 369.15.

Statistical evaluation of the equations is in the accepted range. The correlation coefficient is high with a low standard error. The residual value and residual variance for each series is also low indicating good predictive power of the models. From equation 1 it is observed that two electronic parameters: dipole moment Z component (whole molecule) and VAMP HOMO (whole molecule) negatively contribute (-0.218 and -1.576) for the activity, so electron withdrawing groups may enhance the activity (% Inh).

**RESULTS AND DISCUSSION**

The structures, yields and melting points of the compounds are given in Table 1. Melting points of the synthesized compounds were sharp indicating that the compounds were pure; the yield values of the compounds also suggested that the chemical methods were reliable for the synthesis of the compound. All compounds showed characteristic peaks in the IR and NMR spectroscopic studies.

*Antidepressant Activity*

All synthesized compounds were subjected to antidepressant activity study on Sprague-Dawley rats by despair swim test. Imipramine was used as standard control. The results showed that all compounds displayed antidepressant activity. Among them two compounds (A<sub>3</sub> and A<sub>6</sub>) showed significant antidepressant activity compared with the standard control imipramine (Table 2).

**Table 1.** Analytical and physicochemical data of the synthesized compounds (A<sub>1</sub>-A<sub>11</sub>).

Comp. Code	Mol. Formula	Mol. Wt.	M.P. ° C	Yield %	Elemental analyses		
					Calcd (found)		
					C	H	N
A <sub>1</sub>	C <sub>26</sub> H <sub>26</sub> N <sub>4</sub> O <sub>2</sub> S	458.18	195-200	72	68.10 (67.80)	5.71 (5.50)	10.48 (10.10)
A <sub>2</sub>	C <sub>24</sub> H <sub>21</sub> N <sub>3</sub> O <sub>3</sub> S	431.13	235-238	75	66.80 (66.50)	4.91 (4.51)	9.74 (9.61)
A <sub>3</sub>	C <sub>26</sub> H <sub>23</sub> N <sub>3</sub> O <sub>2</sub> S	441.54	205-207	67	70.72 (70.65)	5.25 (5.10)	9.52 (9.23)
A <sub>4</sub>	C <sub>24</sub> H <sub>20</sub> ClN <sub>3</sub> O <sub>2</sub> S	449.95	230-232	71	64.06 (65.80)	4.48 (4.20)	9.34 (9.05)
A <sub>5</sub>	C <sub>25</sub> H <sub>22</sub> ClN <sub>3</sub> O <sub>2</sub> S	463.11	202-205	78	64.72 (64.60)	4.78 (4.40)	9.06 (8.95)
A <sub>6</sub>	C <sub>25</sub> H <sub>22</sub> N <sub>4</sub> O <sub>4</sub> S	474.14	265-267	69	63.28 (63.01)	4.67 (4.25)	11.81 (11.20)
A <sub>7</sub>	C <sub>24</sub> H <sub>20</sub> ClN <sub>3</sub> O <sub>2</sub> S	449.10	230-233	72	64.06 (65.85)	4.48 (4.10)	9.34 (9.01)
A <sub>8</sub>	C <sub>24</sub> H <sub>20</sub> N <sub>4</sub> O <sub>4</sub> S	460.50	234-238	65	62.60 (62.10)	4.38 (4.12)	12.17 (12.01)
A <sub>9</sub>	C <sub>24</sub> H <sub>20</sub> N <sub>4</sub> O <sub>4</sub> S	460.50	210-215	65	62.60 (62.10)	4.38 (4.31)	12.17 (11.95)
A <sub>10</sub>	C <sub>24</sub> H <sub>19</sub> ClN <sub>4</sub> O <sub>3</sub> S	478.09	185-190	71	60.19 (60.02)	4.00 (3.75)	11.70 (11.20)
A <sub>11</sub>	C <sub>24</sub> H <sub>20</sub> N <sub>4</sub> O <sub>4</sub> S	460.12	240-242	62	62.60 (62.10)	4.38 (4.10)	12.17 (11.95)

**Table 2.** Antidepressant activity of the compounds in despair swim test on rats.

Compound code	Immobility time			% Immobility		
	1 h	5 h	24 h	1 h	5 h	24 h
A <sub>1</sub>	141	148.5	157.5	81.97	81.36	80.76
A <sub>2</sub>	148.5	153.5	156	86.33	84.10	80.00
A <sub>3</sub>	143.5	149	153.5	83.43	81.64	78.71
A <sub>4</sub>	150	156	158	87.20	85.47	81.02
A <sub>5</sub>	153.5	157.5	163.5	89.24	86.30	83.84
A <sub>6</sub>	140	143	145	81.39	78.35	74.35
A <sub>7</sub>	143.5	146.5	157.5	83.43	80.27	80.76
A <sub>8</sub>	140	150	159	81.39	82.19	81.58
A <sub>9</sub>	153	161	160	88.95	88.21	82.05
A <sub>10</sub>	146	153.5	153.5	84.88	84.10	78.71
A <sub>11</sub>	158.5	162.5	162.5	92.15	89.40	83.33
Control	172	182.5	195	100	100	100
Imipramine (std.)	136.5	150.5	154.5	79.41	82.49	79.26

**Table 3.** Equations generated between log (% Inh) and descriptors

Sr. No.	Equation	N	S	R	r <sup>2</sup>	r <sup>2</sup> <sub>cv</sub>	F
series (A <sub>1</sub> -A <sub>9</sub> and B <sub>1</sub> -B <sub>9</sub> )	Y = - 0.218*X <sub>3</sub> - 1.576 X <sub>2</sub> - 13.218	11	0.364	0.835	0.697	0.487	13.816

where Y = log (% Inh) ; X<sub>1</sub>: ClogP; X<sub>2</sub> = VAMP HOMO (whole molecule); X<sub>3</sub> = dipole moment Z component (whole molecule); X<sub>4</sub> = inertia moment 2 length (whole molecule)

Significance of the terms -N= No. of molecules; s = standard error --- less is better; r = correlation coefficient – higher is better > 0.7 ; r<sup>2</sup><sub>cv</sub> = cross validated r<sup>2</sup> - higher is better > 0.5, F value = higher is better; observed and predicted data and graphs are presented in Table 4 and Graph I for the series

**Table 4.** Observed and predicted log (% Inh) value data for 11 compounds

Comp. No.	Observed Value	Predicted Value	Residual Value	Residual Variance
A <sub>1</sub>	1.842983	1.83868347	-0.0043	0.0057
A <sub>2</sub>	1.821448	1.825048019	0.0036	0.0078
A <sub>3</sub>	1.828724	1.819724327	-0.009	0.0049
A <sub>4</sub>	1.722634	1.718733923	-0.0039	0.0198
A <sub>5</sub>	1.835881	1.840780732	0.0049	0.0073
A <sub>6</sub>	1.828724	1.836424327	0.0077	0.0044
A <sub>7</sub>	1.821448	1.807048019	-0.0144	0.0347
A <sub>8</sub>	1.835881	1.829880732	-0.006	0.0184
A <sub>9</sub>	1.828724	1.830024327	0.0013	0.0092
A <sub>10</sub>	1.828724	1.836424327	0.0077	0.0044
A <sub>11</sub>	1.828724	1.830024327	0.0013	0.0092

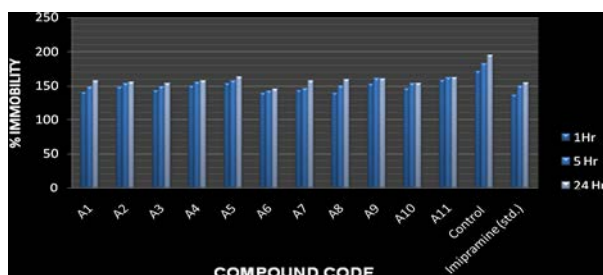


**Fig.1.** Antidepressant effects of schiff base derivatives of benzothiazepine compared with the control group, imipramine used as standard compound.



**Fig. 2.** Antidepressant activity (Forced Swim Test in Rat) of the synthesized compounds

### CONCLUSION

We investigated the importance of functional group substitutions in the structural framework of the compounds for their antidepressant activity. All compounds showed significant antidepressant activity at a dose of 25 mg/kg. The compounds A<sub>3</sub>

and A<sub>6</sub> showed better activity. Finally, the encouraging result of the antidepressant activity displayed by these compounds may be of interest for further structural modifications to the lead compound and for next level studies in the hope of finding a new potent antidepressant prescription.

### REFERENCES

- 1.R.C Kessler, K.A McGonagle, Zhao S., et al., *Arch. Gen. Psychiatry*, **51**, 8-19 (2003)
- 2.Robins L., Regier D., *Psychiatric Disorders in America*, New York: Free Press, 2004.
- 3.B. Petit – Demouliere, F. Chenu, M. Bourin. Forced swimming test in mice: A review of antidepressant activity. *Psychopharmacology*, **177**, 245-255 (2005). <http://dx.doi.org/10.1007/s00213-004-2048-7>
- 4.V. Castagne, P. Moser, S. Roux, R. D Porsolt. Rodent models of depression: Forced swim and tail suspension behavioral despair tests in rats and mice. *Current Protocols in Pharmacology* 2010; **49**: 5.8.1-5.8.14.
- 5.T.C. Baghai, Volz HP, H J. Moller, *World J. Biol. Psychiatry*, **7**, 198 (2006). <http://dx.doi.org/10.1080/15622970601003973>
- 6.K.Mogilaiah, K.Vidya, T. Kumara, *Ind. J. Chem.*, **48B**, 599 (2009).
- 7.R. D. Porsolt,, N Blavet, M Jalfre, *Eur. J. Pharmacol.*, **47**, 379 (1978).
- 8.R. D. Porsolt, A. Bertin, M Jalfre, *Arch. Int. Pharmacodyn.*, **229**, 327 (1977).

## QSAR-ИЗСЛЕДВАНЕ, СИНТЕЗА И АНТИ-ДЕПРЕСАНТНО ИЗСЛЕДВАНЕ НА НЯКОИ НОВИ ПРОИЗВОДНИ НА SCHIFF-ОВИ БАЗИ С БЕНЗОТИАЗЕПИН

Н. С. Дигхе<sup>\*1</sup>, П. С. Шинде<sup>1</sup>, С. Б. Викхе<sup>1</sup>, С. Б. Дикхе<sup>2</sup>, Д. С. Мусмаде<sup>3</sup>

<sup>1</sup> *Департамент по фармацевтична химия, Селскостопански фармацевтичен колеж  
„Правара“, Лони, Индия*

<sup>2</sup> *Департамент по фармакология, Селскостопански фармацевтичен колеж „Правара“,  
Лони, Индия*

<sup>3</sup> *Департамент по фармацевтична химия, Колеж по фармацевтично обучение и  
изследвания, Копаргаон, Индия*

Постъпила на 16 януари, 2015 г.; коригирана на 29 април, 2015 г.

(Резюме)

В тази работа се съобщава за синтезирането, охарактеризирането и оценяването на фармакологичната активност на някои нови производни на Schiff-ови бази с бензотиазепин. Чистотата на синтезираните съединения е потвърдена с помощта на тънкослойна хроматография. Точките на топене са определени по капиларния метод. Съединенията са охарактеризирани с IR, NMR и мас-спектроскопия. Анти-депресантната активност на всички синтезирани съединения е оценена с теста „despair swim“ върху *Sprague Dawley*-плъхове. Като контрола е използван имипрамин. Всички синтезирани съединения показват анти-депресантна активност. QSAR-изследване на описаните съединения е извършено с използването на софтуер TSAR 3.3 и резултатите са задоволителни. Получените резултати ще са полезни за бъдещи изследвания.

## Synthesis, characterization and thermal behaviour of novel phthalocyanines bearing chalcone groups on peripheral positions

A. A. Kaya

School of Health, Gümüşhane University, TR-29000 Gümüşhane, Turkey

Received January 21, 2015, Revised April 15, 2015

A new nickel, zinc, cobalt, copper and metal-free phthalocyanine was synthesized by nucleophilic aromatic substitution reaction of (E)-3-(3-hydroxyphenyl)-1-phenylprop-2-en-1-one with 4-nitrophthalonitrile and cyclotetramerisation of (E)-4-(3-(3-oxo-3-phenylprop-1-enyl)phenoxy) phthalonitrile. The new compounds were characterized by a combination of IR, <sup>1</sup>H NMR, <sup>13</sup>C NMR, UV-Vis, elemental analysis and MS spectral data. The thermal stabilities of the phthalocyanine compounds were determined by thermogravimetric analysis.

**Keywords:** Phthalocyanine; Macrocyclic; Phthalonitrile; Chalcone; Thermogravimetric Analysis.

### INTRODUCTION

Phthalocyanines (Pcs) form nowadays an important group of organic compounds that belong to the most studied subjects of organic functional materials [1]. However, although no phthalocyanines have been identified in the nature yet, they were some of the first macrocycles that were synthesized and used as model compounds to mimic the biologically important porphyrins [2, 3]. Microwave irradiation is an important improvement in the synthesis of metallophthalocyanines. The most important industrial application of phthalocyanines is the formation of colored complexes with metal cations that are used as highly stable pigments and dyes [4]. In recent years, the applications of metallophthalocyanine (MPc) complexes have expanded to areas such as photosensitizers in photodynamic therapy, photoconducting agents in photocopying machines and electrocatalysts. In addition, they can find commercial applications as: photovoltaic materials in solar cells [5-7], systems for fabrication of light emitting diodes (LED) [8, 9], liquid crystalline [10] and non-linear optical materials [11, 12], sensitizers for photodynamic (PDT) cancer therapy [13, 14], photoconductors in xerography [15], dyes at recording layers for CD-R and DVD-R optical storage discs [16], as well as diverse catalytic systems [17, 18].

In medicine, phthalocyanines have been found to have applications as phototoxic drugs for photodynamic therapy [19-22]. Chalcones belong to the largest class of plant secondary metabolites,

which, in many cases, serve in plant defense mechanisms to counteract reactive oxygen species (ROS) in order to survive and prevent molecular damage and damage by microorganisms, insects, and herbivores. They are known to possess antioxidant character of different extents [23].

Closed shell diamagnetic ions such as Zn<sup>2+</sup>, Al<sup>3+</sup> and Ga<sup>3+</sup> give phthalocyanine complexes with both high triplet yields and long lifetimes of the excited triplet state. Thus, these complexes are expected to exhibit strong photochemical and photodynamic activities due to a higher efficiency in generating reactive oxygen species than porphyrins [19].

Some studies showed that a convenient route for the synthesis of metal-free phthalocyanine (H<sub>2</sub>Pc) from phthalonitrile and metallophthalocyanines from phthalonitrile, phthalimide and phthalic anhydride using hexamethyldisilazane (HMDS). In spite of the potential utility of this approach, reaction times necessary for these reactions are very long at relatively high temperature. For example, the reaction times are 10-24 h at 100-150 °C when metal-free phthalocyanine is synthesized from phthalonitrile, 10-48 h at 150 °C when metallophthalocyanines are synthesized from phthalimide or phthalic anhydride and 10-12 h at 100-125 °C in the case of phthalonitrile [24, 25].

Microwave-promoted organic reactions are well known as environmentally benign methods that can accelerate a great number of chemical processes. In particular, the reaction time and energy input are supposed to be mostly reduced in the reactions that are run for a long time at high temperatures under conventional conditions [26].

In this article, we describe the synthesis and characterization of metal-free phthalocyanine **4** in 1.8-diazabicyclo[5.4.0]undec-7-ene (DBU) and *n*-

\* To whom all correspondence should be sent:  
E-mail: afsinkaya@hotmail.com

pentanol in a Schlenk tube under N<sub>2</sub> and metallophthalocyanines **5-8** by microwave irradiation.

## EXPERIMENTAL

All reactions were carried out under dry nitrogen atmosphere using standard Schlenk techniques. The IR spectra were recorded on a Perkin Elmer 1600 FTIR spectrophotometer, using potassium bromide pellets. <sup>1</sup>H and <sup>13</sup>C NMR spectra were recorded on a Varian Mercury 200 MHz spectrometer in CDCl<sub>3</sub>, and chemical shifts are reported (δ) relative to Me<sub>4</sub>Si as internal standard. Mass spectra were measured on a Varian 711 and VG Zapspec spectrometer. UV-visible absorption spectra were measured by a Unicam UV-visible spectrometer. Melting points were measured on an Electrothermal apparatus. Domestic oven (Arçelik MD 823, 350 W) was used for the synthesis of metallophthalocyanines. A Seiko II Exstar 6000 thermal analyzer was used to record the DTA curves under nitrogen atmosphere with a heating rate of 20 °C min<sup>-1</sup> in the temperature range of 30 to 900 °C using platinum crucibles. Domestic oven was used for all syntheses of phthalocyanines.

### Synthesis of (E)-4-(3-(3-oxo-3-phenylprop-1-enyl)phenoxy)phthalonitrile (3)

(E)-3-(3-hydroxyphenyl)-1-phenylprop-2-en-1-one (**1**) [31]. (1 g, 4.46 mmol) was dissolved in dry DMF (15 ml) under N<sub>2</sub> atmosphere and 4-nitrophthalonitrile (**2**) (0.773 g, 4.46 mmol) was added to the solution. After stirring for 10 min finely ground anhydrous K<sub>2</sub>CO<sub>3</sub> (3.07 g, 22.3 mmol) was added portionwise within 2 h under efficient stirring. The reaction mixture was then stirred under N<sub>2</sub> at 50 °C for 72 h. Then the solution was poured into ice-water (100 ml) and was stirred in the course of 1 day. The solid product was filtered, washed with water and dried *in vacuo* over P<sub>2</sub>O<sub>5</sub>. The product was recrystallized from ethanol. Yield: 1.19 g (76 %), mp: 132 °C; <sup>1</sup>H NMR (CDCl<sub>3</sub>, 200 MHz) δ: 8.02-7.10 (m, Ar-H, olefinic C-H); <sup>13</sup>C NMR (CDCl<sub>3</sub>, 100 MHz) δ: 190.29, 161.66, 154.34, 143.05, 138.07, 137.97, 135.80, 133.43, 131.53, 129.00, 128.79, 126.65, 123.84, 122.61, 121.89, 121.76, 120.25, 117.98, 109.43, 115.58, 115.14; IR (KBr) ν: 3076, 2926-2872, 2227, 1668, 1596, 1490, 1314, 1283, 1250, 1229, 1145, 1019, 844, 781, 688; MS (ES<sup>+</sup>) *m/z*: 350 [M]<sup>+</sup>. Anal. calcd for C<sub>23</sub>H<sub>14</sub>N<sub>2</sub>O<sub>2</sub>: C 78.84, H 4.03, N 8.00; found C 78.54, H 4.06, N 8.02.

### Preparation of metal-free phthalocyanine (4)

(E)-4-(3-(3-oxo-3-phenylprop-1-enyl)phenoxy)phthalonitrile (**3**) (300 mg, 0.86 mmol), DBU (five drops) and dry *n*-pentanol (4 ml) were added in a Schlenk tube. The mixture was heated and stirred at 160 °C for 24 h under N<sub>2</sub>. Thereafter the reaction mixture was cooled to 30 °C and precipitated by adding ethanol. The solid product was filtered and washed with ethanol. The green solid product was chromatographed on silica gel with chloroform/methanol (9:1) as an eluent. Yield: 48 mg (16 %), UV-vis (chloroform) λ<sub>max</sub>: 705(2.85), 669(2.79), 642(2.45), 605(2.25), 396(2.35), 341(2.68) nm; <sup>1</sup>H NMR (CDCl<sub>3</sub>, 200 MHz) δ: 7.73-6.72(m, Ar-H, olefinic C-H); <sup>13</sup>C NMR (CDCl<sub>3</sub>, 100 MHz) δ: 176.12, 172.22, 172.74, 163.30, 162.42, 157.28, 154.46, 146.21, 134.14, 131.12, 130.86, 127.94, 126.42, 124.31, 123.64, 122.89, 118.26, 116.42, 114.18; IR (KBr) ν: 3426, 3060, 2923-2853, 1662, 1571, 1464, 1376, 1269, 1119, 852, 750, 692; MS (ES<sup>+</sup>) *m/z*: 1404 [M+1]<sup>+</sup>. Anal. calcd for C<sub>92</sub>H<sub>58</sub>N<sub>8</sub>O<sub>8</sub>: C 78.66, H 4.13, N 7.98, found C 78.62, H 4.11, N 7.96.

### Nickel (II) phthalocyanine (5)

A mixture of (E)-4-(3-(3-oxo-3-phenylprop-1-enyl)phenoxy)phthalonitrile (**3**) (200 mg, 0.57 mmol), anhydrous metal salt NiCl<sub>2</sub> (18.5 mg, 0.14 mmol), and 2-(dimethylamino)ethanol (3 ml) was irradiated in a microwave oven at 175 °C, 350 W for 8 min. After cooling to room temperature the reaction mixture was refluxed with ethanol to precipitate the product which was filtered off and dried *in vacuo* over P<sub>2</sub>O<sub>5</sub>. The obtained green solid product was purified by column chromatography on silica gel with chloroform-methanol (5:1) as an eluent. Yield: 69 mg (33 %), UV-vis (chloroform) λ<sub>max</sub>: 678(2.88), 653(2.51), 436(2.57), 353(3.21) nm; <sup>1</sup>H NMR (CDCl<sub>3</sub>, 200 MHz) δ: 7.90-6.32 (m, Ar-H, olefinic C-H); <sup>13</sup>C NMR (CDCl<sub>3</sub>, 100 MHz) δ: 199.44, 173.32, 168.71, 162.03, 156.41, 143.80, 142.99, 139.73, 138.06, 133.21, 130.85, 128.79, 125.60, 124.29, 122.86, 121.81, 119.99, 113.81, 113.08, 112.27, 111.86, 110.24, 107.59; IR (KBr) ν: 3060, 2927-2846, 1665, 1577, 1473, 1446, 1330, 1236, 1147, 1093, 1017, 977, 772, 689; MS (ES<sup>+</sup>) *m/z*: 1460 [M]<sup>+</sup>; Anal. calcd for C<sub>92</sub>H<sub>56</sub>N<sub>8</sub>O<sub>8</sub>Ni: C 75.60, H 3.83, N 7.67; found C 75.63, H 3.81, N 7.69.

### Zinc (II) phthalocyanine (6)

A mixture of (E)-4-(3-(3-oxo-3-phenylprop-1-enyl)phenoxy)phthalonitrile (**3**) (200 mg, 0.57 mmol), anhydrous metal salt Zn(CH<sub>3</sub>COO)<sub>2</sub> (29 mg, 0.14 mmol), and 2-(dimethylamino)ethanol (3

ml) was irradiated in a microwave oven at 175 °C, 350 W for 6 min. After cooling to room temperature the reaction mixture was refluxed with ethanol to precipitate the product which was filtered off and dried *in vacuo* over P<sub>2</sub>O<sub>5</sub>. The obtained green solid product was purified from the column chromatography on silica gel with chloroform-methanol (6:1) as an eluent. Yield: 107 mg (51 %), UV-vis (chloroform)  $\lambda_{\text{max}}$ : 682(3.12), 651(2.45), 400(2.99), 353(3.16) nm; <sup>1</sup>H NMR (CDCl<sub>3</sub>, 200 MHz)  $\delta$ : 7.98-6.87 (m, Ar-H, olefinic C-H) ; <sup>13</sup>C NMR (CDCl<sub>3</sub>, 100 MHz)  $\delta$ : 186.44, 174.23, 171.02, 166.88, 161.54, 157.44, 151.13, 146.97, 141.85, 132.72, 130.16, 129.58, 128.78, 124.88, 121.42, 120.13, 119.17, 118.42, 110.02, 105.00; IR (KBr)  $\nu$ : 3061, 2927-2851, 1664, 1578, 1484, 1393, 1314, 1236, 1179, 1089, 1045, 977, 880, 773; MS (ES<sup>+</sup>)  $m/z$ : 1467 [M+1]<sup>+</sup>; Anal. calcd for C<sub>92</sub>H<sub>56</sub>N<sub>8</sub>O<sub>8</sub>Zn : C 75.26, H 3.82, N 7.63; found C 75.24, H 3.86, N 7.62.

#### Cobalt (II) phthalocyanine (7)

A mixture of (E)-4-(3-(3-oxo-3-phenylprop-1-enyl)phenoxy) phthalonitrile (**3**) (200 mg, 0.57 mmol), anhydrous metal salt CoCl<sub>2</sub> (18.5 mg, 0.14 mmol) and 2-(dimethylamino)ethanol (3 ml) was irradiated in a microwave oven at 175 °C, 350 W for 8 min. After cooling to room temperature the reaction mixture was refluxed with ethanol to precipitate the product which was filtered off and dried *in vacuo* over P<sub>2</sub>O<sub>5</sub>. The obtained green solid product was purified by column chromatography on silica gel with chloroform-methanol (5:1) as an eluent. Yield: 95 mg (46 %), UV-vis (chloroform)  $\lambda_{\text{max}}$ : 672(2.75), 618(2.32), 302(3.16) nm; IR (KBr)  $\nu$ : 3061, 2927-2846, 1665, 1577, 1473, 1329, 1237, 1179, 1095, 1017, 977, 881, 773, 689; MS (ES<sup>+</sup>)  $m/z$ : 1460 [M]<sup>+</sup>; Anal. calcd for C<sub>92</sub>H<sub>56</sub>N<sub>8</sub>O<sub>8</sub>Co: C 75.59, H 3.83, N 7.67; found: C 75.94, H 3.60, N 7.31.

#### Copper (II) phthalocyanine (8)

A mixture of (E)-4-(3-(3-oxo-3-phenylprop-1-enyl)phenoxy) phthalonitrile (**3**) (200 mg, 0.57 mmol), anhydrous metal salt CuCl<sub>2</sub> (19.1 mg, 0.14 mmol) and 2-(dimethylamino)ethanol (3 ml) was irradiated in a microwave oven at 175 °C, 350 W for 5 min. After cooling to room temperature the reaction mixture was refluxed with ethanol to precipitate the product which was filtered off and dried *in vacuo* over P<sub>2</sub>O<sub>5</sub>. The obtained green solid product was purified by column chromatography on silica gel with chloroform-methanol (6:1) as an eluent. Yield: 73 mg (35 %), UV-vis (chloroform)  $\lambda_{\text{max}}$ : 684(2.83), 618(2.42), 298(3.17) nm; IR (KBr)

$\nu$ : 3061, 2928-2846, 1664, 1577, 1479, 1446, 1314, 1237, 1146, 1092, 1017, 977, 773, 690; MS (ES<sup>+</sup>)  $m/z$ : 1466 [M+1]<sup>+</sup>; Anal. calcd for C<sub>92</sub>H<sub>56</sub>N<sub>8</sub>O<sub>8</sub>Cu: C 75.35, H 3.82, N 7.64; found C 75.33, H 3.85, N 7.62.

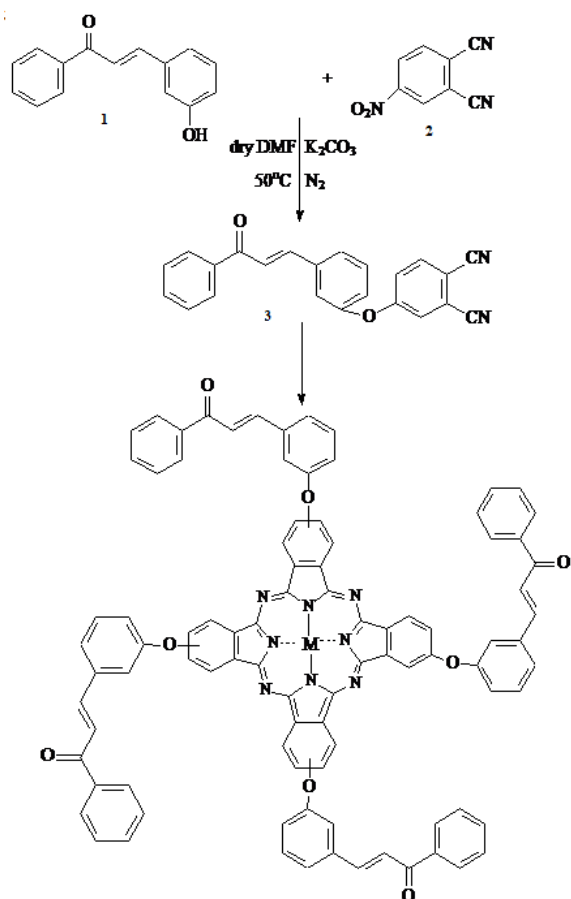
## RESULTS AND DISCUSSION

Synthesis of (E)-4-(3-(3-oxo-3-phenylprop-1-enyl)phenoxy) phthalonitrile **3** was carried out by the reaction of 4-nitrophthalonitrile (**2**) and (E)-3-(3-hydroxyphenyl)-1-phenylprop-2-en-1-one (**1**) in the presence of K<sub>2</sub>CO<sub>3</sub> in dry DMF. Final purification of the phthalonitrile derivative **3** by recrystallization afforded **3** with satisfactory elemental analysis and mass spectral data. In the <sup>1</sup>H-NMR spectrum of the phthalonitrile derivative **3**, the OH group of compound **1** disappeared as expected. The disappearance of OH and the presence of C≡N functional group at 2227 cm<sup>-1</sup> in the IR spectrum of compound **3** confirm the formation of the desired compound **3**. The <sup>13</sup>C-NMR spectrum of the phthalonitrile derivative **3** indicated the presence of nitrile carbon atoms at 115.58, 115.14 (C≡N) ppm.

The metal-free phthalocyanine **4** was synthesized by heating a mixture of phthalonitrile derivative **3**, DBU and dry n-pentanol in a Schlenk tube. The IR spectrum of the metal-free phthalocyanine **4** shows 3426 cm<sup>-1</sup> (N-H) vibrations. The disappearance of the C≡N stretching vibration in the IR spectrum of phthalonitrile derivative **3** suggested the formation of compound **4**. In the <sup>1</sup>H-NMR spectrum of this compound **4** the inner core protons of Pc-2H could not be observed due to strong aggregation of molecules [27]. The mass spectrum of this compound at (m/z): 1404 [M+1]<sup>+</sup> supports the proposed formula for this structure. The elemental analysis confirmed the structure of compound **4** (Fig. 1). The transition metal complexes were prepared from the phthalonitrile derivative **3** and the corresponding metal salt by microwave irradiation in 2-(dimethylamino) ethanol at 175°C, 350 W. The IR spectra of the metal-free compound **4** and the metallophthalocyanine compounds **5-8** are very similar. The significant difference is the presence of (N-H) vibrations of the inner phthalocyanine core which are assigned to a weak band at 3426 cm<sup>-1</sup> in the metal-free molecule. These bands disappear in the spectra of the metallophthalocyanine complexes. The disappearance of the C≡N stretching vibration in the IR spectra of compound **3** suggested the formation of compounds **5-8**. The NMR characteristics of the nickel compound **5** and zinc



the compound **6** were similar to those of the precursor dicyano compound **3** and the metal-free phthalocyanine compound **4**. In the mass spectrum of Ni, Zn, Co and Cu phthalocyanines, the presence of molecular ion peaks at ( $m/z$ ): 1460  $[M]^+$ , 1467  $[M+1]^+$ , 1460  $[M+1]^+$ , 1466  $[M+1]^+$  respectively, confirmed the proposed structures (Fig. 1). The elemental analyses of the metallophthalocyanines **5-8** were satisfactory.



Compound	<b>4</b>	<b>5</b>	<b>6</b>	<b>7</b>	<b>8</b>
M	2H	Ni (II)	Zn(II)	Co(II)	Cu(II)

**Fig. 1.** Synthesis of metal-free phthalocyanine and metallophthalocyanines

The UV-vis absorption spectra of compounds **4-8** in chloroform at room temperature are shown in Figs. 2 and 3. In general, phthalocyanines show typical electronic spectra with two strong absorption regions, one in the UV region at about 300-350 nm related to the B band and the other in the visible region at 600-700 nm related to the Q band. The split Q bands in compound **4**, which are characteristic for metal-free phthalocyanines, were observed at  $\lambda_{\max} = 705, 669$  nm, respectively. These intense Q bands indicate monomeric species, as species with  $D_{2h}$  symmetry show two intense absorption bands around 700 nm [28]. Such split Q band absorptions are due to the  $\pi \rightarrow \pi^*$  transition

from the HOMO to the LUMO of the phthalocyanine ring related to the fully conjugated  $18\pi$  electron system. The presence of strong absorption bands in compound **4** in the near UV region at  $\lambda_{\max} = 341$  nm also shows Soret region B bands which have been ascribed to the deeper  $\pi \rightarrow \pi^*$  levels of LUMO transitions [29].

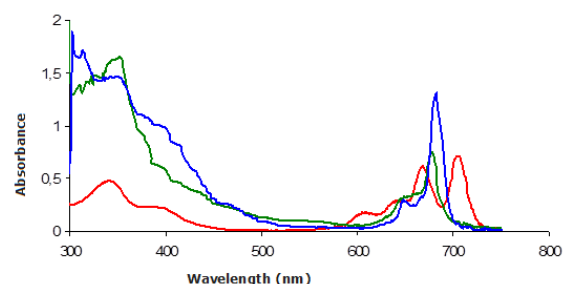


**Fig. 2.** UV-vis spectra of  $H_2Pc$  (—),  $NiPc$  (—) and  $ZnPc$  (—) complexes

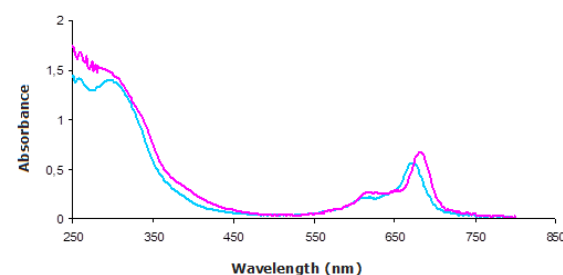


**Fig. 3.** UV-vis spectra of  $CoPc$  (—) and  $CuPc$  (—) complexes

The UV-vis absorption spectra of the metallophthalocyanines **5-8** show intense Q band absorptions at  $\lambda_{\max} = 678, 682, 672, 684$  nm, respectively. The single Q bands in the metal derivatives and the split form in their metal-free derivatives are characteristic [30].

The thermal behaviour of the metallophthalocyanines were investigated by TG/DTA. Although the thermal stabilities of phthalocyanines are well known, the phthalocyanine compounds are not stable above 292 °C. The initial and main decomposition temperatures are given in Table 1. The initial decomposition temperatures decreased in the order:  $8 > 6 > 7 > 5$ .

**Table 1.** Thermal properties of the metallophthalocyanines

Compound	M	Initial decomposition temperature in °C	Main decomposition temperature in °C
<b>5</b>	Ni	292	336
<b>6</b>	Zn	308	391
<b>7</b>	Co	300	399
<b>8</b>	Cu	357	393

## CONCLUSION

In this work, we describe the synthetic procedure and characterization of new metal-free and metallophthalocyanines. A dinitrile monomer was synthesized by nucleophilic aromatic substitution of (E)-3-(3-hydroxyphenyl)-1-phenylprop-2-en-1-one onto 4-nitrophthalonitrile.

The newly developed methods for the synthesis of phthalocyanine are easier, more economical, and less time-consuming. The microwave energy facilitates the synthesis. In addition, the thermal properties of the new phthalocyanines were examined by thermogravimetric analysis. Phthalocyanines are known as compounds of high thermal stability. So this property enables the use of phthalocyanines as technological materials.

## REFERENCES

1. N. B. McKeown, ed. Phthalocyanine materials: Synthesis, Structure and Function, Cambridge University Press; Cambridge, 1998.
2. F. H. Moser, A. L. Thomas, The Phthalocyanines; CRC: Boca Raton, 1983.
3. A. Burczyk, A. Loupy, D. Bogdal, A. Petit, *Tetrahedron*, **61**, 179 (2005).
4. C. Leznoff, A. Lever, eds. Phthalocyanines: properties and applications, vols.1-4. New York: VCH, 1993.
5. T. Anthopoulos, T. Shafai, *Appl. Phys. Lett.* **82**, 1628 (2003).
6. D. Wrobel, A. Boguta, In: Molecular Low Dimensional and Nanostructured Materials for Advanced Technology; Graja A, ed., Kluwer Academic: The Netherlands, 2002.
7. Ch. Pannemann, V. Dyakonov, J. Parisi, Hild, D. Wohrle, *Synth. Met.*, **121**, 1585 (2001).
8. M. Ishii, Y. Taga, *Appl. Phys. Lett.*, **80**, 3430 (2002).
9. S. H. Jung, J. H. Choi, J. H. Yang, W. J. Cho, C. S. Ha, *Mater. Sci. Eng. B.*, **85**, 160 (2001).
10. J. Sluven, C. Gorller-Walrand, K. Binnemans, *Mater. Sci. Eng. C*, **18**, 229 (2001).
11. G. de la Torre, P. Vazquez, F. Agullo-Lopez, T. Torres, *J. Chem. Mater.*, **8**, 1671 (1998).
12. Torres, T. de la Torre, G. Garcia-Ruiz, J. Synthesis of New Push-Pull Unsymmetrically Substituted Styryl Metallophthalocyanines: Targets for Nonlinear Optics. *Eur. J. Org. Chem.* **9**, 2323-2326 (1999).
13. I. Rosenthal, *Photochem. Photobiol.*, **53**, 859 (1991).
14. S. Muller, V. Mantareva, N. Stoichkova, H. Kliesch, A. Sobki, D. Wohrle, M. Shopova, *J. Photochem. Photobiol. B*, **35**, 167 (1996).
15. K. Y. Law, *Chem. Rev.*, **93**, 449 (1993).
16. D. Birkett, *J. Chem. Educ.*, **79**, 1081 (2002).
17. R. Raja, P. Ratnasamy, *J. Catal.*, **170**, 244 (1997).
18. A. Sorokin, B. Meunier, *Eur. J. Inorg. Chem.*, **9**, 1269 (1998).
19. H. Ali, J. E. van Lier, *Chem. Rev.*, **99**, 2379 (1999).
20. R. K. Pandey, *J. Porphyrins Phthalocyanines*, **4**, 368 (2000).
21. I. J. MacDonald, T. J. Dougherty, *J. Porphyrins Phthalocyanines*, **5**, 105 (2001).
22. M. R. Detty, S. L. Gibson, S. J. Wagner, *J. Med. Chem.*, **47**, 3897 (2004).
23. J. Vaya, P. A. Belinky, M. Aviram, *Free Rad. Biol. Med.*, **23(2)**, 302 (1997).
24. H. Uchida, H. Yoshiyama, P. Y. Reddy, S. Nakamura, T. Toru, *Bull. Chem. Soc. Jpn.*, **77**, 1401 (2004).
25. A. Shaabani, R. Maleki-Moghaddam, A. Maleki, A. H. Rezayan, *Dyes and Pigments*, **74**, 279 (2007).
26. A. Loupy, Microwave in organic synthesis. Weinheim: Wiley-VCH; 2002.
27. C. F. von Nostrum, S. J. Picken, J. Schouten, R. J. M. Nolte, *J. Am. Chem. Soc.*, **117**, 9957 (1995).
28. A. Lever, *Advances in Inorganic Chemistry*, **7**, 27 (1965).
29. A. W. Snow, J. R. Griffith, N. P. Marullo, *Macromolecules*, **17**, 1614 (1984).
30. A. E. Martin, J. E. Bulkowski, *J. Org. Chem.*, **47**, 412 (1982).
31. K. Radha, T. Pritam, J. K. Mi., C. J. Tae, N. M. Jung, K. Hye-Lin, N. Younghwa, C. Won-Jea, K. Youngjoo, L. Eung-Seok, *Bioorganic & Medicinal Chemistry*, **18**, 3066 (2010).

## СИНТЕЗА, ХАРАКТЕРИЗИРАНЕ И ТЕРМИЧНО ПОВЕДЕНИЕ НА НОВИ ФТАЛОЦИАНИНИ, НОСЕЩИ ХАЛКОНОВАТА ГРУПИ НА ПЕРИФЕРНИ ПОЗИЦИИ

A. A. Kaya

Училище за здраве, Университет Гюмюшхане, TR-29000 Гюмюшхане, Турция

Получена на 21 януари, 2015 г., ревизирана на 15 Април, 2015 г.

(Резюме)

Нови фталоцианини на никел, цинк, кобалт, мед и некомплексен фталоцианин бяха синтезирани чрез реакция на нуклеофилно ароматно заместване на (E) -3 - (3-хидроксифенил) -1-фенилпроп-2-ен-1-он с 4-нитрофталонитрил и циклотетрамеризация на (E) -4- (3- (3-оксо-3-фенилпроп-1-енил) фенокси) фталонитрил. Новите съединения са охарактеризирани чрез комбинация от ИЧ, <sup>1</sup>H ЯМР, <sup>13</sup>C ЯМР, УВ спектрометрия, елементарен анализ и маспектрални данни. Термичните стабилности на фталоцианинови съединения бяха определени чрез термогравиметричен анализ.

## Analysis of the reaction kinetics of aminotoluene molecule through DFT method

B. Eren, Y. Yalcin Gurkan \*

Namik Kemal University, Department of Chemistry, Tekirdag / Turkey

Received May 5, 2015, Accepted May 14, 2015

In this study, the most probable reaction paths of aminotoluene (o-toluidine) molecule with OH radical were analyzed. The optimized geometry was calculated via Gauss View 5. Subsequently, the lowest energy status was found out through geometric optimization via Gaussian 09 programme. The geometric structure analysis and bond lengths were also calculated. This study aims to determine the most probable path for the product distribution of aminotoluene and OH radical interaction in gas phase and aqueous media. Quantum mechanical methods were used to indicate the impact of reaction rate over primary intermediate, hydroxylated intermediate, and finally the impact of water solvent.

With the aim to determine the intermediates occurring at the reaction of aminotoluene degradation, geometric optimization of the reactant and transition status complexes were realized through Density Functional Theory (DFT) method. Based on the Quantum mechanical calculation, all probable rate constants of reaction paths were calculated by using Transition Status Theory (TST). For the determination of the transition status of the reaction, C-O bonds were taken as reference. Activation energy for probable reaction paths of all transition status complexes, and their most stable state were calculated from the thermodynamic perspective for the gas phase and aqueous media. The impact of water solvent was investigated by using COSMO as the solvation model.

Key words: Aminotoluene, hydroxyl radical, DFT calculation, TST, COSMO

### INTRODUCTION

Volatile aromatic compounds constitute a major part of air and water contaminants. They are mainly emitted into the environment from anthropogenic sources such as combustion processes, vehicle emissions and industrial sources, as well as from biogenic processes [1,2]. Organic contaminants exist at very low concentrations in water [3]. Therefore, it is essential that the organic contaminants be removed from drinking water [4]. Natural purification of water systems such as rivers, creeks, lakes, and pools is realized by solar light on earth. Sunbeams initiate the degradation reaction of big organic molecules into smaller and basic molecules, finally providing the formation of CO<sub>2</sub>, H<sub>2</sub>O, and other molecules [5, 6].

In its reactions with organic molecules, OH behaves as an electrophile whereas O is a nucleophile. Thus, OH readily adds to unsaturated bonds while O does not. Both forms of the radical abstract H from C-H bonds and this can result in the formation of different products when the pH is raised to a range where O rather than OH is the reactant. For example, if an aromatic molecule carries an aliphatic side chain, O attacks there by H abstraction whilst OH adds preferentially to the aromatic ring [7]. Hydroxyl radical which is the most reactive type known in biological systems

reacts with every biomolecule it encounters including water. Potentially, every biomolecule is a hydroxyl radical scavenger at different speeds [8]. Aromatic compounds are good detectors since they hydroxylate. In addition, the position of attack to the ring depends on the electron withdrawal and repulsion of previously present substituents. The attack of any hydroxyl radical to an aromatic compound results in the formation of a hydroxylated product [9].

While an intermediate in aminotoluene herbicide synthesis is used in the production of more than 90 paints and pigments, rubber, chemicals and pesticides, it is also used as a hardening agent for epoxy resin systems, a reactive material for the glucose analysis and fibre dyeing in clinic laboratories [10]. Due to the damaging effects of living organisms emitting resistant bad smell, and because of their solubility, aminotoluenes and their derivatives constitute an important water contaminant group. Although many methods are available for the removal of these molecules from water, every method has its own inconvenience [10-13].

In this study, the kinetics of the degradation reaction of aminotoluene and hydroxyl derivatives was analyzed theoretically. With the aim to determine the intermediates obtained from the reaction of aminotoluene degradation, geometric optimization of the reactant and transition status

\* To whom all correspondence should be sent:  
E-mail: yyalcin@nku.edu.tr

complexes were realized through the Density Functional Theory (DFT) method. Based on the quantum mechanical calculation, all probable rate constants of reaction paths were calculated by using Transition Status Theory (TST).

## COMPUTATIONAL SET-UP AND METHODOLOGY

### *Computational models*

The molecular models were created by using the mean bond distances, the geometric parameters of the benzene ring, tetrahedral angles for sp<sup>3</sup>-hybridized carbon and oxygen atoms, and 120° for sp<sup>2</sup>-hybridized carbon atoms. In the calculation of the hydroxylated radicals, the aromatic ring was left planar except for the position of attack. The attacking •OH radical was assumed to form a tetrahedral angle with the C–H bond due to the change in the hybridization state of the carbon at the addition center from sp<sup>2</sup> to sp<sup>3</sup> [2].

### *Molecular Orbital Calculations*

It is possible that in the photocatalytic degradation reactions of organic contaminants, more harmful products may occur than in the original material. Therefore, before experimentally realizing a photocatalytic degradation reaction, it is essential to know what the primary intermediate products are. The most reliable and accurate information is gathered through calculations carried out with quantum mechanical methods. Thus, since the yield produced is the same, the photocatalytic degradation reaction of o-toluidine and its hydroxy derivatives is based on the direct reaction of these molecules with the OH radical.

With this aim, the kinetics of the reactions of aminotoluene and aminotoluene derivatives with OH radicals was theoretically analysed. The study was initiated with aminotoluene and then exposed to OH radical reaction, and the reaction of the yield was modeled at the gas phase. The experimental findings in the scientific literature show that OH radicals detach hydrogen atom from saturated hydrocarbons, and OH is added to unsaturated hydrocarbons and materials of aromatic structure [14]. For this purpose, all possible reaction paths for the analysed reactions were determined, for every reaction path, molecular orbital calculations of reactant, yield, transition state complexes were carried out with the density function theory (DFT), their molecular orbital calculations were realized and their geometries were optimized.

### *Kinetic Data Treatment*

**The aim** of this study was to develop a model providing the outcome of the yield distribution of the photocatalytic degradation reactions. The vibration frequencies, the thermodynamic and electronic features of every structure were calculated using the obtained optimum geometric parameters. Afterwards, the rate constant and activation energy of every reaction was calculated using the Transition State Theory for a temperature of 25°C based on the quantum mechanical calculation results.

In order to find out the rate of reaction, it is necessary to calculate the equilibrium constant. The equilibrium constant is calculated using the partition functions according to mechanical methods. If the equilibrium constant  $K^\ddagger$  is written in terms of partition functions, it is as follows:

$$K^\ddagger = \frac{q^\ddagger}{q_A \cdot q_B}, \quad (1)$$

$q^\ddagger$ ,  $q_A$ ,  $q_B$ : partition functions belonging to transition state complex and reactants. Molecular partition function is as given below:

$$q = q \cdot e^{-E_0/RT}, \quad (2)$$

$E_a$  shows the activation energy, the difference between the zero point energies of transition state complex and reactants [15].

$$k = \frac{k_B T}{h} \cdot \frac{q^\ddagger}{q_A \cdot q_B} \cdot e^{-E_a/RT}, \quad (3)$$

- $k_B$  : Boltzmann constant
- $h$  : Planck constant
- $T$  : absolute temperature

In order to be able to calculate the rate constant, it is necessary to initially calculate the partition function of the activated complex. To realize this calculation, it is essential to know the geometry of the complex and moments of inertia. In addition,  $E_a$  should be known in order to find out the rate constant. The activation energy like the vibration frequency can only be calculated as quantum mechanical.

The most probable reaction path and the yield distribution of the OH radical of every molecule were determined by comparing the obtained results. The optimized geometric structures were drawn via GaussView 5, and the calculations were done via Gaussian 09 packet programme [16].

### *Methodology*

The reaction system under consideration consists of •OH radicals that are open-shell species. It is well-known that open-shell molecules pose severe problems in quantum mechanical

calculations. Therefore, geometry optimization of the reactants, the product radicals, pre-reactive and transition state complexes were performed with the DFT method with the Gaussian 09 package [16]. DFT methods use the exact electron density to calculate molecular properties and energies, taking electron correlation into account. They do not suffer from spin contamination and this feature makes them suitable for calculations involving open-shell systems. The DFT calculations were carried out by the hybrid B3LYP functional, which combines HF and Becke exchange terms with the Lee–Yang–Parr correlation functional.

Choice of the basis set is very important in such calculations. Based on these results, optimizations in the present study were performed at the B3LYP/6-31G(d) level. The forming C–O bonds in the addition paths and the H–O bond in the abstraction path were chosen as the reaction coordinates in the determination of the transition states. Ground-state and transition-state structures were confirmed by frequency analyses at the same level. Transition structures were characterized by having one imaginary frequency that belonged to the reaction coordinate, corresponding to a first-order saddle point. Zero-point vibrational energies (ZPEs) were calculated at the B3LYP/6-31G(d) level [2].

#### Solvent effect model

In aqueous media, water molecules affect the energetics of the degradation reactions of all organic compounds. Moreover, H<sub>2</sub>O induces geometry relaxation on the solutes. The latter effect becomes more important when hydrogen-bonded complexes are present. However, the results obtained in earlier studies indicate that geometry changes have a negligible effect on the energy of the solute in water for both open- and closed-shell structures [17,18]. In this study, to take into account the effect of H<sub>2</sub>O on the energetics and the kinetics of the aminotoluene + •OH reactions, DFT/B3LYP/6-31+G(d) calculations were carried out for the optimized structures of the reactants, the pre-reactive and the transition state complexes and the product radicals, by using COSMO (conductor-like screening solvation model) [18] as the solvation model, implemented in the Gaussian 09 package. The solvent was water at 25 °C, with dielectric constant  $\epsilon = 78.39$  [19].

COSMO is one of the polarizable continuum methods (PCMs). In PCMs, the solute molecule is placed in a cavity surrounded by a polarizable continuum, whose reaction field modifies the energy and the properties of the solute [20]. The geometry of the cavity is determined by the shape

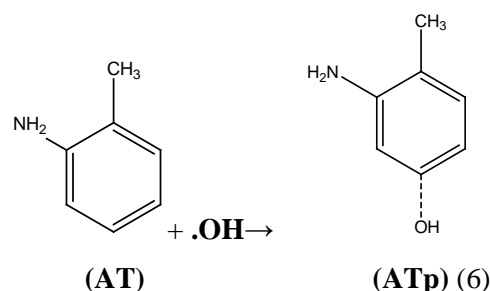
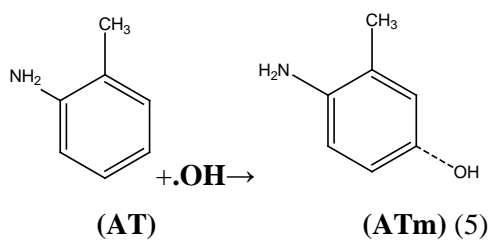
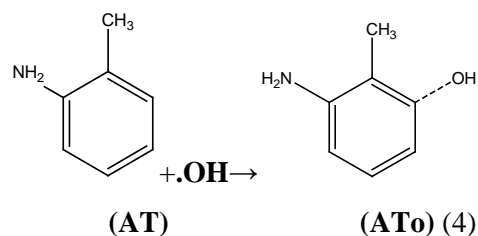
of the solute. The reaction field is described in terms of apparent polarization charges or reaction field factors included in the solute Hamiltonian, so that it is possible to perform iterative procedures leading to self-consistence between the solute wave-function and the solvent polarization. The COSMO method describes the solvent reaction field by means of apparent polarization charges distributed on the cavity surface, which are determined by assuming that the total electrostatic potential cancels out at the surface. This condition can describe the solvation in polar liquids. Hence, it is the method of choice in this study [2].

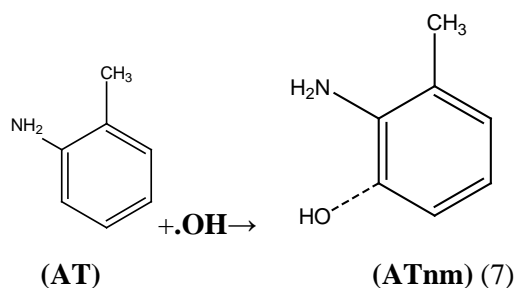
## RESULTS AND DISCUSSION

### Computational modeling

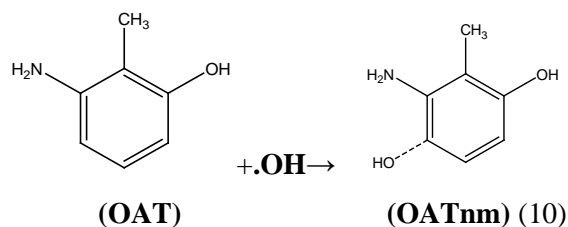
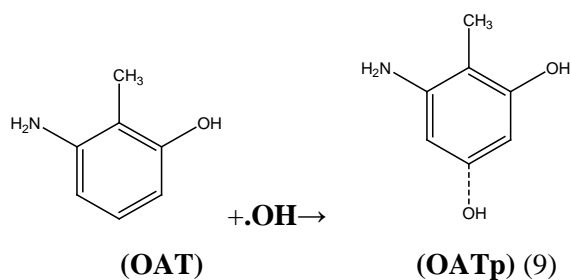
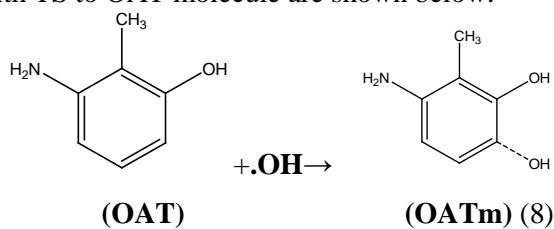
#### Reaction paths

The hydroxyl radical is a very active species and has a strong electrophilic character [21]. Once formed, it can readily attack the aminotoluene molecule and produce the reaction intermediates. •OH radical reactions with aromatic compounds proceed through the following reaction pathway: H-atom abstraction from C–H bonds and addition to aromatic rings [22]. Based on previous results [6,7,8,9,14,23] four different paths for the reaction of aminotoluene(AT) with •OH were determined. The first four paths, o-addition (ATo), m-addition (ATm), p-addition (ATp) and m- addition to NH<sub>2</sub> (ATnm) with TS to AT molecule are shown below:

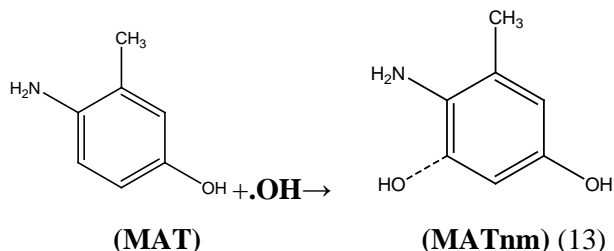
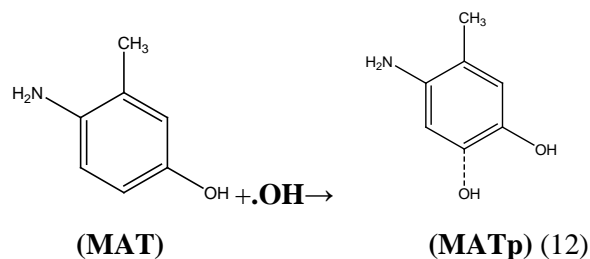
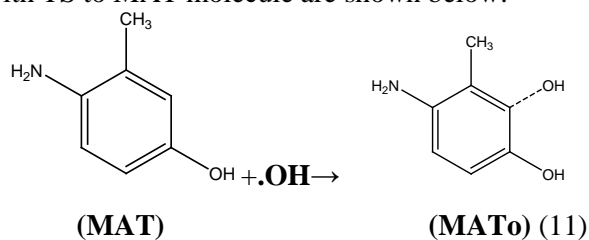




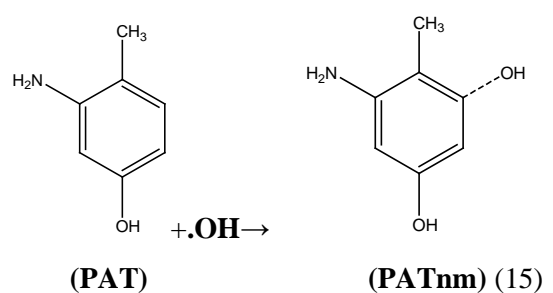
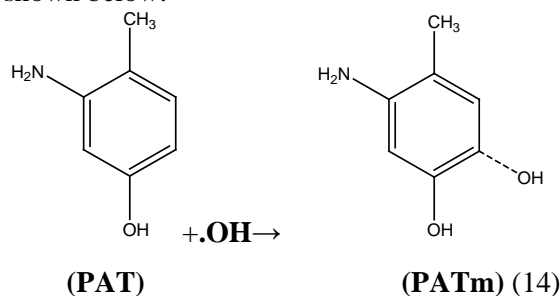
Based on previous results [6,7,8,9,14,23] three different paths for the reaction of 3-hydroxy-2-methyl aniline (OAT) with  $\cdot\text{OH}$  were determined. The first three paths, m-addition (OATm), p-addition (OATp), and m-addition to  $\text{NH}_2$  (OATnm) with TS to OAT molecule are shown below:



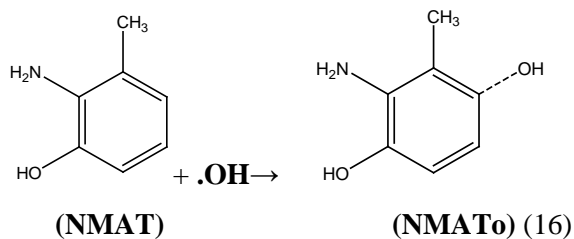
Based on previous results [6,7,8,9,14,23] three different paths for the reaction of 4-hydroxy-2-methyl aniline (MAT) with  $\cdot\text{OH}$  were determined. The first three paths, m-addition (MATo), p-addition (MATp), and m-addition to  $\text{NH}_2$  (MATnm) with TS to MAT molecule are shown below:

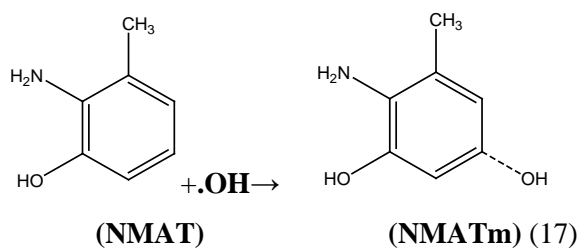


Based on previous results [6,7,8,9,14,23] two different paths for the reaction of 5-hydroxy-2-methyl aniline (PAT) with  $\cdot\text{OH}$  were determined. The first two paths, m-addition (PATm) and m-addition to  $\text{NH}_2$  (PATnm) with TS to PAT molecule are shown below:



Based on previous results [6,7,8,9,14,23] two different paths for the reaction of 2-hydroxy-6-methyl aniline (NMAT) with  $\cdot\text{OH}$  were determined. The first two paths, o-addition (NMATo) and m-addition (NMATm) with TS to NMAT molecule are shown below:





### Transition State Complexes

In this study, reactants were used to find out the transition state complexes. An estimation of the initial geometry was done according to the type of reaction path using the optimum geometric parameters of reactants. C-O bond was chosen as the reaction coordinate while modeling the transition state complexes for the reactions realized with OH addition, and the bond length was changed as 1.850-2.500 Å during calculation. The emerging OH bond length was chosen as the reaction path, and in order to determine the position of the OH radical according to the molecule, the dihedral angles belonging to this group were changed during calculations. Activation energies and their most determined state in thermodynamic terms for gas phase and aqueous media were calculated for the probable reaction paths of all transition state complexes.

According to Fig.1, the C-O bond lengths at four probable transition states of the OH radical were taken as precise measurement. The bond lengths were calculated as AT<sub>o</sub> (2.76 Å), AT<sub>m</sub> (3.44 Å), AT<sub>p</sub> (2.03 Å), AT<sub>nm</sub> (3.63 Å) relatively. The longest C-O bond belongs to AT<sub>nm</sub> TS molecule and it is found out that it occurs later compared to the others. Therefore, it is the most probable transition state.

According to Fig.2, the C-O bond lengths at three probable transition states of the OH radical were measured. The bond lengths were calculated as OAT<sub>m</sub> (2.06 Å), OAT<sub>p</sub> (2.03 Å), OAT<sub>nm</sub> (2.70 Å), MAT<sub>o</sub> (2.09 Å), MAT<sub>p</sub> (2.11 Å), MAT<sub>nm</sub> (2.64 Å), respectively. The longest C-O bonds belong to OAT<sub>nm</sub> and MAT<sub>nm</sub> TS molecules and they are found to occur later than the others. Therefore, they are the most probable transition states.

According to Fig.3, the C-O bond lengths at four probable transition states of the OH radical were measured. The bond lengths were calculated as PAT<sub>m</sub> (2,05 Å), PAT<sub>nm</sub> (2,91 Å), NMAT<sub>o</sub> (2,06 Å), NMAT<sub>m</sub> (2,14 Å), respectively. The longest C-

O bonds belong to AT<sub>nm</sub> and NMAT<sub>m</sub> TS molecules and they are found to occur later than the others. Therefore, they are the most probable transition states.

### CONCLUSIONS

Organic contaminants exist at very low concentrations in water [3]. Therefore, it is essential to remove the organic contaminants from drinking water [4]. Hydroxyl radical which is the most reactive type known in biological systems reacts with every biomolecule it encounters including water. Potentially, every biomolecule is a hydroxyl radical scavenger at a different speed [8]. Aromatic compounds are good detectors since they hydroxylate. In addition, the position of attack to the ring depends on the electron withdrawal and repulsion of previously present substituents [9]. When the Mulliken loads in Table 2 are analysed, the electronegativities of N and O atoms give us information about the bonding state of the OH radical.

In Table 1, the activation energy levels of E<sub>a</sub> gas phase of the TS molecules having the lowest energy at DFT method for every transition state complex are given below:

-7,404 kcal/mol of AT<sub>nm</sub> for AT,  $-1.321 \times 10^1$  kcal/mol of OAT<sub>m</sub> for OAT,  $-5.131$  kcal/mol of MAT<sub>nm</sub> for MAT,  $-1,293 \times 10^1$  kcal/mol of PAT<sub>m</sub> for PAT and  $-6.359$  kcal/mol of NMAT<sub>m</sub> for NMAT are the transition state complexes with the lowest energy. These reveal the most probable transition state complexes in the gas phase. The most rapid occurring transition state complex in the gas phase have the highest values of the k rate constant.

E<sub>a,ecosmo</sub> aqueous media activation energy levels at DFT method are  $0.623 \times 10^1$  kcal/mol of AT<sub>p</sub> for AT,  $0.183 \times 10^1$  kcal/mol of OAT<sub>m</sub> for OAT,  $0.673 \times 10^1$  kcal/mol of AT<sub>nm</sub> for MAT,  $0.763 \times 10^1$  kcal/mol of PAT<sub>nm</sub> for PAT,  $0.210 \times 10^1$  kcal/mol of NMAT<sub>o</sub> for NMAT are the transition state complexes with the lowest energy. This reveals that it is the most probable transition state at aqueous media.

Hydroxyl radicals are used in order to remove organic contaminants from water. In this study, the most probable reaction paths, where OH radical is added to the aromatic ring, were determined.

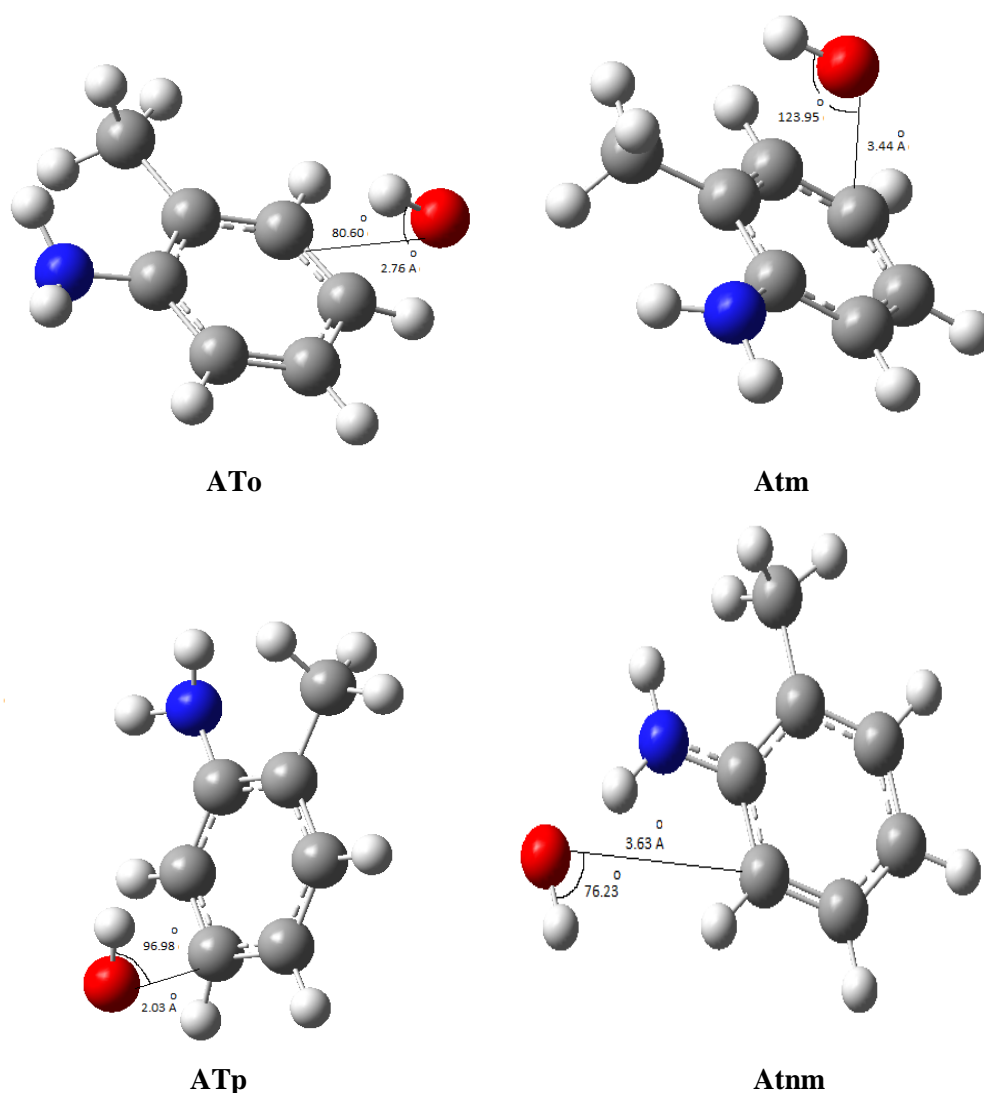


**Fig. 1.** Optimized structures of the transition state complexes of probable reaction paths (4,5,6,7).

**Table 1.** k and energy levels calculated via DFT method

DFT	Ea(kcal/mol)	k	Ea <sub>ecosmo</sub> (kcal/mol)
ATo	-5.964	$1.145 \times 10^{11}$	$5.307 \times 10^1$
ATm	-1.797	$3.738 \times 10^8$	$2.111 \times 10^1$
ATp	-3.480	$1.568 \times 10^9$	<b><math>0.623 \times 10^1</math></b>
ATnm	<b>-7.404</b>	<b><math>2.257 \times 10^{12}</math></b>	$1.927 \times 10^1$
OATm	<b><math>-1.321 \times 10^1</math></b>	<b><math>6.028 \times 10^{15}</math></b>	<b><math>0.183 \times 10^1</math></b>
OATp	-3.275	$1.376 \times 10^9$	$1.211 \times 10^1$
OATnm	-3.077	$1.005 \times 10^9$	$1.856 \times 10^2$
MATo	-4.953	<b><math>2.386 \times 10^{10}</math></b>	$1.647 \times 10^1$
MATp	-4.976	$1.905 \times 10^{10}$	$1.324 \times 10^2$
MATnm	<b>-5.131</b>	$9.504 \times 10^4$	<b><math>0.673 \times 10^1</math></b>
PATm	<b><math>-1.293 \times 10^1</math></b>	<b><math>4.015 \times 10^{15}</math></b>	$0.767 \times 10^1$
PATnm	-4.049	$1.139 \times 10^{10}$	<b><math>0.763 \times 10^1</math></b>
NMATo	-5.402	$5.070 \times 10^{10}$	<b><math>0.210 \times 10^1</math></b>
NMATm	<b>-6.359</b>	<b><math>2.505 \times 10^{11}</math></b>	$0.607 \times 10^1$



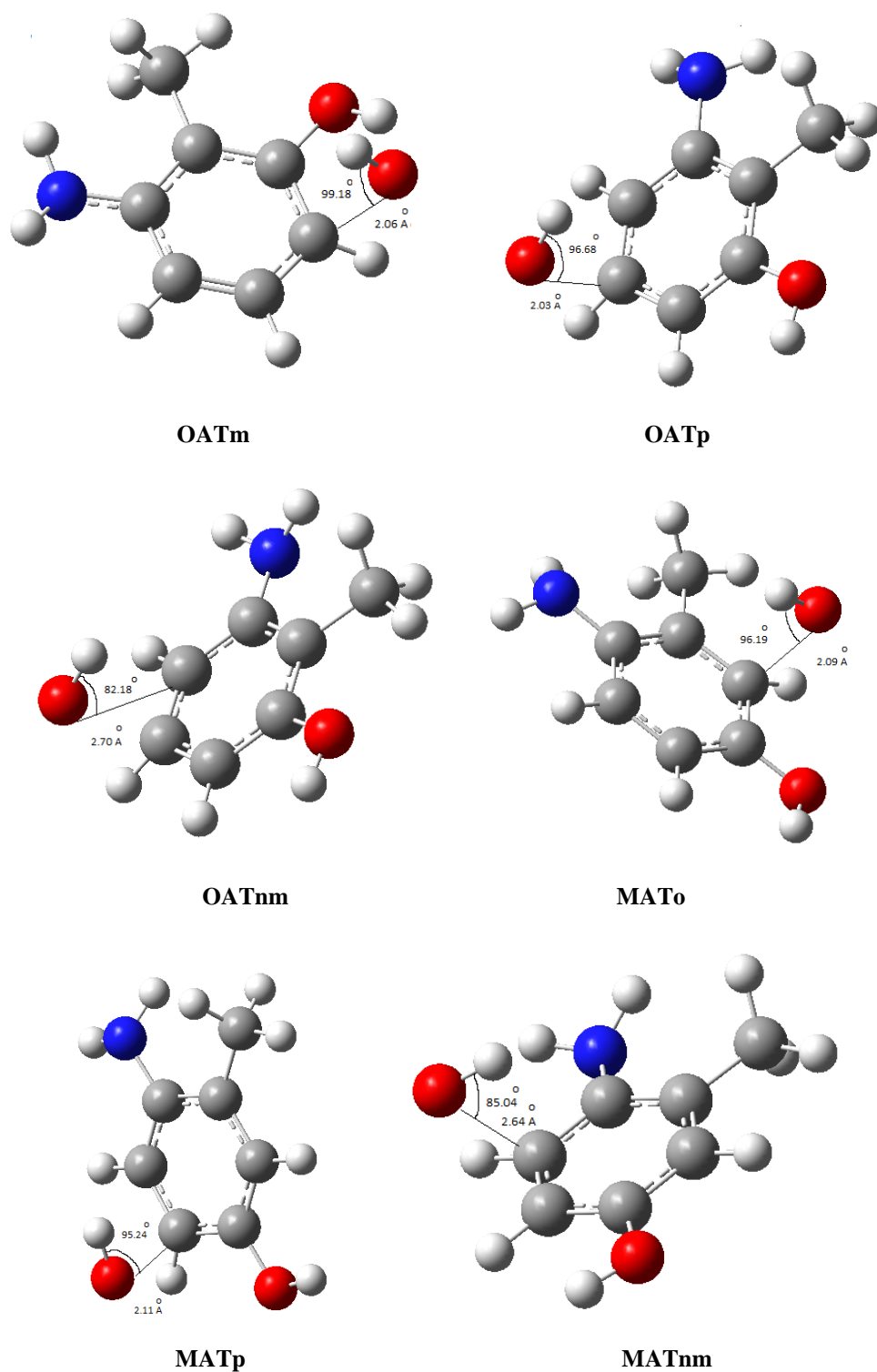


**Fig. 2.** Optimized structures of the transition state complexes of probable reaction paths (8, 9, 10).

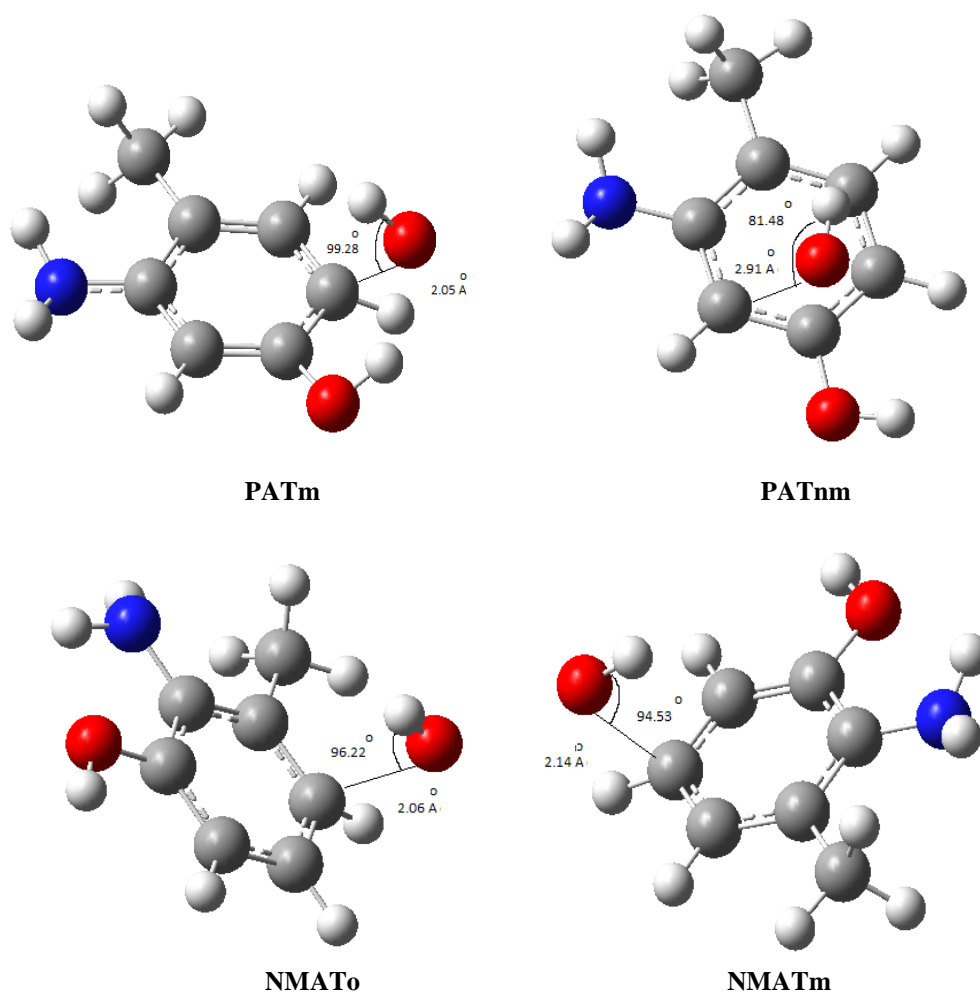


Fig. 3. Optimized structures of the transition state complexes of probable reaction paths (11, 12, 13, 14).

Table 2. Mulliken loads of the heavy atoms of the studied molecules

AT		ATo		ATm		ATp	
11 C	-0.079158	11 C	-0.068813	11 C	-0.084916	11 C	-0.060090
15 N	-0.152651	15 N	-0.128493	15 N	-0.145308	15 N	-0.145132
		18 O	-0.219771	18 O	-0.114680	18 O	-0.209659
ATnm		OAT		OATm		OATp	
11 C	-0.063830	10 C	-0.062126	10 C	-0.055300	10 C	-0.040231
15 N	-0.068889	14 N	-0.151131	14 N	-0.118889	14 N	-0.144576
18 O	-0.231787	17 O	-0.246327	17 O	-0.226425	17 O	-0.240401
				19 O	-0.285348	19 O	-0.204711
OAT nm		MAT		MATo		MATp	
10 C	-0.041225	10 O	-0.253210	10 O	-0.216734	10 O	-0.216065
14 N	-0.145082	12 N	-0.160178	12 N	-0.151373	12 N	-0.149771
17 O	-0.240589	15 C	-0.074152	15 C	-0.049042	15 C	-0.057486
19 O	-0.211082			19 O	-0.202878	19 O	-0.206673
MATnm		PAT		PATo		PATm	
10 O	-0.243592	10 C	-0.086504	10 C	-0.005234	10 C	-0.067938
12 N	-0.150491	14 N	-0.152124	14 N	-0.221558	14 N	-0.119865
15 C	-0.063696	17 O	-0.245155	17 O	-0.252320	17 O	-0.224289
19 O	-0.097024			19 O	-0.095696	19 O	-0.285990
PATnm		NMAT		NMATo		NMATm	
10 C	-0.074263	10 C	-0.076104	10 C	-0.050241	10 C	-0.066739
14 N	-0.144674	14 O	-0.262806	14 O	-0.239830	14 O	-0.256092
17 O	-0.229721	16 N	-0.141021	16 N	-0.133101	16 N	-0.114022
19 O	-0.097927			19 O	-0.220675	19 O	-0.223159

**Acknowledgements:** The authors greatly appreciate Namik Kemal University Research Foundation for financial support. Project number: NKUBAP.00.10.AR.12.05

#### REFERENCES

1. B.J. Finlayson-Pitts, J.N. Pitts Jr., Chemistry of the Upper and Lower Atmosphere, Academic Press, San Diego, 2000.
2. A. Hatipoglu, D. Vione, Y. Yalçın, C. Minero, Z. Çınar, *Journal of Photochemistry and Photobiology A: Chemistry*, **215**, 59 (2010).
3. K. Verschueren, "Handbook of Environmental Data on Organic Chemicals" Second Ed., Van Nostrand Reinhold Company, New York, 1983.
4. J. C. English, V. S. Bhat, G. L. Ball, C. J. McLellan, *Original Research Article Regulatory Toxicology and Pharmacology*, **64**, 2, 269 (2012).
5. R.W. Matthews, D.F. Ollis, H. Al-Ekabi, Photocatalytic Purification and Treatment of Water and Air:in, Elsevier Science Publishers, 1993, p. 121.
6. A. Taicheng, L. Sun, G. Li, S. Wan, *Journal of Molecular Catalysis A:Chemical*, **333** (1–2), 128 (2010).
7. V.G. Buxton, L.C. Greenstock, P.W. Helman, B.A. Ross, *Journal of Physical and Chemical Reference Data*, **17**, 513 (1988).
8. M. Anbar, P. Neta, *Int. J. Radiat Isot*, **18**, 495 (1965).
9. B. Halliwell, M. Grootveld, J.M.C. Gutteridge, 1988, *Methods of Biochemical Analysis*, 33, 59. Laidler K.J and Meiser, J.H, 1982. *Physical Chemistry*, The Benjamin/Cummings Publishing Company Inc., California.
10. IARC Some Aromatic Amines, Organic Dyes, and Related Exposures. IARC Monogr Eval Carcinog Risks Hum, **99**, 1 (2010). PMID:21528837
11. Monogr Eval Carcinog Risk Chem Man, **16**, 1 (1978).
12. IARC Monogr Eval Carcinog Risks Chem Hum, **27**, 1 (1982). PMID:6955259
13. IARC Monogr Eval Carcinog Risks Hum Suppl, **7**, 1 (1987). PMID:3482203
14. IARC Monogr Eval Carcinog Risks Hum, **77**, 1 (2000). PMID:11236796
15. P.W. Atkins, Physical Chemistry, 6th edition, Oxford University Press 1998, P.W. Atkins and R.S. Friedman, 1997, Molecular Quantum Mechanics, 3rd Ed., Oxford University Press Inc., New York.
16. I.N. Levine Quantum Chemistry, Allyn and Bacon Inc., Boston 1983, I.N. Levine, Quantum Chemistry i, Allyn and Bacon, Boston MA 1991, J.P. Lowe, Quantum Chemistry, 2nd Ed., Academic Press, USA 1993.
17. M.J. Frisch, G.W. Trucks, H.B. Schlegel, G.E. Scuseria, M.A. Robb, J.R. Cheeseman, J.A. Montgomery Jr., T. Vreven, K.N. Kudin, J.C. Burant, J.M. Millam, S.S. Iyengar, J. Tomasi, V. Barone, B. Mennucci, M. Cossi, G. Scalmani, N. Rega, G.A. Petersson, H. Nakatsuji, M. Hada, M. Ehara, K. Toyota, R. Fukuda, J. Hasegawa, M. Ishida, T. Nakajima, Y. Honda, O. Kitao, H. Nakai, M. Klene, X. Li, J.E. Knox, H.P. Hratchian, J.B. Cross, C. Adamo, J. Jaramillo, R. Gomperts, R.E. Stratmann, O. Yazyev, A.J. Austin, R. Cammi, C. Pomelli, J.W. Ochterski, P.Y. Ayala, K. Morokuma, G.A. Voth, P. Salvador, J.J. Dannenberg, V.G. Zakrzewski, S. Dapprich, A.D. Daniels, M.C. Strain, O. Farkas, D.K. Malick, A.D. Rabuck, K. Raghavachari, J.B. Foresman, J.V. Ortiz, Q. Cui, A.G. Baboul, S. Clifford, J. Cioslowski, B.B. Stefanov, G. Liu, A. Liashenko, P. Piskorz, I. Komaromi, R.L. Martin, D.J. Fox, T. Keith, M.A. Al-Laham, C.Y. Peng, A. Nanayakkara, M. Challacombe, P.M.W. Gill, B. Johnson, W. Chen, M.W. Wong, C. Gonzalez, J.A. Pople, Gaussian 09, Revision B.04, Gaussian, Inc., Pittsburgh, PA, 2009.
18. J. Andzelm, C. Kölmel, A. Klamt, *J. Chem. Phys.* **103**, 9312 (1995).
19. V. Barone, M. Cossi, *J. Phys. Chem. A.*, **102**, 11 1995 (1998).
20. J.B. Foresman, Æ. Frisch, Exploring Chemistry with Electronic Structure Methods, Gaussian Inc., Pittsburgh, PA, 1996.
21. N.S. Hush, J. Schamberger, G.B. Bacskay, *Coord. Chem. Rev.* **249**, 299, (2005).
22. V. Brezová, M. Ceppan, E. Brandsteterova, M. Breza, L. Lapcik, *J. Photochem. Photobiol. A: Chem.* **59**, 3 (1991).
23. M. Kılıç, G. Koçturk, N. San, Z. Çınar, *Chemosphere*, **69**, 9, 1396 (2007).
24. I. Suh, D. Zhang, R. Zhang, L.T. Molina, M.J. Molina, *Chem. Phys. Lett.* **364**, 454 (2002).

## АНАЛИЗ НА РЕАКЦИОННАТА КИНЕТИКА НА МОЛЕКУЛАТА НА АМИНОТОЛУЕН ЧРЕЗ DFT-МЕТОДА

Б. Ерен, И. Ялчин Гуркан \*

*Департамент по химия, Университет „Намик Кемал“, Текирдаг, Турция*

Постъпила на 5 май, 2015 г.; приета на 5 май, 2015 г.

(Резюме)

В тази работа се анализират най-вероятните маршрути на реакцията на аминотолуен (о-толуидин) с ОН-радикали. Оптимизираната геометрия е изчислена чрез софтуера Gauss View 5. Най-ниските енергийни нива са намерени чрез геометрична оптимизация с програмата Gaussian 09. Изчислени са и геометричната структура и дължината на връзките. Тази работа има за цел да се определят най-вероятните пътища на продуктите от взаимодействието между аминотолуена и ОН-радикалите в газова и в течна фаза. Използвани са квантово-механични методи за посочване на влиянието на скоростта на реакцията върху първичните преходни съединения, хидроксилираните междинни съединения и на водата като разтворител.

Междинните съединения, геометричната оптимизация на реагентите и преходните комплекси са определени по DFT-метода. На базата на квантово-механични пресмятания с използването на теорията на преходните състояния (TST) са определени всички вероятни скоростни константи. Връзките C-O за взети като референтни при определянето на преходните състояния. Активиращата енергия за вероятните реакционни маршрути за всички преходни комплекси и техните най-устойчиви състояния са изчислени от термодинамична гледна точка за газовата и течната фаза. Въздействието на разтворителя (вода) е изследвано чрез COSMO-софтуер като солватационен модел.

## Electrochemical method for energy production from hydrogen sulfide in the Black sea waters in sulfide-driven fuel cell

D. Uzun<sup>1\*</sup>, E. Razkazova–Velkova<sup>2</sup>, K. Petrov<sup>1</sup>, V. Beschkov<sup>2</sup>

<sup>1</sup>Acad. Evgeni Budevski Institute of Electrochemistry and Energy Systems, Bulgarian Academy of Sciences, Acad. G. Bonchev Str., Bl.10, 1113 Sofia, Bulgaria

<sup>2</sup>Institute of Chemical Engineering, Bulgarian Academy of Sciences, Acad. G. Bonchev Str., Bl. 103,1113 Sofia, Bulgaria

Submitted September 25, 2014; accepted October 30, 2014

The aim of the present research is the development of an economically feasible electrochemical method for extraction of H<sub>2</sub>S contained in Black Sea waters, using it as a fuel in a sulfide/oxygen(air) fuel cell. Low HS<sup>-</sup> concentrations and presence of NaCl, similar to the conditions in the depth of Black Sea, have been investigated. Electrochemical condition for oxidation of sulfide HS<sup>-</sup> directly to sulfite and sulfate on electrode (anode) catalysts have been found. Different anode catalysts for HS<sup>-</sup> oxidation have been tested: graphite, cobalt phthalocyanine (CoPc) and perovskite (La<sub>1.3</sub>Sr<sub>0.7</sub>NiO<sub>4</sub>). No catalytic poisoning has been observed by the oxidation products (sulfite and/or sulfate). Perovskite and CoPc have been found as the more suitable catalyst for this fuel cell system. The characteristics of the sulfide driven fuel cell have been tested with optimized HS<sup>-</sup> anodes and previously developed oxygen (air) cathodes. Electric power of P = 7.5 mW has been obtained.

**Key words:** hydrogen sulfide, sulfide driven fuel cell, Black Sea water.

### INTRODUCTION

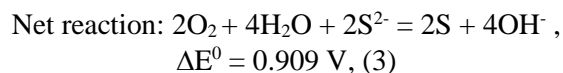
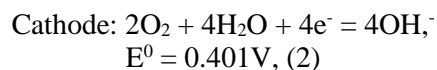
The present work is aimed on the opportunity to recover energy from the hydrogen sulfide in the Black Sea deep waters. It is well known that these waters contain an enormous amount of hydrogen sulfide (as hydrosulfide and sulfide ions) estimated as 4600 Tg, i.e. 4.6 billion tons [1]. The energy content of hydrogen sulfide combined with its large amount suggests its possible application for energy production [2-10]. There are efforts to attack the problem by various methods: low temperature adsorption of hydrogen sulfide from sea waters followed by thermal decomposition [3, 4], electrolysis leading to hydrogen and sulfur production [5], or burning the hydrogen sulfide itself in electric power stations, as proposed by L. Goltsova and L. Yutkin [6].

R&D works exist, dealing with high temperature solid fuel cell operating with hydrogen sulfide in gaseous phase [7], as well as electrochemical process in aqueous media [8-10] with elemental sulfur or poly-sulfides as products. These cells, however, use iron containing catalyst as an electron acceptor at the anode that is heavily corroded by H<sub>2</sub>S and thus they are inappropriate for long term durability.

The present paper is dedicated to the study of H<sub>2</sub>S oxidation at low concentrations for use in a

newly developed H<sub>2</sub>S/O<sub>2</sub> (air) fuel cell, producing electricity as a desirable product in the context of the Hydrogen-Energy-System [11]. The proposed process diagram is presented in Fig. 1. The process produces energy by: pumping saline water (1) and passing it through the anodic compartment of a sulfide-driven fuel cell (3). Atmospheric oxygen (2) is used as oxidizer in the cathodic compartment. The produced energy could be applied for further hydrogen production by splitting water in the electrolyser (4) and produced hydrogen is stored in (6). Clean water is discharged into the sea (5).

The electrochemical reactions in the known fuel cells [8-10] converting sulfide to sulfur are:

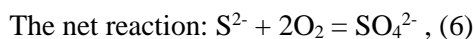
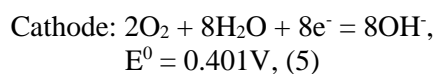
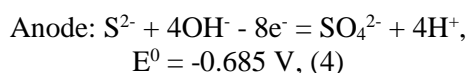


However, the anodic process of sulfide oxidation could be carried out to different final products (elemental sulfur, poly-sulfides, or sulfates). Elemental sulfur and poly-sulfides are market products, but in this process they are produced in low amounts and in a colloidal state. Another disadvantage of elemental sulfur as a final product is the occurrence of anode passivation. An alternative way is the oxidation to sulfate, which is very attractive, since the sulfate anions can be

\*To whom all correspondence should be sent:

E-mail: duzun@bas.bg

returned back to the sea at no pH changes. The electrode reactions leading to sulfate as a final product are as follows:



This process is thermodynamically feasible. The reactions correspond to Eqs. (4-6). The enthalpy of the net reaction is  $\Delta H = -788$  kJ/mole hydrogen sulfide [12]. It is sufficient for production of 1.82 moles of hydrogen, taking into account the losses due to the overpotential. Hence, the proposed fuel cell could be used either for net energy production or for electrolysis ( $\text{H}_2\text{S}$ ) corresponding to Fig.1.

The theoretical open circuit potential for the above process is also higher,  $E_{\text{ocp}} = 1.086$  V [13], compared to the oxidation of sulfide to elemental sulfur, where  $E_{\text{ocp}} = 0.909$  V [13]. The generated electric power may be used further to produce hydrogen from the already de-sulfurized water. It should be noted that sulfide-to-sulfate oxidation

passes through some intermediate reactions (consecutive oxidation of sulfide to sulfur, sulfite and finally to sulfate). Moreover, other reactions are possible, e.g. thiosulfate, dithionate, and polysulfide formation observed at higher initial sulfide concentrations.

The feasible utilization of sulfide ions to produce electromotive force in the fuel cell depends on the cell efficiency, i.e. the conversion rate of sulfide into sulfur or sulfate per unit time in the anodic compartment of the cell. For this reason the choice of appropriate catalysts for sulfide to sulfate oxidation is very important, so different catalysts have been tested in previous studies. Mao et al. [14] discussed various electrochemical methods to convert hydrogen sulfide to its elements, including high temperature electrolysis in alkaline solution using graphite, Pt and  $\text{Mn}^+$  ions. Several authors used ferric and cobalt cations [5,15,16] to catalyse sulfite to sulfate oxidation. Cobalt and carbon compounds, composite compounds like perovskites [5, 17], as well as CoPc [16, 18], have been found to be suitable for sulfide oxidation.

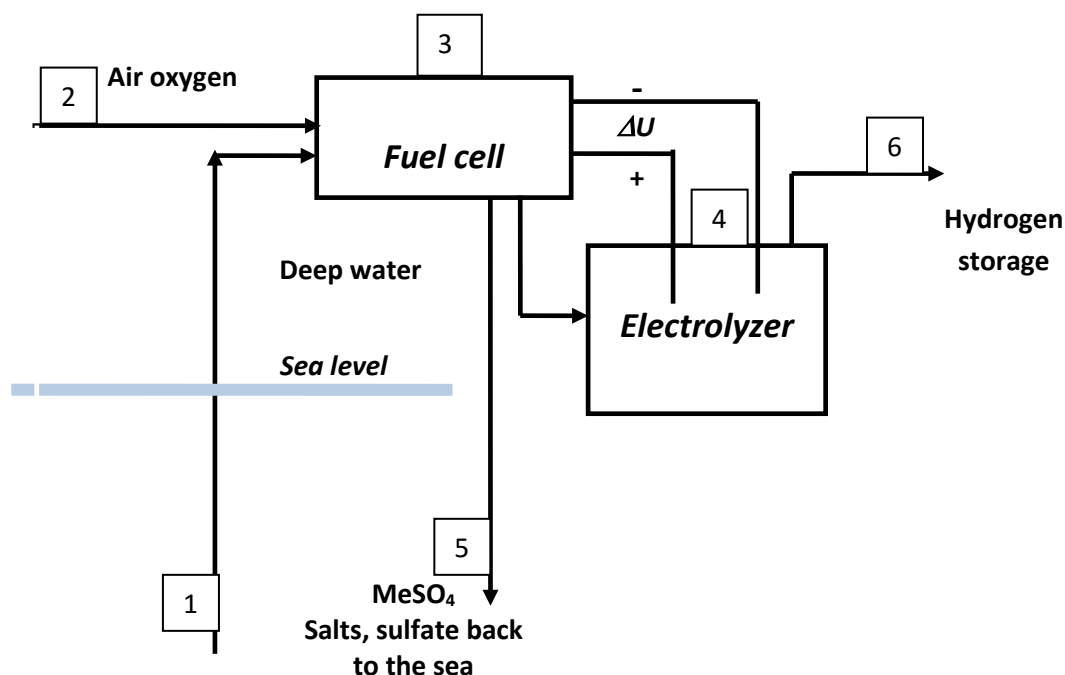


**Fig.1.** Schematically proposed process diagram for hydrogen production by electrolysis using sulfide driving fuel cell: 1- Deep sea waters containing sulfide; 2- Air oxygen; 3- Sulfide driving fuel cell; 4 – Electrolyzer; 5 -  $\text{MeSO}_4$ , sulfates and salts back to the sea; 6 – Hydrogen storage.

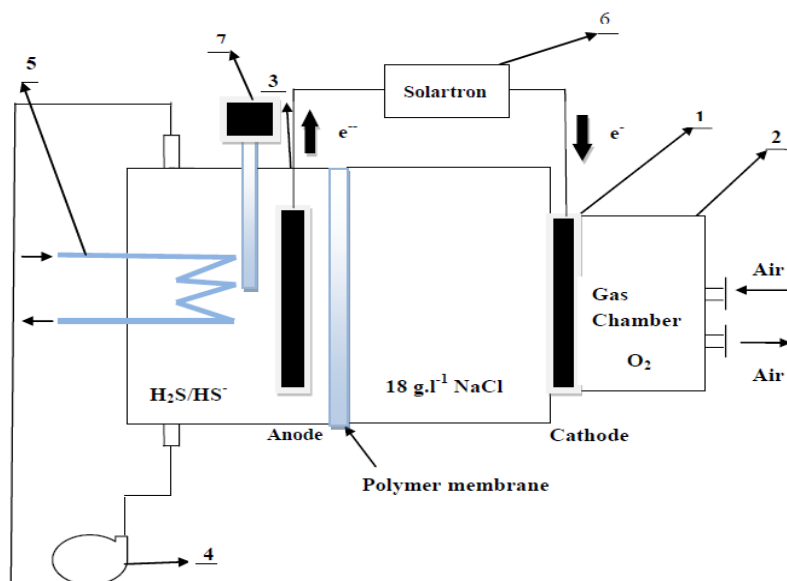


**Fig.2.** Scheme of H<sub>2</sub>S/O<sub>2</sub> fuel cell: 1 – Gas diffusion electrode; 2 - gas chamber; 3 – working electrode (anode); 4 – peristaltic pump; 5 – thermostat; 6 – Solartron; 7 – reference electrode.

## EXPERIMENTAL

### Experimental equipment and conditions

The electrochemical cell and setup are presented schematically in Fig.2. The cell consists of oxygen (air) gas-diffusion electrode (GDE) – (1) with gas chamber - (2) and immersed HS<sup>-</sup> electrode (anode) – (3). The oxygen (air) electrode, similar to the previously developed GDE in the Institute of Electrochemistry and Energy Systems and described in [19, 20].

GDE is double layered: gas diffusion layer of 50 mg.cm<sup>-2</sup> teflonized carbon black (35 % Teflon) and active layer of 20 mg.cm<sup>-2</sup> cobalt-tetra-methoxy-phenyl-porphyrin (CoTMPP) deposited on carbon black. The GDE works quite efficiently in alkaline, as well as in neutral electrolytes, so no experiments have been carried out on air electrode. Our efforts have been focused on anode (HS<sup>-</sup> oxidation electrode) and fuel cell as a whole.

The cell (from plexiglas) volume is 150 ml with possibility of electrolyte circulation – (4), and heating – (5). The anode and cathode electrolyte chambers are separated by a membrane (Nafion, PVC, etc.).

The H<sub>2</sub>S concentration in the electrolyte has been varied in the range 100 – 20 000 mg.l<sup>-1</sup> introduced as NaHS. This range has been selected having in mind two reasons: 1) the electrochemical process is very slow (does not practically occur) at lower concentrations, especially at the naturally encountered concentration of about 9 mg/l [21] and 2) higher concentrations are studied in previous investigations [5, 7]. Supporting electrolyte of 18 g.l<sup>-1</sup> NaCl (similar to the concentration in Black Sea

waters), is added to the electrolyte. The experimental setup in Fig.2 has been used for study fuel cell mode too. A Solartron 1286 Electrochemical Interface – (6), is used for the galvanostatic measurements. A reversible hydrogen electrode (7) by “Gaskatel GmbH”, Germany is used as a reference electrode. A minimum of four measurements were made for each result to achieve better reproducibility. Arithmetic averages are presented in the graphs.

### Electrode preparation

All electrodes studied are of immersed type and have geometrical area of 10 cm<sup>2</sup>.

The electrodes are prepared from a mixture of the catalysts and teflonized carbon black (35% Teflon) as a binder. Two types of carbon black have been used – Vulcan XC-72 and acetylene blacks. The mixture is pressed onto both sides of a stainless steel current collector at 300°C and pressure of 300 atm.

Several home-made catalysts have been studied:

- (i) DG (standard Degussa carbon black) + 20 % CoPc;
- (ii) La<sub>1.3</sub>Sr<sub>0.7</sub>NiO<sub>4</sub> (perovskite);
- (iii) bulk graphite.

### Analytical methods

The total amount of sulfide and sulfite ions was determined iodometrically with starch as indicator [22]. Sulfides were separately determined photometrically with N,N-dimethyl-n-phenylenediamine in presence of Fe(III) with formation of methylene blue [23 - 25]. This method allows increasing the sensitivity of determination

twice. The presence of thiosulfates, sulfites and sulfates was qualitatively checked too. Thiosulfates form a unstable purple complex with Fe (III). The opalescence of the solution after addition of barium cations shows the presence of sulfite and sulfate. The dissolution of the deposit in concentrated hydrochloric acid proves the presence of sulfite, whereas barium sulfate remains non-dissolved [26]

## RESULTS AND DISCUSSION

### *Electrode properties and optimization*

The immersed type electrodes for the oxidation of H<sub>2</sub>S were optimized with respect to the catalyst used, electrode thickness and mass ratio between catalysts and binder, varying one parameter at a time and keeping the others constant.

### *Catalyst optimization*

Four different catalysts were studied:

1. (DG + 20 % CoPc) + 35 % teflonized Vulcan XC-72 (DGCPV);
2. (DG + 20% CoPc) + 35 % teflonized acetylene black (DCPAB);
3. La<sub>1.3</sub>Sr<sub>0.7</sub>NiO<sub>4</sub> + 35 % teflonized Vulcan XC-72 (LSNV)
4. Bulk graphite.

The galvanostatic volt - ampere curves obtained with the different catalysts are presented in Fig.3. It

is seen that the electrodes containing DGCPV and LSNV as catalysts give lower over potential characteristics, so only these two catalysts were used further on.

### *Electrode composition*

The working electrode (anode) potential at a fixed current density ( $i=10 \text{ mA.cm}^{-2}$ ) was selected as a criterion for the quality of the electrode. With this criterion, electrodes with different amounts, resp. ratios of the components were compared to find the optimum composition.

First we wanted to establish the most appropriate amount of catalyst plus teflonized carbon black. For this reason the ratio was held constant (50:50 % wt.) and the total amount was varied. A roughly linear dependence was established between the amount of catalyst plus teflonized carbon black and the anodic potential at  $i=10 \text{ mA.cm}^{-2}$ . Thus the lowest possible amount of the components will be most appropriate from the point of view of over potential. The mechanical stability, however, must also be taken into account. It turns out that about  $60 \text{ mg.cm}^{-2}$  of the mass are needed for the full coverage of the current collector and for a reasonable mechanical stability. So we chose this value for the further optimization.

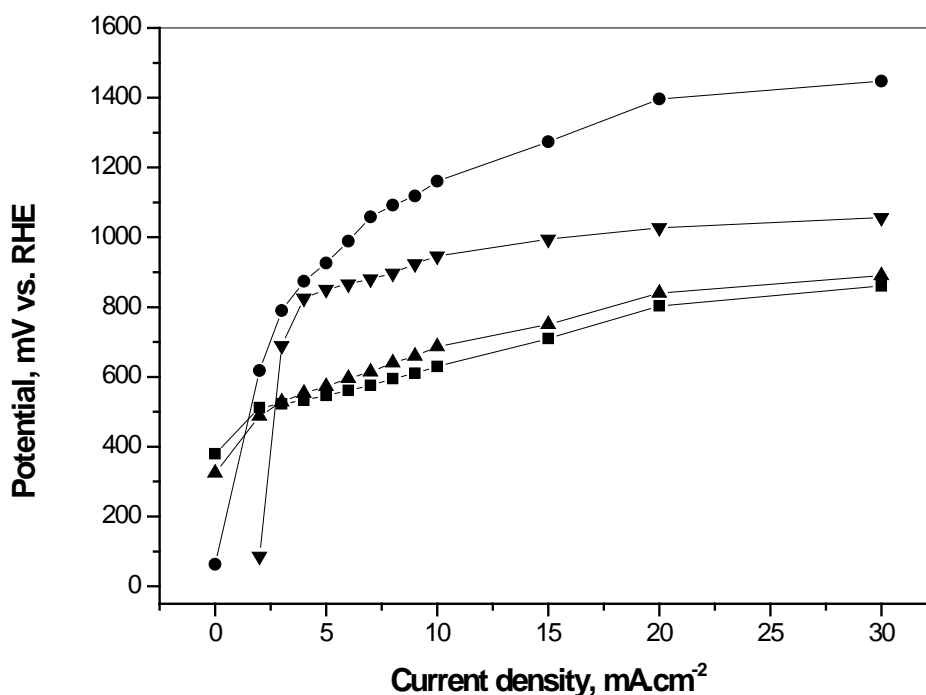


**Fig.3.** Working electrode potential vs. current density for the oxidation of H<sub>2</sub>S with different catalysts: ●– graphite, ▼ – DCPAB, ▲ - DGCPV, ■ - LSNV.; electrolyte - 1g.l<sup>-1</sup> sulfide ions + 18 g.l<sup>-1</sup> NaCl.



Next, the ratio between the binder (35 % teflonized Vulcan XC 72) and the catalyst has to be optimized. Fig. 4 shows the dependence of the working electrode (anode) potential at constant current density ( $i = 10 \text{ mA}\cdot\text{cm}^{-2}$ ) on the amount of  $\text{La}_{1.3}\text{Ni}_{0.7}\text{SrO}_4$  catalyst (in weight %). A pronounced minimum is observed at 45% catalyst, so this value was used further for the preparation of electrodes.

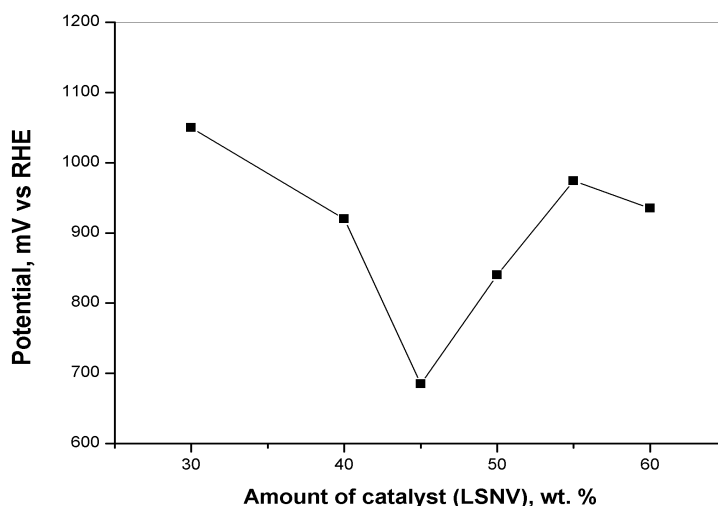


**Fig.4.** Optimization of the amount of catalyst at constant electrode thickness  $-110 \text{ mg}\cdot\text{cm}^{-2}$ . Working electrode – LSNV + teflonized carbon black; electrolyte –  $1 \text{ g}\cdot\text{l}^{-1}$  sulfide ions +  $18 \text{ g}\cdot\text{l}^{-1}$  NaCl.

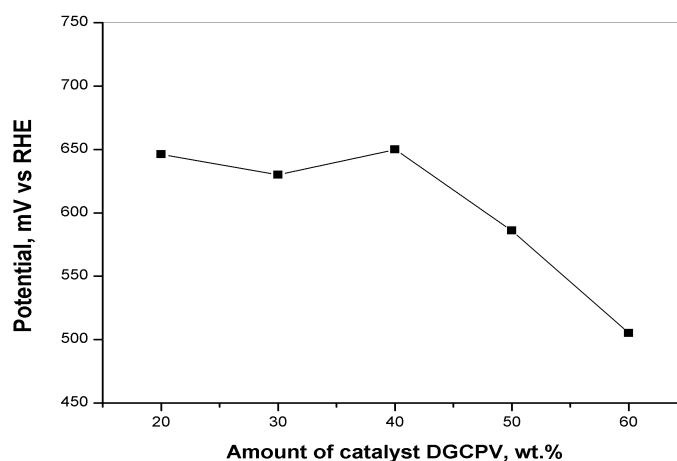


**Fig.5.** Optimization of the amount of catalyst at constant electrode thickness -  $60 \text{ mg}\cdot\text{cm}^{-2}$ . Working electrode – DGCPV + teflonized carbon black; electrolyte -  $1 \text{ g}\cdot\text{l}^{-1}$  sulfide ions +  $18 \text{ g}\cdot\text{l}^{-1}$  NaCl.

The electrochemical characteristics of the optimized electrodes are shown in Fig. 6. It is seen that both electrodes provide fairly similar electrochemical behaviour.

#### *Temperature dependence*

The influence of temperature on the reaction rate is shown in Fig. 7 for the optimized electrode with perovskite catalyst. It may be concluded that increasing the temperature above  $60 \text{ }^\circ\text{C}$  does not

For the (DG + 20 % CoPc) catalyst (Fig. 5) the lowest over potential appears at 50 and 60% catalyst content, but the electrodes are not mechanically stable. So in this case we chose the 30% catalyst content for the further studies because of the small local minimum and the pronounced stability in time.

significantly improve the rate. Tafel-type dependencies can be plotted from the current-potential data for each temperature. Although the slopes of these dependencies indicate the presence of diffusion limitations, they may be used to calculate apparent values for the exchange current densities and to plot an Arrhenius-type dependence (Fig. 8). The apparent energy of activation for the electrochemical reaction, calculated from the slope of the Arrhenius plot is  $E_a = 18.2 \text{ kcal}\cdot\text{mol}^{-1}$ , which

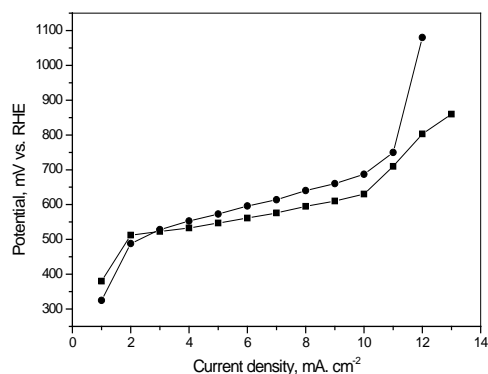


**Fig.6.** Working electrode potential vs. current density for the optimized electrodes: ■ – DGCPV ●– LSNV. Electrolyte - 1 g.l<sup>-1</sup> sulfide ions + 18 g.l<sup>-1</sup> NaCl.

corresponds well with the value found for the catalytic oxidation of sulfides by hydrogen peroxide, [27], i.e.  $E_a = 25.85 \text{ kcal.mol}^{-1}$

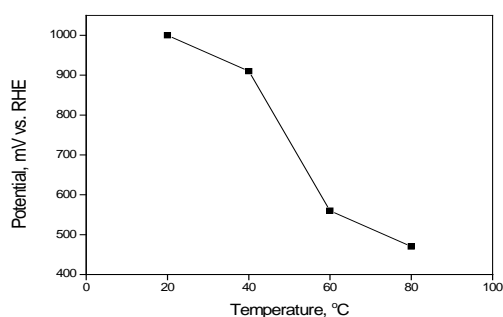


**Fig.7.** Dependence of the electrode potential on the temperature at constant current density ( $i=10 \text{ mA.cm}^{-2}$ ). Working electrode - DGCPV. electrolyte 200 mg.l<sup>-1</sup> sulfide ions + 18 g.l<sup>-1</sup> NaCl.

### *H<sub>2</sub>S driven fuel cell*

The application of H<sub>2</sub>S oxidation for the construction of a fuel cell has been described by Pujare et al. [28] with a solid oxide electrode at high temperature. We would like to show that the electrochemical oxidation of H<sub>2</sub>S at room temperature and low H<sub>2</sub>S concentrations can also be used to promote electromotive force and hence be used as a fuel cell. In order to use the H<sub>2</sub>S/O<sub>2</sub> electrochemical system as a fuel cell, one must ensure a reasonable reaction rate of the electrochemical reaction. As established earlier [21] the natural concentration of H<sub>2</sub>S in the Black Sea waters ( $\approx 9 \text{ mg/l}$ ) is definitely not enough to ensure usable reaction rates and a preliminary preconcentration is needed. In order to check which concentration of H<sub>2</sub>S will yield reasonable reaction rates, we studied the concentration dependence of the electrode potential at our standard galvanostatic conditions ( $i=10 \text{ mA/cm}^{-2}$ ) and in the concentration range discussed in section 2.1. A gradual increase

of the steady state anodic potential at  $i= 10 \text{ mA. cm}^{-2}$  is observed, as seen from Fig. 9, so one can select a suitable concentration for the application as a fuel cell.

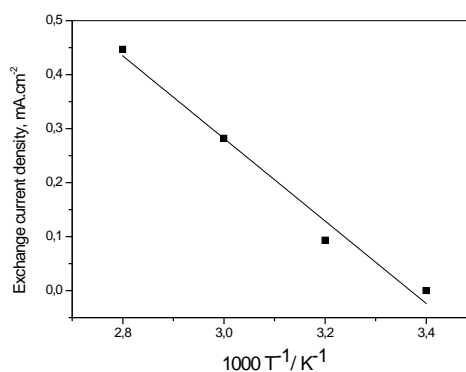


**Fig.8.** Electrochemical Arrhenius plot for the working electrode with LSNV. Electrolyte - 200 mg.l<sup>-1</sup> sulfide ions+ 18 g.l<sup>-1</sup> NaCl.

To study the system behaviour with time, we start with definite H<sub>2</sub>S and SO<sub>3</sub><sup>2-</sup> concentrations and follow their variation in time when a constant current density of  $i=10 \text{ mA.cm}^{-2}$  is imposed on the cell. The initial concentrations were chosen  $C_{\text{H}_2\text{S}} = 186 \text{ mg/l}$  and  $C_{\text{SO}_3} = 243 \text{ mg/l}$  at pH = 11.6 (Table 1). The open circuit potential was about 300 mV and the potential of the working electrode (anode) was  $E = 204 \text{ mV}$ . Oxygen (air) GDE electrode has a constant potential  $E = 750 \text{ mV}$  (RHE) during the whole experiments. As current is imposed, the HS<sup>-</sup> electrode (anode) potential increases and the concentrations of sulfide and sulfite ions change. These concentrations were checked analytically in intervals of 2 hours, the potential was recorded continuously.

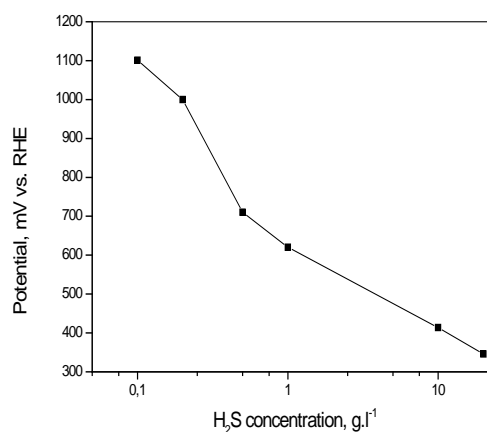


**Fig.9.** Dependence of the steady state working electrode potential on sulfide concentration at constant current density ( $i=10 \text{ mA.cm}^{-2}$ ). Working electrode - DGCPV. Supporting electrolyte 18 g.l<sup>-1</sup> NaCl.

The variation of the working electrode potential with time is shown in Fig. 10 and the variation of the concentrations in Table 1. It is seen that up to the first analytical determination of sulfide and sulfite ions, the potential is already rather high.

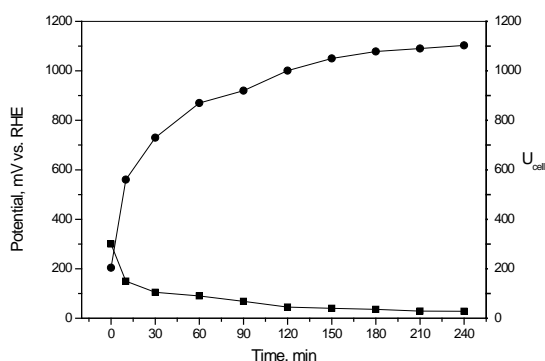


**Fig.10.** Fuel cell mode test (working electrode potential variation with time at constant current density,  $i=10 \text{ mA.cm}^{-2}$ ). Working electrode - DGCPV. Electrolyte –  $186 \text{ mg.l}^{-1}$  sulfide ions +  $18 \text{ g.l}^{-1}$  NaCl, ● – working electrode potential, ■ -  $U_{\text{CELL}}$ .

It should be noted that the decrease in sulfide concentration (Table 1) does not correspond stoichiometrically to the increase in sulfite concentration.

**Table 1.** Experimental data for the time variation of sulfide and sulfite concentrations in the fuel cell mode under galvanostatic conditions:  $i = 10 \text{ mA.cm}^{-2}$

Time, hour	Potential, mV	Concentration of sulfide, $\text{mg.l}^{-1}$	Concentration of sulfite, $\text{mg.l}^{-1}$
0	204	186	243
2	1001	69,7	354
4	1103	10	470

This implies the formation of other sulfur-containing intermediates as well. Please note, however, that after four hours, when the electrochemical process has come to a stop, sulfate ions are qualitatively detectable and no poisoning of the electrode is observed.

The estimated power of the cell used (with  $10 \text{ cm}^2$  electrode) is  $7.5 \text{ mW}$ . The initial cell voltage of  $\approx 500 \text{ mV}$  corresponds to a cell efficiency of  $47 \%$  in the case of complete sulfide to sulfate conversion.

## CONCLUSIONS

Several catalysts have been tested for the anodic oxidation of sulfide to sulfite and sulfate. The electrodes prepared with CoPc and perovskite ( $\text{La}_{1.3}\text{Ni}_{0.7}\text{SrO}_4$ ) have been optimized and showed appropriate electrochemical characteristics. The influence of temperature and  $\text{HS}^-$  concentration has been revealed.

The adequacy of a new developed sulfide driven fuel cell has been tested and proved using optimized electrodes and conditions.  $\text{H}_2\text{S}/\text{O}_2$  fuel cell at room temperature and low  $\text{HS}^-$  concentrations has reached reasonable current densities due to sulfide to sulfite and sulfate oxidation without electrode poisoning

Based on these results we can go further to design practically applicable fuel cell based on sulfide to sulfate oxidation in liquid media at room temperatures.

**Acknowledgement.** This work was supported by the project Hydrogen production from Black Sea water by sulfide-driven fuel cell HYSULFCEL (bs-era.net) of the 7 FP of the European Union, contract DNS7RP 01/32 of the Ministry of Education and Science of Republic of Bulgaria.

## REFERENCES

1. A. Midilli, M. Ay, A. Kale, T. N. Veziroglu, *Int. J. Hydrogen Energy*, **32**, 117 (2007).
2. K. Petrov, *Int. J. Hydrogen Energy*, **16**, 805 (1991).
3. T. Chivers, J.B. Hyne, C. Lau, *Int. J. Hydrogen Energy*, **5**, 499 (1980).
4. S.Z. Baykara, E.H. Figen, A. Kale, T. Nejat Veziroglu, *Int. J. Hydrogen Energy*, **32**, 1246 (2007).
5. K. Petrov, S. Srinivasan, *Int. J. Hydrogen Energy*, **21**, 163 (1996).
6. L. Goltseva, A. Yutkin, Black Sea, Inventor, **2**, 7, (1996).
7. K. Nygren, R. Atanasoski, W. H. Smyrl, E. A. Fletcher, *Energy*, **14**, 323 (1989).
8. D. W. Kalina, E. T. Maas Jr., *Int. J. Hydrogen Energy*, **10**, 157 (1985) -162.
9. B. Dandapani, B.R. Sharifker and J. O'M Bockris, *Sym 21<sup>st</sup> Intersociety Energy Conversion Engineering Conf.*, **1**, 262 (1986).
10. P. K. Dutta, K. Rabaey, Z. Yuan and J. Keller, *Water Res.*, **42** 4965 (2008).
11. J. O'M. Bockris, T. N. Veziroglu, *Int. J. Hydrogen Energy* **8**, 323 (1983).
12. K. H. Naeser, *Physikalisch-Chemische Rechenaufgaben*, VEB Deutscher Verlag fuer Grundstoffindustrie, Leipzig, 1963. (in German).
13. P. U. Rachinskii, P. G. Romankov, D. A. Fridrohsberger, Handbook of Chemistry, Electrode processes, Chemistry – Nauka, Moscow, 2<sup>nd</sup> edn., vol. **3** 1965
14. Z. Mao, A. Anani, R.E. White, S. Srinivasan, A.J. Appleby, *J. Electrochem. Soc.*, **138**, 1299 (1991).
15. J. Zaman and A. Chakma, *Fuel Process. Technol.* **41**, 159 (1995).
16. K. Petrov, I. Nikolov, T. Vitanov, D. Uzun, V. Ognjanov, *Bulg. Chem. Comm.*, **42**, 189 (2010).
17. K.T Chuang, J.C Donini, A.R Sanger, S.V Slavov, *Int. J. Hydrogen Energy*, **25**, 887 (2000).
18. O.M. Ilinitich, Yu.S. Vetchinova, *Catal. Today*, **25**, 423 (1995).

19. I. Iliev, S. Gamburgzev, A. Kaisheva, *J. Power Sources*, **17**, 345 (1986).
20. I. Iliev, A. Kaisheva, Z. Stoynov, H. J. Pauling, Proceedings of the 3<sup>rd</sup> International Battery Recycling Congress, Noordwejk an Zee, The Netherlands (1997)
21. K. Petrov, S.Z. Baykara, D. Ebrasu, M. Gulin, A. Veziroglu, *Int. J. Hydrogen Energy*, **36**, 8936 (2011).
22. N. P. Penchev, B. N. Zagorchev, *Qualitative Analysis, Science and Art* 2<sup>nd</sup> edn., 1956. (in Bulgarian)
23. A. Busev, L. Simon, *Anal. Chem sulfur*, Nauka, Moskow 1975
24. W. Fresenius, G. Jander, *Handbook for Anal. Chem.*, Springer 2<sup>th</sup> edn., 1967
25. M. G. Bapat, B. Z. Scharma, *Anal. Chem.*, **157**, 258 (1957)
26. N. P. Penchev, B. N. Zagorchev, *Analytical Chemistry, Qualitative Analysis*, 1964. (in Bulgarian)
27. N. Ahmad, S. Maitra, B. K. Dutta, F. Ahmad, *J. Env. Sci.*, **211**, 1735 (2009).
28. N.U. Pujare, K.W. Semkow, A.F. Sammells, *J. Electrochem. Soc.*, **134**, 2639 (1987).

## ЕЛЕКТРОХИМИЧЕН МЕТОД ЗА ПОЛУЧАВАНЕ НА ЕНЕРГИЯ ОТ СЕРОВОДОРОДА НА ЧЕРНОМОРСКИТЕ ВОДИ В ГОРИВЕН ЕЛЕМЕНТ ЗАДВИЖВАНА СЪС СУЛФИД

Д. Узун<sup>1\*</sup>, Е. Разказова-Велкова<sup>2</sup>, К. Петров<sup>1</sup>, В. Бешков<sup>2</sup>

<sup>1</sup>Институтът по електрохимия и енергийни системи „Акад. Евгени Будевски“, БАН; 1113 София, ул. Акад.Г.Бончев, бл. 10

<sup>2</sup>Институт по Инженерна химия, БАН; 1113 София, ул. Акад.Г.Бончев, бл. 103

Получена на 25 септември 2014 г., приета на 30 октомври 2014 г.

(Резюме)

Целта на настоящата работа е изследване и развитие на икономически осъществим електрохимичен метод за извличане на H<sub>2</sub>S от водите на Черно море със съдържание (C<sub>H2S</sub> ~ 9 мг.л<sup>-1</sup>), и използването му в горивен елемент H<sub>2</sub>S/O<sub>2</sub> (въздух). Изследвани са разтвори с ниски концентрации на HS<sup>-</sup> и на NaCl, близки до условията в дълбините на Черно море. Намерени са подходящи катализатори, електроди и условия за електрохимично окисление на сулфид HS<sup>-</sup> директно до сулфити и сулфати. Теставани са различни катализатори за анодно окисление на HS<sup>-</sup>: графит, кобалтов фталоцианин (CoPc) и перовскит (La<sub>1.3</sub>Str<sub>0.7</sub>NiO<sub>4</sub>). По вереме на окислението не е наблюдавано каталитично отравяне на продуктите (сулфити и/или сулфати). Измерени са характеристиките на сулфид задвижваният горивен елемент с оптимизирани електроди за окисление на HS<sup>-</sup> (аноде). Получена е електрическа мощност от P = 7,5 MW.

## Electrochemical reduction of sulfur dioxide by oxidation of hydrogen sulfide in aqueous media

D. Uzun<sup>1\*</sup>, E. Razkazova–Velkova<sup>2</sup>, V. Beschkov<sup>2</sup>, G. Pchelarov<sup>1</sup>, K. Petrov<sup>1</sup>

<sup>1</sup>*Institute of Electrochemistry and Energy Systems, Bulgarian Academy of Sciences, Acad. G. Bonchev Str., Bl.10, 1113 Sofia, Bulgaria*

<sup>2</sup>*Institute of Chemical Engineering, Bulgarian Academy of Sciences, Acad. G. Bonchev Str., Bl. 103, 1113 Sofia, Bulgaria*

Received September 25, 2014, Accepted October 30, 2014

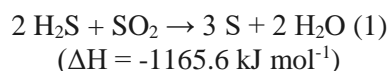
The reduction of sulfur dioxide at high temperature is reported. This article reveals that electrochemical reduction of SO<sub>2</sub> is possible at room temperature. Electrochemical processes for treatment of H<sub>2</sub>S in Black Sea waters and flue gases are presented in order to minimize their environmental impact. We found suitable conditions and electro catalysts for the realization of the process to reduce the flue gases from thermal power plants along the coast of the Black Sea and to solve the problem of hydrogen sulfide in the deep Black Sea waters.

**Key words:** Sulfur dioxide reduction, Hydrogen sulfide oxidation, Black Sea.

### INTRODUCTION

Various kinds of electrode materials were utilized in the past, namely mercury, gold, platinum, bismuth, copper, iron phthalocyanine on graphite and uranium-iron alloys. The electrochemical reduction of sulfur dioxide in aqueous solutions has been investigated since the thirties of the last century. The studies mentioned above focus on obtaining sodium dithionate (sodium hydrosulfite), an important product in industry. Previous studies do not fully explain the electrochemical process in the reduction of sulfur dioxide [1].

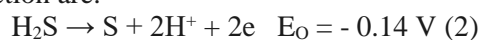
The chemical reduction of SO<sub>2</sub> together with the oxidation of H<sub>2</sub>S is the basis for the so-called Claus process, in accordance with the following general reaction:



The Claus process takes place at temperatures above 1300 °C [2], however, by utilizing different catalysts these can be reduced to 250-850 °C. The use of different types of composite compounds containing transition metals significantly reduces the temperatures at which the above reaction takes place, but does not solve the problem entirely [3-5]. An example of the use of catalysts in the reduction of sulfur dioxide by the oxidation of hydrogen sulfide in accordance with the above reaction using methane at temperatures of up to 1000 °C is given in [6].

The thermodynamic potentials of oxidation and

reduction are:



These electrochemical redox reactions can occur due to the potential difference of  $\Delta E = 0.30 \text{ V}$  as indicated for reactions 2 and 3, which follow from the theory for concurrent redox reactions (corrosion) on dispersed micro-galvanic elements [7].

Their speed is determined with the aid of volt-ampere characteristics in accordance with the so called additive principle [8].

An advantage of these electrochemical reactions is that they are able to completely convert the initial reagents (concentrations of CH<sub>2</sub>S, SO<sub>2</sub> = 0 [9], which is difficult given the chemical kinetics [10].

In accordance with the theory, we consider the pair H<sub>2</sub>S and SO<sub>2</sub>. The oxidation of hydrogen sulfide was studied in our previous work, the most suitable catalyst and conditions were found while the catalysts and binder were optimized by varying one parameter at a time and keeping the others constant.

The simultaneous reduction of SO<sub>2</sub> and the purification of hydrogen sulfide and sulfur dioxide fluids are reviewed in this work. The purpose of the investigation is to examine the process of oxidation of hydrogen sulfide and the reduction of sulfur dioxide in the chemical reactor by electrochemical (galvanic) route under normal atmospheric conditions. This is part of a project to simultaneously extract the sulfur dioxide contained in the smoke fumes generated by coal power plants

\*To whom all correspondence should be sent:  
E-mail: duzun@bas.bg

and hydrogen sulfide from sea water along the Black Sea coastline.

## EXPERIMENTAL CONDITIONS

### Apparatus

We utilized a three-electrode cell to complete the electrochemical reduction of sulfur dioxide. In the present work we used sulfurous acid to attain an environment where we have sulfur dioxide (~5-6% SO<sub>2</sub>). Also we set aside 18 g/l NaCl, equivalent to the content of salt in the waters of the Black Sea. We added 1 M NaOH in order to equilibrate the conditions under which we studied the oxidation of hydrogen sulfide [11]. The cell had a capacity of 50 ml in volume. The electrolyte was stirred continuously with a magnetic stirrer. The sulfurous acid was 1/5 of the total amount of the solution. We obtained a sulfur dioxide content of about 1%, the same as the quantity found in the smoke fumes generated by coal power plants.

Shown in Fig.1 is a three-electrode cell for electrochemical reduction of sulfur dioxide. With the help of the cell in conjunction with a Solartron 1280 and by constantly stirring with a magnetic stirrer, we measured the polarization curves and the reduction of sulfur dioxide in different solutions

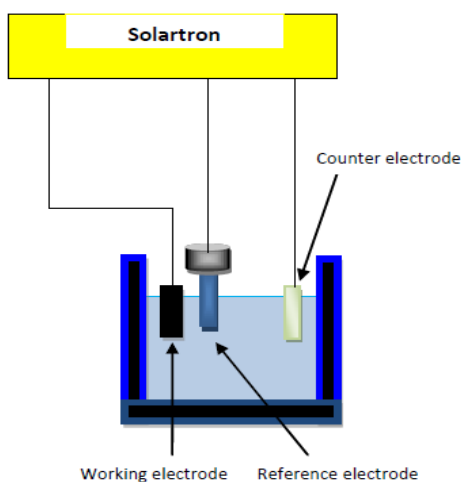


Fig.1. Three-electrode cell

The diagram shown in Fig.1 presents a model three-electrode cell with the help of which our measurements were carried out.

Shown in Fig. 2 is a chemical reactor in which the simultaneous oxidation of hydrogen sulfide and reduction of sulfur dioxide takes place. The electrolyte is stirred constantly with a magnetic stirrer. The catalyst Degussa carbon + 20% CoPc deposited on 35% teflonized Vulcan XC-72 is placed in the reactor.

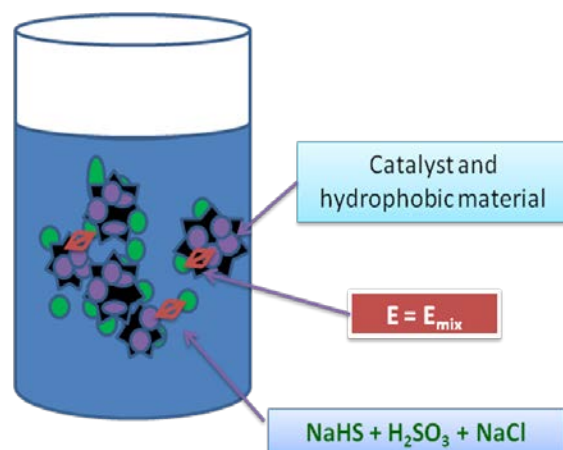


Fig.2. Chemical reactor

### Preparation of the electrode for SO<sub>2</sub> reduction

All electrodes studied are of the immersed type and have a geometrical area of 1 cm<sup>2</sup>. The electrodes are prepared from a mixture of the catalysts and teflonized carbon black (35%. Teflon) as a binder. Two types of carbon black were used – Vulcan XC-72 and acetylene black. The mixture is pressed onto both sides of a stainless steel current collector at 300 °C at a pressure of 300 atm. Several home-made catalysts as well as CoPc [12] were deposited on carbon and pyrolyzed. Commercial catalysts were also studied:

- (i) DG (standard Degussa carbon black) + 20 % CoPc;
- (ii) La<sub>1.3</sub>Sr<sub>0.7</sub>NiO<sub>4</sub> (perovskite);
- (iii) bulk graphite;
- (iv) DG (standard Degussa carbon black) + 20 % CoPc + 6 % Pt;
- (v) Pt.

### Chemical analysis

The concentrations of hydrogen sulfide and sulfur dioxide after mixing and during the experiment were determined iodometrically and only the sulfide - by masking sulfite with formalin [13,14]. An indication that polysulfides were obtained was the colour change of the solution to yellow-green. On addition of hydrochloric acid it was clarified and a sulfur precipitate appeared (qualitative reaction for polysulfides detection). The opalescence when barium chloride is added indicates the presence of sulfates (qualitative reaction for detection of sulfates) [17].

The total amount of sulfide and sulfite ions was determined iodometrically with starch as indicator. Sulfides were separately determined photometrically with N,N-dimethyl-n-phenylenediamine in presence of Fe(III) with formation of methylene blue [15,16]. This method allows increasing the sensitivity of determination

twice. The presence of thiosulfates, sulfites and sulfates was qualitatively checked too. Thiosulfates form a unstable purple complex with Fe (III). The opalescence of the solution after addition of barium cations shows the presence of sulfite and sulfate. The dissolution of the deposit in concentrated hydrochloric acid proves the presence of sulfite, whereas barium sulfate remains undissolved [17].

## RESULTS AND DISCUSSION

### Reduction of sulfur dioxide

Electrodes of the immersed type (1 cm<sup>2</sup>) were used for the reduction of SO<sub>2</sub>, which were optimized in previous studies for oxidation of H<sub>2</sub>S [11]. They were optimized with respect to the catalyst used, the electrode thickness and mass ratio between catalysts and binder, varying one parameter at a time and keeping the others constant. As a result of the optimizations carried out the electrodes were composed of: (i) - 42 mg 35% teflonized Vulcan XC-72 +18 mg DG (standard Degussa carbon black) + 20% CoPc +6% Pt; (ii) - 42 mg 35% teflonized Vulcan XC-72 +18 mg DG (standard Degussa carbon black) + 20% CoPc; (iii) - 60 mg of 35% teflonized Vulcan XC 72 +50 mg La<sub>1.3</sub> Sr<sub>0.7</sub> NiO<sub>4</sub> (perovskite).

The results obtained are the average values of at least three optimized electrodes.

The volt-ampere dependence curves of the electrodes were obtained for reduction of SO<sub>2</sub> in an electrolyte of 1% vol. sulfurous acid + 1 M NaOH + 18 g/l NaCl. The electrocatalysts utilized were: DG (standard Degussa carbon black) + 20% CoPc; La<sub>1.3</sub>Sr<sub>0.7</sub>NiO<sub>4</sub> (perovskite); bulk graphite; DG (standard Degussa carbon black) + 20% CoPc + 6% Pt; (v) Pt.

Shown in Figure 3 are the optimized electrodes together with the catalysts selected for the reduction

From Figure 3 it can be seen that the substrate used (a) does not affect the catalysts studied by us. Good results were obtained from electrodes made of DG +20% CoPc + 6% Pt (d) containing Pt powder, but following long-term studies we found that the platinum is poisoned. The curves (b) and (c) are DG +20% CoPc and perovskite, respectively; these show that electrodes made of the catalyst cobalt phthalocyanine and perovskite are similar. In our further research the catalyst DG +20% CoPc will be investigated. of sulfur dioxide.

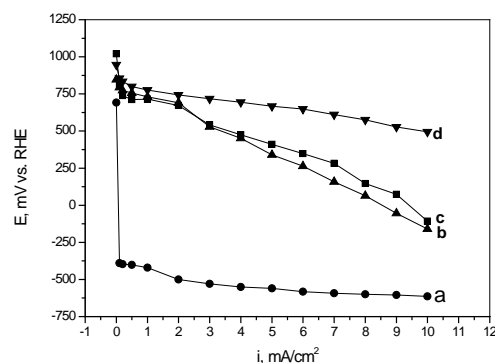


**Fig.3.** Polarization curves of sulfur dioxide reduction in aqueous electrolyte: SO<sub>2</sub> 1% vol. +1 M NaOH + 18 g.l<sup>-1</sup> NaCl. Tested electrodes are: a - type network (stainless steel); b - 35% teflonized Vulcan XC-72 and DG +20% CoPc; - perovskite; d - 35% teflonized Vulcan XC-72 and DG +20% CoPc + 6% Pt.

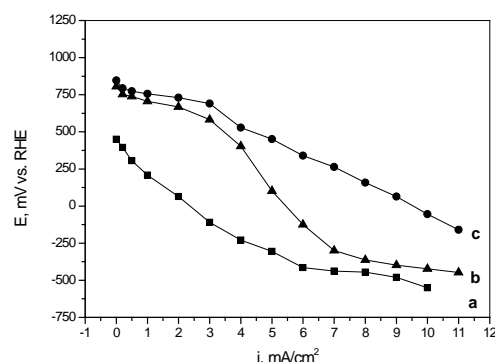


**Fig. 4.** Polarization curves for electrodes from teflonized Vulcan XC-72 and DG + 20 % CoPc, in different electrolytes: a – electrolyte 1 % SO<sub>2</sub> + 18 g/l NaCl; b - electrolyte 1 % SO<sub>2</sub> + 1 M NaOH; c - electrolyte 1 % SO<sub>2</sub> + 18 g/l NaCl + 1 M NaOH.

The catalyst selected was studied in different electrolytes. Shown in Figure 4 are the volt – ampere curves with the SO<sub>2</sub> reduction catalyst 35% Vulcan teflonized XC-72 and DG +20% CoPc in: a - 1% SO<sub>2</sub> + 18 g/l NaCl; b - 1% SO<sub>2</sub> + 1 M NaOH; c - 1% SO<sub>2</sub> + 18 g/l NaCl + 1M NaOH.

The figure shows that at higher currents in the absence of NaCl the conductivity falls [18] as shown by curve (b). It becomes clear from graph (a) that in a solution containing sulfur ions without NaOH, the kinetics of the processes changes yielding sulfur, as seen from the diagram [19].

### Proof of the electrochemical mechanism

The curve of oxidation of hydrogen sulfide (Fig. 5) was investigated in our previous work [11], currently this was utilized in order to substantiate the electrochemical mechanism.

The curve represents the reduction of sulfur dioxide with the optimized electrode containing: (i) 35 % teflonized Vulcan XC-72; (ii) DG + 20 % CoPc (at a ratio of 70:30). The reduction electrolyte was 1% SO<sub>2</sub> + 18 g / l NaCl + 1 M NaOH. From the curves

in Fig. 5 we found the mixed potential and the mixed current. From this it follows that the overall electrochemical reaction rate is  $i \approx 38 \text{ mA/cm}^2$ .

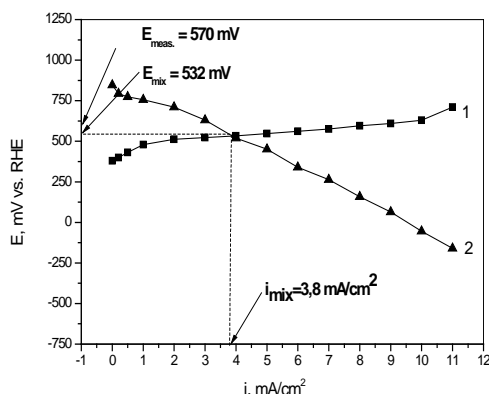


**Fig. 5.** Polarization curves for oxidation of  $\text{H}_2\text{S}$  [10] and reduction of  $\text{SO}_2$ .

The agreement between the mixed potential (in a solution containing hydrogen sulfide and sulfur dioxide  $E_{\text{mix}} (\text{H}_2\text{S}, \text{SO}_2) \approx 570 \text{ mV}$ ) and the potential calculated from the intersection of the partial curves ( $E_{\text{mix}} (\text{partial curves}) = 537 \text{ mV}$ ) is very good, since deviations for the porous electrodes about  $\Delta E \sim 30 \text{ mV}$  are acceptable [20]. This agreement is an indication of the electrochemical mechanism of the process. To confirm this assertion, we needed to measure the total rate of the reaction in the reactor (Fig. 2).

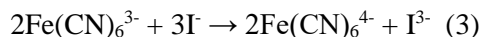
In the reactor shown in Fig. 2 we introduced the two fluids in the form of an electrolyte containing sulfur dioxide and hydrogen sulfide. The catalytic mass corresponded to the above optimized immersed electrode. The amount of  $10 \text{ cm}^2$  teflonized Vulcan XC-72 and catalyst is required for an electrode.

The studies were made using the chemical reactor with a solution (electrolyte)  $1\% \text{ SO}_2 + 18 \text{ g/l NaCl} + 1 \text{ M NaOH} + \text{Na}_2\text{S} \cdot 9\text{H}_2\text{O}$  as shown below (Table 1). The inlet and outlet concentrations, as well as the overall speed of the oxidation/reduction process, were found analytically and were compared with those calculated by the partial electrochemical speed curves,  $i \approx 3,8 \text{ mA/cm}^2$ .

**Table 1.**

Reagent	Initial concentration	Final concentration	$\Delta C$	$i = \Delta C/n.F$ $\text{mA.cm}^{-2}$
$\text{SO}_2 (C_s^{2-}, \text{mg.l}^{-1})$	570 (in 100 ml -57 mg $\text{SO}_3^{2-}$ )	145 (in 100 ml - 14.5 mg $\text{SO}_3^{2-}$ )	42.5 (for two h) - for 1 h 21.25	2.85 $\text{mA.cm}^{-2}$
$\text{H}_2\text{S}(C_s^{2-}, \text{mg.l}^{-1})$	400 (in 100 ml 40 mg $\text{S}^{2-}$ )	100 (in 100 ml 0)	40 (for two h) - for 1 h 20	3.35 $\text{mA.cm}^{-2}$

By matching the results shown in Table 1, we can conclude that the conversion of sulfide is electrochemically preferential as part of the reactants is converted chemically. Such a conclusion was made by Spiro and Freund [21] by exploring the reaction:



From the sketched polarization curves with the optimized electrodes (and catalysts) for the oxidation of hydrogen sulfide and the reduction of sulfur dioxide we found the rate of electrochemical reaction from the points of intersections, in experiments realized in the chemical reactor containing hydrogen sulfide and sulfur dioxide. A catalytic mass was created and micro - galvanic elements were built simultaneously carrying out both reactions, the oxidation of hydrogen sulfide and reduction of sulfur dioxide.

The data shown in Table 1 point to the almost comparable chemical and electrochemical oxidation rates for hydrogen sulfide.

#### *Physical model of the process of oxidation of $\text{H}_2\text{S}$ and reduction of $\text{SO}_2$*

The electrochemical realization of the process is possible due to the launching of novel micro galvanic cells. The physical model of the process is shown in Fig. 6. Schematically shown is a pore electrode (catalyst mass). The structure of the catalytic mass is composed of: (1) teflonized carbon black/charcoal; (2) catalyst DG + 20% CoPc. The catalytic particles are in direct electronic contact through teflonized soot. Performed on these are partial sulfide oxidation reactions (3) and sulfur dioxide reduction (4). Ion contact is achieved through the solution (electrolyte) - (5). These conditions are sufficient for the realization of a galvanic element between the pair  $\text{SO}_2\text{-H}_2\text{S}$ . The hydrogen sulfide is oxidised to sulfur and extends to sulfates (80% of the starting sulfide). The sulfur dioxide is reduced to sulfur by subsequent conversion to sulfates.



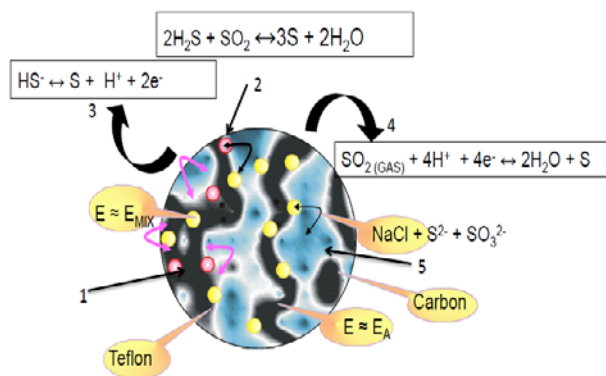


**Fig. 6.** Physical model of the pore of a micro galvanic element with teflonized charcoal /carbon black and catalytic mass for reduction reaction of  $\text{SO}_2$  with the oxidation of  $\text{H}_2\text{S}$  in the electrolyte (1%  $\text{SO}_2$  + 18 g/l  $\text{NaCl}$  + 1 M  $\text{NaOH}$  +  $\text{Na}_2\text{S} \cdot 9 \text{H}_2\text{O}$ ).

### CONCLUSION

The physical model presented illustrates the idea of both oxidation and reduction reactions in solutions containing hydrogen sulfide and sulfur dioxide for purification.

In conclusion we can say that we have found suitable conditions and catalysts for carrying out the simultaneous purification of fluids into hydrogen sulfide and sulfur dioxide. The process can be applied at cape Sinop on the Black Sea coast of Turkey.

**Acknowledgement.** This work was supported by the project Hydrogen production from Black Sea water by sulfide-driven fuel cell HYSULFCEL (bs-era.net) of the 7 FP of the European Union, contract DNS7RP 01/32 of the Ministry of Education and Science of Republic of Bulgaria.

### REFERENCE

1. I. Streeter, A. J. Wain, J. Davis, R. G. Compton, *J. Phys. Chem. B.*, **109**, 18500 (2005).
2. P. F. Cross, *UK Patent Application GB 2503294 A*.
3. EA 000764 B1
4. WO 0153197
5. WO2009055104 (A2)
6. E.P. Fleming, T. C. Fitt, *Ind. Eng. Chem.*, **42**, 2249 (1950).
7. H.M. Jahn, *Grundriss Der Elektrochemie*, (2012).
8. C. Wagner and W. Traud, *Z. Elektrochem.*, **44**, 391 (1938).
9. К. Феттер, *Электрохимическая кинетика*, Изд. „Химия”, 1967.
10. Б.В.Романовский, "Основы химической кинетики", Изд. "Экзамен" 11. Москва, 2006.
11. D. Uzun, E. Razkazova-Velkova, K. Petrov, V. Beschkov, *Bull. Chem Comm.*, Submitted for publication (2014).
12. K. Petrov, I. Nikolov, T. Vitanov, D. Uzun, V. Ognjanov, *Bulg. Chem. Comm.*, **42**, 189 (2010).
13. N. P. Penchev, B. N. Zagorchev, *Qualitative Analysis, Science and Art 2<sup>nd</sup> edn.*, 1956.
14. A. Busev, L. Simon, *Anal. Khim.*, (1975).
15. W. Fresenius, G. Jander, *Handbook for Anal. Chem.*, Springer 4<sup>th</sup> edn., 1967.
16. M. G. Bapat, B. Z. Scharma, *Anal. Chem.* **157**, 258 (1957).
17. N. P. Penchev, B. N. Zagorchev, *Analytical chemistry, Qualitative analysis*, 1964.
18. K. Petrov, S. Srinivasan, *Int. J. Hydrogen Energy*, **21**, 163 (1996).
19. M. A. Siddiqi, J. Krissmann, P. Peters-Gerth, M. Luckas, K. Lucas, *J. Chem. Thermodyn.*, **28**, 685 (1996).
20. A. D. Carbó, *Electrochemistry of porous materials*, 2012.
21. M. Spiro and P. L. Freund, *J. Electroanal. Chem.*, **144**, 293 (1983).

## ЕЛЕКТРОХИМИЧНА РЕДУКЦИЯ НА СЕРЕН ДИОКСИД ЧРЕЗ ОКИСЛЕНИЕ НА СЕРОВОДОРОД ВЪВ ВОДНА СРЕДА

Д. Узун<sup>1\*</sup>, Е. Разказова-Велкова<sup>2</sup>, В. Бешков<sup>2</sup>, Г. Пчеларов<sup>1</sup>, К. Петров<sup>1</sup>

<sup>1</sup>Институтът по електрохимия и енергийни системи „Акад. Евгени Будевски“, БАН; ул. Акад.Г.Бончев, бл. 10, София 1113

<sup>2</sup>Институт по Инженерна химия, БАН; ул. Акад.Г.Бончев, бл. 103, София 1113

Получена на 25 септември 2014 г., приета на 30 октомври 2014 г.

(Резюме)

Работата представя наша оригинална идея за едновременно електрохимично окисление на  $\text{H}_2\text{S}$  и редукция на  $\text{SO}_2$ . На тази основа е разработен електрохимичен метод за почистване на  $\text{H}_2\text{S}$  от водите на Черно море и от димните газове на ТЕЦ. Целта на процеса е да сведе до минимум въздействието на продуктите върху околната среда. Намерени са подходящи условия и електрокатализатори за реализиране на метода за намаляване на димните газове от ТЕЦ по крайбрежието на Черно море. По този начин се решава и проблема със сероводород от Черноморските води.

## Some degree based connectivity indices of nano-structures

M. Veylaki, M. J. Nikmehr\*

<sup>1</sup>Department of Mathematics, Karaj Branch, Islamic Azad University, Karaj, Iran

Received September 11, 2014, Revised March 4, 2015

A topological index of a molecular graph  $G$  is a numeric quantity related to  $G$  which is invariant under symmetry properties of  $G$ . In the present study, several topological indices are computed in linear  $[n]$ -anthracene,  $V$ -anthracene nanotube and nanotori: Zagreb, Randić, Sum-connectivity,  $GA$ ,  $ABC$  indices and Zagreb polynomials.

**Keywords:** Degree based topological indices, Molecular graphs, Linear  $[n]$ -anthracene,  $V$ -anthracene nanotube,  $V$ -anthracene nanotori.

### INTRODUCTION

A graph is a collection of points and lines connecting a subset of them. The points and lines of a graph are called vertices and edges of the graph, respectively. A simple graph is an unweighed, undirected graph without loops or multiple edges. All graphs in this paper are simple. A molecular graph is a simple graph such that its vertices correspond to the atoms and the edges to the bonds. Note that hydrogen atoms are often omitted. In the past years, nano-structures involving carbon have been the focus of an intense research activity which is driven to a large extent by the quest for new materials with specific applications. A topological index is a real number that is derived from molecular graphs of chemical compounds. In organic chemistry, topological indices have been found to be useful in chemical documentation, isomer discrimination, structure-property relationships, structure-activity relationships (SAR) and pharmaceutical drug design. There has been considerable interest in the general problem of determining topological indices [1, 2, 3]. The main goal of this paper is to compute some topological indices and polynomials for a family of linear  $[n]$ -anthracene, lattice of  $V$ -anthracene nanotube and nanotori. The paper is organized as follows: firstly we give the necessary definitions and secondly we compute some topological indice values for the above mentioned nanotubes and nanotori.

### DEFINITIONS

We now recall some algebraic definitions related to the topological indices chosen for the present study. A graph  $G$  consists of a set of

vertices  $V(G)$  and a set of edges  $E(G)$ . The vertices in  $G$  are connected by an edge if there exists an edge  $uv \in E(G)$  connecting the vertices  $u$  and  $v$  in  $G$  such that  $u, v \in V(G)$ . The degree  $d_u$  of a vertex  $u \in V(G)$  is the number of vertices of  $G$  adjacent to  $u$ . There are several topological indices already defined.

The *first Zagreb index* and the *second Zagreb index* have been introduced more than thirty years ago by Gutman and Trinajstić [4]. They respectively are defined as:

$$M_1(G) = \sum_{u \in V(G)} (d_u)^2, M_2(G) = \sum_{uv \in E(G)} d_u d_v$$

In fact, one can rewrite the *first Zagreb index* as:

$$M_1(G) = \sum_{uv \in E(G)} (d_u + d_v)$$

The product-connectivity index, also called *Randić index* of a graph  $G$  and is defined such as:

$$\chi(G) = \sum_{uv \in E(G)} \frac{1}{\sqrt{d_u d_v}}$$

This topological index was first proposed by Randić [5] in 1975. In 2009, Zhou and Trinajstić [6] proposed another connectivity index, named the *Sum-connectivity index*. This index is defined as follows:

$$X(G) = \sum_{uv \in E(G)} \frac{1}{\sqrt{d_u + d_v}}$$

The *geometric-arithmetic (GA) index* is another topological index based on degrees of vertices defined by Vukičević and Furtula [7]:

$$GA(G) = \sum_{uv \in E(G)} \frac{2\sqrt{d_u d_v}}{d_u + d_v}$$

Estrada et al. [8] introduced the *atom-bond connectivity (ABC) index*, which has been applied

\* To whom all correspondence should be sent:  
E-mail: nikmehr@kntu.ac.ir

to study the stability of alkanes and the strain energy of cycloalkanes. This index is defined as follows:

$$ABC(G) = \sum_{uv \in E(G)} \sqrt{\frac{d_u + d_v - 2}{d_u d_v}}$$

Recently, Fath-Tabar [9] put forward the *first and the second Zagreb polynomials* of the graph  $G$ , defined respectively as:

$$ZG_1(G, x) = \sum_{uv \in E(G)} x^{d_u + d_v},$$

$$ZG_2(G, x) = \sum_{uv \in E(G)} x^{d_u d_v}$$

where  $x$  is a dummy variable.

### RESULTS AND DISCUSSION

In this section, at first, we compute index for anthracene graph. Anthracene is a solid polycyclic aromatic hydrocarbon of formula  $C_{14}H_{10}$ , consisting of three fused benzene rings. It is a component of coal tar. Anthracene is used in the production of the red dye alizarin and other dyes.

**Example 3.1.** Let  $G$  be the anthracene graph (Figure 1), there are three types of edges, e. g. edges with endpoints 2 [ $E_1$ ], edges with endpoints 2, 3 [ $E_2$ ] and edges with endpoints 3 [ $E_3$ ].

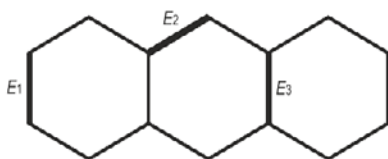


**Fig.1.** Basic structure of an anthracene

These edges are enumerated as 6, 8 and 2 edges of types 1, 2 and 3, respectively.

$$(i) M_1(G) = \sum_{uv \in E(G)} (d_u + d_v) = \sum_{uv \in E_1} (2 + 2) + \sum_{uv \in E_2} (2 + 3) +$$

$$\sum_{uv \in E_3} (3 + 3) = 4 \times 6 + 5 \times 8 + 6 \times 2 = 76$$

$$(ii) M_2(G) = \sum_{uv \in E(G)} (d_u \times d_v) = \sum_{uv \in E_1} (2 \times 2) + \sum_{uv \in E_2} (2 \times 3) +$$

$$\sum_{uv \in E_3} (3 \times 3) = 4 \times 6 + 6 \times 8 + 9 \times 2 = 90$$

$$(iii) \chi(G) = \sum_{uv \in E(G)} \frac{1}{\sqrt{d_u d_v}} = \sum_{uv \in E_1} \frac{1}{\sqrt{2 \times 2}} + \sum_{uv \in E_2} \frac{1}{\sqrt{2 \times 3}} +$$

$$\sum_{uv \in E_3} \frac{1}{\sqrt{3 \times 3}} = \frac{1}{2} \times 6 + \frac{1}{\sqrt{6}} \times 8 + \frac{1}{3} \times 2 = \frac{11 + 4\sqrt{6}}{3}$$

$$(iv) X(G) = \sum_{uv \in E(G)} \frac{1}{\sqrt{d_u + d_v}} = \sum_{uv \in E_1} \frac{1}{\sqrt{2+2}} + \sum_{uv \in E_2} \frac{1}{\sqrt{2+3}} +$$

$$\sum_{uv \in E_3} \frac{1}{\sqrt{3+3}} = \frac{1}{2} \times 6 + \frac{1}{\sqrt{5}} \times 8 + \frac{1}{\sqrt{6}} \times 2 = 3 + \frac{8\sqrt{5}}{5} + \frac{2\sqrt{6}}{6}$$

$$(v) GA(G) = \sum_{uv \in E(G)} \frac{2\sqrt{d_u d_v}}{d_u + d_v} = \sum_{uv \in E_1} \frac{2\sqrt{2 \times 2}}{2+2} + \sum_{uv \in E_2} \frac{2\sqrt{2 \times 3}}{2+3} +$$

$$\sum_{uv \in E_3} \frac{2\sqrt{3 \times 3}}{3+3} = 6 + \frac{2\sqrt{6}}{5} \times 8 + 2 = 3 + \frac{40 + 16\sqrt{6}}{5}$$

$$(vi) ABC(G) = \sum_{uv \in E(G)} \sqrt{\frac{d_u + d_v - 2}{d_u d_v}} + \sum_{uv \in E_1} \sqrt{\frac{2+2-2}{2 \times 2}} +$$

$$\sum_{uv \in E_2} \sqrt{\frac{2+3-2}{2 \times 3}} + \sum_{uv \in E_3} \sqrt{\frac{3+3-2}{3 \times 3}} =$$

$$\sqrt{\frac{2}{4}} \times 6 + \sqrt{\frac{3}{6}} \times 8 + \sqrt{\frac{4}{9}} \times 2 = 7\sqrt{2} + \frac{4}{3}$$

Now we compute first Zagreb, second Zagreb, product-connectivity, sum-connectivity, geometric-arithmetic and atom-bond connectivity indices of a linear [ $n$ ]-anthracene, as described in Example 3.1.

It is seen that  $T = T[n]$  has  $14n$  vertices and  $18n - 2$  edges and the edge set of the graph can be divided in three partitions, e. g.  $E_1(T)$ ,  $E_2(T)$  and  $E_3(T)$ . The following table gives the three types and gives the number of edges in each type.

From table 1, we give an explicit formula for some indices of a linear [ $n$ ]-anthracene, as shown in Figure 2.

**Table 1.** Computing the Number of edges for a linear [ $n$ ]-Anthracene.

$(d_u, d_v)$ where $uv \in E(T)$	Total Number of edges
$E_1 = [2, 2]$	6
$E_2 = [2, 3]$	$12n - 4$
$E_3 = [3, 3]$	$6n - 4$

**Theorem 3.2.** Consider the graph  $T$  of a linear [ $n$ ]-Anthracene. Then

$$(i) M_1(T) = \sum_{uv \in E(G)} (d_u + d_v) = \sum_{uv \in E_1} 4 + \sum_{uv \in E_2} 5 + \sum_{uv \in E_3} 6 = 4 \times 6 + 5 \times (12n - 4) + 6 \times (6n - 4) = 96n - 20$$

$$(ii) M_2(T) = \sum_{uv \in E(T)} (d_u d_v) = \sum_{uv \in E_1} 4 + \sum_{uv \in E_2} 6 + \sum_{uv \in E_3} 9 = 4 \times 6 + 6 \times (12n - 4) + 9 \times (6n - 4) = 126n - 36$$

$$(iii) \chi(T) = \sum_{uv \in E(T)} \frac{1}{\sqrt{d_u d_v}} = \sum_{uv \in E_1} \frac{1}{\sqrt{4}} + \sum_{uv \in E_2} \frac{1}{\sqrt{6}} + \sum_{uv \in E_3} \frac{1}{\sqrt{9}} = \frac{1}{\sqrt{4}} \times 6 + \frac{1}{\sqrt{6}} \times (12n - 4) + \frac{1}{\sqrt{9}} \times (6n - 4) = (2 + 2\sqrt{6})n + \left(\frac{5+2\sqrt{6}}{3}\right)$$

$$(iv) X(T) = \sum_{uv \in E(T)} \frac{1}{\sqrt{d_u + d_v}} = \sum_{uv \in E_1} \frac{1}{\sqrt{4}} + \sum_{uv \in E_2} \frac{1}{\sqrt{5}} + \sum_{uv \in E_3} \frac{1}{\sqrt{6}} = \frac{1}{\sqrt{4}} \times 6 + \frac{1}{\sqrt{5}} \times (12n - 4) + \frac{1}{\sqrt{6}} \times (6n - 4) = (12\sqrt{5} + \sqrt{6})n + \left(3 - \frac{2\sqrt{6}}{3} - \frac{4\sqrt{5}}{5}\right)$$

$$(v) GA(T) = \sum_{uv \in E(T)} \frac{2\sqrt{d_u d_v}}{d_u + d_v} = \sum_{uv \in E_1} \frac{2\sqrt{4}}{4} + \sum_{uv \in E_2} \frac{2\sqrt{6}}{5} + \sum_{uv \in E_3} \frac{2\sqrt{9}}{6} = \frac{2\sqrt{4}}{4} \times 6 + \frac{2\sqrt{6}}{5} \times (12n - 4) + \frac{2\sqrt{9}}{6} \times (6n - 4) = \left(6 + \frac{24\sqrt{6}}{5}\right)n + \left(2 - \frac{8\sqrt{6}}{5}\right)$$



Fig. 2. The molecular graph of a linear [n]-anthracene.

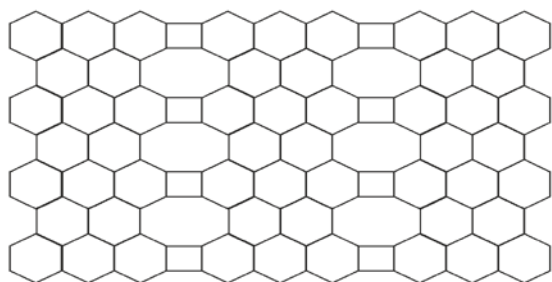


Fig.3. The 2-D graph lattice of  $G=G[p,q]$  with  $p=3$  and  $q=4$ .

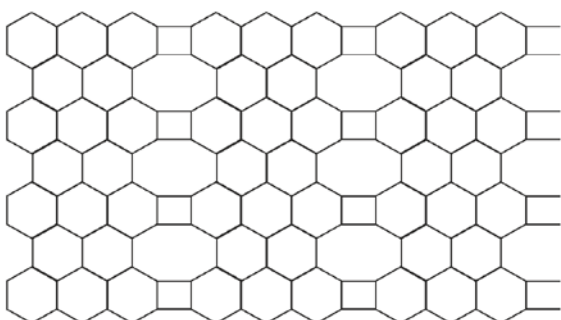


Fig. 4. The 2-D graph lattice of  $K=K[p,q]$  with  $p=3$  and  $q=4$

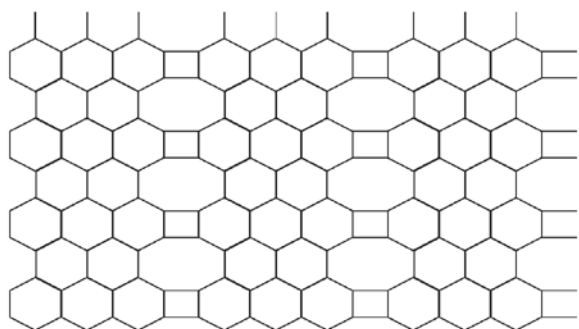


Fig. 5. The 2-D graph lattice of  $L=L[p,q]$  with  $p=3$  and  $q=4$ .

**Theorem 3.3.** Let  $G$  be a 2-dimensional lattice of  $V$ -anthracene (see Figure 3),  $K$  be a lattice of  $V$ -anthracene nanotube (see Figure 4) and  $L$  be a lattice of  $V$ -anthracene nanotori (see Figure 5). Then,  
 $|V(G)| = |V(K)| = |V(L)| = 14pq$ ,  $|E(G)| = 21pq - 3p - 2q$ ,  $|E(K)| = 21pq - 3p$  and  $|E(L)| = 21pq$ .

From table 2, we give an explicit computing formula for some indices of lattice of  $V$ -anthracene nanotube and nanotori, as shown in Figures 3, 4 and 5.

In graph theory, a regular graph is a graph where each vertex has the same number of neighbors, i.e. every vertex has the same degree or valency. A regular graph with vertices of degree  $k$  is called a  $k$ -regular graph or regular graph of degree  $k$ . Now, we need the following lemma to calculate the indices of  $L$ :

**Lemma 3.4.** Let  $G$  be an arbitrary graph. Then  $G$  is  $k$ -regular if and only if one of the followings hold:

1.  $M_1(G) = 2\kappa |E(G)|$ .
2.  $M_2(G) = \kappa^2 |E(G)|$ .
3.  $\chi(G) = \frac{1}{\kappa} |E(G)|$ .
4.  $X(G) = \frac{1}{\sqrt{2\kappa}} |E(G)|$ .
5.  $GA(G) = |E(G)|$ .
6.  $ABC(G) = \frac{\sqrt{2(\kappa-1)}}{\kappa} |E(G)|$

Table 2. Computing the number of edges for molecular graph  $G$ ,  $K$  and  $L$ .

$(d_u, d_v)$ where $uv \in E$	Number of Edges $G$	Number of Edges $K$	Number of Edges $L$
$E_1 = [2, 2]$	$2q+4$	0	0
$E_2 = [2, 3]$	$12p+4q-8$	$12p$	0
$E_3 = [3, 3]$	$21pq-15p-8q+4$	$21pq-15p$	$21pq$

Table 3. Topological indices for the molecular graphs of Figures 3 and 4.

Index	Graph $G$	Graph $K$
$M_1$	$126pq-30p-20q$	$126pq-30p$
$M_2$	$189pq-63p-40q+4$	$189pq-63p$
$\chi$	$7pq+(2\sqrt{6}-5)p+(\frac{2\sqrt{6}-5}{3})q+(\frac{10-4\sqrt{6}}{3})$	$7pq+(2\sqrt{6}-5)p$
$X$	$\frac{7\sqrt{6}}{2}pq+(\frac{12\sqrt{5}}{5}-\frac{5\sqrt{6}}{2})p+(1+\frac{4\sqrt{5}}{5}-\frac{4\sqrt{6}}{3})q+(2-\frac{8\sqrt{5}}{5}+\frac{2\sqrt{6}}{3})$	$\frac{7\sqrt{6}}{2}pq+(\frac{12\sqrt{5}}{5}-\frac{5\sqrt{6}}{2})p$
$GA$	$21pq+(\frac{24\sqrt{6}}{5}-15)p+(\frac{8\sqrt{6}}{5}-6)q+(8-\frac{16\sqrt{6}}{5})$	$21pq+(\frac{24\sqrt{6}}{5}-15)p$
$ABC$	$14pq+(6\sqrt{2}-10)p+(3\sqrt{2}-\frac{16}{3})q+(\frac{8}{3}-2\sqrt{2})$	$14pq+(6\sqrt{2}-10)p$

**Proof.** It is easy to check according to Figure 5. By using Lemma 3.4, consider the Figure 5. We can see that  $V$ -anthracene nanotori graph is 3-regular. So, we illustrate these results in the table below:

**Table 4.** Topological indices for the molecular graphs of Fig. 5.

Index	Graph $L$
$M_1$	$126 pq$
$M_2$	$189pq$
$\chi$	$7pq$
$X$	$\frac{7\sqrt{6}}{2} pq$
GA	$21pq$
ABC	$14pq$

Finally, we will calculate the first and second Zagreb polynomials of the above molecular graphs.

**Theorem 3.5.** The first and second Zagreb polynomials of the above graphs are computed as follows:

- (i)  $ZG_1(G, x) = (12pq - 15p - 8q + 4)x^6 + (12p + 4q - 8)x^5 + (2q + 4)x^4,$
- (ii)  $ZG_2(G, x) = (21pq - 15p - 8q + 4)x^9 + (12p + 4q - 8)x^6 + (2q + 4)x^4,$
- (iii)  $ZG_1(K, x) = (21pq - 15p)x^6 + (12p)x^5,$
- (iv)  $ZG_2(K, x) = (21pq - 15p)x^9 + (12p)x^6,$

$$(v) \quad ZG_1(L, x) = (21pq)x^6,$$

$$(vi) \quad ZG_2(L, x) = (21pq)x^9.$$

**Proof.** By definition of Zagreb polynomials, the proof is clear.

**Acknowledgments:** This article is derived from a doctoral thesis of Maryam Veylaki (Ph.D student) entitled, investigating some topological Indices on molecular graphs. The authors appreciate the support received from the Karaj Branch, Islamic Azad University, Karaj, Iran.

#### REFERENCES

1. M. Eliasi, B. Taeri B, *J. Comput. Theor. Nanosci.*, **4**, 1174 (2007).
2. A. Heydari, B. Taeri, *MATCH Commun. Math. Comput. Chem.*, **57**, 665 (2007).
3. A. Mahmiani, A. Iranmanesh, Y. Pakravesh *Ars Comb.*, **89**, 309 (2008)
4. I. Gutman, N. Trinajstić, *Chem. Phys. Lett.*, **17**, 535 (1972).
5. M. Randić, *J. Am. Chem. Soc.*, **97**, 6609 (1975)
6. B. Zhou, N. Trinajstić, *J. Math. Chem.*, **46**, 1252 (2009)
7. D. Vukičević, B. Furtula, *J. Math. Chem.*, **46**, 1369 (2009).
8. E. Estrada, L. Torres, L. Rodriguez, I. Gutman, *Indian J. Chem.*, **37A**, 849 (1998).
9. H. Fath-Tabar, *Dig. J. Nano-mater. Bios.*, **4**, 189 (2009).

## НЯКОИ СТЕПЕННО БАЗИРАНИ ИНДЕКСИ НА СВЪРЗВАНЕ НА НАНОСТРУКТУРИ

М. Вейлаки \*, М. Дж. Никмер

*Катедра по математика, Клон Карадж, Ислямски университет „Азад“, Карадж, Иран*

Получена на 11 септември 2014 г., ревизирана на 4 март 2015 г.

(Резюме)

Топологичният индекс на молекулен граф  $G$  е число, свързано с  $G$ , който е инвариантно по симетрични свойства на  $G$ . В настоящото проучване се изчисляват няколко топологични индекси за линеен  $[n]$  антрацен,  $V$ -антрацен, нанотръба и нанотори: Загреб, Рандич, сума на свързаност, GA, ABC индекси и Загреб полиноми.

## Multivariate statistical assessment of obesity patients' clinical parameters

R. T. Georgieva-Nikolova<sup>1</sup>, P. A. Gateva<sup>2</sup>, R. K. Hadjiolova<sup>3</sup>, M. P. Slavova<sup>4</sup>, M. M. Nikolova<sup>5</sup>,  
V. D. Simeonov<sup>6\*</sup>

<sup>1</sup>Department of Chemistry and Biochemistry, Faculty of Medicine, Medical University of Sofia, Sofia, Bulgaria

<sup>2</sup>Department of Pharmacology and Toxicology, Faculty of Medicine, Medical University of Sofia, Sofia, Bulgaria

<sup>3</sup>Department of Pathophysiology, Faculty of Medicine, Medical University of Sofia, Sofia, Bulgaria

<sup>4</sup>Institute of Electrochemistry and Energy Systems, Bulgarian Academy of Sciences, Sofia, Bulgaria

<sup>5</sup>Middlesex University, School of Health and Education – London, United Kingdom

<sup>6</sup>Department of Analytical Chemistry, Faculty of Chemistry and Pharmacy, University of Sofia "St. Kl. Okhridski"  
Sofia, Bulgaria

Received December 2, 2014, Revised March 22, 2015

The present study deals with multivariate statistical interpretation of clinical parameters of obesity patients. The goal of the study is to find relationship and similarity between the traditional obesity monitoring characteristics and to determine patterns of similarity between the patients participating in the investigation. Cluster analysis and principal components analysis were used as multivariate statistical methods in the data mining procedure in which 113 patients were included. It has been shown that the status of the patients is dominantly related to parameters characterizing the obesity problem (body mass index, fat mass, weight, degree of obesity etc.) and not so directly with other parameters characterizing mainly the general health status (cholesterol, triglycerides, glucose level etc.). This could help in optimizing the number of clinical variables necessary for monitoring obesity. Further, specific patterns of similarity between patients were defined and the parameters responsible for their formation were determined. In such a way a more individual treatment of the patients becomes possible. A distinctive separation between male and female patients was statistically proven.

It has to be stated that for the first time multivariate statistical analysis is applied for assessment of the health status of obesity patients.

**Key words:** Obesity, clinical parameters, multivariate statistics, health assessment

### INTRODUCTION

Obesity is an issue of worldwide significance, affecting both adults and children. According to the World Health Organisation (WHO), over 400 million people in the world are suffering from it [1]. Obesity is a medical condition, in which the body fat levels are higher than normal and are considered harmful. It occurs as a result of imbalance between an individual's energy consumption through food and his energy expenditure [2].

It may also be triggered by medications or endocrine or psychiatric disorders. As with many other medical conditions, obesity results from the interplay between genetic and environmental factors.

Some medications can cause weight gain or changes in body structure [3]. Some physical and mental conditions and the medications used for their treatment can increase the risk of obesity. Although obesity in itself is not considered a psychiatric

disorder, patients with such are more prone to becoming overweight or obese [4]. Polymorphism in genes controlling the appetite and metabolism, coupled with enough food energy, predisposes to obesity [5]. The percentage of genetic factor-related obesity in the study population varies between 6 and 85% [6, 7]. However, genetic factors only lead to obesity when coupled with environmental ones [8-10].

The dramatic increase in obesity cases worldwide cannot be explained with genetic factors alone [11]. Studies show that obesity is caused by a combination of different factors, rather than a high energy intake and a low expenditure [12].

Metabolic syndrome – a disruption in the body metabolism – results from the excess weight and obesity. Obesity and metabolic syndrome can cause diabetes mellitus type 2, obstructive sleep apnea, some types of cancer, osteoarthritis and osteoporosis, asthma, arterial hypertension, dyslipidemia, gout, liver steatosis, chronic gastroenterocolitis [13, 14].

Men with metabolic syndrome are marked with lower testosterone levels, i.e. sexual 'aging'.

\* To whom all correspondence should be sent:  
E-mail: vsimeonov@chem.uni-sofia.bg

The metabolic syndrome also raises significantly the risk of cancerous formations in the following organs: the prostate, the mammary glands, the endometrium, and the ovaries. The metabolic syndrome also injures the liver and leads to non-alcoholic steatohepatitis and cirrhosis.

Therefore, an assessment of the obesity as a serious medical problem needs large data sets of various indicators. The estimation and the useful information extraction from such big data set requires application of appropriate strategies most effective of which are the methods of the multivariate statistics like cluster analysis and principal components analysis.

The aim of the present study is to classify, model and interpret a clinical data set of obesity patients in order to detect relationships between the parameters or reveal specific patterns of obesity patients. It could be of use for optimization of the monitoring process and applying additional attention to the different groups of affected patients. This is the first ever attempt to interpret clinical data from obesity sufferers by the use multivariate statistical analysis.

## MATERIAL AND METHODS

### *Data collection*

Data from 113 patients (28 male and 85 female) with different degrees of obesity in University Hospital 'Alexandrovska', Sofia, Bulgaria have been used in this study. Totally 40 clinical parameters and sex differentiation were collected for the assessment procedure as follows [15-20]:

1. Sex (not a real parameter, just information);
2. Age, years;
3. Height, cm;
4. Weight, kg;
5. Fat Mass (FM), kg;
6. Fat, % – The percentage of the body fats is calculated in relation to the total patient's weight;
7. Fat-Free Mass (FFM), kg;
8. Muscle Mass (MM), kg;
9. Total body water (TBW), kg;
10. Total body water (TBW), % ;
11. Bone Mass (BM), kg – The obesity patients have lower bone density than this which corresponds to their age [15];
12. Basal Metabolic Rate (BMR), kJ. This is the energy which needs the body at resting to function effectively [16];
13. Basal Metabolic Rate (BMR), kcal;
14. Metabolic Age (MA), years – the age of the metabolism of the body;
15. Visceral Fat Rating – evaluation of the inner abdominal obesity [17];
16. Body Mass Index (BMI), kg/m<sup>2</sup>;

17. Ideal Body Weight (IBW), kg – it is the weight at which the individual has the chance to live longer;
  18. Degree of obesity, %;
  19. Hemoglobin (HGB), g/L
  20. White blood cells (WBC), x10<sup>9</sup>/L;
  21. Red Blood Cells (RBC), x10<sup>12</sup>/L
  22. Hematocrit – HCT, it measures the volume of the erythrocytes in the blood;
  23. Platelets (PLT), x10<sup>9</sup>/L
  24. Mean Corpuscular Volume (MCV), or Mean Cell Volume, fL – MCV is a measure of the average volume of a red blood corpuscle (or red blood cell);
  25. Mean Corpuscular Hemoglobin (MCH), pg;
  26. Mean Corpuscular Hemoglobin Concentration (MCHC), g/L;
  27. Red Blood Cell Distribution Width (RDW), % – is useful biomarker in the determining of cardiovascular risk;
  28. Mean platelet volume (MPV), fL, – lower values of MPV are present in the aplastic anemia [18];
  29. Alanine aminotransferase (ALAT), U/L;
  30. Aspartate aminotransferase (ASAT), U/L – reveals fatty liver [19];
  31. Creatinine, μmol/L – a parameter of the kidney function;
  32. Cholesterol, mmol/L – Total cholesterol is assessed for determination of the damage of the fat metabolism and estimation of the risk of cardiovascular diseases.
  33. High-Density Lipoproteins (HDL), mmol/L – parameter for the risk of cardiovascular diseases.
  34. Low-Density Lipoproteins (LDL), mmol/L ;
  35. Triglycerides (TG), mmol/L ;
  36. High-sensitivity C-reactive protein (hs CRP), mg/L;
- Parameters 32 – 36 estimate the risk of cardiovascular diseases.
37. Oral Glucose Tolerance Test (OGTT), mmol/L – The most important diagnostic value has the fasting glucose, OGTT 0 [20];
  38. OGTT 120 (2h after administration) with 75 g glucose;
  39. Glycated Hemoglobin – Hb A<sub>1c</sub>, %. A parameter for the long-term blood glucose;
  40. Immuno-Reactive Insulin (IRI), mU/L – obesity is associated with hyperinsulinism;
  41. C-peptide, ng/mL – is a component of the proinsulin.

### *Multivariate statistics*

In the present study Cluster analysis (CA) and Principal Components Analysis (PCA) were used. Both methods are well documented and used in many multivariate statistical studies for data modeling, data projection and data interpretation

procedures. They belong to the classical data mining approaches and represent a serious part of the intelligent data analysis strategies [21].

CA is well-known and widely used multivariate statistical approach. In order to cluster objects characterized by a set of variables (e.g. patients by clinical parameters), one has to determine their similarity. A preliminary step of data scaling is necessary (e.g. autoscaling or z – transform) where normalized dimensionless numbers replaces the real raw data values. Thus, even serious differences in absolute values are scaled to similar ranges. Then, the similarity or the distance between the objects in the variable space can be determined usually by calculation of the Euclidean distance. There is a wide variability of clustering (linkage) algorithms but the typical ones include the single linkage, the average linkage or the Ward's method. The representation of the results of the cluster analysis is performed by a tree-like scheme called dendrogram.

PCA is a typical display method, which allows to estimate the internal relations in the data set. There are different variants of PCA but basically, their common feature is that they produce linear combination of the original columns in the data matrix (data set) responsible for the description of the variables characterizing the objects of observation. These linear combinations represent a type of abstract measurements (factors, principal components) being better descriptors of the data structure (data pattern) than the original (chemical or physical) measurements. Usually, the new abstract variables are called latent factors and they differ from the original ones named manifest variables. It is a common finding that just a few of the latent variables account for a large part of the data set variation. Thus, the data structure in a reduced space can be observed and studied.

## RESULTS AND DISCUSSION

As already mentioned the data set consists of 113 cases (patients) and 40 clinical parameters [113x40]. The data set was analyzed by CA (z-transform of the raw data; squared Euclidean distances as similarity measures; Ward's method of linkage and Sneath's criterion for cluster significance) and by PCA (Varimax rotation mode). The main goals of the multivariate statistical data treatment were:

1. to find relationships between the clinical parameters and based on the relationships to determine significant indicators in the treatment of the problem;
2. to find patterns of similarity between the patients treated and to determine discriminant factors (clinical parameters) for each pattern;
3. to define the latent factors responsible for the data set structure and to relate them to the clinical parameters used.

In the first run of the statistical analysis all patients were involved. In Fig. 1 the clustering of clinical parameters for all patients is presented.

Two significant clusters are formed at level  $2/3D_{max}$ :

K1 (*Age, MetaAg, Crea, GlyHb, OGTT0, OGTT12, RDW, Trig, CHOL, LDL, TBW%, HDL, MCV, MCHC, MPV, MCH, ALAT, ASAT*) and

K2 (*Hei, IdBW, BMRc, BoneM, MusM, FFM, BMR, TBW, RBC, HCT, HGB, Wei, FatM, BMI, DegOb, VisFat, Fat, CRP, IRI, CPEP, WBC, PLT*)

In these two clusters some subclusters could be defined but, in general, there is a significant similarity between the clinical indicators for obesity. All indicators are generally divided in two big groups:

Obesity indicators (dominantly in cluster K2)

General health status indicators (dominantly in cluster K1)

There is an option to select smaller number of parameters when assessing the state of obesity and the general health status of the patients, which is related to the obesity syndrome.

In the next dendrogram (Fig. 2) the clustering of all 113 patients is shown. Two major clusters are formed (the number of patients is reduced for better readability of the graph but the clustering involved all patients). The separation is achieved by sex: cluster 1 (the smaller cluster) consists of totally 29 cases with 24 male patients and 5 female patients; cluster 2 (the bigger one) consists of totally 84 cases with 80 female and 4 male patients. Therefore, there is a significant separation between male and female obesity cases.

If the average values for each clinical parameters for the two clusters formed are compared (Table 1) and comparable values from



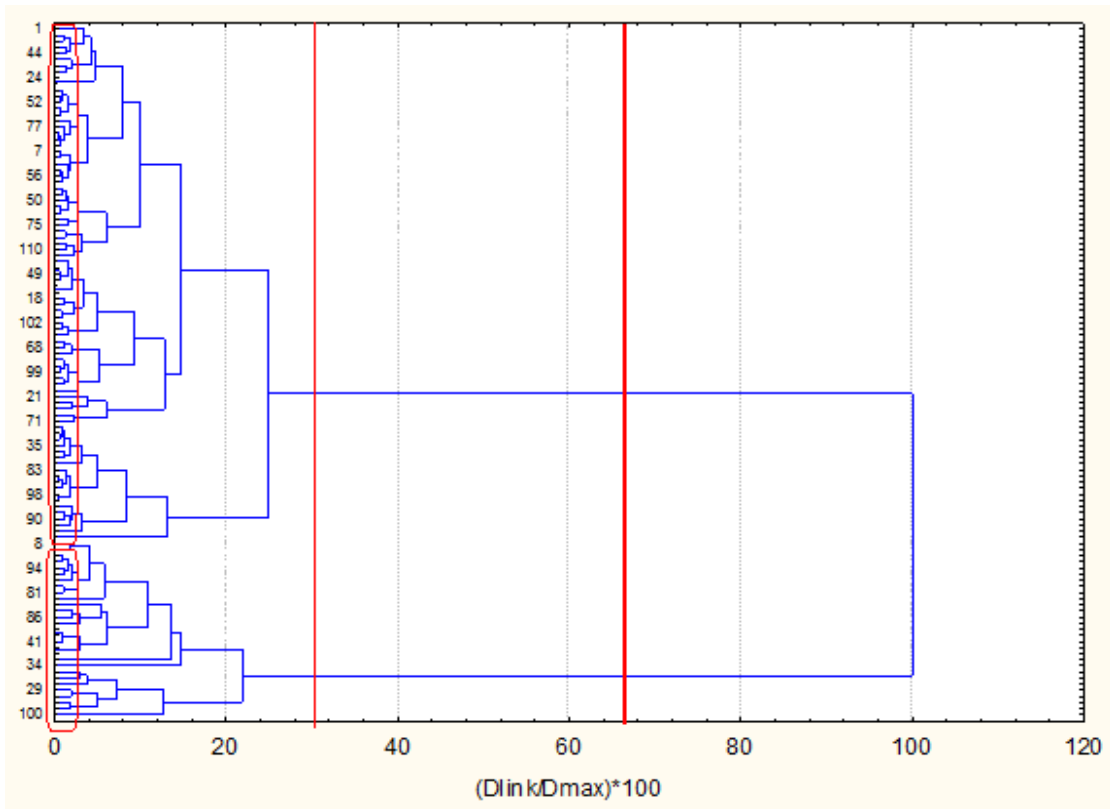


**Fig 1.** Hierarchical dendrogram for clinical parameters (all patients)

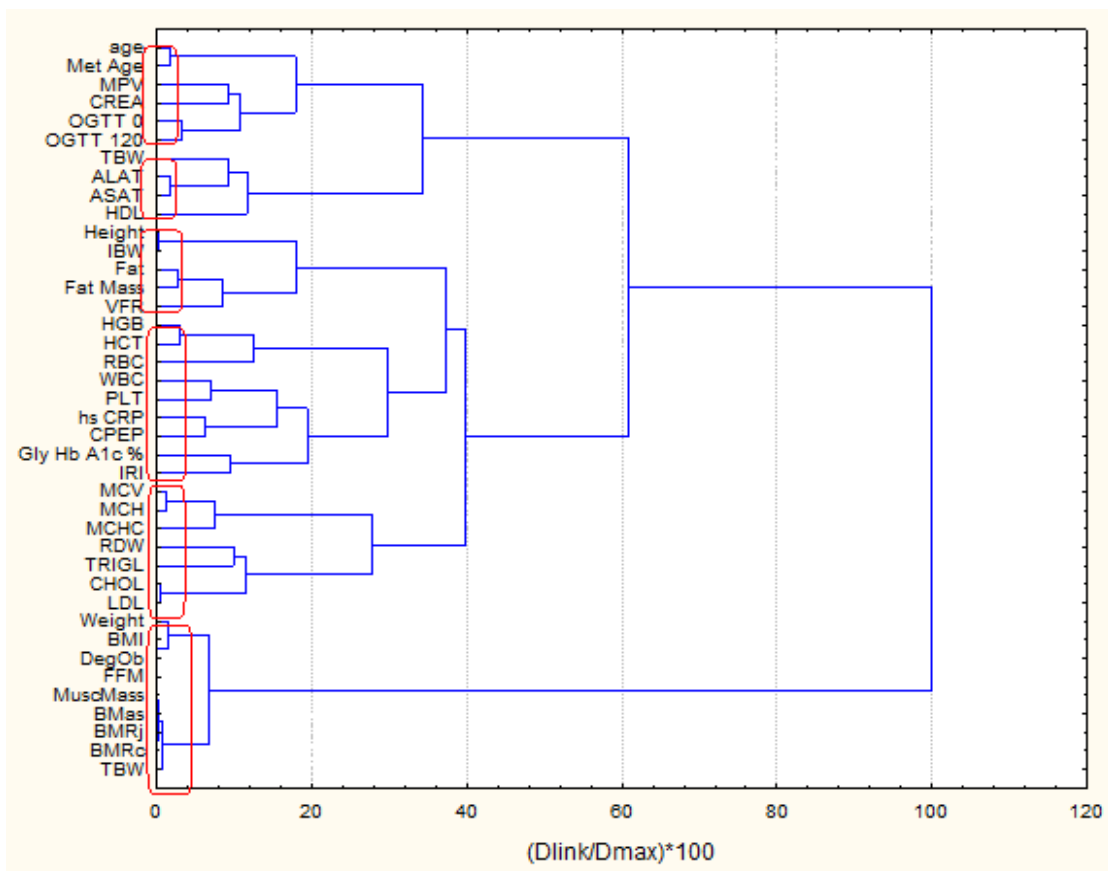


**Fig 2.** Hierarchical dendrogram for clustering of 113 patients

both clusters differ around 50 % following conclusions could be mentioned:

There is no significant difference between lots of the clinical indicators for each one of the clusters formed. In general, the members of the "male" cluster show higher values for many of the "obesity" indicators like weight, fat mass, FFM, muscle mass, TBW, bone mass, BMR, visceral fat, BMI, ideal body weight, degree of obesity, HGB. Probably, it has to be expected due to objective reasons – men are physically stronger and more affected by obesity. The other clinical parameters related to the general health status (blood parameters, glucose parameters, liver parameters) are quite similar in both clusters.

It was interesting to separate the data set into "male" and "female" subsets and try to interpret separately both subsets.

The hierarchical dendrogram for linkage between clinical parameters for male patients is given (Fig. 3).

Six clusters are formed:

K1: *TBW BMRc BMR Bone Mass MuscMass CPR FFM DegOb BMI Weight VisFat*

K2: *LDL CHOL TRIG RDW MCHC MCH MCV*

K3: *IRI GLYHb CPEP PLT WBC RCB HCT HGB*

K4: *FatM Fat IBW Height*

K5: *HDL ASAT ALAT TBWc*

K6: *OGTT120 OGTT0 CREA MPV MetAg Age*

**Table 1.** Average values for the clinical parameters for clusters 1 and 2

Clinical parameter	Cluster 1 ("male")	Cluster 2 ("female")
Age	45.97	49.08
Height	176.79	161.40
Weight	<b>133.51</b>	88.42
Fat	39.77	41.13
Fat Mass	<b>54.00</b>	37.07
FFM	<b>79.53</b>	51.35
Muscle mass	<b>75.62</b>	48.78
TBW	<b>57.69</b>	36.69
TBW %	45.10	42.14
Bone Mass	<b>3.92</b>	2.60
BMR kJ	<b>10392.07</b>	6344.89
BMR ccal	<b>2483.76</b>	1580.42
Metabolic Age	59.41	60.39
Visceral Fat	<b>20.93</b>	10.86
BMI	42.92	33.85
Ideal Body	68.93	57.60
Degree of obesity %	<b>95.12</b>	54.05
HGB	152.17	132.96
WBC	8.38	7.17
RBC	5.08	4.59
HCT	0.45	0.40
PLT	248.55	279.93
MCV	89.14	87.42
MCH	30.01	32.24
MCHC	336.38	333.04
RDW	17.44	13.50
MPV	8.28	8.43
ALAT	28.79	20.40
ASAT	22.97	19.48
CREA	78.50	66.82
CHOL	5.35	5.55
HDL	1.27	1.45
LDL	3.26	3.42
TRIG	1.87	1.52
CRP	7.91	5.67
OGTT0	5.85	5.30
120OGTT	6.62	5.99
GlyHbA1	5.81	5.68
IRI	<b>23.21</b>	14.36
CPEP	5.04	3.76

It is seen that the parameters are clustered in groups related to the obesity (K1, K4), blood indicators (K2, K3), liver parameters (K5) and glucose indicators and age (K6).

This separation is confirmed in principle by the application of principal components analysis. Six latent factors are responsible for explanation of nearly 70 % of the total variance of the system. Factor loadings are presented and the significant ones are marked by bold (Table 2).

The first latent factor (conditional name "obesity factor") indicates the close relationship between the indicators for obesity. It is interesting to note that the parameter "metabolic age" is negatively correlated to the other parameters with significant factor loadings. CPEP and IRI could be also included in this group of indicators although their factor loadings are lower than the required 0.70 level. The second principal component ("glucose level factor") stands for over 11 % of the total variance and indicates logical relationship between glucose level and age. Several blood indicators are also included. The third hidden variable is related to PC1 since it includes other important obesity indicators ("fat indicators factor") and explains over 10 % of the total variance. The fourth principal component is related to the blood quality parameters ("blood parameters factor"). The last two latent factors indicate the role of several indicators for the general health status like cholesterol and triglycerides or blood quality (platelets) It is worth to mention that a certain number of clinical indicators do not contribute significantly to the description of the obesity syndrome (GlyHb, CRP, HDL, ASAT, ALAT). This conclusion offers an opportunity for experimentation aiming optimal selection of significant obesity indicators for male patients.

For female patients (Fig. 4) the clinical indicators are generally divided into two major cluster (the first one included typical obesity parameters and some blood quality characteristics; the second one links glucose level, liver function, general health status parameters along with metabolic age and age). A closer look into the groups could reveal (cluster significance according Sneath of  $1/3 D_{\max}$ ) five clusters of parameters:

K1: *BMR TBWc BMRc BoneMass MuscMass FFM*  
 K2: *CRP Fat VisFat DegOb BMI FatM Weight*  
 K3: *RDW PLT WBC IBW Height*  
 K4: *LDL CHOL MPV MCH MCHC MCV HDL TBW %RBC HCT HGB*  
 K5: *ASAT ALAT CPEP IRI OGTT120 OGTT0 TRIG GLyHb CREA MetA Age*

The "female clustering" resembles the "male" one revealing groups of similarity related to obesity

indicators (K1, K2), blood, liver and glucose indicators (K3, K4, K5).

The factor loadings for this subset of patients are shown after carrying out principal components analysis (Table 3).

Five latent factors are responsible for the data structure in the female subset (explanation of nearly 60 % of the total variance). PC1 and PC2 are typical "obesity indicators factors", since PC3 and PC5 include "blood" and glucose level" indicators. PC 4 reveals a specific relationship for parameters defining general health status (age, ideal body weight, cholesterol, LDL). Even more indicators than those in the case with male patients remain insignificant for explanation of the data structure: HGB, WBC, PLT, MCH, MCHC, MPV, ALAT, ASAT, CREA, CHOL, HDL, TRIG, CRP, CPEP (Table 3).

There is a slight difference between the clustering of the clinical indicators for male and female patients – those for female patients are grouped more compact (less clusters) which is an indication for higher level of similarity between the indicators for the general health status (blood, liver, glucose).

In the next step of the statistical analysis it was of substantial interest to understand if there are specific patterns among the groups of male and female patients and to determine the discriminant indicators for these patterns.

The hierarchical dendrogram for 28 male obesity patients is shown (Fig. 5).

Two significant clusters could be determined:

K1: 6, 7, 8, 9, 10, 11, 12, 13, 14, 20, 24, 25, 26

K2: 1, 2, 3, 4, 5, 15, 16, 17, 18, 19, 21, 22, 23, 27, 28

The clustering of 85 female obesity patients is shown (Fig. 6).

Four clusters are found as follows:

K1: 67, 22, 79, 29, 12

K2: 83, 46, 42, 21, 49, 85, 48, 43, 84, 82, 47, 72, 45, 74, 63, 44, 27, 18, 77, 14

K3: 39, 66, 52, 37, 78, 81, 80, 76, 25, 35, 24, 34, 20, 65, 10, 75, 73, 61, 71, 69, 64, 26, 60, 53, 28, 50, 31, 11, 5, 13, 4

K4: 16, 62, 9, 59, 58, 56, 38, 8, 41, 40, 17, 68, 30, 7, 54, 36, 6, 57, 51, 15, 3, 33, 19, 70, 55, 32, 23, 2,

For identification of discriminant indicators the averages of each parameter for each cluster (both for male and female patients) were determined (Table 4, Table 5).

For male patients: two different patterns are identified among the group of totally 28 male obesity patients. The first pattern (cluster 1) consists of 13 patients characterized by high indication of most of the parameters (weight, fat content, fat mass, FFM, muscle mass, BMI, TBW, bone mass, degree of

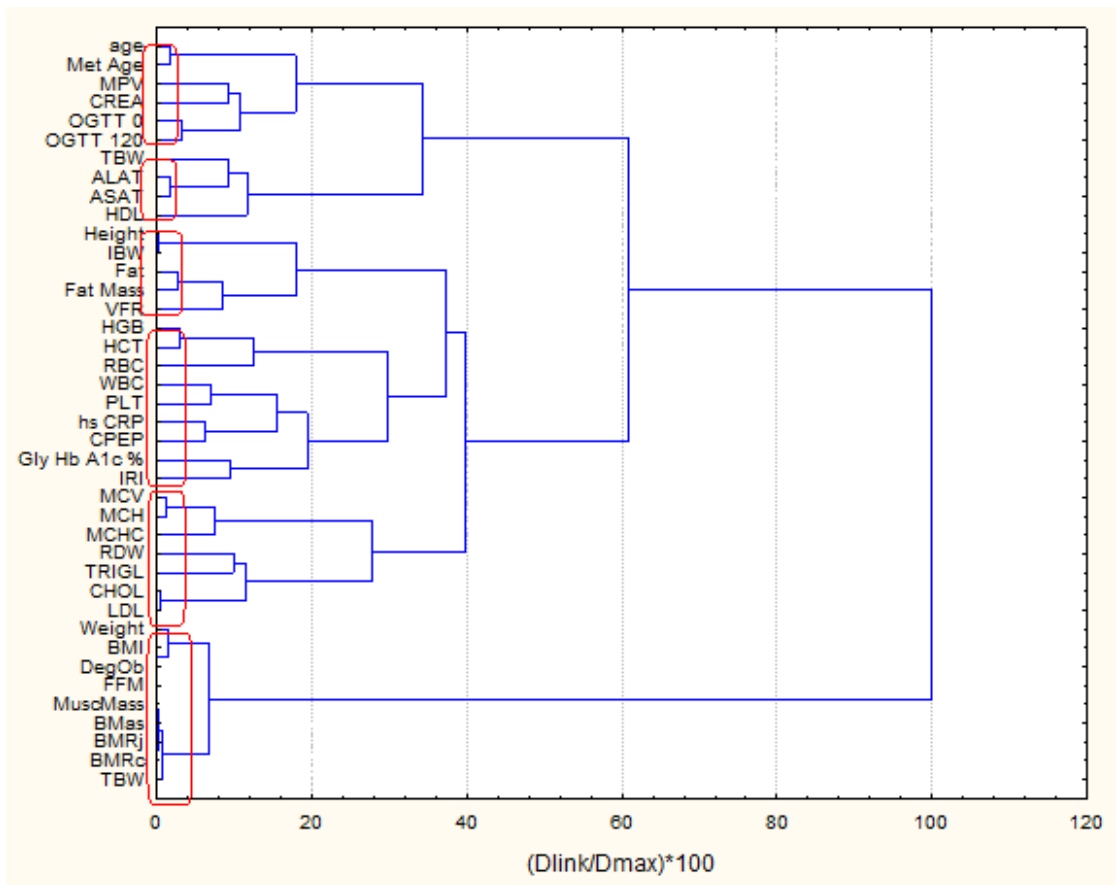


Fig. 3. Hierarchical dendrogram for clinical parameters for male patients

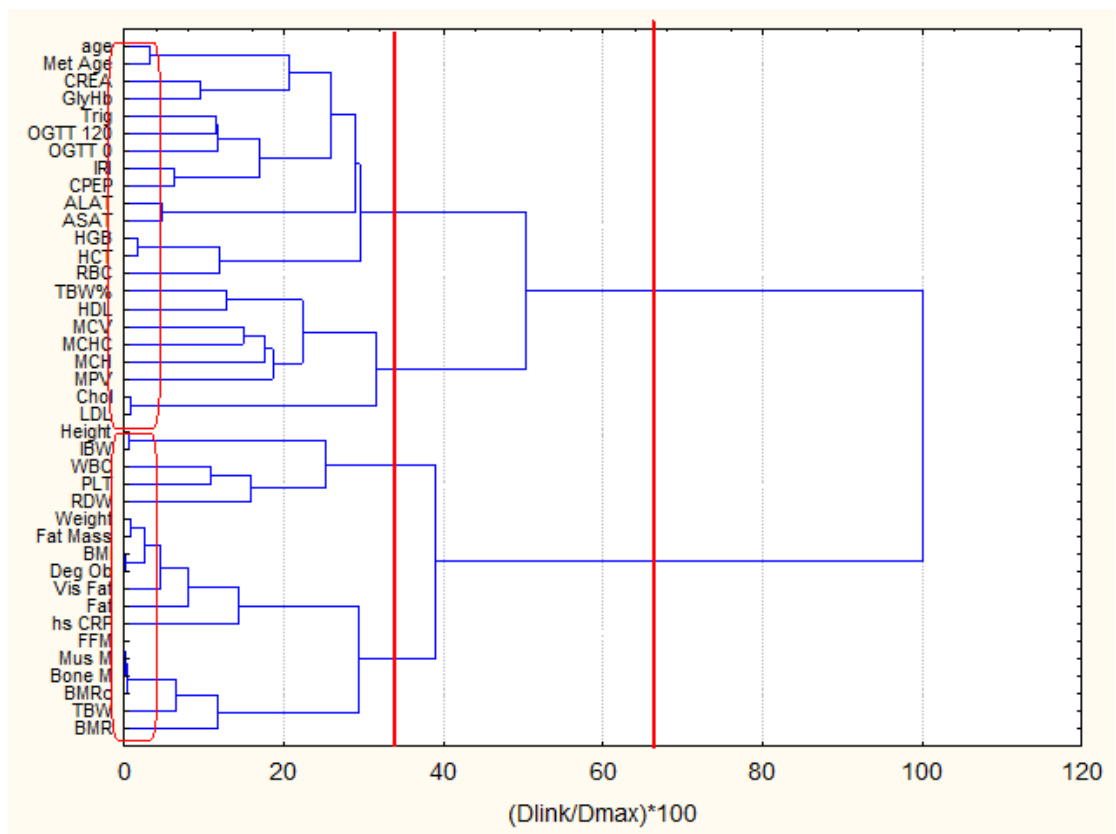


Fig. 4. Hierarchical dendrogram for clinical parameters for female patients

**Table. 2.** Factor loadings for male patients (significant loadings are marked by bold)

Variable	PC- 1	PC 2	PC- 4	PC 3	PC -6	PC- 5
age	-0,45	<b>0,703</b>	-0,171	-0,036	0,180	-0,197
Height	0,40	-0,113	0,035	<b>0,628</b>	-0,519	0,122
Weight	<b>0,872</b>	-0,004	0,024	0,478	0,000	0,007
Fat	-0,11	0,002	0,125	<b>0,926</b>	0,132	0,091
Fat Mass	0,44	-0,011	0,104	<b>0,863</b>	0,042	0,044
FFM	<b>0,982</b>	0,005	-0,060	-0,048	-0,039	-0,029
Muscle Mass	<b>0,985</b>	0,004	-0,061	-0,049	-0,039	-0,029
TBW, kg	<b>0,984</b>	0,004	-0,022	0,065	0,049	0,020
TBW, %	-0,001	0,141	-0,016	<b>-0,702</b>	0,051	0,030
Bone Mass	<b>0,98</b>	0,019	-0,043	-0,033	-0,045	-0,030
BMR, kJ	<b>0,99</b>	-0,002	-0,050	0,026	-0,017	-0,026
BMR, ccal	<b>0,99</b>	-0,002	-0,050	0,026	-0,017	-0,026
Meta Age	<b>-0,57</b>	0,497	-0,152	0,304	0,087	-0,181
Vis Fat	0,25	0,229	-0,111	<b>0,532</b>	0,469	0,019
BMI	<b>0,89</b>	0,063	0,028	0,277	0,268	-0,039
I B W	0,37	-0,094	0,026	<b>0,612</b>	-0,551	0,119
Deg obes	<b>0,89</b>	0,063	0,030	0,278	0,267	-0,039
HGB	-0,11	-0,489	<b>0,751</b>	0,172	0,131	-0,131
WBC	0,14	-0,238	0,042	0,089	<b>0,760</b>	0,284
RBC	-0,08	<b>-0,607</b>	-0,489	0,081	0,108	-0,269
HCT	-0,16	<b>-0,509</b>	0,371	0,166	0,304	-0,328
PLT	0,16	0,046	-0,076	-0,006	<b>0,745</b>	0,193
MCV	-0,07	0,281	<b>0,865</b>	0,065	0,129	0,052
MCH	-0,05	0,192	<b>0,927</b>	0,072	-0,004	0,173
MCHC	0,03	-0,048	<b>0,695</b>	0,035	-0,205	0,290
RDW	-0,10	-0,217	0,148	-0,130	-0,081	<b>0,599</b>
MPV	0,00	<b>0,701</b>	0,192	-0,053	0,025	-0,236
ALAT	0,04	0,003	0,078	0,083	-0,147	0,085
ASAT	-0,10	0,289	0,142	0,105	-0,138	-0,024
CREA	-0,01	0,482	0,474	-0,176	-0,251	0,173
cholesterol	-0,14	0,078	0,174	0,101	0,268	<b>0,846</b>
HDL	-0,38	0,051	0,041	-0,149	0,156	-0,288
LDL	-0,05	0,030	0,207	0,109	0,228	<b>0,826</b>
triglycerides	0,08	0,109	-0,048	0,181	0,061	<b>0,702</b>
hs CRP	0,37	0,305	0,241	0,375	0,311	-0,022
OGTT 0	0,16	<b>0,804</b>	0,109	-0,002	-0,058	0,145
OGTT 120	0,09	<b>0,876</b>	0,046	0,093	0,077	-0,054
Gly Hb A1c	0,37	0,303	0,223	-0,330	0,253	0,027
IRI	<b>0,55</b>	0,273	-0,003	0,290	-0,024	-0,193
CPEP	<b>0,59</b>	0,360	-0,100	0,234	0,110	-0,074
Expl.Var %	26.2	11.4	9.2	10.6	6.9	7.6

**Table 3.** Factor loadings for female patients (significant loadings are marked by bold)

Variable	PC- 1	PC - 2	PC - 3	PC 5	PC-4
age	-0,261	0,402	0,219	0,025	<b>0,602</b>
Height	0,388	0,021	-0,311	0,091	<b>-0,621</b>
Weight	<b>0,862</b>	0,446	0,114	0,047	-0,166
Fat	0,243	<b>0,898</b>	0,029	0,046	-0,125
Fat Mass	<b>0,697</b>	0,656	0,099	0,051	-0,179
FFM	<b>0,959</b>	0,013	0,117	0,031	-0,113
Muscle Mass	<b>0,959</b>	0,008	0,111	0,029	-0,116
TBW	<b>0,810</b>	-0,092	0,020	0,014	-0,083
TBW, %	-0,126	<b>-0,921</b>	-0,014	-0,045	0,051
Bone Mass	<b>0,958</b>	0,027	0,114	0,049	-0,112
BMR, kJ	<b>0,615</b>	-0,132	0,258	0,175	-0,080
BMR, ccal	<b>0,960</b>	0,104	0,113	0,032	-0,159
Metabolic Age	-0,132	<b>0,728</b>	0,154	0,016	0,435
Visceral Fat Rating	0,482	<b>0,733</b>	0,303	0,009	0,058
BMI	<b>0,798</b>	0,487	0,219	0,003	0,070
I B W	0,353	0,017	-0,289	0,099	<b>-0,634</b>
Deg of obesity	<b>0,794</b>	0,489	0,223	0,004	0,066
HGB	0,062	0,066	0,472	<b>-0,800</b>	0,081
WBC	<i>0,396</i>	<i>0,050</i>	<i>0,280</i>	<i>-0,042</i>	<i>-0,255</i>
RBC	0,184	-0,005	<b>0,692</b>	0,120	0,001
HCT	0,110	0,094	0,557	<b>-0,655</b>	0,123
PLT	<i>0,241</i>	<i>-0,010</i>	<i>-0,042</i>	<i>0,204</i>	<i>-0,283</i>
MCV	<i>-0,116</i>	<i>0,091</i>	<i>-0,179</i>	<i>-0,783</i>	<i>0,130</i>
MCH	<i>0,068</i>	<i>-0,087</i>	<i>-0,090</i>	<i>-0,196</i>	<i>-0,021</i>
MCHC	<i>-0,063</i>	<i>-0,029</i>	<i>-0,176</i>	<i>-0,441</i>	<i>-0,064</i>
RDW	0,261	0,010	0,089	<b>0,723</b>	-0,064
MPV	<i>-0,213</i>	<i>0,243</i>	<i>-0,031</i>	<i>-0,077</i>	<i>-0,108</i>
ALAT	<i>0,307</i>	<i>-0,045</i>	<i>0,344</i>	<i>-0,007</i>	<i>0,166</i>
ASAT	<i>0,100</i>	<i>-0,070</i>	<i>0,338</i>	<i>0,083</i>	<i>0,233</i>
CREA	<i>-0,060</i>	<i>0,341</i>	<i>0,167</i>	<i>-0,169</i>	<i>0,156</i>
cholesterol	0,032	-0,006	-0,128	-0,011	<b>0,836</b>
HDL	<i>-0,096</i>	<i>-0,308</i>	<i>-0,498</i>	<i>-0,012</i>	<i>0,308</i>
LDL	0,041	0,012	-0,065	-0,036	<b>0,760</b>
triglycerides	<i>0,122</i>	<i>0,375</i>	<i>0,391</i>	<i>0,101</i>	<i>0,287</i>
hs CRP	<i>0,435</i>	<i>0,355</i>	<i>0,032</i>	<i>0,062</i>	<i>0,089</i>
OGTT 0	0,158	0,096	<b>0,651</b>	-0,072	-0,005
OGTT 120	-0,225	0,140	<b>0,645</b>	0,140	0,115
Gly Hb A1	<i>0,127</i>	<i>0,093</i>	<i>0,467</i>	<i>0,001</i>	<i>0,103</i>
IRI	0,469	0,183	<b>0,607</b>	0,139	-0,251
CPEP	<i>0,190</i>	<i>0,365</i>	<i>0,448</i>	<i>0,157</i>	<i>-0,144</i>
Expl.Var %	22.4	12.1	10.2	6.7	8.5

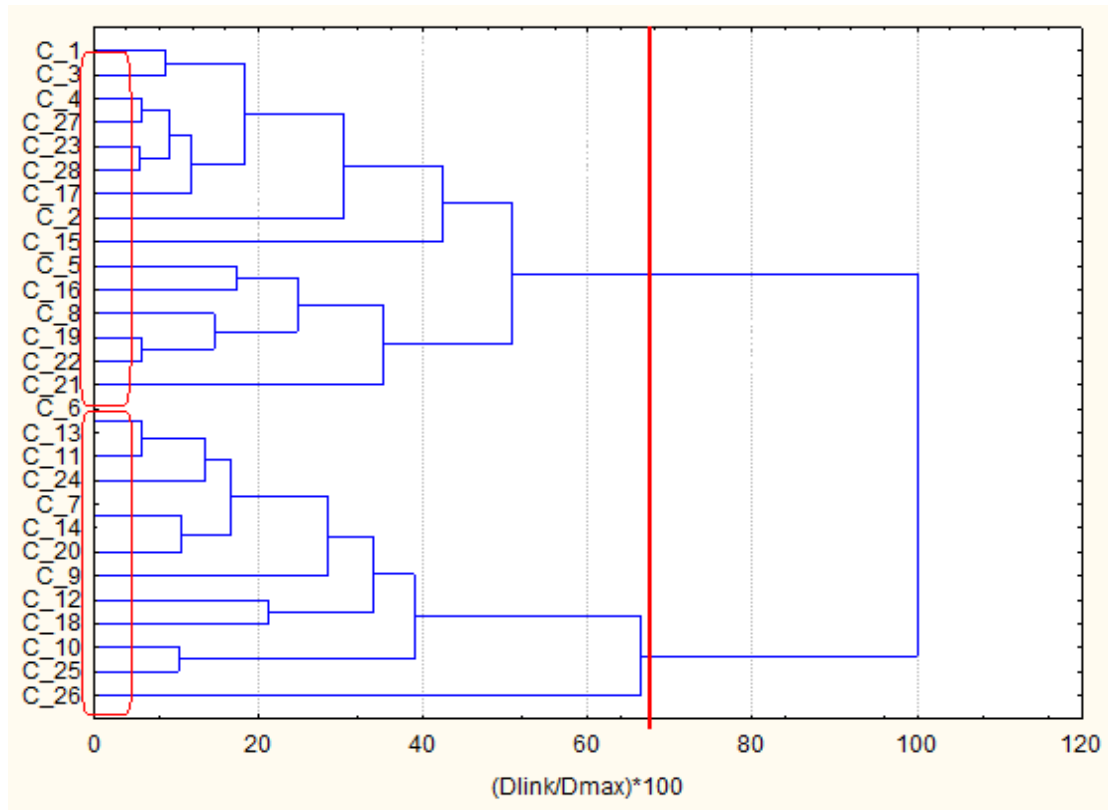


Fig. 5. Hierarchical dendrogram for 28 male obesity patients

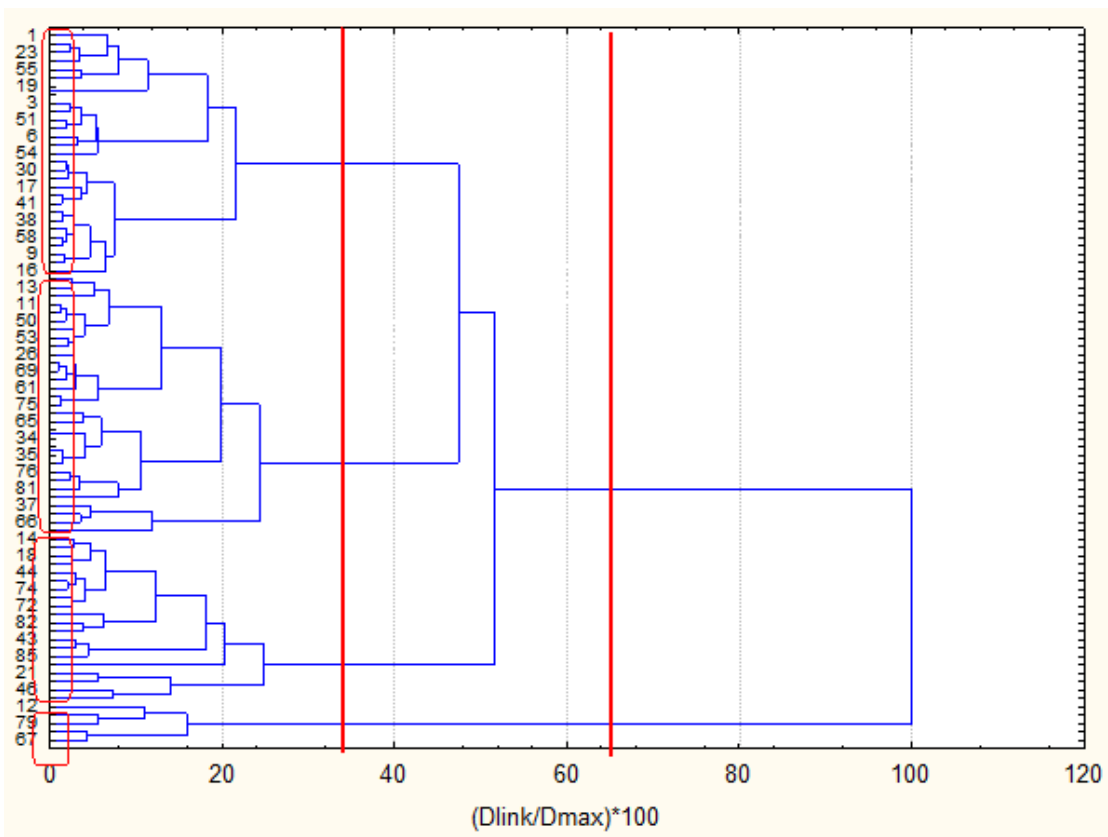


Fig. 6. Hierarchical dendrogram for female patients

obesity or 23 out of all 40 parameters are with higher values). Obviously, this is the pattern of the *most affected patients with bad levels of obesity indicators*. Surprisingly, this is the group with the lower average age which proves the assumption that obesity starts recently in early age, even before 40. The second pattern (cluster 2) represents the rest of 15 patients with the relatively better levels of obesity indicators. They show only three higher levels of indicators forage, metabolic age (this is a logical relationship and ASAT but with very close value to that of values of cluster 1.

So, this pattern could be conditionally named *patients with acceptable and controlled obesity problem*. It is important to note that for 14 parameters (out of all 40) the average levels are almost equal for the patients of both patterns among them cholesterol, LDL, HDL, several blood parameters, glucose level, ALAT.

Thus, they do not have important discriminating effect for the group of male patients. It could be recommended to use mainly obesity indicators for establishing the obesity status of the patients and to separate them into different patterns needing respective medical care and treatment.

The situation with the female patients is slightly different. Four groups of similarity are formed.

Cluster 1 (Table 5) includes only 5 cases (out of 85) having highest obesity indicators values – weight, fat, degree of obesity, BMI etc. This is definitely the pattern of *most affected female patients with bad levels of obesity indicators*. The group is of relatively young age (although not the lowest average age) and it is a troubling symptom. Cluster 2 with 20 cases resembles group of relatively young patients with better obesity indicators. This corresponds entirely to the concept of the statistical recognition as pattern of *patients with acceptable and controlled obesity problem*. Cluster 3 in the case with female patients with lowest average age covers the pattern of the *patients with starting obesity problem*.

The number of cases is 31 out of 85 i.e. the biggest group of female patients. The forth cluster of 29 female patients reveals the pattern of *patients with chronic obesity problem*. This is cluster having relatively high average age but with levels of obesity close to cluster 1. This is proof that obesity is more spread among female patients and already in young age. As in the situation with the male patients the blood, liver and glucose indicators for all obesity patterns do not differ significantly.

For both groups of patients (male and female) the major separation is a result of differences between the obesity indicators, so that they are the only

discrimination parameters for the various clusters (patterns of patients).

**Table. 4.** Average values for clinical parameters for clusters of male patients

Parameter	Cluster 1	Cluster 2
Age	40.62	53.53
Height	181.38	173.80
Weight	145.77	106.81
Fat	41.15	33.97
Fat Mass	59.85	36.46
FFM	85.92	70.35
Muscle mass	81.72	66.87
TBW	64.57	51.95
TBW %	44.35	49.59
Bone Mass	4.20	3.47
BMR kJ	11399.85	8862.27.0
BMR ccal	2724.62	2128.13
Metabolic Age	54.46	65.47
Visceral Fat	22.31	18.60
BMI	44.26	35.02
I B W	72.48	67.09
Deg. obesity %	101.22	59.19
HGB	155.08	149.2
WBC	8.94	7.25
RBC	5.14	5.08
HCT	0.46	0.45
PLT	259.46	232.40
MCV	89.15	88.45
MCH	30.27	29.57
MCHC	339.23	333.67
RDW	21.83	13.63
MPV	8.06	8.49
ALAT	27.54	30.47
ASAT	19.69	26.60
CREA	73.53	81.09
CHOL	5.55	5.17
HDL	1.18	1.47
LDL	3.40	3.00
TRIG	2.19	1.57
CRP	7.82	4.18
OGTT0	5.74	5.85
120OGTT	6.22	6.89
GlyHbA1	5.81	5.75
IRI	26.26	15.98
CPEP	5.92	4.16

**Table. 5.** Average values for clinical parameters for clusters of female patients

Parameter	Cluster 1	Cluster 2	Cluster 3	Cluster 4
Age	43.6	43.3	41.1	61.1
Height	165.4	164.7	162.4	157.6
Weight	151.3	105.3	78.4	86.7
Fat	50.2	45.5	36.7	43.7
Fat Mass	76.0	48.2	29.3	38.1
FFM	75.4	57.1	49.0	48.6
Muscle mass	71.6	54.2	46.6	46.2
TBW	51.5	41.6	35.6	33.2
TBW %	37.8	39.6	45.1	39.9
Bone Mass	3.8	2.9	2.5	2.5
BMR kJ	10142.0	6337.8	6271.1	6260.1



BMR ccal	2424.0	1783.4	1498.8	1496.2
Metabolic Age	58.6	58.3	50.2	72.2
Visceral Fat	22.8	12.4	7.2	12.6
BMI	55.4	38.9	29.7	34.9
I B W	60.3	59.7	58.4	54.7
Deg. obesity	151.9	76.7	35.4	58.6
HGB	145.4	129.1	133.0	134.0
WBC	10.3	7.9	7.0	6.7
RBC	5.1	4.7	4.4	4.5
HCT	0.4	0.4	0.4	0.4
PLT	290.4	316.8	284.5	250.0
MCV	85.8	83.6	89.2	88.9
MCH	28.8	40.7	29.9	29.7
MCHC	329.0	329.5	335.8	333.8
RDW	14.5	14.4	13.2	13.2
MPV	8.1	8.6	8.2	8.6
ALAT	23.8	24.5	18.2	19.1
ASAT	18.2	22.7	17.9	18.6
CREA	70.9	61.0	64.9	74.0
CHOL	5.3	5.2	5.3	6.1
HDL	1.2	1.4	1.5	1.5
LDL	3.3	3.1	3.3	3.8
TRIG	1.8	1.5	1.2	1.8
CRP	14.8	6.3	4.6	6.9
OGTT0	5.9	5.3	5.1	5.4
120OGTT	6.8	5.2	5.5	6.9
GlyHbA1	6.0	5.6	5.6	5.8
IRI	32.0	18.0	12.9	12.8
CPEP	5.3	3.9	3.6	3.6

### CONCLUSION

For the first time in the medical practice multivariate statistical analysis was applied for interpretation of clinical data of obesity patients. It was found that after carrying out cluster analysis and principal components analysis specific relationships between the clinical parameters and between the obesity patients could be assessed and modelled. A clear difference between male and female patients is proven. The clinical parameters are definitively divided into two major groups (clusters) combining, on one hand, obesity specific parameters and parameters characterizing the general health status, on another. This general result could help in optimization of the monitoring procedures for obesity sufferers.

Several specific patterns among the female and male patients could be also assessed. In principle, these patterns indicate various levels of obesity and could be used for more detailed treatment of the problem with respect to the patterns identified.

### REFERENCES

1. B. Caballero, *Epidemiol. Rev.*, **29**, 1 (2007).
2. R. Sturm, *Public Health*, **121**, 492 (2007).
3. D.W. Haslam, W.P. James, *Lancet*, **366**, 1197 (2005).
4. R.F. Kushner, , D.H. Bessesen, Treatment of the Obese Patient. Contemporary Endocrinology. Totowa, NJ, Humana Press, 2007.
5. J.S. Flier, *Cell*, **116**, 337 (2004).
6. W. Yang, T. Kelly, He, J., *Epidemiol. Rev.*, **29**, 49 (2007).
7. S. Farooqi, S. O'Rahilly, *Endocr. Rev.*, **27**, 710 (2006).
8. P. Poirier, *Arterioscler. Thromb. Vasc. Biol.*, **26**, 968 (2006).
9. G. Kolata, Rethinking thing: The new science of weight loss– and the myths and realities of dieting. New York: Picador, 2007.
10. A.J. Walley, J.E. Asher, P. Froguel, *Nat. Rev. Genet.*, **10**, 431 (2009).
11. D. Yach, D. Stuckler, K.D. Brownell, *Nat. Med.*, **12**, 62 (2006).
12. L.A. Barness, J.M. Opitz, E.Gilbert-Barness, *Am. J. Med. Genet. A*, **143A**, 3016 (2007)
13. G.A. Bray, *J. Clin. Endocrinol. Metab.*, **89**, 2583 (2004).
14. H.N. Sweeting, *Nutr. J.*, **6**, 32 (2007).
15. E.A. Greco, R. Fornari, F. Rossi, V. Santemma, G. Prossomariti, C. Annoscia, A. Aversa, M. Brama, M. Marini, L.M. Donini, G. Spera, A. Lenzi, C. Lubrano, S. Migliaccio, *Int. J. Clin. Pract.*, **64**, 817 (2010).
16. Bosy-Westphal, W. Braun, B. Schautz, M.J. Müller, *Front. Physiol.*, **25**, 4 (2013).
17. K. Rabe, M. Lehrke, K.G. Parhofer, U.C., *Mol. Med*, **14**, 741 (2008).
18. S. Liu, J. Ren, G. Han, G. Wang, G. Gu, Q. Xia, J. Li, *Eur. J. Med. Res.*, **17**, 3 (2012).
19. Y. Elitsur, Z. Lawrence, *Med. J.*, **100**, 67 (2004).
20. V.M. Cambuli, M. Incani, S. Pilia, T. Congui, M.G. Cavallo, E. Cossu, F. Sentinelli, S.Mariotti, S. Loche, M.G. Baroni, *Diabetes Metab. Res. Rev.*, **25** 528, (2009).

## МНОГОВАРИАЦИОННА СТАТИСТИЧЕСКА ОЦЕНКА НА КЛИНИЧНИ ПАРАМЕТРИ НА ПАЦИЕНТИ СЪС ЗАТЛЪСТЯВАНЕ

Р. Т. Георгиева-Николова<sup>1</sup>, П. А. Гатева<sup>2</sup>, Р. К. Хаджийолова<sup>3</sup>, М. П. Славова<sup>4</sup>, М. М. Николова<sup>5</sup>, В.  
Д. Симеонов<sup>6\*</sup>

<sup>1</sup>*Катедра по химия и биохимия, Медицински факултет, Медицински университет, София, България*

<sup>2</sup>*Катедра по фармакология и токсикология, Медицински университет, София, България*

<sup>3</sup>*Катедра по патофизиология, Медицински университет, София, България*

<sup>4</sup>*Институт по електрохимия и енергийни системи, Българска академия на науките, София, България*

<sup>5</sup>*Университет Мидълсекс, училище по здравеопазване и образование, Лондон, Великобритания*

<sup>6</sup>*Катедра по аналитична химия, Факултет по химия и фармация, Софийски университет "Св. Кл. Охридски"  
София, България*

Постъпила на 2 декември, 2014 г., коригирана на 22 март, 2015 г.

(Резюме)

Настоящото проучване се отнася за многовариационна статистическа интерпретация на клинични параметри на пациенти със затлъстяване. Целта на проучването е да открие връзки и подобие между традиционно наблюдаваните характеристики при затлъстяване и да определи модели на подобие между пациентите, участващи в изследването. Кластерен анализ и анализ на главни компоненти бяха използвани като многовариационни статистически методи за изследване на данните от проучването, в което бяха включени 113 пациенти. Беше установено, че състоянието на пациентите основно се определя от параметрите, характеризиращи затлъстяването (фактор на телесното тегло, мастна тъкан, телесна маса, степен на затлъстяване и др.) и много по-слабо зависи от параметрите, характеризиращи тяхното общо здравно състояние (общ холестерол, триглицериди, ниво на глюкоза и др.). Това може да помогне за оптимизиране на броя на клиничните променливи, които са необходими за контрол на затлъстяването. Освен това, бяха определени специфични модели на подобие между пациентите и параметрите, отговорни за тяхното формиране. Това дава възможност за по-индивидуално лечение на пациентите. Статистически беше доказано характерното разделяне на мъжете и жените пациенти.

Може да се каже, че за първи път многовариационен статистически анализ е приложен за оценка на здравното състояние на пациенти със затлъстяване.

## Morphology and thermal behaviour of poly(methyl methacrylate) /poly(ethylene glycol) /multi-walled carbon nanotubes nanocomposites

G. Q. Liu\*

College of Material Science and Engineering, Henan University of Technology, Zhengzhou, 450001, China.

Received December 25, 2013, Revised July 3, 2015

Poly(methyl methacrylate) /poly(ethylene glycol) /multi-walled carbon nanotubes (PMMA/PEG/MWNTs) nanocomposites were prepared by ultrasonic assisted free radical bulk polymerization. The effect of different weight percent loadings of MWNTs on the morphological and thermal properties of PMMA/PEG/MWNTs nanocomposites had been investigated. It was found that, at low concentration of MWNTs, it could uniformly disperse into PMMA/PEG blends and increase the nucleation density of PEG. Thermal analysis showed that a clear improvement of thermal stability for PMMA/PEG/MWNTs nanocomposites increased with increasing MWNTs content.

**Keywords:** PMMA, PEG, MWNTs, morphology, thermal behaviour

### INTRODUCTION

Polymer nanocomposites with lower nanofiller's loading display more superior properties than conventional composites, and have increasingly drawn attention because of their many advantages such as flexible features, easy processing, and lightweight [1-9], especially polymers/carbon nanotubes (CNTs) nanocomposites [10-13]. CNTs are ideal fillers for polymer nanocomposites and have high Young modulus, tensile strength, good electrical conductivity and thermal conductivity, together with the need for only small volume fractions to obtain desired properties; therefore, polymers/CNTs nanocomposites could use for the development of advanced multifunction materials [14-16].

Generally, CNTs can consist of single-walled carbon nanotubes (SWNTs) and multi-walled carbon nanotubes (MWNTs). They can be prepared by three techniques: laser ablation, arc discharge and chemical vapour decomposition (CVD) [17]. Among them, CVD is the most commonly used method for mass production of different types of CNTs. Although SWNTs offer the opportunity for much lower loading versus MWNTs to achieve the same electrical properties, enhancing mechanical properties even further [18], MWNTs are widely used as a result of lower unit cost, greater availability and fewer dispersion challenges compared with SWNTs.

Linear poly(methyl methacrylate) (PMMA) can form stable blends with linear poly(ethylene oxide) (PEO) due to van der Waals type bonding between the PMMA chains and the planar PEO segments

[19-21], which is among the most studied polymer systems; however, its relatively poor heat resistance hinders specific applications; therefore, many studies are reported in the literature concerning PMMA nanocomposites [22-27]. In this work, to enhance and utilize the properties of PMMA/PEG, especially to improve heat resistance, PMMA/PEG/MWNTs nanocomposites were prepared by ultrasonic assisted free radical bulk polymerization. The effects of MWNTs on the morphology, crystal structure and thermal stability of PMMA/PEG/MWNTs nanocomposites were investigated. This paper is aimed at presenting the fabrication methods of nanocomposites and the CNTs-modified properties of polymer.

### EXPERIMENTAL

#### Material

MWNTs were purchased from Shenzhen Nano-Technologies Port Co. Ltd., China, with a purity of above 96 %, average length of microns, and surface area of  $4.26 \text{ m}^2 \cdot \text{g}^{-1}$ . Methyl methacrylate (MMA) and azobisisobutyronitrile (AIBN) were of analytical grade obtained from the Chengdu Reagent Factory. Ethylene glycol dimethacrylate (EGDMA) was purchased from Aldrich Chemical Co. MMA was distilled under reduced pressure before use. AIBN, used as a radical initiator, was recrystallized from methanol solution. EGDMA was used as a cross-linker without further purification. Polyethylene glycol (PEG, Aldrich,  $M_n=2000$ ) was dried by heating at  $70 \text{ }^\circ\text{C}$  for 7 hrs under vacuum, which also played a role of an organic dispersant.

\* To whom all correspondence should be sent:  
E-mail: mikepolymer@126.com

### Preparation of PMMA/PEG/MWNTs nanocomposites

Firstly, MWNTs were immersed in 3 mol·l<sup>-1</sup> nitric acid (HNO<sub>3</sub>) and refluxed for 8 hrs, subsequently washed with distilled water until the pH of MWNTs solution was ca. 7, finally obtained after dried in a vacuum oven at 90 °C for 40 hrs. Adding the gained MWNTs (0.5-3 wt.%), MMA (54.5-57 wt.%) and PEG (38 wt.%) into a two-necked flask, the mixtures was sonicated using a bath sonicator for 1 hr. AIBN (1 wt.%) as an initiator, and EGDMA (3.5 wt.%) as a crosslinker, were added and nitrogen gas was purged into the flask to remove oxygen. Polymerization was carried out with constant stirring at 60 °C for 10 min. Then, the reaction mixture injected into the space between two glass plates separated by polyethylene spacers (3 mm thick) and continued to polymerize by ultrasonic assisting at 55 °C for 24 hrs. The prepared PMMA/PEG/MWNTs nanocomposites were quenched and then dried under vacuum at room temperature for 72 hrs to remove unreacted monomers.

### Characterizations

MWNTs size analysis was performed on a Microtrac S3000 analyzer (Microtrac Software Co., USA). The spherulitic morphology was observed and photographed through a polarized optical microscope (POM, a Jiangnan XPR-2, China) equipped with a digital camera. Thermogravimetric analysis (TGA) measurement was performed using TGA-7 (Perkin-Elmer). The thermal analyses were carried out with a differential scanning calorimeter (DSC, DuPont 9900) over a temperature range from -70 to 155 °C at a heating rate of 10 °C·min<sup>-1</sup>, purged with nitrogen gas, and quenched with liquid nitrogen. The cell was calibrated using an indium standard; the weight of the sample was 5-10 mg. SEM observation was carried out with a JSM-5900LV scanning electron microscopy. TEM measurements were carried out on a FEI Fecnai F20 S-Twin transmission electron microscope, operating at an accelerating voltage of 200 kV.

## RESULTS AND DISCUSSION

It is well known that the dispersion of CNTs in the polymer matrix and their interfacial interactions are the key factors to ultimately determine many properties of polymers/CNTs nanocomposites, including improving the mechanical, electrical, and thermal performances of the polymer matrix. The TEM image of as as-received MWNTs is shown in Fig.1 (a) and their diameter distribution is measured, as shown in Fig.1 (b). The specifications

of MWCNTs are as follows: 93 % MWNTs smaller than 100 nm with average diameters = 68 nm, and about 0.8 % larger than 200 nm.

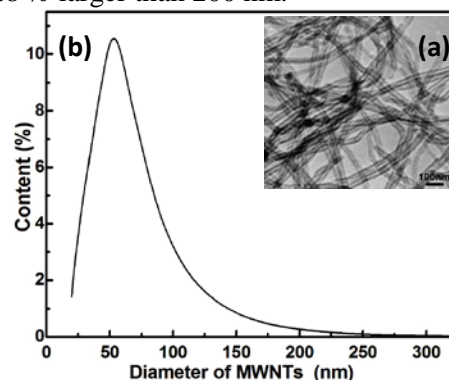


Fig. 1. TEM image (a) and distribution of diameter (b) for as-received MWNTs.

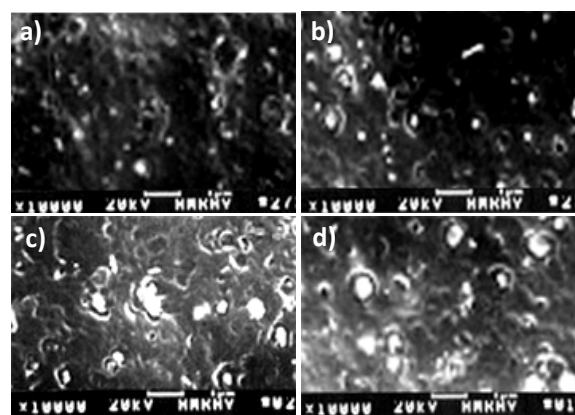
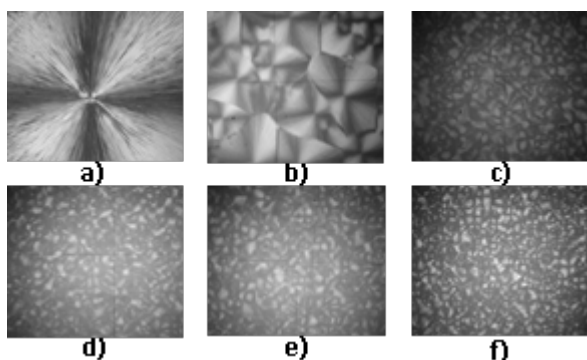


Fig. 2. SEM images of PMMA/PEG/MWNTs nanocomposites. a) PMMA/PEG/0.5 wt.% MWNTs, b) PMMA/PEG/1 wt.% MWNTs, c) PMMA/PEG/2 wt.% MWNTs, d) PMMA/PEG/3.0 wt.% MWNTs.

To reveal dispersion of MWNTs in the PMMA/PEG blends, the cryo-fractured surfaces of the nanocomposites were investigated in detail by SEM, as shown in Fig. 2 a) - d). A fibrous fractured surface is observed due to the elongation at break of PMMA/PEG/MWNTs nanocomposites; the random dispersed bright dots because of MWNTs high conductivity are the ends of the broken carbon nanotubes [28]. In addition, it is found that some MWNTs are broken apart, and, as a result of poor interfacial adhesion, some MWNTs are pulled out of the matrix before the breakage, forming caves on the fractured surface; moreover, other MWNTs are observed with their one end still strongly embedded in the PMMA/PEG blends as an inset. Such interesting and typical breakage phenomenon of the MWNTs indicates that a strong interfacial adhesion exists between MWNTs and PMMA/PEG blends and that the load transfer takes place efficiently from the matrix to the nanotubes. The strong is usually responsible for the significant enhancement of the mechanical properties [29]. This interfacial

adhesion may be ascribed to the following facts: carboxylic acid groups could be formed at the open ends and at defect sides of the side walls of CNTs after the strong acid treatment [30, 31], therefore, the hydrogen bonds could exist in between the PEG hydroxyl group and the carbonyl group of MWNTs, which would help to disperse MWNTs in PMMA/PEG/MWNTs nanocomposites.

At low concentration of MWNTs, from Fig. 2 a) and 2 b), it can be seen that the bright dots (i.e., MWNTs) embedded in the PMMA/PEG blends and the caves (i.e., MWNTs) pulled out from the PMMA/PEG blends are well dispersed; however, with an increase in MWNTs concentration, from Fig. 2 c) and 2 d), a nonuniform dispersion of MWNTs is observed in the nanocomposites, and a large aggregate of MWNTs having a diameter of over 500 nm is presented; while in the case of pristine MWNTs, its diameter is about 70 nm, as shown in Fig. 1. Those indicate that the MWNTs were dispersed as nanotubes aggregates due to the imperfect mixing of the masterbatch.



**Fig. 3.** Spherulitic morphologies of a) neat PEG2000, b) PMMA/PEG2000, c) PMMA/PEG2000/0.5 wt.% MWNTs, d) PMMA/PEG/1 wt.% MWNTs, e) PMMA/PEG/2 wt.% MWNTs, and f) PMMA/PEG/3.0 wt.% MWNTs crystallized at 0 °C by POM ( $\times 20$ ).

When the content of MWNTs is no more than 1.0 wt.%, owing to producing carboxylic or hydroxylic groups on the surface of the MWNT, which ensures the high dispersion quality of the MWNTs and prevents the severe aggregation of MWNTs [32, 33], reasonably uniform distribution of the MWNTs is observed in Fig. 2 a) and 2 b). On the other hand, at compositions containing greater amounts of MWNTs, a small amount of aggregates is shown in Fig. 2 c) and 2 d). These results are in good agreement with the results of Wu et al. and Bikiaris et al. who reported that increasing the content of SiO<sub>2</sub> leads to larger agglomerates [34, 35]; this is also the case in PMMA/PEG/MWNTs nanocomposites. In fact, there are more or less agglomerates of MWNTs formed in Fig. 2.

The effect of MWNTs on the spherulitic morphology of PEG blends was studied by POM. Fig. 3 shows the spherulitic morphology of neat PEG2000, PMMA/PEG blends and PMMA/PEG/MWNTs nanocomposites crystallized at 0 °C. Well-developed spherulite grows to a size of about 2000  $\mu\text{m}$  in diameter in the case of neat PEG2000, as shown in Fig. 3 a). Spherulites are the basic morphology for polymers crystallized from melting or concentrated solutions, which are high-order crystal structures with spherical textures composed of lamellar crystallites shaped like ribbons that radiate from the center, separated by amorphous material [16]. For the PMMA/PEG blends, as shown in Fig. 3 b), it is clear that the presence of PMMA networks limited the PEG spherulites growth. Parts c), d), e), and f) of Fig. 3 illustrate the POM images of PEG spherulites after nanocomposites preparation with MWNTs. It is clear that the size of PEG spherulites becomes smaller in the presence of MWNTs, indicative of the increase of nucleation density; some smaller and imperfect spherulites with diameter less than 200  $\mu\text{m}$  are observed to grow rapidly, impinge quickly with surrounding spherulites, and restrict further growth. Spherulitic morphology studies indicate that the nucleation density of PEG is improved due to the presence of MWNTs in the nanocomposites and MWNTs seem very effective as a nucleation agent.

It is of great interest to study the effect of the incorporation of MWNTs on the crystal structure of PEG in the nanocomposites. Fig. 4 illustrates the WAXD patterns of neat PEG2000 and PMMA/PEG/MWNTs nanocomposites, which were crystallized at 0 °C for 12 hrs.

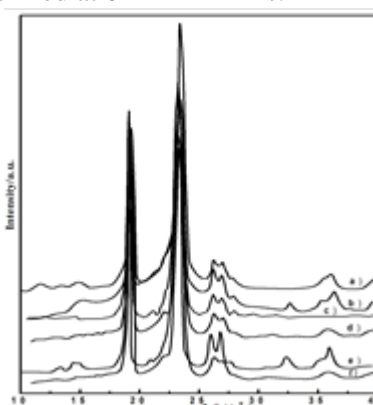


**Fig. 4.** WAXD patterns of a) neat PEG2000, b) PMMA/PEG2000, c) PMMA/PEG2000/0.5 wt.% MWNTs, d) PMMA/PEG2000/1 wt.% MWNTs, e) PMMA/PEG2000/2 wt. % MWNTs, f) PMMA/PEG2000/3 wt. % MWNTs.

It should be noted that PEG2000 and PMMA/PEG/MWNTs nanocomposites have

similar diffraction patterns, and so are their diffraction angles and crystal plane distances. Neat PEG2000 shows two main diffraction peaks at about 18.9° and 23.1°, whose positions don't change in PMMA/PEG/MWNTs nanocomposites, which demonstrates that neat PEG2000 and PMMA/PEG/MWNTs nanocomposites have similar crystal structure and crystal cell type, and there are no significant distortions of the crystal structures of PEG in nanocomposites. In other words, the crystal structure of PEG has not been changed by the procedure of blending, and therefore, there are no chemical changes at all. The main difference between neat PEG2000 and PMMA/PEG/MWNTs nanocomposites is that the diffraction peak height and half-width of the former are lower and narrower than those of the latter, which means that the dimension of spherulites becomes smaller and the degree of crystallization decreases; the result is consistent with POM results.

It is of great interest to study the melting behavior of neat PEG2000, PMMA/PEG2000 and its nanocomposites because crystal structures and crystallinity play significant roles in the mechanical and other properties of crystalline polymers. DSC analysis is a generally convenient method for analyzing first order transitions like melting.

Fig. 5 shows the thermal diagram measured during heating.

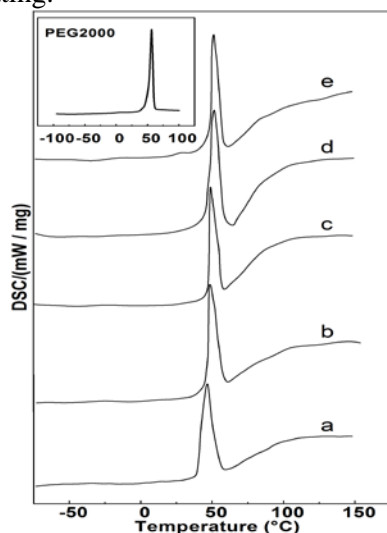


**Fig. 5.** DSC scans of neat PEG2000, PMMA/PEG2000 (a), PMMA/PEG2000/0.5 wt.% MWNTs (b), PMMA/PEG2000/1 wt.% MWNTs (c), PMMA/PEG2000/2 wt.% MWNTs (d), and PMMA/PEG2000/3 wt.% MWNTs (e).

The PMMA/PEG/MWNTs nanocomposites possess a melting endothermic peak ( $T_m$ ) during heating; it can be observed that  $T_m$  increase slightly in the PMMA/PEG/MWNTs nanocomposite compared with those in PMMA/PEG blend, and increase with increase of MWNTs concentration, as

shown in Table 1, which indicates that the MWNTs presence does not prevent PEG crystallization, and act as an nucleation reagent for the PEG crystallization; meanwhile, the melting enthalpy ( $\Delta H_m$ ) which are determined from the area under the endotherm, are increased in the nanocomposites as compared with that of PMMA/PEG blend in Table 1. The weight crystallinity indexes ( $X_c$ ) of the PEG phase, PMMA/PEG2000 and PMMA/PEG2000/MWNTs nanocomposites are calculated from:

$$X_c = \Delta H_m / \Delta H_{PEG}^{\circ} \quad (1)$$

Where  $\Delta H_{PEG}^{\circ}$  is the heat of fusion per gram of 100 % crystalline PEG (from literature data [36],  $\Delta H_{PEG}^{\circ} = 45 \text{ cal}\cdot\text{g}^{-1}$ ).

**Table 1.** DSC results for PEG2000, PMMA/PEG2000 and its nanocomposites.

Sample	$T_m$ (°C)	$\Delta H_m$ (J/g)	$X_c$ (%)
PEG2000	57	178	94
PMMA/PEG2000	46.5	26.5	14
PMMA/PEG2000/0.5 wt% MWNTs	48.6	30.2	16
PMMA/PEG2000/1.0 wt% MWNTs	49.7	32.3	17
PMMA/PEG2000/2.0 wt% MWNTs	50.8	34.1	18
PMMA/PEG2000/3.0 wt% MWNTs	51.7	35.9	19

Although  $X_c$  of PMMA/PEG2000 and PMMA/PEG2000/MWNTs nanocomposites are much lower than that of pure PEG2000, they increase with increasing of MWNTs content for PMMA/PEG2000/MWNTs nanocomposites. From above results, compared to PMMA/PEG blends, it can be concluded that the incorporation of MWNTs enhances the crystallization of PEG2000 in the nanocomposites, which should be attributed to the strong heterogeneous nucleation of MWNTs [26].

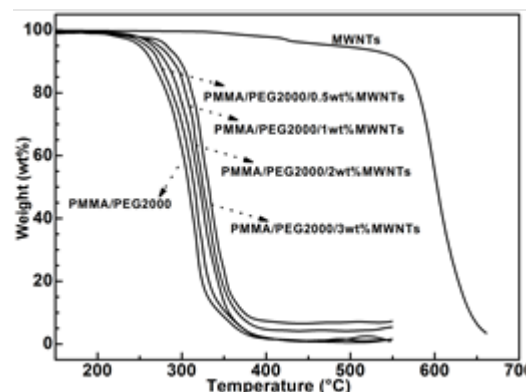


**Fig. 6.** TGA curves of MWNTs, PMMA/PEG2000 and PMMA/PEG2000/MWNTs nanocomposites.

Fig. 6 shows TGA thermograms of PMMA/PEG blend, MWNTs and PMMA/PEG/MWNTs nanocomposites. The decomposition temperature (onset of inflection) for PMMA/PEG blend is lower than those of its nanocomposites, indicating that the thermal stability of nanocomposites has been improved because of addition of MWNTs. Besides that, the residual weight of PMMA/PEG/MWNTs nanocomposites left increases steadily with the increase of MWNTs loading. As shown in Fig. 6, the weight loss at 345 °C for PMMA/PEG blend is about 85 %, whereas PMMA/PEG/MWNTs nanocomposites are only around 49 - 79 %. This also indicates that the thermal stability of PMMA/PEG blend is significantly improved on incorporation of MWNTs.

Fig. 7 shows the dependence of the decomposition temperature ( $T_d$ , 5 % weight loss temperature) on MWNTs content. PMMA/PEG blend and pure MWNTs start to lose weight at 251 °C and 467 °C, respectively. It can be seen that the overall thermal stability of PMMA/PEG/MWNTs nanocomposites, compared with PMMA/PEG blend, is clearly improved; in Fig. 7, the addition of 0.5 wt % MWNTs causes the decomposition temperature of PMMA/PEG blend increase more than 7 °C. The thermal stability of PMMA/PEG/MWNTs nanocomposites may be closely related to following factors: the dispersion state and the loading content of MWNTs.

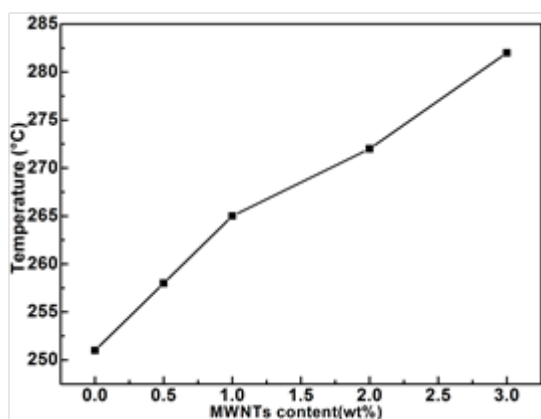


Fig. 7. Decomposition temperature ( $T_d$ , 5 % weight loss temperature) as a function of MWNTs loading.

The decomposition temperature of PMMA/PEG/MWNTs nanocomposites increases slightly with increasing MWNTs loading content, probably due to the ease of compact char formation for the nanocomposites during the thermal degradation; more importantly, CNTs is a kind of excellent flame retardant material, which may be ascribed to the following factors: a) high heat conduction ability of CNTs promotes the consumption of heat [37]; b) CNT as electron

acceptor can capture high-energy radicals during the thermal degradation process [38, 39].

On the other hand, high concentration MWNTs would definitely prevent its fine dispersion, and more aggregation or bundles could often be formed because of van der Waals force among the MWNTs, thus deteriorating the thermal stability of the nanocomposites. It is necessary to research the competing effect between the dispersion state and the loading content of MWNTs in depth.

## CONCLUSIONS

MWNTs were dispersed into PMMA/PEG blends through ultrasonic assisting with 0.5 %; 1 %; 2 % and 3 % (wt/wt) of MWNTs loadings.

Morphological analysis shows that, at low concentration of MWNTs, it is well dispersed; however, with an increase in MWNTs concentration, it is a nonuniform dispersion, and a large aggregate of MWNTs having a diameter of over 500nm is formed. The POM images of PEG spherulites becomes smaller in the presence of MWNTs; DSC analysis showed that  $T_m$  increased very slightly in the PMMA/PEG/MWNTs nanocomposites compared with those in PMMA/PEG blend, and increased with increase of MWNTs concentration. The analysis of thermal degradation in airflow showed a clear improvement of thermal stability for PMMA/PEG/MWNTs nanocomposites, proportionally to MWNTs content.

## REFERENCES

1. A. Allaoui, S. Bai, H. M. Cheng, J. B. Bai, *Compos. Sci. Technol.*, **62**, 1993 (2002).
2. S. J. Park, M. S. Cho, S. T. Lim, H. J. Choi, M. S. Jhon, *Macromol. Rapid Comm.*, **24**, 1070 (2003).
3. Y. B. Zou, Y. C. Feng, L. Wang, X. B. Liu, *Carbon*, **42**, 271 (2004).
4. E. N. Konyushenko, J. Stejskal, M. Techova, J. Hradil, J. Kovářová, M. Cieslar, J. Y. Hwang, K. H. Chen, I. Sapurina, *Polymer*, **47**, 5715 (2006).
5. M. K. Yeh, N. H. Tai, J. H. Liu, *Carbon*, **44**, 1 (2006).
6. N. Grossiord, J. Loos, O. Regev, C. E. Koning, *Chem. Mater.*, **18**, 1089 (2006).
7. A. Maity, M. Biswas, *J. Ind. Eng. Chem.*, **12**, 311 (2006).
8. S. T. Kim, J. Y. Lim, B. J. Park, H. J. Choi, *Macromol. Chem. Phys.*, **208**, 514 (2007).
9. F. H. Zhang, R. G. Wang, X. D. He, C. Wang, L. N. Ren, *J. Mater. Sci.*, **44**, 3574 (2009).
10. Y. Wang, R. Cheng, L. Liang, Y. Wang, *Compos. Sci. Technol.*, **65**, 793 (2005).
11. J. C. Kearns, R. L. Shambaugh, *J. Appl. Polym. Sci.*, **86**, 2079 (2002).
12. X. Tong, C. Liu, H. Cheng, H. Zhao, F. Yang, X. Zhang, *J. Appl. Polym. Sci.*, **92**, 3697 (2004).

13. B. Safadi, R. Andrews, E. A. Grulke, *J. Appl. Polym. Sci.*, **84**, 2660 (2002).
14. M. Terrones, *Annu. Rev. Mater. Res.*, **33**, 419 (2003).
15. F. H. Gojny, M. H. G. Wichmann, B. Fiedler, W. Bauhofer, K. Schulte, *Compos. Part A: Appl. S.*, **36**, 1525 (2005).
16. E. T. Thostenson, Z. Ren, T. Chou, *Compos. Sci. Technol.*, **61**, 1899 (2001).
17. H. W. Goh, S. H. Goh, G. Q. Xu, K. P. Pramoda, W. D. Zhang, *Chem. Phys. Lett.*, **379**, 236 (2003).
18. J. N. Coleman, U. Khan, J. Blau, Y. Gun'ko, *Carbon*, **44**, 1624 (2006).
19. H. Ito, T. P. Russell, G. D. Wignall, *Macromolecules*, **20**, 2213 (1987).
20. J. Straka, P. Schmidt, J. Dybal, B. Schneider, J. Spevacek, *Polymer*, **36**, 1147 (1995).
21. X. Lu, R. A. Weiss, *Macromolecules*, **25**, 3242 (1992).
22. H. Schmidt, I. A. Kinloch, A. N. Burgess, A. H. Windle, *Langmuir*, **23**, 5707 (2007).
23. S. Pande, R. B. Mathur, B. P. Singh, T. L. Dhama, *Polym. Compos.*, **30**, 1312 (2009).
24. A. K. Pradhan, S. K. Swain, *J. Mater. Sci. Technol.*, **28**, 391 (2012).
25. G. Gonçalves, S. M. Cruz, A. Ramalho, J. Grácio, P. A. Marques, *Nanoscale*, **4**, 2937 (2012).
26. R. Ormsby, T. McNally, C. Mitchell, N. Dunne, *J Mater Sci Mater Med.*, **21**, 2287 (2010).
27. R. Ormsby, T. McNally, P. O'Hare, G. Burke, C. Mitchell, N. Dunne, *Acta Biomater.*, **8**, 1201 (2012).
28. D. Chen, M. Wang, W. D. Zhang, T. Liu, *J. Appl. Polym. Sci.*, **113**, 644 (2009).
29. G. X. Chen, H. S. Kim, B. H. Park, J. S. Yoon, *Polymer*, **47**, 4760 (2006).
30. S. T. Kim, H. J. Choi, S. M. Hong, *Colloid Polym. Sci.*, **285**, 593 (2007).
31. J. Liu, A. G. Rinzler, H. Dai, J. H. Hafner, R. K. Bradley, P. J. Boul, A. Lu, K. Shelimov, C. B. Huffman, F. Rodriguez-Macias, Y. S. Shon, T. R. Lee, D. T. Colbert, R. E. Smalley, *Science*, **280**, 1253 (1998).
32. S. J. Park, S. T. Lim, M. S. Cho, H. M. Kim, J. Joo, H. J. Choi, *Curr. Appl. Phys.*, **5**, 302 (2005).
33. Y. Zhao, Z. Qiu, W. Yang, *J. Phys. Chem. B*, **112**, 16461 (2008).
34. C. L. Wu, M. Q. Zhang, M. Z. Rong, K. Friedrich, *Compos. Sci. Technol.*, **62**, 1327 (2002).
35. D. N. Bikiaris, A. Vassiliou, E. Pavlidou, P. Karayannidis, *Eur. Polym. J.*, **41**, 1965 (2005).
36. E. Martuscelli, C. Silvestre, C. Glomondi, *Die Makromolekulare Chemie*, **186**, 2161 (1985).
37. J. J. Ge, H. Hou, Q. Li, M. J. Graham, A. Greiner, D. H. Reneker, ... & S. Z. Cheng, *J. Am. Chem. Soc.*, **126**, 15754 (2004).
38. P. C. P. Watts, P. K. Fearon, W. K. Hsu, N. C. Billingham, H. W. Kroto and D. R. M. Walton, *J. Mater. Chem.*, **13**, 491 (2003).
39. M. S. P. Shaffer, A. H. Windle, *Adv. Mater.*, **11**, 937 (1999).

## МОРФОЛОГИЯ И ТЕРМИЧНИ ОТНАСЯНИЯ НА НАНОКОМПОЗИТИ ОТ ПОЛИ(МЕТИЛ-МЕТАКРИЛАТ/ПОЛИ(ЕТИЛЕНГЛИКОЛ) С МНОГОСТЕННИ ВЪГЛЕРОДНИ НАНОТРЪБИ

Г. К. Лю

Колеж по материалознание и инженерство, Технологичен университет Хенан, Женгжоу, 450001, Китай

Постъпила на 25 декември, 2013 г.; коригирана на 3 юли, 2015 г.

(Резюме)

Изготвени са многостенни въглеродни нанотръби (MWNTs) с нано-композити от поли(метил-метакрилат/поли(етиленгликол) (PMMA/PEG/MWNTs). Приложена е радикалова обемна полимеризация под действието на ултразвук. Изследван е ефекта на различните процентни натоварвания с MWNTs върху морфологичните и термичните свойства на нанокompозитите от PMMA/PEG/MWNTs. Намерено е, че при ниски концентрации многостенните въглеродни нанотръби се диспергират равномерно в смесите от PMMA/PEG и повишават плътността на зародишообразуване на PEG. Термичният анализ показва, че има ясно изразено подобрене на термичната стабилност на нанокompозитите PMMA/PEG/MWNTs с повишаване на съдържанието на MWNTs.



## Synthesis and characterization of some lanthanide metal complexes Ce(III), Gd(III), Nd(III), Tb(III) and Er(III) with sulfasalazine as sulfa drug

M. G. Abd El-Wahed<sup>1</sup>, S. M. El-Megharbel<sup>1,2</sup>, M. Y. El-Sayed<sup>1</sup>, Y. M. Zahran<sup>1</sup>, M. S. Refat<sup>2,3\*</sup>

<sup>1</sup>Department of Chemistry, Faculty of Science, Zagazig University, Egypt

<sup>2</sup>Department of Chemistry, Faculty of Science, Taif University, 888 Taif, Kingdom Saudi Arabia

<sup>3</sup>Department of Chemistry, Faculty of Science, Port Said, Port Said University, Egypt

Received December 6, 2013, Revised May 13, 2015

The complexation between lanthanides metal ions like Ce(III), Eu(III), Nd(III) and La(III) with sulfasalazine (H<sub>3</sub>suz) produced 1:1 molar ratio (metal : sulfasalazine) as a monodentate via OH group and give general formula: Na<sub>2</sub>[M(Hsuz)(Cl)<sub>3</sub>(H<sub>2</sub>O)]·xH<sub>2</sub>O, where: M= Ce, Eu, Nd and La, x= 2 and 10. The resulted sulfasalazine compounds were assigned by Infrared, <sup>1</sup>H-NMR and electronic spectra. Thermogravimetric analysis and kinetic thermodynamic parameters have proved the thermal stability feature of sulfasalazine complexes. The anti-microbial activities of the lanthanides metal complexes of sulfasalazine recorded a significant effect against some bacteria and fungi.

**Keywords:** Sulfasalazine; lanthanide metal ions; complexation; antimicrobial activity

### INTRODUCTION

Sulfa drugs have attracted special attention for their therapeutic importance as they were used against a wide spectrum of bacterial ailments [1-9]. Also, some sulfa drugs were used in the treatment of cancer, malaria, leprosy and tuberculosis [4]. The importance of the very interesting features of metal coordinated systems is the concerted spatial arrangement of the ligands around the metal ions [10]. Although the complexes of the sulfa drugs have been investigated in the solid state, relatively was known about their solution chemistry in particular their mixed-ligand complexes [8, 11]. The formation and characterization of binary and mixed-ligand complexes, involving iminodiacetic acid and sulfa drugs as sulfadiazine and sulfadiazamide, were investigated [8, 11, 12]. Sulfasalazine H<sub>3</sub>suz (Fig. 1) 2-hydroxy-5-[[4-[(2-pyridinylamino) sulfonyl]phenyl]azo]benzoic acid; is a sulfa drug, a derivative of Mesalazine (5-aminosalicylic acid abbreviated as 5-ASA), used primarily as an anti-inflammatory agent in the treatment of inflammatory bowel diseases as well as rheumatoid arthritis [13-16]. When dealing with the interaction between drugs and metal ions in living systems, a particular interest has been given to the interaction of metal ions with antibiotics, which has been widely used in medicine both towards human beings and animals [17, 18]. In particular the interaction between transition metals and β-lactamic antibiotics such as cephalexin has

been recently investigated by several physicochemical and spectroscopic methods, and with detailed biological data [19-22]. Many properties when administered in the form of metallic complexes. Probably the most widely studied cation in this respect is Cu(II), since a host of low-molecular-weight copper complexes have been proven beneficial against several diseases such as tuberculosis, rheumatoid, gastric ulcers, and cancers [23-29] of the complexation of sulfa drugs did not focus on the coordination behavior, but only dealt with the solution state and crystal structures of its metal complexes.

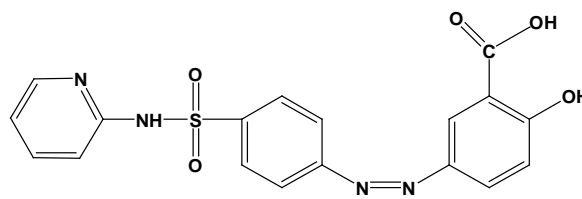


Fig. 1. Sulfasalazine (H<sub>3</sub>suz) drug ligand.

The complexation of sulfasalazine (H<sub>3</sub>suz) with some of transition metals have been investigated [30]. Three types of complexes, [Mn(Hsuz)(H<sub>2</sub>O)<sub>4</sub>].2H<sub>2</sub>O, [M(Hsuz)(H<sub>2</sub>O)<sub>2</sub>].xH<sub>2</sub>O (M= Hg(II), ZrO(II) and VO(II), x=4, 8 and 6, respectively) and [M(Hsuz)(Cl)(H<sub>2</sub>O)<sub>3</sub>].xH<sub>2</sub>O (M=Cr(III) and Y(III), x= 5 and 6, respectively) were obtained and characterized by physicochemical and spectroscopic methods. The IR spectra of the complexes suggest that the sulfasalazine behaves as a monoanionic bidentate ligand. The thermal decomposition of the complexes as well as thermodynamic parameters

\* To whom all correspondence should be sent:  
E-mail: msrefat@yahoo.com

( $E^*$ ,  $\Delta H^*$ ,  $\Delta S^*$  and  $\Delta G^*$ ) were estimated using Coast-Redfern and Horowitz-Metzger equations. In vitro antimicrobial activities of the H<sub>3</sub>suz and the complexes were tested. The complexes of sulfasalazine(H<sub>3</sub>suz) with some of alkaline-earth metals Mg(II), Ca(II), Sr(II) and Ba(II) have been investigated [31]. Sulfasalazine complexes were synthesized and characterized by spectroscopic tools; Infrared spectra, electronic and mass spectra. The IR spectra of the prepared complexes were suggested that the H<sub>3</sub>suz behaves as a bi-dentate through the carboxylic and phenolic groups. The molar conductance measurements gave an idea about the non-electrolytic behavior of the H<sub>3</sub>suz complexes. The thermal decomposition processes for metal(II) complexes of H<sub>3</sub>suz viz: [M(Hsuz)(H<sub>2</sub>O)<sub>4</sub>] (where M= Mg(II), Ca(II), Sr(II) or Ba(II)) have been accomplished on the basis of TG/DTG and DTA studies, and the formula conforms to the stoichiometry of the complexes based on elemental analysis. The kinetic analyses of the thermal decomposition were studied using the Coast-Redfern and Horowitz-Metzger equations. The antitumor and antimicrobial activities of the H<sub>3</sub>suz and their alkaline-earth metals(II) complexes were evaluated. Sulfasalazine is composed by sulfapyridine (SP) and 5-amino salicylic acid (5-ASA) with a diazo bond linkage. 5-ASA is considered to be the active component in the therapy of inflammatory bowel disease, while SASP and SP are effective in the therapy of rheumatoid disease [32-34]. The complexation behaviour of mesalazine (5-aminosalicylic acid; 5-ASA) towards the transition metal ions namely, Cr(III), Mn(III), Fe(III), Co(II), Ni(II), Cu(II) and Zn(II) have been examined by elemental analyses, magnetic measurements, electronic, IR and <sup>1</sup>H-NMR. Thermal properties and decomposition kinetics of all complexes are investigated. The interpretation, mathematical analyses and evaluation of kinetic parameters of all thermal decomposition stages have been evaluated using Coast-Redfern equation. The free ligand and its metal complexes have been tested in vitro against *Aspergillus niger* and *Candida albicans* fungi and *Pseudomonas aeruginosa*, *Escherichia coli*, *Bacillus subtilis* and *Staphylococcus aureus* bacteria in order to assess their anti-microbial activity than the parent 5-ASA drug [35]. Herein, in this work we prepare chelates of Ce(III), Eu(III), Nd(III) and La(III) with Sulfasalazine drug molecule. The solid chelates are characterized using different physico-chemical methods like elemental analyses (C, H, N, S and metal content), IR, UV-vis spectra, <sup>1</sup>H-NMR and thermal analyses (TG and

DTG). Antimicrobial activity test of the complexes are studied.

## EXPERIMENTAL

### Physical measurements

Carbon and hydrogen contents were determined using a Perkin-Elmer CHN 2400. The metal content was found gravimetrically by converting the complexes into their corresponding oxides. Infrared spectra were recorded on Bruker FT-IR Spectrophotometer (4000-400 cm<sup>-1</sup>) in KBr pellets. The UV-vis spectra were studied in the DMSO solvent with a concentration of 1.0x10<sup>-3</sup> M for the H<sub>3</sub>suz and their complexes using Jenway 6405 spectrophotometer with 1cm quartz cell, in the range 800-200 nm. Molar conductance of the freshly prepared solutions of H<sub>3</sub>suz complexes with 1.0x 10<sup>-3</sup> M in DMSO were measured using Jenway 4010 conductivity meter. <sup>1</sup>H-NMR spectra were recorded on a Varian Gemini 200 MHz spectrophotometer using DMSO-d<sub>6</sub> as solvent. Thermogravimetric analyses (TGA and DTG) were carried out in a dynamic nitrogen atmosphere (30 ml/min) with a heating rate of 10 °C/min using Shimaduz TGA-50H thermal analyzer.

### Antimicrobial activity test

According to [36], the hole well method was applied. The investigated isolates of bacteria were seeded in tubes with nutrient broth (NB). The seeded NB (1 cm<sup>3</sup>) was homogenized in the tubes with 9 cm<sup>3</sup> of melted (45 °C) nutrient agar (NA). The homogeneous suspensions were poured into petri dishes. The holes (diameter, 4 mm) were done in the cool medium. After cooling 2x10<sup>-3</sup> dm<sup>3</sup> of the investigated compounds were applied using a micropipette. After incubation for 24 h in a thermostat at 25-27 °C, the inhibition (sterile) zone diameters (including disk) were measured and expressed in mm. An inhibition zone diameter of over 7 mm indicates that the tested compounds are active against the bacteria under investigation. The antibacterial activities of the investigated compounds were tested against *Escherichia coli* (Gram -ve), *Bacillus subtilis* (Gram +ve) and antifungal (*Aspergillus niger* and *Penicillium* activities).

### Materials and methods

All chemicals used were of analytical grade where possible and were purchased from Aldrich and Merck companies and sulfasalazine drug was presented from Egyptian international pharmaceutical industrial company (EIPICO). The complexes were prepared by mixing sulfasalazine

(2 mmol) and metal chlorides of Eu(III), Ce(III), Nd(III) and La(III) (1.0 mmol) in mixed solvent MeOH/H<sub>2</sub>O (50/50%; 40 cm<sup>3</sup>), then pH of the solution was adjusted to 8-9 with 1 M NaOH solution and the reaction mixture was stirred at 60 °C for 2 h and left to stand overnight. The precipitated complexes were filtered off, washed with MeOH and H<sub>2</sub>O and dried in vacuum at room temperature under anhydrous CaCl<sub>2</sub>.

## RESULTS AND DISCUSSION

The elemental analysis (CHN) agrees quite well with the speculated structure of the colored sulfasalazine complexes (Table 1). The prepared complexes have brown color. They are thermally stable above >250 °C, soluble in DMSO and DMF. The conductivity values measured in DMSO at room temperature are located in the range of non-electrolytes [37] for Ce(III), Eu(III), Nd(III) and La(III)/H<sub>3</sub>suz complexes while complexes behaves as 1:1 non-electrolytes. The interpretation concerning decreasing of conductivity values back to the deprotonation of both OH of carboxylic and OH of phenolic groups for the sulfasalazine ligand. This assumption proves that free ligand acts in a bidentate fashion via carboxylic and phenolic groups and also attributed to the participation of carboxylic group as a monodentate chelate.

### Infrared spectra

The infrared spectra of sulfasalazine and its complexes exhibited with the main coordination bands which reveal the mode of bonding and are summarized in Table 2. Concerning the sulfasalazine complex, the most important region in the infrared spectra of all complexes and the H<sub>3</sub>suz

free ligand (~1700-1300 cm<sup>-1</sup>) is selected and assigned in Table 2 as follows; In contrast to the assignments data of sulfasalazine, Ce(III), Eu(III), Nd(III) and La(III) complexes show no absorption band at 1677 cm<sup>-1</sup>, characteristic to the ν(C=O) vibration of the carboxylic group (in case of free H<sub>3</sub>suz ligand), that is indicative of the involvement of the carboxylic group in the coordination with metal ion. The peaks at 1655 cm<sup>-1</sup> (vs) Ce(III)/Hsuz, 1652 cm<sup>-1</sup> (vs) for Eu(III)/Hsuz, 1649 cm<sup>-1</sup> (s) for Nd(III)/Hsuz, 1654 cm<sup>-1</sup> (vs) for La(III)/Hsuz complexes, respectively, are absent in the spectrum data of the free H<sub>3</sub>suz and can be assigned to the asymmetric stretching vibration of the carboxylate group, ν<sub>as</sub>(COO<sup>-</sup>). The spectra of Na<sub>2</sub>[M(Hsuz)(Cl)<sub>3</sub>(H<sub>2</sub>O)].xH<sub>2</sub>O (M= Ce(III), Eu(III) Nd(III) and La(III), x= 2 and 10 respectively) complexes also have medium to strong intensity band in the range of 1437-1456 cm<sup>-1</sup>. This band is absent in spectrum of H<sub>3</sub>suz and interpretive to the symmetric vibration of the ν<sub>s</sub>(COO<sup>-</sup>) group. Deacon and Phillips [38] studied the criteria that can be used to distinguish between the three binding states of the carboxylate complexes. These criteria are: (i) ν >200cm<sup>-1</sup> (where ν = [ν<sub>as</sub>(COO<sup>-</sup>)- ν<sub>s</sub>(COO<sup>-</sup>)], this relation is found in case of unidentate carboxylato complexes, (ii) bidentate or chelating carboxylato complexes exhibit ν significantly smaller than ionic values (ν <100 cm<sup>-1</sup>) and finally (iii) bridging complexes show ν comparable to ionic values (ν ~150 cm<sup>-1</sup>). The observed ν for all the sulfasalazine complexes is > 200 cm<sup>-1</sup> which confirms a unidentate interaction of the carboxylate group.

**Table 1.** Elemental analyses and physical data of suzH and its complexes

Complexes	Mwt	Color	Content ((calculated) found)					Am Ω <sup>-1</sup> cm <sup>-1</sup> mol <sup>-1</sup>
			% C	% H	% N	% Cl	% M	
Ce(III)	698.5	Brown	(30.11)	(2.79)	(7.39)	(14.03)	(18.49)	9.2
			30.26	2.79	7.19	14.44	18.31	
Eu(III)	854.5	Brown	(24.97)	(4.08)	(6.13)	(11.64)	(16.63)	5.9
			25.63	4.52	6.40	12.60	17.95	
Nd(III)	702.5	Brown	(29.95)	(2.78)	(7.35)	(13.96)	(18.93)	8.7
			30.56	4.92	7.38	15.23	20.82	
La(III)	697.5	Brown	(30.16)	(2.80)	(7.40)	(14.06)	(18.36)	6.8
			30.73	2.83	8.43	15.73	19.57	

**Table 2.** Main IR data of the suzH and its metal complexes

Compound	V(O-H)	V(C-O)	δ(OH)	V <sub>as</sub> (COO)	V <sub>s</sub> (COO)	ΔV(COO)	V(M-O)
H <sub>3</sub> suz	--	1281	1393	1625	1427	--	--
Ce(III)	3430	1239	1374	1655	1449	206	529
Eu(III)	3383	1239	1378	1652	1437	215	538-458
Nd(III)	3423	1240	1380	1649	1441	208	439
La(III)	3422	1240	1382	1654	1456	198	411

A broad diffuse band of strong to medium strong intensity in the 3500-3350  $\text{cm}^{-1}$  region may be assigned to the OH stretching vibration for the coordinated and uncoordinated water molecules in the  $\text{H}_3\text{suz}$  complexes. It is note-worthy to say that when the media of precipitation is sodium hydroxide, this means that the sodium salt of sulfasalazine is formed so, the stretching vibration band of  $\nu$  (OH) of carboxylic group. As is also difficult distinction between the  $\nu$  (OH) phenolic group of sulfasalazine and the stretching vibrational bands of water molecules because of the overlapping values, and appear in one place. To ascertain the involvement of  $\nu$  (OH) of phenolic group of sulfasalazine in the coordination process to the followed by the stretching vibration bands of  $\nu$  (C-O) in all sulfasalazine complexes, examination of the  $\text{H}_3\text{suz}$  complexes found that the  $\nu$  (C-O) shifted to lower wave number from 1281  $\text{cm}^{-1}$  in case of free ligand to 1239 to 1240  $\text{cm}^{-1}$  in case of their complexes. This result indicates that the phenolic group participated in the complexation and the  $\text{H}_3\text{suz}$  ligand acted as bidentate. The lower shift of  $\delta$ (OH) from 1393  $\text{cm}^{-1}$  in the free  $\text{H}_3\text{suz}$  ligand to 1374-1382  $\text{cm}^{-1}$  in their complexes is another factor confirming the involvement of OH phenolic group in the coordination process. The presence of  $\nu$ (M-O) stretching vibrations at two bands: 538-458  $\text{cm}^{-1}$  for Eu(III)/Hsuz and one band: 529  $\text{cm}^{-1}$  for Ce(III)/Hsuz, 439  $\text{cm}^{-1}$  for Nd(III)/Hsuz and 411  $\text{cm}^{-1}$  for La(III)/Hsuz, supports coordination by  $\text{H}_3\text{suz}$  ligand as a bidentate monoanionic chelating agent via OH of carboxylic and phenolic groups [39].

#### Electronic spectra

The electronic spectra of the free  $\text{H}_3\text{suz}$  and their metal complexes were measured and listed in Table 3.

**Table 3.** Electronic spectral data of the sulfasalazine metal complexes

Compound	$\lambda_{\text{max}}$ (nm)	Assignment
Ce (III)	226, 246, 260,	$\pi$ - $\pi^*$ trans n- $\pi^*$ trans
	268,308, 332,	
	389	
	427, 601, 701,	
Eu(III)	787	$\pi$ - $\pi^*$ trans n- $\pi^*$ trans
	226, 248, 259,	
	270, 296, 332	
	597, 704	
Nd(III)	228, 269, 298,	$\pi$ - $\pi^*$ trans n - $\pi^*$ trans
	332	
	403, 427, 591	
	215, 227, 231,	
La(III)	245, 251, 262,	$\pi$ - $\pi^*$ trans n- $\pi^*$ trans
	270, 306, 332	
	428, 591	

There are some absorption peaks at ranged from 215-390 nm (225, 280, 290, 360, 390 nm) and at 415 nm, which are assigned to  $\pi$ -  $\pi^*$  and n- $\pi^*$  transitions within the organic moiety of sulfasalazine ligand. On the other hand, there are two absorption ranges at 215-389 nm and 403-787 nm, due to  $\pi$ - $\pi^*$  and n- $\pi^*$  transitions, respectively, within the  $\text{H}_3\text{suz}$  complexes. The electronic absorption spectra of all  $\text{H}_3\text{suz}$  complexes show a bathochromic shift comparable to free ligand within n- $\pi^*$  transition region [40-45]. This shift attributed to the place of complexation and the change in the electronic configuration for the  $\text{H}_3\text{suz}$  complexes resulted.

#### $^1\text{H-NMR}$ spectra

The  $^1\text{H-NMR}$  spectra presented the persuasive confirmation of the coordination modes. Thus, the  $^1\text{H-NMR}$  spectra of complexes (Fig. 2) on comparing with those of spectrum of the free sulfasalazine indicate that,  $\text{H}_3\text{suz}$  ligand acts as bidentate ligand through the phenolic OH group and carboxylic OH group.  $^1\text{H-NMR}$  spectra of complexes were carried out in  $\text{DMSO-d}_6$  as a solvent, the data obtained are in agreement with the suggested coordination through the carboxylic and phenolic groups by absence of the signals of two protons which exist in the free ligand about  $\delta$ = 11.00 and 5.00 ppm, respectively, and due to different chemical environments the signals of aromatic protons at 6.00–8.00 ppm are present with decreasing intensities.

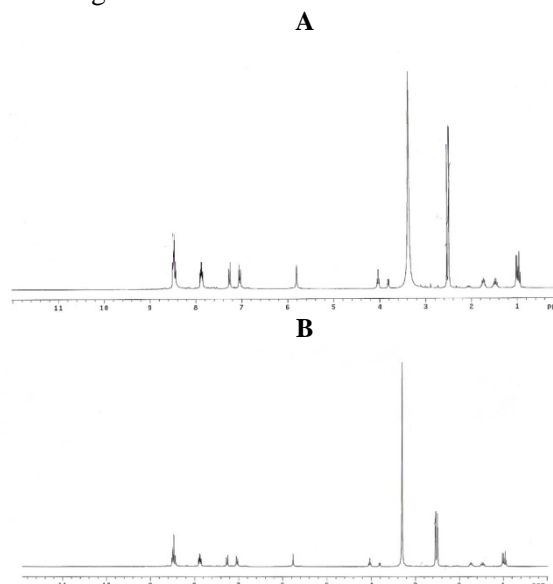


**Fig. 2.**  $^1\text{H-NMR}$  spectra of (A) Eu(III)/Hsuz and (B) Nd(III)/Hsuz complexes

#### Thermal analysis

The thermal decomposition curves (TG/DTG and DTA) are given in Fig. 3, while the TG weight loss data, DTG and DTA peak temperatures are

existed in Table 4. The results showed that the complexes lost its hydration water below 573 K, within the temperature range 573-653 K the coordinated water molecules were liberated. The anhydrous complexes displayed the decomposition of the organic ligand within the temperature range 673-1073 K leading to metal oxide. The metal contents were calculated from the residual contents and were found to be in good agreement with the results of elemental analysis.  $\text{Na}_2[\text{Ce}(\text{suzH})(\text{Cl})_3(\text{H}_2\text{O})] \cdot 2\text{H}_2\text{O}$  complex was thermally decomposed in three successive decomposition steps within 327-1073 K, the first decomposition step (obs= 5.0%, calc= 5.4%) within the temperature range 327-519 K, may be attributed to the liberation of the two hydrated water molecules. The second decomposition step found within the temperature range 519-768 K (obs= 45.6%, calc= 45.3%), which are reasonably accounted for by the removal of  $(3\text{C}_2\text{H}_2+2\text{HCN}+\text{SO}_2+1.5\text{Cl}_2+0.5\text{O})$ . The rest of sulfasalazine molecule was removed on the third step within the temperature range 768-1073 K (obs= 27.9%, calc= 27.4%). The decomposition of the ligand molecule ended with a final oxide residue of  $\text{CeO}_{1.5}$ .

The TG curve of  $\text{Na}_2[\text{Eu}(\text{suzH})(\text{Cl})_3(\text{H}_2\text{O})] \cdot 10\text{H}_2\text{O}$  complex indicates that the mass change begins at 352 K and continues up to 814 K. the first mass loss corresponds to the liberation of the three hydrated water molecules (obs= 7.9%, calc= 8.0%). The second decomposition step occurs in the range 600-814 K and corresponds to the loss of  $(2\text{C}_2\text{H}_2+\text{SO}_2+2\text{HCN}+2\text{HCl}+5.5\text{H}_2\text{O}+\text{O}_2)$  (obs= 43.2%, calc= 43.7%). The final decomposition step occurs in the range 814-1073 K and corresponds to the loss of  $(5\text{C}_2\text{H}_2+\text{HCl}+\text{N}_2+2\text{CO})$  (obs= 29.2%, calc= 29.3%). DTG profile shows three endothermic peaks, the first at 352 K corresponds to the melting of the complex, while the second at 600 K corresponds to the dehydration and decomposition of the complex. The third broad endothermic peak corresponds to the final decomposition of the organic ligand to the  $\text{EuO}_{1.5}$ .

To make sure about the proposed formula and structure for the Nd complex, thermo gravimetric (TG) and differential thermo gravimetric (DTG) was carried out for this complex under  $\text{N}_2$  flow. The thermal decomposition for  $\text{Na}_2[\text{Nd}(\text{suzH})(\text{Cl})_3(\text{H}_2\text{O})] \cdot 2\text{H}_2\text{O}$  complex occurs in three steps. The first degradation step take place in the range of 298-344 K and it is corresponds to the elimination of  $2\text{H}_2\text{O}$  molecules due to weight loss (obs, =5.8% and calc=5.4%).

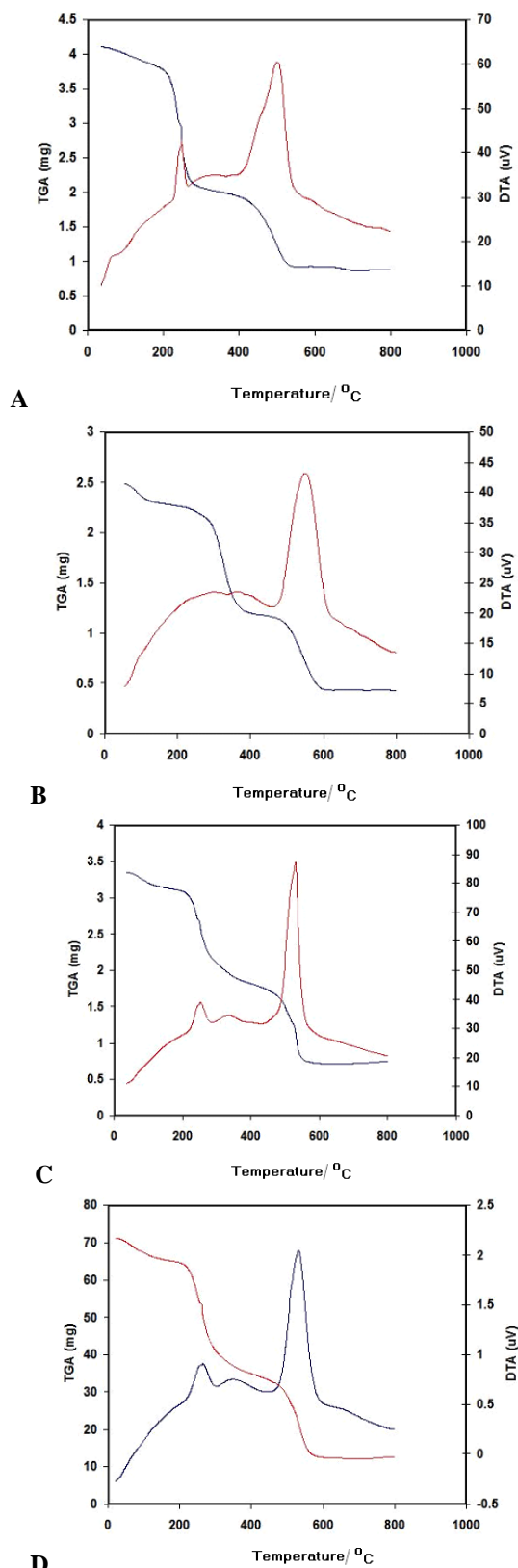


**Fig. 3.** TG and DTG curves of (A): Ce-sulfasalazine, (B): Eu-sulfasalazine, (C): Nd- sulfasalazine and (D): La-sulfasalazine

The second step fall in the range 523-803 K which is assigned to loss of  $(3\text{C}_2\text{H}_2+2\text{HCN}+\text{SO}_2+\text{Cl}_2+0.5\text{O})$  with a weight loss

(obs=38.7% and calc=39.0%). The final step fall in 803 K was accompanied by mass loss (obs=32.1% and calc=31.9%) which is assigned to loss of (4C<sub>2</sub>H<sub>2</sub>+N<sub>2</sub>+2CO+0.5Cl<sub>2</sub>). The (NdO<sub>1.5</sub>) is the final product remains stable till 1073 K.

The Na<sub>2</sub>[La(suzH)(Cl)<sub>3</sub>(H<sub>2</sub>O)].2H<sub>2</sub>O complex was thermally decomposed in three successive decomposition steps with in the temperature range 352-1073 K. the first decomposition step (obs= 6.0%, calc= 5.4%) within the temperature range 352-600 K, may be attributed to the liberation of two hydrated water molecules.

The second decomposition steps found within the temperature range 534-803 K (obs= 35.5%, calc= 35.5%) which corresponds to loss of (2C<sub>2</sub>H<sub>2</sub>+2HCN+SO<sub>2</sub>+Cl<sub>2</sub>+0.5O). The rest of sulfasalazine molecule was removed on the final step within the temperature range 803-1073 K and corresponds to loss of (2.5C<sub>2</sub>H<sub>2</sub>+N<sub>2</sub>+ 2CO+HCl) (obs= 27%, calc= 27.3%). The decomposition of the ligand molecule ended with a final oxide residue of LaO<sub>1.5</sub> contaminated carbon atoms.

In the present investigation, the general thermal behaviors of the sulfasalazine complexes in terms of stability ranges, peak temperatures and values of kinetic parameters, are shown in Table 5 and Fig. 4.

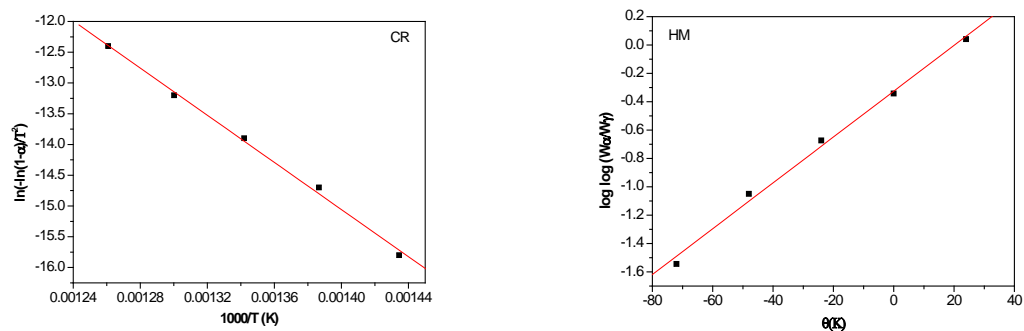
The kinetic and thermo dynamic parameters have been evaluated using the Coats-Redfern and Horowitz-Metzger equations [46, 47]. The entropy of activation, ΔS\*, was calculated. The enthalpy activation, ΔH\*, and Gibbs free energy, ΔG\*, were calculated from; ΔH\* = E\* - RT and ΔG\* = ΔH\* - TΔS\*, respectively. The thermodynamic behavior of the all complexes of sulfasalazine with some lanthanide(III) metal ions is non-spontaneously (more ordered) reactions (ΔS is negative value), endothermic reactions (ΔH>0) and endergonic (ΔG >0) during the reactions. The thermodynamic data obtained with the two methods are in harmony with each other. The correlation coefficients of the Arrhenius plots of the thermal decomposition steps were found to lie in the range ~ 0.99, showing a good fit with linear function. It is clear that the thermal decomposition process of all sulfasalazine complexes is non-spontaneous, i.e., the complexes are thermally stable.

*Structure of the sulfasalazine complexes*

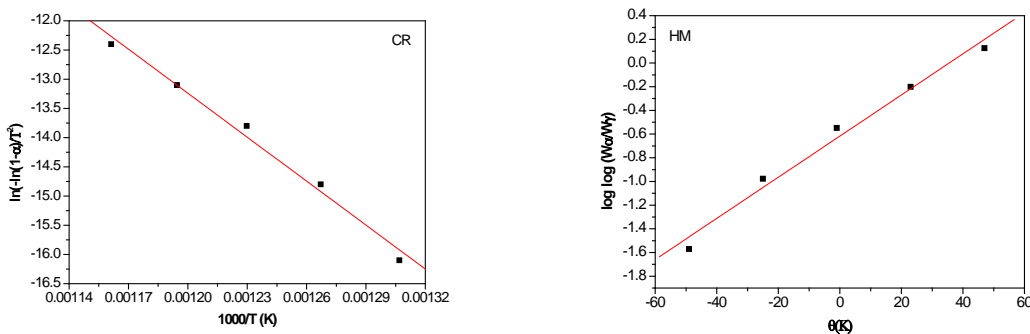
Finally on the basis of the above studies, the suggested structures of the sulfasalazine complexes can be represented in Fig. 5.

**Table 4.** Thermal data of sulfasalazine and its complexes

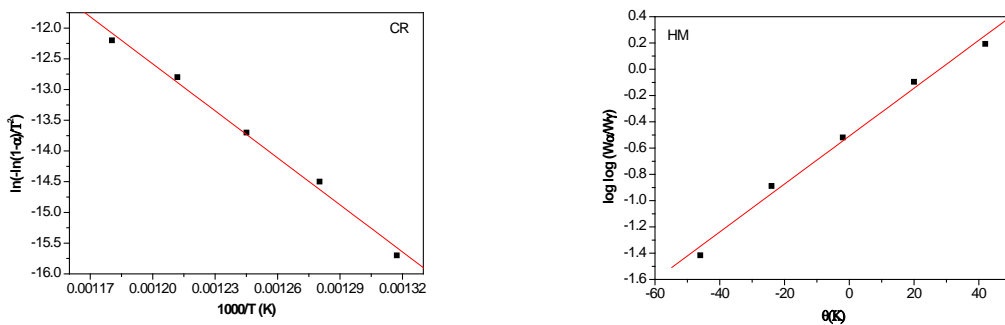
Compound	Step	Temp range (°C)	DTG peak (°C)	TG weight		Assignments
				Calc	Found	
Ce(III)	1	50-150	54.59	5.4	5.0	2H <sub>2</sub> O
	2	200-250	246.73	45.3	45.0	3C <sub>2</sub> H <sub>2</sub> +2HCN+SO <sub>2</sub> +1.5Cl <sub>2</sub> +0.5O
	3	260-500	495.97	27.4	27.9	4C <sub>2</sub> H <sub>2</sub> +N <sub>2</sub> +2CO CeO <sub>1.5</sub> +Na <sub>2</sub> O
Eu(III)	1	40-180	80	8.0	7.9	3H <sub>2</sub> O
	2	200-330	327.43	43.7	43.2	2C <sub>2</sub> H <sub>2</sub> +SO <sub>2</sub> +2HCN+2HCl+5.5H <sub>2</sub> O+ O <sub>2</sub>
	3	350-800	541.82	29.3	29.2	5C <sub>2</sub> H <sub>2</sub> +N <sub>2</sub> +2CO+ HCl EuO <sub>1.5</sub> + Na <sub>2</sub> O
Nd(III)	1	30-150	71.50	5.4	5.8	2H <sub>2</sub> O
	2	200-450	250	39.0	38.7	3C <sub>2</sub> H <sub>2</sub> +2HCN +SO <sub>2</sub> +Cl <sub>2</sub> +0.5O
	3	500-800	530	31.9	32.1	4C <sub>2</sub> H <sub>2</sub> +0.5Cl <sub>2</sub> +N <sub>2</sub> +2CO NdO <sub>1.5</sub> + Na <sub>2</sub> O
La(III)	1	50-150	62.36	5.4	6.0	2H <sub>2</sub> O
	2	200-250	261	35.5	35.5	2C <sub>2</sub> H <sub>2</sub> +2HCN+SO <sub>2</sub> +Cl <sub>2</sub> +0.5O
	3	560-800	530	27.3	27.0	2.5C <sub>2</sub> H <sub>2</sub> +N <sub>2</sub> + 2CO+0.5Cl <sub>2</sub> LaO <sub>1.5</sub> + Na <sub>2</sub> O



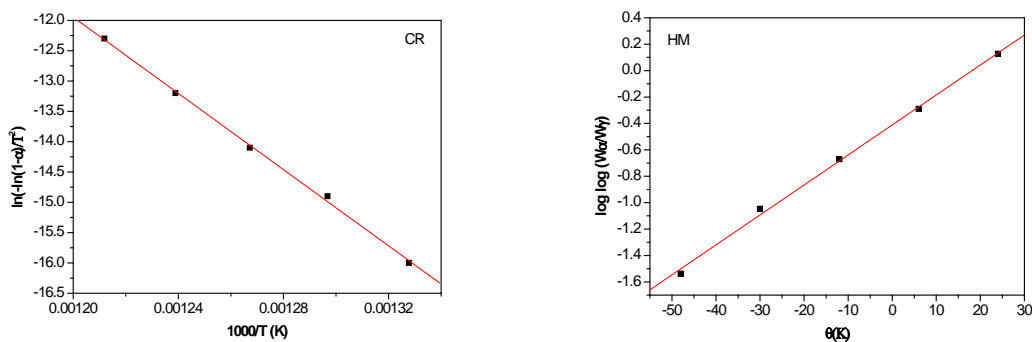
Ce(III) complex



Eu(III) complex



La(III) complex



Nd(III) complex

Fig. 4. Coat-Redfern (CR) and Horowitz and Metzger (HM) curves for sulfasalazine complexes

**Table 5.** Thermodynamic parameters of the thermal decomposition of sulfasalazine complexes

Thermodynamic Parameters	Methods		Complexes	
	CR	HM		
r	0.99836	0.99732	Ce(III)	
E*	1.59E+05	1.83E+05		
A	6.17E+08	2.56E+10		
ΔS*	-	-		
	8.45E+01	5.35E+01		
ΔH*	1.53E+05	1.77E+05		
ΔG*	2.18E+05	2.18E+05		
r	0.99408	0.99172		Eu(III)
E*	2.09E+05	2.20E+05		
A	1.33E+11	1.39E+12		
ΔS*	-	-		
	4.03E+01	2.08E+01		
ΔH*	2.02E+05	2.14E+05		
ΔG*	2.35E+05	2.31E+05		
r	0.99645	0.99536	La(III)	
E*	2.12E+05	2.26E+05		
A	4.29E+11	5.13E+12		
ΔS*	-	-		
	3.05E+01	9.86E+00		
ΔH*	2.05E+05	2.20E+05		
ΔG*	2.30E+05	2.28E+05		
r	0.99926	0.99885		Nd(III)
E*	2.61E+05	2.79E+05		
A	1.22E+15	2.06E+16		
ΔS*	3.57E+01	5.92E+01		
ΔH*	2.55E+05	2.72E+05		
ΔG*	2.26E+05	2.25E+05		

*Antimicrobial activity*

The results of antimicrobial activities (bacteria and fungi) in vitro of sulfasalazine ligand and their complexes Table 6 and Fig. 6, show that, the Na<sub>2</sub>[La(suzH)Cl<sub>3</sub>(H<sub>2</sub>O)].2H<sub>2</sub>O test complex have high activities against A. niger>B. subtilis>pencillium. On the other hand, Ce(III), Eu(III) and Nd(III) sulfasalazine complexes have antimicrobial activities against B. subtilis and pencillium These results clearly obviously that, some metal ions after complexation give the sensitive nature for the ligand against some bacteria and fungi.

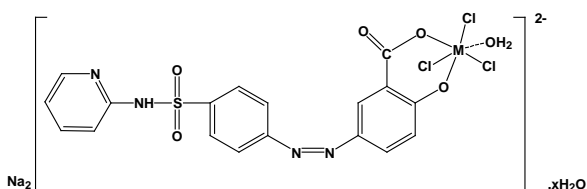


**Fig 5.** Mode of chelation of sulfasalazine complexes, where M= Ce(III), Eu(III), Nd(III) and La(III); X= 2 and 10.

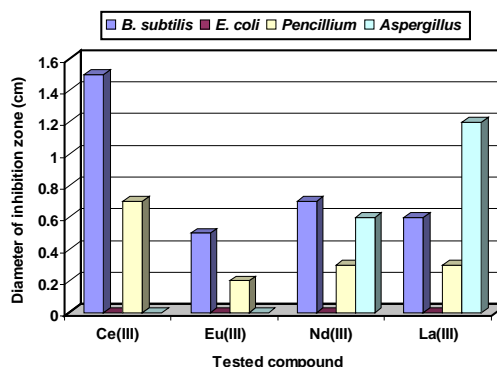


**Fig. 6.** Microbial test for sulfasalazine complexes

**Table 6.** Antimicrobial activity of sulfasalazine complexes.

Tested compounds	Diameter of inhibition zone (cm)			
	B. subtilis	E. col	P.rotatum	A.niger
Ce(III)	1.5	0	0.7	0
Eu(III)	0.5	0	0.2	0
Nd(III)	0.7	0	0.3	0.6
La(III)	0.6	0	0.3	1.2

REFERENCES

- 1.D.B. Clyson, J. A. S. Pringle, G. M. Ranses, *Biochem. Pharmacol.*, **16**, 614 (1967).
- 2.W.N. Beerlev, W. Pelers, K. Mager, *Ann. Trop. Med. Parasitol.*, **26**, 288 (1960).
- 3.G. Tarbini, *Inst. Congr. Chemother. Proc. 5<sup>th</sup>*, **2**, 909 (1967).
- 4.Hoffman La Roches Co., Swiss Patent 416648 (1967).
- 5.L.H. Schmidt, *Ann. Rev. Microbiol.*, **23**, 427 (1969).
- 6.C. Sharaby, *Synth. React. Inorg. Met. Org. Chem.*, **35** 133 (2005).
- 7.A. Vaichulis, US Patent 3,272,352 (1966).
- 8.M.M. Shoukry, E.M. Shoukry, *Int. J. Chem.*, **2**, 81 (1991).
- 9.C. Sharaby, *Spectrochim. Acta Part A.*, **66(4)**,1271 (2007).
- 10.J. B. Castledine, A.F. Fell, R. Modin, B. Sellberg, *J. Chromatogr.*, **592**, 27 (1999).
- 11.W. M. Hosny, *Synth. React. Inorg. Met.- Org. Chem.*, **29**, 361 (1999).
- 12.W. M. Hosny, *Synth. React. Inorg. Met.- Org. Chem.*, **27**, 197 (1999).
- 13.C. M. Bell, F. M. Hebal, *Am. J. Gastroenterol.*, **92**, 2201 (1997).
- 14.O.DiavCirtin, Y.Park, G.Veerasuretharam, *Gastroenterology.*, **114**, 23 (1998).
- 15.W.Sandborn , L.Sutherland , D.Pearson , G.May , R. Modigliani , C.L.Prantera *Cochrane Database Syst. Rev.*, CD000543 (2000).
- 16.S.B.Hanauer, W.J.Sandborn, A.Kornbluth, S.Katz, M. Safdi. *Am J Gastroenterol.* , **100**, 2478 (2005).



17. J. Klostersky, D. Danean, D. Weerts, *Chemotherapy*, **18**, 191 (1973).
18. A. Zaki, E. C. Schreiber, I. Welikly, J. R. Knill H. J. Hubsher, *J. Clin. Pharmacol.*, **14**, 1180 (1974).
19. F. M. Abdel-Gawad, N. M. el-Guinidi, M. N. Ibrahim, *J. Drug Res.*, **17**, 197 (1987).
20. J. Lozano, J. Borrás, *J. Inorg. BioChem.*, **31**, 187 (1987).
21. M. I. H. Helaleh, E. S. M. Nameh, *An. Quim. Int.*, **94**, 160 (1998).
22. J. R. Anaconda, *J. Coord. Chem.*, **54**, 355 (2001).
23. G. N. Mukherjee, S. Beau, T. Ghosh, *J. Indian Chem. Soc.*, **70**, 1043 (1993).
24. S. Tabassum, F. Amirand, S. H. Rafiqi, *Main Group Metal Chem.*, **19**, 245 (1996).
25. Z -F. Chen, S. Kang, H. Liang, F. Yi, K -B. Yu, R -G. Xiong, X -Z. You, *Appl. Organometal. Chem.*, **17**, 887 (2003).
26. Z -F. Chen, S. Kang, S -M. Shi, B F. Abrahams, H. Liang, *J. Mol. Struct.*, **882**, 134 (2008).
27. S. Kang, Z -F Chen, J. Guangxi, *Normal University*, **26**, 789 (2006).
28. D.H. Brown, A.J. Lewis, W.E. Smith, J.W. Teape, *J. Med. Chem.*, **23**, 729 (1980).
29. G. M. Golzar Hossain, A. J. Amoroso, A. Banu K. M.A. Malik, *Polyhedron*, **26**, 967 (2007).
30. M. G. Abd El-Wahed, M. S. Refat, S. M. El-Megharbel, *Indian academy of science*, **32**, 205 (2008).
31. M. S. Refat, F. S. Mohamed, *Spectrochimica Acta part A, Molecular and Biomolecular Spectroscopy*, **82**, 108 (2011).
32. K. M. Das, R. Dubin, *Clin pharmacokinet.*; **1** 406 (1976).
33. C. Fischer, K. Maier, E. Stumpf, U. von Gaisberg, U. Klotz, *Eur J Clin Pharmacol*; **25**, 511 (1983).
34. H. A. Bird, *Br J Rheumatol*, **34**; 16 (1995).
35. H. M. Soliman, G. M. Gehad, *Spectrochimica Acta part A, Molecular and Biomolecular Spectroscopy*, **107**, 8 (2013).
36. R. Gupta, R. K. Saxena, P. Chatarvedi, J. S. Virdi, *J. Appl. Bacteriol.*, **87**, 378 (1995).
37. W. J. Geary *Coord., Chem. Rev.*, **7**, 81 (1971).
38. G. B. Deacon, R. J. Philips, *Coord. Chem. Rev.*, **33**, 227 (1980).
39. K. Nakamoto, *Infrared and Raman spectra of inorganic and coordination compounds*, 4 th ed., Wiley, New York, 1986.
40. M. G. Abd El-Wahed, M. S. Refat, S. M. El-Megharbel, *Chem. Pharm. Bull.*, **56 (11)**, 1585 (2008).
41. M. G. Abd El-Wahed, M. S. Refat, S. M. El-Megharbel, *Spectrochim. Acta A*, **70**, 916 (2008).
42. M. S. Refat, *J. Mol. struct.*, **842**, 24 (2007).
43. M. G. Abd El-Wahed, M. S. Refat, S. M. El-Megharbel, *J. Mol. Struct.*, **888**, 416 (2008).
44. M.G. Abd El-Wahed, M.S. Refat, S.M.El-Megharbel, *J. Mol. Struct.*, **892**, (2008) 402.
45. M.,S.,Refat, *J.Mol.struct.*, **969**, 163,(2010).
46. A.W. Coats, J. P. Redfern, *Nature*, **201**, 68 (1964)
47. H.W. Horowitz, G. Metzger, *Anal. Chem.*, **35**, 1464 (1963).

## СИНТЕЗА И ОХАРАКТЕРИЗИРАНЕ НА НЯКОИ КОМПЛЕКСИ НА ЛАНТАНИДИТЕ Ce(III), Gd(III), Nd(III), Tb(III) И Er(III) СЪС СУЛФАСАЛАЗИН КАТО СУЛФА-ЛЕКАРСТВА

М. Г. Абд Ел-Уахед<sup>1</sup>, С. М. Ел-Мегарбел<sup>1,2</sup>, М. И. Ел-Сайед<sup>1</sup>, Я. М. Захран<sup>1</sup>, М. С. Рефат<sup>2,3\*</sup>

<sup>1</sup>Департамент по химия, Факултет за наука, Университет Загазиг, Египет

<sup>2</sup>Департамент по химия, Факултет за наука, Университет Таиф, 888 Taif, Кралство Саудитска Арабия

<sup>3</sup>Департамент по химия, Факултет за наука, Университет в Порт Сауд, Египет

Постъпила на 6 декември, 2013 г.; Коригирана на 13 май, 2015 г.

(емюзер)

Комплексообразуването между йони на лантанидите (напр. Ce(III), Eu(III), Nd(III) и La(III)) със сулфасалазин (H<sub>3</sub>suz) дава комплекси с моларно съотношение 1:1 (метал : сулфасалазин) като монодендантичрез хидроксилна група и с обща формула Na<sub>2</sub>[M(Hsuz)(Cl)<sub>3</sub>(H<sub>2</sub>O)]·xH<sub>2</sub>O, където M= Ce, Eu, Nd и La, x = 2 и 10. Получените съединения за охарактеризирани с инфрачервени, <sup>1</sup>H-NMR и електронни спектри. Доказана е тяхната термична стабилност чрез термогравиметричен анализ, термодинамични и кинетични изследвания. Тези комплексни съединения на лантанидите със сулфасалазина показват анти-микробна активност спрямо някои бактерии и гъбички.

## Adaptive mutation particle swarm optimized BP neural network in state-of-charge estimation of Li-ion battery for electric vehicles

Feng Jin<sup>1,2</sup>, He Yong-ling<sup>1</sup>

<sup>1</sup> School of Transportation Science and Engineering of Beijing University of Aeronautics and Astronautics, Beijing 100191;

<sup>2</sup> Department of Automobile Engineering, Guilin University of Aerospace Technology, Guilin 541004

Submitted May 12, 2014

The state of charge (SOC) of Li-ion battery on electric vehicle (EV) is highly nonlinear. The randomly selected initial parameters of BP neural network can cause significant inaccuracy and long training time. In the study presented in this paper, an optimized BP neural network, with its initial parameters optimized by adaptive particle swarm optimization (PSO) algorithm, was used to estimate the Li-ion battery's state of charge (SOC). The performance on BP neural network estimation, as well as the optimized performance with adaptive mutation PSO was analyzed. A model for adaptive mutation PSO- BP neural network was established for battery SOC estimation. Experimental results show that: using BP neural network optimized by adaptive mutation PSO for SOC estimation of Li-ion battery of EV, can overcome the shortcomings of easily trapped to local optimum, long training time and so on. It also reduces the estimation deviation.

**Key words:** Adaptive mutation; particle swarm optimization; BP neural network; state of charge

### INTRODUCTION

State of charge (SOC) estimation is a key technology of battery management system (BMS) of electric vehicles (EV). Accurate estimation of SOC not only avoids the danger of over-charging and over-discharging which may damage the battery, but also helps creating a better battery control strategy, which allows more effective control and more precise prediction of driving range. This will help approaching the goal of energy saving, environmental protection, and battery life extension for EV [1, 2].

SOC of battery cannot be measured directly. Instead, it can be estimated from some physical properties of the battery, such as terminal voltage, current, temperature, etc. The accuracy of estimation is affected by many factors, i.e. voltage, charge-discharge rate, power, temperature, life cycle, internal resistance, internal pressure, self-discharge rate, etc. These factors have strong nonlinear relationship with SOC. Therefore it is difficult to establish an accurate mathematical model [3, 4].

The commonly used methods for SOC estimation include Ah counting method, open circuit voltage (OCV) method, the linear model method; neural network method and Kalman filter (KF) method [2]. Ah counting method can get the battery charge and discharge electricity by the integral of current times the time. If the initial SOC

is known, this method can be approached on-line SOC testing. But the algorithm also has some drawbacks such as, the Coulomb efficiency is difficult to be measured accurately and the accumulated sampling error is large, and so forth. It is not suitable for the occasions where the voltage and current change dramatically. Therefore, Ah counting method does not meet the requirement of EV for long-term use [5]. Some studies proposed improved Ah counting method that an equivalent Coulomb efficiency was defined to alleviate these problem with an SOC estimation method combined with the open circuit voltage method, Kalman filter, and Ah counting method. The SOC estimate error using this method relative to a discharge test was only 2.3%, satisfies the 8% SOC estimate precision requirement of EV. However, this method also comprises the problem of high requirement of model accuracy, large amount of calculation, high requirement of hardware, and couldn't meet the requirements for commercialization [6]. The most obvious drawback of OCV method is that battery must be relaxed for a long time before each measurement to eliminate the battery polarization effects which affects accuracy of voltage value. So this method is not suitable for online estimation of battery' SOC. The most effective use of OCV method is in initial SOC estimation after EV's long time standing so it is often used in combination with the Ah counting method. A recent study [7] proposed an equivalent circuit network to describe the polarization effect of the battery in OCV method. The recursive least square algorithm with

\* To whom all correspondence should be sent:  
E-mail: daewoo\_feng@126.com

forgetting was applied to implement the on-line parameter calibration. The maximum and mean relative errors are 1.666% and 0.01% respectively, in a hybrid pulse test. The linear model method which is based on linear equation established by the relationship between current, voltage, SOC variation and the former SOC value, is suitable for the low-current situation, which makes it only applicable to the lead-acid battery. The KF method is a useful tool for optimal state estimation of systems. Using the temporal transfer relationship of a system, this approach estimates the state of system with a set of recursive formula. It is suitable for noise filter in the harsh environment like EV driving process. However, the KF needs a proper equivalent circuit model of the battery to describe the characteristics of charging and/or discharging, of which the internal parameters are often difficult to determine. Meanwhile, for large amount of calculation, the system requires a higher speed processor which means higher cost [8].

The neural network method presumes a highly non-linear system, applicable to SOC estimation of all kinds of battery. But, it needs a large number of experiment data for training [9, 10]. Since the initial weights and thresholds of neural network are selected randomly, each training result of the network is different and the range of deficiency is large. Finding the proper network parameters takes a great amount of time. However, using power battery testing equipment, training samples all-inclusive for covering the entire work range can be collected and use to train the neural network. On this basis, the forecast accuracy of neural network can be improved as long as the proper network can be constructed and the initial weights and thresholds could be optimized [11].

In this paper, the BP neural network optimized with adaptive mutation PSO would be proposed for estimation of battery SOC. First, the characteristics of BP (Back Propagation) neural network and the modeling process will be introduced. Then, the initial weights and thresholds of BP neural network optimized by adaptive mutation PSO will be taken into the BP neural network to establish the SOC estimator. Finally, the proposed method will be tested in UDDS cycles and the simulation results are compared with the actual values.

### ESTABLISHMENT OF BP NEURAL NETWORK

#### BP Neural Network

BP network is a multi-layer forward network with hidden layer and error feedback. It has good learning and adaptive capacity as to solve the

learning problem of the connection weights of implied unit in a multi-layer network. As of today it is the most widely used neural network [12]. The basic principle of BP neural network algorithm is the gradient steepest descent method, which can minimize the total errors by adjusting the network weights. That is, the gradient search technology minimizes the error of the mean square value of actual output. In fact, multi-layer network using BP learning algorithm contains the forward and reverse spread of two stages. The input information from the input layer is propagated through the hidden layer to output layer and processed layer-by-layer during the forward propagation process [11,13]. The structure of BP neural network is showed as Fig.1.

The input of the  $i$ -th neuron in hidden layer is showed as below under the sample  $p$ :

$$o_i = f\left(\sum_{j=1}^m w_{ij}x_j - \theta_i\right) \tag{1}$$

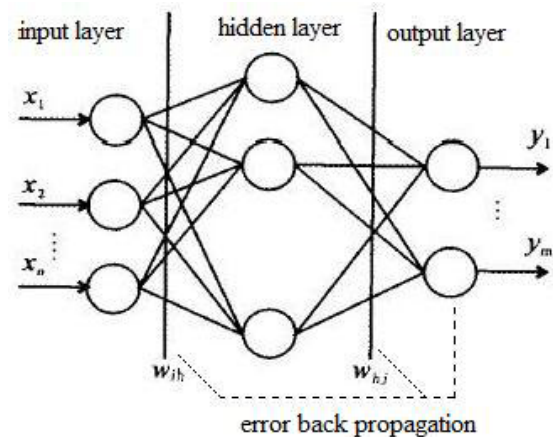


Fig.1. The structure of BP neural network.

Where  $o_i$  is the output value of the  $i$ -th neuron in the hidden layer,  $w_{ij}$  is the connection weight between the  $j$ -th neuron in input layer and the  $i$ -th neuron in the hidden layer,  $x_i$  is the input value of the  $j$ -th neuron in input layer,  $\theta_i$  is the threshold of the  $j$ -th neuron of input layer,  $f$  is the activation function of the hidden layer.

The output of the  $k$ -th neuron in the output layer is:

$$y_k = g\left(\sum_{i=1}^q w_{ki}o_i - \theta_k\right) \tag{2}$$

Where,  $y_k$  is the output value of the  $k$ -th neuron in output layer,  $w_{ki}$  is the connection weight between the  $k$ -th neuron in output layer and the  $i$ -th neuron in hidden layer,  $\theta_k$  is the threshold of the  $k$ -th neuron of output layer,  $g$  is the activation function of the output layer.

If the output value is not the expected, back propagation then begins. The error signal is returned along the original connection channel, then, the value of connection weights of each layers are modified to make the error signal less at the same time.

The error function  $J$  can be expressed as:

$$J = \frac{1}{2} \sum_{k=1}^L (t_k - o_k)^2 \quad (3)$$

Where,  $L$  is the number of output layer,  $t_k$  is the target value.

### Weight coefficient of output layer adjustment

The weight coefficient is adjusted according to the opposite direction of function gradient, which make the network gradually converge. According to the gradient method, the correction formula of each neuron weight coefficient of output layer is as follows:

$$\Delta w_{ki} = -\eta \frac{\partial J}{\partial w_{ki}} = \eta o_k (1 - o_k) (t_k - o_k) o_i \quad (4)$$

Similarly, the correction formula of the each neuron weights coefficient of hidden layer is as follow:

$$\Delta w_{ij} = -\eta \frac{\partial J}{\partial w_{ij}} = \eta o_i (1 - o_i) \left( \sum_{k=1}^L ((t_k - o_k) o_k (1 - o_k) w_{ki}) \right) o_j \quad (5)$$

### Collection of testing sample

When using BP neural network algorithm for SOC estimation of Li-ion battery, the first thing is the collection of training samples and testing samples. The number of training samples should be large and all-inclusive for covering the entire work range. There are many impact factors in SOC estimation. Considering the purpose of this research is to verify the rationality of the algorithm, only current and voltage's influence are taken into account [14].

Simulation software ADVISOR (Advanced Vehicle Simulator) is developed by National Renewable Energy Laboratory (NREL) of the United States for the management of the development of hybrid drive systems. Because the battery data in this software is from experiment done by NREL, its data is relatively accurate and comprehensive. In this paper, experiment samples would be acquired under different working conditions using a virtual EV which contains a 6Ah Li-ion battery manufactured by SAFT Company of the Unite State. The working conditions include constant speed of 8 km h<sup>-1</sup>, constant speed of 72kmh<sup>-1</sup>, constant speed of 144 km h<sup>-1</sup>, FTP cycle

and UDDS cycle. The relationship curve between speed and time is shown as Fig. 2 in the example of UDDS cycle.

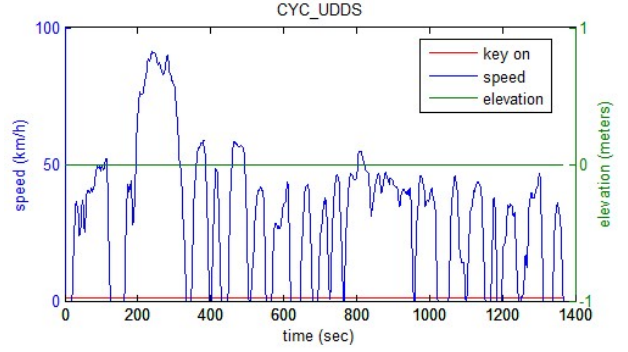


Fig. 2. EPA Urban Dynamometer Driving Schedule (UDDS)

The above working condition simulates the situations of EV at low speed, medium speed, high speed and urban road, covering the entire typical driving pattern and has strong representation. In order to collect sufficient data for the neural network training and testing, each of simulation working condition was looped to execute from SOC being 1 until SOC being 0. Each parameter of EV battery including voltage value and current value was sampled at the frequency of 1 during the simulation process and there were total of 12925 sets of data. The 2386 sets of data sampled during UDDS cycle were for testing, the other data were grouped as 160-set samples according to the principles of uniform distribution for training [15, 16]. Fig. 3 to Fig.5 shows the sample value when virtual EV drives during one period of UDDS cycle.

### Sample preprocessing

From above figure we can see that current and voltage samples have difference in the order of magnitude. In order to avoid this problem which would make the network error larger, samples should be normalized first. Meanwhile, samples normalization can also help the convergence of network's training speed accelerate. The common samples normalization methods includes maximum and minimum method and average variance method. For the reason to simplify the problem, maximum and minimum method was employed in this paper.

$$x_k = (x_k^* - x_{min}) / (x_{max} - x_{min}) \quad (6)$$

Where,  $x_k$  is the  $k$ -th sample factor after normalization,  $x_k^*$  is the  $k$ -th sample factor before normalization,  $x_{max}$  is the maximum value of sample factor before normalization and  $x_{min}$  is the minimum value of sample factor before normalization.

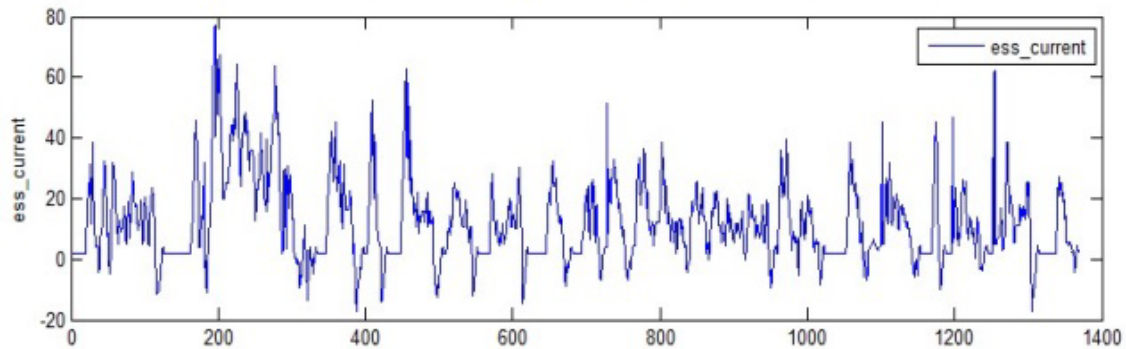


Fig. 3. Current profile sampled during UDDS cycles.

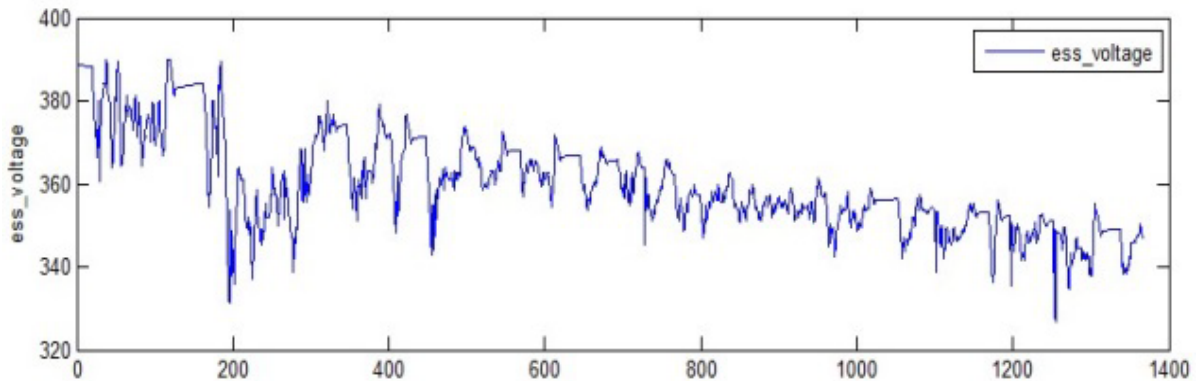


Fig. 4. Voltage profile sampled during UDDS cycles.

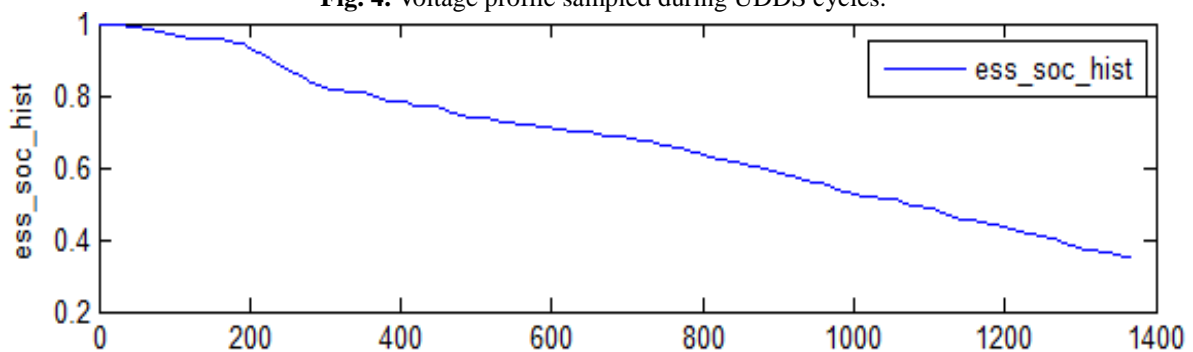


Fig. 5. SOC profile sampled during UDDS cycles.

**The hidden layer of BP neural network**

The number of nodes in hidden layer of BP neural network has a great impact on network’s prediction accuracy. If the nodes number is too small, the network does not have sufficient learning and needs to increase the frequency of training, so the training accuracy may be less than desired. However, if the number of nodes is too much, it will make the training time too long and the network easy to over-fitting. The number of nodes has a direct relationship with the requirements, input and output nodes of the problem. The following two equations can be used as reference formula to select the optimum node number of hidden layer [17].

$$L = \sqrt{(m+n)} + a \tag{7}$$

Where  $L$  is the number of nodes of hidden

layer,  $m$  is the number of node of output layer,  $n$  is the number of nodes of input layer,  $a$  is a constant between 0 and 10.

$$L = \log_2 n \tag{8}$$

Where  $n$  is number of nodes of input layer.

Base on the above conditions, the number of nodes of hidden layer should be determined through thorough testing. In this study, number of nodes of the hidden layer are 5. The established BP neural network is shown as Fig. 6.

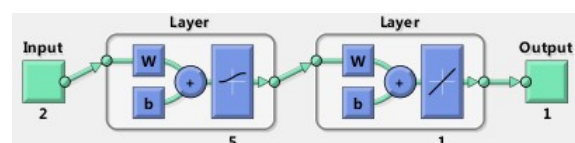


Fig. 6. The BP neural network.

### Weight and threshold of bp neural network optimized by PSO

Since the initial weights and thresholds of BP neural network are selected randomly, each training result of the network is different and range of deficient is large. Finding the proper network parameters takes a great amount of time. If the initial weights and thresholds of BP neural network are optimized by particle swarm optimization algorithm, the forecast accuracy of network can be improved.

Particle swarm optimization (PSO) is a new evolutionary algorithm developed in recent years. Similar to genetic algorithm (GA), PSO find the optimal solution by iteration, starting at a random solution. However it does this in a simpler way. PSO find the global optimum by following the current optimal value without “crossover” or “mutation” like GA. Compared with generic algorithm, PSO is easier to implement, has enhanced global searching capability, higher precision and faster convergence. Using PSO to optimize the initial weights and thresholds of BP network can shorten the network training time, improve the convergence, enhance network generalization ability and reduce error [18, 19].

The algorithm assumes that there are a number of particles in a population, and each particle has a position vector and velocity vector. The position vector and velocity vector of the  $i$ -th particle can be expressed as:

$$X_i = [x_{i1}, x_{i2}, \dots, x_{id}] \quad (9)$$

$$V_i = [v_{i1}, v_{i2}, \dots, v_{id}] \quad (10)$$

Where  $d$  represents the dimension of the solution space and its value is also the possible solutions. Particles can find the optimal solution by iteration through constantly moving in search space. The basic formula is:

$$v_{ij}^{k+1} = \omega v_{id}^k + c_1 r_1 (p_{ij}^k - x_{ij}^k) + c_2 r_2 (p_{gj}^k - x_{ij}^k) \quad (11)$$

$$x_{ij}^{k+1} = x_{ij}^k + v_{ij}^{k+1} \quad (12)$$

Where  $i = 1, 2, \dots, N$  and  $j = 1, 2, \dots, d$ ,  $v_{ij}$  are flight speed of the  $i$ -th particle,  $x_{ij}$  is position of the  $i$ -th particle,  $\omega$  is the inertia factor,  $c_1$  and  $c_2$  are acceleration factor which is positive constant,  $r_1, r_2$  are the random number on the interval  $[0, 1]$ ,  $p_{ij}$  is the best position of the  $i$ -th particle currently find.  $p_{gj}$  is the best position of global population currently find.

The initial positions and velocities of the particle swarm are generated randomly, and then they

iterate according to the formula 11 and formula 12. Particles continue to modify their velocities and positions according to  $p_{ij}$  and  $p_{gj}$  in each of the iterations, so that particles approach to the global optimal solution. There are 21 ( $2*5+5+5*1+1$ ) parameters that need to be optimized for a BP neural network with topology structure of  $[2, 5, 1]$ .

### Adaptive mutation algorithm establishment

PSO algorithm iteratively update by tracking the most optimal particle. Once a particle finds the optimal value, the other particles will quickly move close to it. However, the traditional algorithms have the problems of early convergence when the optimal value is trapped to local optima. It is necessary to enhance the basic PSO algorithm to avoid the premature convergence problem. The reason of premature convergence is large lost in population diversity. When algorithm escapes from local optima before convergence, it can continue searching in other area in solution space and finally find the global optima [20].

In this study, a random number in the iterative formula serves as mutation condition. Once the particles are greater than iteration threshold value, it mutates to be a random number. In this way, some of the particles can maintain the diversity for optimization from the current optimal conditions. The optimized algorithm with adaptive mutation can be established as:

$$x_{ij}^{k+1} = \begin{cases} x_{ij}^k + v_{ij}^{k+1} & r_1 \leq m \\ rand & r_1 > m \end{cases} \quad (13)$$

Where,  $m$  is the mutation threshold.

The basic parameters of adaptive mutation PSO algorithm are set as the following: The population size is 20, the maximum number of iterations is 200, learning factor  $c1 = c2 = 1.49$ , Speed range is on interval  $[-1, 1]$ , the position range is on interval  $[-1, 1]$ , the adaptive mutation threshold  $m = 0.8$ . First, fitness value is compared between PSO with adaptive mutation and the basic PSO. Fig.7 shows the fitness curve without adaptive mutation and Fig.8 shows the fitness curve with adaptive mutation.

As can be seen in Fig.8, although the optimization process of PSO algorithm without adaptive mutation is obvious, it converged quickly at first, but stopped at the 120 generation and trapped in local optima. In contrast, the PSO algorithm with adaptive mutation continues finding the optimal solution during the whole evolution process as shown in Fig.9.

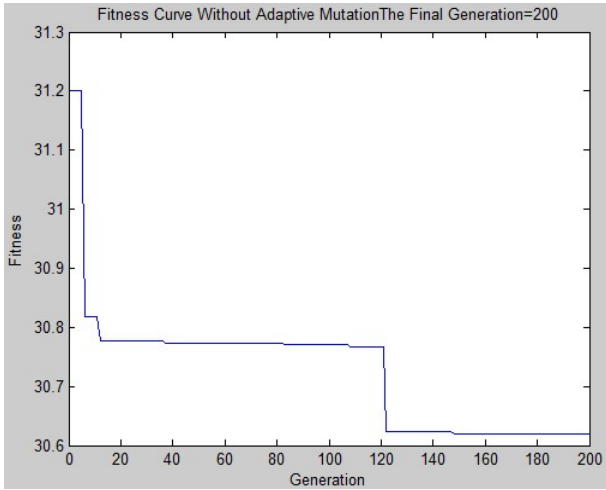


Fig. 7. Fitness curve without adaptive mutation.

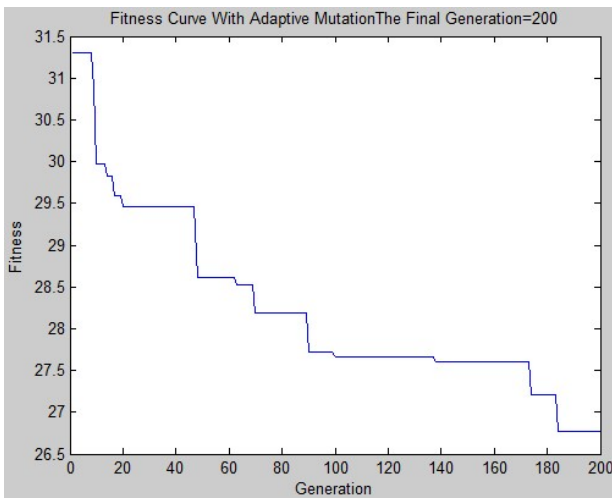


Fig. 8. Fitness curve with adaptive mutation.

## EXPERIMENT

### Experiment process

To verify the effect of BP neural network whose initial weights and threshold are optimized by adaptive mutation PSO, experiment and simulation were conducted. Experiments were conducted under UDDS conditions to illustrate the algorithm. Before starting the test, the Li-ion battery was fully charged (SOC=100%). Current and voltage value sampled from UDDS cycle in Advisor were imported into BP neural network for simulation. And then, the simulation result was compared with the experiment result done by NREL.

UDDS stands for Urban Dynamometer Driving Schedule. It refers to a United States Environmental Protection Agency (EPA) mandated dynamometer test on fuel economy that represents city driving conditions, which is used for light duty vehicle testing. Each cycle time is 1369 seconds, 7.45 miles, with average speed of 31.52 kmh<sup>-1</sup>.

Conditions cycle was shown as Fig.2. In this paper, several cycles of UDDS were employed to verify the SOC estimation algorithm. The voltage and current profiles sampled during UDDS cycles were shown in Fig.3 and Fig.4.

From above figure we can see, the battery was in a rapidly changing dynamic process under the UDDS cycle. The current and voltage change very quickly. Simulation under this working cycle can test the generalization ability of BP network well.

### Experimental result

To verify the performance of SOC estimation by adaptive mutation PSO-BP neural network for Li-ion battery of EV, we compared with standard BP neural network. Two kinds of model were trained with uniform training samples and set with uniform parameters, of which learning rate  $lr$  was 0.05, inertia factor  $mc$  was 0.9, number of iterations was 5000, error target was 10E-5. Meanwhile, relative errors between estimation value and experiment value were compared to illustrate their magnitude of error. Relative error was defined as follows:

$$Error = \frac{soc_s - soc_t}{soc_t} \quad (14)$$

Where,  $Error$  is the relative error,  $soc_s$  is the estimation value of SOC and  $soc_t$  is experiment value of SOC.

Experimental and simulation results were shown in Fig.9-12. Fig.9 and Fig.10 showed the actual and the estimated SOC during the entire charging process. Fig.11 and Fig.12 showed the relative error between the actual SOC and the estimated SOC.

From the estimation curve and error curve, estimated SOC by adaptive mutation PSO-BP algorithm matched the actual SOC well. It could follow the actual value trend. The relative error was small (about 8%) in the range of SOC from 1 to 0.15. However, the relative error became larger as the SOC decreases below 0.15. Considering the fact that SOC of EV's power battery is in the range from 0.2 to 0.8, the error was acceptable. Estimated SOC by standard BP algorithm can also follow the trend of experiment value. However, the relative error was large, more than 10% in the range of SOC from 1 to 0.15. Its estimation precision was lower than adaptive mutation PSO-BP algorithm. In summary, using adaptive mutation PSO-BP neural network has better precision in SOC estimation of EV's power battery than standard BP algorithm.

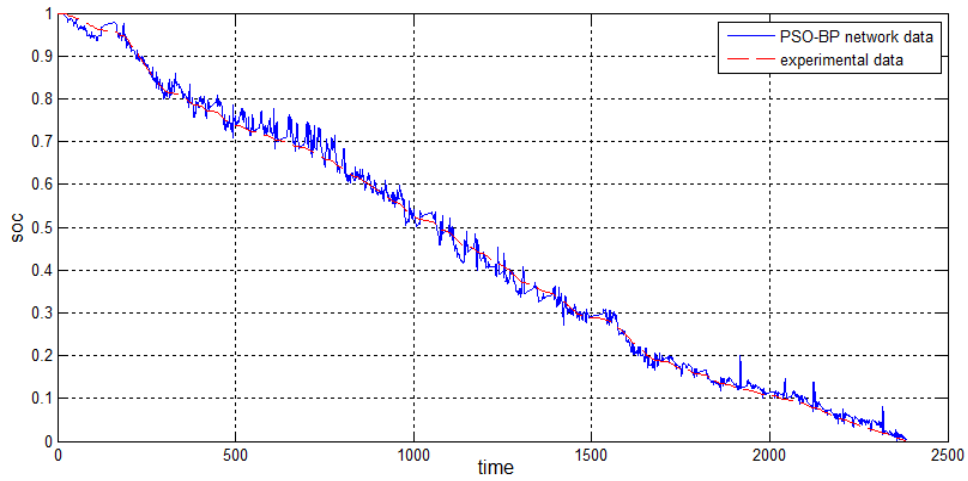


Fig. 9. SOC curves with adaptive mutation PSO-BP and experiment.

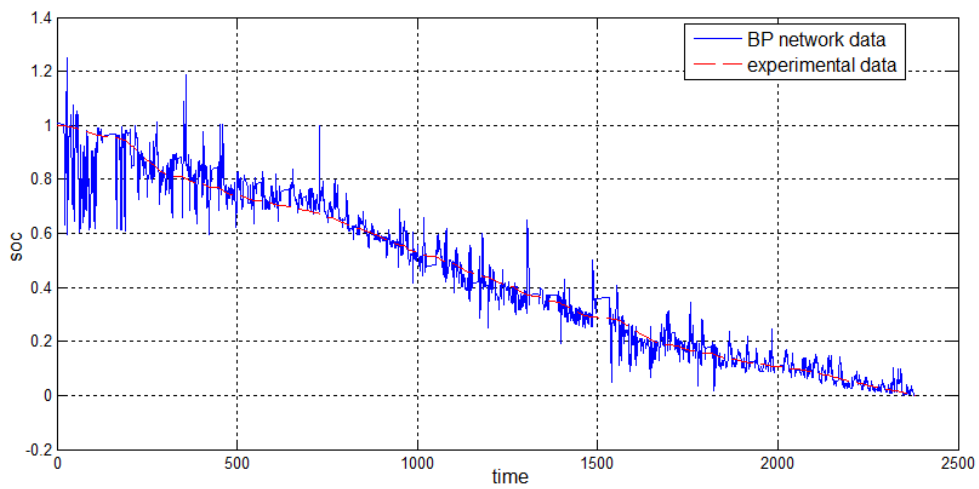


Fig. 10. SOC curves with BP network and experiment.

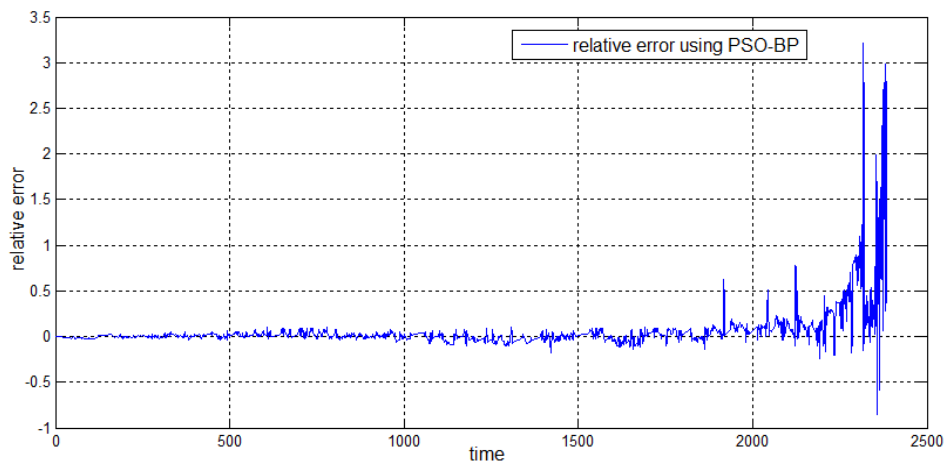


Fig. 11. Relative error between adaptive mutation PSO-BP and experiment.



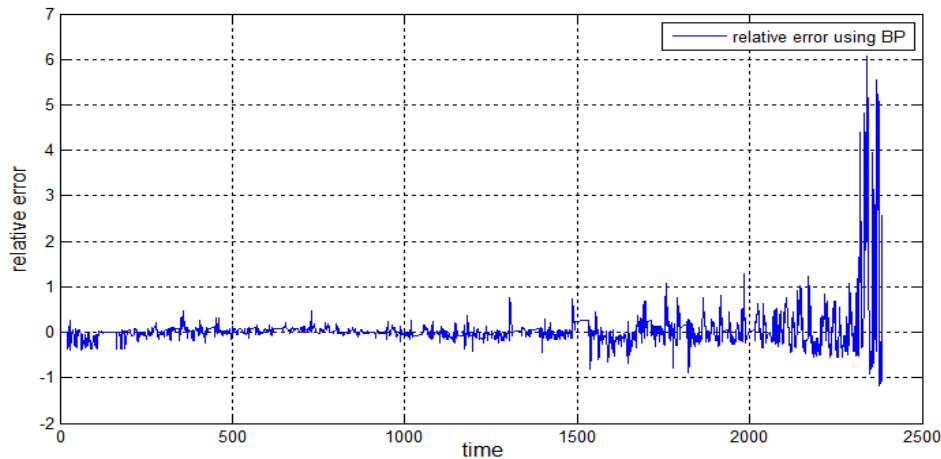


Fig. 12. Relative error between BP network and experiment.

## CONCLUSION

Battery SOC estimation is one of the most important tasks in the EV's BMS. Not only is it the basic parameter to decide the vehicle control strategy, but also it helps drivers using battery power reasonably as to control and predict the driving range. In this paper, EV's power battery SOC estimation algorithm is proposed based on BP neural network whose initial parameters optimized by adaptive mutation PSO. Finally, the experiment demonstrated the basic performance of the algorithm. The results are as follows:

(1) The convergence rate of adaptive PSO-BP neural network is not only faster than BP neural network but also has strong ability of global optimization.

(2) Using BP neural network for EV's power battery SOC estimation is feasible. Furthermore, the algorithm with its initial parameters optimized by adaptive mutation PSO has better performance than basic BP neural network and has higher accuracy in the SOC estimation of EV's power battery. So it has application value.

**Acknowledgments.** The authors gratefully acknowledge the support of the Beijing University of Aeronautics and Astronautics and the Guilin University of Aerospace Technology. The work is supported by the project of the Guilin University of Aerospace Technology under Grant No. X12Z002.

## REFERENCES

1. Feng Jin, He Yong-ling. *Advanced Material Research*, **490-495**, 3854 (2012).
2. Feng Jin, He Yong-ling, *J. Theor. Appl. Inform. Technol.*, **48**, 1398 (2013).
3. Lin Chen-tao, Wang Jun-ping, CHEN Quan-shi,

- Battery Bimonthly*, **134**, 376, (2004) (in Chinese).
4. Yinjiao Xing, Wei He, M. Pecht, Kwok Leung Tsui, *Appl. Energy*, **113**, 106 (2014).
5. Wu Hong-jie, Qi Bo-jin, Zheng Min-xin, Liu Yong-zhe, *J. Beijing Univ. Aeronautics Astronautics*, **33**, 945 (2007) (in Chinese).
6. Lin Cheng-tao, Chen Quan-shi, Wang Jun-ping, HuanG Wen-hua, Wang Yan-chao, *J. Tsinghua Univ. (Sci & Tech)*, **46**, 247 (2006) (in Chinese).
7. Hu Xiao-song, Sun Feng-chun, ZoU Yuan, *J. Central South Univ. Technol.*, **18**, 1525 (2011).
8. Xia Chao-ying, Zhang Shu, Sun Hong-tao. *Chinese J. Power Sources*, **31**, 414 (2007) (in Chinese).
9. M. Charkhgard, M. Farrokhi, *IEEE Trans. Industr. Electronics*, **57**, 4178 (2010).
10. Jaemoon Lee, Oanyong Nam, B.H. Cho, *J. Power Sources*, **174**, 9 (2007).
11. V. Valdez, A. Jojutla, IEEE Neural networks conference, **39**, 193 (2006).
12. G. Das, P.K. Pattnaik, S.K. Pattnaik, S.K. Padhy, *Expert Systems with Applications*, **41**, 3491 (2014).
13. Yu Chang-guan. Modern control theory and applications, second ed., Harbin Institute of Technology, Press. Harbin, 2007 (in Chinese).
14. Liu Rui-hao, Sun Yu-kun, Chen Kun-hua, *Electrical Measurement & Instrumentation*, **48**, 34 (2011) (in Chinese).
15. Lei Xiao, Chan Qing-quan, Liu Kaipei, Ma Li, *Trans. China Electrotech. Soc.*, **23**, 81 (2008) (in Chinese)
16. G. L. Plett, *J. Power Sources*, **134**, 277 (2004).
17. Liu Qiu-li, Ma Xiao-jun, Yuan Dong, Su Jian-qiang, *Computer Eng.*, **38**, 143 (2012) (in Chinese).
18. M. Carvalho, T.B. Ludermir, Sixth International conference on hybrid intelligent systems, **6**, 2 (2006).
19. Gan Xu-sheng, Duanmu Jing-shun, Meng Yue-bo, CONG Wei, *J. Central South Univ. Technol.*, **20**, 1592 (2013).
20. A. Alfi, *Acta Automatica Sinica*, **37**, 541 (2011).

## ОЦЕНКА НА ЗАРЕЖДАНЕТО НА ЛИТИЕВО-ЙОННИ БАТЕРИИ С ПОМОЩТА НА АДАПТИВНА МУТАЦИЯ И ОПТИМИЗАЦИОНЕН АЛГОРИТЪМ С РОЯК НА ЧАСТИЦИ ПРИ НЕВРОННИ МРЕЖИ С ОБРАТНО РАЗПРОСТРАНЕНИЕ

Фенг Джин<sup>1,2</sup>, Хе Йонг-линг<sup>1</sup>

<sup>1</sup> Училище по транспорт и инженерство при Университета по авионавтика и астронавтика в Бейджин, Бейджин 100191, Китай

<sup>2</sup> Департамент по автомобилно инженерство, Университет по космически технологии, Гуйлин 541004, Китай

Постъпила на 12 май, 2014 г.

(Резюме)

Състоянието на зареждане (SOC) на литиево-йонните батерии за електромобилите (EV) е силно нелинейно. Произволният избор на началните параметри на невронните мрежи с обратно разпространение (BP) може да причини значителна неточност и дълго време за трениране. В настоящето изследване се въвежда BP оптимизирана невронна мрежа с начални параметри, оптимизирани чрез алгоритъм, основаващ се на рояк на частици (PSO) с цел оценяване на състоянието на зареждане на литиево-йонна батерия (SOC). Анализирани са поведението на BP-невронната мрежа, както и оптимизираното поведение с адаптивна мутация. Съставен е модел на адаптивна мутация PSO-BP невронна мрежа, описващ състоянието на зареждане на батерията SOC. Експерименталните резултати показват, че чрез използването на BP-невронната мрежа, оптимизирана чрез адаптивна мутация PSO за оценка на SOC на литиево-йонните батерии за електромобили се преодоляват недостатъците от попадане на целевата функция в локален минимум, дълги времена на трениране и пр.

## The annual emissions of sulfur gases from different tidal flats in the Yellow River Delta, China

Li Xinhua<sup>1\*</sup>, Sun Zhigao<sup>2</sup>, Guo Honghai<sup>3</sup>, Zhu Zhenlin<sup>1</sup>

<sup>1)</sup> Shan Dong Institute of Agriculture Sustainable Development, Ji Nan 250100, China,

<sup>2)</sup> Key Laboratory of Coastal Zone Environmental Processes, Yanta Institute of Coastal Zone Research (YIC), Chinese Academy of Sciences (CAS), Yanta 264003)

<sup>3)</sup> Institute of Resource and Environment, Shandong Academy of Agricultural Sciences (SAAS)

Submitted May 12, 2014

The annual emission of sulfur gases (H<sub>2</sub>S and COS) from different tidal flats in the Yellow River Delta, China were studied from February to December 2013 by using static chamber-gas chromatography technique. The result showed that the annual emissions of H<sub>2</sub>S and COS were featured with obvious seasonal variations. For the full year, the high tidal flats, middle tidal flats and low tidal flats were all the emission sources for H<sub>2</sub>S, and the range was on the order of 0.14-7.31 μg·m<sup>-2</sup>·h<sup>-1</sup>, 0.22-6.38 μg·m<sup>-2</sup>·h<sup>-1</sup> and 0.23-8.80 μg·m<sup>-2</sup>·h<sup>-1</sup> respectively, and the means were 3.37 μg·m<sup>-2</sup>·h<sup>-1</sup>, 1.98 μg·m<sup>-2</sup>·h<sup>-1</sup> and 3.29 μg·m<sup>-2</sup>·h<sup>-1</sup> respectively. For COS, the high tidal flats were also the emission sources, while the middle tidal flats and the low tidal flats were the sink, and the range was on the order of -1.16-2.52 μg·m<sup>-2</sup>·h<sup>-1</sup>, -3.32-1.25 μg·m<sup>-2</sup>·h<sup>-1</sup> and -5.53-1.78 μg·m<sup>-2</sup>·h<sup>-1</sup> respectively, and with means of 0.68 μg·m<sup>-2</sup>·h<sup>-1</sup>, -0.09 μg·m<sup>-2</sup>·h<sup>-1</sup> and -0.17 μg·m<sup>-2</sup>·h<sup>-1</sup> respectively. The annual emissions of H<sub>2</sub>S and COS from the different tidal flats in the Yellow River Delta China were significantly affected by the annual seasonal variation, and the emissions of H<sub>2</sub>S and absorptions of COS from the different tidal flats were mainly concentrated in the growing season of plants (from May to October). In the different tidal flats areas, the annual emission amounts of H<sub>2</sub>S and COS were also different, among which H<sub>2</sub>S was manifested as low tidal flats > high tidal flats > middle tidal flats, and COS as high tidal flats > low tidal flats > middle tidal flats.

**Key words:** Yellow River Delta; Tidal flats; Sulfur gases; Annual emission; China

### INTRODUCTION

Volatile sulfur gases were an important part of the sulfur cycle in nature, it had a great impact on the environment and was closely related to acid deposition, the greenhouse effect, aerosol formation and other processes [1, 2]. Sulfur gases emitted from the nature were one of the main sources of sulfur gases in the atmosphere. According to the estimates the sulfur gases from natural sources were equal to such gases from human activities [3, 4]. However, the greater spatial, and temporal variability, of natural sources of sulfur gases emission, coupled with limited monitoring data, has brought great uncertainty to the global sulfur budget [5, 6]. Wetlands were one of the most important natural sources of sulfur emissions, and sulfur gases emitted from wetlands were generally one, or several orders of magnitude higher than those emitted from inland due to their unique natural and ecological conditions [7]. Scholars had researched on the emission fluxes of sulfur gases,

its effect factors and its emission mechanism in freshwater marshes, salt marshes, coastal waters and different types of wetlands [8-15].

The researches have shown that the emissions of sulfur gases from the wetlands had greater spatial and temporal variability, and the kind of sulfur gases emitted from the wetlands were mainly hydrogen sulfide (H<sub>2</sub>S), carbonyl sulfide (COS), dimethyl sulfide (DMS), carbon disulfide (CS<sub>2</sub>), mercaptanes (MeSH) and dimethyl disulfide (DMDS), and so on [8-11,13, 16]. Among them, H<sub>2</sub>S was highlighted by a higher emission flux in the saline wetland along inshore areas and seashore [17], and was also closely related to carbon mineralization and methane emissions [18-21]; COS was a kind of reduced sulfur compound with the highest abundance in the atmosphere [22] and it was controversial in understanding about its source/sink [23]. Sulfur gases were released mainly from the decomposition of organic matter and sulfate reduction, and its emissions rate was affected by many factors, such as temperature, tides, redox potential, vegetation type, and so on

\* To whom all correspondence should be sent:

E-mail: xinhuali\_2088@126.com

[3,9,10,13,24].

The Yellow River is well known as a sediment-laden river, and the Yellow River Delta are China's best preserved, and largest warm temperate, nascent wetlands, and are also a typical estuarine wetlands. They are an important bird habitat, breeding ground, transit station, with a classic permissivity, fragility, rarity and are of international importance. The Yellow River on average delivers an annual input of  $1.0 \times 10^9$ t of sediment into the estuary, with about 45% of the deposition in the coastal zone. This provides the material basis for the development of tidal estuaries. The re-shaping caused by the frequent swings and marine dynamics of the Yellow River tail forms the Delta's broad tidal wetlands. With a total area of about 964.8km<sup>2</sup>, accounting for 63.06% of the total area of the Yellow River Delta [25]. This area is one of the important ecological zones of the Yellow River Delta. Under the interactive influence of tides, overflow and other marine dynamics along with estuarine runoff, sediment and other land-based forces, the difference in intensity among these forces and the varying lengths of flooding time, give the Yellow River Delta coastal tidal area an obvious horizontal belt character, forming parallel high, middle and low tidal flats in a seaward direction [26]. This is accompanied by a succession of typical natural biomes. From the low tidal flats to medium tidal flats to high tidal flats, it is mainly *Suaeda salsa* communities, *Suaeda salsa-Tamarix chinensis* communities and *Suaeda salsa-Phragmites australis* communities that are successively encountered (Xing, et al. [27]). This parallel-shaped distribution of low mass and vegetation, pulsing the impact of land-sea interaction inevitably, cause differences in the biological substances circulating throughout the sub-tidal zone wetland ecosystem, thereby affecting the stability of the wetlands so that their appearance and structure are always in flux.

Current research on the biogenic elements cycle in the tidal flats of the Yellow River Delta China mainly focused on the accumulation and distribution features of plant elements (C, N, P, S

and trace elements) [28,29], distribution of elements in soils [30,31] and greenhouse gas emissions [31-34]. To date, the studies on the emissions of sulfur gases from the tidal flats in Yellow River Delta china were still lacking, so the paper was to determine the annual emissions of sulfur gases from the different tidal wetlands in Yellow River Delta China by using static chamber-gas chromatography technique, so as to provide essential data for evaluating the influence of sulfur gases emission on atmospheric environment, understanding the relationship between the emission of H<sub>2</sub>S and CH<sub>4</sub> and further studying on the sulfur cycle in the natural wetland of the Yellow River Delta, China .

## 1. MATERIALS AND METHODS

### 1.1 Site study

This study was conducted from February to December 2013 at the typically experimental plots located in the Nature Reserve of Yellow River Delta (37°35'N~38°12'N, 118°33'E~119°20'E) in Dongying City, Shandong Province, China. The nature reserve is of typical continental monsoon climate with distinctive seasons; summer is warm and rainy while winter is cold. The annual average temperature is 12.1°, the frost-free period is 196 days, and the effective accumulated temperature is about 4300 °. Annual evaporation is 1962 mm and annual precipitation is 551.6 mm, with about 70 percent of precipitation occurs between June and August. The soils in the study area are dominated by intrazonal tide soil and salt soil, and the main vegetations include *Phragmites australis*, *S. salsa*, *Triarrhena sacchariflora*, *Myriophyllum spicatum*, *chinensis* and *Limonium sinense* [27].

The typical experiment area was selected in the coastal tidal wetland situated at the north of the mouth of the Yellow River. In the typical experiment area, the 3 typical sample points including high tidal flats ((37°46'7.25"N, 119°09'55.54"E), middle tidal flats (37°46'11.62"N, 119°09'56.09"E) and low tidal flats (37°46'15.95"N, 119°09'57.44"E) were selected, and it's vegetation distribution was continuous, and

the vegetation of high tidal flats, middle tidal flats and low tidal flats was *Suaeda Salsa-Phragmites australis*, the *Suaeda Salsa-Tamarix Chinensis* and *Suaeda Salsa* community respectively. Three repeated monitoring points were distributed in the each tidal flats, and the total monitoring points were 9, and the gas samples were collected every month or every two month, each sampling period was at 8:00-10:00am.

### 1.2 Collection and analysis of gas samples

Gas samples are collected with closed chamber method [24]. The chamber was made of polycarbonate with an internal height of 100cm, covered an area of 0.25m<sup>2</sup> (50cm in length and 50 cm in width) of test field. Each chamber, in the internal top had a small fan for mixing the air. To avoid disturbing the soil, the chamber were placed on a stake driven into the soil installed in December 10, 2011, meanwhile the boardwalk were installed for minimizing disturbance to the test field during sampling. Four gas samples of the chamber air were collected into a 1000ml Tedlar bag by a small sampling pump at a flow rate of 2000 ml.min<sup>-1</sup> at 0, 20, 40 and 60 min after the chamber was set up. The sulfur fluxes were determined by measuring the temporal change of the concentration in the air inside the chamber. Therefore a positive values refers to the emission from the wetland to the atmosphere and negative values to the absorption into the plants and soil of wetlands.

The concentrations of H<sub>2</sub>S and COS were determined as described in detail by Li et al. [24].

### 1.3 Statistical analysis

Data graphics are made available with Origin7.5 and statistical analysis is developed with SPSS13.0.

## 2. RESULTS AND DISCUSSION

### 2.1 Annual emission characteristics of sulfur gases from the different tidal wetlands in Yellow River Delta, China

**2.1.1 Annual emission characteristics of sulfur gases from the high tidal flats.** The high tidal flats are located between the high tide level and neap tide level, with a width in the range of 1-9 km

range. It is mainly composed of *Suaeda salsa-Phragmites australis* communities. The annual emissions of H<sub>2</sub>S and COS were shown in Fig.1, the annual emissions of H<sub>2</sub>S and COS from the high tidal flats both showed significant seasonal variation (Fig.1), and the annual emission range of H<sub>2</sub>S was 0.14-7.31μg·m<sup>-2</sup>·h<sup>-1</sup>, with a mean of 3.29 μg·m<sup>-2</sup>·h<sup>-1</sup>, and a variation coefficient of 81.7%.

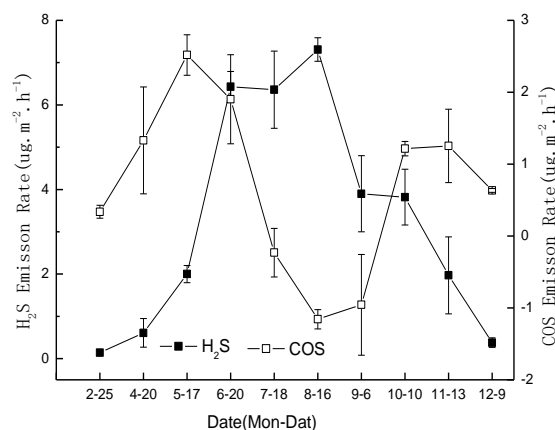


**Fig.1** The annual emissions of H<sub>2</sub>S and COS from the high tidal flats.

From February-August, the emission flux of H<sub>2</sub>S increased, and peak emissions occurred in August, and from September to December, the emission amount of H<sub>2</sub>S began to decrease. The annual emission of COS showed alternating emission-absorption characteristics, and the range of COS annual emission was -1.16-2.52μg·m<sup>-2</sup>·h<sup>-1</sup>, with a mean of 0.68 μg·m<sup>-2</sup>·h<sup>-1</sup>, and a variation coefficient of 175.0%. From February to May, the emission amount of COS increased, and afterwards gradually decreased. Absorption was manifested in July, the emergence of the absorption peak was seen in August with the value of -1.16μg·m<sup>-2</sup>·h<sup>-1</sup>. The weak absorption was shown in September, and from October to December, the emission flux of COS took over to release.

### 2.1.2 Annual emission characteristics of sulfur gases from the middle tidal flats

The middle tidal flats are located between the neap tide level and the neap tide low tide level with a width up to 1-4 km. It is mainly composed of *Suaeda salsa-Tamarix chinensis* communities.

These are *Suaeda salsa* communities with

transition phases to *tamarisk* communities or *Phragmites australis* communities. In the middle tidal flats, the annual emissions of H<sub>2</sub>S and COS also showed significant seasonal variation (Fig.2).

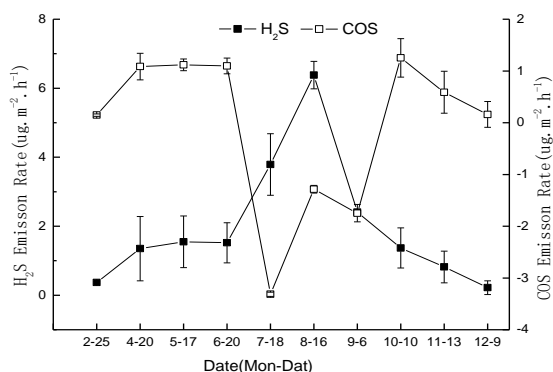


**Fig.2.** The annual emissions of H<sub>2</sub>S and COS from the middle tidal flats.

The annual emission range of H<sub>2</sub>S was 0.22-6.38  $\mu\text{g}\cdot\text{m}^{-2}\cdot\text{h}^{-1}$ , with a mean of  $1.98\mu\text{g}\cdot\text{m}^{-2}\cdot\text{h}^{-1}$ , and a variation coefficient of 93.8%, as an H<sub>2</sub>S release source. From February to August, the emission amount of H<sub>2</sub>S showed an increasing trend, and appeared the emission peak in August, then the emission amount of H<sub>2</sub>S gradually decreased, and the lowest value appeared in December. The emission amount of COS was in the range of -3.32-1.25  $\mu\text{g}\cdot\text{m}^{-2}\cdot\text{h}^{-1}$ , with a mean of  $-0.09\mu\text{g}\cdot\text{m}^{-2}\cdot\text{h}^{-1}$ , and a variation coefficient of 732.2% with large variability. From an annual point of view, the middle tidal flat was a weak sink for COS. The variation of COS emission showed fluctuations, among which, the emission amount of COS manifested from February to June, then volatile absorption was seen from July to September, and the absorption peak ( $-3.32\mu\text{g}\cdot\text{m}^{-2}\cdot\text{h}^{-1}$ ) appeared in July, and from October to December, COS emissions were seen again, while the emission amount of COS decreased.

**2.1.3 Annual emission characteristics of sulfur gases from the low tidal flats.** The low tidal flats are located between the neap tide low tide level and the low tide level. The low tidal flats are narrow with an average width of 0.5-2 km. They are mainly composed of *Suaeda salsa*-*Phragmites australis* communities which are succession pioneer communities in the Yellow River Delta wetlands.

The annual emissions of H<sub>2</sub>S and COS from the low tidal flats had a clear seasonal variation (Fig.3), in which the emission range of H<sub>2</sub>S was from 0.23  $\mu\text{g}\cdot\text{m}^{-2}\cdot\text{h}^{-1}$  to 8.80  $\mu\text{g}\cdot\text{m}^{-2}\cdot\text{h}^{-1}$ , with a mean of 3.37  $\mu\text{g}\cdot\text{m}^{-2}\cdot\text{h}^{-1}$ , and a variation coefficient of 85.7%, as an H<sub>2</sub>S release source.

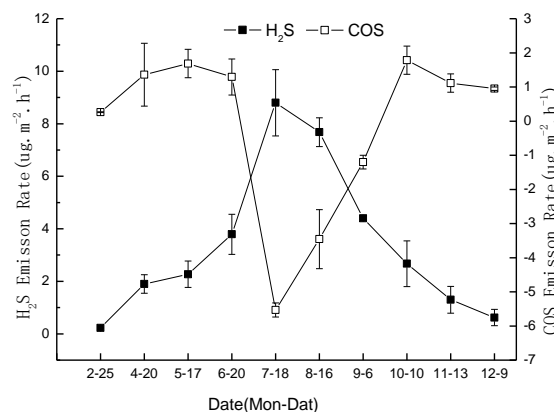


**Fig.3.** The annual emissions of H<sub>2</sub>S and COS from the low tidal flats

The emission mode of H<sub>2</sub>S was a single peak, and from February to July, the emissions amount of H<sub>2</sub>S increased gradually until the peak discharge manifested in July, and from July to December, the emissions amount of H<sub>2</sub>S gradually decreased. While the annual emission of COS showed alternating emission-absorption characteristics, and the range of the COS emission amount was -5.53-1.78  $\mu\text{g}\cdot\text{m}^{-2}\cdot\text{h}^{-1}$ , with a mean of  $0.17\mu\text{g}\cdot\text{m}^{-2}\cdot\text{h}^{-1}$ , and a variation coefficient of 506.4% which showed a large amount of variability for COS emission. From February to June, there were emissions of the COS, but there was little change in the emission amounts. From July to September, absorption of COS was manifested, and the absorption peak occurred in July, as  $-5.53\mu\text{g}\cdot\text{m}^{-2}\cdot\text{h}^{-1}$ , then weak emission was also manifested from October to December and the emission amount decreased.

**2.2. Comparison of the annual emissions of sulfur gases from the different tidal flats in the Yellow River Delta, China**

Previous studies have indicated that the sulfur gases emissions from wetlands were significantly affected by annual and seasonal changes, as well as plant growth [10,11]. Looking at the full year,

temperature was relatively high from May to October in the Yellow River Delta, China, and this was also growth season for plants. From November to the following April, the temperature was relatively low, and it was the season when plants are dying off, a non-growing season. We calculated the average emission amounts of H<sub>2</sub>S and COS from the different tidal flats in the plant growth season and non-growth season according to this division (Table 1). From Table 1 we can see that the averaged emission amounts of H<sub>2</sub>S from the high tidal flats, middle tidal flats and low tidal flats in the growing season were 6.4, 4.1, and 4.9 times higher than that in the non-growing season respectively. It can be seen that H<sub>2</sub>S emissions were mainly concentrated in the growing season. For the COS, the averaged emission value in the high tidal flats showed emissions in both the growth and non-growth seasons, in the growing season, although there was periodic absorption in high tidal flats, its absorption capacity was less than the middle tidal flats and middle tidal flats, resulted in overall emission in the plant growing season. While the middle tidal flats and low tidal flats were different from the high tidal flats, and they showed absorption in the growth season and emission in the non-growth season which was well agreed with the results of Fall [36] and Whelan et al. [13].

From an annual perspective, the averaged emission amount of the H<sub>2</sub>S from the low tidal flats was the highest (3.37 μg·m<sup>-2</sup>·h<sup>-1</sup>) which was related to the low tidal flats near the sea and effecting strongly by tidal, followed by the high tidal flats (3.29 μg·m<sup>-2</sup>·h<sup>-1</sup>) and the middle tidal flats (1.98

μg·m<sup>-2</sup>·h<sup>-1</sup>). In terms of COS, the averaged emission amount from the high tidal flats was the highest (0.68 μg·m<sup>-2</sup>·h<sup>-1</sup>), followed by the low tidal flats manifesting absorption, and that from the middle tidal flats was the lowest with weak absorption. The reasons for the different H<sub>2</sub>S and COS amounts in each tidal flats may be related to differences in research samples in terms of vegetation type, soil matrix, hydrothermal interaction and salinity conditions, or other relevant conditions. There is a need to explore these areas in future studies.

### 3. CONCLUSIONS

The emissions of H<sub>2</sub>S and COS from the different tidal flats in the Yellow River Delta China were all shown with obvious seasonal variations. For the full year, the high tidal flats, middle tidal flats and low tidal flats were emission sources for H<sub>2</sub>S, and the range was on the order of 0.14-7.3 μg·m<sup>-2</sup>·h<sup>-1</sup>, 0.22-6.38 μg·m<sup>-2</sup>·h<sup>-1</sup> and 0.23-8.80 μg·m<sup>-2</sup>·h<sup>-1</sup> respectively, and with means of 3.29 μg·m<sup>-2</sup>·h<sup>-1</sup>, 1.98 μg·m<sup>-2</sup>·h<sup>-1</sup> and 3.37 μg·m<sup>-2</sup>·h<sup>-1</sup> respectively. For COS, the high tidal flats manifested emissions, while the middle tidal flats and the low tidal flats manifested absorption, the range was on the order of -1.16-2.52 μg·m<sup>-2</sup>·h<sup>-1</sup>, -3.32-1.25 μg·m<sup>-2</sup>·h<sup>-1</sup> and -5.53-1.78 μg·m<sup>-2</sup>·h<sup>-1</sup> respectively, and with means of 0.68 μg·m<sup>-2</sup>·h<sup>-1</sup>, -0.09 μg·m<sup>-2</sup>·h<sup>-1</sup> and 0.-0.17 μg·m<sup>-2</sup>·h<sup>-1</sup> respectively.

The H<sub>2</sub>S and COS emissions from the different tidal flats in the Yellow River Delta China were significantly affected by annual seasonal variation, which caused that H<sub>2</sub>S emission and COS

**Table 1.** The average emission flux of H<sub>2</sub>S and COS in plant growing season and non growing season from different tidal flats in the Yellow River Delta China.

Sulfur gases	Time	Average Emission Fluxes (μg·m <sup>-2</sup> ·h <sup>-1</sup> )		
		High tidal flat	Middle tidal flat	Low tidal flat
H <sub>2</sub> S	Growing Season (May-October)	4.97	2.84	4.93
	Non-growing Season (November-April)	0.78	0.69	1.01
	Annual Average	3.29	1.98	3.37
COS	Growing Season (May-October)	0.55	-0.48	-0.90
	Non-growing Season (November-April)	0.89	0.50	0.92
	Annual Average	0.68	-0.09	-0.17

absorption were mainly concentrated in the growing season. In different tidal wetland areas, H<sub>2</sub>S and COS emission amounts were different, among which H<sub>2</sub>S was manifested as low tidal flats > high tidal flats > middle tidal flats, and COS as high tidal flats > low tidal flats > middle tidal flats. The differences may be related to vegetation types, tidal action, the soil matrix, hydrothermal interaction, salinity conditions, or other relevant conditions. Future in-depth studies are required.

**Acknowledgements:** the authors would like to acknowledge the financial support of the National Nature Science Foundation of China (No. 41103036), and also to thank Han Yi, Sun Wenguang and Sun Wanlong for their friendly help with gases sampling and analyzing.

#### REFERENCES

- V.P. Aneja, *J. Air Waste Manag. Assoc.*, **40**, 469 (1990).
- V. Robert, S. Richard, S.C. Artz, et al., *Atmosph. Environ.* (2014, in press).
- M.O. Andreae, W.A. Jaeschke, In: R.W. Howarth, J.W.B. Stewart, M. Ivanou (eds), *Sulphur Cycling in the Continents*. New York: John Wiley & Sons, 1992, pp.27-61.
- P. Brimblecombe, *The Global Sulfur Cycle*, 559 – 591(2014).
- Z. Yang, L. Kong, J. Zhang, et al. *Science Total Environ.*, **224**, 1 (1998).
- F. Tassi, F. Capecchiacci, L. Gianninia, et al. *Environ. Pollution*, **180**, 111 (2013).
- D. Istvan, R.D. Delaune. *Organic Geochem.*, **23**, 283 (1995).
- V.P. Aneja, S.O. Farwell, E. Robinson E, et al. *J. Air Pollution Control Assoc.*, **31**, 256 (1981).
- M.C. Morrison, M.E Hines, *Atmosph. Environ.*, **24**, 1771 (1990).
- R.D. Delaune, I. Devai, C.W. Lindau, *Estuarine, Coastland Shelf Science*, **54**,1003 (2002).
- Li X.H., Liu J. S., Yang J.S., *Environ. Sci.*, **27**, 2145 (2006).
- Zhou C.F., An S.Q., Zhao C.J., et al. *Marine Sci.*, **33**, 17 (2009).
- M.E. Whelan, Dong-Ha Min, R.C. Rhew. *Atmosph. Environ.*,**73**, 131 (2013).
- Yi Z.G., Wang X.M., Sheng G.Y., et al., *Agriculture, Ecosystems & Environment*, **123**, 116 (2008).
- Yi Z.G., Wang X.M., Sheng G.Y., et al., *Environ. Chem.*, **28**, 574 (2009).
- D.J. Cooper, W.Z. Demello, W.J. Cooper et al. *Atmosph. Environ.*, **21**, 7 (1987).
- R.W Howarth, *Biogeochemistry*, **1**, 5 (1984).
- D.B. Nedwell, A. Watson, *Soil Biol. Biochem.*, **27**, 893 (1995)
- S.D. Bridgham, D. Updegraff, J. Pastor, *Ecology*, **79**, 1545 (1998).
- Long Y.Y., Liao Y, Zhang K, et al. *Ecol. Eng.*,**60**, 438 (2013).
- G.J. Scott, D.B. Edward, A. Thor, et al., *Chem. Geol.*, **371**, 9 (2014).
- U. Kuhn, C. Ammann, A. Wolf, et al., *Atmosph. Environ.*, **33**, 995 (1999).
- S.F. Watts, *Atmosph. Environ.*, **34**, 761(2000).
- Li X.H., Liu J.S., Jia Y.Q., *J. Instrum. Analysis*, **25**, 68 (2006).
- Cui B.S., Yang Q.C., Yang Z.F., et al., *Ecol. Eng*, **35**, 1090 (2009).
- Li Y.F., Huang Y.L., Li S.S., *Acta Ocenologica Sinica*, **13**, 662 (1991).
- Xing S.J., Chi J.B., Zhang J.F., et al., *J. Northeast Forestry Univ.*, **31**, 85 (2003).
- Mou X.J, Sun Z.G, Liu X.T., *Acta Prataculturae Sinica*, **21**, 45 (2012).
- Sun Z.G, Mou X.J., Tian H.Q., et al., *Ecol. Eng.*, **53**, 153 (2013).
- Yu J.B., Chen X.B., Sun Z.G., et al., *Acta Scientiae Circumstantiae*, **30**, 855 (2010).
- Sun Z.G, Wang L.L., Tian H.Q., et al. *Chemosphere*, **90**, 856 (2013).
- Jiang H.H., Sun Z.G, Wang L.L., *Chinese J. Environ. Sci.*, **33**, 565 (2012).
- Chen Q.F., Ma J.J., Liu J.H., et al.,. *Int. J. Biodeterioration & Biodegratation*, **85**, 646 (2013).
- Zhang L.H., Song L.P., Zhang L.W., et al., *Ecol. Eng.*, Part A, **61**, 82 (2013).
- Sun W.L., Sun Z.G, Sun W.G., et al., *Acta Prataculturae Sinica*,**1**, 104 (2014).
- R. Fall, D.L. Albritton, R.C. Fehsenfeld, et al., *J. Atmosph. Chem.* **6**, 341 (1988).



## ГОДИШНИ ЕМИСИИ ОТ СЯРА-СЪДЪРЖАЩИ ГАЗОВЕ В ПРИЛИВНИТЕ ПЛИТЧИНИ В ДЕЛТАТА НА ЖЪЛТАТА РЕКА, КИТАЙ

Ли Ксинхуа<sup>1\*</sup>, Сунн Жигао<sup>2</sup>, Гуо Хонгхай<sup>3</sup>, Жу Женлин<sup>1</sup>

<sup>1)</sup> *Институт по устойчиво развитие на земеделието Шандонг, Жи Нан 250100, Китай*

<sup>2)</sup> *Ключова лаборатория за екологични процеси в крайбрежните зони, Институт за изследвания в крайбрежните зони в Янта (YIC), Китайска академия на науките, Янта 264003, Китай*

<sup>3)</sup> *Институт по ресурси и околна среда, Шандонг'ска академия по земеделски науки (SAAS), Шандонг, Жи Нан, Китай*

Постъпила на 12 май, 2014 г.

(Резюме)

Изследвани са годишните емисии на сяра-съдържащи газове (сероводород и карбонил-сулфид) от различни приливни плитчини в делтата на Жълтата река за периода от февруари до декември, 2013 г. с помощта на статично пробонабиране и газ-хроматографска техника. Резултатите показват наблюдаеми сезонни колебания на изследваните вещества. За целогодишния период източник на сероводород са високите, средните и ниските плитчини. Интервалите от концентрации са от порядъка съответно  $0.14-7.31 \mu\text{g}\cdot\text{m}^{-2}\cdot\text{h}^{-1}$ ,  $0.22-6.38 \mu\text{g}\cdot\text{m}^{-2}\cdot\text{h}^{-1}$  и  $0.23-8.80 \mu\text{g}\cdot\text{m}^{-2}\cdot\text{h}^{-1}$ , като средните стойности са  $3.37 \mu\text{g}\cdot\text{m}^{-2}\cdot\text{h}^{-1}$ ,  $1.98 \mu\text{g}\cdot\text{m}^{-2}\cdot\text{h}^{-1}$  и  $3.29 \mu\text{g}\cdot\text{m}^{-2}\cdot\text{h}^{-1}$ . За карбонил-сулфида, високите плитчини са източник на замърсяване, докато средните и ниските са по-скоро консуматори, при концентрации от порядъка на  $-1.16-2.52 \mu\text{g}\cdot\text{m}^{-2}\cdot\text{h}^{-1}$ ,  $-3.32-1.25 \mu\text{g}\cdot\text{m}^{-2}\cdot\text{h}^{-1}$  и  $-5.53-1.78 \mu\text{g}\cdot\text{m}^{-2}\cdot\text{h}^{-1}$ . Средните стойности на концентрациите са съответно  $0.68 \mu\text{g}\cdot\text{m}^{-2}\cdot\text{h}^{-1}$ ,  $-0.09 \mu\text{g}\cdot\text{m}^{-2}\cdot\text{h}^{-1}$  и  $-0.17 \mu\text{g}\cdot\text{m}^{-2}\cdot\text{h}^{-1}$ . Годишните емисии на сероводород и карбонил-сулфид от различните приливни плитчини в делтата на Жълтата река се влияят значително от годишните сезонни колебания, като емисиите на сероводород и карбонил-сулфид са главно в периода на растителен растеж (от май до октомври). В различните плитчини годишните емисии на двата замърсителя са различни, като сероводородът се проявява най-много в ниските, после във високите и накрая в средните плитчини. Карбонил-сулфидът най-много се проявява във високите плитчини.

## Influence of fumed silica on the properties of cushion packaging materials based on bagasse pith and bisulfite spent liquor

Yanna Lv<sup>1,2\*</sup>, Beihai He<sup>1,3</sup>, Yali Wu<sup>4</sup>

<sup>1</sup> State Key Laboratory of Pulping and Papermaking Engineering, South China University of Technology, 510640 Guangzhou, China

<sup>2</sup> Department of Media and Communication, Guangdong Industry Technical College, 510300 Guangzhou, China

<sup>3</sup> National Engineering Research Center of Papermaking & Pollution Control, South China University of Technology, 510640 Guangzhou, China

<sup>4</sup> Department of Food, Guangdong Industry Technical College, 510640 Guangzhou, China

Submitted May 1, 2014

In this work, biodegradable cushion packaging materials based on bagasse pith, magnesium bisulfite spent liquor and hydrophilic fumed silica were prepared via press-molding method and the effects of silica nanoparticles on the physical properties and biodegradation of the packaging materials were investigated. Results showed that the addition of silica nanoparticles increased the apparent density and the static compressive strength of bagasse pith cushion packaging materials. When the silica loading was within the critical value, the compressive strength was found to increase with the increase of specific surface areas of fumed silica due to a fine dispersion of nanofillers in the matrix. The morphology of fumed silica nanoparticles and the dispersion state of silica nanoparticles in the matrix were studied by transmission electron microscopy and scanning electron microscopy, respectively. The morphological analyses indicated that the reinforcement effect of fumed silica was the consequence of silica filler-matrix and silica filler-filler interactions. Biodegradation assays revealed that the presence of silica in the packaging materials reduced the biodegradation rate after 15 days of incubation in liquid nutrient medium.

**Key words:** Fumed silica, bagasse pith, cushion packaging material, biodegradation

### INTRODUCTION

Cushion packaging materials protect fragile and delicate products against shock and vibration during shipping and handling. Generally, expanded polystyrene (EPS) and expanded polyethylene (EPE) are popular materials for this application due to their adequate mechanical strength and low cost. However, these foams are not biodegradable and recyclable, causing a serious white pollution. Therefore, manufacturers and consumers are looking for alternative materials that are eco-friendly and cheap, and possess good cushioning properties [1].

The biomass cushion packaging materials based on plant fiber have become a research hotspot all over the world due to their degradation and wide sources of raw materials. Many researchers have developed degradable cushion packaging materials with straw fibers (wheat straw fiber, rice straw fiber, bagasse fiber, rice husk fiber, etc.) [2-4]. Most of the research is still on laboratory level, and the

improvements in production technology and functional properties of materials will require further study.

Bagasse is a by-product of the sugarcane milling process and has adequate chemical and mechanical properties for paper making [5-7]. However, 30%–40% of the spongy structured bagasse pith in the sugarcane bagasse has adverse effect on the pulp quality; therefore, efficient removal of pith is a prerequisite in papermaking enterprise [8, 9]. In China, the annual output of sugar cane is 6 million tons, and the ratio of oven dry bagasse is about 13%, which means about 6.5 million tons [10]. The impressively abundant bagasse pith is mainly utilized as fuel for heating and power generation, but it can be used for more value-added products. Spongy bagasse pith has certain elasticity and resilience after being dried, thus, it can endow materials with good cushion performance without the need for foaming agents. The use of bagasse pith for producing biomass cushion packaging material is a way to enhance its added value.

Magnesium lignosulfonate, the major component of sulfite pulping waste liquor of sugarcane bagasse, is characterized by good

\* To whom all correspondence should be sent:  
E-mail: lvyanna2006@gmail.com

adhesion and degradability. The sugars and derivatives in the pulping waste liquor further enhance its adhesion ability via synergistic effect [11]. Therefore, acid sulfite pulping waste liquor can be used as an adhesive mixed with bagasse pith to produce degradable cushion packaging materials.

Some researchers compounded plant fibers with biodegradable adhesives to produce biodegradable packaging materials. Studies showed that high plant fiber fractions can help reduce the cost per unit volume of packaging materials. However, the strength of the materials consequently decreases [12, 13]. Therefore, fumed silica is selected as the reinforcing filler of the bagasse pith cushion packaging materials in this experiment. Fumed silica ( $\text{SiO}_2$ ) is usually employed as an enhancing agent in thermoplastic polymers and rubber to increase their mechanical properties, such as toughness and tensile strength. Bouaziz et al. [14] reported the reinforcement mechanism of  $\text{SiO}_2$  in polypropylene composites. Zhang and coworkers [15] studied the impact of silica content on tensile modulus and impact strength of high-density polyethylene. Prasertsri and Rattanasom [16] investigated the effects of loading and surface area of fumed silica on stiffness and tear strength. As far as we are aware, however, no work has been done on the reinforcement by fumed silica of plant fiber-based materials.

Therefore, this study aims to prepare cushion packaging materials based on bagasse pith, magnesium bisulfite spent liquor, and fumed silica via press-molding process and to investigate the effects of fumed silica on the physical and mechanical properties of the cushion packaging materials. The biodegradation of the specimen is also reported in this paper. Interfacial studies were made with scanning electron microscopy (SEM) to illustrate the silica reinforcement mechanism.

## MATERIALS AND METHODS

### *Experimental equipment design*

The experimental equipment for preparing the biodegradable cushion packaging materials (BCPMs) used in this study was designed by Tianjin Sichuang Jingshi Technology Co. Ltd. (Tianjin, China). The equipment consists of top pressure plate, lower pressure plate, inner mold, and outer mold. During drying, water in packaging materials evaporated from the small holes in the copper mesh. The outer mold is made of 3 mm-thick stainless steel plates to ensure the shape of the inner mold.

### *Materials and chemicals*

The bagasse pith with 13.36% moisture content and the spent liquor with 52% solid content were supplied by Jiangmen Sugarcane Chemical Factory (Group) Co. Ltd. (Guangdong, China). The fraction of bagasse pith passing a 10-mesh sieve was used in all experiments. The spent liquor from the magnesium bisulfite pulping process of bagasse was used as the adhesive.

Analytical-grade sodium hydroxide was purchased from Guangzhou Chemical Reagent (Guangdong, China) and was used for pH adjustment. Three types of hydrophilic fumed silica nanoparticles from Guangzhou GBS High-Tech & Industry Co. Ltd. (Guangdong, China), were used as reinforcing filler. These three types were HL150, HL200 and HL380 with nominal SSAs of 150, 200 and 380  $\text{m}^2 \text{g}^{-1}$ , respectively. The physical and chemical properties of silica are shown in Table 1. The surface area and porosity measurements were performed using an ASAP 2020 (Accelerated Surface Area and Porosimetry) machine. Surface properties were evaluated through nitrogen gas physisorption process. The SSA of the fumed silica was calculated according to the Brunauer-Emmett-Teller (BET) procedure [17]. The surface area contribution according to pore dimensions was also determined according to the Barrett-Joiner-Holenda (BJH) method [18].

In the following discussion, the cushion packaging materials are labeled referring to the name of silica nanoparticle and its weight content. For example, pith-HL200-1 indicates that pith and 1 wt% HL200 were used as matrix and filler, respectively.

### *Preparation of the BCPMs*

The BCPMs were manufactured on the basis of previous results [19]. The solid content of the spent liquor was 52%, and the mass ratio of bagasse pith to bisulfite spent liquor (on solid content basis) was 2:1. The amount of lignin sulfonate in the adhesive was determined by its solid content. Under certain experimental conditions, BCPMs had a low apparent density, the lowest water absorption capacity and good mechanical properties.

The magnesium bisulfite spent liquor (pH 4.5) was placed in a plastic beaker. Then, sodium hydroxide was added until the spent liquor became neutral which ensured that the cushion packaging materials could be directly contacted with the packaged articles. Finally, silica (1%-15% relative to oven dry bagasse pith) was charged to the neutralized spent liquor for filler dispersion. The mixed solution and the bagasse pith were stirred

together for 2 min in the SHR-10A high-speed mixer (Zhangjiagang Gelan Machinery Co., Ltd., China). The homogeneously blended ingredients were discharged to the molds and compressed by a Micro press machine. The materials were processed at a set pressure of 52KPa and time of 30 s. After the molding process, the materials in the inner molds were dried at  $155 \pm 2^\circ\text{C}$  for 45 min in an air oven. Eventually, the BCPMs were obtained after demolding.

**Table 1.** Physical and chemical properties of fumed silicas.

Sample	BET surface area ( $\text{m}^2\text{g}^{-1}$ )	BJH adsorption cumulative surface area of pores (1.7-300nm)( $\text{m}^2\text{g}^{-1}$ )	pH value
HL150	138.6± 1.1	106.8	4.33
HL200	154.4± 1.1	119.9	4.83
HL380	325.5± 2.6	246.3	4.17
HL150	138.6± 1.1	106.8	4.33

#### BCPMs biodegradability

Biodegradability of BCPMs was characterized by the weight-loss method [20]. Table 2 shows the reagents and dosages to confect the mineral salt medium (MSM).

The ingredients of a medium developed for screening of BCPMs strain were bagasse pith and MSM. Solid media were prepared by the addition of 1.5% agar to the above mentioned medium. Soils from Jiangmen Sugarcane Chemical Factory (Group) Co. Ltd, the lotus pond of the campus as well as the surrounding area of the waste plants were taken as samples, which were transferred into a shake flask containing MSM medium. The fungal strains were domesticated at  $30^\circ\text{C}$  and 150 rpm for 5 days in MSM medium with bagasse pith as the sole carbon source. After that, the MSM plate was coated by the dilution coating method using bagasse pith as the sole carbon source. Five strains were selected from colonies growing faster and in good condition, and then were streaked onto the MSM plate. Finally single colonies were inoculated on the slant and prepared for the determination of degradation rate.

**Table 2.** Reagents and dosages to confect the MSM.

Reagent	Dosage (g)	Reagent	Dosage (g)
NaCl	1.0	$(\text{NH}_4)_2\text{SO}_4$	2.0
$\text{K}_2\text{HPO}_4$	1.0	$\text{MnCl}_2 \cdot 7\text{H}_2\text{O}$	0.001
$\text{MgSO}_4$	1.0	$\text{ZnSO}_4 \cdot 7\text{H}_2\text{O}$	0.001
$\text{CaCO}_3$	2.0	$\text{FeSO}_4 \cdot 7\text{H}_2\text{O}$	0.001

Weight-loss method was applied to determine BCPMs degradation rate. First, BCPMs liquid medium was prepared and discharged into three

250 mL Erlenmeyer flasks, respectively. The liquid was sterilized under 0.105 MPa for 30 min. Under aseptic operational conditions, the strains were selected from the slant mentioned above, then inoculated into the prepared medium and incubated for 15 days at  $30^\circ\text{C}$  and 150 rpm. The BCPMs which were not degraded were separated from the Erlenmeyer flask by filtering. The samples were purified with distilled water and then dried to constant weight at  $60^\circ\text{C}$  in an air oven. Afterwards, the mass of the samples after degradation was weighed, and the weight loss of BCPMs before and after degradation was calculated. The degradation rate of BCPMs can be converted to the weight-loss rate [21]. The weight loss rate is described by Eq. (1).

$$W = \frac{m_1 - m_2}{m_1} \times 100\% \quad (1)$$

where W is the degradation rate,  $m_1$  is the mass of the samples before degradation,  $m_2$  is the mass of the samples after degradation.

#### BCPMs characterization

*Apparent density.* The length, width and thickness of the samples were measured with a manual vernier caliper (Guanglu, China). The apparent density was calculated as the relationship between weight and volume according to the GB8168-2008 Testing Method of Static Compression for Packaging Cushioning Materials. The reported values are the averages of six determinations for each formulation.

*Mechanical properties.* The mechanical properties of the samples were investigated through static compression tests. The tests included compressive stress-strain ( $\sigma$ - $\epsilon$ ) and static cushion factor-strain evaluations. Static compression tests were performed according to GB8168-2008 on five specimens that were stored for 24 h at  $23 \pm 2^\circ\text{C}$  and  $50 \pm 2\%$  relative humidity using a CMT4204 universal testing machine (MTS China Co. Ltd.) operated at a speed of  $12 \pm 2$  mm/min.

#### TEM analysis

The particle sizes and morphologies of silica were examined by transmission electron microscopy (TEM, JEOL JEM-2010HR). Samples were prepared by placing droplets of a suspension of silica powders in anhydrous alcohol on copper grids.

#### SEM analysis

The morphologies of BCPMs before and after degradation were characterized by field emission scanning electron microscopy (SEM, FEI Quanta

400F). The fracture surfaces of samples were coated with gold using a vacuum sputter-coater before observation.

## RESULTS AND DISCUSSION

### TEM analysis of fumed silica

Fig. 1 presents TEM micrographs of three kinds of fumed silica used in this study. It was found that fumed silica nanoparticles were sphere shaped and connected as grape bunches. Nanoparticles were prone to agglomerate due to hydrogen bonds between the surface hydroxyl groups of silica. The forces between the agglomerates were easily destroyed using mechanical agitation and the aggregation process was reversible [22].

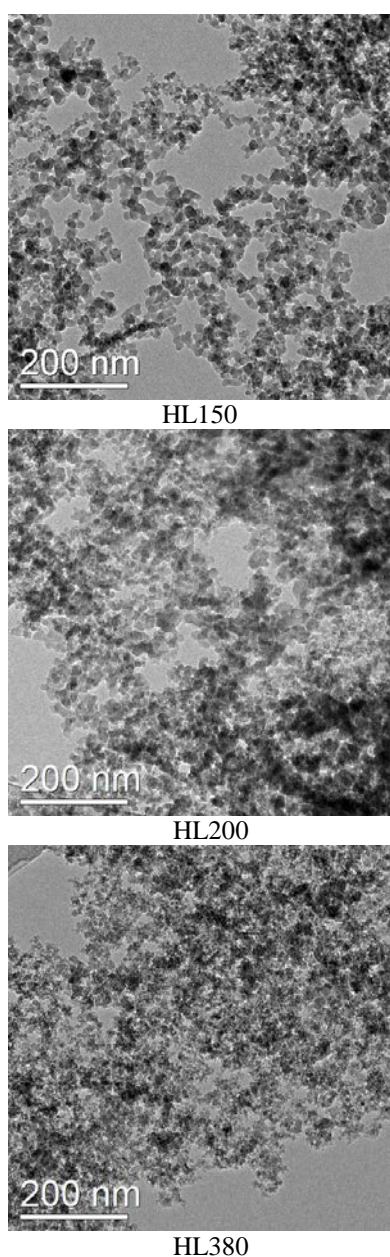


**Fig. 1.** TEM micrographs of fumed silica nanoparticles.

The dispersion of fumed silica in the polymer matrix affected the mechanical behavior of the resulting composites.

The particle size of silica could be indirectly reflected from the specific surface area ( $S_{BET}$ ). Small diameter particles had high specific surface area. TEM analysis showed that the mean diameter of HL150, HL200 and HL380 ranged from 10 to 18 nm, 8 to 14 nm and 4 to 10 nm, respectively, consistent with  $S_{BET}$  test results.

### Apparent densities of BCPMs

The apparent densities of BCPMs with different silica loadings are shown in Fig. 2. It is seen that cushion packaging materials with silica have higher apparent densities compared with materials without silica, which was  $0.204 \text{ g/cm}^3$  [19]. The apparent densities of BCPMs increased with the increasing silica loading.

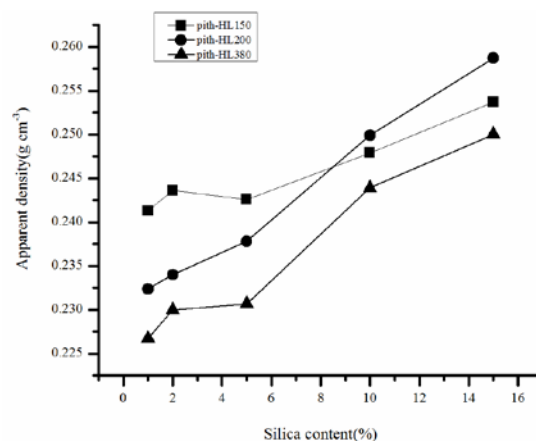


**Fig. 2.** Effects of silica loadings on BCPMs apparent densities.

Given the same silica loading, BCPMs with HL380 reinforcement has the minimum apparent density. Compared with HL150 and HL200, HL380 has the largest specific surface area, more silanol groups (Si-OH) on the surface, more additional cross-linking reactions produced from the chemical reaction with phenolic hydroxyl groups (Ph-OH) and sulfonic groups in the molecular chains of magnesium lignosulfonate, and higher network strength of the reinforcement system. Therefore, HL380 underwent the minimum volume deformation under same molding pressure of 52 KPa. When silica loading exceeded 10 wt%, BCPMs with HL200 reinforcement achieved higher apparent density than BCPMs with HL150 reinforcement. This finding may be ascribed to maximum volume deformation of BCPMs with HL200 reinforcement under external forces.

The number of silanol groups in HL200 was greater than in HL150. In addition, the interparticle interaction of HL200 was stronger than that of

HL150. Therefore, HL200 particles were prone to agglomerate as the amount of the particles increased [23]. The HL200 aggregates yielded a poor dispersion within the bagasse pith/ bisulfite spent liquor matrix and led to more matrix defects. Poor dispersion and matrix defects could lower the effective stress transfer at the interface and cause large volume deformation of BCPMs. In the experiment, the loadings of fumed silica increased from 1 wt% to 15 wt%, whereas the apparent density of BCPMs varied from 0.22 g/cm<sup>3</sup> to 0.26 g/cm<sup>3</sup>. The addition of lightweight amorphous silica powder had little effect on the apparent density of BCPMs. Fumed silica is beneficial for maintaining the low apparent density of cushion packaging material.

### Mechanical properties of BCPMs

**Effect of silica loading.** To analyze the effect of silica loading on the cushion performance of BCPMs, 1 wt% HL150, HL200 and HL380 silica were added to the samples. The corresponding static compressive stress-strain curves are shown in Fig. 3.

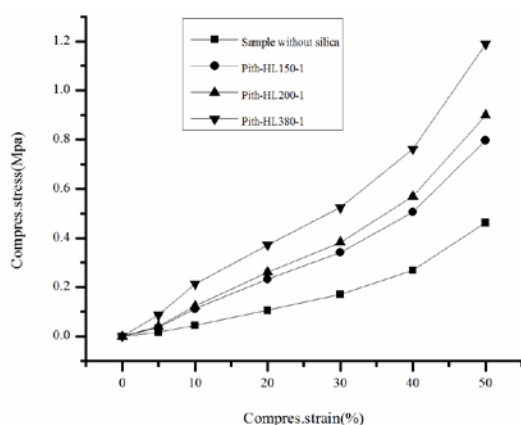


**Fig. 3.** Static compression properties of BCPMs with and without silica.

BCPMs without silica can withstand stress of 0.17 MPa, whereas BCPMs with HL150, HL200 and HL380 can withstand stress of 0.31MPa, 0.36MPa and 0.48 MPa, respectively, under the same strain of 30%. This finding indicates the significant effect of silica loading in improving the compression strength of BCPMs. The stress-strain diagram shows that under the same strain conditions, stress increased at first and then decreased with the increase in silica loadings. Such variation in trend can be analyzed qualitatively based on the microstructure of the interface between silica and adhesive. Magnesium lignosulfonate is the major component of bisulfate spent liquor serving as the adhesive in this experiment. The molecules of lignosulfonate

contain various active functional groups such as hydroxyl groups (including alcoholic hydroxyl groups and phenolic hydroxyl groups), sulfonic groups, and carboxy groups [24] that can combine with silanol groups on the silica surface to develop chemical bonds, and enhance the binding between nanoparticles and adhesive. The increase of silica loading may contribute more silanol groups to the system and expand the contact area with pulping spent liquor, developing more cross-linking joints, which is good for stress transfer. Thus, the load capacity of the adhesive membrane formed on the surface of the material finally increased. The effects of silica loading on the static compressive stress-strain curve of BCPMs were studied under the same specific surface area ( $S_{BET}$ ) of fumed silica. The results are shown in Fig. 4.

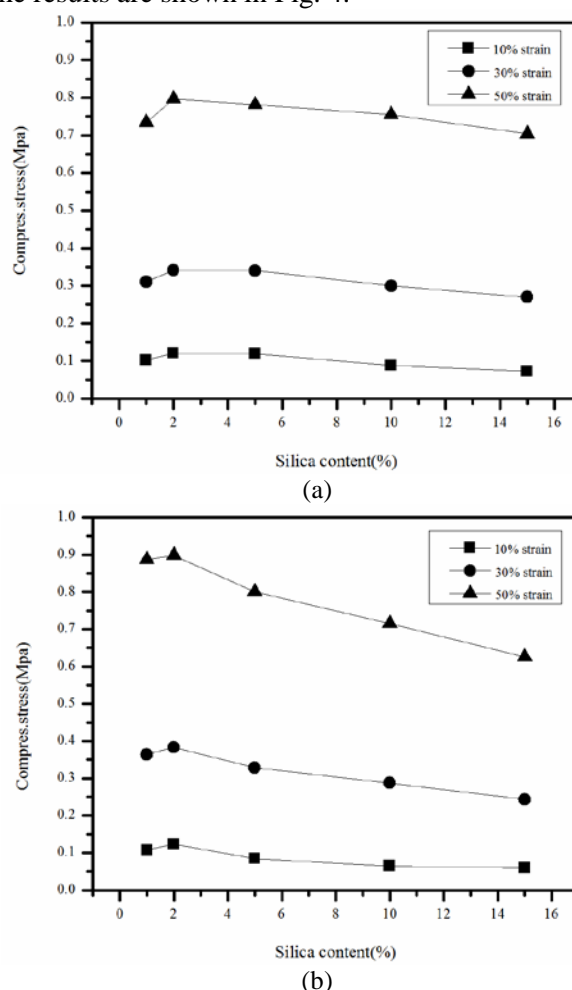


**Fig. 4.** Static compression properties of BCPMs filled with different silica loadings: (a) HL150; (b)HL200.

By contrast, less than 5 wt% HL150 and less than 2 wt% HL200 served as inorganic rigid fillers scattered evenly in the bagasse pith and spent liquor compound, which can expand the region of stress concentration and absorb certain deformation, thus increasing the compressive stress. Given that silica

was dispersed in the pulping spent liquor first in this experiment, the silica-adhesive interfacial adhesion was improved with the increase in silica loading. However, excessive silica loading may lead to bigger sizes of the agglomerates in the adhesive, which increases the defects of BCPMs, thus decreasing compressive stress accordingly.

The comparison of drop points in Figs. 4(a) and 4(b) showed that BCPMs with higher than 2 wt% HL200 silica as reinforcing filler have poor mechanical properties, which are caused by the agglomeration of HL200 with high surface energy. The result is similar to the observations reported by Kantala et al. [22].

*Effect of silica specific surface area.*

Specific surface area is one of the most important morphological parameters of fumed silica without surface modification [23]. The effects of  $S_{BET}$  on the cushioning property of BCPMs were studied under the same silica loading conditions. The results are displayed in Fig.5.

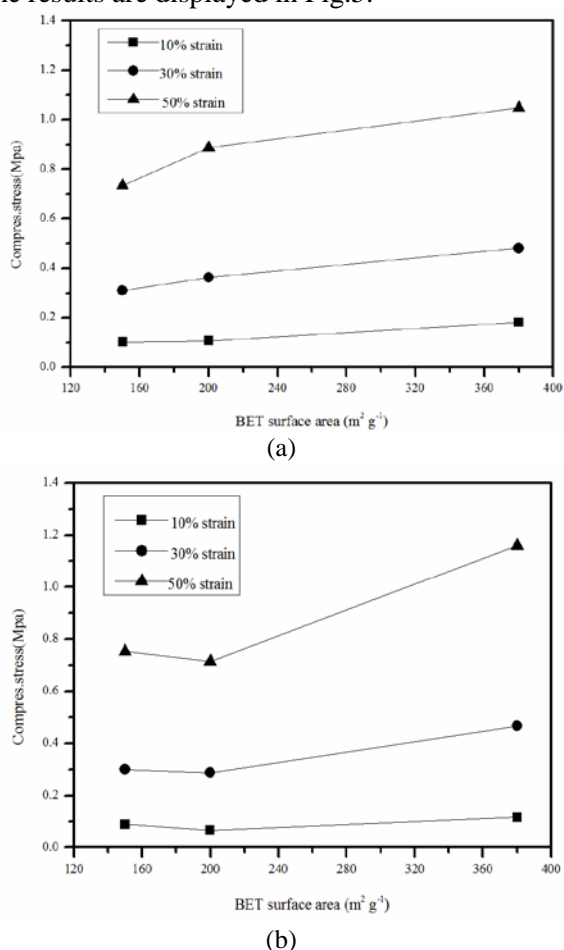


**Fig. 5.** Static compression properties of 1 wt% (a) and 10 wt% (b) filled BCPMs with various silica  $S_{BET}$ .

As shown in Fig. 5, stress of BCPMs containing 1 wt% silica increased with the increase of silica contents. A further increase in compression strength

was observed under high compressive strain condition. When  $S_{BET}$  of silica increased from 200 to 380 m<sup>2</sup> g<sup>-1</sup>, the compressive stress increased by 0.08MPa with the strain of 10%, 0.12MPa with the strain of 30% and 0.16MPa with the strain of 50%. This is probably due to the increased interfacial area between adhesive and silica nanoparticles with high  $S_{BET}$  value. Nevertheless, when the silica loading was up to 10 wt%, BCPMs with HL200 reinforcement can withstand less stress than HL150. The results showed that once silica loading exceeded the critical value, the filler-filler interaction was dominant, which resulted in weak interactions between silica particles and matrix. The compression strength of BCPM decreased in its macro performance.

The cushion factor-maximum static stress curves of BCPMs with three kinds of silicas are presented in Fig.6. The specific surface area of silica had a significant effect on the cushioning properties of BCPMs. Higher  $S_{BET}$  values resulted in a higher cushion factor, revealing that the BCPMs became stiffer.

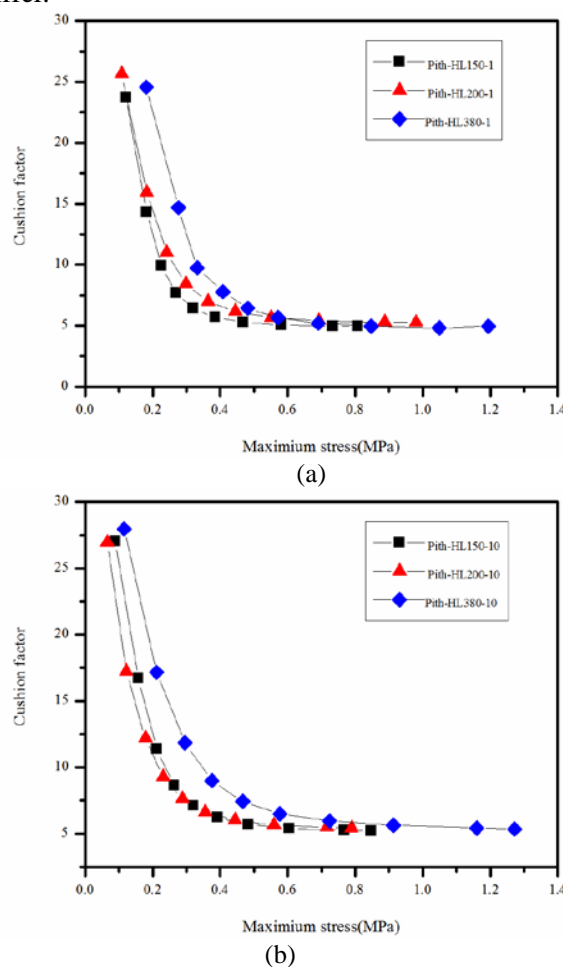


**Fig. 6.** Static cushion factors of 1 wt% (a) and 10 wt% (b) filled BCPMs with various silica  $S_{BET}$ .

Compared with high-density EPS with apparent density of  $0.0226 \text{ g/cm}^3$ , BCPMs display a lower cushion factor under high compressive stress ( $>0.4 \text{ MPa}$ ), and perform well in a more extensive stress range [25]. These data indicate that better protection and lower BCPMs consumption could be achieved in packing heavy fragile articles. In addition, BCPMs is superior to nondegradable EPS with respect to mechanical and electronic products as well as large household appliances.

#### SEM Analysis

The morphology of BCPMs was studied by SEM in order to evaluate the dispersion state of silica particles in the bagasse pith/ bisulfite spent liquor matrix. The particles observed in Fig.8 and Fig.9 are fumed silica.

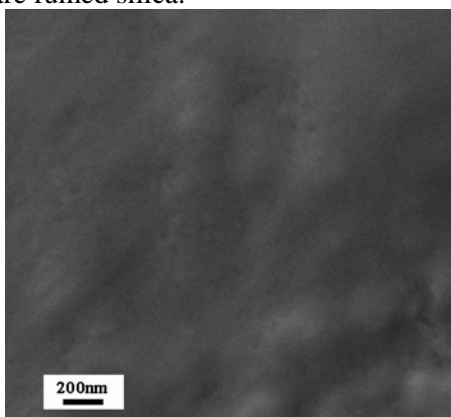


Fig. 7. SEM micrographs of BCPMs without silica.

It can be seen from Fig. 7 that the surfaces of BCPMs are covered by a layer of dense membrane from magnesium bisulfate spent liquor. The fumed silica particles are dispersed into the adhesive membrane. Therefore, the compressive stress was transferred from the membrane onto the rigid phase [14], and fumed silica particles reinforced the BCPMs. The increase of  $S_{\text{BET}}$  led to bigger sizes of the agglomerates. By comparing the images in Figs. 8 and 9, it can be seen that the size of HL200 agglomerates is larger than that of HL150.

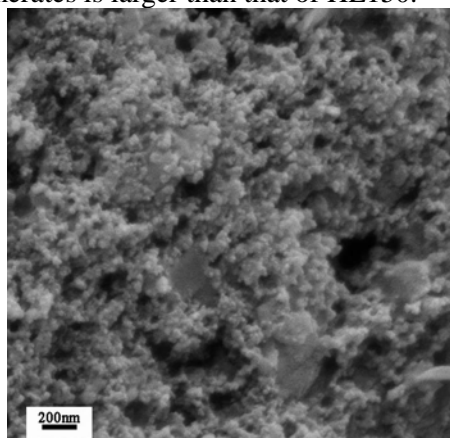


Fig. 8 SEM micrographs of BCPMs with 10 wt% HL150.

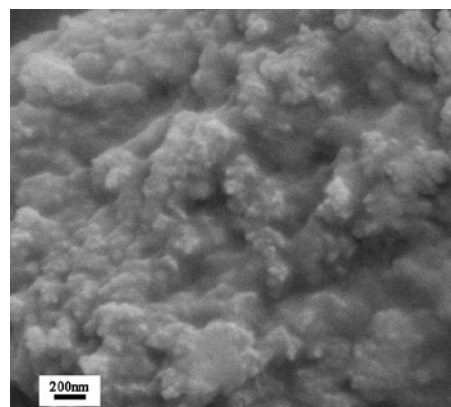


Fig. 9. SEM micrographs of BCPMs with 10 wt% HL200.

These silica agglomerates became the stress concentration points as the BCPMs were compressed, making the BCPMs more prone to damage. This finding is in accordance with the change trend of the mechanical properties of BCPMs.

#### Biodegradation

Previous studies have proved that there were large amounts of hemicellulose in bagasse pith and the degradation of hemicellulose mainly makes use of molds [26]. In the experiment, the samples were cultured with molds for 15 days in submerged culture with shake flask, and then the biodegradation rate of BCPMs was measured by the weight-loss method. The weight loss was observed for the BCPMs without silica and with 10 wt% HL200 (52.5% and 45.7%, respectively) after 15 days. The presence of silica particles in the BCPMs reduced the biodegradation rate. The BCPMs with 10 wt% HL200 were left to dry in an air oven at  $60 \text{ }^\circ\text{C}$  after degradation, and then the degradation state was observed by SEM.

The SEM micrographs of the BCPMs surfaces before and after degradation treatment are shown in Fig. 10. The micrographs clearly show that the surfaces of the BCPMs are covered by a film formed by the adhesive before degradation treatment. The film was dense and thick. After degradation treatment, the BCPMs became thinner, and the surface was dotted by different-sized holes because of erosion.

#### CONCLUSIONS

Biodegradable cushion packaging materials based on bagasse pith, magnesium bisulfite spent liquor and hydrophilic fumed silica were prepared via press-molding method. The experimental results revealed that the dispersion of fumed silica within the matrix and the size distribution of silica nanofiller aggregates had a significant effect on the



properties of BCPMs. The apparent densities of BCPMs increased with the increase of silica loading. Given the same silica loading, BCPMs reinforced by the silica with largest specific surface area has minimum apparent density. From the study of the cushioning properties, it was found that the addition of fumed silica improved the compression strength of BCPMs. However, excessive silica loading may lead to bigger sizes of the agglomerates in the adhesive, which increases the defects of BCPMs, thus decreasing compressive stress accordingly. When the silica loading was within the critical value, the compressive strength was found to increase with the increase of specific surface areas of fumed silica due to a fine dispersion of nanofillers in the matrix.

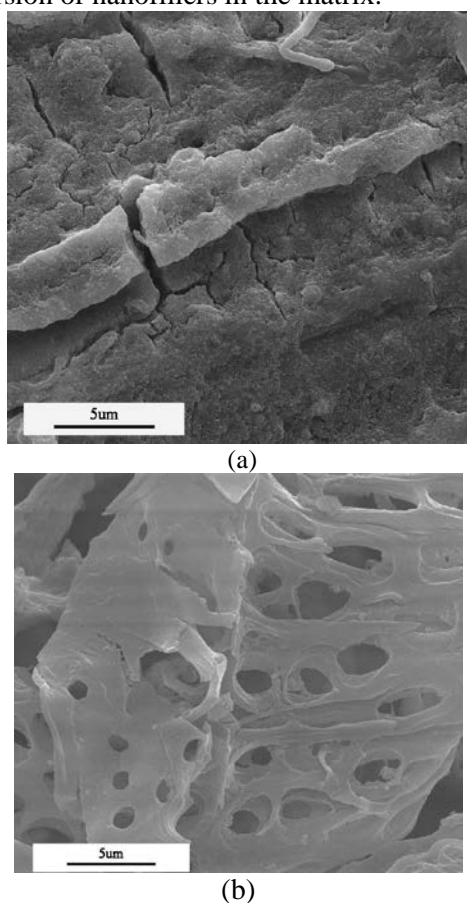


**Fig. 10.** SEM micrographs of BCPMs surface: (a) before degradation treatment (b) after degradation treatment.

The morphological analyses indicated that the reinforcement effect of fumed silica was the consequence of silica filler-matrix and silica filler-filler interactions.

BCPMs had good cushioning properties within a large stress range, and good degrading performance in mold conditions. Compared with high-density EPS, BCPMs can be used for packing heavy delicate articles.

**Acknowledgements:** The authors wish to thank the Guangzhou GBS High-Tech & Industry Co., Ltd. for offering hydrophilic fumed silica nanoparticles.

#### REFERENCES

1. Y. Chen, Z.Y. Zhang, Y. Ishikawa, T. Maekawa, *Trans. ASAE*, **45**, 1051 (2006).
2. S. Shibata, Y. Cao, I. Fukumoto, *Polym. Compos.*, **26**, 689 (2005).
3. L. K. Chen, Q. F. Zhang, Z. F. Lei, Y. H. Wang, X. L. Dong, *Packaging Engineering*, **32**, 11 (2011). (in Chinese)
4. F. Y. Li, K. K. Guan, P. Liu, G. Li, J. F. Li, *Int. J. Polymer Sci.*, **70**, 1 (2014).
5. R.K. Sharma, K.R. Yadav, V.L. Maheshwari, R.M. Kothari, *Crit. Rev. Biotechnol.*, **20**, 237 (2000).
6. S. Hedjazi, O. Kordsachia, R. Patt, A. Latibari, U. Tschirner, *Holzforchung*, **62**, 142 (2008).
7. A. Khakifirooz, F. Ravanbakhsh, A. Samariha, M. Kiaei, *BioResources*, **8**, 21 (2013).
8. J. A. Lois-Correa, *Ingeniería Investigación y Tecnología*, **13**, 417 (2012).
9. S.K. Paul, K.S. Kasiviswanathan, *Ippta*, **10**, 1 (1998).
10. H. Y. Zhan, *China Pulp and Paper*, **29**, 56 (2010). (in Chinese)
11. H.H. Nimz, *Wood Adhesives Chemistry and Technology*, A. Pizzi, (ed.), Marcel Dekker, New York. (1983).
12. J.E. Van Dam, M.J. van den Oever, E.R. Keijsers, J.C. van der Putten, C. Anayron, F. Josol, A. Peralta, *Ind. Crop. Prod.*, **24**, 96 (2006).
13. S. Shibata, *BioResources*, **7**, 5381 (2012).
14. A. Bouaziz, M. Jaziri, F. Dalmas, V. Massardier, *Polym. Eng. Sci.*, **54**, 2187 (2014).
15. M. Q. Zhang, M. Z. Rong, H. B. Zhang, K. Friedrich, *Polym. Eng. Sci.*, **43**, 490 (2003).
16. S. Prasertsri, N. Rattanasom, *Polym. Test.*, **31**, 593 (2012).
17. S. Brunauer, P.H. Emmett, E. Teller, *J. Am. Chem. Soc.*, **60**, 309 (1938).
18. E. Barret, L. Joyner, P. Holenda, *J. Am. Chem. Soc.*, **73**, 373 (1951).
19. Y.N. Lv, J. Z. Ou, K. J. Chen, The Second International Papermaking and Environment Conference, W, L.J., Ni, Y.H., Hou, Q.X., and Liu, Z. (eds.), China Light Industry Press, Bei Jing. (2009).
20. F. Li, H. Yang, Z.Q. Guo, Z.Y. Wang, Y. Wang, D.B. Liu, H.M, Xia, S. Chen, *Journal of Northeastern University*, **43**, 127 (2011).
21. H.J. Hou, F.S. Chen, X.L. Cheng, B.W. Gong, *Plastics Science and Technology*, **37**, 40 (2009).

- 22.C. Kantala, E. Wimolmala, C. Sirisinha, N. Sombatsompop, *Polym. Adv. Technol.*, **20**, 448 (2009).
- 23.M. J. Wang, M.D. Morris, Y. Kutsovsky, *Kautschuk, Gummi & Kunststoffe*, **61**, 107 (2008).
- 24.D. J. Yang, Y. G. Du, J.G. Fu, X. Q. Qiu, *CIESC J.*, **61**, 1859 (2010).
- 25.C. Liu, Y. D. Ren, *Packaging Engineering*, **31**, 117 (2010).
- 26.R.Sanzjuan, J.Anzaldo, J.Vargas, J.Turrado, R.Patt, *Eur. J. Wood & Wood Prod.*, **59**, 447 (2001).

## ВЛИЯНИЕ НА ОПУШЕН СИЛИЦИЕВ ДИОКСИД ВЪРХУ СВОЙСТВАТА НА МЕКИ ОПАКОВЪЧНИ МАТЕРИАЛИ НА ОСНОВАТА НА СЪРЦЕВИНА ОТ БАГАСА И БИСУЛФИТНА ОТПАДЪЧНА ЛУГА

Янна Лв<sup>1,2\*</sup>, Бейхай Хе<sup>1,3</sup>, Яли У<sup>4</sup>

<sup>1</sup> Държавна лаборатория по инженерство на целулозата и хартията, Южен китайски технологичен университет, Гуанчжу, Китай

<sup>2</sup> Департамент по медии и съобщения, Технически колежпромишлено-технически колеж Гуандонг, Гуанчжу, Китай

<sup>3</sup> Национален инженерно-изследователски център по хартия и контрол на замърсяванията, Южен китайски технологичен университет, Гуанчжу, Китай

<sup>4</sup> Департамент по храните, Технически колежпромишлено-технически колеж Гуандонг, Гуанчжу, Китай

Постъпила на 1 май, 2014 г.

(Резюме)

В настоящата работа се съобщава за биоразградими опаковъчни материали, основани на сърцевината от багаса, отпадъчна бисулфитна луга, съдържаща магнезий и хидрофобен опушен силициев диоксид. Материалите са приготвени чрез леене под налягане. Изследван е ефектът на добавените наночастици от силициев диоксид върху физичните свойства и биодеградационните отнасяния. Резултатите показват, че добавянето на наночастици от силициев диоксид повишава привидната плътност и здравината към статично свиване на меки опаковъчни материали от сърцевина на багаса. Когато натоварването със силициев диоксид е в границите на критичните стойности, здравината на свиване расте с нарастването на специфичната повърхностна площ на опушения силициев диоксид поради фината дисперсия от наночастици в матрицата. Морфологията на наночастиците от опушения силициев диоксид и на дисперсионното им състояние са изучени с трансмисионна и сканираща електронна микроскопия. Морфологичните анализи показват, че ефектът на усилване от опушения силициев диоксид е в следствие на взаимодействия пълнеж-матрица и пълнеж-пълнеж. Пробите показват, че в присъствие на силициев диоксид в опаковъчните материали, тяхната биоразградимост намалява след престой от 15 дни в течна хранителна среда.

## Synthesis of Cu<sub>2</sub>O nanocrystals and their agricultural application

Wang Qiang

College of Chemistry and Pharmaceutical Sciences, Qingdao Agriculture University, Qingdao, 266109, PR China

Submitted May 1, 2014

A series of cuprous oxide (Cu<sub>2</sub>O) nanocrystals with different structures were synthesized by reductive reaction. The nanocrystals were obtained in an aqueous mixture of CuSO<sub>4</sub>, fructose, NaOH and templates at 45-75°C. We developed a facile one-pot route for the synthesis of Cu<sub>2</sub>O by simple adjustment of the template quantity. The novel particles were analyzed by SEM and XRD. These verified that the average sizes for the cubic, octahedral, petaloid and spherical structures were approximately 450, 180 and 360 nm, respectively. The octahedral Cu<sub>2</sub>O was selected for the further experiments due to the smallest size of its particles. The agricultural application performance like anti-alga experiments and inhibition zone method showed that about 4.9×10<sup>3</sup> N.cm<sup>-2</sup> diatom was noticed on the surface and the inhibition rate of the novel mixture towards *Colletotrichum capsici* was 90%, as soon as 70 mg nano-Cu<sub>2</sub>O was added into 100 mL culture media. Similar results were obtained in sea water after 120 days of exposure.

**Key words:** Cu<sub>2</sub>O, synthesis, performance, agricultural application.

### INTRODUCTION

It is witnessed that fouling is a destructive natural phenomenon that affects almost every economic sector, causing annually billions of dollars in damage and disorder [1-3]. The most common and efficient antifouling method was painting antifouling coatings containing biocides like TBT (tetra-*n*-butyl tin) which often had detrimental non-target environmental effects during its application, particularly in marine water. As soon as the environmentally disastrous effect of TBT coatings was noticed by the following research, the UN International Maritime Organization had decided to ban the use of TBT in antifouling coatings by the end of Jan. 1, 2008 [4]. Consequently, there still exists a desperate need for high-effective and environment-friendly alternatives [5-7]. Considering environmental protection, many researchers had developed two ways to resolve the matter by the end of last decade: one was constructing micro/nano-surfaces like low energy surface and superamphiphobic surface that physically released the accumulated fouling. The other was applying environmentally friendly biocides like Cu<sub>2</sub>O that chemically inhibited most of marine organisms by leaching some biocides [8-11]. In order to unite these advantages and simplify the operation, our present work aimed at studying the synergistic performance of environmental biocides with sub-micro cuprous

oxide and functional acrylic resin. It was reported that Cu<sub>2</sub>O was still the dominant biocide in antifouling coating. But seldom papers disclosed the relationship between crystal morphology, particle size, functional acrylic resin and antifouling performance. Fortunately, there were lots of papers about the synthesis of particles of different size and morphology. The Cu<sub>2</sub>O particles with cubic, octahedral and spherical structures were interesting not only because excellent antibacterial properties could be investigated with great certainty, but also because synthetic conditions of controlling the particle morphology could be achieved. Generally speaking, templates were universally applied during micro/nano-particles synthesis. Yu *et al.* [12] reported the synthesis of Cu<sub>2</sub>O nano-whiskers by using cetyl-trimethyl ammonium bromide (CTAB). Zeng *et al.* [13] reported Cu<sub>2</sub>O nanocrystals with size of 70 nm produced at 160-220°C by using hexadecylamine. Dong *et al.* [14] reported the synthesis of micro/nano Cu<sub>2</sub>O by using NH<sub>2</sub>-NH<sub>2</sub> as a reducing agent. Huang *et al.* [15] synthesized eight nanocrystals of different morphology by changing the quantity of NH<sub>2</sub>OH. All these suffered from the use of either high temperature, random morphology or toxic reducing agents.

According to atom economy, it would be desirable to develop a simple synthetic approach at mild conditions to synthesize Cu<sub>2</sub>O of different morphology like cubic, octahedral and spherical structures without waste disposal or high temperature. Recently, the common fact was accepted that the template played an important role in nanocrystal synthesis and stability. The β-

---

\* To whom all correspondence should be sent:  
E-mail: wangqian\_qau@163.com

cyclodextrin ( $\beta$ -CD) derivative,  $\alpha$ -1,4-linked D-glucopyranose polymer, was selected as a promising template. It is funnel shaped with hydrophilic groups outside, and lipophilic alkyl groups inside. There was little information about  $\beta$ -CD and its derivatives as soft templates to synthesize Cu<sub>2</sub>O nanocrystals. This kind of hydrophilic-lipophilic template not only realized proper molecule-cages, but could improve the stability of nano-particles. In this paper, a typical Cu<sub>2</sub>O biocide of various size and particle morphology was synthesized by direct reduction with fructose. Then, the novel coating containing acrylic resins copolymerized with VTMS (containing  $-\text{Si}(\text{OCH}_3)_3$  as a cross-linking group) with Cu<sub>2</sub>O was produced. Furthermore, the synergistic antifouling performance of the coating was investigated in Qingdao offshore.

## EXPERIMENTAL

### Material

The algae of *Nitzschia flosterium* were provided by the laboratory of alga at the Ocean University of China. The algae were cultivated in a biological culture box and prepared for the following anti-alga experiments. All nutrient salts were purchased from Alfa. Methyl methacrylate (MMA), butyl acrylate (BA) and vinyltrimethoxysilane (VTMS) were obtained from Qingdao Haida Chemical Co. Ltd (CN). All these materials were industrial grade products, which were used as received without further purification. Copper sulfate (CuSO<sub>4</sub>),  $\beta$ -cyclodextrin ( $\beta$ -CD), fructose and toluene were obtained from BASF (CN). 2,2'-Azobis (2-methylpropionitrile) (AIBN) was obtained from Changzhou Watson Fine Chemical Co. Ltd. (CN). Deionized water (17.8 M $\Omega$ ) was used for all solution preparations.

### Synthesis of Cu<sub>2</sub>O by "one-pot" reduction reaction

It is known that continuous efforts have been made to focus on efficient approaches for the synthesis of Cu<sub>2</sub>O nanocrystals because of their remarkable antifouling and antibacterial properties. The multi-component reaction was one of the most efficient methods because it was a synthetic operation without the need for isolation of the intermediates [16,17]. The one-pot reaction was highly effective for the synthesis of Cu<sub>2</sub>O nanocrystals with different shapes of cubic, octahedral and spherical structures via multi-component reaction of fructose, CuSO<sub>4</sub> and NaOH in  $\beta$ -CD solution. The raw material solutions were placed in a water bath at 45-75°C. Then 0.04g soft

templates like  $\beta$ -CD, cellulose and PG-200, were added to 10 mL of 1M CuSO<sub>4</sub> under stirring. Five minutes later, 30 mL of 1M NaOH and 2M fructose solutions were added to the former solution. The total solution volume was about 40 mL. The solution was kept in the water bath for half an hour in order to promote the reaction and then was centrifuged at 3000 rpm for 4 min. After the top solution was decanted, the precipitate was washed with 10 mL of a 1:1 volume ratio of C<sub>2</sub>H<sub>5</sub>OH and H<sub>2</sub>O. The precipitate was centrifuged and washed at least three times using the former solution to remove the remainders. The precipitate was dispersed in 10 mL of absolute C<sub>2</sub>H<sub>5</sub>OH for storage and analysis.

### Synthesis of acrylic resin copolymerized with VTMS

The free radical copolymerization of multi-monomers represents a versatile tool for the formation of copolymers. In the current study n-butyl acrylate and methyl methacrylate were synthesized via high-temperature acrylate synthesis in a one-pot-one-step procedure with radicals [18].

A mixture of 0.71 g of 2,2'-azobisisobutyronitrile (AIBN), 0.63 mol of methyl methacrylate, 0.26 mol of butyl acrylate, and 0.037 mol of VTMS, was put into a conical flask to obtain a clear solution after ultrasonic oscillation. The toluene was deoxygenated by purging with nitrogen in a 250 ml round-bottomed flask for at least 10 min. A small amount of radicals (1%, w/w) was added before the reaction. Otherwise the copolymerization was blocked or out of control. Then, the mixture was fed by an injector into 100 mL of toluene with a motor stirrer at 80°C-86°C. These monomers were copolymerized at 550 - 600 rpm for 1 h. Once the reaction was completed, which was evident from the change in the appearance of the doped solution, additional 0.55 g of AIBN was added to enhance the polymerization rate for more 3 h. The final product was saved in dark environment without air and water vapor [19]. The product was transparent and glutinous. The formation of copolymer structure was evidenced by IR (KBr): appearance of absorption peaks at 1770 cm<sup>-1</sup>, 1149 cm<sup>-1</sup> and 1387 cm<sup>-1</sup> confirmed the presence of C=O,  $-\text{Si}-\text{O}-\text{Si}-$  and  $-\text{Si}-\text{OCH}_3$ , respectively.

### Anti-algal activity test

*Algae cultivation.* The algae of *Nitzschia flosterium*, a typical fouling organism, were transferred to a conical flask containing NaNO<sub>3</sub>: 14.96 g, NaH<sub>2</sub>PO<sub>4</sub>·2H<sub>2</sub>O: 1.0 g, Na<sub>2</sub>SiO<sub>4</sub>·9H<sub>2</sub>O: 10.1 g, and distilled water. The flask was sterilized

for 15 min at 120°C. The nutrient salts (with or without silicate, as appropriate) were weighed exactly by electronic analytical balance. The algae were cultivated in a biological culture box for seven days at 21±1°C. In order to accelerate alga growth, the flask was stirred at least three times during the day-time. The culture box was under continuous illumination of cool-white fluorescent tubes at 3000-4000 lux with a 12 h light/dark cycle, coinciding with alga growth law [20,21].

*Anti-algal colonization.* There were two coatings; one group (coating containing Cu<sub>2</sub>O) and the other group (coating without Cu<sub>2</sub>O). The coatings were prepared on glass (30mm×70mm×5mm) without any flaws like pinholes or uneven surface. Until the solvent volatilizes, every tested example was vertically put into the alga pool, in order to avoid deposition of alga. As soon as the tested examples were placed into the culture pool, some bacteria directly colonized the surface. A few hours later, *Nitzschia flosterium* was successively gathering onto the coating surfaces following the bacterial colonization. After seven days, the surface of every tested coating was washed at least 30 times with 10 mL of distilled water without addition of a nutrient by an adjustable air-displacement pipette. Then the anti-alga property was evaluated by the counting method under stereo microscope as soon as possible, in case the algae were getting dead in distilled water. All tests were conducted in triplicate in three different parallel experiments.

#### *Antifouling property of the novel coatings*

The antifouling property of the novel coating was investigated according to GB 5370-85 [22]. Uncoated panels (control panels) were used to assess the fouling resistance rating. The main bio-fouling organisms observed were green algae and encrusting species like hydroids, bryozoans and barnacles. The marine coating systems were exposed in vertical position to sea water for 5 months (June to October). At first, the low-carbon steel test plates (150mm×250mm×3mm) were polished with sandpaper and coated within 8 hours or before rusting occurred with the appropriate anticorrosive coatings. Two kinds of Cu<sub>2</sub>O were tested, one was the traditional product, and the other was octahedral nanocrystalline product. Then we brushed the antifouling coatings following the formulation shown in Table 1.

These panels dried at least 7 days without direct sunshine during daytime and were fastened by nylon ropes. The tested samples were vertically immersed in sea water at 1 to 1.5 m depth at the

No.8 harbor of Qingdao, east of China. The examples were traced and photographed during the effective antifouling period.

**Table 1.** Composition of antifouling coating (unit: g).

No.	Acrylic resin	Cuprous oxide	Functional group	Assistant	Xylene
A	31	25 (nanocrystal)	0	2	12
B	31	25a (nanocrystal)	VTMS	2	11
C	31	25	0	2	12
D	31	25	VTMS	2	11

## RESULTS AND DISCUSSION

### *One-pot synthesis of Cu<sub>2</sub>O nanocrystals*

Previously, Cu<sub>2</sub>O nanocrystals were fabricated by mixing deionized water, CuSO<sub>4</sub>, cetyltrimethyl ammonium bromide, fructose and NaOH in the listed order. We considered that this synthetic method was a good starting point to synthesize these particles. We had witnessed the role of soft templates during the nanoparticles synthesis in our previous work. Hydroxyethyl-β-CD was selected because of the strong interaction of hydroxyl groups with Cu<sup>2+</sup>, thus the OH<sup>-</sup> groups had little chance to destroy the interaction. Then the following reduction reaction was confined in the molecule-cages of the hydroxyethyl-β-CD, thus the reunited nanoparticles were resolved. The proper templates not only were critical for the nano-confinement effect, but also effected electrostatic repulsion. At the same time, we tested the influence of the reaction temperature on the Cu<sub>2</sub>O shape. A series of Cu<sub>2</sub>O nanostructures of the cubic, octahedral and spherical type were synthesized. The products were conserved in alcohol. The XRD patterns of the one-pot reduction reaction composed of cubic, octahedral and spherical crystals showed that both Cu<sub>2</sub>O (PDF 00-005-0667) crystals were highly crystalline after a post deposition procedure (Figure 1). No impurity peaks from CuO (PDF 00-045-0937) or copper metal (PDF 00-004-0836) are seen in the following figure.

*The quantity of NaOH increased the particle size without templates.* The reaction was conducted under vigorous stirring. The fructose solution was directly added to the reactor without keeping constant temperature. Figure 2 shows the SEM images of the Cu<sub>2</sub>O nanocrystals synthesized with different NaOH quantities. Some different Cu<sub>2</sub>O shapes appear in the picture, due to the changing reaction temperature because of the addition of fructose solution. The size of Cu<sub>2</sub>O particles increased with increasing NaOH quantity. The average particle sizes for the octahedral structure

were about 0.2, 3, 5, and 8 μm (see Figure 2). The results showed that NaOH quantity hardly influences the {100} faces, so there was little change of the morphology, yet enlarged the size of the particle [23].

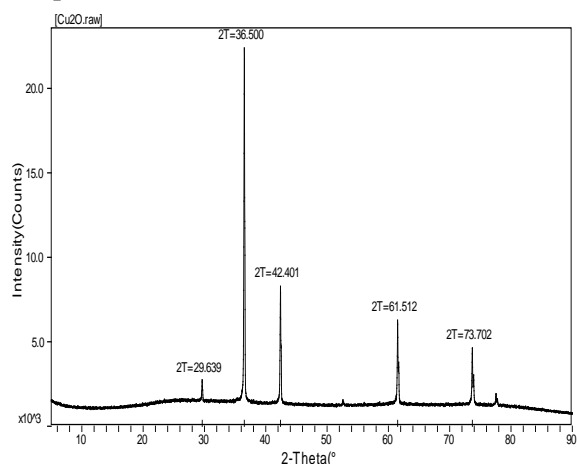


**Fig.1.** XRD pattern of Cu<sub>2</sub>O of one-pot synthesis.

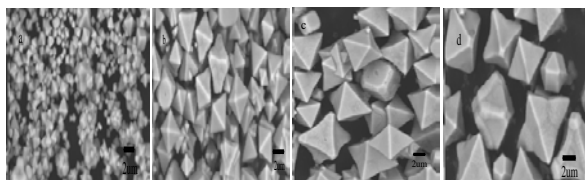


**Fig. 2.** SEM images of the Cu<sub>2</sub>O nanocrystals synthesized at different NaOH concentrations: (a) 1 M, (b) 2 M, (c) 3M, (d) 4M.

In addition, it is known that the concentration of Cu<sup>2+</sup> is getting lower with increasing NaOH quantity because of the equilibrium constant. So less Cu<sup>+</sup> was produced and particle density was lower comparing to the control solution. Thus larger and larger crystals of Cu<sub>2</sub>O were observed with the increase in NaOH concentration.

The different templates influenced the Cu<sub>2</sub>O particles. After the same quantity of templates (0.4% w/w) was dissolved in water, the other constituents except the reducing agent were mixed in a thermostatic bath. In order to promote the reaction, the fructose solution was warmed-up before being poured into the mixture. The anticipated shapes of the octahedral nanocrystals were observed. The particle size is about 0.2 μm to 0.5 μm, as is seen from Figure 3.

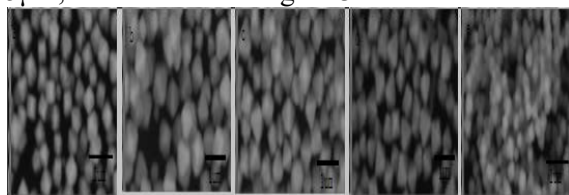


**Fig. 3.** SEM images of the Cu<sub>2</sub>O nanocrystals.

It was realized that uniformity and stabilization of Cu<sub>2</sub>O was achieved in hydroxyethyl-β-CD

solution. It contributed to the coordination complexes between Cu<sup>2+</sup> and the hydroxyl groups surrounding its funnel structure; the Cu<sup>2+</sup> was divided in the molecular space by the template, thus the chance of continuous crystal growth was blocked. As soon as the starch played its role, an amorphous mass of nano-Cu<sub>2</sub>O was obtained through several rinses with alcohol and water. The HEC (hydroxyethyl cellulose) has poor solubility, thus it had weak effect to regulate the particle size. In terms of Cu<sub>2</sub>O size, PEG-200 (polyethyleneglycol) and CMC (carboxymethyl cellulose) were inferior to the β-CD synthesized in different templates: (a) β-CD, (b) HEC, (c) PEG-200, (d) CMC, (e) starch.

The quantity of template influenced the particle shapes and size. In order to avoid changing the reaction temperature during the addition of fructose solution, all original materials were heated in a water bath. Figure 2 shows the octahedral nanocrystal synthesized when 0.04 g of hydroxyethyl-β-CD was added (the amount of Cu(OH)<sub>2</sub> was 0.01 mol). Figure 2a shows many crystal shapes and different sizes due to the non-templates controlling. When the template played its role, there was distinct evidence that uniform morphology appeared and the average particle sizes for the octahedra were about 300, 400, 200, 180 and 350 nm (see Figure 4). We could say that nanocrystals were synthesized by one-pot reduction reaction without bringing environmental burden like toxic reducing agents.

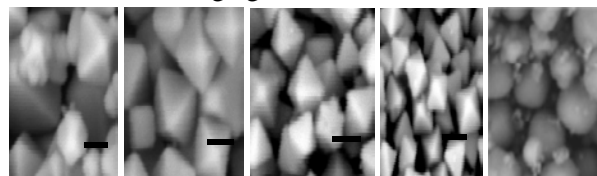


**Fig. 4.** SEM images of the Cu<sub>2</sub>O nanocrystals synthesized with different β-CD quantities: (a) 0% (W/W), (b) 0.01% (W/W), (c) 0.02% (W/W), (d) 0.4% (W/W), (e) 0.08% (W/W).

With the increasing quantity of hydroxyethyl-β-CD, spherical particles were obtained and the template also was found in the image, probably because of the changing viscosity; this verified that templates imposed strong restrictions on crystal growth. Considering the particle size and nanocrystals morphology, the 0.4% (w/w) of hydroxyethyl-β-CD was screened out.

The reaction temperature influenced the particle morphology. Previously, cuprous oxide of different morphology like spherical, cubic, octahedral, polygonal nanostructures, was synthesized at random as shown in Figure 2. It was necessary that we control not only the particle morphology but the

particle size. Figure 3 shows the SEM images of Cu<sub>2</sub>O synthesized under control in hydroxyethyl- $\beta$ -CD solution. By progressively increasing the reaction temperature, spheres, cubes and octahedra were synthesized. The crystal growth rule gave that the final morphology depended on the growth velocity. It was authenticated that faster growth velocity of the crystal face is related to its faster disappearance. The following figure gives us clear explanation of the fact that the nanocrystals morphology is dependent on the growth velocity of {100} facets and {111} facets.

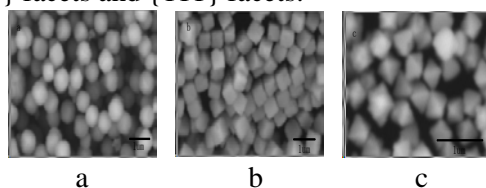


**Fig. 5.** SEM images of the Cu<sub>2</sub>O nanocrystals synthesized at different reaction temperatures: (a) 45°C, (b) 55°C, (c) 65°C.

Once the two facets had the same or similar growth velocity, the spherical shape was observed at a temperature of 45°C. On the contrary, had they different growth velocities, the cubic shape appeared owing to the {100} facets being exposed, at a temperature of 55°C. So it was believed that the concentration of Cu<sup>+</sup> was under control, that is to say, provided adjustable growth velocity of {111} facets, thus all kinds of nanocrystals morphology could be synthesized in theory [23]. As soon as the temperature reached 65°C, the octahedral shape appeared in the SEM image (see Figure 5 for the particle morphology). In fact, at least six different morphologies were found during our experiments, unfortunately these appeared irregularly. So there is still a lot of work needed to explore the field. The average particle sizes for the spheres, cubes and octahedra were 360, 450, and 270 nm, respectively (see Figure 4). The controlled release of Cu<sup>2+</sup> and the nanocrystals stability was realized by the functional hydroxyethyl- $\beta$ -CD template.

### Coating performance

Table 2 shows the general information on the prepared tested coatings before the exposure in the ocean. It can be noticed that the performance of the

**Table 2.** General information on the prepared coatings.

	A	B	C	D	Inspection
Appearance	Red glutinous	Red glutinous	Red glutinous	Red glutinous	GB 1729
Dry to touch	1	1	1	1	GB1728-88
Impact strength/kg.cm <sup>-1</sup>	<10	20	<10	20	GB1732-89
Flexibility/mm	4	3	4	3	GB1731-79
Contact-angle/°	88	96	86	90	Contact-angle meter

coating B and coating D was superior to that of acrylic resin (coating C). As a result of the helix of Si-O- bond and reticular structure, the impact strength, flexibility and hydrophobicity were enhanced. The water contact angle of coating B containing nanocrystal Cu<sub>2</sub>O increased to 96 $\pm$ 1°, because the nano-structure had higher surface energy, the water was not inclined to spreading wetting. Comparing to the traditional coatings, that containing nanocrystals without functional monomer (VTMS) also gave the expected properties like water contact angles. We believe that the functional surface was constructed following the siloxane groups hydrolyzing with hydroxyl or other active groups. It is worth mentioning that the water contact angles were measured at least at five different points and the water droplet was not more than 1  $\mu$ l.

**Anti-algal capacity.** From Figure 6 it is evident that all tested coatings showed a good inhibition performance towards *Nitzschia flosterium* as expected.

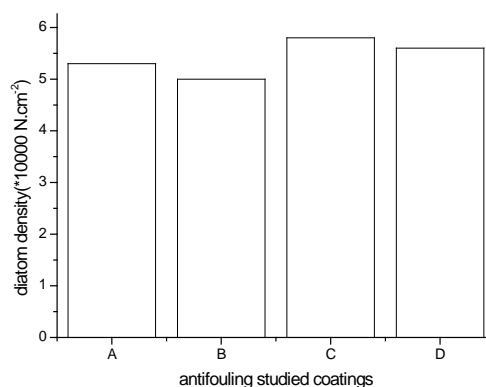


**Fig. 6.** Settlement density of *Nitzschia flosterium* on the tested coatings.

There was less *Nitzschia flosterium* on the B-board containing nanocrystals than on the other tested coatings. Believing that settlement of *Nitzschia flosterium* was by gravity, one would expect the same settlement density on all four surfaces [24, 25]. However, there were more diatoms adhering to the coating-C-surface, comparing to coating B and D owing to the microstructure of the surface.

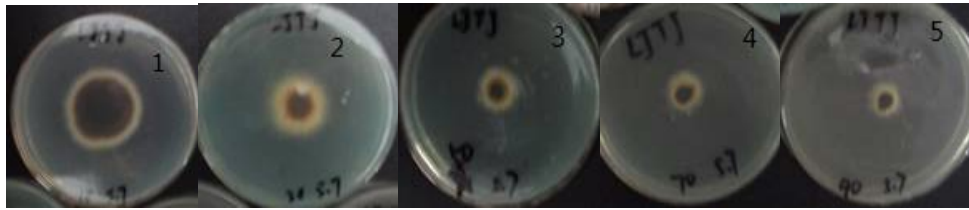


**Fig. 7.** Antibacterial images of  $\text{Cu}_2\text{O}$  towards *Colletotrichum capsici* (LJTJ) by the oxford cup method. The concentration of particles was 0.1 mg/L, 0.3 g/L, 0.5 g/L, 0.7 g/L, 0.9 g/L, corresponding to the number from one to five

The ingredient of VTMS was inclined to move to the surface in application, taking coating-B for instance, the low- surface-energy property was becoming evident, thus the alga hardly adhered to the constructed surface. The anti-alga performance of nano- $\text{Cu}_2\text{O}$  was superior to the others, as shown in Figure 7. This is an evidence that the nanocrystals had a strong action with the cell walls of bacteria, once there was less bacteria; there was less alga-settlement.

**Antibacterial activity.** According to our former experiments, the nanoparticles were added into the culture media, which was scattered by sonic oscillator. *Colletotrichum capsici* was selected because it was common in north plantation. The following figures gave us the direct data and images about the novel particles in our experiment.

The antibacterial ability of the novel particles towards *Colletotrichum capsici* is shown in Fig. 7. The diameter of fungal zone was getting smaller and smaller with the increasing of  $\text{Cu}_2\text{O}$ . After 5 days, a concentration of 0.7 g/L  $\text{Cu}_2\text{O}$  was added, and the expected antibacterial activity was noticed.

**Results for ocean plates of offshore platform.** The four test plates covered with antifouling coatings were immersed in sea-water suspended under the offshore platform, and the experiment was carried out for about 120 days.

In this special period the marine organisms like algae and barnacles grow vigorously. The results of the periodic photographs are shown in Table 3.

Bio-fouling was considered to have four distinct stages according to their different attachment. The first step was that dissolved organic matter (DOM) and molecules such as protein fragments and polysaccharides accumulated onto the submerged substrates [26-28]. Then, bio-films were gradually obtained owing to the quantity of microorganisms, especially the bacterial colonies. They adhered to the surface of the under-water man-made engineering and shielded themselves in an extra-cellular matrix of polysaccharide, protein and nucleic acids. It was a typical step of the following fouling. As soon as the bio-film came into being, algae and macro-fouling organisms like bryozoans, mussels, barnacles, tunicates and tubeworms colonized the surface without hesitation where

perhaps the fouling organisms adapted themselves to adhere [27,29,30].

**Table 3.** Tracing pictures of ocean plates of offshore platform.

	30d	60d	120d
A			
B			
C			
D			
b l a n k			

Based on successive photographic records, we investigated the antifouling property of the novel coatings from the tested panels of surface-attached marine organisms under the experimental platform. Based on tracing pictures (Table 3), marine algae, barnacles and other marine organisms were invariably found to be the dominant fouling during about 150 days. The blank board was heavily covered with mud and marine fouling like green marine algae. Yet we could see no marine fouling on the other tested board for one month. Over a stretch of four months, there were less macro-organisms and mollusks accumulating on the surfaces of the tested coatings. Up to 150 days submerging under the platform, the last step was active. More barnacles had settled on most of the tested plates except coating-B. At the same time, we noticed that some parts of the tested coatings



had already been destroyed by these fouling organisms. Coating-B showed superior antifouling performance to the others owing to the interaction of VTMS and nano-Cu<sub>2</sub>O. We reviewed the performance of the tested boards and analyzed the antifouling property of the coatings abiding by the bio-fouling mechanism. We gradually realized that the components interaction properly delayed the fouling-organisms accumulation. As we advanced our cognition of objectively explaining the antifouling performance with the experiments, a few doubts were gradually cleared. The functional monomer- VTMS containing the - Si(OCH<sub>3</sub>)<sub>3</sub> was hydrolyzed into reticular structure. The acrylic polymerized with VTMS served as a warehouse to supply Cu<sub>2</sub>O. When it came to sustained-release property, the reticular structure of -Si-O- links played as a compact net which made Cu<sub>2</sub>O difficult to be quickly washed away by sea water. Furthermore, the nanocrystals had high effective and non-selective germicide effect owing to nano-Cu<sub>2</sub>O which more easily adhered on the germ than the large particles. Once the bio-film was destroyed, fouling organisms had no chance of attachment. Therefore, the novel surface retarded the fouling organisms during five-month exposure. From the figures above we can clearly see that the novel coating containing VTMS and nano-Cu<sub>2</sub>O had a good antifouling performance comparing to the traditional products, even during the peak vigorous growth period of barnacle and other marine fouling.

### CONCLUSIONS

In this work, a series of Cu<sub>2</sub>O nanocrystals were synthesized via one-pot reductive reaction. Different structures like cubes, spheres and octahedra with sizes of 180-450 nm were realized by adjusting the reaction temperature in  $\beta$ -cyclodextrin solution. At the same time, the related experiments with the novel coating containing nano-Cu<sub>2</sub>O and VTMS showed significant antifouling performance around the offshore, especially in the peak growth period of marine macro-organisms. We witnessed a promising synergy towards antifouling and noticed that there is still a lot of work to do to find out the relationships between structure and antifouling, the components ratio, and so on.

**Acknowledgement.** This work was supported by the basis of the Qingdao science and technology plan (13-1-4-233-jch).

### REFERENCES

1. M. E. Callow, J. A. Callow, *Biofouling*, **15**, 49 (2000).
2. P. Molino, R. Wetherbee, *Biofouling*, **24**, 365 (2008).
3. P. Y. Qian, S. Lau, H. U. Dahms, S. Dobretsov, T. Harder, *Mar. Biotechnol.*, **9**, 399 (2007).
4. S. M. Evans, A. C. Birchenough, M.S. Brabcat, *Mar. Pollution Bull.*, **40**, 204 (2000).
5. K. A. Dafforn, J. A. Lewis, E. L. Johnston, *Mar. Pollution Bull.*, **62**, 453 (2011).
6. P. Pagliara, C. Caroppo, *TOXICON*, **60**, 1203 (2012).
7. M. R. Mohammad, H. H. Chun, H. Park, *Macromol. Res.*, **19**, 8 (2011).
8. X. F. Yan, L. M. Yu, X. L. Jiang, *Periodical Ocean Univ. China*, **43**, 64 (2013) (in Chinese).
9. C. Bressy, A. Margailan, *Prog. Org. Coat.*, **66**, 400 (2009).
10. L. Marlène, M. André, B. Christine, *Chem. Rev.*, **112**, 4347 (2012).
11. W. W. Cong, L.M. Yu, *Chemical Research in Chinese University*, **27**, 803 (2011).
12. Y. Yu, F. P. Du, C. Jimmy, *J. Solid State Chem.*, **177**, 4640 (2004).
13. L. Dong, L. M. Yu, X.H. Jiang, *Chinese J. Inorg. Chem.*, **12**, 2013(2008) (in Chinese).
14. W. C. Huang, L. M. Yu, Y. C. Yang, M. H. Huang, *J. Am. Chem. Soc.*, **134**, 1261 (2012).
15. K. X. Yao, X. M. Yin, T. H. Wang, H.C. Zeng, *J. Am. Chem. Soc.*, **132**, 6131 (2010).
16. S. L. Schreiber, *Chem. & Eng. News* **81**, 51 (2003).
17. P. Dalko, L. Moisan, *Angew. Chem. Int. Ed.*, **40**, 3726 (2001).
18. G. Odian, Principle of polymerization (4th ed.). New York: Wiley-Interscience, 2004.
19. Q. Wang, Z. N. Yu, L.M. Yu, *JBTE*, **10**, 1 (2011).
20. M. Beutler, K.H. Wiltshire, B. Meyer, C. Moldaenke, C. Lüring, M. Meyerhöfer, U.P. Hansen, H. Dau, *Photosynth. Res.*, **72**, 39 (2002).
21. F. Guo, L. J. Zhu, C. H. Ke, S. Q. Zhou, *J. Xiamen University (Natural Science)*, **44**, 831 (2005).
22. GB/T 5370-85, Antifouling panels in shallow submergence
23. T. Sugimoto, F. Shiba, *Colloids and Surfaces A: Physicochemical and Engineering Aspects*, **164**, 205 (2000).
24. P. G. Verity, C. Y. Robertson, C. R. Tronzo, *Limnol. Oceanogr.*, **37**, 1434 (1992).
25. A. Nishida, K. Ohkawa, I. Ueda, H. Amamoto, *Biomol. Eng.*, **20**, 381(2003).
26. D. M. Yebra, S. Kiil, C.E. Weinell, K.D. Johansen: *Prog. Org. Coat.*, **57**, 56 (2006).
27. P. Stoodley, K. Sauer, D. G. Davies, J. W. Costerton, *Ann. Rev. Microbiol.*, **56**, 187 (2002).
28. B. Natalia, A. Beatriz, R. Romagnoli, *Prog. Org. Coat.*, **74**, 411 (2012).
29. M. R. Parsek, P.K. Singh, *Ann. Rev. Microbiol.*, **57**, 677 (2003).
30. Y. Bautista, M. P. Gomez, C. Ribes, V. Sanz, *Prog. Org. Coat.*, **70**, 358 (2011).

## СИНТЕЗ НА НАНОКРИСТАЛИ ОТ $\text{Cu}_2\text{O}$ И ТЯХНОТО ПРИЛОЖЕНИЕ В ЗЕМЕДЕЛИЕТО

Ванг Кианг

*Колеж по химия и фармация, Агрономически университет в Ксингдао, Китайска народна република* <sup>2)</sup>

Постъпила на 1 май, 2014 г.

(Резюме)

Синтезирани са различни нанокристали от купроокис( $\text{Cu}_2\text{O}$ ) с различна структура чрез редукционна реакция. Нанокристалите са получени от водни разтвори на  $\text{CuSO}_4$ , фруктоза, натриева основа и шаблони при 45-75°C. Разработена е проста, едностадийна синтеза на  $\text{Cu}_2\text{O}$  чрез контролиране на количеството на шаблоните. Тези нови частици са изследвани чрез SEM и XRD. Потвърдено е, че средните размери за кубичните, октаедричните и сферичните структури са с размери съответно 450, 180 и 360 nm. Октаедричният  $\text{Cu}_2\text{O}$  е избран за следващи експериментални изследвания заради най-малките си размери. Експериментите са относно агрономически приложения (напр. против развитие на алги) по метода на зоната на инхибиране. Те показват, че на повърхността се забелязват около  $4.9 \times 10^3 \text{ N.cm}^{-2}$  кремъчни водорасли. Степента на инхибиране е 90% спрямо *Colletotrichum capsici*, ако се добавят 70 mg нано- $\text{Cu}_2\text{O}$  в 100 mL културална среда. Подобен резултат е получен в морска вода след 120-дневна експозиция.

## Adsorption kinetics of phosphate from aqueous solutions by waste iron sludge

Weiwei Zhang<sup>1\*</sup>, Yan Shi<sup>2</sup>

<sup>1</sup> College of Environmental Science and Engineering, Tongji University, 1239 Siping Road, Shanghai 200092, P. R. China

<sup>2</sup> North China University of water Resources and Electric Power, 36 Beihuan Road, Zhengzhou 450011, P. R. China

Submitted May 12, 2014

The kinetics of phosphate adsorbed on waste iron sludge was investigated in this study. Static batch adsorption experiments were performed at different initial phosphate concentrations, initial pH and temperature of solution. The initial adsorption rate increased with increasing the phosphate concentration. A shorter time, however, was required to reach adsorption equilibrium at low phosphate concentration due to external surface adsorption. Although the efficacy of phosphate adsorbed on waste iron sludge depended significantly on pH of solution, the adsorption kinetics was relatively independent on pH. Increasing solution temperature contributed to accelerating reaction rate of adsorption and raising the uptake of phosphate adsorbed on waste iron sludge. The kinetic process of phosphate adsorbed on waste iron sludge could be well described by both pseudo second-order and Elovich kinetic models, indicating chemisorption occurred. The simulation of intra-particle and Boyd model demonstrated that the intra-particle diffusion occurred, but the liquid film diffusion was the rate-limiting step. The of apparent activation energy of adsorption value ( $33.40 \text{ kJ}\cdot\text{mol}^{-1}$ ) also indicated that chemical reaction was not the only rate-limiting step and diffusion was involved within the whole adsorption process. Results of these findings suggested that the intra-particle diffusion and chemisorption occurred in the entire adsorption process, but the mass transfer in the liquid film was the dominant rate-limiting step.

**Key words:** phosphate; waste iron sludge; adsorption; kinetics

### INTRODUCTION

Phosphorus is the most important element causing eutrophication of water bodies, such as lakes and reservoirs [1]. Hence the removal of phosphate from wastewater has drawn much attention.

Chemical precipitation using various precipitants is an effective way to remove phosphate from wastewater, but large amounts of chemical sludge are produced in these processes [2]. Phosphate can be also removed by metabolism of microorganisms, but removal efficiency of phosphate is sensitive to environmental factors, such as temperature, pH and dissolved oxygen [3]. The removal of phosphate by adsorption has aroused wide attention because of simple operation, sustainable efficiency and producing less sludge [4]. The key for adsorption is to seek out an appropriate adsorbent.

Many types of adsorbents for phosphate removal have been investigated in recent years, such as aluminum oxides/aluminum hydroxide [5], calcium silicate [6], zeolite [7], calcined Mg-Mn-layered double hydroxides [8], iron oxide tailings [4], Fe-Mn binary oxide [9], polymeric ligand exchanger [10]. In order further to reduce costs, using industrial wastes, such as activated red mud [11], blast furnace slag [12] or fly ash [13], as adsorbents to remove phosphate from aqueous solutions has become a hot topic.

Dewatered aluminum or iron sludges are produced during the process of drinking water treatment when aluminum or iron salts are used as coagulants to remove turbidity. Previous studies [14, 15] mainly focused on using dewatered aluminum sludge to adsorb phosphate from aqueous solutions because of aluminum salt being more used as coagulant. However, iron salt, as an alternative coagulation, are considered more and more due to the physiological disorders caused by the residual aluminum [16]. Large amounts of iron based coagulants used in drinking water treatment plant will produce dewatered iron sludge. Thus the utilization of dewatered iron sludge is urgent. Ding studied the efficacy, equilibrium and thermodynamics of phosphate adsorbed on dewatered iron sludge [2]. However, there is a significant gap in knowledge on the kinetic characteristics of phosphate adsorbed on dewatered iron sludge, which is crucial to better understanding the removal mechanism of phosphate and designing the reactor of adsorption.

Accordingly, this study is aimed to (1) investigate the effects of environmental factors, such as initial phosphate concentration, initial pH of solution and temperature of solution, on kinetics of phosphate adsorbing on waste iron sludge; (2) find an appropriate kinetic model to quantitative describe the kinetics of phosphate adsorbed on waste iron sludge; (3) analyze the diffusion mechanism of phosphate from bulk solution to surface of waste iron sludge.

\* To whom all correspondence should be sent:

E-mail: zww\_227@126.com

## MATERIALS AND METHODS

### Adsorbent

Dewatered iron sludge was supplied by a local drinking water treatment. The sludge was dried at 105°C for 8 h, then it was ground and sieved. The particles whose diameters were below 100 µm were used as adsorbents in this study.

### Chemicals and adsorbate

All chemicals used in this study were AR grade, and purchased from Sinopharm Chemical Reagent Co., Ltd., China. Potassium dihydrogen phosphate (KH<sub>2</sub>PO<sub>4</sub>) was used as adsorbate in this study. And a stock solution of phosphate (P, 50 mg L<sup>-1</sup>) was prepared by dissolving accurately weighed sample of potassium dihydrogen phosphate in ultra-pure water. Test samples with various concentrations of phosphate used in adsorption experiments were prepared by diluting the stock solution with distilled water where needed.

### Adsorption procedure

The effects of different phosphate concentrations, initial pH of solution and temperatures of solution on the kinetics of phosphate adsorbed on waste iron sludge were investigated by batch adsorption mode. Taking 5 mg L<sup>-1</sup> phosphate adsorbed on waste iron sludge as an example illustrated experimental process. First, waste iron sludge (0.2 g) was added into a series of conical flasks containing 50 mL phosphate solution with the concentration of 5 mg P/L, respectively. These conical flasks were sealed with lids. Then they were put into water bath and were mixed at a constant speed of 150 rpm at 303 K. These samples were taken out at preset time intervals and filtered using a 0.45 membrane, respectively. The phosphates in filtrates were measured using a UV-visible spectrophotometer (UV-2450PC, Shimadzu, Japan) at 700 nm according to standard method [17]. The similar kinetic experiments were conducted at other conditions. All experiments were carried out in triplicate and average values were reported herein.

The amount of phosphate adsorbed on iron sludge at any time,  $q_t$  (mg P/g), is calculated by equation (1).

$$q_t = (C_0 - C_t)V / m \quad (1)$$

Where  $C_0$  and  $C_t$  (mg L<sup>-1</sup>) are the concentration of phosphate in aqueous solution at initial and time  $t$ , respectively;  $V$  (L) is the volume of solution,  $m$  (g) is the mass of iron sludge.

## RESULTS AND DISCUSSION

### Effect of initial phosphate concentration on kinetics

The experiments were conducted by varying initial phosphate concentration from 5 to 15 mg/L in order to study the influence of initial phosphate concentration on the kinetics of phosphate adsorbed on waste iron sludge. The results are depicted in Fig. 1. They demonstrate the similar trend for all initial phosphate concentrations: initially the amount of phosphate adsorbed on waste iron sludge increases rapidly, then increases slowly with increasing adsorption time, and finally keeps approximately constant.

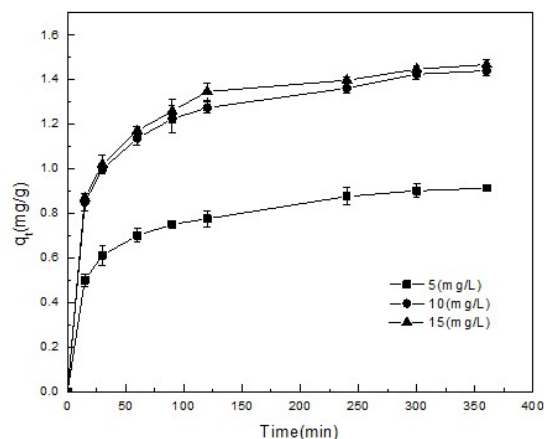


**Fig. 1.** Adsorption kinetics of phosphate on waste iron sludge at different initial phosphate concentrations (Conditions: 0.2 g adsorbent, 50mL solution, 150rpm stirring speed, 303K temperature, pH 7.0).

This indicated that the adsorption of phosphate on waste iron sludge was fast at initial stage of adsorption. This was because the abundantly unused active adsorption sites adsorbed swiftly phosphate from aqueous solutions at initial stage of adsorption. The adsorption rate, however, decreased gradually with increasing adsorption time. This was attributed to the sharp reduction of available adsorption sites. In addition, it was also observed from Fig. 1 that the initial adsorption rate increased with increasing initial phosphate concentration. This could be explained by the fact that high phosphate concentration accelerated the diffusion process of phosphate from bulk solution to the adsorbent surface [18]. Compared to high phosphate concentration (10 mg L<sup>-1</sup>, 15 mg L<sup>-1</sup>), the time required to reach adsorption equilibrium was shorter at low phosphate concentration (5 mg L<sup>-1</sup>). This might be because the external surface of adsorbent played a major role at low phosphate concentration, resulting in shorter equilibrium time. On the other hand it took longer time for phosphate to diffuse into the pores at high phosphate concentration, leading to the longer time required to reach equilibrium. The uptake of phosphate increased rapidly with increasing phosphate concentration from 5 to 10 mg L<sup>-1</sup>, also indicating that phosphate diffused into pore and the internal sites were made

full use of. However, the uptake of phosphate increased slightly when concentration of phosphate varied from  $10 \text{ mg L}^{-1}$  to  $15 \text{ mg L}^{-1}$ , showing that the active sites had been exhausted.

#### Effect of initial pH of solution on kinetics

The value of solution pH is a key factor for adsorption due to affecting the chemical performances of adsorbent and adsorbate. In order to investigate the effect of initial pH of solution on the kinetics of phosphate adsorbed on waste iron sludge, experiments were performed at varying initial pH from 3.0 to 11.0 with 0.1 M HCl or 0.1 M NaOH solutions. The results were shown in Fig. 2.

Fig. 2 shows that the uptake of phosphate adsorbed on waste iron sludge varied indistinctly when pH of solution ranged from 5.0 to 7.0, showing phosphate could be well removed by waste iron sludge.

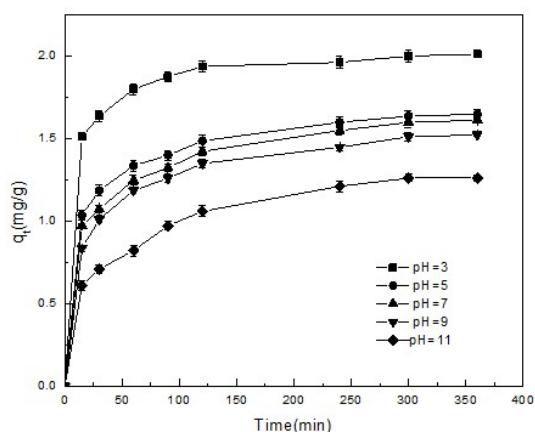


**Fig. 2.** Adsorption kinetics of phosphate on waste iron sludge at different initial pH of solution (Conditions:  $10 \text{ mg/L}$  phosphate concentration,  $50 \text{ mL}$  solution,  $0.2 \text{ g}$  adsorbent,  $150 \text{ rpm}$  stirring speed,  $318 \text{ K}$  temperature).

However, the uptake of phosphate decreased slightly with increasing pH of solution to 9.0. This could be explained by the concept of isoelectric point. The isoelectric point of iron or aluminum oxides/hydroxides was usually considered as around pH 8.0 [19, 20]. The surfaces of waste iron sludge were charged negatively at pH 9.0. The electrostatic repulsion between surface of adsorbent and phosphate ions in solution made it difficult that phosphate ions were adsorbed on waste iron sludge, resulting the decrease in uptake of phosphate. It was also observed from Fig. 2 that the uptake of phosphate decreased rapidly when pH of solution increased from 9 to 11. This might be because the hydroxyl ions competed for adsorption sites with phosphate ions besides electrostatic repulsion at pH 11.0. However, the uptake of phosphate increased swiftly with decreasing the value of pH from 4.0 to

3.0. Hydrogen ions interacting with the basic functional groups of iron sludge made it easier to remove phosphate by the chemistry chelating of ferric or ferrous ions at pH 3.0, causing the increase in uptake of phosphate. Although the efficacy of phosphate adsorbed on waste iron sludge depended on pH of solution (shown in Fig. 2), the time achieving the adsorption equilibrium at different pH of solution kept approximately identical. This implied that the kinetics of phosphate adsorbed on waste iron sludge was independent on the initial pH of solution.

#### Effect of temperature of solution

The effects of solution temperature on the kinetics of phosphate adsorbed on waste iron sludge were investigated by varying solution temperature from  $293 \text{ K}$  to  $318 \text{ K}$ . The results were given in Fig. 3.

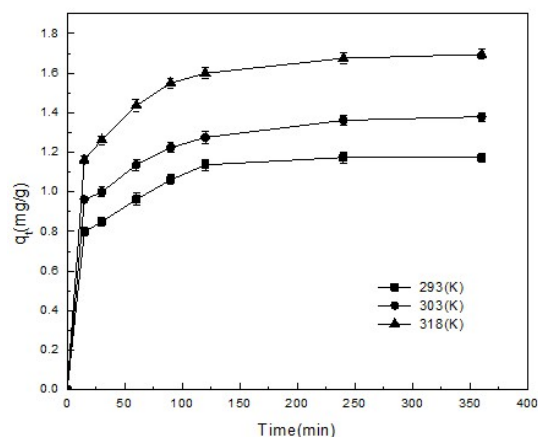


**Fig. 3.** Adsorption kinetics of phosphate on waste iron sludge at different temperature of solution (Conditions:  $10 \text{ mg/L}$  phosphate concentration,  $50 \text{ mL}$  solution,  $0.2 \text{ g}$  adsorbent,  $150 \text{ rpm}$  stirring speed, pH 7.0).

The rate of phosphate adsorbed on waste iron sludge increased rapidly with raising solution temperature from  $293 \text{ K}$  to  $318 \text{ K}$  at initial stage of adsorption. From a view of kinetics, the higher the solution temperature is, the faster the motion of phosphate ions in solution. This accelerated the diffusion rate of phosphate ions from bulk solution to surface of waste iron sludge, resulting in an increase in the rate of phosphate adsorbed on iron sludge. In addition, elevating solution temperature contributed to phosphate ions in solution gaining energy and becoming activated ions, accelerating reaction rate of adsorption. Meanwhile, the decrease in dynamic viscosity of water and resistance with increasing solution temperature made phosphate easy to diffuse from bulk solution onto surface of adsorbent [21]. This was also a reason causing the rapid increase in adsorption rate. Fig. 3 also demonstrated that for an identical time,

the uptake of phosphate adsorbed on waste iron sludge increased with elevating solution temperature. This might be because high temperature enhances phosphate penetration into the internal pores thus making internal adsorption sites fully used.

#### *Kinetic model of phosphate adsorbed on waste iron sludge*

Quantitatively data on kinetics of phosphate adsorption on waste iron sludge contribute to analyze and predict adsorption mechanism as well as to provide useful parameters for designing adsorption unit. Some frequently used kinetic model equations include pseudo first-order, pseudo second-order and Elovich ones.

Based on the assumption that the rate of change of adsorbed solute with time is proportional to the difference in equilibrium adsorption capacity and the adsorbed amount, the pseudo-first-order kinetic model [22] can be expressed by equation (2).

$$q_t = q_e [1 - \exp(-k_1 t)] \quad (2)$$

Where  $q_e$  (mg g<sup>-1</sup>) is the amount of phosphate adsorbed on waste iron sludge at equilibrium;  $t$  (min) is adsorption time;  $k_1$  (min<sup>-1</sup>) is the rate constant of pseudo first-order model.

The pseudo second-order kinetic model [23] is based on the assumption that the rate-limiting step involves chemisorption which involved covalent forces through sharing or exchange of electrons between adsorbent and adsorbate, and is described by equation (3).

$$q_t = k_2 q_e^2 t / (1 + k_2 q_e t) \quad (3)$$

Where  $k_2$  (g mg<sup>-1</sup> min<sup>-1</sup>) is the rate constant of pseudo second-order model.

The Elovich kinetic model [24] is a semi-empirical model used to describe the chemical adsorptive behavior of adsorbate adsorbed on heterogeneous surface, and is given by equation (4).

$$q_t = \frac{1}{\beta} \ln(1 + \alpha \beta t) \quad (4)$$

Where  $\alpha$  (mg g<sup>-1</sup> min<sup>-1</sup>) is the initial adsorption rate constant;  $\beta$  (g mg<sup>-1</sup>) is related to the extent of surface coverage and activation energy for chemisorption.

These three kinetic models were used to fit these experimental data of phosphate adsorbed on waste iron sludge under various environmental conditions in this study. All the model parameters and correlation coefficient ( $R^2$ ) were evaluated by non-linear regression using OriginPro 8.5 software. The standard deviation was calculated by equation (5).

$$S.D. = \sqrt{\frac{\sum [(q_{t,exp} - q_{t,cal}) / q_{t,exp}]^2}{n-1}} \quad (5)$$

Here  $n$  is the number of data points, and  $q_{t,exp}$  is the experimental value of uptake at time  $t$ , and  $q_{t,cal}$  is the value of uptake calculated by kinetic model at time  $t$ . The fitted results are given in Table 1, and the validity of different kinetic models is evaluated by correlation coefficient and standard deviation.

It is shown in Table 1 that compared to the pseudo second-order and Elovich kinetic models, the values of correlation coefficient fitted by the pseudo first-order kinetic model are much smaller. However, the values of standard deviation are much larger. In addition, for the pseudo first-order model, equilibrium adsorption capacity obtained from experiments do not agree with the values calculated by model. These results show that the pseudo first-order kinetic model do not describe well the kinetic process of phosphate adsorbed on waste iron sludge.

For the pseudo second-order and Elovich kinetic models, the correlation coefficients with high values ( $R^2 > 0.98$ ) are close and the standard deviations with small values are close too. The equilibrium adsorption capacity obtained from experiments perfectly agrees with the values by pseudo second-order model. These results demonstrate that the pseudo second-order and Elovich kinetic models can well describe the kinetic process of phosphate adsorbed on waste iron sludge, implying that chemical sorption occurs in the adsorption process

#### *Diffusion mechanism of phosphate onto waste iron sludge*

The removal process of pollutant adsorbed on adsorbent generally included three consecutive rate-limiting steps [25]: (1) pollutants from bulk solution crossed the boundary film formed around adsorbent to external surface of adsorbent, which was called as liquid film diffusion; (2) pollutants diffused from external surface into internal adsorption sites of pores, which was called as intra-particle diffusion; (3) pollutants were adsorbed onto adsorption sites. The influence of the third step on whole adsorption rate was usually negligible because of the fact that adsorption reaction was very fast. Thus the whole adsorption rate of pollutants adsorbed on adsorbent was generally controlled by the liquid film or/and intra-particle diffusion.

The intra-particle diffusion model [23] was expressed by equation (6).

$$q_t = k_{id} t^{1/2} + C_i \quad (6)$$

**Table 1.** Pseudo first-order model, pseudo second-order model, and Elovich model of phosphate adsorbed on waste iron sludge.

Factors	Pseudo first-order model ( $q_t = q_e(1 - \exp(-k_1t))$ )				Pseudo second-order model ( $q_t = \frac{k_2 q_e^2 t^2}{1 + k_2 q_e t}$ )				Elovich model ( $q_t = \ln(1 + abt)/b$ )				
	$q_e$ (mg/g)	$q_{e,cal}$ (mg/g)	$k_1$ (1/min)	$R^2$	S.D. (%)	$q_{e,cal}$ (mg/g)	$k_2$ (g/(mg min))	$R_2$	S.D. (%)	$\alpha$	$\beta$	$R^2$	S.D. (%)
$C_0$ (mg/L)													
5	0.914	0.836	0.9405	0.9405	10.10	0.917	0.0733	0.9866	4.97	0.4506	7.7164	0.9990	1.42
10	1.450	1.324	0.0542	0.9497	11.95	1.437	0.0564	0.9899	7.91	1.3855	5.4278	0.9985	4.07
15	1.485	1.363	0.0534	0.9562	8.78	1.476	0.9925	0.9925	3.84	1.5124	5.3396	0.9957	2.52
pH													
3	2.014	1.921	0.0903	0.9777	5.61	2.015	0.0874	0.9967	2.28	202.1656	6.3642	0.9962	2.20
5	1.650	1.526	0.0610	0.9489	8.89	1.647	0.0568	0.9886	4.44	2.7719	5.0943	0.9990	1.07
7	1.613	1.477	0.0525	0.9292	11.25	1.610	0.0479	0.9803	6.36	1.2558	4.6978	0.9986	1.61
9	1.525	1.409	0.0458	0.9496	9.75	1.542	0.0431	0.9910	4.34	0.7553	4.5940	0.9977	1.91
11	1.362	1.184	0.0275	0.9174	16.93	1.317	0.0300	0.9720	9.99	0.1743	4.3664	0.9945	4.60
T(K)													
293	1.175	1.102	0.0667	0.9462	8.34	1.190	0.1693	0.9838	5.15	3.2111	7.4142	0.9903	3.85
303	1.380	1.269	0.0748	0.9450	9.46	1.365	0.2289	0.9832	5.50	5.9797	6.8135	0.9962	2.34
318	1.696	1.588	0.0716	0.9622	7.94	1.704	0.4899	0.9921	3.89	8.0229	5.5291	0.9948	2.34

Where  $k_{id}$  ( $\text{mg g}^{-1} \text{min}^{-1/2}$ ) was the intra-particle diffusion rate constant, and  $C_i$  represented the boundary layer effect which meant that the larger the intercept was, the greater the contribution of the surface sorption in the rate controlling step.

Based upon the intra-particle diffusion theory, the intra-particle diffusion was the only rate limiting step of adsorption process if the plot of  $q_t$  against  $t^{1/2}$  was a straight line and passed the origin, otherwise, other steps along with intra-particle diffusion might be also involved.

In order to interpret the diffusion removal process of phosphate from bulk solution onto waste iron sludge, the intra-particle diffusion model was used to fit the experimental data of kinetics at different initial phosphate concentrations ( $5 \text{ mg L}^{-1}$  and  $10 \text{ mg L}^{-1}$ ) in this study. The results are presented in Fig. 4 and Table 2. The fitted results demonstrate that the plots of  $q_t$  versus  $t^{1/2}$  are not linear within the whole adsorption time, but each plot is divided into two segments and each segment gives a good linear form. However, all these lines do not pass through the origin. These results above imply that the intra-particle diffusion is not the only rate-limiting step and other diffusion process, such as liquid film diffusion, affects the adsorptive rate of phosphate adsorbed on waste iron sludge.

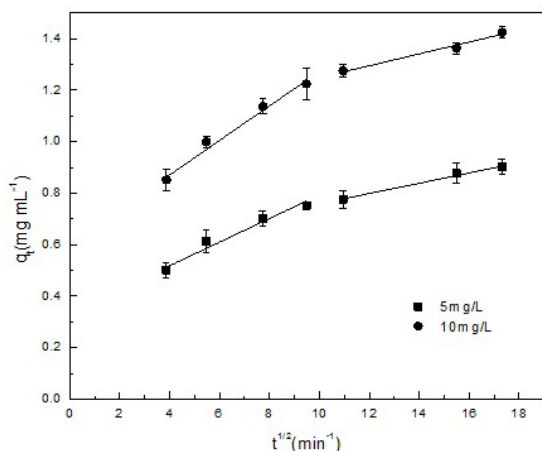


**Fig. 4.** Plots of intra-particle diffusion model for the adsorption of phosphate on waste iron sludge at different initial phosphate concentrations.

In order to ascertain the factual rate-limiting step during the process of phosphate adsorbed on waste iron sludge, Boyd model was used to further fit the

**Table 2.** Constants and correlation coefficients of intra-particle diffusion model for phosphate adsorption on waste iron sludge

$C_0$ (mg/L)	Intra-particle diffusion model					
	$K_{id1}$ ( $\text{mg}/(\text{mL min}^{1/2})$ )	$C_1$	$R^2$	$K_{id2}$ ( $\text{mg}/(\text{mL min}^{1/2})$ )	$C_2$	$R^2$
5	0.0436	0.3514	0.9480	0.0201	0.5577	0.9829
10	0.0655	0.6173	0.9764	0.0228	1.0212	0.9583

kinetic data at different initial phosphate concentrations. The Boyd model [26] was given by equation (7).

$$Bt = -0.4977 - \ln\left(1 - \frac{q_t}{q_e}\right) \tag{7}$$

Where  $B$  is a constant.

The value of  $Bt$  at different adsorption time  $t$  was calculated by equation (7), and the values of  $Bt$  were plotted against  $t$ . Based on the Boyd model it must be expected that the adsorption process on is controlled by the intra-particle step if the plots of  $Bt$  versus  $t$  were linear and passed through the origin. Otherwise, the adsorption rate must be controlled by the liquid film diffusion.

The results fitted by the Boyd model are given in Fig. 5 and Table 3. Fig. 5 demonstrates that although Boyd plots give well straight lines at different initial phosphate concentration, they both do not pass through the origin, implying that the adsorption rate of phosphate on waste iron sludge was dominantly controlled by the liquid film diffusion. The value of  $B$  was obtained from the slope of the plot of  $Bt$  versus  $t$ , and they were also listed in Table 3. It was observed from Table 3 that the values of  $B$  at different initial phosphate concentrations were much smaller than 1, further verifying that the removal rate of phosphate adsorbed on waste iron sludge was mainly affected by the liquid film diffusion [27].

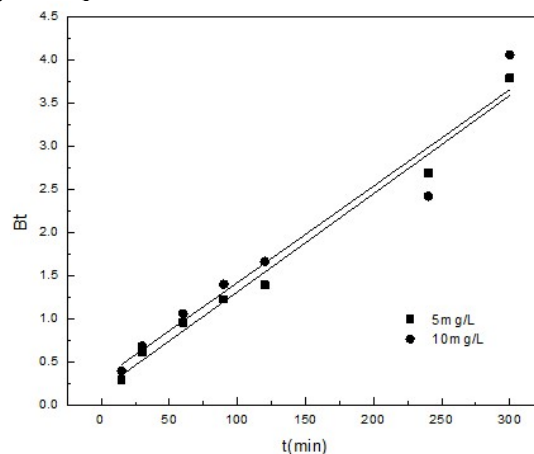


**Fig. 5.** Boyd plots of phosphate adsorbed on waste iron sludge at different initial phosphate concentrations.



## Apparent activation energy of adsorption

The conventional thermodynamic parameters, such as standard Gibbs free energy change ( $\Delta G^0$ ), standard enthalpy change ( $\Delta H^0$ ) and standard entropy change ( $\Delta S^0$ ), cannot describe the reaction rate of adsorption. An empirical equation of Arrhenius type [28], shown in Equation (8) is given to describe the relation of temperature and the constant of reaction rate.

$$\ln(k_2) = \ln A - \frac{E_a}{RT} \quad (8)$$

Where  $k_2$  ( $\text{g}\cdot\text{mg}^{-1}\cdot\text{min}^{-1}$ ) was the rate constant obtained from the pseudo second-order kinetic model,  $E_a$  ( $\text{kJ}\cdot\text{mol}^{-1}$ ) was the apparent activation energy of adsorption,  $T$  (K) was the absolute temperature of solution,  $R$  ( $8.314 \text{ J}\cdot\text{mol}^{-1}\cdot\text{K}^{-1}$ ) was the molar gas constant and  $C$  was a constant.

According to equation (8), a straight line of  $\ln(k_2)$  against  $1/T$  can be obtained, and the value of  $E_a$  can be calculated by the slope of the straight line above. The magnitude of apparent activation energy of adsorption can give an idea what control the reaction rate of adsorption. The experimental data of kinetics at different temperature of solution (shown in Table 1) were used to calculate the apparent activation energy of phosphate adsorbed on waste iron sludge (shown in Fig. 6). Fig. 6 showed that the plot of  $\ln(k_2)$  against  $1/T$  gave a good straight line ( $R^2=0.9770$ ). The apparent activation energy of phosphate adsorbed on waste iron sludge calculated by the slope ( $k_{\text{slope}}=-4017.1$ ) was  $33.40 \text{ kJ}\cdot\text{mol}^{-1}$ , indicating that chemical reaction was not the only rate-limiting step and diffusion (liquid film and pore diffusion) was involved within the whole adsorption process [29]. These were consistent with the results of kinetics and diffusion mechanism studies.

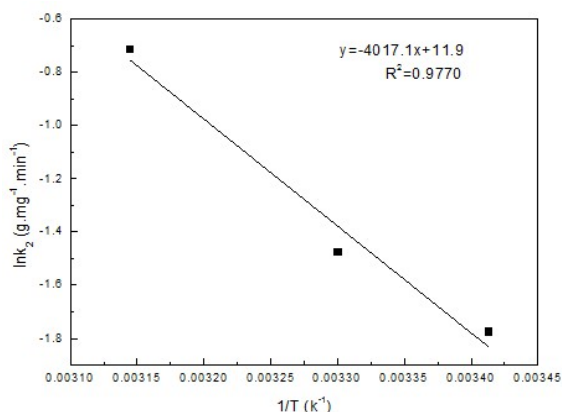


Fig. 6. Arrhenius plot of phosphate adsorbed on waste iron sludge.

## CONCLUSION

The present study showed that the kinetics of phosphate adsorbed on waste iron sludge was affected to varying degrees by various environmental factors. The initial adsorption rate increased with increasing the phosphate concentration. The shorter time, however, was required to reach adsorption equilibrium at low phosphate concentration due to external surface adsorption. Although the efficacy of phosphate adsorbed on waste iron sludge depended on pH of solution significantly, the adsorption kinetics was relatively independent on pH of solution. Elevating solution temperature contributed to accelerating reaction rate of adsorption and raising the uptake of phosphate adsorbed on waste iron phosphate adsorbed on waste iron sludge depended on pH of solution significantly, the adsorption kinetics was relatively independent on the solution pH.

Elevating solution temperature contributed to accelerating reaction rate of adsorption and raising the uptake of phosphate adsorbed on waste iron sludge. Both pseudo-second-order and Elovich kinetic models could well describe the kinetic process of phosphate adsorbed on waste iron sludge. The intra-particle diffusion and chemisorptions occurred in whole adsorption process, but the liquid film was the dominant rate-limiting step.

## REFERENCES

- Huang, W. Y., Li, D., Zhu, Y., Xu, K., Li, J. Q., Han, B. P., Zhang, Y.M., *Mater. Res. Bull.* **48**, 4974 (2013).
- Ding, L., Wu, C., Deng, H. P., Zhang, X. X., Wang, Q. F., *Fresenius Environ. Bull.* **21**, 1268 (2012).
- Gong, G. Z., Ye, S. F., Tian, Y. J., Wang, Q., Ni, J., Chen, Y. F., *J. Hazard. Mater.* **166**, 714 (2009).
- Zeng, L., Li, X., Liu, J., *Water Res.* **38**, 1318 (2004).
- S. Tanada, M. Kabayama, H. Kawasaki, T. Sakiyama, T., Nakamura, T., Araki, M. and Tamura, *J. Colloid Interf. Sci.*, **257**, 135 (2003).
- D.C. Southam, T.B. Lewis, A.J. McFarlane, J.H. Johnston, *Curr. Appl. Phys.*, **4**, 355 (2004).
- E. Chmielewska, R. Hodossyova, *Fresenius Environ. Bull.*, **22**, 598 (2013).
- R. Chitrakar, S. Tezuka, A. Sonoda, K. Sakane, K. Ooi, T. Hirotsu, *J. Colloid Interf. Sci.*, **290**, 45 (2005).
- Zhang, G., Liu, H., Liu, R., Qu, J. (2009), *J. Colloid Interf. Sci.*, **335**, 168 (2009).
- Ding, L., Wu, C., Deng, H.P., Zhang, X.X., *J. Colloid Interf. Sci.*, **376**, 224 (2012).
- Zhang, H.Y., Zhang, L.Y., Guo, W., Wu, W. S., Zhang, M. L., Han, L., *Fresenius Environ. Bull.*, **21**, 1539 (2012).
- Qiu, L.P., Wang, G.W., Zhang, S. B., Yang, Z.X., Li, Y.B., *Water Sci. Technol.*, **65**, 1048 (2012).
- Wang, Y.R., Tsang, D.C.W., W.E. Olds, P.A. Weber, *Environ. Technol.* **34**, 3177 (2013).

14. K.C. Makris, D. Sarkar, R. Datta, *Environ. Pollut.*, **140**, 9 (2006).
15. Yang, Y., Zhao, Y., A. Babatunde, Wang, L., Ren, Y., Han, Y., *Sep. Purif. Technol.*, **51**, 193 (2006).
16. S. Bolognin, L. Messori, D. Drago, C. Gabbiani, L. Cendron, P. Zatta, *Int. J. Biochem. Cell Biol.* **43**, 877 (2011).
17. APHA, (1998) Standard Methods for the Examination of Water and Wastewater, 20 ed., Washington, DC.
18. Ding, L., Deng, H. P., Han, X., Dong, L., Wang, P., D. de Ridder, *Fresenius Environ. Bull.* **19**, 2548(2010).
19. Wei, X., R.C Viadero, S. Bhojappa, *Water Res.* **42**, 3275 (2008).
20. Babatunde, Zhao, Y., Yang, Y., P. Kearney, P., *Chem. Eng. J.* **136**, 108 (2008).
21. H. Nadaroglu, E. Kalkan, N. Demir, *Desalination*, **251**, 90-95 (2010).
22. A.Y. Dursun, O. Tepe, G. Uslu, G. Dursun, Y. Saatci, *Environ. Sci. Pollut. R.* **1** (2013).
23. E.M.Ö. Kaya, A.S. Özcan, Ö. Gök, A. Özcan, *Adsorption*, **1** (2013).
24. M. Ahmad, S. S.Lee, S.-E.Oh, D. Mohan, D.H. Moon, Lee, Y.H., Y.S. Ok, *Environ. Sci. Pollut. R.* **1** (2013).
25. M.A. Ahmad, N.K. Rahman, *Chem. Eng. J.*, **170**, 154 (2011).
26. S. Madala, S.Kumar Nadavala, S. Vudagandla, V.M. Boddu, K. Abburi, *Arabian J. Chem.* (2013, inn press),. <http://dx.doi.org/10.1016/j.arabjc.2013.07.017>
27. Y.Z. Niu, R.J. Qu, C.M. Sun, C.H., Wang, Chen, H., Ji, C. N., Zhang, Y., Shao, X., Bu, F.L., *J. Hazard. Mater.*, **244**, 276 (2013).
28. H. Nollet, M. Roels, P. Lutgen, P. Van der Meeren, W. Verstraete, *Chemosphere*, **53**, 655-665 (2003).
29. N.Y. Mezenner, A. Bensmaili, *Chem. Eng. J.*, **147**, 87 (2009).

## КИНЕТИКА НА АДСОРБЦИЯТА НА ФОСФАТИ ОТ ВОДНИ РАЗТВОРИ ВЪРХУ ОТПАДЪЧНА ЖЕЛЯЗНА ТИНЯ

Уеиуей Жанг<sup>1\*</sup>, Ян Ши<sup>2</sup>

<sup>1</sup> Колеж по екологични науки и инженерство, Университет Тонгдзи, Шанхай, Китай

<sup>2</sup> Северно-китайски университет по водни ресурси и електроенергия, Женгжу, Китай

Постъпила на 12 май, 2014 г.

(Резюме)

Изследвана е кинетиката адсорбцията на фосфати върху отпадъчна желязна тиня. Проведени са статични експерименти в периодичен режим при различни начални концентрации, стойности на рН и температури. Началните скорости на адсорбция нараства с нарастване концентрацията на фосфати. По-кратки времена са нужни за достигане на равновесие при по-ниски концентрации на фосфати поради адсорбцията на външна повърхност. Въпреки че ефективността на адсорбция зависи значително от рН на разтвора, кинетиката остава относително независима от рН. Повишението на температурата води до повишаване скоростта на адсорбция и повишаване на усвояването на фосфатите, адсорбирани от желязната тиня. Кинетиката на адсорбция може да се опише добре както с уравнение от псевдо-втори порядък, така и с кинетичния модел на Елович, показвайки възможността за хемисорбция. Симулационните експерименти по модела на Бойд и с вътрешна дифузия и адсорбция показват, е налице вътрешна дифузия, но масопренасянето в течния граничен слой е скоростно-определящият стадий. Определената привидна активираща енергия на адсорбция ( $33.40 \text{ kJ} \cdot \text{mol}^{-1}$ ) също показва, че химичната реакция не е единственият скоростно-определящ стадий и че дифузията има влияние върху цялостния процес на адсорбция.

## Determination of CO<sub>2</sub>/crude oil system interfacial tension and dynamic interfacial tension by ADSA method

Wang Xin<sup>1</sup>, Liu Lifeng<sup>2</sup>, Lun Zengmin<sup>1</sup>, Lv Chengyuan<sup>1</sup>

<sup>1</sup> Sinopec Research Institute of Petroleum Exploration & Production, Beijing 100083, China

<sup>2</sup> PetroChina Research Institute of Petroleum Exploration & Development, Beijing 100083, China 541004

Submitted May 4, 2014

ADSA was used to measure the interfacial tension of CO<sub>2</sub>/crude oil system under simulated-formation conditions of temperature of 355.65K and pressure ranging from 7MPa to 23MPa. The test results indicated that the equilibrium interfacial tension of CO<sub>2</sub>/crude oil system decreased as the systematic pressure increased. Intense mutual diffusion happened when CO<sub>2</sub> was in contact with crude oil. CO<sub>2</sub> extracted the light components of crude oil and was constantly dissolved in the crude oil, both processes ultimately achieving homeostasis. The dynamic interfacial tension between CO<sub>2</sub> and crude oil was large at the initial contact. After that, the interfacial tension gradually decreased, and finally reached dynamic balance. In addition, the interfacial tension of the CO<sub>2</sub>/crude oil system decreased greatly with time as the systematic pressure increased.

**Key words:** ADSA; diffusion; equilibrium interfacial tension; CO<sub>2</sub>/crude oil system; dynamic interfacial tension

### INTRODUCTION

Miscible flooding technology is considered as one of the most cost-effective methods of EOR [1,2]. There is a variety of gases that can be injected; CO<sub>2</sub> for its wide sources and good flooding effect has been widely put into practical application in oil fields. The key for miscible flooding technology is to determine the minimum miscibility pressure between injection agent and crude oil [3-7]. The common experimental methods are slim-tube displacement test [8-12], rising bubble and vanishing interfacial tension (VIT) technique [13-15]. The latter technique has many advantages, e.g., ease of operation and visuality. ADSA was used to measure the relationship between the equilibrium interfacial tension and pressure of CO<sub>2</sub>/crude oil system under the conditions of the stratum temperature, make sure how the interfacial tension changes with time, and get the variation of the dynamic interfacial tension with pressure.

### EXPERIMENTAL

#### *Experimental apparatus*

High temperature and pressure interfacial tension meter, made by the French production company ST, was used in the experiments. The core of the device is a reactor with a window, operating at a temperature of 0 ~ 200 K, and a maximum working pressure of 70MPa. The needle used in the experiments was 0.81mm.

ADSA is the most accurate method to measure the

interfacial tension under high temperature and high pressure conditions. At first use the pump to form droplets on the stainless steel needle department, then take photographs of the droplets shape by an amplifying camera system, after that use the computer image processing system to get the outer contour of the oil droplets. Using the data of the needle diameter corrected by image magnification and the density of light phase and heavy phase, ultimately calculate the interfacial tension. The experimental apparatus is shown in Fig. 1.

#### *Experimental samples*

Crude oil was provided by Zhongyuan oilfield, formation temperature 355.65 K. CO<sub>2</sub> gas produced by Beijing Hua Yuan Co., purity of 99.995%, and petroleum ether produced by Sinopharm Chemical Reagent Company were used.

#### *Experimental procedure*

The experimental steps are as follows:

(1) Wash the whole experimental system with petroleum ether, and use hot nitrogen to remove residual petroleum ether.

(2) Do vacuum.

(3) Pump the oil sample into the injector with a manual pump.

(4) Start heating when both reactor and oil injector pump reach the set temperature (355.65K), then introduce CO<sub>2</sub> into the reactor pressurized with a manual pump. Shut valve until the reactor pressure stabilizes.

(5) Push oil slowly into the reactor through the oil injection pump, the formed small droplets around

\* To whom all correspondence should be sent:  
E-mail: wangxin\_bj@yeah.net

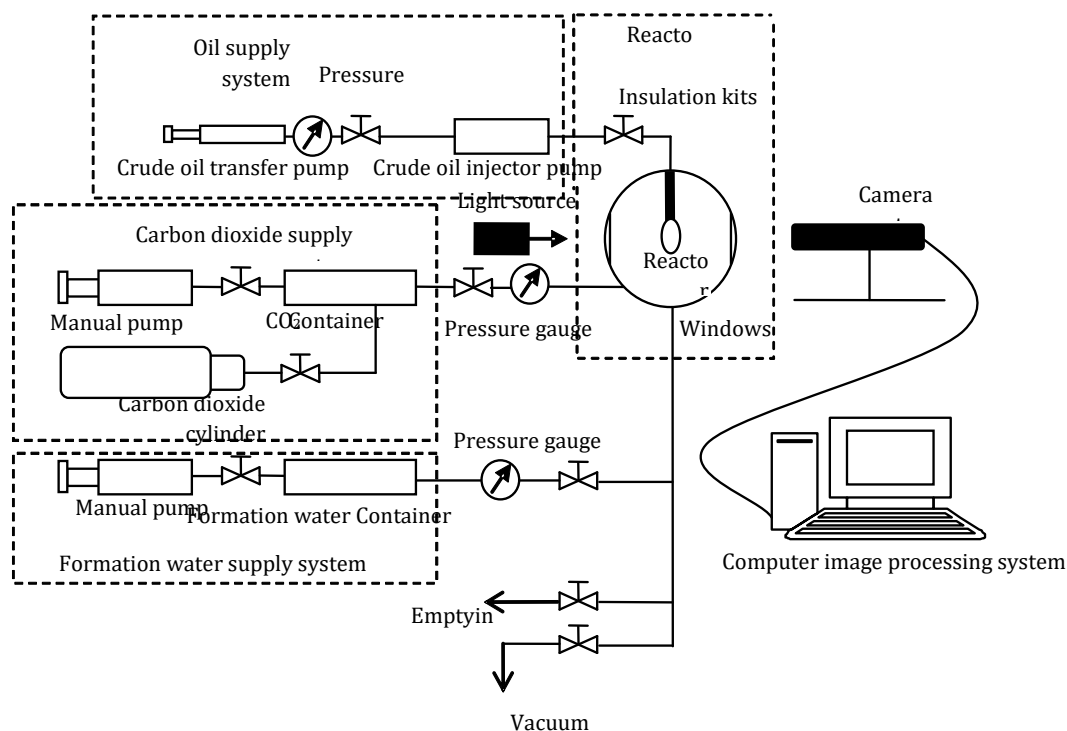


**Fig.1** The schematic for the determination of interfacial tension by the pendant drop method

the probe are maintained for a period of time. Photograph the images of droplets by the camera system. Each droplet holds no less than 15 minutes, and each pressure point refers to at least three droplets. Finally, get the interfacial tension according to the shape of droplets.

(6) Adjust the experimental pressure and repeat step (5) and step (6) until the end of the experiment.

### EXPERIMENTAL PHENOMENA AND RESULTS ANALYSIS

#### CO<sub>2</sub>/Crude oil equilibrium interfacial tension

*Experimental Phenomena.* (1) Dissolution and Extraction Effect. During the experiment, there is a medium exchange as the oil drop from the tip of the needle interacts with CO<sub>2</sub> from the reactor on the condition that the experimental pressure is higher than the bubble point pressure [16-18]. CO<sub>2</sub> is constantly dissolved into the oil droplets, and the light group of oil droplets is spread to CO<sub>2</sub> [19-22]. At the beginning of the contact between oil and CO<sub>2</sub>, the reaction is much stronger, and the light component of crude oil is constantly dissolved by supercritical CO<sub>2</sub> [23-25], as shown in Figure 2. After some dissolution and extraction, the heavy component of crude oil will be left behind, and the crude oil and CO<sub>2</sub> will eventually reach equilibrium state as shown in Figure 3. The interfacial tension at this moment can be considered as the equilibrium interfacial tension.

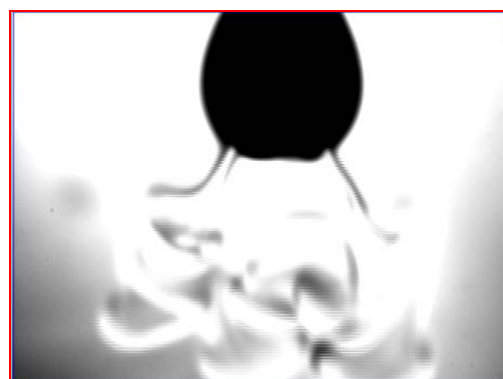


**Fig. 2.** Initial phase.

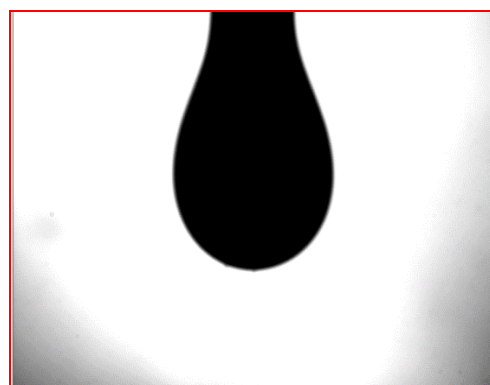


**Fig. 3.** Equilibrium phase.

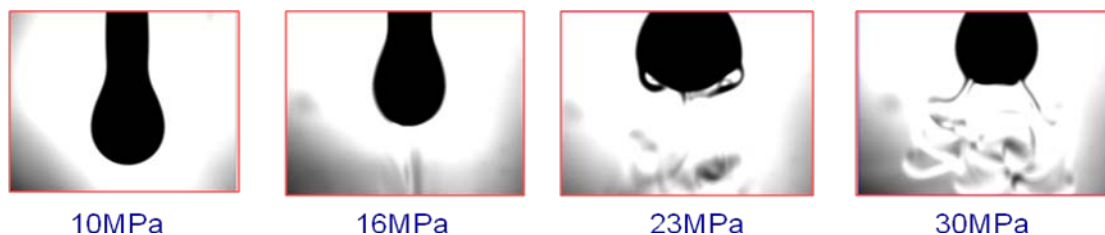


Fig. 4. Images of the pendant oil drop in CO<sub>2</sub>/crude oil system under different pressures.

(2) Effect of Pressure on the Dissolution and Extraction. It can be seen from the experiment that, as the pressure increases, the extraction of crude oil increases, and the interface between CO<sub>2</sub> and crude oil becomes unstable. A small amount of light components can be extracted out at a pressure of 16MPa, but the extraction effect becomes more significant when the pressure reaches 30MPa, as shown in Figure 4.

*Experimental curve.* The relationship between interfacial tension and pressure is shown in Figure 5.

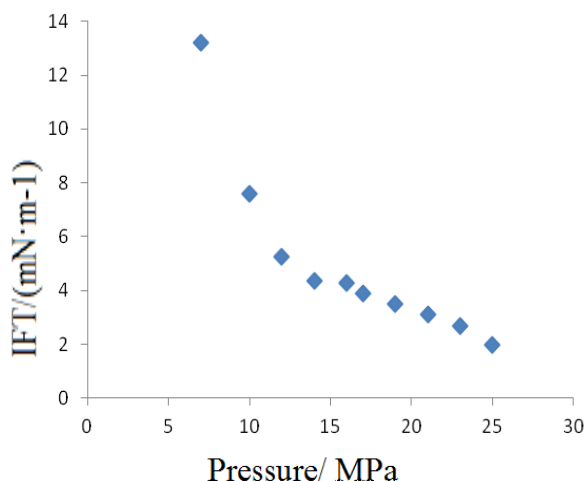


Fig. 5 Interfacial tension of CO<sub>2</sub>/crude oil system under different pressures.

The equilibrium interfacial tension between crude oil and CO<sub>2</sub> decreases with the increase in pressure. The minimum miscibility pressure of the system calculated by the extrapolation method is 18.97MPa. When the pressure is lower than 18.97MPa, the interfacial tension decreases rapidly; but when the pressure reaches 18.97MPa, the interfacial tension decrease gets slower.

*Dynamic interfacial tension between crude oil and CO<sub>2</sub>*

The experiment showed that the interaction between CO<sub>2</sub> and crude oil is strong at the early stage, but with the extraction of light component of crude oil by CO<sub>2</sub>, and the dissolution of CO<sub>2</sub> into the oil, the interfacial tension between them changes. In order to study the effect of this process

on the interfacial tension, the effect of contact time on the interfacial tension between crude oil and CO<sub>2</sub> was tested.

Figures 6 and 7 compare the curves of CO<sub>2</sub>/crude oil interfacial tension change with time at two different pressures. It can be seen from the figures that the interfacial tension between CO<sub>2</sub> and oil is large at the initial contact; but as the contact is getting longer, the interfacial tension decreases gradually, and eventually reaches dynamic balance. In addition, the higher the pressure, the larger is the magnitude of CO<sub>2</sub>/crude oil interfacial tension. The value of the equilibrium interfacial tension under 12MPa is more than 90% of the initial interfacial tension, but it turns to 80% at a pressure of 21MPa. Obviously, the interaction between CO<sub>2</sub> and oil is stronger, and the change of interfacial tension is bigger at a higher pressure. The actual reservoir CO<sub>2</sub> flooding belongs to multi contact miscible flooding; after the contact of CO<sub>2</sub> and oil, and multiple extraction and dissolution, the oil and CO<sub>2</sub> eventually get miscible. This leads to the interfacial tension between crude oil and CO<sub>2</sub> as an inevitable result of dynamic change.

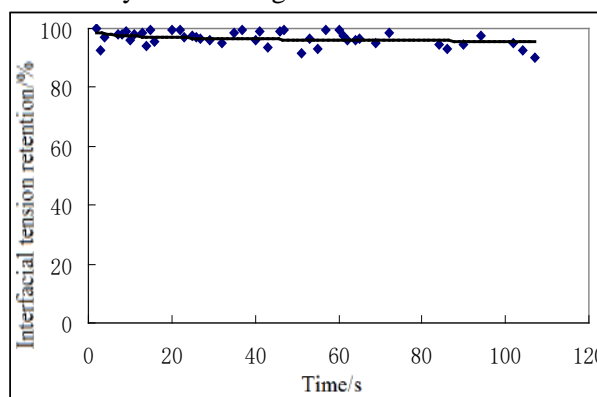


Fig.6. The curve of CO<sub>2</sub>/crude oil system interfacial tension change with time under 12MPa.

**CONCLUSION**

1. Using the ADSA method, the interaction between CO<sub>2</sub> and crude oil can be followed through the reactor under simulated-formation conditions of temperature and pressure. There is a strong mutual diffusion at the beginning of the contact of CO<sub>2</sub> and crude oil, and as the pressure goes higher, both dissolution and extraction increase.

2. Experimental determination of CO<sub>2</sub> and crude oil interfacial tension data was performed under the conditions of temperature of 355.65K and pressure ranging from 7MPa to 23MPa. Experimental results show that CO<sub>2</sub>/crude oil equilibrium interfacial tension decreases with the increase in pressure.

3. The interfacial tension between CO<sub>2</sub> and oil is large at the initial contact, then gradually decreases with time, and eventually reaches dynamic balance. Moreover, the higher the pressure, the larger is the magnitude of CO<sub>2</sub>/crude oil interfacial tension change with time.

**Acknowledgments.** The authors gratefully acknowledge the support of the Beijing University of Aeronautics and Astronautics and the Guilin University of Aerospace Technology. The work is supported by the project of the Guilin University of Aerospace Technology under Grant No. X12Z002.

#### REFERENCES

1. Y. Zuo, J. Chu, S. Ke, T. Guo, *J. Petrol. Sci. Eng.*, **8**, 315 (1993).
2. B. Liu, P. Zhu, Z. Yong, et al. *Acta Petrol. Sinica*, **23**, 56 (2002).
3. D. Yang, Y. Gu. SPE-102481-MS, *SPE Annual Technical Conference and Exhibition*, USA (2006).
4. H. Ronde, SPE-24877-MS, *SPE Annual Technical Conference and Exhibition*, USA (1992).
5. K.D. Hagedorn, F.M. Orr, SPE-25169-PA, *SPE Advanced Technology Series*, **2**, 2 (1994).
6. B. Peng, H. Luo, G. Chen, C. Sun, *Acta Petrolei Sinica*, **28**, 3 (2007).
7. C. Sun, W. Wang, G. Chen, et al. *Journal of China University of Petroleum: Edition of Natural Science*, **30**, 5 (2006).
8. B.T. Campbell, F.M. Orr Jr, SPE-11958-PA, *Society of Petroleum Engineers Journal*, **25** 5 (1985).
9. Z. Novosad, L.R. Sibbald, T.G. Costain *J. Can. Pet. Technol.*, **29**, 1 (1990).
10. G.C. Wang, SPE-15085-MS, *SPE California Regional Meeting*, USA (1986).
11. M. Stukan, W. Abdallah, SPE-161279-MS, *Abu Dhabi International Petroleum Conference and Exhibition*, UAE, (2012).
12. L.R. Sibbald, Z. Novosad, T.G. Costain, *SPE Reservoir Engineering*, **6**, 3 (1991).
13. F.B. Thomas, X.L. Zhou, D.B. Bennion, et al., *J. Can. Pet. Technol.*, **33**, 2 (1994).
14. D. Yang, Y. Gu, SPE-89366-MS, *SPE/DOE Symposium on Improved Oil Recovery*, USA, (2004).
15. A.M. Elsharkawy, F.H. Poettmann, *Energy & Fuels*, **10**, 2 (1996).
16. Orr, F.M., Yu, A.D., Lien, C.L., SPE-8813-PA, *Society of Petroleum Engineers Journal*, **21**, 4 (1981).
17. D.B. Bennion, S. Bachu. SPE-114479-MS, *SPE Annual Technical Conference and Exhibition*, USA, (2008).
18. K. Jessen, F.M. Orr, SPE-110725-PA, *SPE Reservoir Evaluation & Engineering*, **11**, 5 (2008).
19. M. Dong, S. Huang, S.B. Dyer, et al., *Journal of Petroleum Science and Engineering*, **31**, 1 (2001).
20. D.N. Rao, *Fluid Phase Equilibria*, **139**, 2 (1997).
21. S. Siregar, P. Mardisewojo, D. Kristanto, R. Tjahyadi, SPE-57300-MS, *SPE Asia Pacific Improved Oil Recovery Conference*, Malaysia, (1999).
22. U.W.R. Siagian, R.B. Grigg, SPE-39684-MS, *SPE/DOE Improved Oil Recovery Symposium*, USA, (1998).
23. A.Y. Zekri, S.A. Shedid, R.A. Almehaideb, SPE-104750-MS, *International Symposium on Oilfield Chemistry*, (2007).
24. D.N. Rao, J.I. Lee, *Journal of Colloid and Interface Science*, **262**, 2 (2003).
25. R.A. DeRuiter, L.J. Nash, M.S. Singletary, SPE-20523-PA, *SPE Reservoir Engineering*, **9**, 2 (1994).

## ОПРЕДЕЛЯНЕ НА РАВНОВЕСНОТО И ДИНАМИЧНОТО МЕЖДУФАЗНО НАПРЕЖЕНИЕ НА СИСТЕМАТА ВЪГЛЕРОДЕН ДИОКСИД/ПЕТРОЛ ПО ADSA-МЕТОДА

Ванг Ксин<sup>1</sup>, Лю Лифенг<sup>2</sup>, Лун Зенгмин<sup>1</sup>, Льв Ченгян<sup>1</sup>

<sup>1</sup> Изследователски институт по изследване и производство на петрол „Синопек“, Бейджин, Китай

<sup>2</sup> Изследователски институт по изследване и производство на петрол „Петролайн“, Бейджин, Китай

Постъпила на 4 май, 2014 г.

(Резюме)

Използван е ADSA-методът за измерване на междуфазовото напрежение в системата CO<sub>2</sub>/суров петрол при симулирани условия на температура от 355.65 K и налягания в интервала от 7MPa до 23MPa. Тестовите резултати показват, че равновесното междуфазово напрежение намалява с нарастване на налягането в системата. Интензивна взаимна дифузия протича когато CO<sub>2</sub> е в контакт със суровия петрол и постоянно се разтваря в петрола, като накрая се достига до устойчиво състояние. Динамичното междуфазно напрежение между фазите е високо при първоначалния контакт. След това то постепенно намалява, като в края на контакта се достига динамично равновесие. Освен това междуфазното напрежение в системата CO<sub>2</sub>/суров петрол намалява значително при повишение на налягането.

## Convection-diffusion modelling for chemical pollutant dispersion in the joint of artificial lake using finite element method

De-Sheng Li

*School of Science, Anhui Science and Technology University, Donghua Road 9#, Fengyang 233100, China*

Submitted May 12, 2014

**Abstract.** A convection-diffusion mathematical model is adopted to describe the chemical contamination dispersion problem in the joint of artificial lake. We consider the problem into 2-dimensional discussion limited to the surface of the joint. Under this assumption, the mathematical formulation of the pollution model comprises the mass conservation, which describes convection, turbulent diffusion and emission of the pollutant, illustrated by a convection-diffusion equation. We construct and analyse (discrete) boundary conditions for an implicit difference scheme. The finite element method is used to get the numerical solution of the convection-diffusion equation to insight into the variation of temperature and concentration fields. Especially, different with other similar research, a stochastic model of Lévy flights is employed to calculate the dispersion tensor coefficients, which heavily relies on the soil orography, stability class, distance of pollutant source and surface roughness. Consider the degradation of chemicals, we can also get form the concentration of time and space distribution by the instantaneous source of pollution. The experimental result of simulation shows that the progress of chemical pollutant dispersion in the joint of artificial lake is not only related to the velocity of water fluid, degradation rate, dispersion coefficient, and initial concentration, but also to the geometrical shape of the a horn mouth to the main body of the artificial lake. It also can be concluded that the Finite Element Method of Convection-Diffusion model is suitable, accurate and efficient for this kind of pollution problem.

**Key words:** Environmental Impact, Chemical Pollutant Dispersion, Convection-Diffusion Problem, Finite Element Method

### INTRODUCTION

Nowadays, the common fact that the release of waste materials from chemical and industrial facilities into water bodies could harm heavily the human health and the environment is broadly accepted in both academia and industry. According to literature [1,2] one typical environmental problem in current due to the dispersion of solutes in water bodies is the fate of the total residual chlorine in rivers. Unfortunately, in most developing countries, this kind of phenomenon is very common especially in inland rivers and lakes.

An artificial lake, sometimes called reservoir, is often a storage pond or impoundment from a dam which is used to store water. Artificial lakes may be created in river valleys by the construction of a dam or may be built by excavation in the ground or by conventional construction techniques such as brickwork or cast concrete. It is characterized by the neat geometric shapes that composed by a rectangular cavity connected to the river and a horn mouth to the main body reservoir as shown in Fig. 1. Due to the trait of large capacity and decreasing velocity of the fluid, the pollution is usually very serious in the joint of artificial lake [3]. In this research our aim is to investigate the dispersion of chemical contamination in the joint which is only

related to the upstream pollution detection, but also affects the human and animal health downstream.

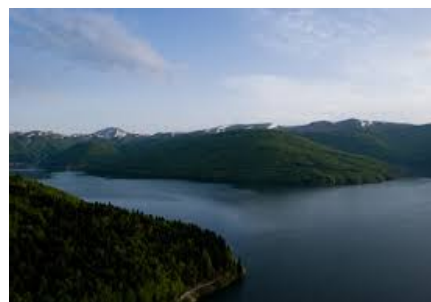


**Fig. 1.** The landscape of the joint of artificial lake.

Then, we should establish the strict mathematical model for the proposed problem. In general, modeling of contamination dispersion often plays an important role in environmental science, not only because of its capability to assess the importance of the relevant processes, but also to describe the deterministic relationship between emissions and concentrations/depositions. Typical modeling and techniques include non-reactive (e.g., dispersion modeling) and reactive (e.g., photochemical modeling); deterministic models (e.g., Gaussian, Lagrangian and Eulerian ones) and stochastic models [4,5].

Among these models, convection- diffusion problem [6-11], launched by the research in fluid science, also concentrate on the physical/chemical quantities carried by mass points in fluid flow, such

\* To whom all correspondence should be sent:  
E-mail: ldsy2006@126.com

as the concentration of the substance in the dissolved fluid flow in the process of change rule. These changes generally include convection, diffusion, and its attenuation of physical measurement of some physical and/or chemical causes or growth process. Convection diffusion phenomenon in the research of environmental protection is often met in fluid mechanics. In the research of fluid science, convection-diffusion equation is a consolidation of the diffusion and convection equations, and describes physical /chemical phenomena where particles, energy, or other physical/chemical quantities are transferred inside a physical/chemical system due to two processes: diffusion and convection. Under some contexts, it could be also called the advection-diffusion equation, drift-diffusion equation, Smoluchowski equation [12] or scalar transport equation [13].

In this article, we use the finite element method to get the numerical solution of the convection-diffusion equation to insight into the variation of temperature and concentration field. Specially, different with other similar research in [5,14], a stochastic model of Lévy flights is employed to calculate the dispersion tensor coefficients according to the concrete stochastic models, which are heavily rely on the soil orography, stability class, distance of pollutant source and surface roughness. Consider the degradation of chemicals, we can also get form the concentration of time and space distribution by the instantaneous source of pollution.

## PROBLEM FORMULATION

### *Rationale and assumption*

The rationale of the finite element method for convection-diffusion problem is shown below. First, denote the physical quantity fields (such as concentration field, velocity field temperature field, and so forth) as a finite collection of discrete points. According the initial and boundary conditions mesh the grid and generate the boundary conditions. Then establish and solve the algebraic equation on these discrete points to acquire the approximate solutions. Note that the convergence of the solution should be discussed. When the solution is not convergent, it is necessary to establish new discrete control equation to be resolved until the convergent one.

Before formalizing the problem, we should give some preliminary assumptions. Firstly, we consider the problem into 2-dimensional discussion limited to the surface of the lake. Therefore the pollutant's density has to be lower than the water's to make this assumption valid, for instance, the oil pollutant often taken as the example. Moreover, in this article, we present an Eulerian model of pollutant which on this

scale never reacts significantly with other composites similar to the literature [15].

### *Dispersion of the pollutant*

Here we adopt a non-reactive model for one pollutant in order to simplify the numerical method proposed, but it is not difficult to generalize to several reactive pollutants. At last, we assume the water flows are steady, so the first stage is used to compute the velocity field of the lake surface, while the second stage determines the flow of the pollutant measured by a local and time-dependent concentration:  $C(x,y,t)$ .

The mathematical formulation of the water bodies' pollution model is the equation of mass conservation, which describes convection, turbulent diffusion and emission of the pollutant, illustrated by the following convection- diffusion equation:

$$\frac{\partial C}{\partial t} + \vec{v} \cdot (-k\vec{\nabla}C + \vec{v}C) = f \text{ in } \Omega \times (0, t_f)$$

s.t.

$$\frac{\partial C}{\partial t} + \vec{v} \cdot \vec{q} = 0, \forall (x, y) \in A, \vec{q} = -k\vec{\nabla}C + \vec{v}C$$

endowed with proper initial and boundary condition for the pollutant concentration  $C(x,y,t)$ , which stands for the concentration of pollutant [kg] per [m<sup>3</sup>] water. The vector  $\vec{q}$  stands for the flow [kg/m<sup>2</sup>-s]. The equation  $\vec{q} = -k\vec{\nabla}C + \vec{v}C$  demonstrates the flow and the concentration of the pollutant obeying the relationship called behavior law, which is a mathematical relation between the gradients of a function and its dual function. In this work, boundary conditions are artificial specified since the river estuary never owns a nature boundary. The turbulent diffusivity tensor  $k$  could be employed into Gaussian perturbation or Lévy flights which will be explained in the latter subsection. The contamination source  $f$  is standing for a term of generation/elimination [kg/m<sup>3</sup>-s]. The space domain of water bodies  $S \in \mathbb{R}^2$  lays over a given surface, and  $t_f$  denotes the final time. The vector  $\vec{v}$  is the local field velocity of the flow.

### *Diffusivity tensor using Lévy flights*

For the diffusivity tensor, we only consider the model on the transport and diffusion of pollutants emitted by industrial wastewater; hence we adopt the stochastic models (Gaussian perturbation, random walk and so forth). By diffusion, we understand an aggregation of dispersive processes which are of diffusion type in a mathematical sense, i.e. resulting from a random walk (Brownian motion, Einsteinian diffusion). For a good introduction into the research, see e.g. [16].



Under these premises, the concentration of the pollutants assumes the form of a stochastic distribution in two-dimensional space, and let it fit the coefficients of turbulent diffusivity tensor hereunder:

$$k = \begin{bmatrix} k_{xx} & 0 \\ 0 & k_{yy} \end{bmatrix}$$

where  $x$  and  $y$  are those associated with the horizontal plane.

The stochastic models could be used to obtain the empirical coefficients  $k_{xx}$  and  $k_{yy}$  on basis of orography, fluid stability and so forth. The value of them could be calculated as,

$$k_{xx} = k_{yy} = \frac{\sigma^2 \det(\vec{V})}{2r}$$

where  $r$  is the distance from the pollutant source and  $\sigma$  is the dispersion tensor coefficients according to the concrete stochastic models, which are heavily rely on the soil orography, stability class, distance of pollutant source and surface roughness (c.f. [17]).

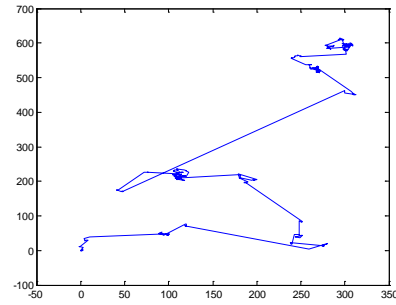
In recent related researches, Gaussian models are used to be the stochastic model to generate the empirical coefficients in paper [5]. However, compared to Gaussian distribution, Lévy distribution is advantageous since the probability of returning to a previously visited site is smaller than for a Gaussian distribution, irrespective of the value of  $\mu$  chosen. So in our research, another random walk method, Lévy flights, is employed to this work. Lévy flights, named after the French mathematician Paul Pierre Lévy, are Markov processes [18]. After a large number of steps, the distance from the origin of the random walk tends to a stable distribution. Lévy flights, which can be characterized by an inverse square distribution of step length, may optimize the random search process when targets are scarce and scarcity of resources. In contrast, Brownian motion is usually suited for the case when there is a need to locate abundant prey or targets.

Mathematically, Lévy flights are a kind of random walk whose step lengths meet a heavy-tailed Lévy alpha-stable distribution, often in terms of a power-law formula,  $L(s) \sim |s|^{-1-\beta}$  where  $0 < \beta \leq 2$  is an index. A typical version of Lévy distribution can be defined as according to reference [19]

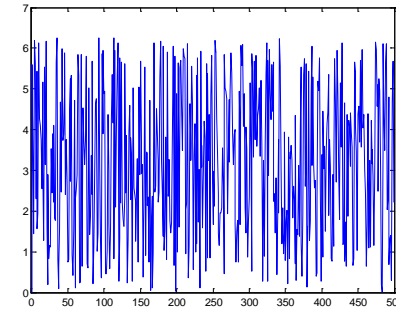
$$L(s, \gamma, \mu) = \begin{cases} \sqrt{\frac{\gamma}{2\pi}} \exp\left[-\frac{\gamma}{2(s-\mu)}\right] \frac{1}{(s-\mu)^{3/2}}, & 0 < \mu < s < \infty; \\ 0, & s \leq 0. \end{cases}$$

As the change of  $\beta$ , this can evolve into one of Lévy distribution, normal distribution and Cauchy distribution. Taking the 2D-Lévy flights for instance, the steps following a Lévy distribution as in Fig.

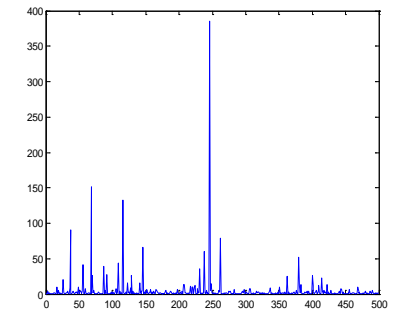
2(b), while the directions of its movements meet a uniform distribution as in Fig. 2(a). As shown in Fig. 2(c), an instance of the trajectory of 500 steps of random walks obeying a Lévy distribution. Note that the Lévy flights are often efficient in exploring unknown and large-scale search space than Brownian walks. One reason for this argument is that the variance of Lévy flights  $\delta^2(t) \sim t^{3-\beta}$  increases faster than that of Brownian random walks, i.e.,  $\delta^2(t) \sim t$ .



(a) Distance



(b) Angle values



(c) Step lengths

**Fig. 2.** 2D Lévy flights in 500 steps

### Velocity field of the water body

The following assumptions are made in order to compute the water speed field: one is incompressible flow and the other is non-viscous flow. These could result into the consequence described by the following equations:

$$\vec{\nabla} \cdot \vec{V} = 0, \text{rot} \vec{z} = 0$$

where the unit vector  $\vec{z}$  is the direction vector normal to the lake. Now, we assume another function  $\psi$ , called stream-function, defined by :

$$u = \frac{\partial \psi}{\partial y}, v = -\frac{\partial \psi}{\partial x}$$

where  $u$  and  $v$  are the two horizontal components of the water speed field. Thus, if such a potential exists, then insertion into the rotational equation gives a single governing equation (Laplace equation) to be solved:

$$\Delta\psi = 0, \forall (x, y) \in A$$

For a steady-state flow, the trajectories of the fluid-particles are within the streamlines. It is possible to demonstrate that these streamlines are simply described by the equality:

$$\psi = \bar{\psi}$$

Coming from this last relationship, the boundary conditions are easily set when prescribing a different value to each boundary limited by two successive mouths similar to a 'wall' forbidding any crossover (the shore for instance). One of the boundary has to be prescribed as a zero value for  $\psi$ . The value of  $\psi$  will be defined according to the inflow/outflow of the relevant separating mouth in nearby boundaries. To each inflow and to each outflow corresponds a 'jump' of the value of  $\psi$ . A constant value for  $\psi$  defines a streamline

### Variational form

The finite element method is based on the discretization of a variational form corresponding to each equation of the problem.

Based on the Eq. (1), the Galerkin variational problem [20] is corresponding to the mechanical principle of virtual work, i.e., for a static equilibrium of the system, the virtual work about the forces of all external forces along with the virtual displacement could be expressed as the following equation,

$$\begin{aligned} W &= \iint_S \varphi(x, y) \left( \vec{\nabla} \cdot (-k\vec{\nabla}C + \vec{V}C) + \frac{\partial C}{\partial t} \right) dx dy \\ &= \sum \iint_{S_e} k\vec{\nabla}\varphi(x, y) \cdot (\vec{\nabla}C) dx dy \\ &\quad - \oint_{\partial S} k\varphi(x, y) \cdot (\vec{\nabla}C) \cdot \vec{n} ds \\ &\quad + \sum \iint_{S_e} \varphi(x, y) \left( \vec{\nabla} \cdot (\vec{V}C) \right) dx dy \\ &\quad + \sum \iint_{S_e} \varphi(x, y) \frac{\partial C}{\partial t} dx dy \end{aligned}$$

where  $\varphi(x, y)$  stands for any trial function,  $S$  is the total lake surface and  $\partial S$  the limit of the lake. Once the division of the domain (called meshing) into elementary surfaces (called finite elements) is done, then the weak form is discretized and appears as a sum of elementary terms. Because the numerical solution of the above pollution model is critical to use accurate and stable numerical methods. In our

work, we use a combination of Galerkin and upwind finite element method to simulate the chemical pollutant dispersion in river estuary.

### Discrete forms of FEM

Let us discuss the Discrete forms of FEM. Firstly,  $T$  is a collection of continuous piecewise linear function under triangulation, which is a linear space on real number field. Every function  $T(x, y)$  in  $T$  could be expressed as:

$$T(x, y) = \sum_{i=1}^{N_p} T_i N_i(x, y) = \langle N_1, N_2, N_3 \rangle \begin{Bmatrix} T_1 \\ T_2 \\ T_3 \end{Bmatrix}, (x, y) \in \bar{S}$$

where  $T_i$  is the value of  $T(x, y)$  on the spot of  $P_i$ .  $N_i(x, y)$  are called the linear interpolation functions on element  $e$ . The linear interpolation function  $N_i(x, y)$  get the value 1 on the spot of  $P_i$ , but around  $P_i$  get nonzero values.. Based on these interpolation function, any trail function  $\varphi(x, y)$  could be expressed linearly as below:

$$\varphi(x, y) = \langle \varphi_1, \varphi_2, \varphi_3 \rangle \begin{Bmatrix} N_1 \\ N_2 \\ N_3 \end{Bmatrix}$$

Then the linear interpolation functions on element  $e$  have the solution as follows:

$$\begin{cases} N_1(x, y) = \frac{1}{2A^e} [y_{32}(x_2 - x) - x_{32}(y_2 - y)] \\ N_2(x, y) = \frac{1}{2A^e} [y_{13}(x_3 - x) - x_{13}(y_3 - y)] \\ N_3(x, y) = \frac{1}{2A^e} [y_{21}(x_1 - x) - x_{21}(y_1 - y)] \end{cases}$$

Thus, the gradient vector of  $T$  could be expressed as:

$$\vec{\nabla}T = \begin{Bmatrix} \frac{\partial T}{\partial x} \\ \frac{\partial T}{\partial y} \end{Bmatrix} = \begin{bmatrix} \frac{\partial N_1}{\partial x} & \frac{\partial N_2}{\partial x} & \frac{\partial N_3}{\partial x} \\ \frac{\partial N_1}{\partial y} & \frac{\partial N_2}{\partial y} & \frac{\partial N_3}{\partial y} \end{bmatrix} \begin{Bmatrix} T_1 \\ T_2 \\ T_3 \end{Bmatrix}^e = [B]\{T\}^e ;$$

$$\vec{\nabla}\varphi = \begin{Bmatrix} \frac{\partial \psi}{\partial y} \\ -\frac{\partial \psi}{\partial x} \end{Bmatrix} = \begin{bmatrix} \frac{\partial N_1}{\partial y} & \frac{\partial N_2}{\partial y} & \frac{\partial N_3}{\partial y} \\ -\frac{\partial N_1}{\partial x} & -\frac{\partial N_2}{\partial x} & -\frac{\partial N_3}{\partial x} \end{bmatrix} \begin{Bmatrix} \psi_1 \\ \psi_2 \\ \psi_3 \end{Bmatrix}^e$$

$$= \langle \psi \rangle^e \begin{bmatrix} B(2, :) \\ -B(1, :) \end{bmatrix}^T$$

$$\vec{\nabla}\varphi = \langle \varphi_1, \varphi_2, \varphi_3 \rangle^e \begin{bmatrix} \frac{\partial N_1}{\partial x} & \frac{\partial N_1}{\partial y} \\ \frac{\partial N_2}{\partial x} & \frac{\partial N_2}{\partial y} \\ \frac{\partial N_3}{\partial x} & \frac{\partial N_3}{\partial y} \end{bmatrix} = \langle \varphi \rangle^e [B]^T$$

Besides, we can write the gradient matrix  $[B]$  as follows:

$$[B] = \begin{bmatrix} \frac{\partial N_1}{\partial x} & \frac{\partial N_2}{\partial x} & \frac{\partial N_3}{\partial x} \\ \frac{\partial N_1}{\partial y} & \frac{\partial N_2}{\partial y} & \frac{\partial N_3}{\partial y} \end{bmatrix} = \frac{1}{2A^e} \begin{bmatrix} y_{23} & y_{31} & y_{12} \\ x_{32} & x_{13} & x_{21} \end{bmatrix}$$

Hence, the elementary weak form, which is

necessary to calculate the speed field, can be discretized as follows:

$$\begin{aligned} W_\psi &= \sum_{e=1}^{nelt} W_\psi^e = \sum_{Se} \iint k \vec{v} \varphi(x, y) \cdot (\vec{v} C) dx dy \\ &= \sum_{Se} \iint \langle \varphi \rangle^e [B]^T k [B] \{C\}^e dx dy \\ &= \sum_{Se} \langle \varphi \rangle^e \iint [B]^T k [B] dx dy \{C\}^e \\ &= \sum_{Se} \langle \varphi \rangle^e [K]_\psi^e \{C\}^e \end{aligned}$$

with the elementary stiffness matrix being defined by the relation :

$$[K]_\psi^e = A^e k [B]^T [B]$$

where  $A^e$  is the surface of the relevant element.

The weak form corresponding to the equation of diffusion-transport can be discretized as

$$W_C = W_{C1} + W_{C2}$$

Where:

$$\begin{aligned} W_{C1} &= \sum_{e=1}^{nelt} W_{C1}^e \\ &= \sum_{Se} \iint \varphi(x, y) (\vec{v} \cdot (\vec{v} C)) dx dy \\ &= \sum_{Se} \iint \varphi(x, y) \vec{v} \cdot (\vec{v} C) dx dy \\ &= \sum_{Se} \iint \langle \varphi \rangle^e \begin{Bmatrix} N1 \\ N2 \\ N3 \end{Bmatrix} \langle \psi \rangle^e \begin{bmatrix} B(2, :) \\ -B(1, :) \end{bmatrix}^T [B] \{C\}^e dx dy \\ &= \sum_{Se} \langle \varphi \rangle^e \iint \begin{Bmatrix} N1 \\ N2 \\ N3 \end{Bmatrix} dx dy \langle \psi \rangle^e \begin{bmatrix} B(2, :) \\ -B(1, :) \end{bmatrix}^T [B] \{C\}^e \\ &= \sum_{Se} \langle \varphi \rangle^e \frac{A^e}{3} \begin{Bmatrix} 1 \\ 1 \\ 1 \end{Bmatrix} \langle \psi \rangle^e [B]^T \begin{bmatrix} B(2, :) \\ -B(1, :) \end{bmatrix} \{C\}^e \\ &= \langle \varphi \rangle^e [K]_C^e \{C\}^e \end{aligned}$$

Then the definition of the transport matrix  $[K]_C^e$  could be written as following:

$$[K]_C^e = \frac{A^e}{3} \begin{Bmatrix} 1 \\ 1 \\ 1 \end{Bmatrix} \langle \psi \rangle^e [B]^T \begin{bmatrix} B(2, :) \\ -B(1, :) \end{bmatrix}$$

The components of the vector  $\langle \psi \rangle^e$  are the nodal values of the triangular element, which outputs are resulting from the first step of the solving procedure (water velocity field).

$$\begin{aligned} W_{C2} &= \sum_{e=1}^{nelt} W_M^e = \sum_{Se} \iint \varphi(x, y) \frac{\partial C}{\partial t} dx dy \\ &= \sum_{Se} \langle \varphi \rangle^e \iint \begin{Bmatrix} N1 \\ N2 \\ N3 \end{Bmatrix} \langle N1, N2, N3 \rangle dx dy \{\dot{C}\}^e \\ &= \sum_{Se} \langle \varphi \rangle^e [M]^e \{\dot{C}\}^e = \sum_{Se} \langle \varphi \rangle^e \frac{A^e}{12} \begin{bmatrix} 2 & 1 & 1 \\ 1 & 2 & 1 \\ 1 & 1 & 2 \end{bmatrix} \{\dot{C}\}^e \end{aligned}$$

where the mass matrix is relevant to the temporal term and defined by :

$$[M]^e = \frac{A^e}{12} \begin{bmatrix} 2 & 1 & 1 \\ 1 & 2 & 1 \\ 1 & 1 & 2 \end{bmatrix}$$

What's more, the components of the vector  $\{\dot{C}\}^e$  are the temporal derivatives of the concentration value at the nodes.

At the end of the assembly step, which consists in summing up the whole set of elementary contributions for the global system, we can write the two equations systems hereunder:

(1) Solving the water speed field:

$$W_\psi = 0$$

(2) Transport of the pollutant with the help of the water field speed:

$$W_C = 0$$

Considering stability of function, we use an explicit schema to the diffusion of the pollutant in the lake corresponds one equations system. There are no boundary conditions of the Dirichlet's type for this equations system. The necessary and boundary condition for the pollutant is over the whole contour of the lake: there must be a reflexion of the pollutant over the whole contour. This is a Neumann's type of boundary condition.

The system to be solved is therefore the following:

$$[M] \{\dot{C}\} + [K_\psi + K_C] \{C\} = \{F_C\}$$

where vector  $\{F\}$  results of the introduction of the initial condition.

$$\begin{aligned} [M] \frac{\{C\}^{n+1} - \{C\}^n}{\Delta t} + [K_\psi + K_C] \{C\}^n &= \{F_C\}^n \\ \{C\}^{n+1} &= ([I] - \Delta t [M]^{-1} [K_\psi + K_C]) \{C\}^n \\ &\quad + \Delta t [M]^{-1} \{F_C\}^n \\ [G] &= [I] - \Delta t [M]^{-1} [K_\psi + K_C] \end{aligned}$$

We put  $l_i$  the eigenvalues of the matrix  $[M]^{-1} [K_\psi + K_C]$ , with  $l_i \geq 0$ . Therefore:  $\lambda_i = 1 - l_i$  is the stable scheme if

$$0 \leq \lambda_i \leq 1, \Delta t \leq \frac{1}{l_i^{max}}$$

To the diffusion of the pollutant in the joint corresponds one equations system. There is no boundary condition of the Dirichlet's type for this equation system. The necessary and boundary condition for the pollutant is over the whole contour of the joint surface: there must be a reflexion of the pollutant over the whole contour. This is a Neumann's type of boundary condition.

$$e \vec{q} \cdot \vec{n} = -75 \text{ W/m} \quad (\text{Neumann})$$

$$\begin{aligned} - \oint_{\partial S} k_e \varphi(x, y) \cdot (\vec{\nabla} T) \vec{n} ds &= \sum_{i^e} \int \varphi(-75) ds \\ &= \sum \langle \varphi_1, \varphi_2 \rangle^e \frac{l^e(-75)}{2} \{1\} \end{aligned}$$

However, in the other cases, the Cauchy's type of boundary condition is considered.

$$e \vec{q} \cdot \vec{n} = h_e(T - T_{air})$$

So the last component of Eq. (3) could be written as :

$$\begin{aligned} & - \oint_{\partial S} k_e \varphi(x, y) \cdot (\vec{\nabla} T) \vec{n} ds \\ &= \sum_{i^e} \int \varphi h_e (T - T_{air}) ds \\ &= \sum_{i^e} \int \langle \varphi \rangle^e \begin{Bmatrix} N1 \\ N2 \end{Bmatrix} h_e \langle N1 \quad N2 \rangle \{T\}^e ds \\ & - \sum_{i^e} \int \langle \varphi \rangle^e \begin{Bmatrix} N1 \\ N2 \end{Bmatrix} h_e T_{air} ds \\ &= \sum \langle \varphi_1, \varphi_2 \rangle^e \frac{h_e l^e}{6} \begin{bmatrix} 2 & 1 \\ 1 & 2 \end{bmatrix} \begin{Bmatrix} T1 \\ T2 \end{Bmatrix}^e \\ & - \sum \langle \varphi_1, \varphi_2 \rangle^e \frac{h_e l^e T_{air}}{2} \{1\} \\ &= \sum \langle \varphi_1, \varphi_2 \rangle^e \left( \frac{h_e l^e}{6} \begin{bmatrix} 2 & 1 \\ 1 & 2 \end{bmatrix} \begin{Bmatrix} T1 \\ T2 \end{Bmatrix}^e \right. \\ & \left. - \frac{h_e l^e T_{air}}{2} \{1\} \right) \end{aligned}$$

### SOLVING STAGES

To calculate the solving procedure, the transport modeling of the chemical pollutant by the speed field has to satisfy the following stages:

**Step 0.** Preprocessing of the parameters.

**Step 1.** Soling the speed field equation:

$$[K_\psi] \{\psi\} = \{F_\psi\}$$

**Step 2.** Regulating the initial condition on C:

$$C(x_0, y_0, t = 0) = C_0$$

**Step 3.** Choosing the time step  $\Delta t$ .

**Step 4.** Iterating on the discrete time.

**Step 4.1** Resolution of the concentration increment between time 'n' and time 'n+1':

$$\begin{aligned} \{[M] + \Delta t [K_\psi + K_C]\} \{\Delta C_n^{n+1}\} \\ = \Delta t (\{F_C\} - [K_\psi + K_C] \{C^n\}) \end{aligned}$$

**Step 4.2** Update the solution:

$$\{C^{n+1}\} = \{C^n\} + \{\Delta C_n^{n+1}\}$$

**Step 5.** Postprocessing of the results.

## EXPERIMENTAL RESULTS AND ANALYSIS

### Time and space distribution of pollutant concentration formed by transient source

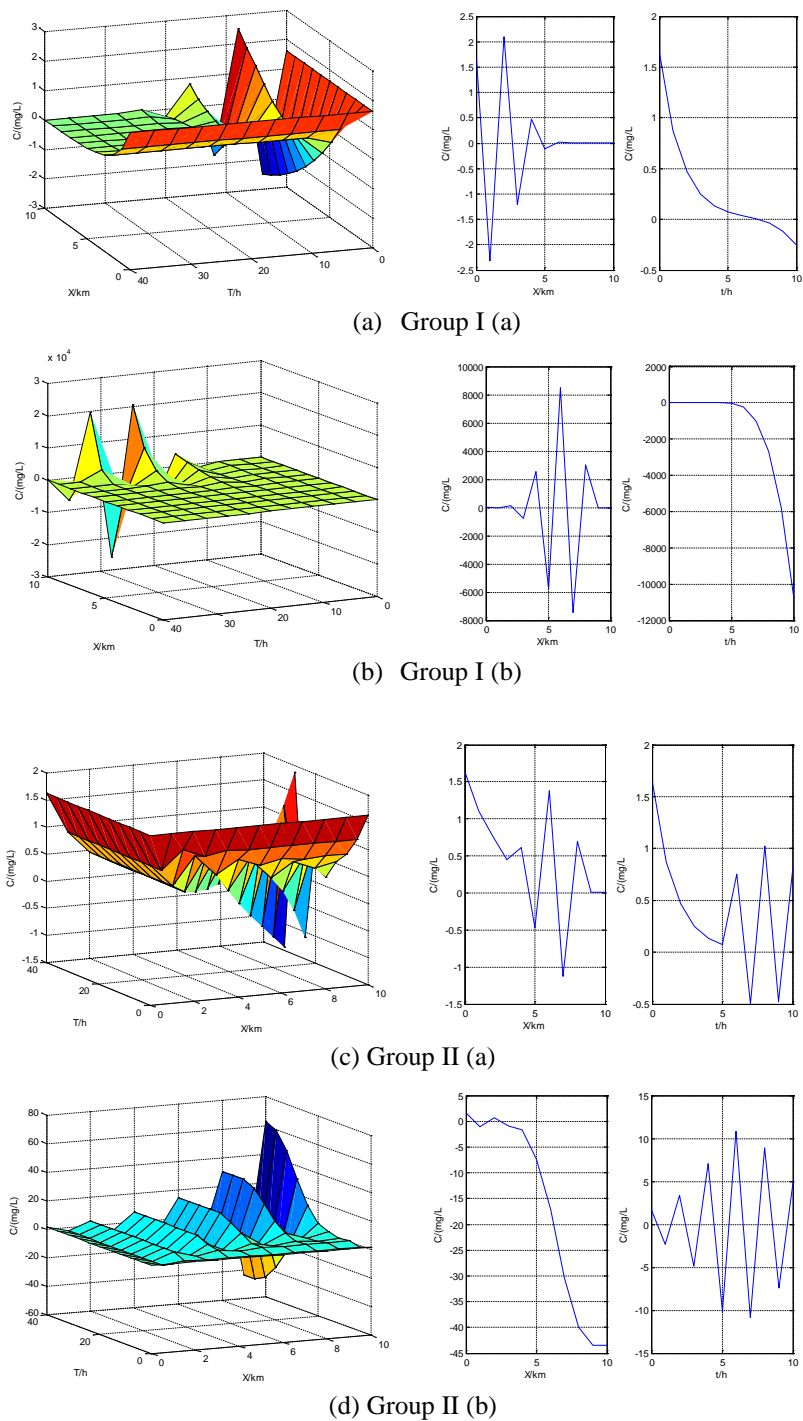
In this simulation, we investigate the time and space distribution of pollutant concentration formed by transient source. As shown in Table 1, the experiment is divided into two groups. Group I presents the case with a low flow velocity of 0.05km/h, while Group II with a high flow velocity of 0.5km/h. Each group consists of two tries with different pollutants degradation rate constant, i.e., 0.16 and 0.84. The initial concentration C0 is fixed to 1.63mg/L.

**Table 1.** Time and space distribution of concentration by transient source.

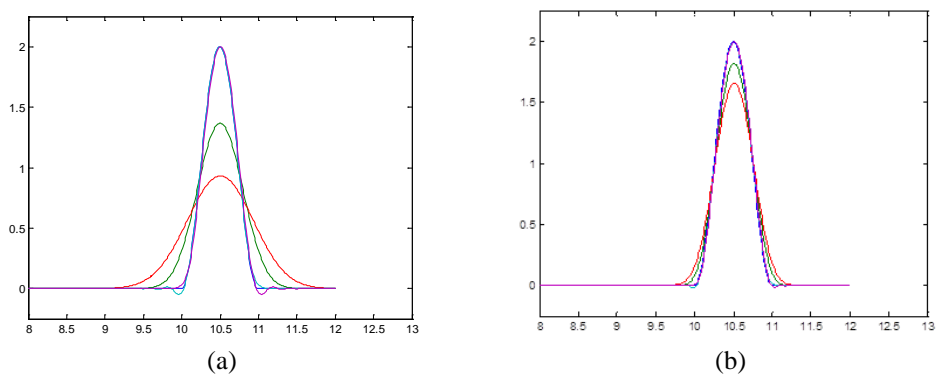
Group	Type	u [km/h]	P	C <sub>0</sub> [mg/L]
Group I	(a)	0.05	0.16	1.63
	(b)	0.05	0.84	1.63
Group II	(a)	0.5	0.16	1.63
	(b)	0.5	0.84	1.63

Fig. 3 (a)-(d) illustrates the time and space distribution of pollutant concentration formed by transient source. The vertical coordinates denote the pollutant concentration. From Fig. 3 (a) and (b), we can clearly see that concentration shocks up and down about 0, and declines rapidly with the time elapses, regardless of degradation rate constant. However, in the Fig. 3 (c) and (d), the concentration varies with the change of distance obviously. Moreover, the fluid may carry the pollutant downstream fast so that the concentration is large when far from the transient source.

Concentration of suspended particles increases near the bed with increase of settling velocity, as it proceeds towards downstream. It is interesting to note that with increase of settling velocity the elongation in the concentration profiles is mostly prominent near the bed surface. This is because the heavier particles travel most of the time very close to the bottom, where the velocity gradient is greater than any other region; this means, that the greater the velocity gradient, the larger the longitudinal dispersion [27].



**Fig. 3.** Time and space distribution of pollutant concentration formed by transient source.



**Fig. 4.** Dimensionless, steady, concentration profiles at various downstream distances from the source.

### Temperature transport and heat flow of chemical pollutants

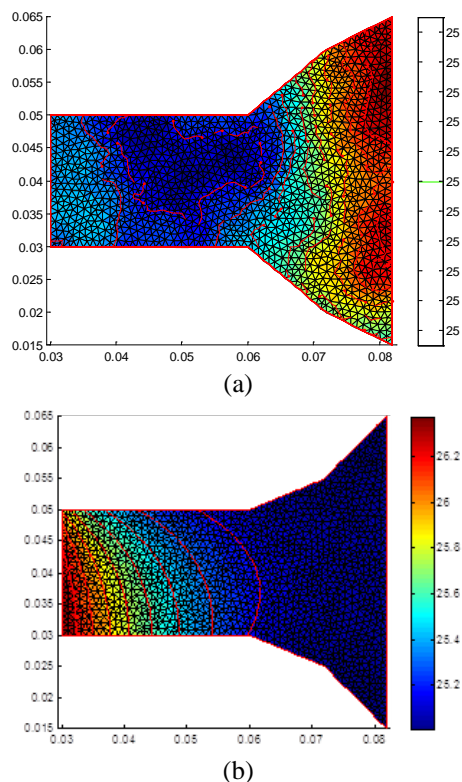
In this subsection, we are investigating the joint geometry's the influence for the temperature transport of chemical pollutants. This facet of research is meaningful as the downstream creature such as fishes and other stream biota are very sensitive to the variation of temperature. On the other hands, the chemical pollutants in industrial wastewater, such as, metallurgical or chemical fibre wastewater, always take higher temperature than the water bodies.

In reality, according to the different geometrical morphology, the joint of artificial lake can be classified as into two types, i.e., Parabolic Joint and Hyperbolic Joint, which own different kind of horn mouth to the main body reservoir.

The parameter setting of simulation is shown in Table 2, where  $N_{nt}$  is the number of nodes,  $N_{elt}$  the number of elements, and  $N_{barres}$  the number of barriers elements. It also presents the numerical solutions of pollutants temperature in PJ and HJ.

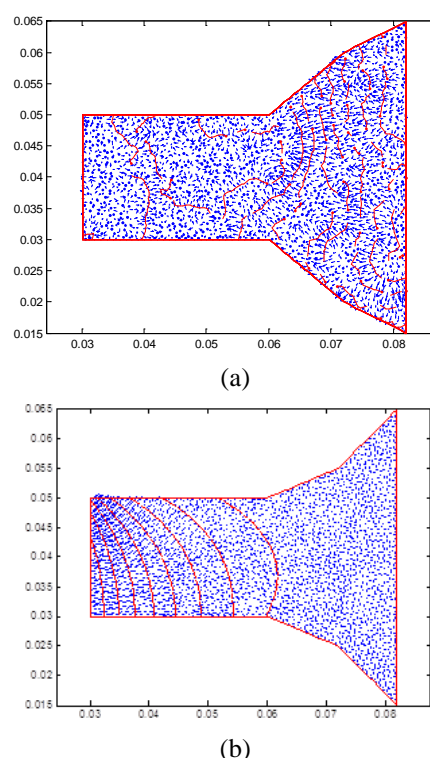
**Table 2.** Numerical solutions of diffusion of pollutants temperature

Joint Type	$N_{nt}$	$N_{elt}$	$N_{barres}$	Minimum field solution	Maximum field solution
Parabolic Joint (PJ)	1496	2990	181	25	25
Hyperbolic Joint (HJ)	1408	2823	202	25.00859600	26.37535877



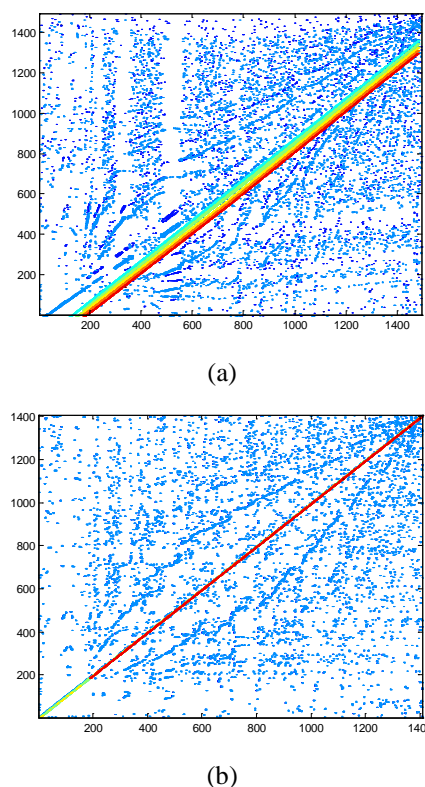
**Fig. 5.** Temperature transport of chemical pollutants in PJ and HJ

Fig. 5 describes the temperature transport of chemical pollutants in PJ and HJ. In Fig. 5(a), the temperature field is non-gradient because the chemical pollutants present a different diffusion and the diversity of directions. It also can be seen that the temperature in the horn mouth of PJ is higher than the rectangular cavity. Therefore, in this kind of joint, the temperature transport and heat flow of chemical pollutants may seriously affect the survival of the downstream creature. Whereas in the case depicted by Fig. 5(b), the temperature field of pollutants decrease rapidly because of the uniform thermal plume. Hence, the water body of this kind of horn mouth is not easy to be affected by the variation of temperature. The Fig. 6 illustrates the heat flow of chemical pollutants with isothermal in PJ and HJ.



**Fig. 6.** Heat flow of chemical pollutants with isothermal in PJ and HJ.

Consider for the coefficients of turbulent diffusivity under the cases of PJ and HJ, the landscape of the global stiffness matrices are shown in Fig. 7(a) and (b) respectively. Note that the matrices are block-tridiagonal, clearly showing the random distribution on the  $N_{nts}$ . It can be seen that the block before  $N_{barres}$  (with green diagonal line) is sparser than the block after  $N_{barres}$  (with red diagonal line) in both Fig. 7(a) and (b). Moreover, in Fig. 7 (a), there exist some discontinuous blocks but continuous in Fig. 7(b). According to our treatment to the coefficients of turbulent diffusivity, the matrices should follow a distribution by Lévy flights.



**Fig. 7** Heat flow of chemical pollutants with isothermal in PJ and HJ.

This can be verified in both Fig. 8 (a) and (b), where the temporal residue vectors are illustrated. In this figures, the coefficients of turbulent diffusivity is transformed as the 1-dimesion steps.

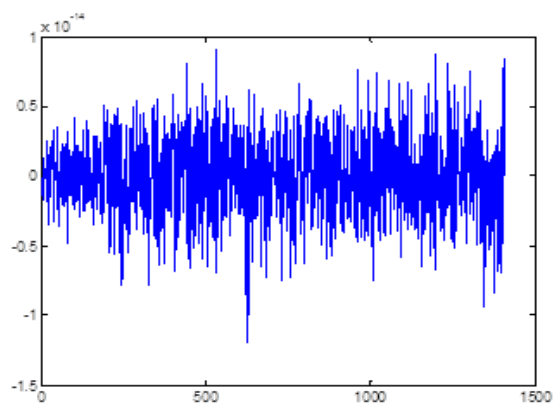


**Fig. 8.** Coefficients of turbulent diffusivity following a distribution by Lévy flights.

### CONCLUSIONS

In this paper, we investigate the chemical contamination dispersion problem in the joint of artificial lake; a convection-diffusion mathematical model is adopted to describe it. We consider the problem into 2-dimensional discussion limited to the surface of the joint. Firstly, for the diffusivity tensor, we only consider the model on the transport and diffusion of pollutants emitted by industrial

wastewater; hence we adopt a new kind of stochastic models, Lévy flights, to model it. The latter simulation proved this the correctness of the random distribution. Then we also investigate the time and space distribution of pollutant concentration formed by transient source and found that the fluid may carry the pollutant downstream fast so that the concentration is large when far from the transient source. Concentration of suspended particles increases near the bed with increase of settling velocity, as it proceeds towards downstream. It is interesting to note that with increase of settling velocity the elongation in the concentration profiles is mostly prominent near the bed surface. At last, we investigate the joint geometry's the influence for the temperature transport of chemical pollutants. In the kind of PJ, the temperature transport and heat flow of chemical pollutants may seriously affect the survival of the downstream creature. Whereas, the water body of the kind of horn mouth of HJ is not easy to be affected by the variation of temperature.

**Acknowledgements:** The research was supported by the National Natural Science Foundation of China (No.61201250), the Natural Science Foundation of Anhui Province (No. 1308085 QF103), the Natural Science Foundation of Educational Government of Anhui Province (No. KJ2013B073), and the Talent Introduction Special Fund of Anhui Science and Technology University (No. ZRC2011304). The authors sincerely thank the anonymous reviewers for their constructive comments and helpful suggestions.

### REFERENCES

1. C.S. Lew, W.B. Mills, J.Y. Loh, *Hybrid Methods Eng.*, **1**, 19 (1999).
2. B.S. Mazumder, D.C. Dalal, *J. Comp. Appl. Math.*, **126**,: 185 (2000).
3. S. Hong, E.J. Won, H.J. Ju, Korea, *Marine Polln Bull.*, **60**,: 308 (2010).
4. P. Bossew, G. Kirchner, *J. Environ. Radioact.*, **73**, 127 (2004).
5. L. Ferragut, M.I. Asensio, J.M. Cascón, *Adv. Eng. Software*, **65**, 191 (2013).
6. L. Monte, *J. Environ. Radioact.*, **101**, 134 (2010).
7. M. Ehrhardt, R.E. Mickens, *Appl. Math. Comp.*, **219**, 6591 (2013).
8. R.K. Lin, T.W.H. Sheu, *J. Comp. Phys.*, **208**, 493 (2005).
9. L.E. Bittencourt Sampaio, *Computers & Fluids*. **67**, 87 (2012).
10. M. Remešíková, *Appl. Math. Comp.*, **184**, 116 (2007).
11. A. Rodríguez-Ferran, M.L. Sandoval, *Adv. Eng. Software*, **38**, 439 (2007).
12. S. Chandrasekhar, *Reviews Modern Physics*, **15**, 1 (1943).
13. Computational fluid dynamics in industrial

- combustion. CRC Press, 200.
14. J. Wang, N. Zabaras, *Int. J. Heat Mass Transfer*, **49**, 939 (2006).
  15. I. Lagzi, D. Kármán, T. Turányi, et al. *J. Environ. Radioact.*, **75**, 59 (2004).
  16. K. Roth, Soil Physics Lecture Notes. Institute of Soil Science (v3.2), University of Hohenheim, D-70593 Stuttgart, Germany, 1996.
  17. J.H. Seinfeld, Atmospheric chemistry and physics of air pollution. John Wiley and Sons, Inc.: 1986
  18. M. Jamil, H.J. Zepernick, Levy Flights and Global Optimization. In: Swarm Intelligence and Bio-Inspired Computation: Theory and Applications, London, 2013. Pp. 49-72.
  19. X.S. Yang, S. Deb, NaBIC 2009. World Congress on. IEEE. Pp. 210-214.
  20. D.N. Karamouzis, *Water Resources Manag.*, **6**, 35 (1992).
  21. A. Krefit, A. Zuber, *Chem. Eng. Sci.*, **33**, 1471 (1978).
  22. O.V. Konshin, *Health Physics*, **63**, 301 (1992).
  23. R.H. Velasco, M. Belli, U. Sansone, S. Menegon, *Health Physics*, **64**, 37 (1993).
  24. J.P. Toso, R.H. Velasco, *J. Environ. Radioact.*, **53**, 133 (2001).
  25. M.R. Raupach, B.J. Legg, *J. Fluid Mech.*, **136**, 111 (1983).
  26. P.J. Sullivan, H. Yip, *Math. Phys.* **38**, 409 (1987).
  27. B.M. Sumer, *J. Fluid Mech.*, **65**, 11 (1974).

## МОДЕЛИРАНЕ ПО МЕТОДА НА КРАЙНИТЕ РАЗЛИКИ НА КОНВЕКТИВНАТА ДИФУЗИЯ ПРИ РАЗСЕЙВАНЕТО НА ХИМИЧЕСКИ ЗАМЪРСИТЕЛИ В ИЗКУСТВЕН ВОДОЕМ

Де-Шенг Ли

Научен колеж, Университет за наука и технология "Ануи", Фенгианг 233100, Китай

Постъпила на 12 май, 2014 г.

(Резюме)

Разработен е математичен модел за описанието на дисперсията на химични замърсители в устието на изкуствен водоем, основан на конвективната дифузия. Разгледана е двумерната задача в област, ограничена до повърхността на канала. При тези предпоставки моделът се основава на уравнението за съхранение на масата с отчитане на конвективната и турбулентната дифузия. Съставени са и са анализирани гранични условия с помощта на неявна диференчна схема. Методът на крайните елементи е използван за да се получи числено решение на уравнението на конвективната дифузия и да се получат полетата на разпределение на концентрациите и на температурата. Успоредно с това е използван стохастичният метод на Lévy за определянето на коефициентите в дисперсионния тензор, който силно зависи от орографията на почвата, класа на стабилност, разстоянието от източника на замърсяване и повърхностната грапавина. Отчитайки разлагането на химическите вещества може да се открие времето и пространственото разпределение на моментен източник на замърсяване. Симулационните експерименти показват, че разпространението на замърсяването в устието на водоема зависи не само от скоростта на флуида, скоростта на разлагане, дисперсионния коефициент и началната концентрация, но и геометричната форма на устието.

Може да се заключи, че методът на крайните елементи е подходящ в случая на конвективна дифузия; той е точен и ефикасен в този клас проблеми на замърсяването.



## **ERRATUM**

Because of an error in the publishing procedure an acknowledgment in the article “Behaviour of eggshell membranes at tensile loading” by M.J. Strnková, Š. Nedomová, J. Trnka, J. Buchar and V. Kumbár, published in Bulgarian Chemical Communications (2014), Volume 46, Special issue B (pp. 44 – 48) is missing. It should be read as:

***Acknowledgement:** The authors would like to acknowledge the support of IP 17/2014 IGA MENDELU and of the Institute of Thermomechanics AS CR, v. v. i. of the Czech Academy of Sciences through institutional support No. RVO: 61388998.*



## BULGARIAN CHEMICAL COMMUNICATIONS

### Instructions about Preparation of Manuscripts

**General remarks:** Manuscripts are submitted in English by e-mail or by mail (in duplicate). The text must be typed double-spaced, on A4 format paper using Times New Roman font size 12, normal character spacing. The manuscript should not exceed 15 pages (about 3500 words), including photographs, tables, drawings, formulae, etc. Authors are requested to use margins of 3 cm on all sides. For mail submission hard copies, made by a clearly legible duplication process, are requested. Manuscripts should be subdivided into labelled sections, e.g. **Introduction, Experimental, Results and Discussion, etc.**

**The title page** comprises headline, author's names and affiliations, abstract and key words.

Attention is drawn to the following:

a) **The title** of the manuscript should reflect concisely the purpose and findings of the work. Abbreviations, symbols, chemical formulas, references and footnotes should be avoided. If indispensable, abbreviations and formulas should be given in parentheses immediately after the respective full form.

b) **The author's** first and middle name initials, and family name in full should be given, followed by the address (or addresses) of the contributing laboratory (laboratories). **The affiliation** of the author(s) should be listed in detail (no abbreviations!). The author to whom correspondence and/or inquiries should be sent should be indicated by asterisk (\*).

**The abstract** should be self-explanatory and intelligible without any references to the text and containing not more than 250 words. It should be followed by key words (not more than six).

**References** should be numbered sequentially in the order, in which they are cited in the text. The numbers in the text should be enclosed in brackets [2], [5, 6], [9–12], etc., set on the text line. References, typed with double spacing, are to be listed in numerical order on a separate sheet. All references are to be given in Latin letters. The names of the authors are given without inversion. Titles of journals must be abbreviated according to Chemical Abstracts and given in italics, the volume is typed in bold, the initial page is given and the year in parentheses. Attention is drawn to the following conventions:

a) The names of all authors of a certain publications should be given. The use of “*et al.*” in

the list of references is not acceptable.

b) Only the initials of the first and middle names should be given.

In the manuscripts, the reference to author(s) of cited works should be made without giving initials, e.g. “Bush and Smith [7] pioneered...”. If the reference carries the names of three or more authors it should be quoted as “Bush *et al.* [7]”, if Bush is the first author, or as “Bush and co-workers [7]”, if Bush is the senior author.

**Footnotes** should be reduced to a minimum. Each footnote should be typed double-spaced at the bottom of the page, on which its subject is first mentioned.

**Tables** are numbered with Arabic numerals on the left-hand top. Each table should be referred to in the text. Column headings should be as short as possible but they must define units unambiguously. The units are to be separated from the preceding symbols by a comma or brackets.

Note: The following format should be used when figures, equations, *etc.* are referred to the text (followed by the respective numbers): Fig., Eqns., Table, Scheme.

**Schemes and figures.** Each manuscript (hard copy) should contain or be accompanied by the respective illustrative material as well as by the respective figure captions in a separate file (sheet). As far as presentation of units is concerned, SI units are to be used. However, some non-SI units are also acceptable, such as °C, ml, l, etc.

The author(s) name(s), the title of the manuscript, the number of drawings, photographs, diagrams, etc., should be written in black pencil on the back of the illustrative material (hard copies) in accordance with the list enclosed. Avoid using more than 6 (12 for reviews, respectively) figures in the manuscript. Since most of the illustrative materials are to be presented as 8-cm wide pictures, attention should be paid that all axis titles, numerals, legend(s) and texts are legible.

The authors are asked to submit **the final text** (after the manuscript has been accepted for publication) in electronic form either by e-mail or mail on a 3.5” diskette (CD) using a PC Word-processor. The main text, list of references, tables and figure captions should be saved in separate files (as \*.rtf or \*.doc) with clearly identifiable file names. It is essential that the name and version of

the word-processing program and the format of the text files is clearly indicated. It is recommended that the pictures are presented in \*.tif, \*.jpg, \*.cdr or \*.bmp format, the equations are written using "Equation Editor" and chemical reaction schemes are written using ISIS Draw or ChemDraw programme.

The authors are required to submit the final text with a list of three individuals and their e-mail addresses that can be considered by the Editors as potential reviewers. Please, note that the reviewers should be outside the authors' own institution or organization. The Editorial Board of the journal is not obliged to accept these proposals.

## EXAMPLES FOR PRESENTATION OF REFERENCES

### REFERENCES

1. D. S. Newsome, *Catal. Rev.–Sci. Eng.*, **21**, 275 (1980).
2. C.-H. Lin, C.-Y. Hsu, *J. Chem. Soc. Chem. Commun.*, 1479 (1992).
3. R. G. Parr, W. Yang, *Density Functional Theory of Atoms and Molecules*, Oxford Univ. Press, New York, 1989.
4. V. Ponec, G. C. Bond, *Catalysis by Metals and Alloys* (Stud. Surf. Sci. Catal., vol. 95), Elsevier, Amsterdam, 1995.
5. G. Kadinov, S. Todorova, A. Palazov, in: *New Frontiers in Catalysis* (Proc. 10th Int. Congr. Catal., Budapest, 1992), L. Guzzi, F. Solymosi, P. Tetenyi (eds.), Akademiai Kiado, Budapest, 1993, Part C, p. 2817.
6. G. L. C. Maire, F. Garin, in: *Catalysis. Science and Technology*, J. R. Anderson, M. Boudart (eds), vol. 6, Springer-Verlag, Berlin, 1984, p. 161.
7. D. Pocknell, *GB Patent 2 207 355* (1949).
8. G. Angelov, PhD Thesis, UCTM, Sofia, 2001.
9. JCPDS International Center for Diffraction Data, Power Diffraction File, Swarthmore, PA, 1991.
10. *CA* **127**, 184 762q (1998).
11. P. Hou, H. Wise, *J. Catal.*, in press.
12. M. Sinev, private communication.
13. <http://www.chemweb.com/alchem/articles/1051611477211.html>.

## CONTENTS

Academician Panayot R. Bontchev - In memoriam .....	745
S. Hina, M. I. Rajoka, P.B. Savage, S. Roohi, T. H.Bokhari, Labeling, quality control and biological evaluation of <sup>99m</sup> Tc-vibramycin for infection sites imaging .....	747
Chr. B. Boyadjiev, M. D. Doichinova, B. Chr. Boyadjiev, Some problems in the column apparatuses modeling...	755
N. Dr. Dermendzhieva, E. N. Razkazova-Velkova, V. N. Beschkov, Kinetics of oxidation of sulfide ions in model solutions of sea water .....	766
H. Yilmaz, Analysis in terms of environmental awareness of farmers' decisions and attitudes in pesticide use: the case of Turkey .....	771
K. Ignatova, Effect of H <sub>3</sub> BO <sub>3</sub> and Na <sub>3</sub> citrate on the conditions of electrodeposition of Ni-Co alloy from citrate electrolyte .....	776
Ž. Šmelcerović, M. Rangelov, E. Cherneva, G. Kocić, S. Stojanović, T. Jevtović-Stoimenov, Ž. Petronijević, D. Yancheva, Inhibition mechanism and molecular modeling studies of the interactions of 6-(propan-2-yl)-3-methyl-morpholine-2,5-dione with xanthine oxidase .....	783
V. N. Hubenov, S. N. Mihaylova, I. S. Simeonov, Anaerobic co-digestion of waste fruits and vegetables and swine manure in a pilot-scale bioreactor .....	788
D. B. Dzhonova-Atanasova, Sv. Ts. Nakov, E. N. Razkazova-Velkova, N. N. Kolev, Pressure drop of highly efficient Raschig Super-Ring packing for column apparatuses .....	793
A. Jouyban, M. Khoubnasabjafari, F. Martinez, A model to predict the solubility of drugs in ethanol + propylene glycol mixtures at various temperatures .....	800
H. Alinezhad, K. Nemati, M. Zare, Efficient one-pot room-temperature synthesis of 2-imidazolines from aldehydes .....	804
M. Momayezan, M. Ghashang, S. A. Hassanzadeh-Tabrizi, Barium aluminate nano-spheres grown on the surface of BaAl <sub>2</sub> O <sub>4</sub> : a versatile catalyst for the Knoevenagel condensation reaction of malononitrile with benzaldehyde .....	809
S. Gutzov, P. Stoyanova, K. Balashev, N. Danchova, S. Stoyanov, Preparation and optical properties of colloidal europium(III) diphenanthroline nitrate hydrate .....	816
Y. V. Hubenova, M. Y. Mitov, Application of cyclic voltammetry for determination of the mitochondrial redox activity during subcellular fractionation of yeast cultivated as biocatalysts .....	821
M. Y. Mitov, E. Y. Chorbadzhiyska, L. Nalbandian, Y. V. Hubenova, Synthesis and characterization of dip-coated CoB-, NiB- and CoNiB-carbon felt catalysts .....	825
F. Sheikholeslami-Farahani, A. S. Shahvelayati, Solvent-free one-pot synthesis of highly functionalized benzothiazolodiamides via Ugi four-component reaction .....	830
N. S. Dighe, P. S. Shinde, S. B. Vikhe, S. B. Dighe, D. S. Musmade, QSAR study, synthesis and anti-depressant studies of some novel schiff base derivatives of benzothiazepine .....	837
A. A. Kaya, Synthesis, characterization and thermal behaviour of novel phthalocyanines bearing chalcone groups on peripheral positions .....	844
B. Eren, Y. Yalcin Gurkan, Analysis of the reaction kinetics of aminotoluene molecule through DFT method .....	849
D. Uzun, E. Razkazova-Velkova, K. Petrov, V. Beschkov, Electrochemical method for energy production from hydrogen sulfide in the Black sea waters in sulfide-driven fuel cell .....	859
D. Uzun, E. Razkazova-Velkova, V. Beschkov, G. Pchelarov, K. Petrov, Electrochemical reduction of sulfur dioxide by oxidation of hydrogen sulfide in aqueous media .....	867
M. Veylaki, M. J. Nikmehr, Some degree based connectivity indices of nano-structures .....	872
R. T. Georgieva-Nikolova, P. A. Gateva, R. K. Hadjiolova, M. P. Slavova, M. M. Nikolova, V. D. Simeonov, Multivariate statistical assessment of obesity patients' clinical parameters .....	876
G. Q. Liu, Morphology and thermal behaviour of poly(methyl methacrylate) /poly(ethylene glycol) /multi-walled carbon nanotubes nanocomposites .....	889
M. G. Abd El-Wahed, S. M. El-Megharbel, M. Y. El-Sayed, Y. M. Zahran, M. S. Refat, Synthesis and characterization of some lanthanide metal complexes Ce(III), Gd(III), Nd(III), Tb(III) and Er(III) with sulfasalazine as sulfa drug .....	895
Feng Jin, He Yong-ling, Adaptive mutation particle swarm optimized BP neural network in state-of-charge estimation of Li-ion battery for electric vehicles .....	904
Li Xinhua, Sun Zhigao, Guo Honghai, Zhu Zhenlin, The annual emissions of sulfur gases from different tidal flats in the Yellow River Delta, China .....	913
Yanna Lv, Beihai He, Yali Wu, Influence of fumed silica on the properties of cushion packaging materials based on bagasse pith and bisulfite spent liquor .....	920
Wang Qiang, Synthesis of Cu <sub>2</sub> O nanocrystals and their agricultural application .....	929
Weiwei Zhang, Yan Shi: Adsorption kinetics of phosphate from aqueous solutions by waste iron sludge .....	937
Wang Xin, Liu Lifeng, Lun Zengmin, Lv Chengyuan, Determination of CO <sub>2</sub> /crude oil system interfacial tension and dynamic interfacial tension by ADSA method .....	945
	963

<i>De-Sheng Li</i> , Convection-diffusion modelling for chemical pollutant dispersion in the joint of artificial lake using finite element method .....	949
<i>ERRATUM</i> .....	959
<i>INSTRUCTIONS TO THE AUTHORS</i> .....	961

## СЪДЪРЖАНИЕ

<i>С. Хина, М. И. Раджока, П. Б. Саваж, С. Рухи, Т.Х. Бокхари</i> , Белязане, качествен контрол и биологична оценка на 99mTc-вибрамицин за определяне на инфектирани зони .....	754
<i>Хр. Б. Бояджиев, М. Д. Дойчинова, Б. Хр. Бояджиев</i> , Проблеми при моделиране на колонни апарати.....	765
<i>Н. Др. Дерменджиева, Ел. Н. Разказова – Велкова, В. Н. Бешков</i> , Кинетика на окислението на сулфидни йони от моделни разтвори на морска вода .....	770
<i>Х. Йилмаз</i> , Анализ на екологично съобразените ерешения на фермерите в турция за употребата на пестициди .....	775
<i>К. Игнатова</i> , Ефект на $H_3BO_3$ и $Na_3$ цитрат върху условията на електролитно отлагане на Ni-Co сплави от цитратен електролит .....	782
<i>Ж. Шмелцерович, М. Рангелов, Е. Чернева, Г. Коцич, С. Стоянович, Т. Йевтович-Стоименов, Ж. Петрониевич, Д. Янчева</i> , Механизми на инхибиране и молекулно моделиране на на взаимодействията на 6-(пропан-2-ил)-3-метил-морфолин-2,5-дион с ксантин оксидаза .....	787
<i>В. Н. Хубенов, С. Н. Михайлова, И. С. Симеонов</i> , Анаеробна биодеградация на смеси от отпадни плодове и зеленчуци и свински тор в пилотен биореактор .....	792
<i>Д. Б. Джонова-Атанасова, Св. Ц. Наков, Е. Н. Разказова-Велкова, Н. Н. Колев</i> , Хидравлично съпротивление на високоефективния пълнеж Raschig Super-Ring за колонни апарати .....	799
<i>А. Джуйбан, М. Хубнасабджафари, Ф. Мартинез</i> , Модел за предсказване на разтворимостта на лекарства в смеси от етанол и пропилен-гликол при различни температури .....	803
<i>Х. Алинежад, К. Немати, М. Заре</i> , Ефективна едностадийна синтеза при стайна температура на 2-имидазолини от алдехиди .....	808
<i>М. Момаезян, М. Гашанг, С.А. Хасанзаде-Табризи</i> , Наносфери от бариев алуминат, израстнали на повърхността на $BaAl_2O_4$ : общо приложим катализатор за кондензацията по Knoevenagel на малонитрол с бензалдехид .....	815
<i>С. Гуцов, П. Стоянова, К. Балашев, Н. Данчова, С. Стоянов</i> , Приготвяне и оптични свойства на колоиден европиев (III) нитрат дифенантролин хидрат .....	820
<i>Й. В. Хубенова, М. Й. Митов</i> , Приложение на цикличната волтаперометрия за определяне на митохондриална редокс активност по време на вътреклетъчно фракциониране на дрожди култивирани като биокатализатори .....	824
<i>М. Й. Митов, Е. Й. Чорбаджийска, Л. Налбандиан, Й. В. Хубенова</i> , синтез и охарактеризиране на CoV-, NiV- и CoNiV- катализатори отложени върху въглеродно кече .....	829
<i>Ф. Шейхолеслами-Фарахани, А.С. Шахвеляти</i> , Едностадийна синтеза на високо-функционални бензотиазол-диамиди без разтворител чрез четири-компонентна реакция на Ugi .....	836
<i>Н. С. Дигхе, П. С. Шинде, С. Б. Викхе, С. Б. Дикхе, Д. С. Мусмаде</i> , QSAR-изследване, синтеза и анти-депресантно изследване на някои нови производни на schiff'ови бази с бензотиазепин .....	843
<i>А. А. Кая</i> , Синтеза, характеризирани и термично поведение на нови фталоцианини, носещи халконовата групи на периферни позиции .....	848
<i>Б. Ерэн, И. Ялчин Гуркан</i> , Анализ на реакционната кинетика на молекулата на аминотолуен чрез DFT-метода .....	858
<i>Д. Узун, Е. Разказова-Велкова, К. Петров; В. Бешков</i> , Електрохимичен метод за получаване на енергия от сероводорода на черноморските води в горивен елемент, задвижван със сулфид .....	866
<i>Д. Узун, Е. Разказова-Велкова, В. Бешков, Г. Пчеларов, К. Петров</i> , Електрохимична редукция на серен диоксид чрез окисление на сероводород във водна среда .....	871
<i>М. Вейлаки, М. Дж. Никмер</i> , Някои степенно базирани индекси на свързване на наноструктури .....	875
<i>Р. Т. Георгиева-Николова, П. А. Гатева, Р. К. Хаджийолова, М. П. Славова, М. М. Николова, В. Д. Симеонов</i> , Многовариационна статистическа оценка на клинични параметри на пациенти със затлъстяване .....	888
<i>Г. К. Лю</i> , Морфология и термични отнасяния на нанокompозити от поли(метил-метакрилат/поли(етилен-гликол) с многостенни въглеродни нанотръби .....	894
<i>М. Г. Абд Ел-Уахед, С. М. Ел-Мегарбел, М. И. Ел-Сайед, Я. М. Захран, М. С. Рефат</i> , Синтеза и охарактеризиране на някои комплекси на лантанидите Ce(III), Gd(III), Nd(III), Tb(III) и Er(III) със сулфасалазин като сулфа-лекарства .....	903
<i>Фенг Джин, Хе Йонг-линг</i> , Оценка на зареждането на литиево-йонни батерии с помощта на адаптивна мутация и оптимизационен алгоритъм с рояк на частици при невронни мрежи с обратно разпространение .....	912
<i>Ли Ксинхуа, Сунн Жигао, Гуо Хонгхай, Жу Женлин</i> , Годишни емисии от сярна-съдържащи газове в приливните плитчини в делтата на Жълтата река, Китай. ....	919
<i>Янна Льв, Бейхай Хе, Яли У</i> , Влияние на опушен силициев диоксид върху свойствата на меки опаковъчни материали на основата на сърцевина от багаса и бисулфитна отпадъчна луга .....	928
<i>Ванг Куанг</i> , Синтез на нанокристали от $Cu_2O$ и тяхното приложение в земеделието .....	936
	965

<i>Уеуей Жанг, Ян Ши, Кинетика на адсорбцията на фосфати от водни разтвори върху отпадъчна желязна тиня .....</i>	944
<i>Ванг Ксин, Лю Лифенг, Лун Зенгмин, Лв Ченгян, Определяне на равновесното и динамичното междуфазно напрежение на системата въглероден диоксид/петрол по adsa- метода .....</i>	948
<i>Де-Шенг Ли, Моделиране по метода на крайните разлики на конвективната дифузия при разсейването на химически замърсители в изкуствен водоем .....</i>	958
<i>ИНСТРУКЦИЯ ЗА АВТОРИТЕ .....</i>	961